P-T history and $^{40}Ar/^{39}Ar$ dating of the Jinshuikou group, Eastern Kunlun Mountains, Qinghai, China

C.J.C. Bontje

Master research project & thesis
Student number: 1822411
Supervisors: J.R. Wijbrans & F.M. Brouwer
May 2015

VU University
Amsterdam

Front page: Field area at sample location 5, close to the village of Jinshuikou.

Abstract

The Kunlun Mountains, located along the northern margin of the Tibetan Plateau in Qinghai, Western China play an important role in the collision history between Eurasia and India. However, not much research has been done on both metamorphic P-T conditions and geochronology. A combined P-T modelling and $^{40}Ar/^{39}Ar$ dating study on the Jinshuikou group in the Kunlun Mountains revealed a metamorphic event of Silurian – Devonian age. Peak conditions of amphibolite to granulite facies of 750°C, 13 kbar and 800°C, 10 kbar are at higher pressure and lower temperature conditions than previously found by Liu et al. (2005). Dating of hornblende, biotite, muscovite and K-feldspar of metamorphic and intrusive rocks from the Jinshuikou group revealed four age groups: 1) 450.27 ± 22.60 Ma till 403.25 ± 17.89 Ma; 2) 353.40 ± 14.62 Ma till 263.43 ± 9.97 Ma; 3) 252.58 ± 8.87 Ma till 199.86 ± 43.37 Ma and 4) 215.11 ± 5.48 Ma till 184.26 ± 7.52 Ma. These groups all correspond to important accretion phases of microcontinents to the Eurasian continent with corresponding magmatic events. Ages found display cooling rather than forming ages and are (partially) reset by new pulses of magmatic intrusions.

By combining P-T modelling with the thermal history based on argon dates from this study and U-Pb zircon and AHe ages from literature, initial cooling rates of 10 – 14°C/Ma between 430 and 400 Ma were found, decreasing exponentially to 2.0°C/Ma between 400 and 300 Ma. Reheating of sample locations 1 and 5 by Permian – Triassic intrusions caused another phase of exponential cooling, followed by a fluctuation around 250°C due to several phases of granitic intrusions. A paleo geothermal gradient of 50°C/km between peak metamorphism and present is assigned to the Jinshuikou group, which implies a denudation rate of 0.1 km/Ma and total unroofing of 40 km.

Table of contents

1. Introduction

The Kunlun Mountains, located along the northern margin of the Tibetan Plateau in Qinghai, Western China, play an important role in the collision history between Eurasia and India. However, not much research has been done on both metamorphic P-T conditions and geochronology. By investigating the metamorphic grade and internal variations therein, combined with timing of metamorphism by $^{40}Ar/^{39}Ar$ dating of selected samples from the Jinshuikou group in the Kunlun Mountains, we hope to improve the understanding of its tectonic history.

This research is a collaboration between VU University Amsterdam and China University of Geosciences Wuhan. A fieldwork for a period of one week was carried out in the Kunlun Mountains in July 2012. During this fieldwork gneisses, amphibolites and granites (both syn- and post metamorphic) were sampled at five locations along a transect in the Jinshuikou group. The transect was orientated along the strike of the mountain belt over a distance of approximately 430 km.

1.1. Background

The Kunlun Mountains were accreted against the southern margin of Eurasia as one of a series of microcontinents and island-arcs positioned in the Tethys ocean during the Paleozoic and Mesozoic (Dewey et al., 1988; Xiao et al., 2003; Yin and Nie, 1996; Zhiqin et al., 1997). The final collision event in this series is the Indo-Asian collision during the Cenozoic, which started between 70-34 Ma (Aitchison et al., 2007; Mo et al., 2008; Royden et al., 2008; Zhu et al., 2005). Evidence for accretion towards the Eurasian continent is clear as deformation in each subsequent unit becomes younger southwards across the plateau (Dewey et al., 1988).

From recent studies it appears that the convergence of the Kunlun Mountains lasted at least from Early Paleozoic up to Cenozoic (Liu et al., 2005; Mock et al., 1999). From this long lasting sequence of orogenetic phases, four age groups of different tectonic events in the Kunlun Mountains were identified by Liu et al. (2005) and Arnaud et al. (2003), of which at least two could be ascribed to distinct metamorphic events of granulite and amphibolite facies of Middle Silurian - Late Devonian and Triassic age. This was followed by magmatic intrusions and partial overprinting of earlier fabrics. The third age group of Middle Jurassic – Lower Cretaceous age represents a sinistral deformation regime as strike-slip structures in mylonites. The last age group represents late-stage exhumation during the Himalayan orogenesis of Oligocene age.

1.2. Project aim

This project aims to investigate the tectonic history of the Kunlun Mountains and more specifically the Jinshuikou group. This will be done by thermodynamic modelling of samples collected on a west-east transect along the eastern Kunlun Mountains, using the computer program Perple_X (Connolly, 2005). $^{40}Ar/^{39}Ar$ dating of these samples will hopefully give an idea of the timing of different events. Combining these results, P-T-t paths for different locations in the Kunlun Mountains can be resolved, providing information on the tectonic history and ultimately differences therein for different parts of the Kunlun Mountains.

In chapter 2, an overview of the geological setting will be given, followed by the research methodology in chapter 3. Then, results of the $^{40}Ar/^{39}Ar$ dating will be shown in chapter 5, and of the thermodynamic modelling in the program Perple_X (Connolly, 2005) in chapter 6, followed by the discussion and conclusions in chapters 7 and 8 respectively.

2. Geological setting

The study area is located in the eastern Kunlun Mountains, on the north-eastern edge of the Tibetan plateau. The Kunlun Mountains are part of the Himalayan-Tibetan orogen, which is in turn part of the Himalayan-Alpine system and stretches from Spain in the west, to Indonesia in the east (Yin and Harrison, 2000). During the Palaeozoic to Mesozoic, subsequent accretion of microcontinents to the southern margin of the Eurasian continent formed the orogen (Yin and Nie, 1996). These continents include amongst others the North- and South Tarim block, North- and South China block, Qaidam block, Qiangtang block and Lhasa block. A short reconstruction of the plate configuration and formation of the Himalayan-Tibetan orogen after (Yin and Nie, 1996) will be given. The simplified tectonic model is shown in Figure 1. In this figure, the future Kunlun Mountains and Altyn Tagh fault are indicated.

During the Silurian to mid-Devonian, the South Tarim and Qaidam block moved northward, causing subduction of a small paleo-ocean underneath the North Tarim and North China block and subsequent collision (Dai et al., 2013) (Figure 1A). Evidence for this accretion and subduction is found in widespread Silurian and Early-Devonian granites across the Eastern Kunlun range (Figure 2) and hornblende, muscovite and biotite $^{40}Ar/^{39}Ar$ ages (Chen et al., 2002; Liu et al., 2005). This was followed by subduction of this group underneath the Siberia-Kazakhstan plate during the Devonian (Figure 1B). During the Carboniferous – Permian the South China block started to subduct underneath the North China-Qaidam plate and a magmatic arc formed along the southern margin of the Qaidam block, where in the future the Kunlun Mountains will be (Figure 1C). In the Late Permian, collision of the South China block with the North China-Qaidam plate started, propagating from east to west. Widespread granitoids from this period can be found (Dai et al., 2013) (Figure 2). Simultaneous subduction of the Paleo-Tethys occurred both northward and southward (Dai et al., 2013; Yin and Nie, 1996). Due to this collision, earlier suture zones were reactivated as strike-slip faults and the Qaidam block was pushed to the west during the Triassic (Figure 1D). During the late-Triassic to Cretaceous, subsequently the Qiangtang and Lhasa block (also called Gangdise terrain) were attached, forming the later so called Qinghai-Tibet plateau (Figure 1E). The timing of these events is strengthened by occurrence of Late Triassic and Early Jurassic granitoids (Dai et al., 2013) and an age group of 104-172 Ma which may be related to ductile deformation along the Xidatan fault due to the northward accretion of the Lhasa block (Liu et al., 2005). During the Paleogene, the India-Asia collision began, propagating from west to east. Ongoing compression resulted in the formation of thrusts and folds in the Qiangtang block, south of the Kunlun Mountains. In the Cenozoic, activation of the Altyn Tagh and Kunlun sinistral strike-slip faults north of the Qinghai-Tibet plateau, led to eastward extrusion of the plateau (Dewey et al., 1988) and to separation of the Kunlun Mountains into the western- and eastern Kunlun (Figure 1F).

Today, the Kunlun Mountains separate the Qinghai-Tibet plateau from the Qaidam and Tarim block in the north (Roger et al., 2003), which are on its turn separated by the Altyn Tagh sinistral strike-slip fault. The Kunlun mountain range follows the sinistral Kunlun fault (Van der Woerd et al., 2000) and stretches east for 2000 km into the Qilian and Qinling Mountains (Mattauer et al., 1985). Both the Qaidam and the Tarim block are rigid regions that resisted deformation. Therefore it is probable that deformation was strongly focused in the Kunlun and Altyn Tagh faults (Dewey et al., 1988).

The geology of the eastern Kunlun Mountains is dominated by a broad Palaeozoic arc with a superposed Late Permian – Triassic arc, together referred to as the Kunlun batholith (Yin and Harrison, 2000) (Figure 2). The western part of this batholith consists of Middle to Late Proterozoic gneiss, schist and marble, overlain by marine deposits (Yin and Harrison, 2000). Dating of gneissic basement rocks near the Golmud-Lhasa highway with the Rb-Sr method gave an age of 1846 ± 109 Ma (Zhang and Zheng, 1994) in (Yin and Harrison, 2000). Protoliths of both the metamorphic and granitic sequences in

the Jinshuikou group were dated between 1339 Ma and 2468 ± 46 Ma (Ba et al., 2012; Liu et al., 2005; Long et al., 2006; Yu et al., 2005; Zhang et al., 2003). Extensive granitic intrusions in the Eastern Kunlun batholith give predominantly ages of 290-190 Ma (Dai et al., 2013; Harris et al., 1988; Li et al., 2013; Liu et al., 2005; Mock et al., 1999). According to Yin and Harrison (2000), the local volcanic deposits together with large amounts of submarine strata, suggest that the eastern Kunlun Mountains experienced a rifting event in the Early Permian. Subsequent, northward subduction of the Songpan-Ganzi-Hoh Xil terrain beneath the Kunlun batholith led to volcanic eruptions and intrusion of granites forming the superposed arc. Alternatively, the superposed arc could be related to southward subduction of the Qilian terrain north of the Qaidam block (Yin and Harrison, 2000).

The eastern Kunlun orogen can be subdivided into three different tectonic units, namely the Northern, Middle and Southern Zone. These are separated by respectively the North- and Central Kunlun fault (Liu et al., 2005; Zhang et al., 2012). The Southern Zone is bounded to the south by the South Kunlun fault. The northern zone is an Early Paleozoic fold belt, containing Ordovician marine sediments and low-grade metamorphic rocks (Liu et al., 2005). The Middle Zone mainly consists of Middle to Late Proterozoic metamorphic sequences overlain by Devonian and Carboniferous rocks and Paleozoic and Mesozoic granitic intrusions (Liu et al., 2005; Zhang et al., 2012). The Southern Zone is similar to the Middle Zone, but contains more Triassic successions (Liu et al., 2005). The metamorphic sequences in the Middle Zone can be divided into the Binggou formation, the Xiaomiao formation and the Baishahe formation (Zhang et al., 2012), of which the Baishahe and Xiaomiao formations together constitute the Jinshuikou Group (Zhang et al., 2012). The Binggou formation contains marbles, slates and meta-sandstones. The Baishahe formation consists of gneisses and marbles, with minor amounts of amphibolites, migmatites and schists. Their protoliths were greywackes, limestones and intermediate to basic volcanic rocks. The Xiaomiao formation consists of granulites, schists and minor amounts of marbles. Their protoliths were likely a suite of volcanic-sedimentary rocks that underwent low amphibolite-facies metamorphism.

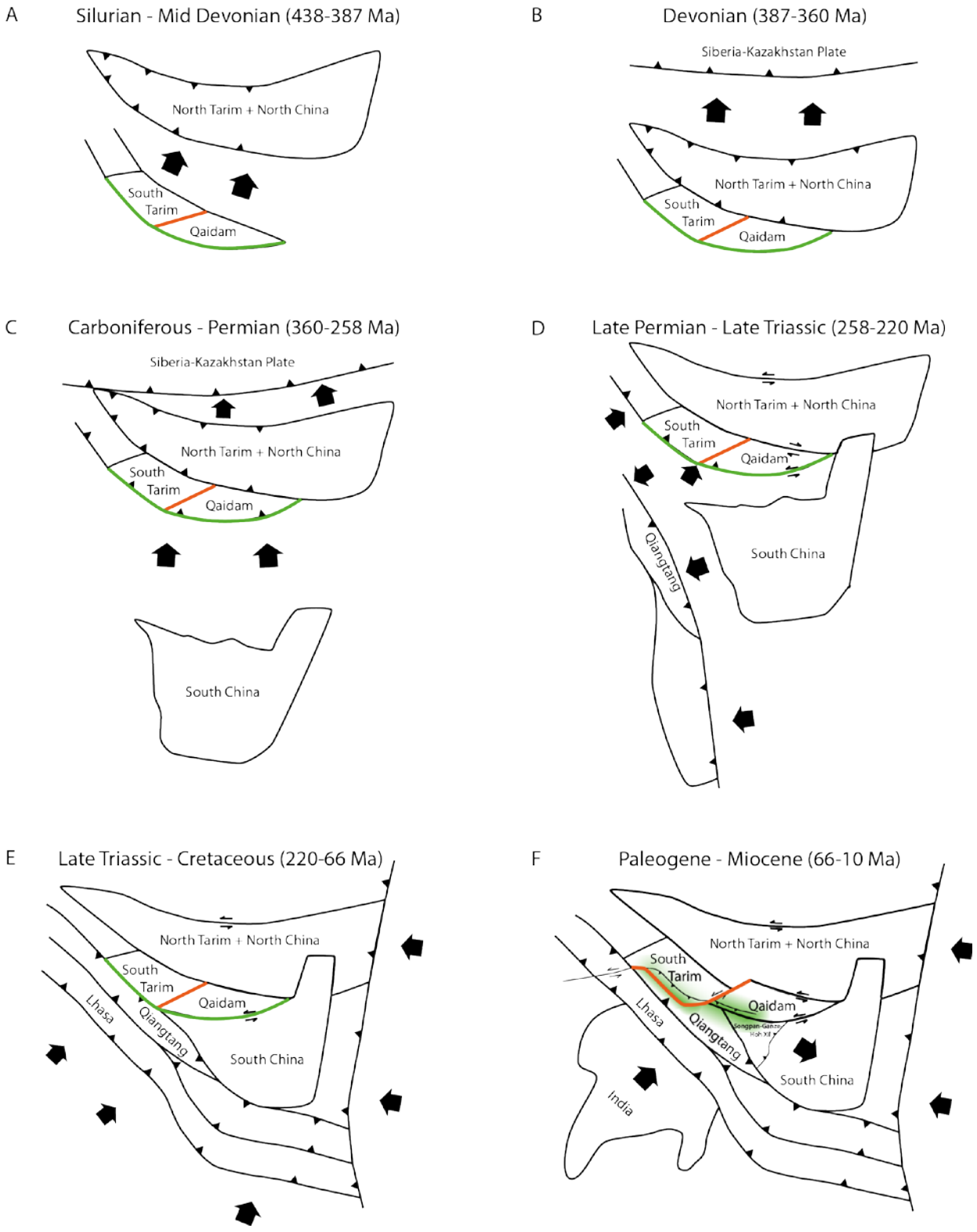

Figure 1. Simplified tectonic history of the Himalayan-Tibetan orogen. Green in figures A-E indicates future Kunlun mountains; orange indicates future Altyn Tagh fault. Figure F shows the Kunlun thrust system in green and the Altyn Tagh fault in orange. Modified after (Yin and Nie, 1996).

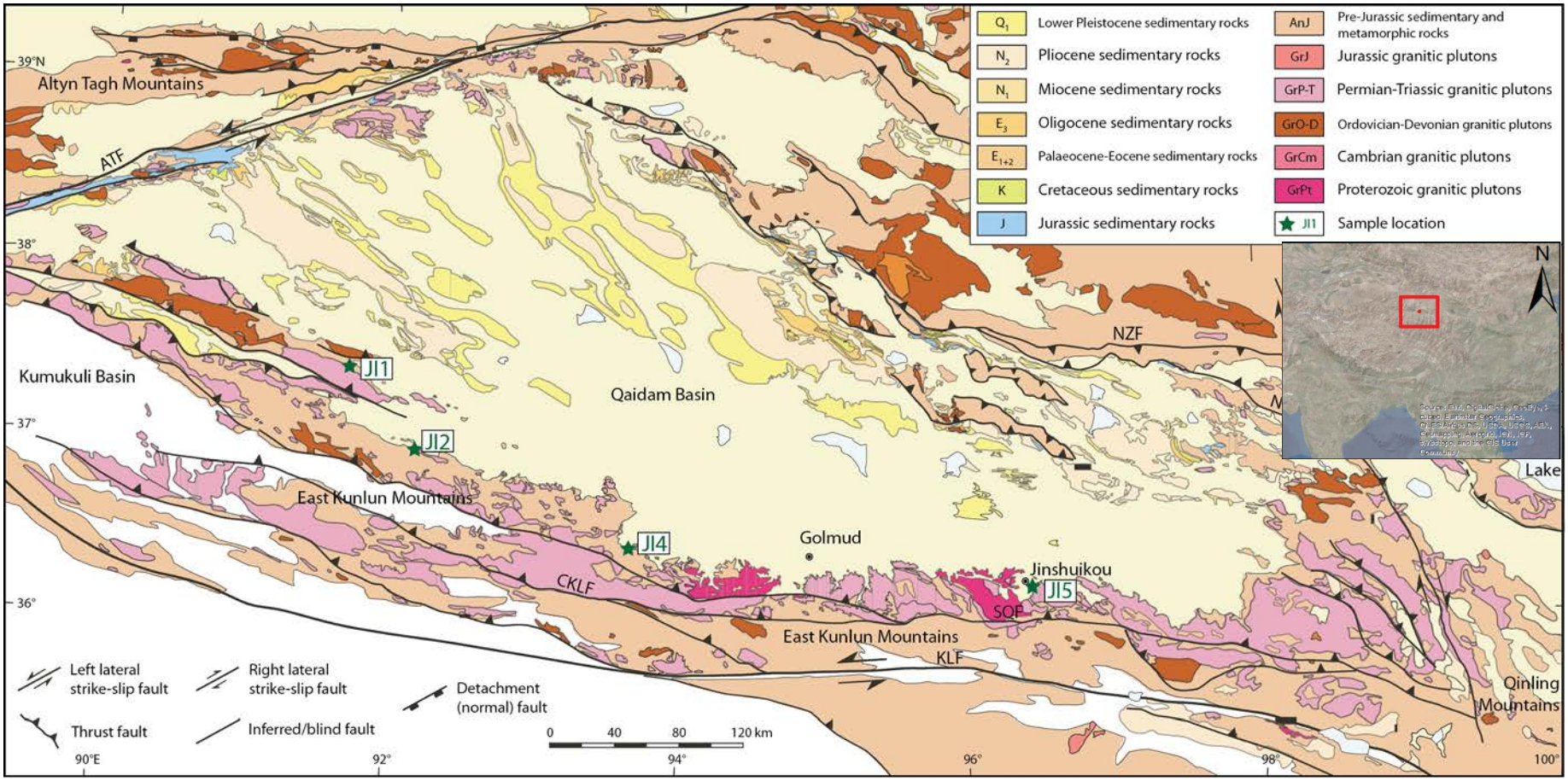

Figure 2. Geological map of the Eastern Kunlun Mountains and surroundings. Sample locations are indicated with a green star. Explanation of abbreviations: ATF = Altyn Tagh Fault, NZF = North Zongwulongshan Fault, NQF = North Qaidam Fault, CKLF = Central Kunlun Fault, SQF = South Qaidam Fault, KLF = Kunlun Fault. Modified after Chen et al. (2012)

3. Methodology

In this chapter the used methodology for this research is described. First a fieldwork was carried out where samples were gathered. Depending on the state of alteration and on the mineralogy, samples were selected for thermodynamic modelling and for argon dating. In the following paragraphs, procedures for these measurements are described.

3.1. Fieldwork and sample selection

Fieldwork was carried out in the summer of 2012, between July 18 and 24. Within the Jinshuikou group, sixteen samples were collected along a transect parallel to the strike of the Kunlun Mountains, running from 290 km west to 130 km east of the city of Geermu (Golmud), in the Qinghai province, Western China (Figure 2). Samples from amphibolites and gneisses were used for both thermodynamical modelling and argon dating. For argon dating also granites that intruded these rocks were sampled. Also quartz lenses were sampled for fluid inclusion analysis (this would be in the context of a future study). Due to limited time in the field, the main purpose of the fieldwork was to collect samples rather than doing a structural analysis.

Thin sections were produced of all samples to identify minerals and alteration using optical microscopy. From the metamorphosed samples, the ones with minor alteration were chosen for thermobarometry and equally divided between this project and the project of Huijgen (2015). Most samples were processed for mineral separation for argon dating as almost all samples contained (minor amounts of) either K-feldspar, amphibole, biotite or white mica. A list of the samples including rock type and type of analyses can be found in Table 1.

Sample	Rocktype	Thermodynamic modelling	Argon dating
JI-1-1	Amphibolite	X	X
JI-1-3	Biotite Gneiss	X	X
JI-1-4	Amphibolite gneiss	X	X
JI-2-1	Garnet amphibolite	X	
JI-2-2	Biotite gneiss	X	X
JI-4-2	Biotite Gneiss	X	X
JI-4-3	Amphibolite	X	X
JI-4-5	Mylonite		X
JI-4-6	Garnet amphibolite	X	
JI-4-7	Granite	X	X
JI-5-1	Granite with garnet		X
JI-5-2	Granite with Cr micas		X
JI-5-3	Hornblende hornfels	X	X
JI-5-4	Mafic intrusion		
JI-5-5	Gabbro		X
JI-5-7	Late post tectonic granite	X	X

Table 1. Samples and rock types used in this study. Thermodynamic modelling samples indicated in yellow are analysed in this study; samples in green are analysed in the study of Huijgen (2015); pink samples are used in both studies.

3.2. Thermobarometry

For thermobarometry, both whole rock major element analyses, and single crystal in situ major element spot analyses are needed. Therefore, Li-tetraborate glass beads were produced from whole rock powders in order to perform XRF (X-ray fluorescence) measurements and thin sections were used for electron microprobe measurements (EMP) on selected near surface locations in single crystals. The obtained data was used to derive a P-T model with the program Perple_X (Connolly, 2005). This methodology is described in more detail below.

3.2.1. XRF measurements

Whole rock XRF analysis of major elements will provide vital knowledge on the composition of the rocks. In this section the procedure of preparation of the samples for XRF measurements and execution of the measurements is described.

3.2.1.1. Preparation

Samples were crushed by a jaw crusher up to a particle size of <1 cm. Approximately 100 g of this crushed material was used for XRF preparations; the rest was used for mineral separation for argon dating. 100 g of the material was put in an agate mill for one minute, grinding the sample to a silt grain size. By using a planetary mill with agate pots for one hour this grain size was reduced further to clay size.

The clay sized material was dried in an oven at 100°C for one day. Subsequently, 1.2000 g of this material was further heated at 1000°C for 30 minutes to remove all volatiles and eventually remove organic material and carbonate. The difference in weight before and after heating to 1000°C will determine the Loss On Ignition (LOI), which is a measure for the OH and CO_3 content. Then 1.0000 g of ignited powder was mixed with 4.0000 g of spectroflux 110 (lithium tetraborate : lithium metaborate in a 66.5 : 33.5 wt% ratio). The mixed powder was put in a platinum cup, heated to 1150°C in the Perl'X 3 machine and poured out into a platinum disk, creating a flat, glass bead with dimensions of approximately 4 cm diameter and 4 mm thick.

3.2.1.2. Measurements

XRF measurements on the beads were carried out with the PANalytical MagiX Pro, based at the VU University Amsterdam. The following major element oxides were measured: Fe_2O_3 + FeO (total Fe listed as Fe_2O_3) , MnO, TiO_2, CaO, K_2O, P_2O_5, SiO_2, Al_2O_3, MgO, Na_2O and BaO.
Table 2 shows the accuracy of the measurements as measured on andesite standard AGV-1 P4925 that was co-processed with the project.

	Fe_2O_3	MnO	TiO_2	CaO	K_2O	P_2O_5	SiO_2	Al_2O_3	MgO	Na_2O	BaO
Delta (%)	-0,1	4,5	-0,1	0,7	1,4	-0,2	1,3	0,6	-4,8	0,2	-1,3
Average (N=51)	6,76	0,096	1,049	4,973	2,960	0,499	59,624	17,248	1,457	4,267	0,136
Recommended value	6,77	0,092	1,05	4,94	2,92	0,5	58,84	17,15	1,53	4,26	0,137

Table 2. Accuracy of the major element oxides as measured on laboratory standard AGV-1 P4925 using the PANalytical MagiX Pro XRF spectrometer at the VU university Amsterdam.

3.2.2. Electron microprobe measurements for thermobarometry

The same rock samples as used for XRF measurements were used for electron microprobe measurements (EMP). Polished thin sections of these samples were coated with a conductive carbon layer. Per thin section, five to six locations were indicated for measurements. Locations were chosen such that the same type of different minerals in coherence with each other and possibly containing zonation could be measured in each location.
Measurements were carried out on the JEOL JXA 8800M at the VU University. An acceleration voltage of the primary electron beam was 15 kV, beam current was 20 nA and a beam diameter of 5 µm were used. As different kind of minerals were measured in each location, it was not possible to defocus the beam for measurements of Na and K. Calibration was done against natural standards as listed in Table 3. A ZAF correction was applied to the data (Reed, 2005).

Standard	Element
Diopside	Si, Ca
Forsterite	Mg
Ilmenite	Ti
Jadeite	Na
Fayalite	Fe

Table 3. Standards used for EMP measurements

3.2.3. Thermodynamic modelling

For thermodynamic modelling, Perple_X version 6.6.8. by Connolly (1990), updated in 2012, was used. This is a set of FORTRAN77 coded programmes which calculate phase diagrams, phase equilibria and thermodynamic data, based on minimization of Gibbs free energy of mineral reactions. The various programmes in the Perple_X package each serve for a different part of the process of calculating a pseudosection, a phase diagram which shows the fields of stability of different mineral assemblages at a given bulk-rock composition, and defining mineral composition and modal abundances. Programs of Perple_X used for this study are BUILD, VERTEX, PSSECT, WERAMI, PSTABLE, PSVDRAW and MEEMUM. In addition the program PyWerami version 2.0.1 by Lexa (2011) was used to display data produced in WERAMI. Table 4 shows a short description of the functionality of each of these routines.

Program	Purpose
BUILD	Define compositional variables, boundary conditions, and data sources to be used for the actual calculation.
VERTEX	Calculate the pseudosection.
PSSECT	Plot the pseudosection as calculated in VERTEX.
WERAMI	Calculate isopleths and modal abundances.
PyWerami	Visualize isopleths and modal abundances.
PSTABLE	Plot cumulative modal abundance against P, T or X.
PSVDRAW	Plot profiles.
MEEMUM	Define properties at specified conditions in the pseudosection.

Table 4. Programs used for performing thermodynamic modelling.

In the BUILD file, a thermodynamic data file, a fluid equation of state file and a solution model file need to be defined. For all three, the default setting is used, hp02ver.dat (Holland and Powell, 1998a), and solution_model.dat, respectively. A more detailed description of how to use the programs can be found

in Pietersen (2013). In a separate document (Basic Perple_X manual, version 2015), a roadmap of how Perple_X was used in this study to arrive at acceptable pseudosections is given.

3.3. Argon dating

Argon dating is based on the decay of ^{40}K to ^{40}Ar and ^{40}Ca with a half-life of 1250 Ma (McDougall and Harrison, 1999). As precision of the K/Ar method is generally lower than that of the $^{40}Ar/^{39}Ar$ method, the latter is used for this study.

For this method, samples have to be irradiated in order to transform a small proportion of ^{39}K into ^{39}Ar. Subsequently, relative abundances of ^{40}Ar, ^{39}Ar, ^{38}Ar, ^{37}Ar and ^{36}Ar are measured in a Hiden quadrupole mass spectrometer. As $^{40}Ar^{*}/^{39}Ar_{K}$ is proportional to $^{40}Ar^{*}/^{40}K$, where $^{40}Ar^{*}$ represents the radiogenic argon component, the age can be calculated.

3.3.1. Preparation for argon dating

A high (preferably > 1.0%) potassium content is needed in order to perform argon dating. Therefore, minerals with a high potassium content such as K-feldspar, amphibole, biotite and white mica were separated from the samples. Subsequently radiation of the samples took place in the NRG HFR radiation facility of Petten, The Netherlands.

3.3.1.1. Mineral separation

The material left over from the jaw crusher was sieved for size fractions 32 - 125 µm, 125 - 250 µm, 250 - 500 µm and 500 - 1000 µm. The different fractions were washed using demineralised water and put in an ultrasonic bath as to get rid of small particles attached to the grains. Mineral separation and measurements are easier on coarser material. Therefore, for each target mineral, the coarsest fraction was optically chosen and used for further treatment.
By using a range of heavy liquids with different densities in the centrifuge LOC 50, minerals were separated from each other.

Table 5 lists the liquid densities used for separation of the different minerals.

Mineral	Liquid density (g/cm^3)
K-feldspar	2.54 – 2.59
Biotite	3.05 – 3.20
Amphibole	3.05 – 3.20

Table 5. Heavy liquids used for mineral separation. White mica was separated using only the Faul table.

For further purification of K-feldspar and amphibole, the Frantz magnet was used. By applying a variable electric current on the magnet, the minerals will be separated according to their magnetic susceptibility. Contaminated grains will be separated from the fresh grains as the contamination generally has a different magnetic susceptibility.

Further purification of biotite and separation of white mica was done using the Faul table. This is a vibrating plate that separates grains according to shape. Platy minerals such as micas will be transported to the end of the table, whereas round grains will drop off in the beginning. As there was enough clean material of white mica present in the samples, it was not needed to use heavy liquids for a first separation.

Finally, a 3% HNO_3 solution was added for 5 minutes to all minerals to remove surface contamination on the grains. Mineral separation was completed by hand picking using a small vacuum cleaner, resulting in 5 till 100 mg of clean sample.

3.3.1.2. Electron microprobe measurements

As potassium content, heterogeneity and zoning are important factors for argon dating, EMP measurements were carried out on roughly ten minerals per rock sample to check for these factors. The potassium content was verified with EDS (Energy Dispersive Spectroscopy) on the EMP facility at the VU University Amsterdam. Samples which did not contain enough potassium for dating according to EDS measurements were excluded from further measurements. EMP Measurements of the core, middle and rim of the grains using the wavelength dispersive spectroscopes were carried out in order to detect changes in chemical compositions over growth time. For the process of EDS and EMP measurements mineral mounts of the cleaned samples selected for argon dating were made by gluing separate minerals to a plastic layer, filling the gaps with resin and final polishing. These mounts were coated with a conductive carbon layer and subsequently measured. The same EMP facility and settings were used as for the thin section measurements.

3.3.1.3. Radiation

In order to have ^{39}Ar present, the clean minerals need to be irradiated with fast (2-7 MeV) neutrons. This was carried out in the High Flux Reactor in Petten, The Netherlands in the RODEO cadmium shielded position on July 15, 2012. In this facility the samples are exposed to a fast neutron field for 18 hours with 1MWH, changing some of the ^{39}K into ^{39}Ar. In order to define how much ^{39}K is transformed into ^{39}Ar, the amount of radiation on each samples, known as the irradiation parameter *J* or flux, has to be determined. This parameter is calculated using a standard sample which is radiated together with the samples of interest (unknowns). The absolute K/Ar age of the standard sample should be very accurately dated. This absolute age in combination with dating of the standard after irradiation using the $^{40}Ar/^{39}Ar$ method enables us to calculate the irradiation parameter by using Equation 1. For this research, the in-house standard Drachenfels with a known age of 24.99 ± 0.07 Ma is used (Wijbrans et al., 1995).

Equation 1. Calculating the irradiation parameter

$$J = \frac{e^{\lambda t} - 1}{{}^{40}Ar^{*}/{}^{39}Ar_{K}}$$

Samples were packed in aluminium packages and stacked together in an aluminium tube for radiation as shown in Figure 3. Standard samples were provided with an extra cupper layer to easily tell the difference between standards and unknowns. Standard samples were put in every two to four samples, trying to keep the speciation of the standards equal in order to calculate the flux change over the samples using a linear interpolation. Figure 4 shows the J-values of all standard samples used in this study. Figure 1A linear interpolation of the J-factor on two subsequent standards is used to calculate the flux on each individual sample as the difference in flux change over the standards is rather substantial. Therefore a total linear regression is not favourable. As becomes clear from Figure 4 standard xc1 displays a strange flux deviating from the expected value in line with the other standards.

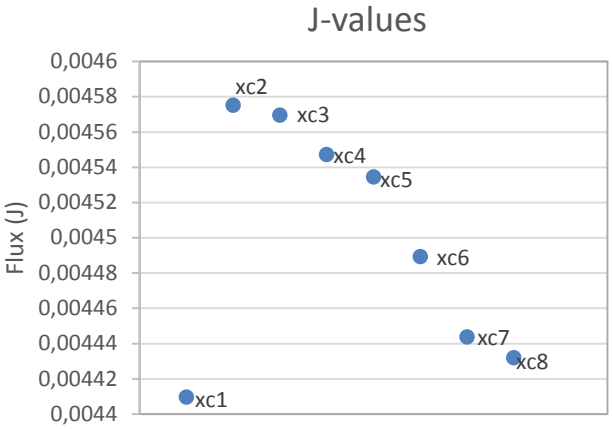

Figure 4. J-values for the individual standard samples. As flux changes between two subsequent samples vary substantial, linear interpolation between two subsequent standards is used rather than a total regression. Distance between two standards is roughly constant.

Figure 3. Packing sequence for irradiation. Difference between standards and unknowns is obvious from the cupper around the standard samples. The total length of this wrap is 5 cm.

3.3.2. Measurements with AGES

Sample measurements were carried out on the AGES (Automated Gas Extraction System) at the VU University, Amsterdam. A CO_2 laser beam is directed onto the mineral with a varying intensity, causing the mineral to (partly) melt. During this melting, argon is released from the crystal lattice and let into the cleaning part of the extraction line. In this phase, two SAES getters and a cold finger with an operating temperature of 250°C and -40°C respectively will ensure that undesired elements are trapped before the gas reaches the Hiden quadrupole mass spectrometer where ^{40}Ar, ^{39}Ar, ^{38}Ar, ^{37}Ar and ^{36}Ar are measured in fifteen cycles.

Blanks are frequently measured to keep track of unexpected contaminations from either the line itself, or the previous measured sample. For single grain fusion measurements this is every four measurements; for stepwise heating experiments, the frequency is every two measurements. For the blank measurement, the same routine as for a sample is followed, except that the laser has an intensity of 0. Air measurements which are used for correcting for the atmospheric ^{40}Ar present in the sample, are measured four times a month.

3.3.2.1. Single grain fusion

When a rock has experienced a complex tectonic history, this may be represented in different age peaks for single grain measurements. Therefore single grain measurements were carried out on three biotite samples, namely JI 4-2, JI 4-7 and JI 5-1. Grains of biotite were loaded in a 185 hole cupper disk with one grain per hole. Per sample, thirty replicates were loaded to get a good idea of the spread of the ages. Each grain was heated once by the laser at an intensity of 80 W. This resulted in a molten grain after heating and it was assumed that all argon was released at once.

3.3.2.2. Stepwise heating

For establishing an absolute age of the transition through the closing temperature of a certain mineral, stepwise heating experiments were done. Roughly twelve grains per sample per hole were loaded in a 21 hole cupper disk. In approximately fifteen steps with increasing laser intensity, all argon was released from the mineral structure. The heating scheme is slightly different for different minerals and chosen such that the amount of ^{39}Ar released in each step is roughly similar. For biotite the following scheme was used: 15W, 17.5W, 20W, 22.5W, 25W, 27W, 29W, 32W, 35W, 38W, 42W, 46W, 100W, 150W. For K-feldspar the scheme was as following: 20W, 25W, 30W, 35W, 40W, 47W, 55W, 70W, 90W, 100W, 110W, 130W, 150W, 200W, 270W. And for hornblende the scheme was as following: 15W, 18W, 21W, 23W, 25W, 27W, 28W, 30W, 33W, 35W, 40W, 46W, 120W, 170W, 230W. For white mica the following scheme was used: 10W, 12W, 13W, 14W, 15W, 16W, 17W, 18W, 19W, 20W, 23W, 32W, 150W, but probably due to the mineral structure of white mica this scheme contained still too large steps in intensity increase. As the step size cannot be decreased further, the laser beam width was doubled in order to reduce the intensity of the laser on a single spot. As fine tuning of these schemes was carried out on one sample per mineral type, the scheme might not be ideal for all samples.

3.3.3. Data reduction

Age calculations from the obtained data were done using the Microsoft Excel add-in ArArCALC by Koppers (2002). This software enables to do age calculations and correct for blank measurements, air measurements and J-factor.

As the produced gas is measured in 15 cycles with a total measurement time of approximately thirty minutes, deviations might occur in measurements from the beginning and end. Mainly in the beginning, measurements might be off as equilibrium between the isotopes is not yet reached. Therefore, all measurements are manually checked in ArArCALC and wrong measurements in the beginning of the 15 cycles (often the first two) are deleted. Subsequently, ArArCALC calculates the age, amount of argon released, isochron ($^{40}Ar/^{36}Ar$ versus $^{39}Ar/^{36}Ar$), inverse isochron ($^{36}Ar/^{40}Ar$ versus $^{39}Ar/^{40}Ar$), age plateau and K-Ca plateau. Blank measurements are processed the same way and corrections on the sample measurements are done automatically.

Data reduction for the standard measurements is done in the same way, resulting in a J-value for the neutron flux. Linear interpolation of the J-values gives a value to use for the unknown age calculations. This value can be inserted in the sample parameters of the unknown age file and results in automatic recalculation of the age.

The ratio of $^{36}Ar/^{40}Ar$ for the air measurements is compared to the internationally used value of 298.56 ± 0.31 (Lee et al., 2006). Deviation from this value is calculated by ArArCALC and listed as an MDF value. This value can be incorporated in the unknown measurements in the same way as the J-value to correct for the air contribution of argon in the sample.

In some measurements, the amount of ^{36}Ar in the sample is almost 0. If this is the case, it might happen that the measurement of ^{36}Ar in the blank is (slightly) higher than during the sample measurements. This results in an unnatural low error on the age calculation. In order to work with more natural error values, the value of ^{36}Ar in the sample is changed to blank+1. This adjustment only affects the error to a more natural value, but leaves the measured age unchanged.

3.3.4. Excess argon and recoil effects

In an ideal case, the mineral dated acts as a closed system, in which all argon originates from the decay within the mineral. However, this is often not the case and argon can move in and out the crystal lattice before reaching the closure temperature. When this happens, so-called excess ^{40}Ar ($^{40}Ar_E$) can be present, which affects the age calculations. Incorporating $^{40}Ar_E$ in minerals during or after crystallization

can be caused by overpressure of ^{40}Ar in the surroundings due to for instance increased heat by an intrusion (Harrison and McDougall, 1980).

^{40}Ar can be either radiogenic (formed by the decay of ^{40}K), atmospheric (in a $^{40}Ar/^{36}Ar$ ratio of 298.56 ± 0.31 (Lee et al., 2006)) and non-radiogenic (e.g. 'excess'). In age spectra calculations the amount of atmospheric ^{40}Ar is calculated from the amount of ^{36}Ar, assuming that all ^{36}Ar is atmospheric. The remaining amount of ^{40}Ar is thought to be radiogenic and used for the age calculation. However, with this approach the $^{40}Ar_E$ is not determined and therefore calculated ages may be too high and thus meaningless. In order to detect the $^{40}Ar_E$, normal- and inverse isochron plots should be made ($^{40}Ar/^{36}Ar$ versus $^{39}Ar/^{36}Ar$ and $^{36}Ar/^{40}Ar$ versus $^{39}Ar/^{40}Ar$ respectively). In these diagrams the deviation of measurements from the atmospheric $^{40}Ar/^{36}Ar$ ratio becomes clear and with that the presence of excess ^{40}Ar.

Another effect which could make the age calculations unreliable is recoil of ^{39}Ar during irradiation. The neutron beam which activates the $^{39}K(n,p)^{39}Ar$ reaction with a recoil energy of ~300 keV enables ^{39}Ar to recoil out of the mineral (Ching-Hua and Onstott, 1989). Especially in biotite this effect cannot be ignored (Ching-Hua and Onstott, 1989; Hess et al., 1987). These minerals may, although appearing homogeneous, contain small scale alteration products which can accommodate ^{39}Ar which recoiled out of the biotite (Hess et al., 1987). Therefore $^{40}Ar/^{39}Ar$ spectra may be influenced. According to Hess and Lippolt (1986) this effect can also be observed in white mica, hornblende and K-feldspar, although in much smaller scale than for biotites.

In order to find out if recoil could have taken place in samples used in this study, element distribution maps of different biotite grains were made in order to detect alteration products within seemingly unaltered grains. To do so, Fe, Mg, K, Si, Ti, Ca and Al were mapped out over a 500 × 500 µm range with the EMP facility at the VU University Amsterdam, using an acceleration voltage of 15 kV, beam current of 2.5 nA, a fully focused beam and a measurement interval of 0.50 µm.

4. Petrological results

Within the study area, different rock-types have been found. In this chapter, an overview will be given on the petrography and mineral assemblages, whole rock geochemistry and mineral geochemistry.

4.1. Petrography

The Jinshuikou group consists of metamorphic rocks of amphibolite facies metamorphic grade, including amphibolites and gneisses. In the upper part of the Jinshuikou group, the rocks are often mylonitized, whereas in the lower part of the group, rocks are often migmatized. Figure 5 shows slightly mylonized rocks on the left and partly migmatized rocks on the right. Syn- and posttectonic intrusions of granite and gabbro can be found in between the metamorphic rocks. The heat of these intrusions created contact metamorphic hornfels in the east of the section. The presence of intrusive rocks increases towards the east, whereas the amount of metamorphic rocks decreases. Thin section descriptions of all samples can be found in Appendix I. Table 6 shows a summary of the mineral abundances of all samples. An explanation of mineral abbreviations used in this study can be found in Paragraph 6.

Figure 5. (left) Slightly mylonized rocks in the top of the Jinshuikou group. (right) Slightly migmatized rocks in the lower part of the group with Jan Wijbrans, supervisor of this research as scale indicator.

4.1.1. Amphibolite

The amphibolite samples show a mineral assemblage of amp + pl ± bio ± q ± ep ± cz/zo ± sph ± cc ± chl ± gt ± metal oxides ± ru. Sample JI 4-6, shows a large amount (30%) of fresh garnet and in sample JI 2-1 we find relics of garnet, almost completely replaced by amp + pl + metal oxides. These are remains of an earlier (peak) metamorphic part of the history of the rock. The other amphibolites do not show any hints of garnet. Occurrences of chl + pl (ab) in all amphibolite samples and epidote or cz/zo in all samples but JI 4-3 gives evidence for the course of the retrograde path into greenschist facies. Also the seemingly unstable habit of amphibole with irregular mineral edges and being partly replace by chlorite or metal oxides is evidence for recrystallization along this retrograde path. Samples JI 1-1, JI 1-4 and JI 2-1 also display presence of late calcite, indicating introduction of a CO_2 fluid into the system. Figure 6 shows a typical example of an amphibolite.

4.1.2. Gneiss

The gneiss samples in the Jinshuikou group all show a mineral assemblage of q + bio + pl + kfs ± mica ± ru ± zo/cz ± chl ± cc ± metal oxides ± zr ± ap. In all gneisses, either plagioclase or K-feldspar is partly replaced by clayminerals. JI 1-3 and JI 2-2 contain muscovite, although in JI 1-3 this is partly replaced by chlorite. In JI 2-2 almost all biotite is replaced by chlorite, only leaving tiny patches within the grains as proper biotite. Quartz generally shows undulose extinction and banding of felsic and mafic minerals is often deformed. Figure 6 and Figure 7 show typical examples of a gneiss. In the case of gneiss JI 1-3 the development of a crenulation at cm scale is note, with an S2 developing parallel to the orientation of the hammer on the photograph (Figure 7).

Figure 7. Strongly deformed banding in JI 1-3.

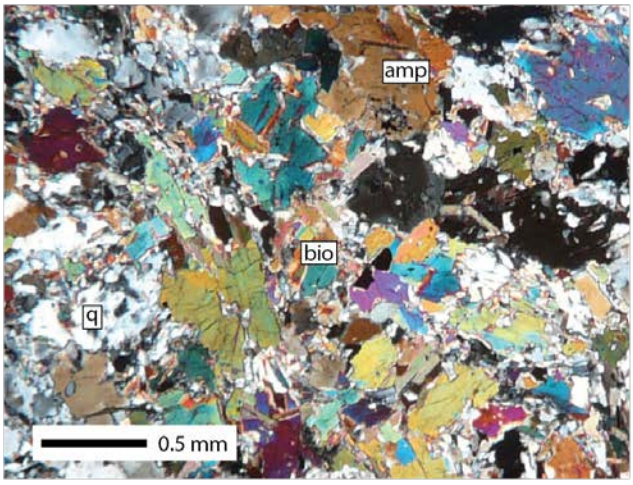

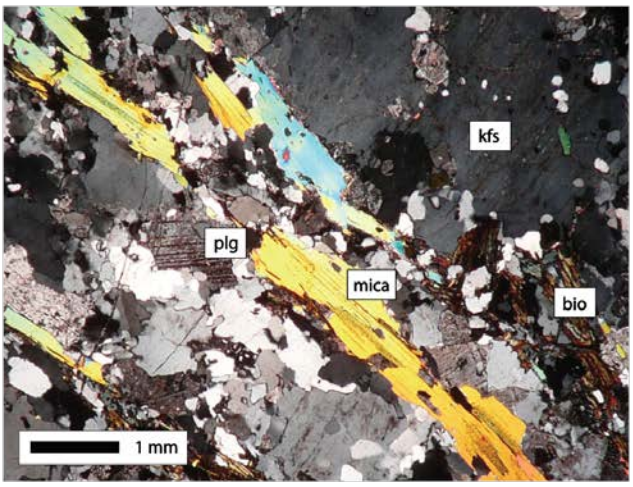

Figure 6. JI 4-3, a typical example of an amphibolite with randomly orientated anhedral amphiboles. (right) JI 2-2, a typical example of a gneiss with mica banding and plagioclase partly replaced by clayminerals. indicator.

4.1.3. Granite

The granite samples show a mineral assemblage of q + pl + kfs + bio ± ep ± gt ± mica ± zo ± chl ± ap ± zr ± metal oxides. JI 4-7, JI 5-1 and JI 5-2 show an unstable habit in which epidote or amphibole is growing instead of biotite, garnet and feldspar. These samples show rather large crystal sizes of on average 2 mm, with outliers up to 20 mm. In contrast, JI 5-7 shows small crystal sizes with a maximum of 1 mm. From structural relations in the field it was already concluded that the latter is a posttectonic granite, whereas granites JI 4-7, JI 5-1 and JI 5-2 are syn-tectonic. Figure 8 shows a typical example of a granite from the Jinshuikou group with large crystals up to 4 mm and often garnet present.

4.1.4. Gabbro

The gabbro samples show a mineral assemblage of amp + ol + bio + metal oxides + pl + ru + q ± zo ± chl ± ap ± cpx and were only found in the eastern area of the Jinshuikou group. Biotite occurs only in fairly small amounts (< 2%) and relatively large amounts of metal oxides overgrow plagioclase and in JI 5-4 also olivine and quartz. Figure 9 shows a typical example of a gabbro with the mentioned mineral assemblage and a grain size up to 2 mm.

4.1.5. Hornblende hornfels

The hornblende hornfels sample shows a mineral assemblage of amp + q + bio + pl + metal oxides. Within this sample amphibole and plagioclase are represented both as phenocrysts and in the matrix. Phenocrysts have a size up to 4 mm and display clear zoning. The matrix contains grains with an average size of 0.05 mm. The phenocrysts seem generally unstable and are partly replaced by biotite and metal oxides. Figure 10 shows a hornblende hornfels.

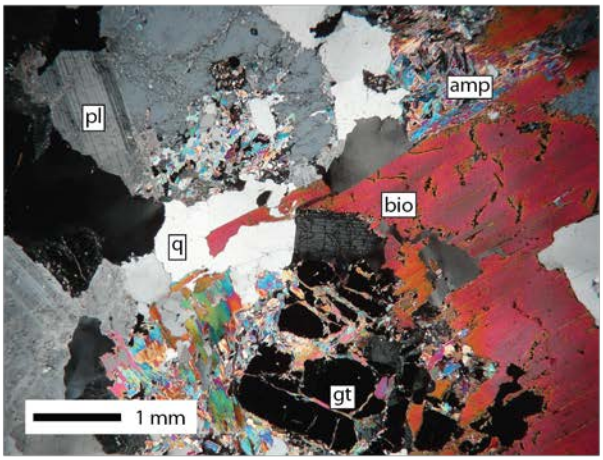

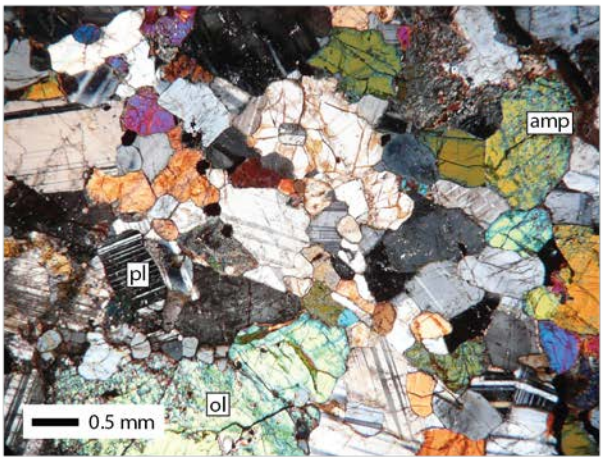

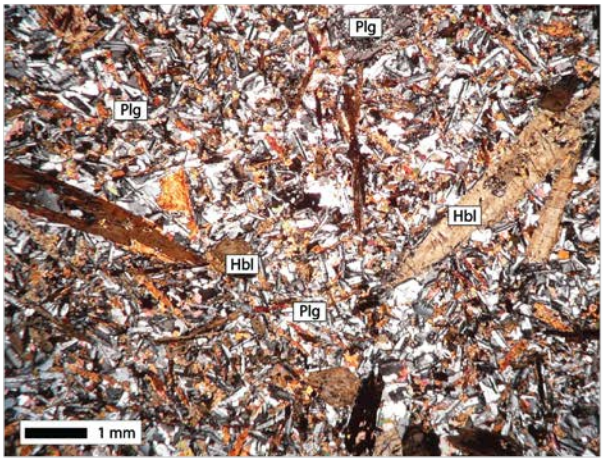

Figure 8. (top left) JI 5-2, a typical example of a granite with large crystals up to 4 mm.

Figure 9. (top right) JI 5-5, a typical example of a gabbro with metal oxides overgrowing plagioclase and olivine.

Figure 10. (bottom left) JI 5-3, a typical example of a hornblende hornfels containing phenocrysts of hornblende and plagioclase which are unstable and partly replaced by biotite and metal oxides.

Sample	q	amp	bio	ep	gt	Metal oxide	pl	kfs	mica	zo/cz	sph	chl	cc	ru	ilm	zr	ap	ol	cpx
JI 1-1	5	60	2	5			15			3	5	1	5						
JI 1-3	45		20				7	5	15	5		2							
JI 1-4	25	40	5	5			10	2		2	1	3	5	2					
JI 2-1	1	70(66)			3(10)	5	10(8)			3	5		1(0)	1					
JI 2-2	35		<1		<1		25	25	8	<1		5		<1		acc	acc		
JI 4-2	65		20				10	7								acc			
JI 4-3	20	50	5			3	10	7			3						2		
JI 4-5	65		3			5	10	5				10	3			acc			
JI 4-6	20	25	10		30		2	2		6	1			acc	5	1	2		
JI 4-7	35		15	5		3	25	20		1						1			
JI 5-1	50		10		5+20		10	10								acc			
JI 5-2	40	10	10		5		20	15											
JI 5-3	20	10+30	10			2	2+25					1		1					
JI 5-4	40	15	acc			10	15			5		3		2			acc	10	
JI 5-5	2	25	2			5	20							2				40	5
JI 5-7	50		15				15	10	5			5							

Table 6. Mineral abundances in percent of all samples; acc stands for accessory. For JI 2-1, the number between brackets is the assumed amount before alteration of garnet. JI 5-1 has a 5% fresh and 20% altered garnet. For JI 5-3 the double numbers of amphibole and plagioclase stand for phenocryst + matrix.

4.2. Whole rock geochemistry

For all metamorphic samples and granites JI 4-7 and JI 5-7 XRF major element analyses were carried out to determine the whole rock geochemistry. The results are listed in Appendix II. For all samples but JI 4-6 also the LOI was determined. It should be noted that for iron, no distinction can be made between Fe^{2+} and Fe^{3+} during measurements. So although Fe_{total} is measured, it is listed as Fe_2O_3 in the tables.

From the TAS classification (Figure 11), it is clear that the (garnet) amphibolites JI 1-1, JI 2-1, JI 4-3 and JI 4-6 display a basaltic composition. The amphibolite gneiss JI 1-4 and hornblende hornfels JI 5-3 show a basaltic andesite composition. Biotite gneiss JI 1-3 and JI 4-2 and granite JI 4-7 show a dacitic composition whereas the gneiss JI 2-2 and granite JI 5-7 display a rhyolitic composition. For samples JI 4-5. JI 5-1, JI 5-2, JI 5-4 and JI 5-5 no XRF analysis was carried out.

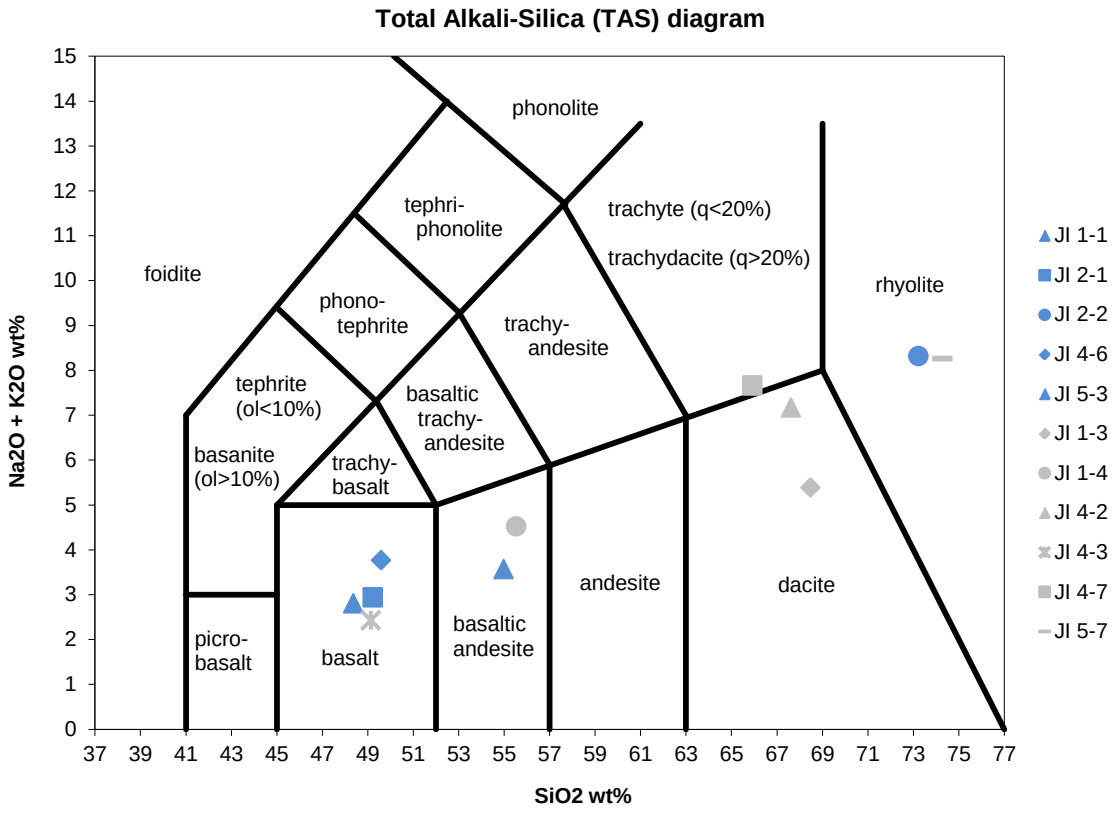

Figure 11. TAS classification of the samples used in this study. Blue samples are the ones used for thermodynamic modeling in this study and argon dating; grey samples are only used for argon dating. Thermodynamic modeling on the latter is performed by Huijgen (2015).

4.3. Mineral geochemistry

EMP spot analyses were carried out both on thin sections of the samples which were selected for thermodynamic modelling and on mineral mounts of the minerals picked for argon dating. The chemical results are shown in Appendix III (mineral mounts) and IV (thin sections). Measurement locations are shown in Appendix IV . In the following sections, mineralogical compositions of feldspars, amphiboles, garnets and micas will be shown and details will be explained.

4.3.1. Feldspar

For each sample 10-30 feldspar measurements were done. Locations for these measurements in the thin sections were chosen randomly in order to define the range in compositions within one rock. When zoning was obvious from backscattered images, both core and rim of a grain were measured. As can be seen in Figure 12, samples JI 1-1, JI 2-1, and JI 5-3 show only plagioclase compositions varying from albite to anorthite. Samples JI 2-2 and JI 4-6 also show K-feldspar compositions. In samples JI 2-1, JI 2-2 and JI 4-6 the feldspars are not in equilibrium as can be seen from the segregation in Figure 13.

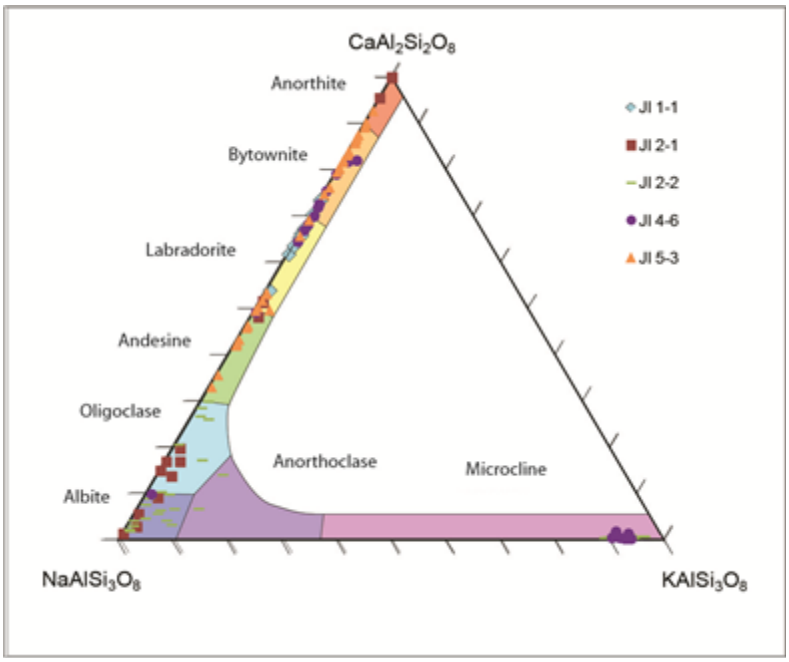

Figure 12. Ternary diagram of EMP measurements on feldspars in samples used for thermodynamic modeling.

After mineral separation, EMP measurements were also carried out on K- feldspars from samples JI 1-1, JI 1-3, JI 1-4, JI 2-2, JI 4-2, JI 4-3, JI 4-5, JI 4-7, JI 5-1, JI 5-2, JI 5-5 and JI 5-7 in order to determine how potassium content changes within the mineral and how this might influence the $^{40}Ar/^{39}Ar$ dating. Results per rock type are shown in Figure 14. Within error, no changes are visible and therefore will not influence argon dating results.

4.3.2. Garnet

Garnet compositions are shown in Figure 15. Sample JI 2-1 only contains altered garnets of which only the outer parts remained (Figure 16). However, compositions are very similar throughout the sample as is clear from Figure 15. Also sample JI 4-6 shows very uniform garnet compositions. Both samples contain very Mg-poor garnet.

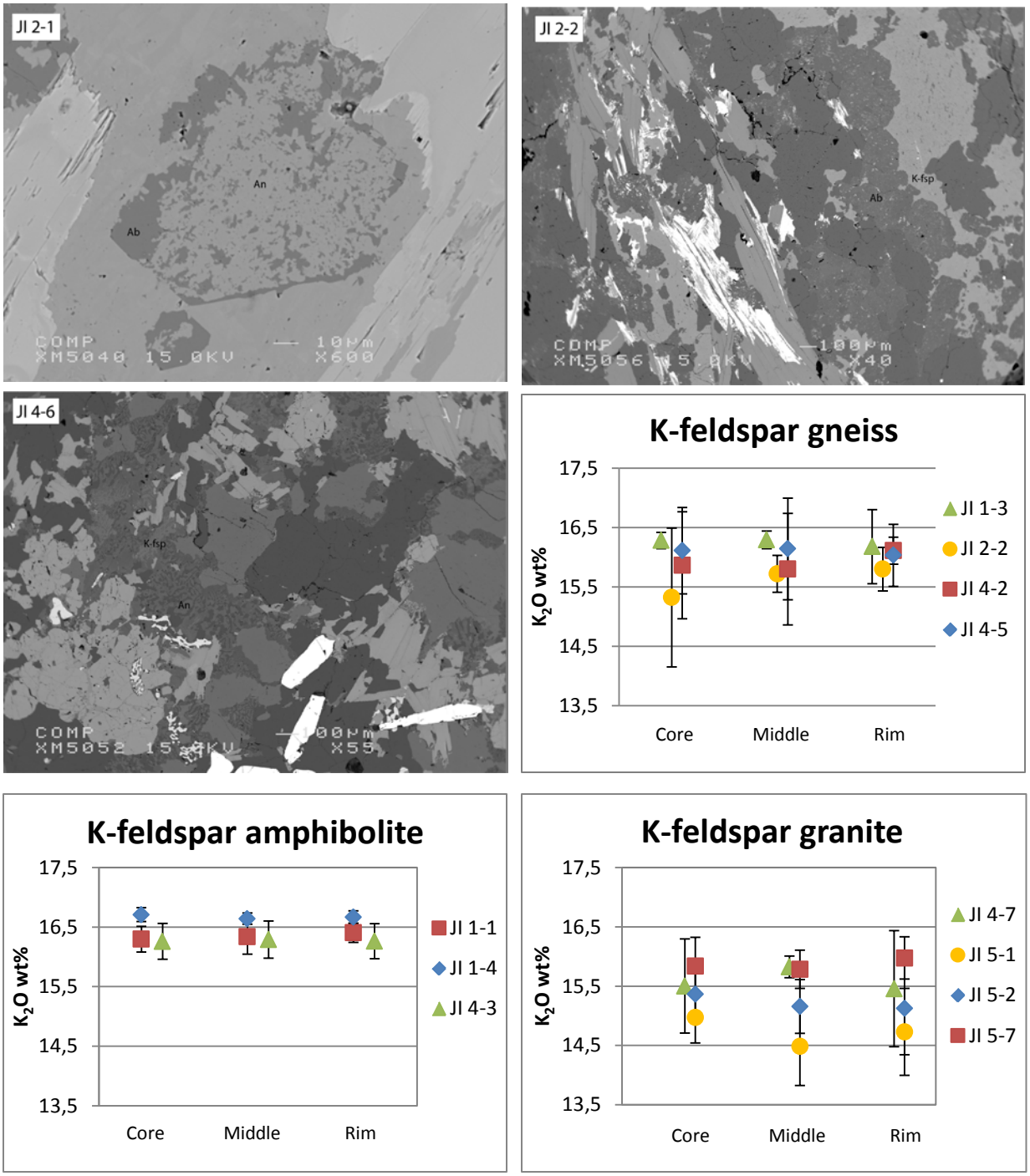

Figure 13. Backscattered images of feldspar in sample JI 2-1, JI 2-2 and JI4-6. Anorthite rich feldspar is generally darker than K-rich feldspar and lighter than albite rich feldspar. Spots of light and dark feldspar in the same grains develop from segregation of a mineral that is no longer in equilibrium.

Figure 14. K_2O measurements of K-feldspar single crystals of core, middle and rim. Within error, no changes in content occur over the crystals for amphibolite, gneiss and granite rocks. For each measurement, n=12.

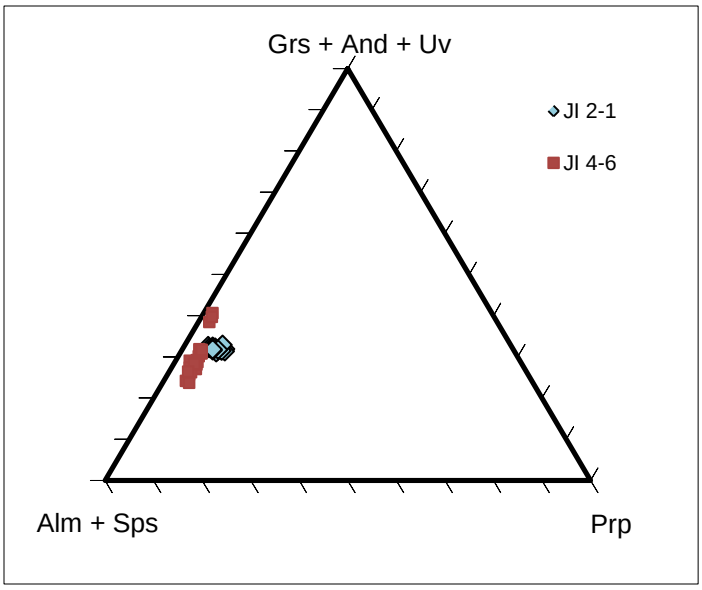

Figure 15. Ternary diagram of EMP measurements of garnet in samples used for thermodynamic modeling.

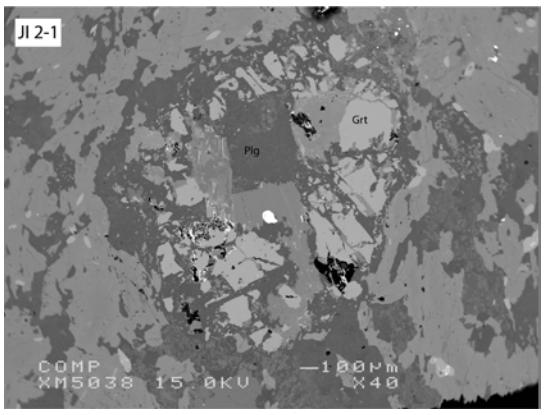

Figure 16. Remaining garnet in sample JI 2-1. Part of the garnet is replaced by plagioclase, amphibole and metal oxides.

4.3.3. Amphibole

Amphiboles in samples JI 1-1, JI 1-4, JI 2-1, JI 4-3 and JI 5-3 all show a calcic composition with $Ca_B \geq 1.5$ and $(Na + K)_A < 0.5$ according to the amphibole classification of Leake et al. (1997). Amphiboles in JI 4-6 also have a calcic composition, but contain more potassium, resulting in a classification of $Ca_B \geq 1.5$; $(Na + K)_A > 0.5$ and $Ti < 0.5$ according to Leake et al. (1997). Figure 17 and Figure 18 show the compositions of all amphiboles. Sample JI 1-1 and JI 4-3 show an obvious trend from ferrotschermakite, through ferrohornblende and magnesiohornblende to actinolite. Sample 1-4 also shows a slight trend from ferrotschermakite to ferrohornblende. For sample JI 5-3, distinction is made between phenocrysts and matrix. The rim of the phenocrysts corresponds in composition to that of the crystals in the matrix. The composition of the phenocryst cores contains more magnesium.

Also for amphibole, EMP measurements on minerals separated for argon dating were carried out. The average composition of the minerals is displayed in Figure 17 and Figure 18 together with error bars, indicating the range of measurements. For sample JI 1-1 and JI 4-3, all single grain measurements showed a quite similar composition as indicated with respectively the light blue diamond and pink dot and associated error bars. As it appears from the thin section measurements that the composition of amphiboles in both samples spreads over a large range, this means that only a small part of the population of amphiboles will be dated. Single grains of sample JI 5-3 show a range in composition from phenocryst to matrix measurements on the thin section. So for dating, an average of all amphiboles will be measured. Also for sample JI 1-4, the whole range of amphibole compositions is included in the grain separates used for argon dating. It was not possible to separate a sufficient amount of amphibole from sample JI 2-1 for dating purposes, so no single crystal measurements were carried out. Figure 19 shows the K_2O content of amphiboles in amphibolite and hornfels measured in the core, middle and rim of the crystals. Within error, no variation in composition is noted within the crystals.

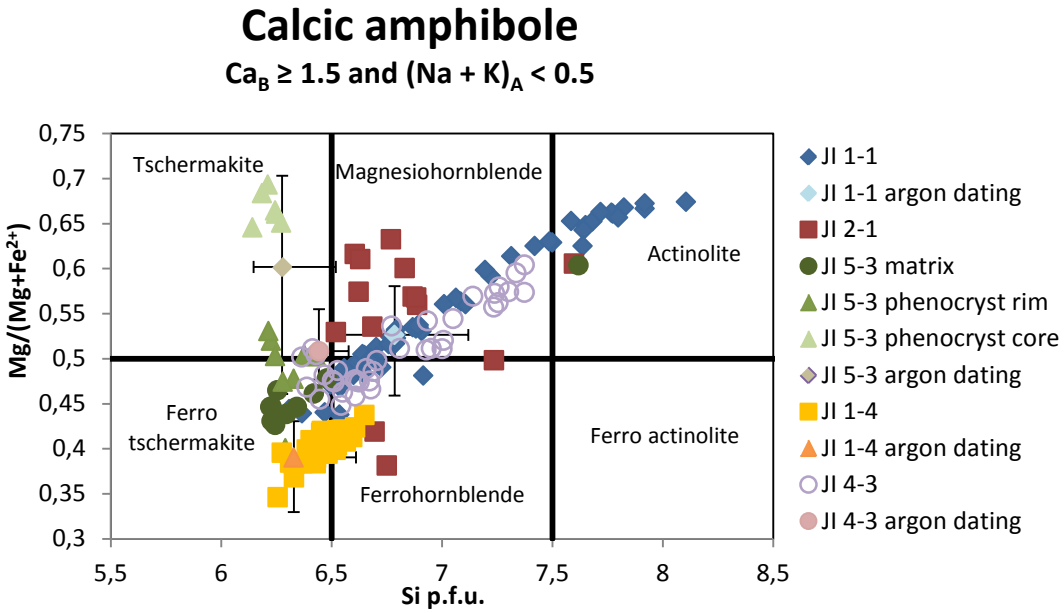

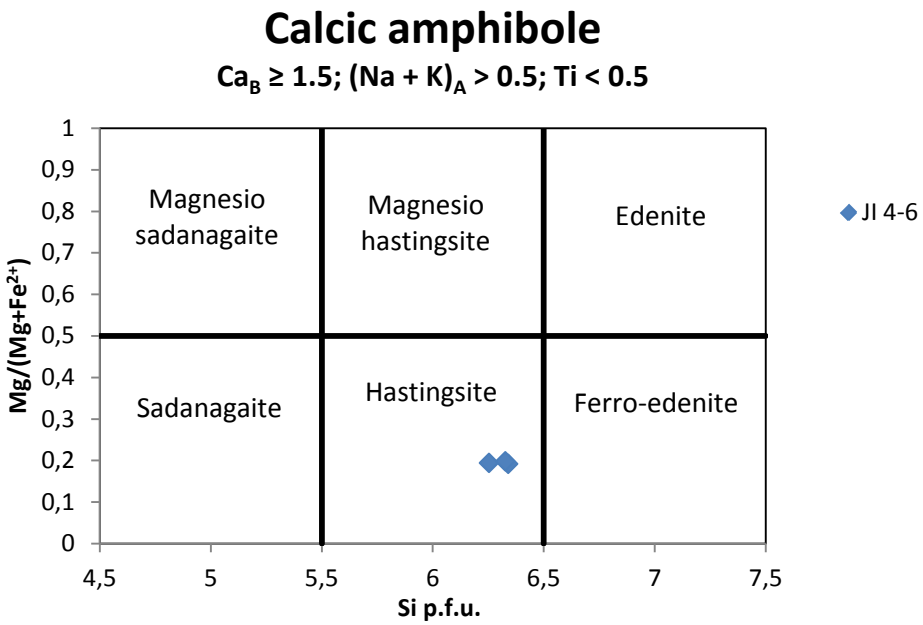

Figure 17. (top) Amphibole compositions from EMP measurements. All amphiboles plot in the calcic amphibole field and $(Na + K)_A < 0.5$ and $Ca_B \geq 1.5$. Composition of grains separated for argon dating is also shown. Error bars on these points indicate the range of compositions of the grains separated for argon dating.

Figure 18. (bottom) Amphibole composition of JI 4-6 with $Ca_B \geq 1.5$; $(Na + K)_A > 0.5$ and Ti < 0.5. JI 4-6 shows a hastingsite composition.

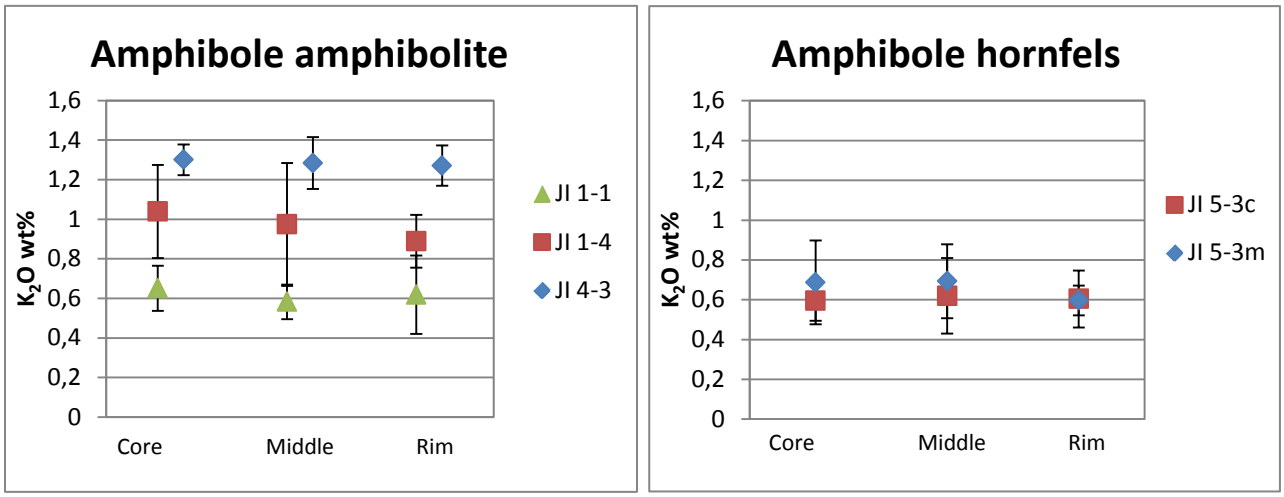

Figure 19. K_2O measurements of hornblende on single crystals in core, middle and rim. Within error, no variation in composition can be observed in the crystal. For all numbers displayed, n=12.

4.3.4. Mica

Micas within the samples used in this study show muscovite, celadonite and biotite compositions. Nomenclature is based on the amount of positive charge per octahedral site, dividing micas into dioctahedral (<2.5 positive charge) and trioctahedral (>2.5 positive charge) (Rieder et al., 1998). Since substitution within micas is based on the replacement of Al by Fe, Mg and Ti in octahedral sites and by Si in tetrahedral sites, this can be shown graphically in a combined graph (Tracy, 1975). Biotite samples should plot along the trioctahedral trend whereas muscovite plots along the dioctahedral trend (Figure 20). As becomes clear from this graph the micas in sample JI 1-1, JI 4-6 and JI 5-3 have a biotite composition whereas micas in JI 2-1 are celadonitic. JI 2-2 contains both biotite and muscovite.

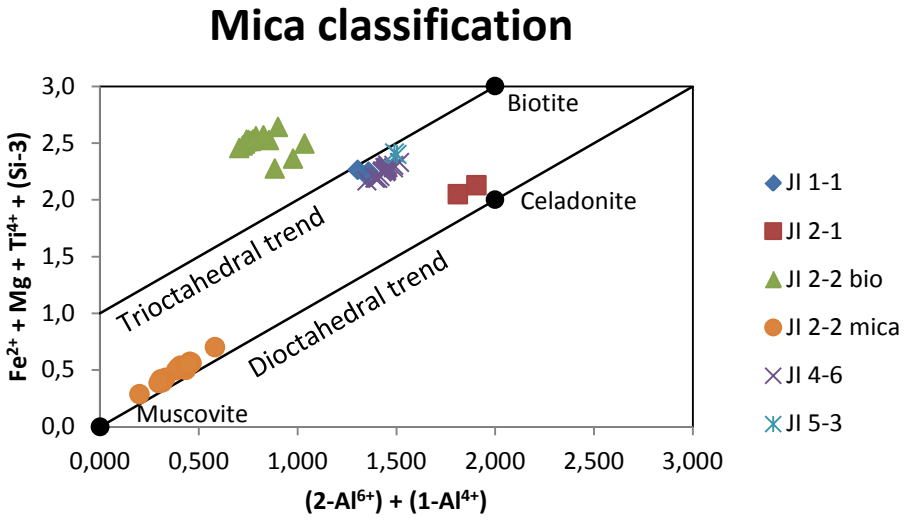

Figure 20. Mica classification after (Tracy, 1975). Ideal endmember compositions are displayed with black dots.

Figure 21 shows the potassium content of micas that are used for $^{40}Ar/^{39}Ar$ dating measured in the core, middle and rim of the samples. Within error, no variation in composition is observed in the samples.

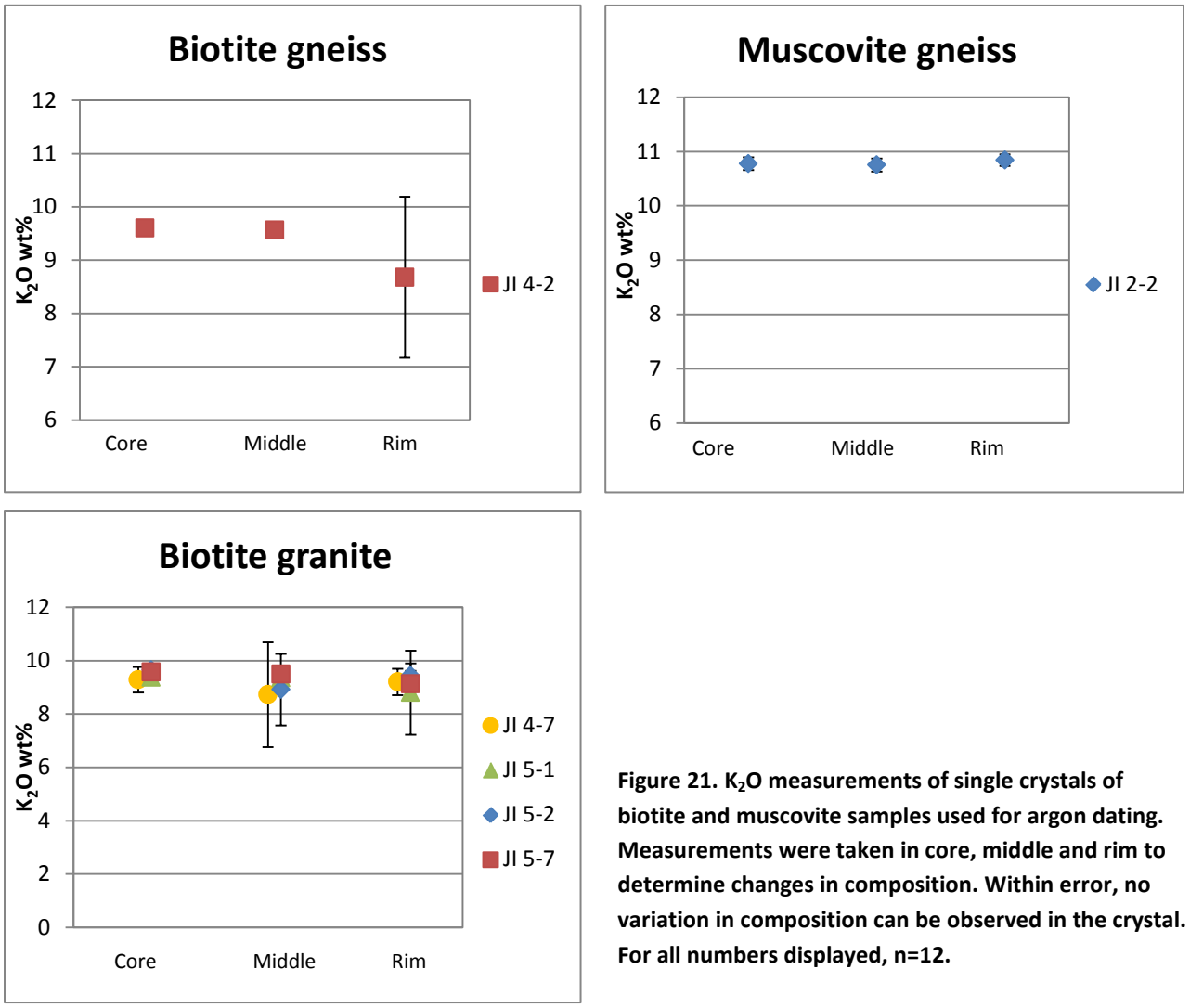

Figure 21. K_2O measurements of single crystals of biotite and muscovite samples used for argon dating. Measurements were taken in core, middle and rim to determine changes in composition. Within error, no variation in composition can be observed in the crystal. For all numbers displayed, n=12.

As was explained in paragraph 3.3.4 intercalation of alteration products with biotite can be used as evidence for possible recoil effects of ^{39}Ar out of the sample. It was not possible to detect alterations on nanometre scale, but on micrometre scale evidence of chlorite alteration in biotite grains was found for sample JI 4-2 (Figure 22). This figure shows a backscattered image of a cluster of biotite grains, together with chemical maps of the same area of K, Ti and Mg on a micrometre scale. Absence of K and Ti together with elevation of Mg in the same regions indicates presence of chlorite. This makes it very plausible that also on a smaller scale alteration products are present. As it is beyond the scope of this project to go into detail on this subject, only chemical maps of one sample were produced. However, the possible effects of argon recoil must be taken into account as biotite alteration products may be expected in other samples as well.

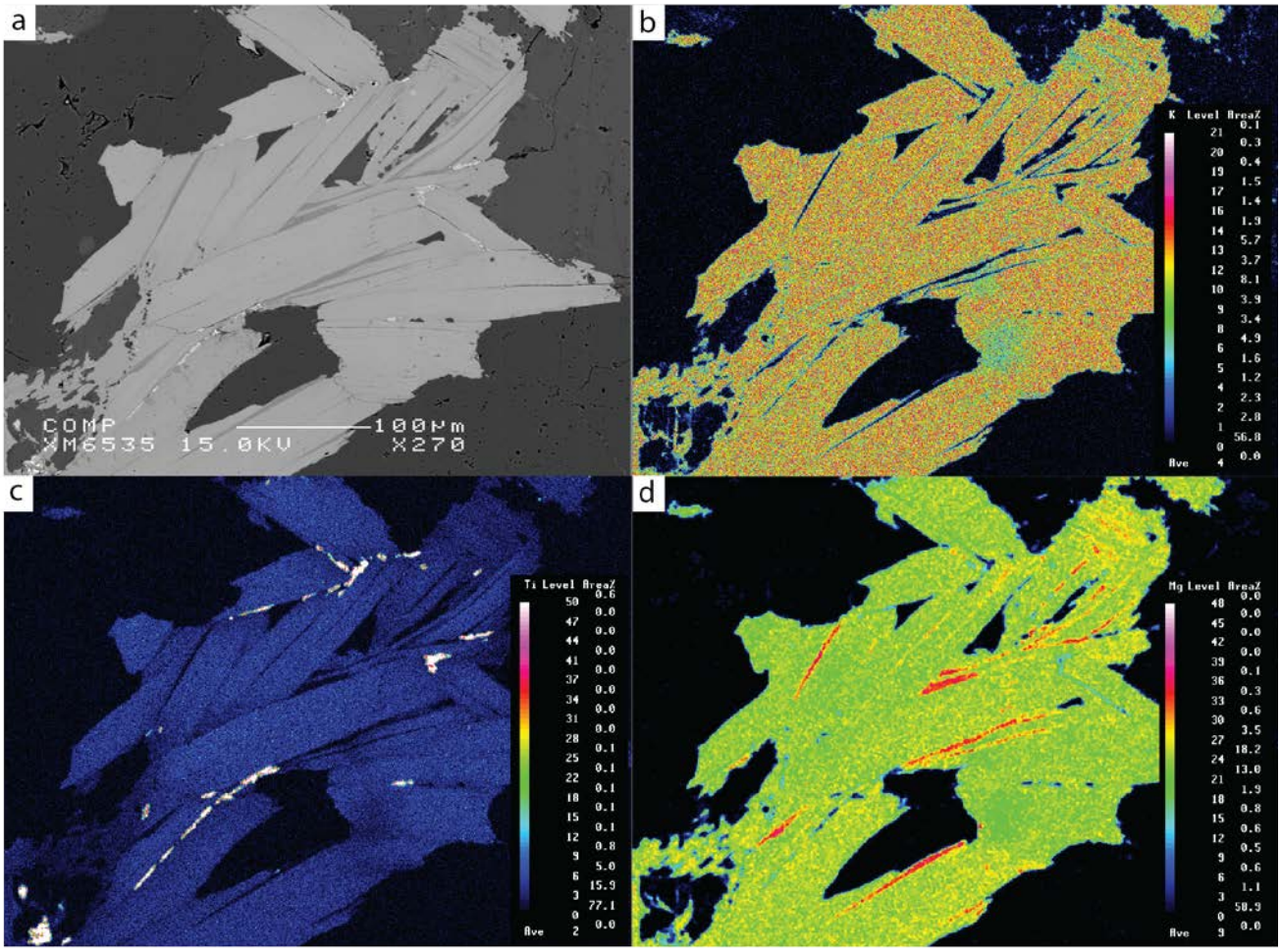

Figure 22. Chemical maps of sample JI 4-2. a) backscattered electron image, b), c) and d) show respectively amounts of K, Ti and Mg. It is clear that darker areas within the biotite crystal shown on figure a) correspond to absence of K and Ti, and elevation of Mg, which points towards chlorite intercalation within the biotite crystals.

5. Argon dating results

In this chapter the results of Ar-Ar dating will be described. Both stepwise heating measurements on biotite, hornblende, K-feldspar and white mica and single grain measurements on biotite were carried out. Not all ages are straightforward plateau ages, but rather closure ages obscured by excess argon and partial resetting. Best estimates for these ages can be divided into four different age groups, namely 450.27 ± 22.60 Ma to 403.25 ± 17.89 Ma, 353.40 ± 14.62 Ma to 263.43 ± 9.97 Ma, 252.58 ± 8.87 Ma to 199.86 ± 43.37 Ma and 215.11 ± 5.48 Ma to 184.26 ± 7.52 Ma. No clear trends in ages from west to east or from top to bottom of the Jinshuikou group were found.

Below, the single measurements will be described in detail and the reasoning underlying the choices for best age estimates is explained. Argon plateau ages can be used when no excess argon is present in the sample, and the plateau contains at least 50% of all radiogenic argon with an MSWD value below 5. Excess argon was found in all but the biotite grains, based on a deviation of single heating steps from the atmospheric isochron. Therefore, no plateau ages except for biotite could be used and ages are thus based on isochron corrections. Within this chapter only the isochron diagrams that are needed for explanation of the age are shown. In these diagrams, green dots are the measurements used for the isochron, blue dots are left out of the calculation. The purple line corresponds to an atmospheric isochron, whereas the pink line corresponds to the isochron as drawn for the included measurements. A 2σ error ellipse for each of the measurements is displayed. A complete overview of all age data including incremental heating summary, age plateau, K-Ca plateau, normal- and inverse isochron diagram is shown in Appendix V.

5.1. Stepwise heating

From stepwise heating experiments, ages for hornblende, biotite, white mica and K-feldspar were obtained for the four sample locations. The results will be described per sample location. An overview of the results is shown in Table 7. Colours indicate rock type; blue = metamorphic, orange = mylonitic, green = intrusive. As not all ages are straightforward measurements, some of the numbers given in Table 7 are best estimates rather than absolute ages. Ages with a * are best estimates based on isochron or lowest step ages; ages with ** are averages based on minimum and maximum ages. Details on these ranges and reason for the best estimates are given in the sample location descriptions below, but on general the lowest reasonable age is used as best estimate as excess argon results in overestimation of the age. Figure 23 shows the ages in map view, separated for metamorphic rocks on the top and intrusive rocks on the bottom. All errors given in this chapter display 2σ errors.

	hbl	bio	mica	kfs
JI 1-1	184.28 ± 58.74*			
JI 1-3				184.26 ± 7.52*
JI 1-4	273.92 ± 4.26*			217.46 ± 10.94*
JI 2-1				
JI 2-2			418.15 ± 2.45	295.37 ± 15**
JI 4-2		307.60 ± 1.64		199.86 ± 43.37*
JI 4-3	403.25 ± 17.89*			263.43 ± 9.97*
JI 4-5				309.34 ± 16.19*
JI 4-6				
JI 4-7		282.91 ± 3.46		207.44 ± 10.12*
JI 5-1		235.75 ± 3.89*		203.02 ± 1.02*
JI 5-2		228.73 ± 2.81		190.52 ± 0.38*
JI 5-3	252.58 ± 8.87*			
JI 5-4				
JI 5-5				241.37 ± 1.15**
JI 5-7		233.26 ± 2.84		242.72 ± 5.38*

Table 7. $^{40}Ar/^{39}Ar$ ages with 2σ error as obtained from stepwise heating experiments. Colours stand for rock type; blue = metamorphic, orange = mylonitic, green = intrusive. Ages with * are best estimates based on isochron or lowest step ages. Ages with ** are averages based on maximum and minimum values.

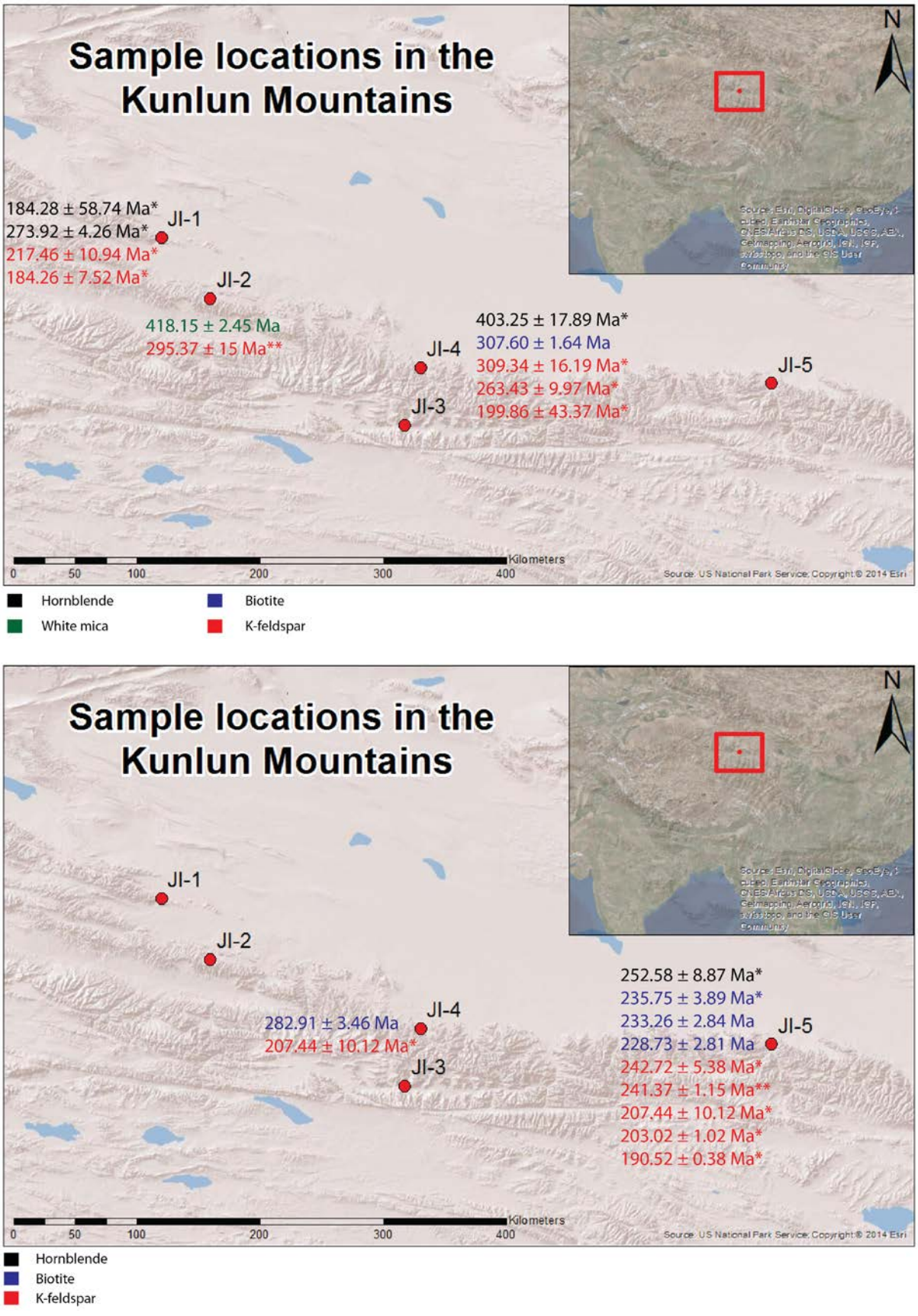

Figure 23. $^{40}Ar/^{39}Ar$ ages per sample location for metamorphic rocks (top) and intrusive rocks (bottom). Colours correspond to the different mineral ages. * is best estimated age, ** is an average age.

5.1.1. Location 1

At the westernmost location three metamorphic rocks were dated, of which two amphibolites JI 1-1 and JI 1-4 and a gneiss JI 1-3. Figure 24 shows the stepwise heating age spectra as obtained for hornblende and K-feldspar of these three samples. Note the difference in vertical scale. Due to excess argon inheritance the age spectra look bumpy and no plateau ages were determined.

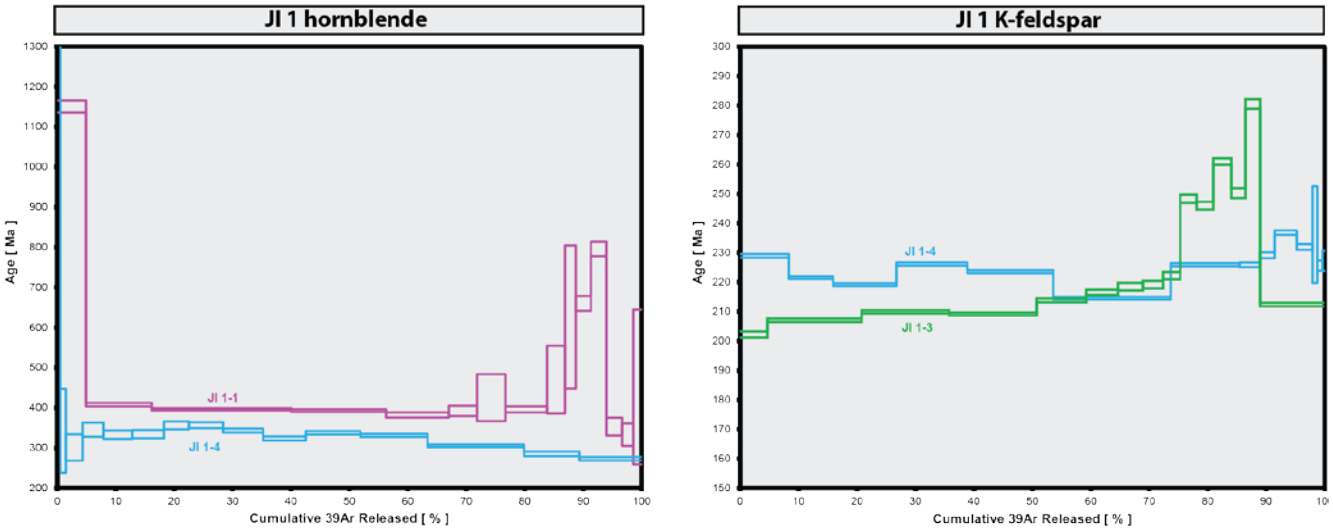

Figure 24. Stepwise heating age spectra for hornblende and K-feldspar measurements on location 1. Due to excess argon inheritance no age plateaus could be determined. Note the difference in vertical scale.

Hornblende in JI 1-1 seems to show a proper plateau in the heating step ages (Figure 24). However the inverse isochron diagram shows obvious evidence for excess argon, obscuring the age (Figure 25). An inverse isochron age for this plateau gives 377.28 ± 9.48 Ma. However, as excess argon results in an overestimation of the age, an inverse isochron age for the middle ten measuring steps is calculated, resulting in 184.28 ± 58.74 Ma. This is thought to be the best estimate of the closure age.

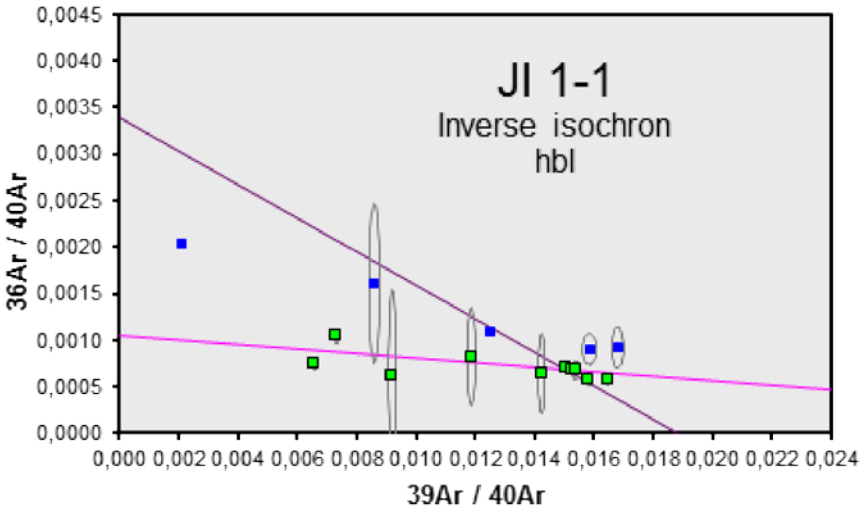

Figure 25. Inverse isochron of hbl from JI 1-1. The middle ten measurements are included.

K-feldspar in JI 1-3 shows a disturbed age pattern (Figure 24) with clear evidence of excess argon from the inverse isochron diagram (Figure 26) as measurements strongly deviate from the atmospheric isochron displayed in purple. An inverse isochron age of all but the first two heating steps is 184.26 ± 7.52 Ma and is thought to be the best estimate as no reasonable age could be obtained otherwise.

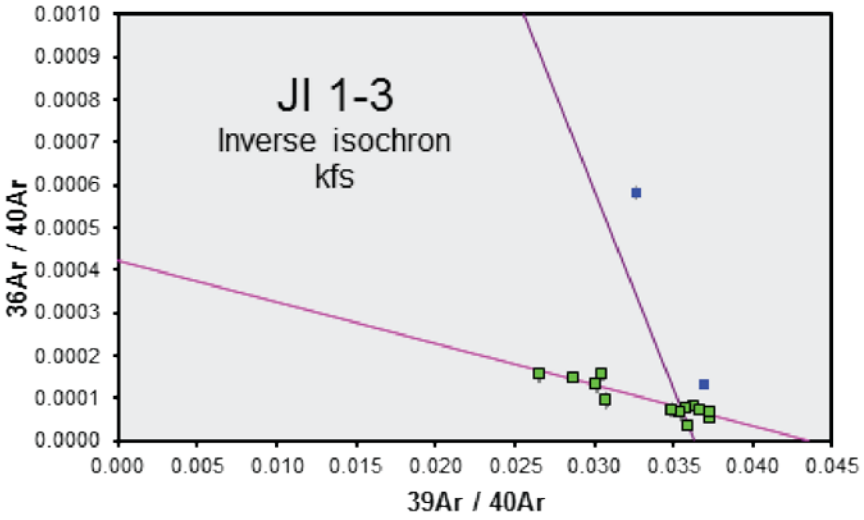

Figure 26. Inverse isochron of kfs from JI 1-3. All but the first two heating steps are included.

Hornblende in sample JI 1-4 does not show a nice plateau (Figure 24) despite of the absence of excess argon in the first twelve heating steps according to the inverse isochron (Figure 27). Therefore an inverse isochron age for this part was determined resulting in 335.65 ± 11.51 Ma. However when looking at the lowest age step at the end of the spectrum the age is 273.92 ± 4.26 Ma which is thought to be the best estimate as excess argon in these steps still results in an age overestimation. This makes the first age of 335.65 ± 11.51 Ma meaningless.

K-feldspar in JI 1-4 shows very clear evidence for excess argon both in the age plateau (Figure 24) and inverse isochron (Figure 28). An inverse isochron of the first seven heating steps was drawn resulting in an age of 217.46 ± 10.94 Ma. As the ages of the different heating steps all vary within the same range, also a total fusion age of 223.23 ± 1.07 Ma with a minimum of 214.52 ± 0.46 and a maximum of 236.82 ± 0.74 Ma was calculated. As excess argon overestimates the age, and no clear lowest step in the heating spectrum is present, the inverse isochron age of 217.46 ± 10.94 Ma is used as a best estimate.

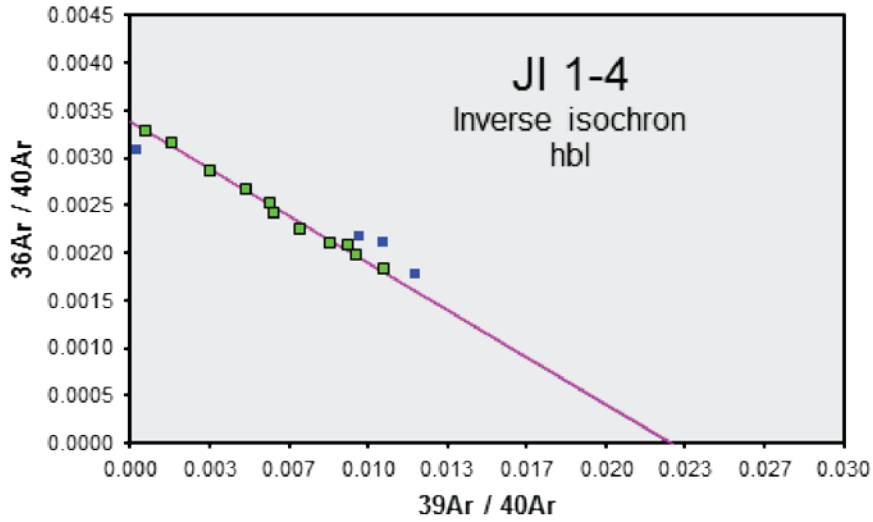

Figure 27. Inverse isochron of hbl from JI 1-4. The first twelve heating steps are included for the isochron. These steps line-up nicely with the atmospheric value, so no excess argon is present.

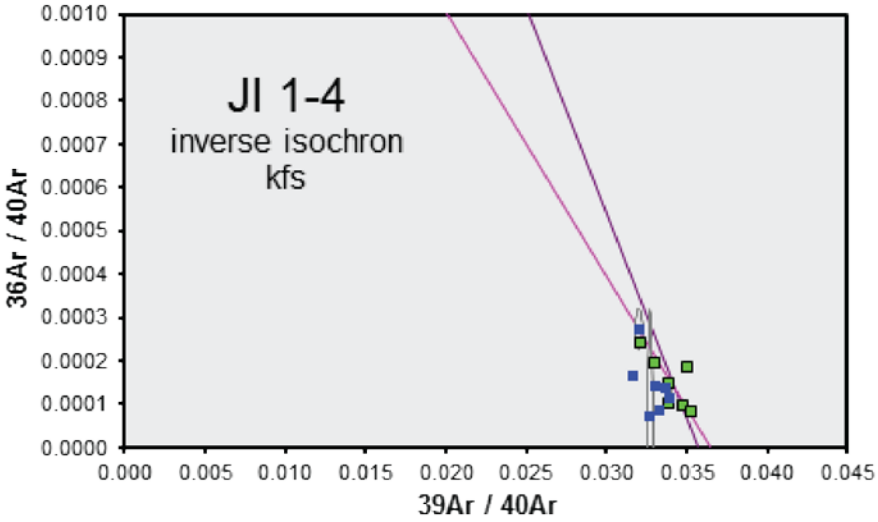

Figure 28. Inverse isochron of kfs from JI 1-4. The first seven heating steps are included in the calculation. All measurements cluster and a best linear fit through a subsequent set of measurements is used for calculating the inverse isochron age.

5.1.2. Location 2

Approximately sixty kilometres to the south-east of the first location another amphibolite (JI 2-1) and gneiss (JI 2-2) were sampled. Figure 29 shows the stepwise heating age spectra for muscovite and K-feldspar of JI 2-2. Unfortunately no potassium containing minerals could be separated from JI 2-1 so no age were obtained for this sample.

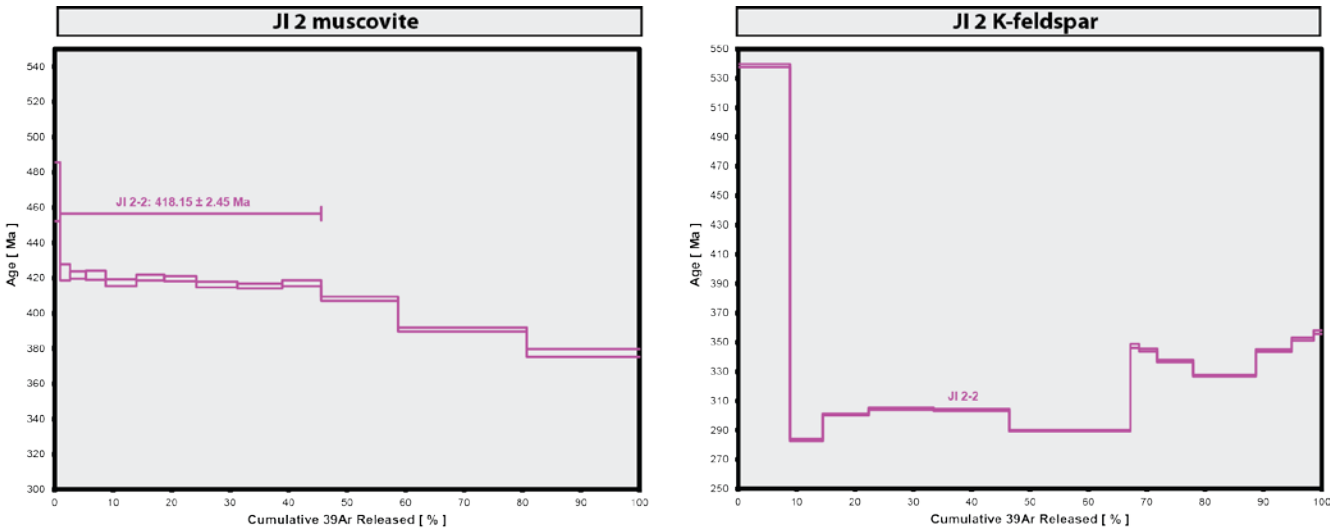

Figure 29. Stepwise heating age spectra for muscovite and K-feldspar measurements on location 2. Due to excess argon inheritance in K-feldspar no age plateau could be determined. Note the difference in vertical scale. For JI 2-1 no potassium containing minerals could be separated.

Muscovite in JI 2-2 gives a nice plateau age of 418.15 ± 2.45 Ma and no signs of excess argon occur. However, the K-feldspar of JI 2-2 does show a disturbed age spectrum (Figure 29) and a cluster of the measurements in the inverse isochron diagram (Figure 30) giving evidence for excess argon. The measurements cluster in the inverse isochron diagram makes it impossible to draw a proper isochron. Therefore the normal isochron diagram is used to calculate an age. Figure 31 shows two normal isochrons drawn for JI 2-2 K-feldspar, one for the first six measurements (isochron 1), and one for the last seven measurements (isochron 2). This results in an age envelope of 237.33 ± 22.14 Ma for isochron 1 and 353.40 ± 14.62 Ma for isochron 2 which are thought to be the extremities, with the real age in between. An average of 295.37 ± 15 Ma is used as best estimate.

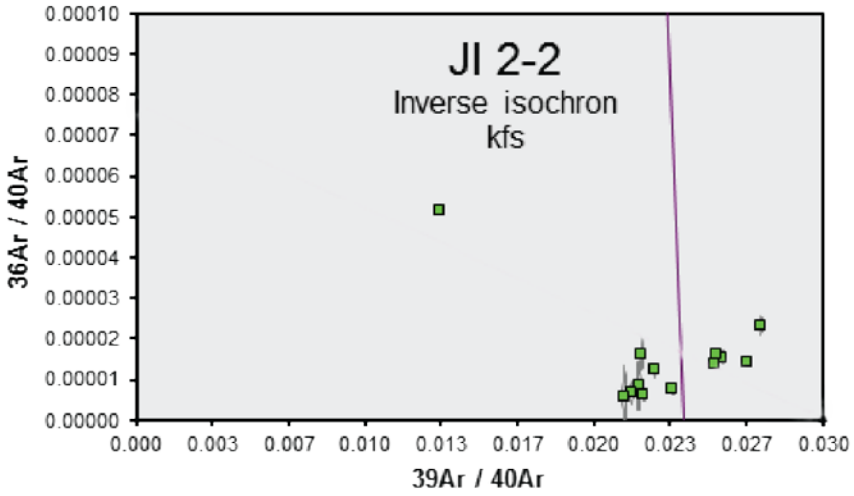

Figure 30. Inverse isochron diagram of kfs for JI 2-2. The measurements show a large spread so no decent inverse isochron could be drawn.

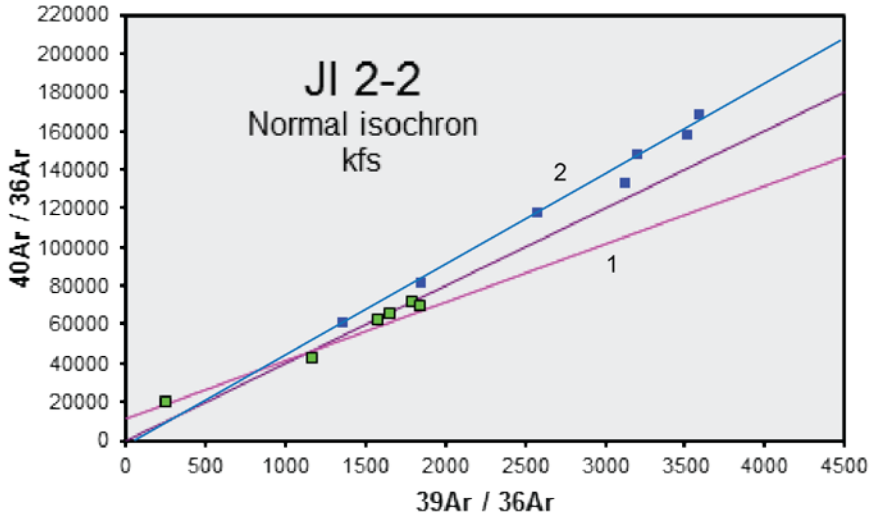

Figure 31. Normal isochron diagram of kfs for JI 2-2. Two isochrons can be drawn through respectively the first six (isochron 1, green dots) and last seven (isochron 2, blue dots) heating steps resulting in an age envelope.

5.1.3. Location 4

From location 4, which is situated roughly in the middle of the entire research area, five samples were sampled. Four of these samples, including a gneiss (JI 4-2), amphibolite (JI 4-3), mylonized gneiss (JI 4-5) and a granite (JI 4-7) are dated. For amphibolite JI 4-6 no ages were determined. Figure 32 shows the stepwise heating age spectra for hornblende, biotite and K-feldspar. All spectra for hornblende and K-feldspar show a disturbed pattern coming from excess argon. However, biotite does show nice plateau ages. A more detailed explanation is given per sample below.

Biotite in JI 4-2 gives a plateau age of 307.60 ± 1.64 Ma. Although the inverse isochron diagram does show a scatter of the measurements, the isochron still agrees with the plateau age. The age spectrum does show a slight climbing staircase pattern with a lowest age of 304.85 ± 1.02 Ma. As this age does not differ within error from the plateau age, it is thought to be the moment at which the system was actually closed.

K-feldspar in JI 4-2 shows a disturbed age spectrum (Figure 32) and clear evidence for excess argon in the inverse isochron diagram (Figure 33). Two isochrons were drawn representing the first four measurements (isochron 1) and the last eight measurements (isochron 2). These give ages of 285.54 ± 11.83 Ma and 199.86 ± 43.37 Ma respectively. The lowest two age steps at the end of the age spectrum give an age of 269.95 ± 5.93 Ma. These lowest steps are supposed to be an upper estimate of the real K-feldspar age as excess argon results in overestimation of the age. As the outer part of the mineral (and thus the first heating steps) should represent younger ages than the inside, and because the lowest age steps of the spectrum lay below the inverse isochron age of isochron 1, the isochron 2 age is used as a best estimate.

Hornblende in JI 4-3 shows a disturbed age spectrum (Figure 32) due to excess argon. The lowest steps at the end of the spectrum with an age of 425.66 ± 4.81 Ma are thought to represent an upper limit of the hornblende age. For the inverse isochron diagram, again two isochrons could be drawn; one for the first six heating steps and one for the last seven steps (Figure 34). Ages of these isochrons are 450.27 ± 22.60 Ma and 403.25 ± 17.89 Ma respectively. The lowest of these ages is thought to be the closest approximation of reality and listed as best estimate.

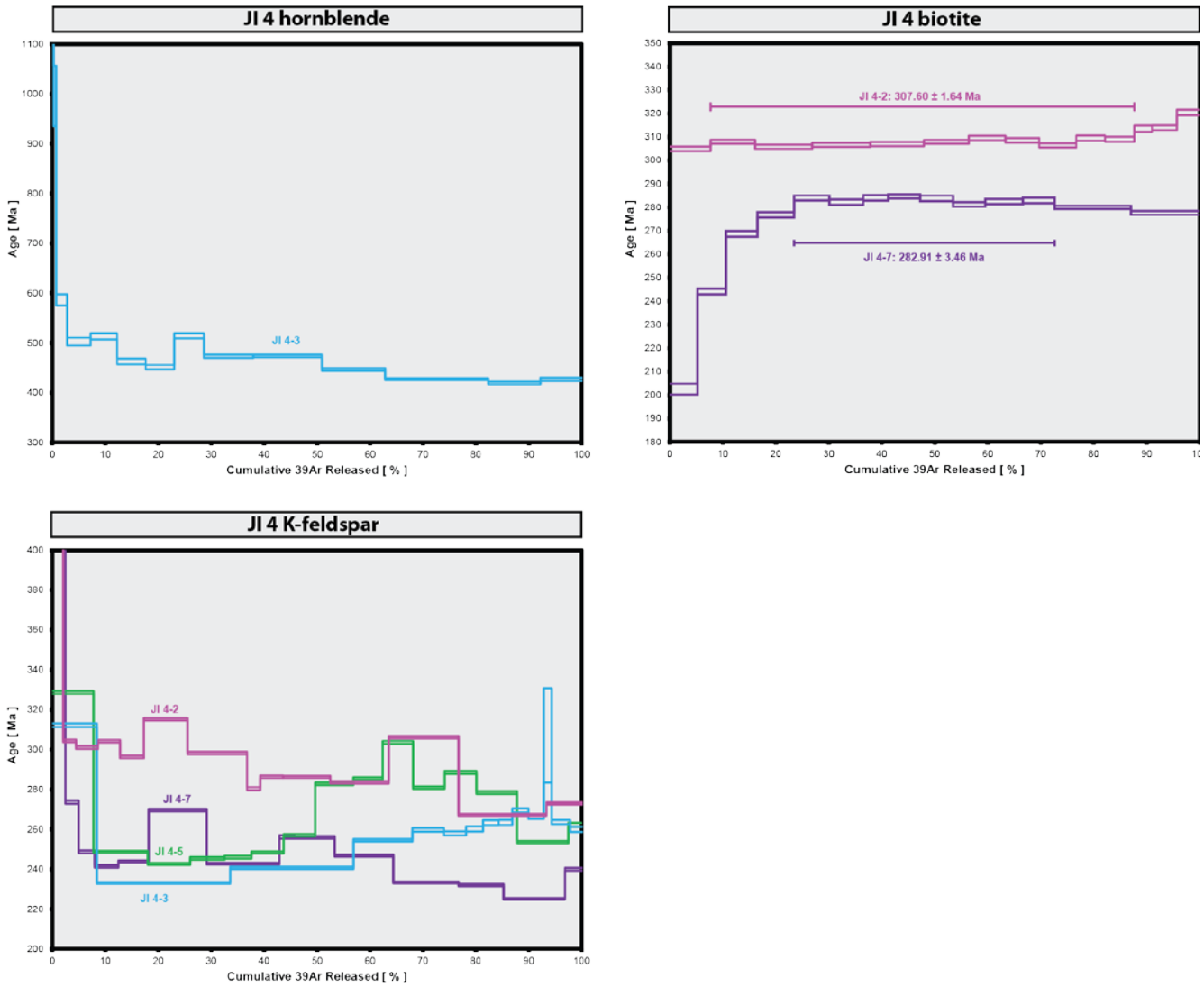

Figure 32. Stepwise heating age spectra for hornblende, biotite and K-feldspar measurements on location 4. Note the difference in vertical scale. All hornblende and K-feldspar age spectra show a disturbed pattern coming from excess argon. Biotite shows nice plateau ages and partial resetting of JI 4-7 resulting in a staircase pattern.

K-feldspar in JI 4-3 shows a stepwise heating spectrum with a staircase pattern at the beginning and a concave downward pattern at the end. The last ten heating steps fall along the atmospheric line in the inverse isochron (Figure 35) and thus no presence of excess argon is assumed. Therefore the inverse isochron age of these steps is assumed to be the best estimate with an age of 263.43 ± 9.97 Ma. The staircase pattern in the first heating steps is interpreted as a partial resetting of the sample. The lowest age step of 233.26 ± 0.51 Ma is thought to represent an upper constraint for the onset of this resetting.

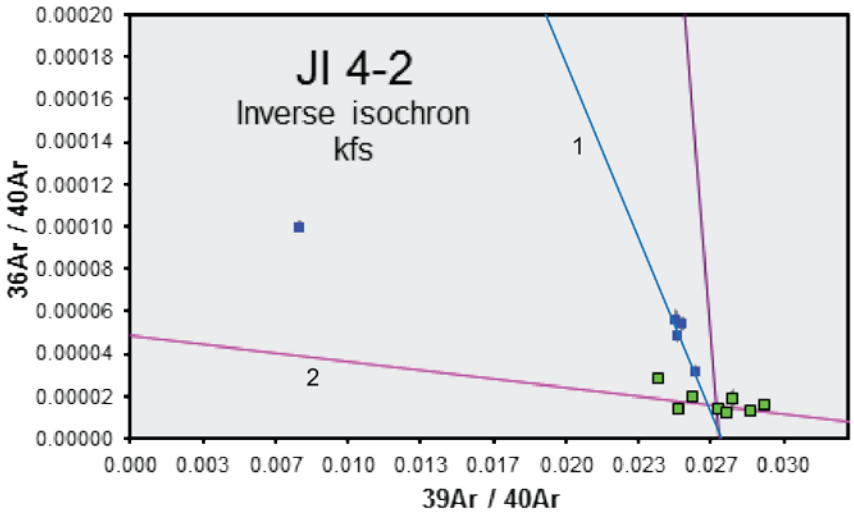

Figure 33. Inverse isochron diagram for K-feldspar in JI 4-2. An isochron for the first four (isochron 1, blue dots) and the last eight (isochron 2, green dots) measurements was drawn.

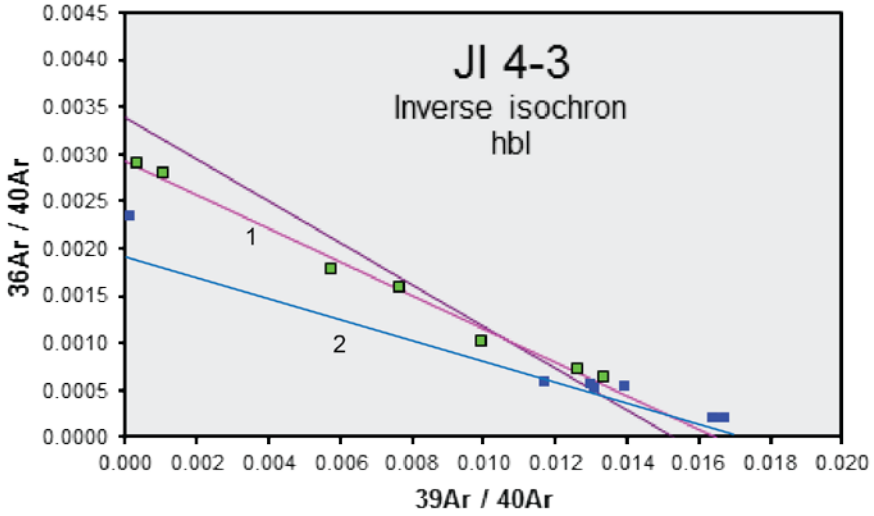

Figure 34. Inverse isochron diagram for hornblende in JI 4-3. An isochron for the first six (isochron 1, green dots) and the last seven (isochron 2, blue dots) measurements was drawn.

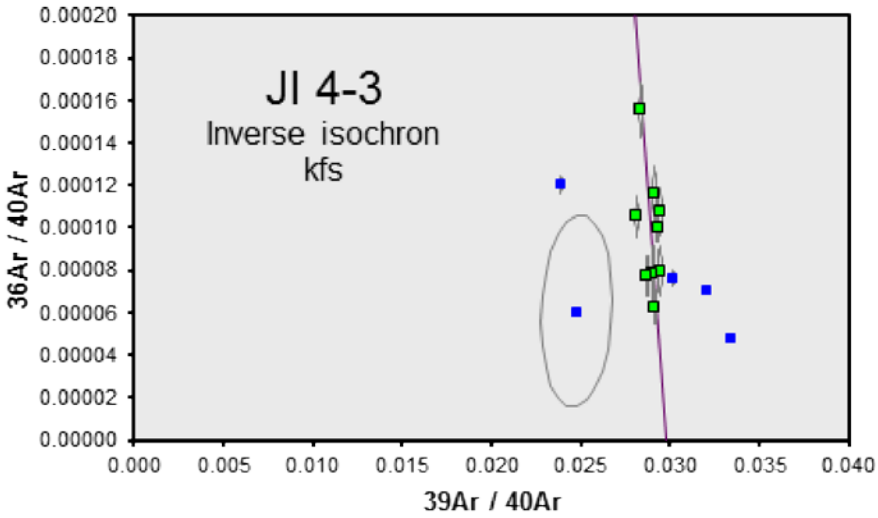

Figure 35. Inverse isochron diagram for K-feldspar in JI 4-3. The last ten heating steps follow the atmospheric isochron in purple.

The K-feldspar age spectrum of JI 4-5 is also disturbed by the presence of excess argon (Figure 32). On the inverse isochron diagram the measurements show a too large scatter to define a decent isochron. Therefore the normal isochron diagram is used. Figure 36 shows the normal isochron diagram with two isochrons drawn for the first seven measurements (isochron 1) and the next five measurements (isochron 2). Ages of these isochrons are 241.35 ± 15.39 Ma and 309.34 ± 16.19 Ma respectively. These ages are thought to represent a cooling age and a partial resetting age as the lowest step of 242.32 ± 0.56 Ma agrees very well with the first isochron age. Therefore the cooling age of 309.34 ± 16.19 Ma is thought to represent the best estimate.

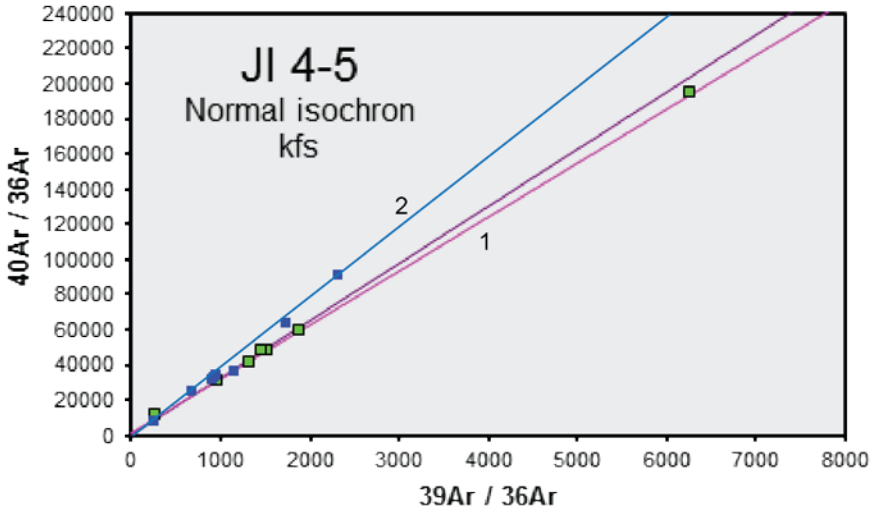

Figure 36. Normal isochron diagram for K-feldspar in JI 4-5. An isochron for the first seven (isochron 1, green dots) and the next five (isochron 2, blue dots) measurements was drawn.

Biotite in JI 4-7 shows a nice plateau age of 282.91 ± 3.46 Ma (Figure 32). No excess argon is observed in these plateau steps. The beginning of the age spectrum shows a climbing staircase pattern with a lowest age of 202.32 ± 2.30 Ma which is interpreted as the moment of partial resetting of the system.

K-feldspar in JI 4-7 again shows a disturbed age pattern (Figure 32) and strong evidence for excess argon in the inverse isochron diagram (Figure 37). The lowest age step at the end of the heating steps is 225.15 ± 0.45 Ma, which is assumed to be an upper limit of the correct age. An inverse isochron age of 207.44 ± 10.12 Ma was determined for the last part of the heating spectrum and assumed to be the best estimate.

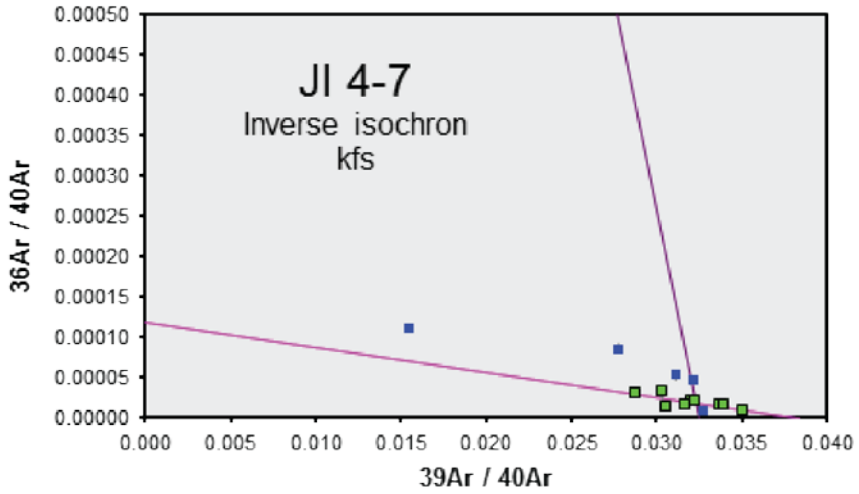

Figure 37. Inverse isochron diagram of kfs for JI 4-7. The last nine heating steps excluding the very last are used for the isochron calculation.

5.1.4. Location 5

On the easternmost location a total of five rocks, three granites, JI 5-1, JI 5-2 and JI 5-7, a hornblende hornfels, JI 5-3 and a gabbro, JI 5-5 were sampled and dated. Step heating age spectra are shown in Figure 38. Note the difference in vertical scale. All K-feldspar spectra are disturbed due to inheritance of excess ^{40}Ar. Biotite spectra do show nice plateaus and staircase patterns due to partial resetting. Age spectra of K-feldspar of samples JI 5-1, JI 5-2 and JI 5-5 inherit a first age step off scale of the diagram. However as there is no scientific meaning to the exact age of this step the diagrams scale was adjusted such that details in the remaining spectra could still be observed.

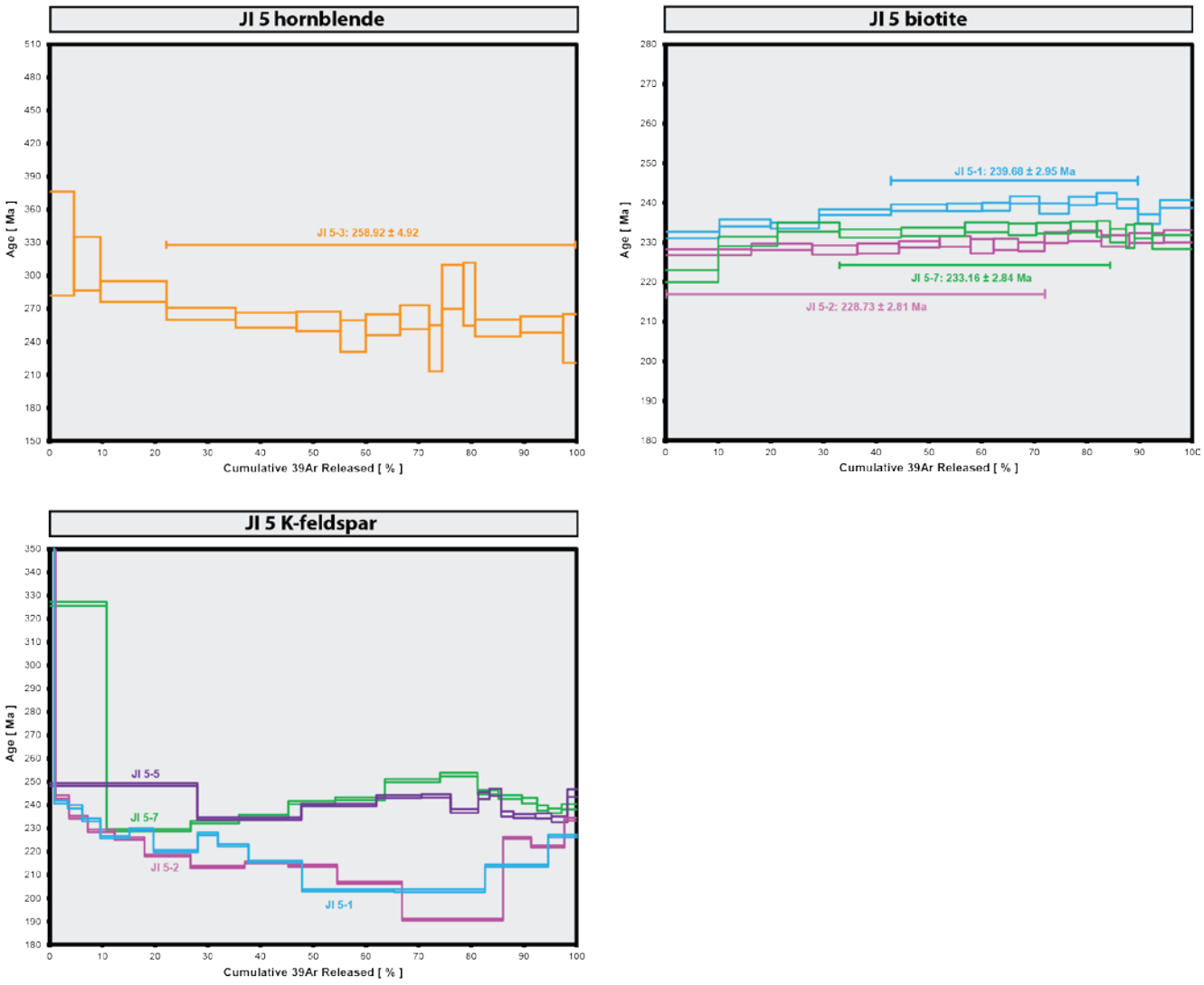

Figure 38. Stepwise heating age spectra for hornblende, biotite and K-feldspar measurements on location 5. Note the difference in vertical scale. All K-feldspar age spectra show a disturbed pattern coming from excess argon. Biotite shows nice plateau ages and partial resetting in a staircase pattern.

Biotite in JI 5-1 shows a clear plateau of 239.30 ± 2.97 Ma (Figure 38). However, from the inverse isochron it becomes clear that excess ^{40}Ar is inherited (Figure 39). Therefore the inverse isochron age of 235.75 ± 3.89 Ma is used as a best estimate. The step heating age spectrum does show a climbing staircase pattern with a lowest step of 231.93 ± 0.80 Ma. As excess argon results in overestimating the age, this age is thought to represent an upper limit of the moment of partial resetting.

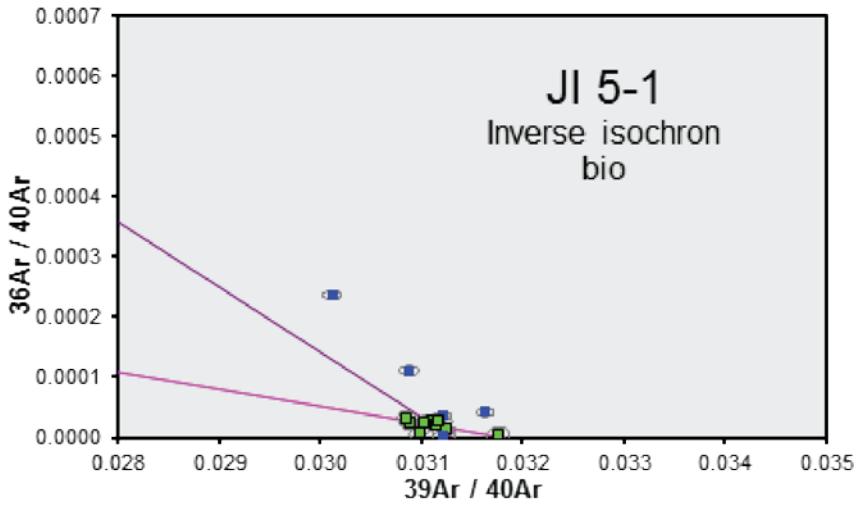

Figure 39. Inverse isochron diagram of bio for JI 5-1. Green dots are used for the isochron calculation and represent the apparent age plateau heating steps.

K-feldspar in JI 5-1 shows clear evidence for excess argon in both the age spectrum (Figure 38) and the inverse isochron diagram (Figure 40). Two inverse isochrons were defined, one for the first seven measurements (isochron 1) and one for the last four measurements (isochron 2). Ages for these isochrons are 215.11 ± 5.48 Ma and 233.20 ± 15.72 Ma respectively. However, as the lowest steps of the age spectrum of 203.02 ± 1.02 Ma are lower than the inverse isochron ages, this age is used as the best estimate.

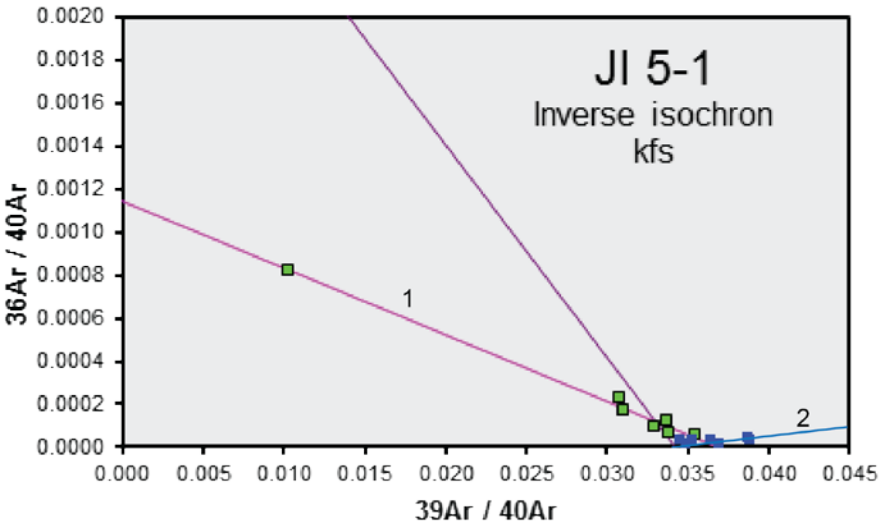

Figure 40. Inverse isochron diagram for kfs in JI 5-1. An isochron for the first seven (isochron 1, green dots) and the last four (isochron 2, blue dots) measurements was drawn.

Biotite in JI 5-2 shows a clear plateau with an age of 228.73 ± 2.81 Ma (Figure 38). The heating steps included in this plateau do not show evidence for excess argon. Also no partial resetting is observed.

K-feldspar in JI 5-2 shows clear evidence of excess argon in both the age spectrum (Figure 38) and the inverse isochron diagram (Figure 41). An inverse isochron was drawn based upon the first part of the heating steps resulting in an age of 190.00 ± 11.25 Ma. The lowest age step of the spectrum with an age of 190.52 ± 0.38 Ma agrees very well with the inverse isochron age and is therefore thought to be the best estimate.

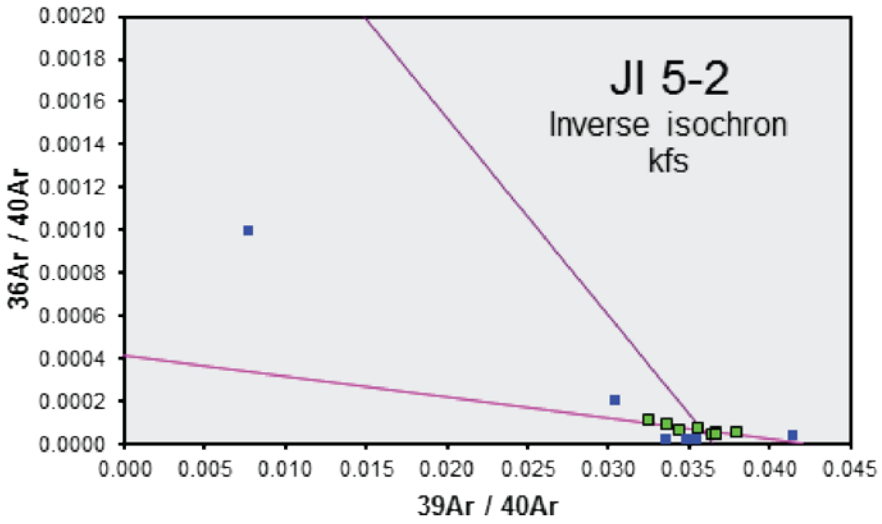

Figure 41. Inverse isochron diagram of kfs for JI 5-2. Green dots are used for the isochron calculation and represent the first part of the heating steps.

Hornblende in JI 5-3 shows a very clear age spectrum of excess argon inheritance with higher ages in the beginning, lowering towards a plateau with an age of 258.92 ± 4.92 Ma (Figure 38). A small amount of inherited excess argon in the plateau steps is evident from the inverse isochron diagram (Figure 42). An inverse isochron with an age of 252.58 ± 8.87 Ma was drawn for the plateau age steps and used as the best estimate.

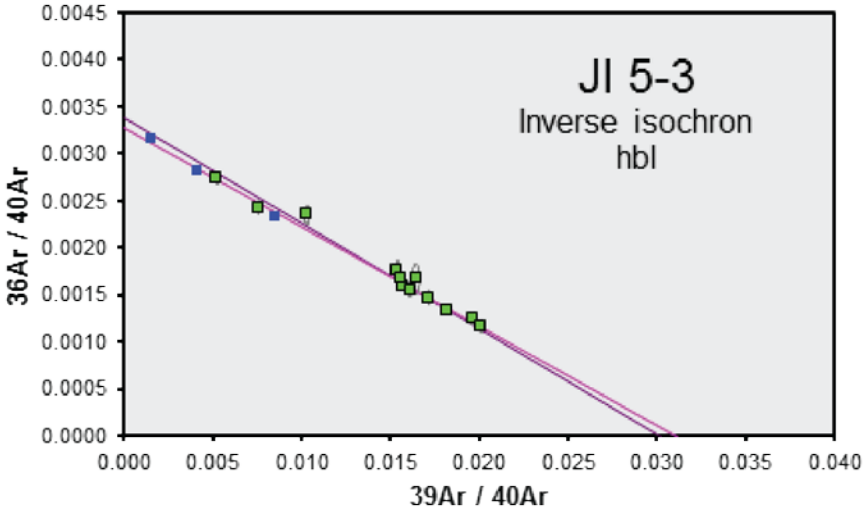

Figure 42. Inverse isochron diagram of hbl for JI 5-3. Green dots are used for the isochron calculation and represent the age plateau steps.

K-feldspar in JI 5-5 shows clear evidence for excess argon. The different steps of the age spectrum all vary around the same age (Figure 38). A total fusion age of 241.37 ± 1.15 Ma with a minimum of 233.76 ± 1.19 Ma and maximum of 248.77 ± 0.54 Ma was determined. As the inverse isochron diagram shows a large scatter of the measurements (Figure 43), no isochron could be drawn and the total fusion age is used as a best estimate of the upper limit of the K-feldspar age.

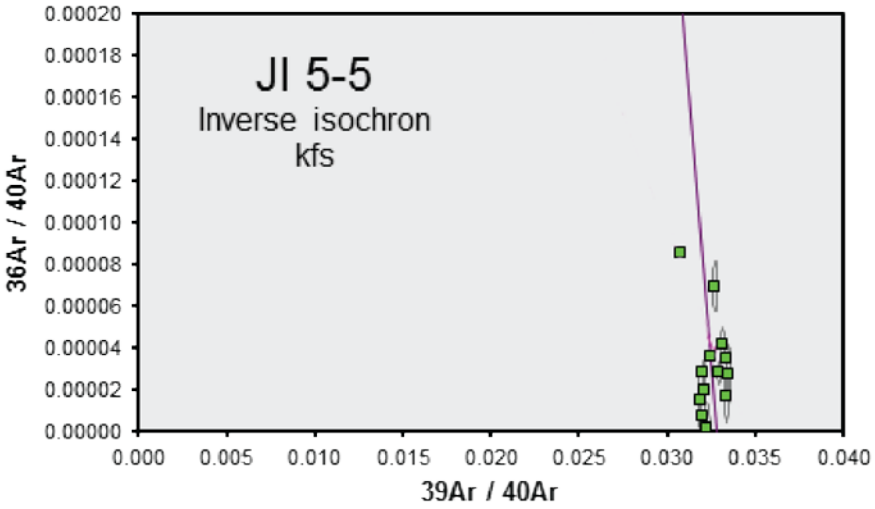

Figure 43. Inverse isochron diagram of kfs for JI 5-5. The large scatter of measurements makes it impossible to determine an isochron.

Biotite in JI 5-7 shows a clear plateau with an age of 233.26 ± 2.84 Ma (Figure 38) and no evidence for excess argon. The first three heating steps show a climbing staircase pattern with a lowest age of 221.48 ± 1.54 Ma, which is thought to be the timing of partial resetting.

K-feldspar in JI 5-7 shows a step heating spectrum of a climbing staircase, followed by a convex downward pattern (Figure 38). For these measurements two inverse isochrons could be drawn (Figure 44). An inverse isochron of the climbing part (isochron 1) results in an age of 193.91 ± 20.33 Ma, whereas an inverse isochron of the downward pattern (isochron 2) results in an age of 242.72 ± 5.38 Ma. The latter follows the atmospheric argon line and thus no excess argon is present. Therefore this is thought to represent the cooling age and is used as best estimate. The staircase pattern is thought to represent a partial resetting phase. The lowest age step in the beginning has an age of 229.26 ± 0.53 Ma, which is older than the inverse isochron age of the staircase. Therefore the inverse isochron age is thought to represent the moment of partial resetting at 193.91 ± 20.33 Ma.

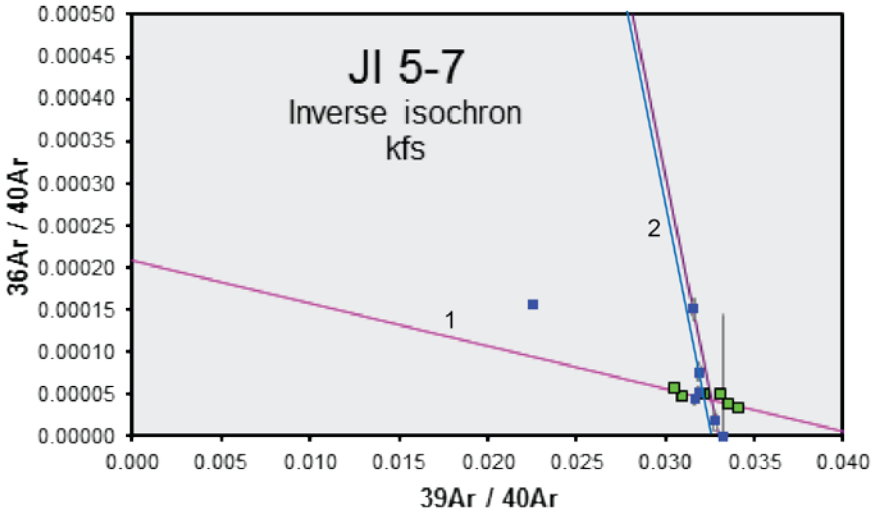

Figure 44. Inverse isochron diagram of kfs for JI 5-7. Two inverse isochrons were drawn, one for the climbing staircase part of the age spectrum (isochron 1, green dots), and one for the concave downward pattern of the age spectrum (isochron 2, blue dots).

5.2. Summary

A summary of the above described ages is shown in Table 8.

Sample	Mineral	Cooling age (Ma)	Resetting age (Ma)	Average age (Ma)
JI 1-1	hbl	184.28 ± 58.74		
JI 1-3	kfs	184.26 ± 7.52		
JI 1-4	hbl	273.92 ± 4.26		
	kfs	217.46 ± 10.94		
JI 2-2	mica	418.15 ± 2.45		
	kfs	353.40 ± 14.62 – 237.33 ± 22.14		295.37 ± 15
JI 4-2	bio	307.60 ± 1.64	304.85 ± 1.02	
	kfs	269.95 ± 5.93	199.86 ± 43.37	
JI 4-3	hbl	403.25 ± 17.89		
	kfs	263.43 ± 9.97	233.26 ± 0.51	
JI 4-5	kfs	309.34 ± 16.19	241.35 ± 15.39	
JI 4-7	bio	282.91 ± 3.46	202.32 ± 2.30	
	kfs	207.44 ± 10.12		
JI 5-1	bio	235.75 ± 3.89	231.93 ± 0.80	
	kfs	233.20 ± 15.72	203.02 ± 1.02	
JI 5-2	bio	228.73 ± 2.81		
	kfs	190.00 ± 11.25		
JI 5-3	hbl	252.58 ± 8.87		
JI 5-5	kfs	241.37 ± 1.15		
JI 5-7	bio	233.26 ± 2.84	221.48 ± 1.54	
	kfs	229.26 ± 0.53	193.91 ± 20.33	

Table 8. Summary of the described ages. Resetting ages are an upper estimate.

5.3. Single grain results

For the single grain measurements, thirty replicates of biotite in samples JI 4-2, JI 4-7 and JI 5-1 were fused in a single event with a laser intensity of 80 W, resulting in age ranges as shown in Figure 45 and Figure 46. These samples were chosen based on amount of biotite grains available and correspond to one gneiss (JI 4-2) and two granites (JI 4-7 and JI 5-1). Figure 45 shows the age per grain measurement for each sample. Error bars display a 2σ error. Colours represent separate age groups that either show a normal distribution within the group or are outliers. Group differentiation is based on visual grouping. Figure 46 shows a probability density curve of the age distribution. Age groups in Figure 45 agree with the peaks of probable ages in Figure 46.

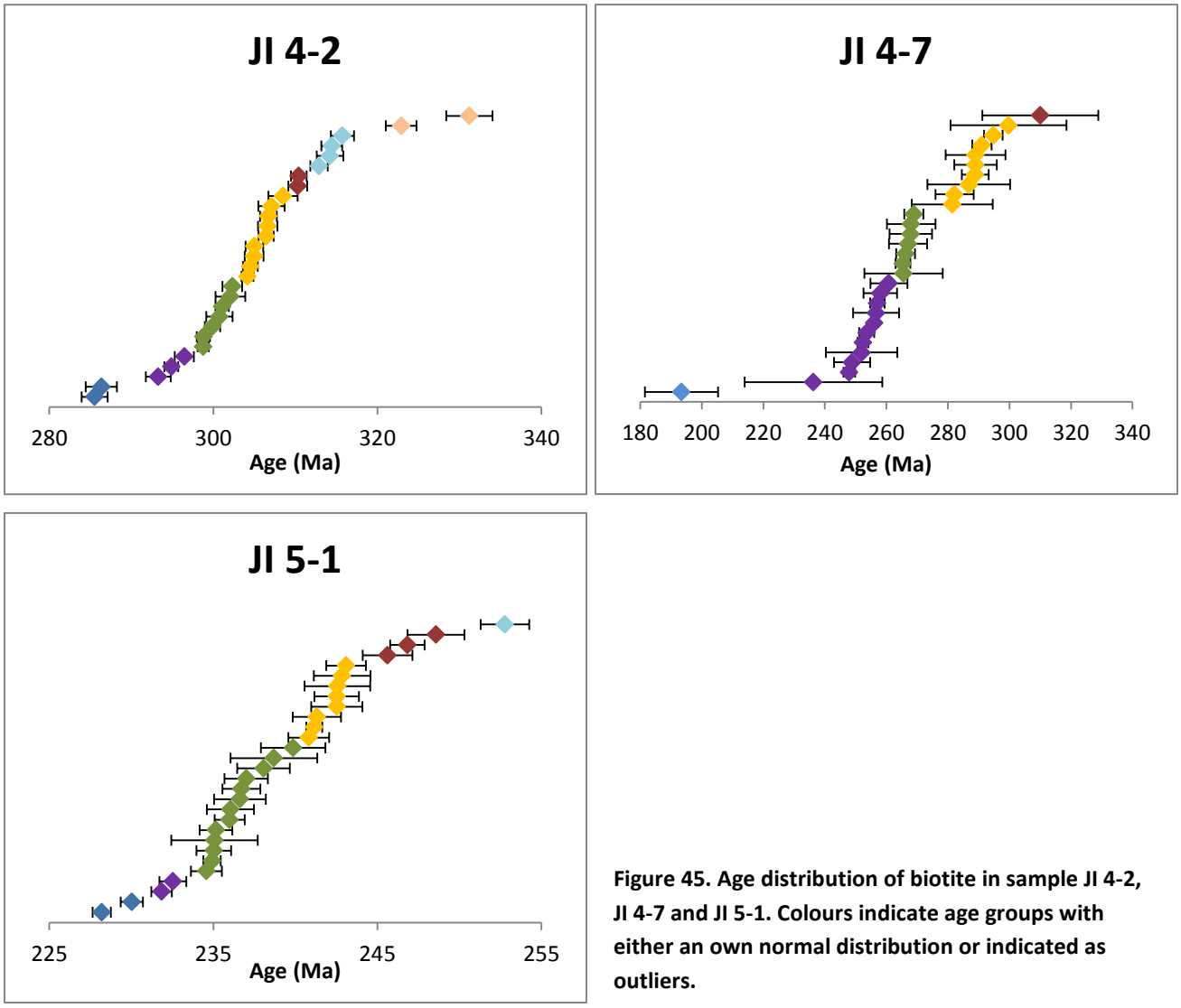

Figure 45. Age distribution of biotite in sample JI 4-2, JI 4-7 and JI 5-1. Colours indicate age groups with either an own normal distribution or indicated as outliers.

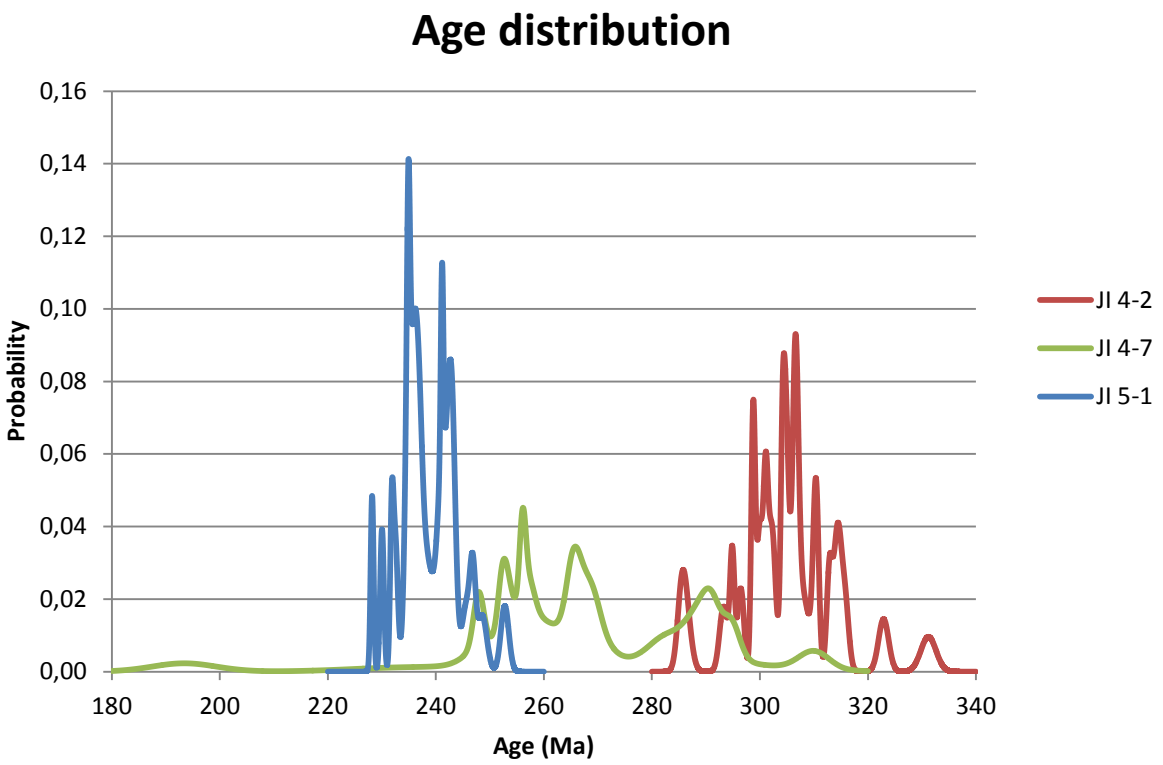

Figure 46. Probability density distribution of single grain ages for biotite in samples JI 4-2, JI 4-7 and JI 5-1. Different age peaks correspond with the age groups as indicated in Figure 45.

For sample JI 4-2 the age range spreads over approximately 45 Ma, from 285.52 ± 1.59 Ma to 331.21 ± 2.82 Ma. On the high- and low end of the range single measurements are present. In the core of the measurements, we can distinguish at least four age groups indicated in Figure 45. Within error, these groups show a similar age with averages from low to high of 300.52 ± 3.14 Ma (green), 305.99 ± 3.56 Ma (orange), 310.35 ± 1.49 Ma (red) and 314.31 ± 2.71 Ma (blue). For sample JI 4-7 the range spreads over almost 120 Ma, from 193.41 ± 11.91 Ma to 310.01 ± 5.55 Ma. On the low end, an extreme outlier is present which deviates more than 40 Ma from the next measurements. Also on the high end an outlier occurs. The core of the measurements can be divided into three different age groups with average ages from low to high of 252.69 ± 29.63 Ma (purple), 267.01 ± 18.37 Ma (green) and 289.19 ± 30.32 Ma (yellow). Sample JI 5-1 shows an age range of almost 25 Ma from 228.20 ± 0.55 Ma to 252.76 ± 1.48 Ma. On both the high and low end of the range four unique measurements occur. The core of the measurements can again be divided into two groups with average ages from low to high of 236.44 ± 1.62 Ma (green) and 242.10 ± 0.87 Ma (yellow). Normal and inverse isochron diagrams of these measurements are shown in Appendix V. The blue dots indicate measurements with relative excess ^{40}Ar. This could be either due to excess ^{40}Ar caused by partial overpressure during exhumation, or loss of ^{39}Ar due to recoil effects during irradiation (Ching-Hua and Onstott, 1989; Hess and Lippolt, 1986). The relative excess ^{40}Ar measurements appear all to be present in the higher age ranges of all three samples, causing an overestimation of the real age. This effect starts to show up on measurements in JI 4-2 with an age over 304.15 ± 0.73 Ma, in JI 4-7 with an age over 265.35 ± 4.98 Ma and in JI 5-1 with an age over 238.04 ± 1.15 Ma. On the low-age side, there is evidence for relative excess ^{36}Ar. There is no clear evidence present for excess ^{40}Ar in the lower age range and these ages are thus more reliable.

6. Thermodynamic modelling results

In order to constrain the metamorphic evolution of the rocks addressed in this study, thermodynamic modelling was carried out using Perple_X Connolly (1990) version 6.6.8. (2012). As described in the methodology (Chapter 3), solution models for each of the minerals in a sample are used. These models describe how elements are built into the crystal lattice and the chemistry dependence on pressure and temperature. The models used in this study were chosen for various reasons as described in Paragraph 6.1 and listed in Table 9.

The findings of each rock sample are discussed in two paragraphs; first the model outcomes are described and in a second paragraph discrepancies between the modelled and observed results are discussed. Endmember mineral abbreviations used in this study follow Holland and Powell (1998, 2002) and are listed in Table 10.

6.1. Solution models

All models with the suffix (stx), (stx7) or (stx8) need a specific thermodynamic data file, which is known to give problems when using other solution models without this addition. Therefore these models were dismissed a priori. For consistency within the study, the same solution models are used in each sample, unless the mineral composition and chemistry did require a specifically different model.

For amphibole, GlTrTsPg is used as it is preferable for use over large pressure ranges due to its limited computational time (solution.dat file, Perple_X package). Other available models for amphibole are Amph(DPW) and cAmph(DP). Amph(DPW) is a more extensive model which takes more endmembers into account and therefore requires much more computational time. A test run was made for sample JI 2-1 to compare the difference between GlTrTsPg and Amph(DPW). It appeared that the shape of stability fields varies greatly among the two models, but the assigned stability field for both tests which compares to the stable mineral assemblage in JI 2-1 lies in the same P-T range. A test run with cAmph(DP) was aborted after 18 hours because of the lengthy computational time, making this model unpractical. Although Amph(DPW) could have been used for the models with a relatively small pressure range, in the interest of consistency, GlTrTsPg was used for all models except JI 4-6. For this sample, GlTrTsPg resulted in stability of amphibole up to unrealistically high temperatures. Therefore Amph(DPW) was used instead.

The Bio(TCC) model was used for biotite as it provides better constraints on the Ti substitution than Bio(HP), which is the other model available. Advantages of Bio(HP) are the extension to cover Mn-solutions, but because Mn is not incorporated in many of the other solution models considered, MnO was not considered in the calculations and therefore the choice for Bio(TCC) was preferable.

For chlorite, solution models Chl(LWV) and its extended version Chl(HP) with a wider range of endmembers were available. In order to reduce computational time, and because there was no obvious reason to choose Chl(HP) instead, Chl(LWV) was used.

The Cpx(l) model was chosen for clinopyroxene. A test run with Cpx(h), the other available model, resulted in unrealistic stability of this phase throughout the entire P-T range whereas Cpx(l) worked fine and only showed stability at P-T conditions where this would be expected. Therefore Cpx(l) was chosen to use in this study.

For feldspar, models for mixtures of either all three, or two endmembers are available. In case both plagioclase and K-feldspar are present in the sample, it was chosen to use the three-endmember model 'feldspar', which is the most straightforward model. For a reasonably simple mineral system such as feldspar this is assumed to be the best option (solution.dat file, Perple_X package). In case a sample

contains only plagioclase, the model Pl(h) was used, being the only plagioclase model available. K-feldspar did not occur on its own, so no solution model for these minerals was used.

For both garnet and orthopyroxene, only Gt(HP) and Opx(HP) were available as all other models had the suffix (stx), (stx7) or (stx8) and could thus not be used together with the models for the other minerals requiring a different thermodynamic data file.

Most models for white mica are focussed on phengite. However, as the samples in this study do not contain phengite, these models were dismissed. The models with the broadest chemical composition are Mica(CHA) and Mica(CHA1). The first does not include Ti substitution whereas the latter does. As Ti does not make out an important part of most white mica analysed in this study, Mica(CHA) was used. Only for JI 2-2, where using Mica(CHA) resulted in excessive stability of rutile, Mica(CHA1) was used.

For both epidote and ilmenite only one solution model was available and therefore Ep(HP) and IlHm(A) were used to model these minerals respectively.

Target mineral	Solution model	Reference
Amphibole	GlTrTsPg	Wei and Powell (2003)
	Amph(DPW)	Dale et al. (2005)
Biotite	Bio(TCC)	Tajčmanová et al. (2009)
Chlorite	Chl(LWV)	Holland and Powell (1998b) edited by Wagner (2012)
Clinopyroxene	Cpx(l)	Gasparik (1984) and (1985)
Epidote – Zoisite	Ep(HP)	Holland and Powell (1998, 2002)
Feldspar	feldspar	Fuhrman and Lindsley (1988)
Garnet	Gt(HP)	Holland and Powell (1998, 2002)
Ilmenite	IlHm(A)	Andersen and Lindsley (1988)
Orthopyroxene	Opx(HP)	Holland and Powell (1996)
Plagioclase	Pl(h)	Newton et al. (1980)
White mica	Mica(CHA)	Coggon and Holland (2002)
White mica	Mica(CHA1)	Auzanneau et al. (2010)

Table 9. Solution models used in this study.

Abbreviation	Mineral	Abbreviation	Mineral
ab	albite	ilm	ilmenite
acti	actinolite	kfs	K-feldspar
amp	amphibole	law	lawsonite
and	andalusite	Mg-hbl	magnesio-hornblende
ank	ankerite	mic	microcline
cc	calcite	mica	white mica
cel	celadonite	mt	magnetite
clin	clinochlore	ol	olivine
cpx	clinopyroxene	phl	phlogopite
crd	cordierite	pl	plagioclase
cz	clinozoisite	prl	pyrophyllite
di	diopsite	q	quartz
dol	dolomite	ri	richterite
fa	fayalite	ru	rutile
Fe-hbl	ferro-hornblende	sid	siderite
Fe-ts	ferro-tschermakite	sill	sillimanite
fosm	Fe-osumilite	sph	sphene (titanite)
gt	garnet	stlp	stilpnomelane
Hbl	hornblende	ts	tschermakite
hed	hedenbergite	vsv	vesuvianite
hem	hematite	wrk	wairakite
herc	hercynite	zo	zoisite

Table 10. Mineral abbreviations as used in this study.

6.2. Amphibolite JI 1-1 model

Sample JI 1-1 shows a mineral assemblage of amp + bio + ep + zo/cz + pl + sph + cc + q. As described in detail in the thin section descriptions (Appendix I), calcite rich lumps are present which are being replaced by clayminerals, ep, zo/cz, cc and amp. Within the amphibole hints of instability in some grains were observed whereas others looked very fresh. From EMP measurements on single grains of amphibole as described in Paragraph 4.3.3 a trend in chemistry from actinolite to ferro-tschermakite is observed.

Solution models used for this sample are: GlTrTsPg, Ep(HP), feldspar, Bio(TCC), Chl(LWV) and Mica(CHA). Model runs are calculated for a FeO + TiO_2 + CaO + K_2O + MgO + Na_2O + SiO_2 + Al_2O_3 + O_2 + H_2O + CO_2 system with SiO_2 as a saturated component and H_2O + CO_2 as a saturated fluid. As none of the solution models includes MnO in the calculations, this oxide is left out of consideration. As this model includes P, T, O_2 and CO_2 as variables, first the O_2 concentration was defined, setting CO_2 to 0. After that, the desired CO_2 concentration was modelled using a fixed O_2 concentration as found in the previous step (see below for a detailed description). The field of stability of the mineral assemblage of this rock fell around the same P-T conditions for both cases, excluding and including CO_2 concentration, although the shape of the stability fields varied.

As it is not possible in Perple_X to model in 3D (eg. P-T-O_2 or P-T-CO_2), seven P-T pseudosections for varying O_2 concentrations were made to define the right amount of O_2 to produce 5% epidote. The right concentration of O_2 for the stability of sample JI 1-1 was chosen based on intersection of modal abundances of minerals present in the sample. Subsequently five pseudosections for varying CO_2 concentrations and a fixed O_2 concentration as found before were made to define the right amount of CO_2 to produce 5% calcite. The right H_2O-CO_2 fluid mixture was also chosen based on intersection of modal abundances of the minerals present in the sample and on chemical compositional isopleths of amphibole and plagioclase. Pseudosections including isopleths for determination of both the O_2 and CO_2 concentration are shown in Appendix VI, Figure 120 till Figure 123 .

Figure 47 shows the pseudosections for sample JI 1-1 in the P-T range of 1-20 kbar and 300-800°C, with a O_2 concentration of 0.04 wt% and a H_2O-CO_2 fluid mixture of 0.7 H_2O + 0.3 CO_2. The stability field which matches the mineral assemblage of the rock is indicated with red in Figure 47 and contains amp +bio + ep + zo + fsp + sph + cc + q. This field ranges from 590 - >800°C and 8 - >19.1 kbar. No upper constraint on this field was modelled as modal abundances of minerals present in the sample and compositional isopleths of these minerals all indicate stability in the lower part of the field <720°C and <11 kbar (see below for details). The mineral assemblage as modelled agrees exactly with the minerals found in the thin section.

Isopleths of modal abundances of all pertinent minerals in the sample cluster around 670-720°C and 9-10.5 kbar (Figure 48). The isopleths as shown in all figures display the average EMP measurements of the pertinent minerals in the thin section, and are tabulated in Appendix IV. If two or more populations of measurements are present, these isopleths are all shown. The stability field as indicated in Figure 47 agrees very well with modal abundances and part of the amphibole isopleths which cluster around 625-675°C and 8.6 kbar (Figure 48). As isopleths for biotite and plagioclase follow the same path and do not intersect, they are plotted as a single line which also runs through the stability field around 625°C and 8.6 kbar.

Single EMP measurements of plagioclase and amphibole are plotted onto the pseudosection as isopleth intersections in Figure 49 in case of an error smaller than 20°C and 0.75 kbar and tabulated in Appendix IV. Amphibole measurements show a very clear trend from 700°C and 9.6 kbar towards 475°C and 2.9 kbar. As only retrograde minerals remained in the sample, only the retrograde path can be determined. Peak conditions derived from these single EMP measurements are 10.9 kbar and 730°C represent the minimum peak conditions the rock has experienced.

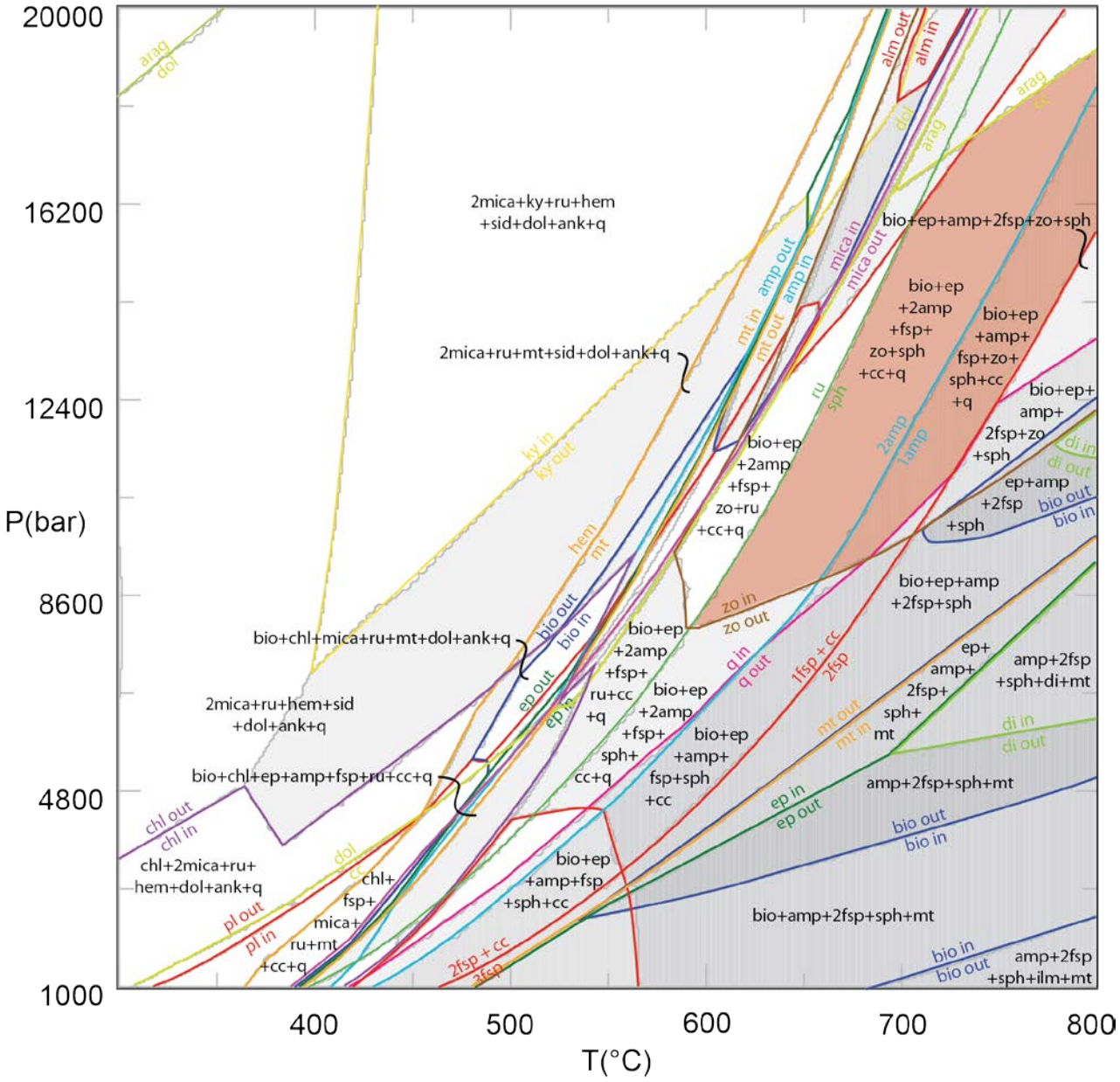

Figure 47. Pseudosection for JI 1-1 with O_2 = 0.04 and CO_2 = 0.3. Stable mineral assemblage amp + bio + ep + zo/cz + pl + sph + cc + q is indicated with the red field. Phase boundaries are indicated with coloured lines and mineral assemblages of most fields are indicated.

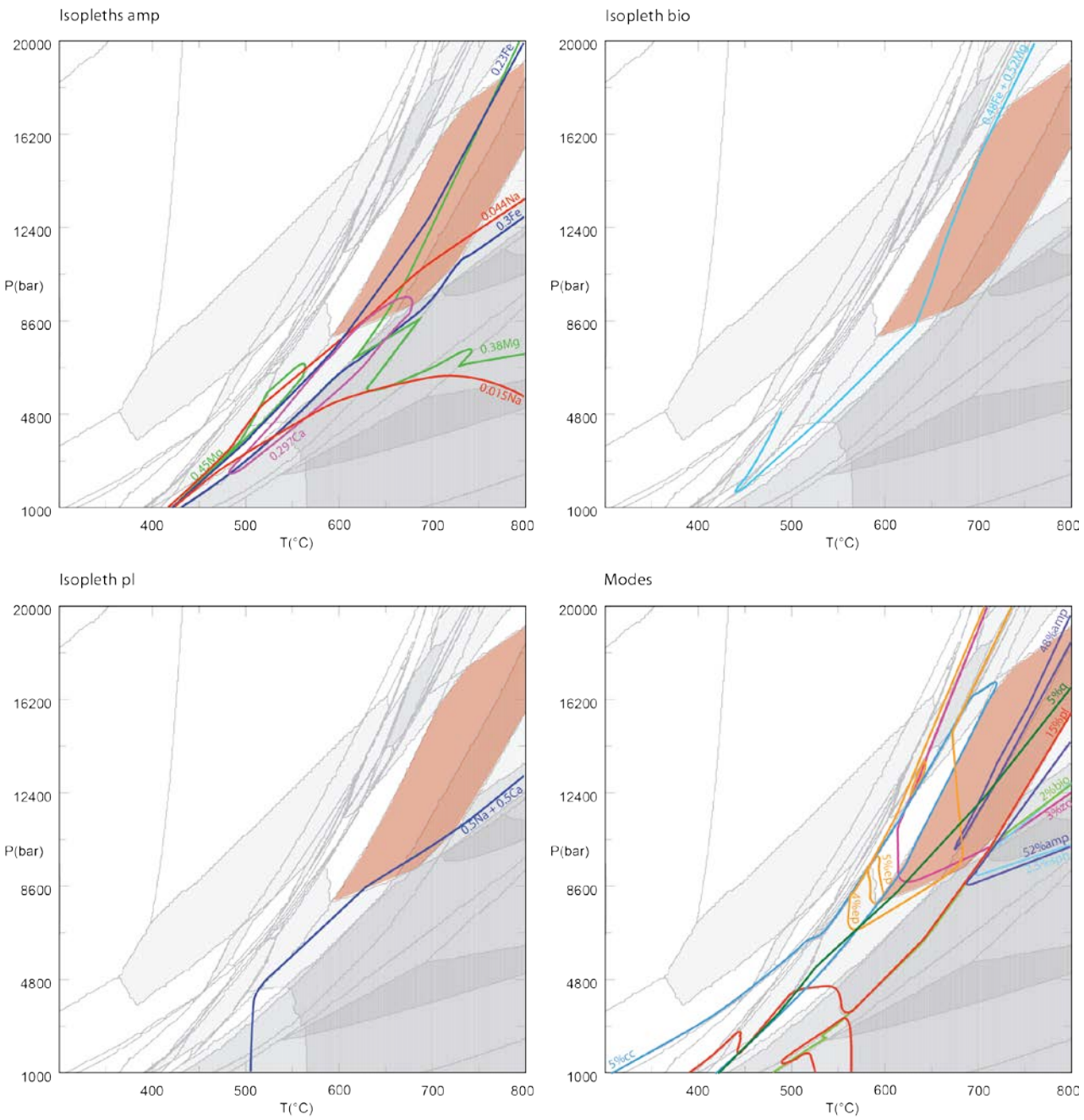

Figure 48. Isopleths of amp, bio and pl and modes of the stable mineral assemblage of JI 1-1.

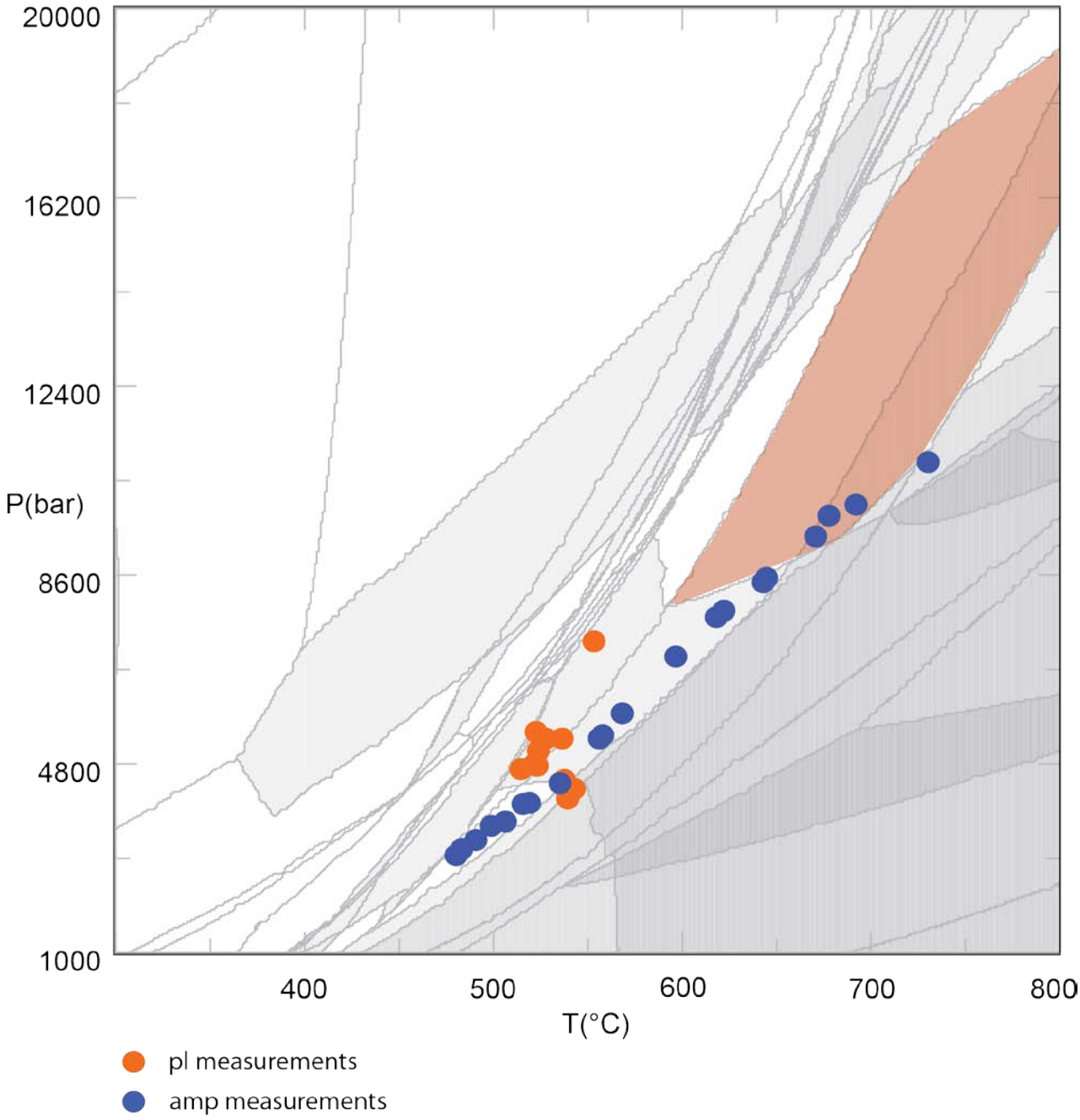

Figure 49. Separate EMP measurements plotted on the pseudosection of sample JI 1-1. Amphibole measurements show a very clear trend from 700°C and 9600 bar towards 475°C and 2900 bar.

6.2.1. JI 1-1 model discussion

For sample JI 1-1 the model had to take into account four variables, namely P, T, O_2 and CO_2. Therefore assumptions had to be made in order to run the model as only modelling in 2D is possible. The most important assumption made is that the effect of the O_2 concentration on the minerals is not influenced by a change in CO_2 – H_2O fluid mixture. Either this assumption or the assumption that the effect of CO_2 concentration on the minerals is not influenced by a change in O_2 concentration had to be made in order to specify either O_2 or CO_2 and model the other. The O_2 concentration was fixed based on the intersect of modal abundance isopleths and compositional isopleth intersections. The O_2 concentration at which a closest approximation of an intersect of all these isopleths occurred was used for further modelling. However, a true intersection was not achieved (Appendix VI, Figure 120 and Figure 121). By assuming that the effect of the O_2 concentration is not affected by a change in CO_2 concentration, a better fit for the mineral modes was not found.

A more preferable, but in the scope of this project too time consuming, option is to adopt an iterating process on this method. By first defining a 'best' O_2 concentration and using this to model the 'best' CO_2 concentration, the first step of this process is achieved. Subsequently the best CO_2 concentration can be used to again model with different O_2 concentrations and see if the best fit of isopleth intersections can be further narrowed down. By continuing this process a better fit could be found in P-T-O_2-CO_2 space.

The model outcome agrees very well with the observed mineral assemblage of amp + bio + ep + zo/cz + pl + sph + cc + q in the thin section. Chemical compositions are reasonably well reproduced in the model with compositional isopleths coming together within a 50°C and 0.2 kbar range. As assumptions are made with each step of the modelling process, this is quite a good achievement. Also mineral modes agree fairly well in the model with thin section observations. Except for amphibole, as for this mineral the maximum mode modelled does not exceed 52%, whereas the sample in reality contains 60%. The discrepancy between the two could be caused by the large trend in amphibole composition which is visible in Figure 50. As not all amphibole is still stable in the sample, unstable grains cause an overestimation from the thin

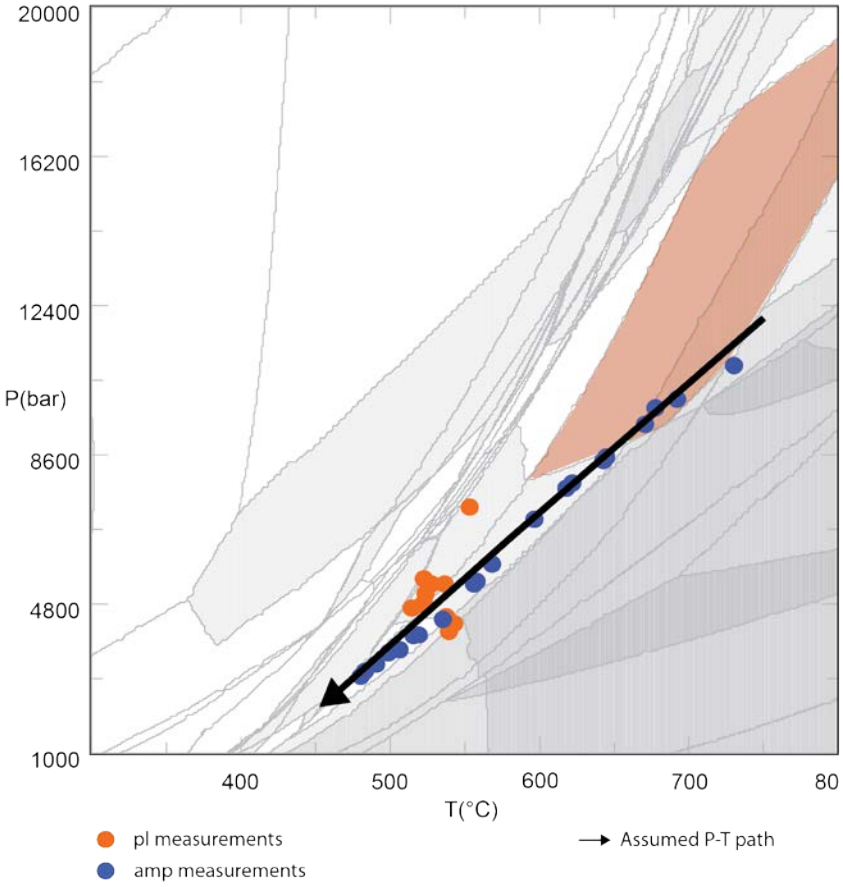

Figure 50. P-T path of sample JI 1-1. As only retrograde minerals remained in the sample, no details on the prograde path can be given.

section, causing the discrepancy.

All mineral modes cluster together within a range of 50°C, from 670 – 720°C, except for calcite which is stable in the right amounts approximately 50°C lower. 2.5% calcite would be stable in the same range as the other minerals, which is half of the amount observed in thin section. This discrepancy could be ascribed to the assumptions made to determine the O_2 and CO_2 concentrations as described above. Figure 50 shows the P-T path which is based on the stability field and single EMP measurements with minimum peak conditions of 10.9 kbar and 730°C. As shown in Figure 17, only a part of the amphibole population is dated by $^{40}Ar/^{39}Ar$ dating. This part corresponds to the amphibole above 600°C in the model, which is above the assumed closure temperature of 450 – 525°C. Therefore cooling ages rather than forming ages are found.

6.3. Garnet amphibolite JI 2-1

Sample JI 2-1 has a mineral assemblage of amp + gt + pl + zo + ru + cc + cel + sph + q. As described in detail in the thin section descriptions (Appendix I) this mineral assemblage is not in equilibrium. Garnet is partially replaced by amphibole and plagioclase and calcite occurs in the pressure shadow of the garnet. Therefore two consecutive 'stable' mineral assemblages are interpreted and modelled, namely: amp + gt + pl + cel + q (early) and amp + pl + zo + ru + cc + sph + cel + q (main).

Solution models used for this sample are: GlTrTsPg, Gt(HP), feldspar and Mica(CHA). Model runs are calculated for a FeO + TiO_2 + CaO + K_2O + MgO + Na_2O + SiO_2 + Al_2O_3 + H_2O (+ CO_2) system with SiO_2 as a saturated component and H_2O or H_2O + CO_2 as a saturated fluid. As the Gt(HP) model is the only one that includes MnO, this oxide is left out of consideration to prevent overestimating garnet stability. Because no distinction can be made between Fe^{2+} and Fe^{3+} in XRF and EMP measurements, Fe_{total} is used and assumed to all be Fe^{2+}. Therefore, no epidote and only pure clinozoisite could be modelled.

Figure 51 and Figure 52 show pseudosections for sample JI 2-1 in a P-T range of 1-15 kbar and 300-800°C, with a pure H_2O fluid and a 0.8 H_2O + 0.2 CO_2 fluid mixture, respectively. The stability field of the early mineral assemblage is indicated with a red field in Figure 51. This assemblage of hbl + gt + pl + cel + sph +q occurs between 625 - 725°C and 10.1 - >15 kbar. The model was not extended to higher pressures in an attempt to identify and upper boundary, because the modal abundances of minerals present in the sample and compositional isopleths of these minerals all indicate stability in the lower part of the field (see below for details). The modelled mineral assemblage contains sphene (titanite), while this mineral was not expected to be stable in the early assemblage as the grains in the thin section look very fresh and texturally late, overgrowing mainly amphibole grains, and were therefore ascribed to later growth.

The stability field of the main assemblage is indicated in red in Figure 52 and shows a modelled mineral assemblage of hbl + ts + pl + zo + cel + sph + cc + q. It ranges from 610 – 635°C and 8.9 – 10.4 kbar. This assemblage matches the observed assemblage in thin section except for rutile. However, rutile appears 1 kbar lower or 40°C higher than the indicated field, so this is not thought to be a major mistake according the assumption that had to be made in order to model the pseudosection.

As it is not possible in Perple_X to model in 3D (e.g., P-T-CO_2), eleven P-T pseudosections for varying CO_2 concentrations were produced. In Figure 53, the stable mineral assemblage amp + pl + sph ± gt ± cc is displayed for each of these pseudosections. A shift can be observed towards higher temperatures with increasing CO_2 concentrations, with approximately 200°C difference between CO_2 = 0.05 and CO_2 = 0.9. The assumed concentration of CO_2 in the fluid for the stable assemblage of sample JI 2-1 was chosen based on modal abundances of minerals present in the sample and on compositional isopleths of amp and pl. These data are shown in Appendix VI. A best fit of isopleth intersections was derived for CO_2 = 0.2.

The isopleths as shown in all figures (Figure 54 and Figure 55) display the average EMP measurements of the pertinent minerals in the thin section, and are tabulated in Appendix IV. If two or more populations of measurements are present, isopleths are shown for each of them. The stability fields as indicated in Figure 51 and Figure 52 are in agreement with the observed modal abundances, which cluster around 640-670°C and 10.1-10.7 kbar for CO_2 = 0 (Figure 54) and around 600-645°C and 9.4-10.1 kbar for CO_2 = 0.2 (Figure 55) and the mineral chemistry of gt, amp and pl (Figure 54 and Figure 55). Isopleth intersections at CO_2 = 0 for amp and gt cluster around 650-680°C and 9.4 kbar, whereas for pl two intersections are present around 650°C; 9.5 kbar and 535°C; 10.3 kbar. At CO_2 = 0.2 isopleths of amphibole do not intersect but narrow between 600-660°C and 8.7-9.7 kbar. Plagioclase isopleths intersect again in two spots at 625°C; 9.2 kbar and 500°C; 4.5 kbar.

Single microprobe measurements are plotted in the pseudosections as isopleth intersections in case of an error smaller than 20 °C and 0.5 kbar. The garnet and albite measurements, which are

assumed to represent the early stable assemblage, were plotted in the pseudosection for CO_2 = 0; the amphibole and plagioclase measurements are representative for the retrograde part of the metamorphic history where a CO_2 fluid was present and were therefore plotted in the pseudosection for CO_2 = 0.2. All stability fields are displayed on the latter in Figure 56.

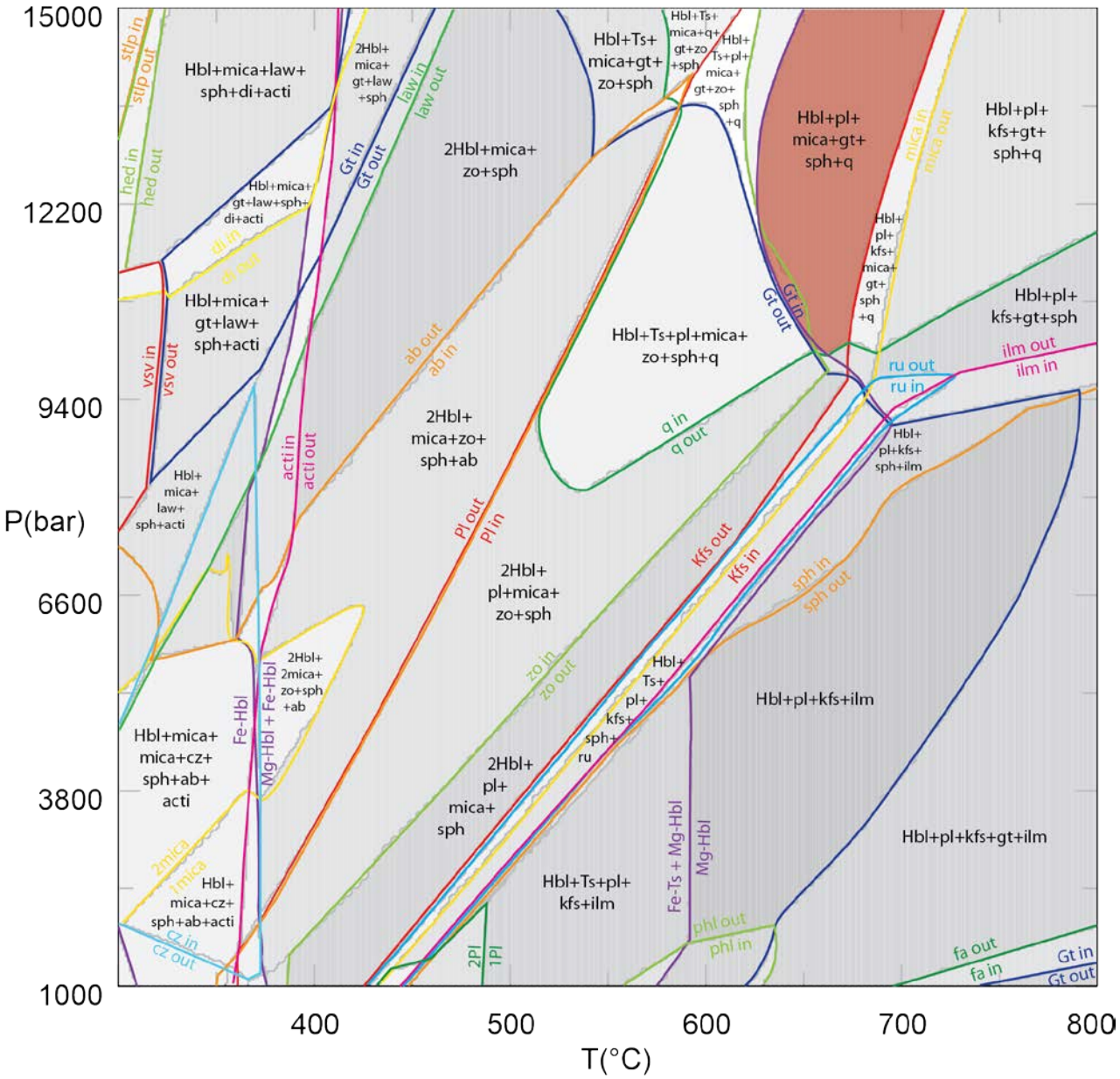

Figure 51. Pseudosection for JI 2-1 with CO_2 = 0. Stable mineral assemblage of hbl + gt + pl + mica + sph + q ± zo is indicated with the red field. Phase boundaries are indicated with coloured lines and mineral stability of most fields are indicated. Note that the names used for amphiboles and micas are not true endmembers but rather nomenclature based on chemistry after Leake et al. (1997) and Rieder et al. (1998).

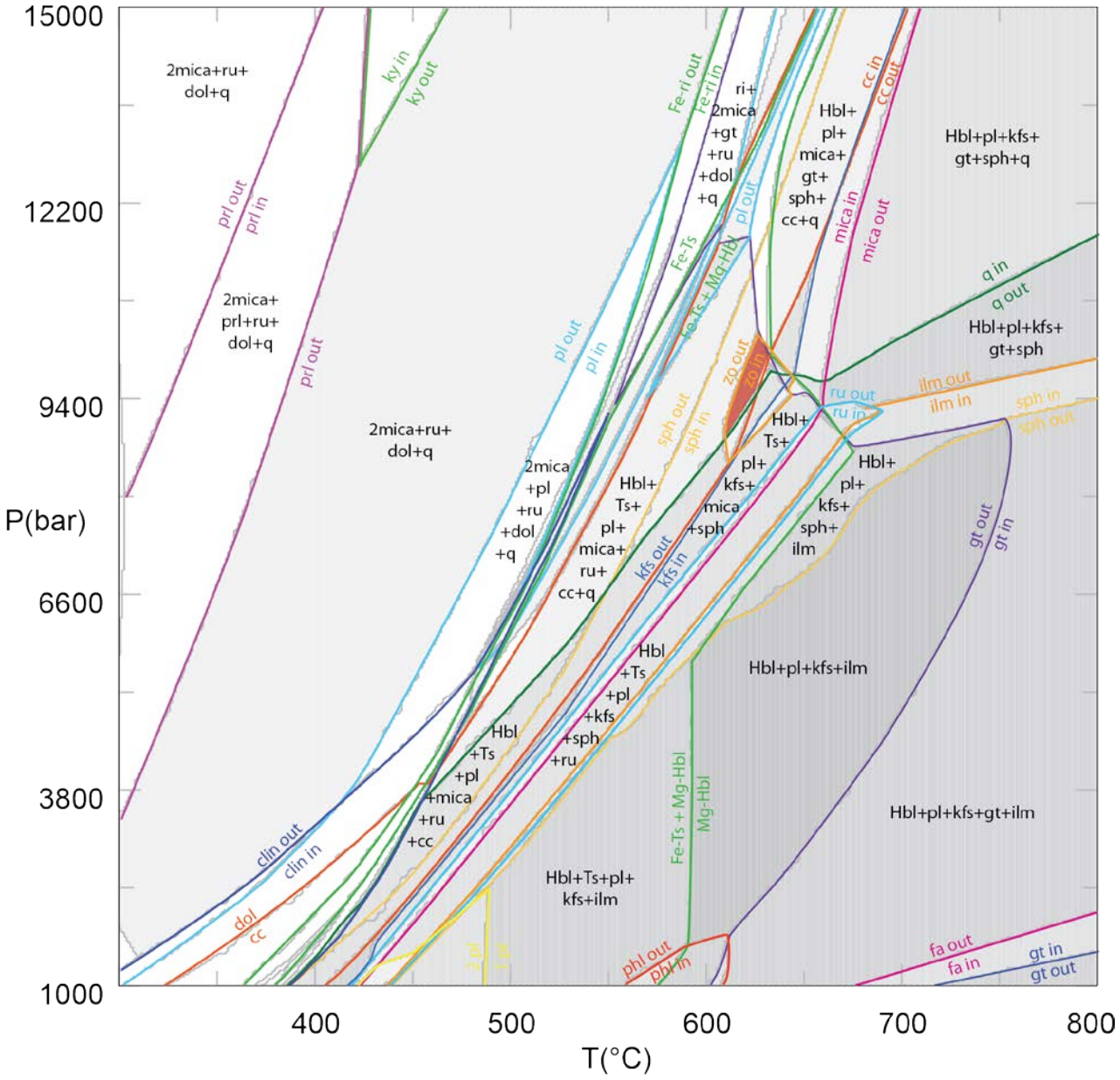

Figure 52. Pseudosection for JI 2-1 with CO_2 = 0.2. Stable mineral assemblage of hbl + ts + pl + mica + zo + sph + cc is indicated with the red field. Phase boundaries are indicated with coloured lines and mineral stability of most fields are indicated. Note that the names used for amphiboles and micas are not true endmembers but rather nomenclature based on chemistry after Leake et al. (1997) and Rieder et al. (1998).

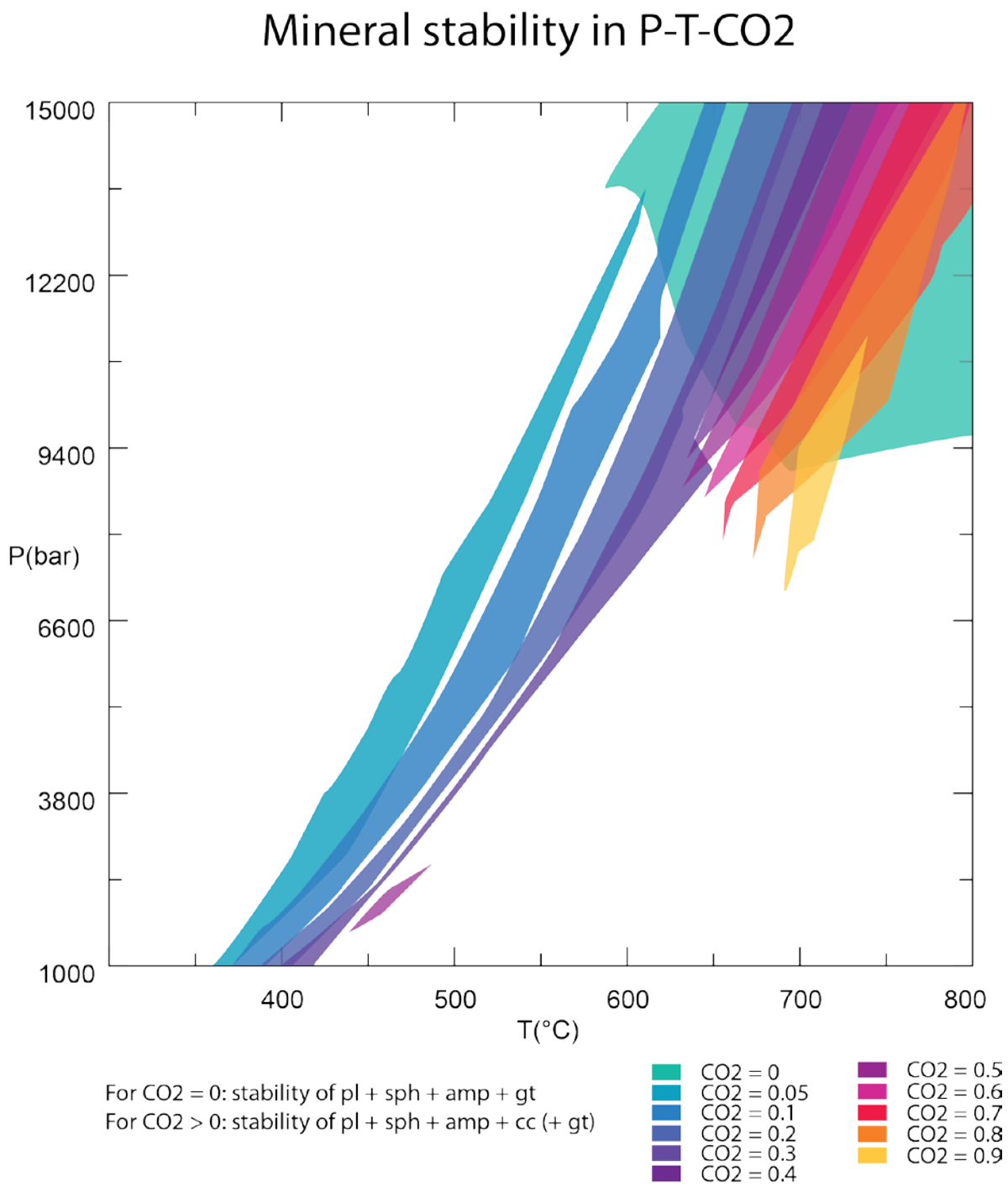

Figure 53. Stability fields of the mineral assemblage amp + pl + sph ± gt ± cc at different CO_2 fluid concentrations. CO_2 concentrations are based on a CO_2 + H_2O mixture with a total of 1. With increasing CO_2 content a shift of stability towards higher temperatures is observed.

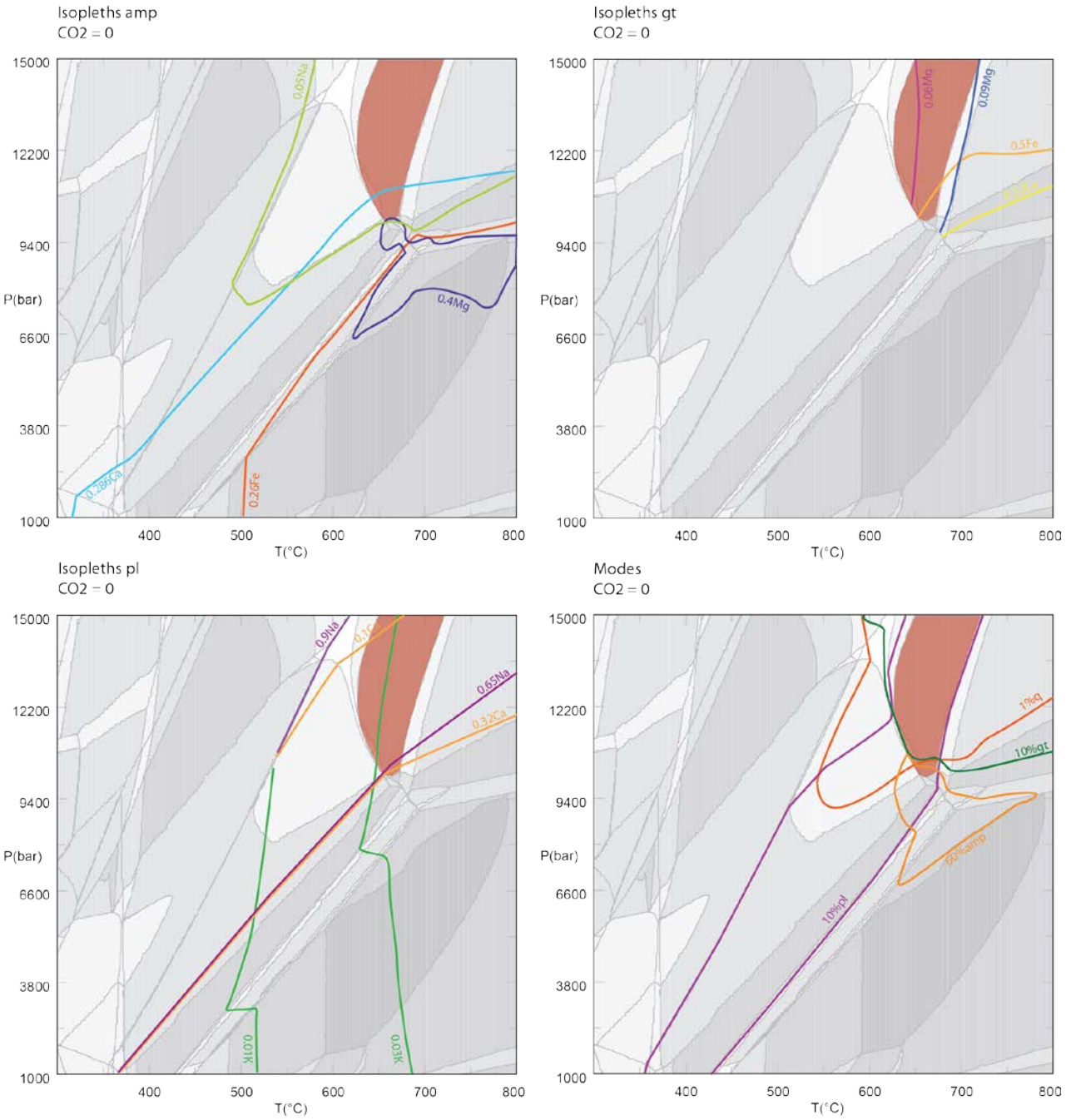

Figure 54. Mineral modes and isopleths of amp, gt and pl. Intersections of isopleths and modal abundances correlate very well to the assumed stability field.

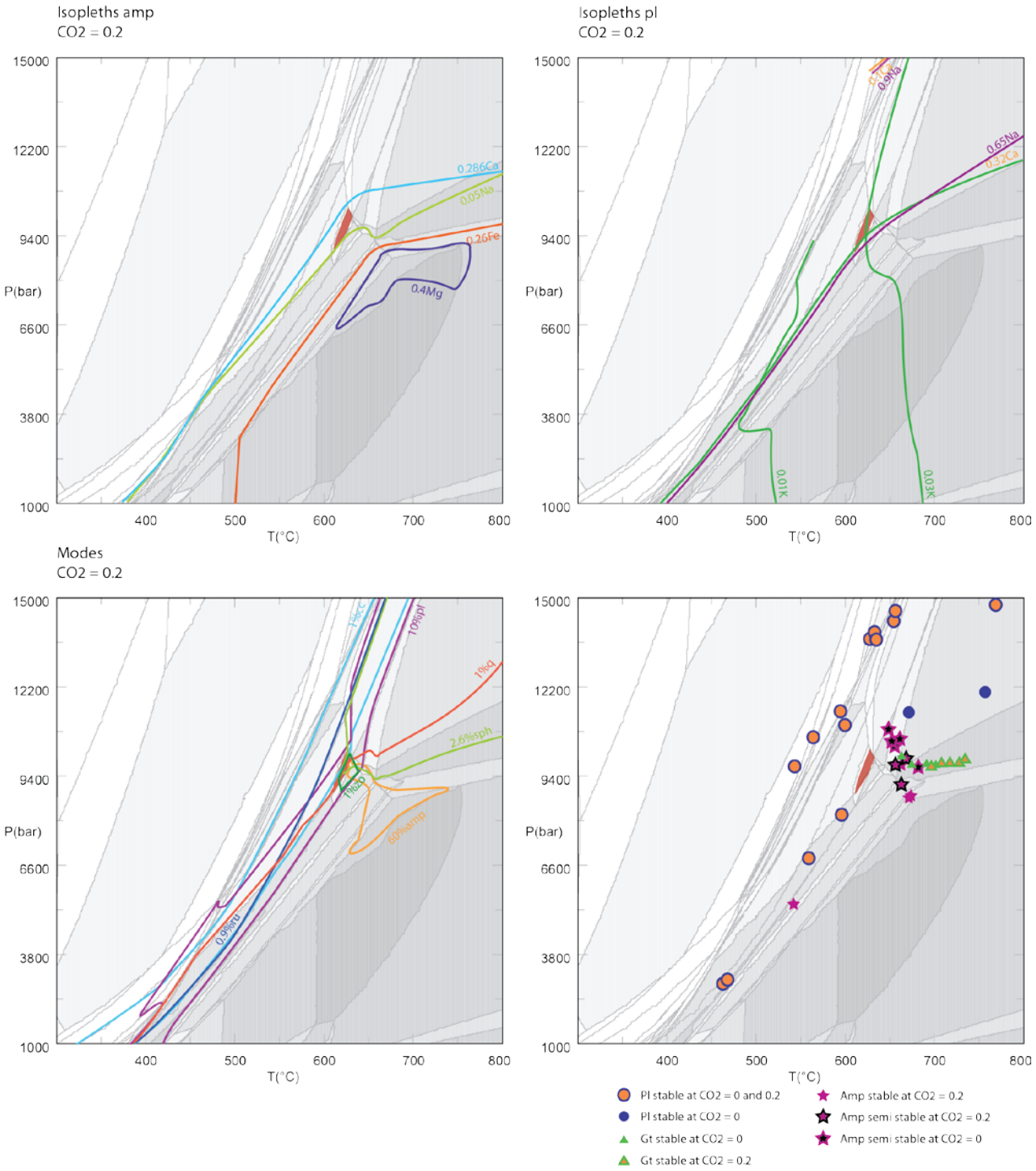

Figure 55 (top). Mineral modes and isopleths of amp and pl. Intersections of isopleths and modal abundances correlate very well with the assumed stability field.

Figure 56 (right). Stability of EMP measurements, displayed on the pseudosection for CO_2 = 0.2.

6.3.1. JI 2-1 model discussion

For sample JI 2-1 two metamorphic stages were identified on the basis of textural information. An early peak metamorphic assemblage of amp + gt + pl + cel + q and a main assemblage of amp + pl + cz + ru + cc + sph + cel + q, (almost completely) excluding garnet was present. The most important assumption for this model is that the whole rock chemical composition did not change through time. However, with the introduction of a CO_2 fluid, it can be expected that other changes in the chemistry occurred as well as an active fluid flow took place, being able to transport molecules. Because isopleth intersections and mineral mode intersections all agree within a range of 30°C and 1 kbar, the assumption appears to be justified. The only discrepancy observed is the modelled amount of amphibole, which does not exceed 60% and is thus slightly (6%) lower than the observed modal abundance. Another assumption is that the fluid was saturated in the sample. However, as garnet is not broken down completely, it is probable that not enough fluid was present to form the retrograde hydrous phases such as biotite or amphibole from the anhydrous garnet, and the assumption of fluid saturation may not be entirely justified during retrogression.

For the main mineral assemblage, the most suitable fluid composition in terms of CO_2 – H_2O proportions was constrained based on the best fit of compositional isopleth intersections for amphibole and plagioclase, in combination with the modal abundances. However, this best fit still resulted in a range of 75°C and 2 kbar for isopleths of amphibole, with no intersection. For plagioclase and the mineral modes, almost perfect intersections at a single point were obtained. As it was assumed that the clinozoisite present was all the pure endmember zoisite, no O_2 was added in the model in order to model epidote. However, from EMP measurements we know that not all of the zoisite is the pure endmember. Adding O_2 to the system might cause the stability fields to shift slightly and also provide a better approximation of intersection of the amphibole compositional isopleths. In addition, the amount of modelled amphibole might deviate from thin section observations because 2% garnet is preserved as relisc, but not modelled as part of the main assemblage. As part of the garnet is replaced by amphibole, a slight shift in mineral modes might happen when all garnet is gone. The choice of amphibole solution model may also have played a role. A single test was carried out, in which stability field boundaries appeared to change drastically, although the P-T conditions at which the mineral assemblage is stable are comparable between both models. Because modelling using Amph(DPW) turned out to be too computationally expensive, the simpler GlTrTsPg model was used.

Single EMP measurements are plotted onto the pseudosection in order to define a P-T path as shown in Figure 57. The shape of the P-T path is based on the single EMP measurements and the stability fields before influx of CO_2 in green and with presence of CO_2 in red. As the moment of influx of the CO_2 fluid that allowed for calcite to appear in the main mineral assemblage is not known, measurements are plotted for both the pure water case and the 0.2 CO_2 case. For garnet it appears that stability is shifted towards 50-100°C higher temperatures with the presence of CO_2 in the fluid. However, as amphibole measurements all coincide with garnet without the presence of CO_2, it is more likely that garnet was formed entirely before the influx of CO_2. Based on the stability of amphibole, the timing of CO_2 influx is determined at 655°C and 10 kbar and indicated in Figure 57.

Plagioclase measurements are stable at higher P-T conditions than garnet, both in the case of presence and absence of a CO_2 fluid. Therefore, all but the last four plagioclase measurements along the path are thought to represent the prograde part of the P-T path with peak conditions of 760°C and 13.6 kbar. As the plagioclase grains generally seem more unstable than amphibole (Appendix IV), it is likely that they were formed during the prograde rather than the retrograde part of the metamorphic history.

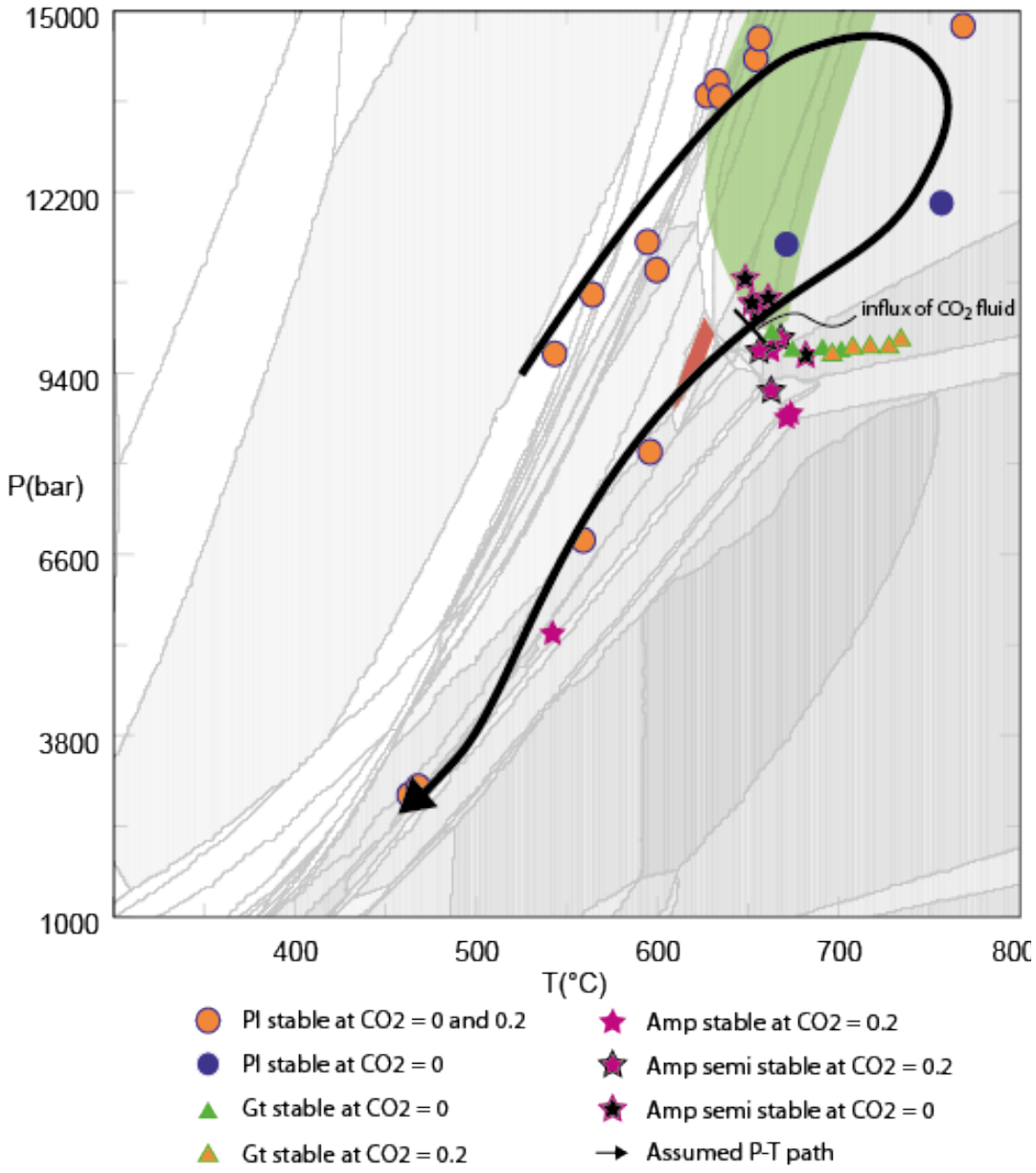

Figure 57. P-T path of sample JI 2-1. Indicated are the stability field before CO_2 influx in green and after in red and the moment of CO_2 influx together with single EMP measurements.

6.4. Gneiss JI 2-2

Sample JI 2-2 shows a mineral assemblage of chl + mica + pl + kfs + q + ru + metal oxides and an accessory amount of zr and ap with relics of gt. This mineral assemblage is modelled using the following solution models: Bio(TCC), Mica(CHA1), feldspar, Chl(LWV), Cpx(I) and Gt(HP). Model runs are calculated for a $FeO + TiO_2 + CaO + K_2O + MgO + Na_2O + SiO_2 + Al_2O_3 + H_2O$ system with SiO_2 used as a saturated component and H_2O as a saturated fluid. MnO was left out of the model as only Gt(HP) incorporates MnO and including it will therefore lead to overestimating the stability of garnet.

Figure 58 shows the pseudosection as modelled for JI 2-2 in the P-T range of 0.001-15 kbar and 300-800°C. As it was determined from the thin section that the chlorite present used to be biotite, the stable mineral assemblage bio + mica + pl + kfs + q + ru is modelled and indicated with a red field which ranges between 410 – 725°C and 0.001 – 12.5 kbar. The green field indicated in Figure 58 is thought to be the present stability as biotite is replaced by chlorite and tiny hints of clinozoisite can be found in the thin section. This field ranges between 300 – 360°C and 0.9 – 3.1 kbar. From the garnet relics, an earlier mineral assemblage of gt + bio + mica + pl + kfs + q is assumed. The stability field corresponding to this assemblage is indicated in blue and ranges between 650 – 715°C and 11.5 – 15 kbar.

In order to assess the effect of the amount of water in the system, and to determine the amount of water used to stabilize the above mentioned stability fields, P-H_2O pseudosections were produced for three different temperatures, 400, 600 and 800°C. Figure 59 shows a P-H_2O diagram with H_2O ranging from 0 – 1 wt%. Lines in the diagram indicate the amount of H_2O used in Figure 58 to form the stable mineral assemblage at the given P and T conditions. More water at the given conditions results in excess water. The amount of water used by the model varies strongly throughout the pseudosection. The red stability field as indicated in Figure 58 corresponds to a H_2O concentration of roughly 0.4 - 0.5 wt%. The availability of water strongly affects the stability of garnet and aluminosilicates: at decreasing water content (0.2 – 0.4 wt%), the stability of garnet starts at lower pressure and temperature, whereas the aluminosilicates are not stable at all at water contents higher than 0.4 wt%. However, as we do not have specified constraints on the realistic amount of water in the model, water saturation was assumed for all models.

The feldspars in this rock are subdivided in primary (albite) and secondary (K-feldspar) minerals based on their stability. Compositional isopleths of mica, biotite and primary and secondary feldspar are shown in Figure 60. Isopleths for mica intersect within the indicated stability field in red at 625°C and 9.75 kbar. Isopleths for feldspar vary in a large range and are thus displayed as 'isopleth fields' rather than lines. These fields for primary feldspar overlap in an approximately 40°C wide band at the lowest pressure towards 90°C at the highest pressure, ranging from ~3 to >15 kbar as indicated in Figure 60. Isopleths of secondary feldspar agree with measured chemistry at least between 0.001 and 15 kbar with increasing temperatures from 400°C at 1 bar up to 550°C at 15 kbar. Furthermore it is assumed that the ratio Fe/Mg in chlorite in the sample is the same as in the modelled biotite. So EMP measurements of these elements in chlorite are compared with isopleths of biotite. This data falls along a line as indicated in Figure 60. As chlorite analyses are compared with modelled biotite, this data might be slightly off and will only indicate an area of assumed stability.

Figure 61 shows the modal abundances of the stable mineral assemblage in the thin section. Modes run parallel in a 150°C wide band around and parallel to the indicated stability field in red in Figure 58. This band overlaps with the mica isopleth intersection and the overlap of isopleths of primary feldspar. Modal abundances of mica and quartz also intersect within the green field. Single EMP measurements of white mica based on K and Al isopleth intersections, and primary feldspar and secondary feldspar based on K and Na isopleths intersections are displayed in Figure 62 in case of an error smaller than 20°C and 0.5 kbar and tabulated in Appendix IV.

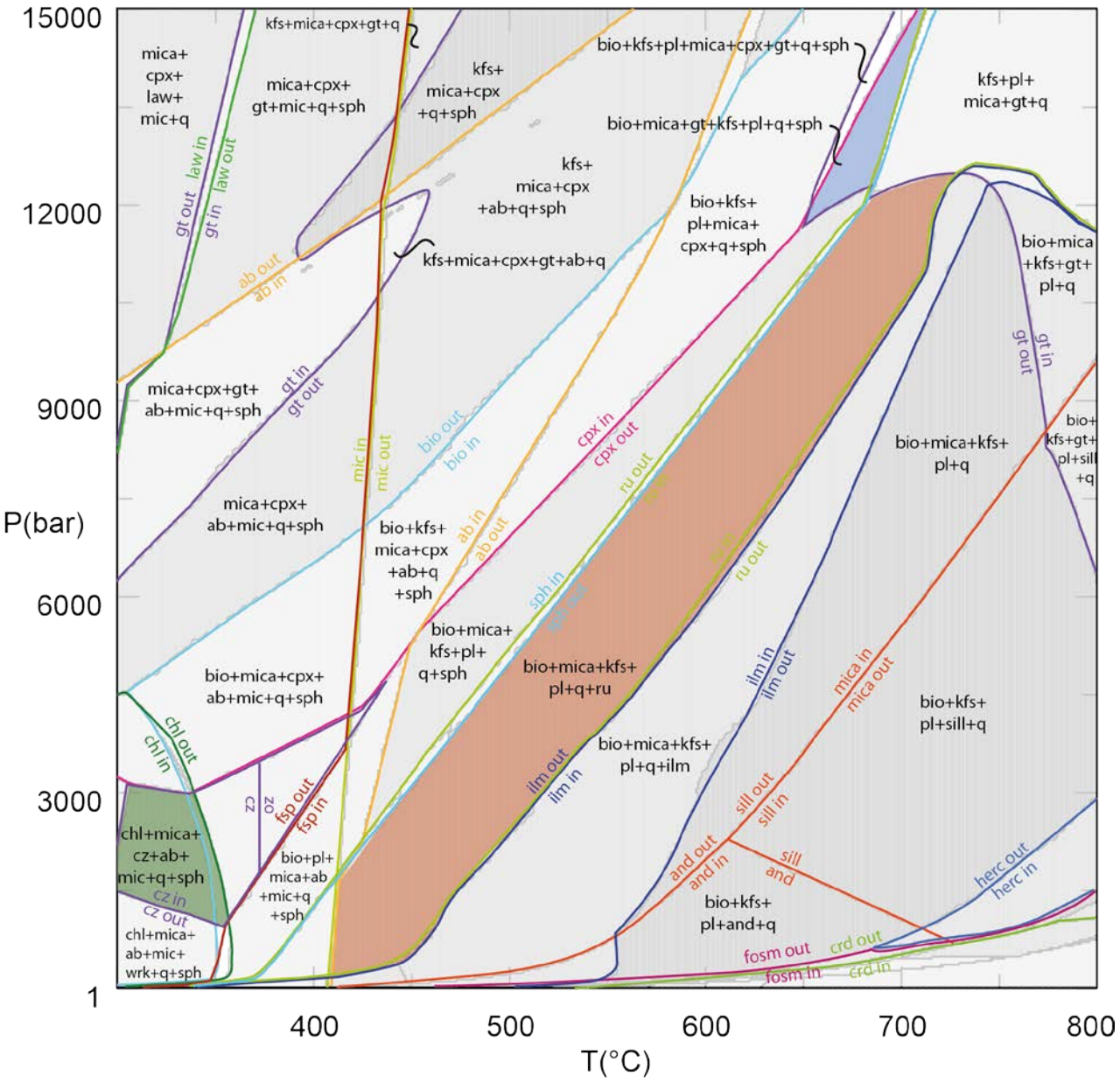

Figure 58. Pseudosection of JI 2-2. Stable mineral assemblage of bio + mica + pl + kfs + ru + q is indicated with the red field. Stable mineral assemblage of chl + mica + ab + mic + q + cz + sph is indicated with the green field. Stable mineral assemblage of gt + bio + mica + pl + kfs + q + sph is indicated with the blue field. Important phase boundaries are indicated with coloured lines and stable mineral assemblages of most fields are indicated.

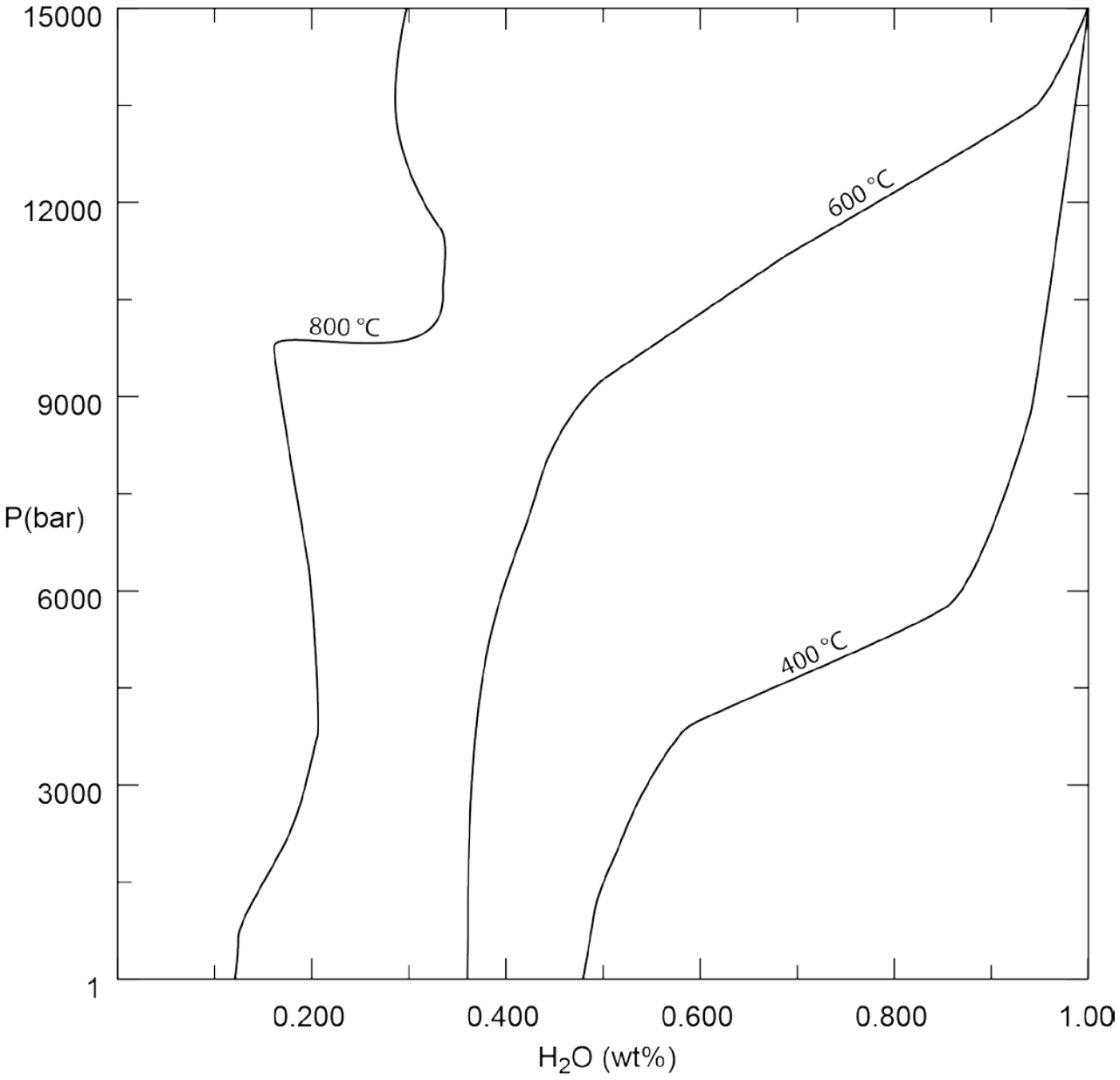

Figure 59. Water content used in the pseudosection of Figure 58 at given pressure and temperature conditions. The stability field indicated in red in the former figure corresponds to a water content of roughly 0.4 – 0.5 wt%.

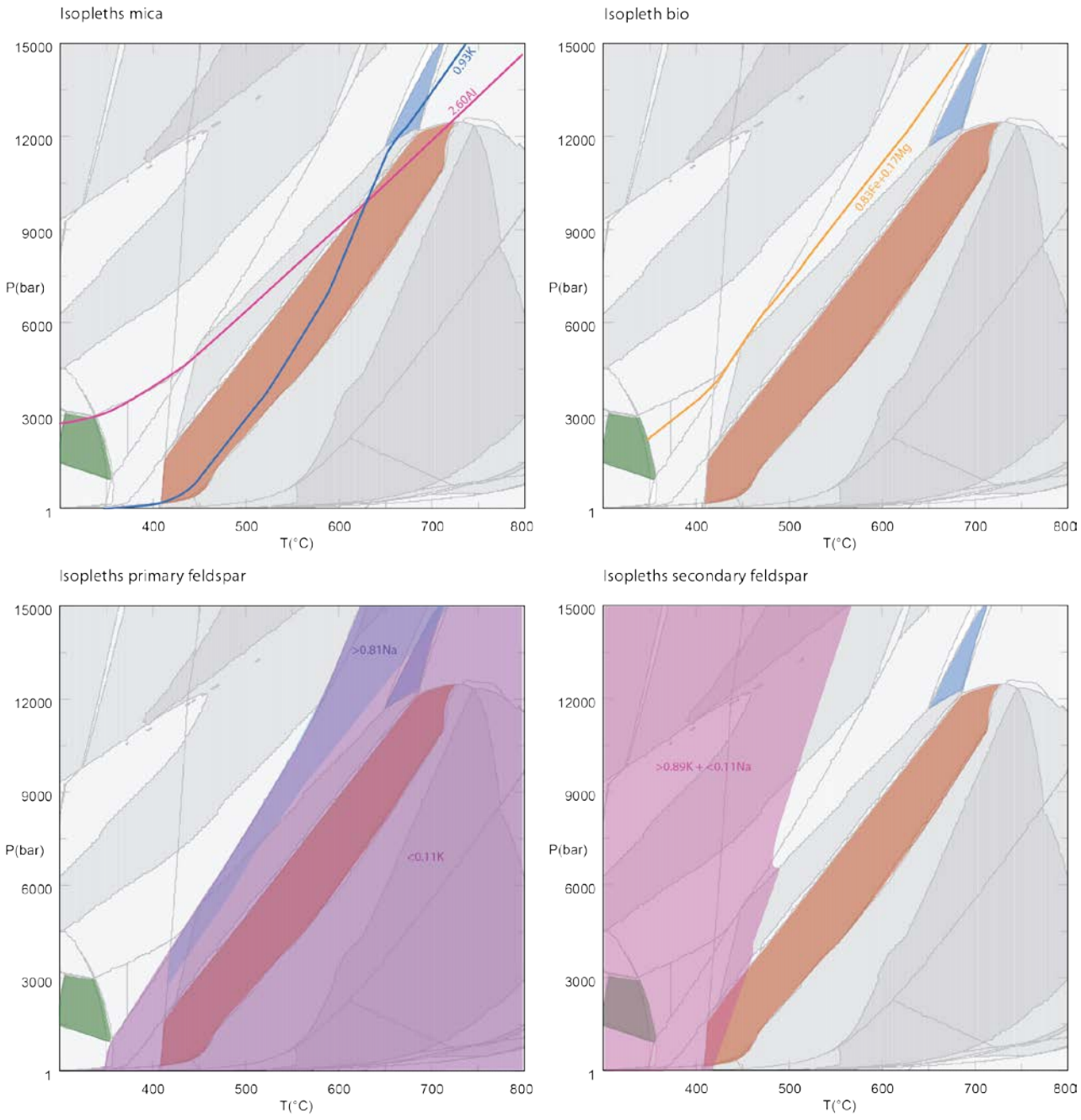

Figure 60. Isopleths of mica, biotite, primary feldspar and secondary feldspar. As data of the feldspars vary over a large range, stability fields are indicated. The mica isopleth is thought to be the most reliable due to instability of the other minerals and thus distortion of the measurements.

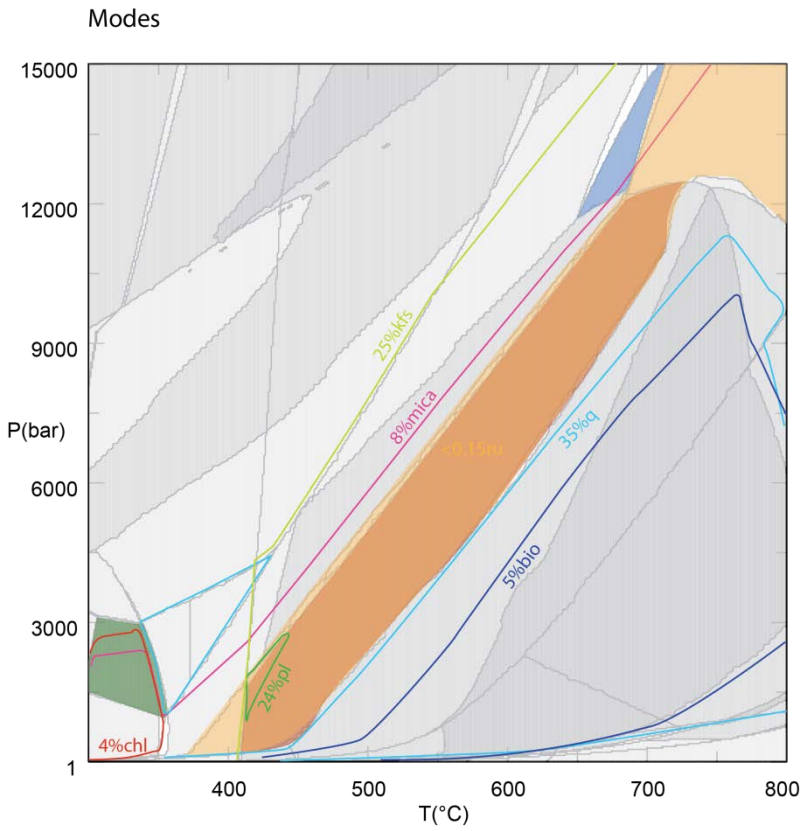

Figure 61. Modal abundances of sample JI 2-2. Modes focus in a parallel band around the stability field as indicated in Figure 58.

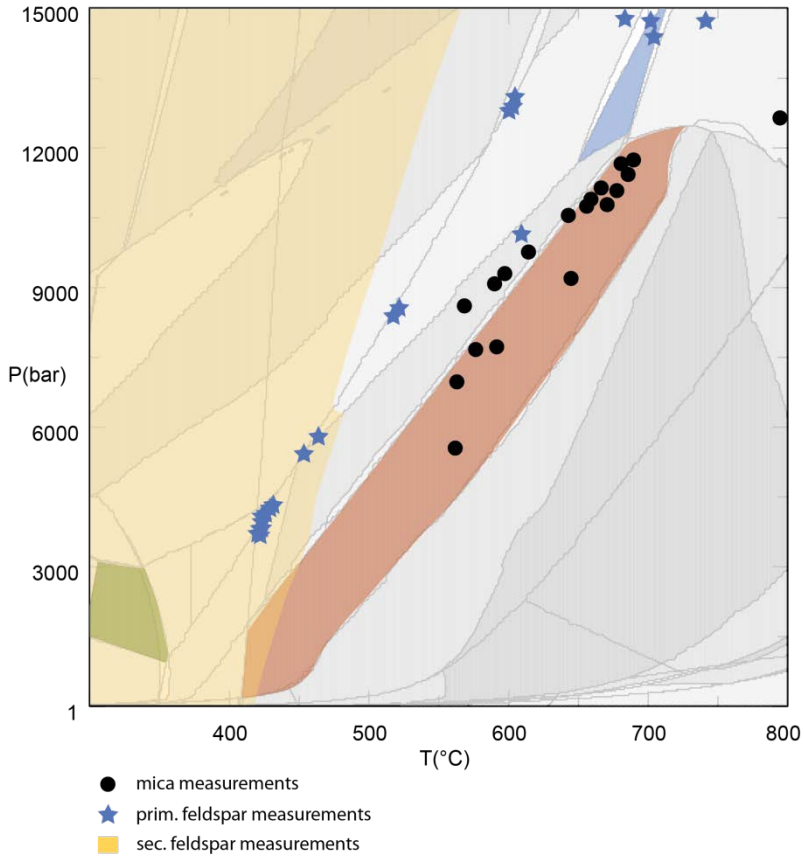

Figure 62. Single EMP measurements of mica and primary feldspar based on isopleth intersections. The stability field of secondary feldspar is indicated as isopleths of Na and K run parallel.

6.4.1. JI 2-2 model discussion

Sample JI 2-2 contains 5% chlorite with relict parts of biotite inside the grains. Therefore, it was assumed that biotite is almost completely replaced by chlorite, which results in two metamorphic stages. From a chemistry point of view this assumption makes sense as plagioclase is unstable, whereas K-feldspar is stable. With replacing biotite by chlorite, potassium got free and stabilized K-feldspar and muscovite. However, it is unclear what phase took up the sodium that was released from the decay of plagioclase.

Although changes in the chemistry are obvious, for modelling the assumption was made that the chlorite chemistry resembles that of the former biotite and thus the stable mineral assemblage was chl/bio + mica + pl + kfs + q + ru + metal oxides. This is probably the reason why modal abundances for biotite and K-feldspar are 150°C apart and do not intersect with the modes of other minerals present in the sample.

For feldspars, a subdivision was made between potassium poor (primary) and potassium rich (secondary) feldspars. For the primary feldspars, compositional isopleth intersections could be drawn. Based on freshness of the grains from BSE (backscattered electron images), a sequence from most to least disturbed chemistry was made. This corresponds very well with the prograde part of the P-T path in Figure 63. This part of the path also corresponds with the compositional isopleth of biotite. Peak metamorphic conditions are displayed in primary feldspar chemistry and the location of the blue stability field including garnet. The retrograde part of the path is based on mica compositional isopleth intersections and the stability field of the present mineral assemblage with biotite (red) and with chlorite (green). The red stability field is based on the presence of rutile. As this mineral is thought to be a late ingrowth, and part of the mica isopleth intersections fall at slightly higher pressures, a wiggle in the P-T path is interpreted. Compositional isopleths of the secondary feldspars run parallel, almost isothermal. Therefore the shape of the P-T path is thought to run along a fairly isobaric line, e.g. perpendicular to the secondary feldspar isopleths. Peak metamorphic conditions are found at 720°C and 14.25 kbar, which falls within the garnet stability field. Only small amounts of garnet are still present in the sample, whereas sample JI 2-1 contains much more remains of garnet. This could have three reasons; 1) either the rock has only been in garnet stability for a relatively short amount of time and therefore not much garnet was formed, 2) enough water was available to enable retrograde reactions and breakdown of garnet, or 3) chemistry was not favourable to form garnets. With less than 1 wt% MnO, CaO and MgO and only 2 wt% FeO, a combination of the latter two is assumed.

For $^{40}Ar/^{39}Ar$ dating, only mica grains with a potassium content between 0.897 and 0.926 p.f.u. were used. This corresponds to the mica EMP measurements in Figure 63 above 625°C. As this temperature lies well above the assumed closure temperature of mica of 325 – 375°C, cooling ages rather than forming ages were found.

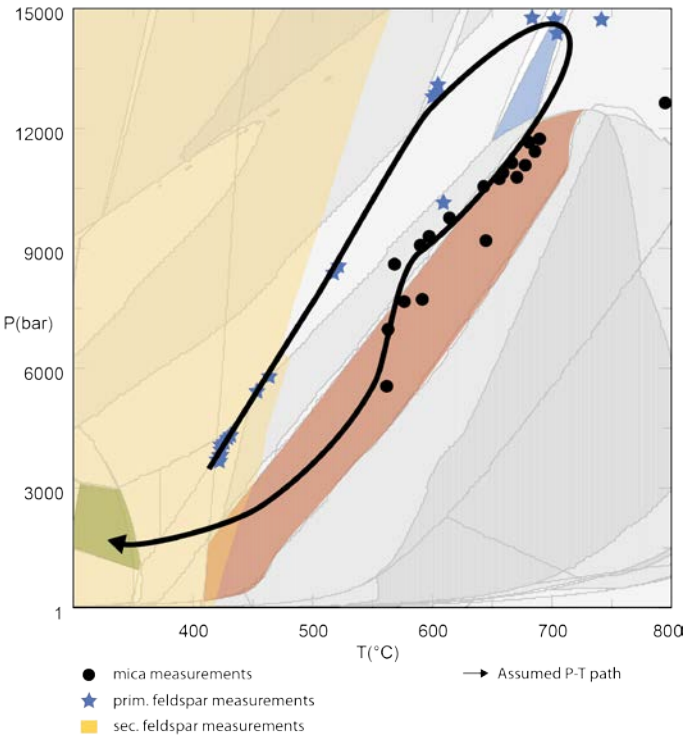

Figure 63. P-T path of sample JI 2-2.

6.5. Granulite JI 4-6

Sample JI 4-6 shows a mineral assemblage of gt + amp + pl + kfs + bio + ep + q + ilm + ap and accessory amounts of ru and al. This mineral assemblage is modelled using the following solution models: Ep(HP), Gt(HP), Amph(DPW), Bio(TCC), feldspar, Mica(CHA), IlHm(A), Cpx(I) and Opx(HP). Model runs are calculated for a $FeO + TiO_2 + CaO + K_2O + MgO + Na_2O + SiO_2 + Al_2O_3 + H_2O + O_2$ system with SiO_2 used as a saturated component and H_2O as a saturated fluid. MnO was left out of the model as only Gt(HP) incorporates MnO. Leaving MnO in would lead to overestimating the stability of garnet. The amount of O_2 added to the system was determined based on the best fit of modal abundance isopleths of the stable mineral assemblage and chemical compositional isopleths of garnet and shown in Appendix VI (Figure 129 and Figure 130). A best fit was found with 0.4 wt% O_2. Amph(DPW) was used instead of GlTrTsPg because this resulted in a better fit for compositional isopleths of amphibole and the absence of amphibole at unrealistic high temperatures.

Figure 64 shows the pseudosection as modelled for JI 4-6 in the P-T range of 1 – 25 kbar and 500 – 1000°C. It has a mineral assemblage of gt + amp + pl + bio + ep + q + ilm ± mt and ranges between 630 – 730°C and 8.2 – 14.8 kbar. The only deviation of this assemblage with the one observed in the thin section is the absence of kfs. In this pseudosection, kfs is only observed where cpx is present and amp is absent.

In order to assess the effect of the amount of water in the system, and to determine the amount of water used to form the above mentioned stability fields, P-H_2O pseudosections were produced for three different temperatures, 600, 700 and 800°C. Figure 65 shows a P-H_2O diagram with H_2O ranging from 0 – 2 wt%. Lines in the diagram indicate the amount of H_2O used in Figure 64 to form the stable mineral assemblage at the given P and T conditions. Larger amounts of water result in excess water. The amount of water used by the model varies strongly throughout the pseudosection. The red stability field as indicated in Figure 64 corresponds to a H_2O concentration of roughly 1.3 – 1.7 wt%. The availability of water strongly affects the stability of garnet. With decreasing water content (0.2 wt%), the stability of garnet starts at lower pressure and temperature (5 kbar and 100°C).

Compositional isopleths of garnet, amphibole, feldspar and biotite are shown in Figure 66. Garnet isopleths cluster very nicely at 780°C and 8.8 kbar. For amphibole the magnesium isopleth cannot be reasonably displayed and is therefore left out of the image. The compositional isopleths of Ca, Na and Fe lay parallel below 675°C and 8 kbar. However, the chemical composition of amphibole in the sample is not well reflected as both for Na and Fe, amounts are too high whereas for Ca they are too low. Feldspar shows two stable groups, one with a roughly 0.4 Na + 0.6 Ca composition and one almost pure K-fsp. Isopleths for the first group intersect at 560°C and 4.8 kbar. For the pure K-fsp stability occurs over 850°C and 21 bar. This seems unrealistic high compared to other samples from the same region. A close to pure K-fsp stability is also observed around 730 – 850°C and 9 – 10 kbar. The biotite Mg + Fe isopleth falls within the same range as the other isopleth intersections.

Figure 67 shows the modal abundances of the stable mineral assemblage ep, bio, gt, kfs, pl, q and ilm. This data clusters around 740 – 760°C and 13-15.4 kbar, which is at slightly higher P-T conditions than the stability field of the mineral assemblage. Amphibole shows only a maximum of 10% modal abundance in the model whereas 25% is observed in thin section. Therefore amphibole is left out of the image.

Single EMP measurements of feldspar, garnet, amphibole and biotite are plotted on the pseudosection as isopleth intersections in Figure 68 in case of an error smaller than 20°C and 0.75 kbar and tabulated in Appendix IV. As isopleths for biotite and amphibole are parallel over a large range, stability fields for these minerals are displayed.

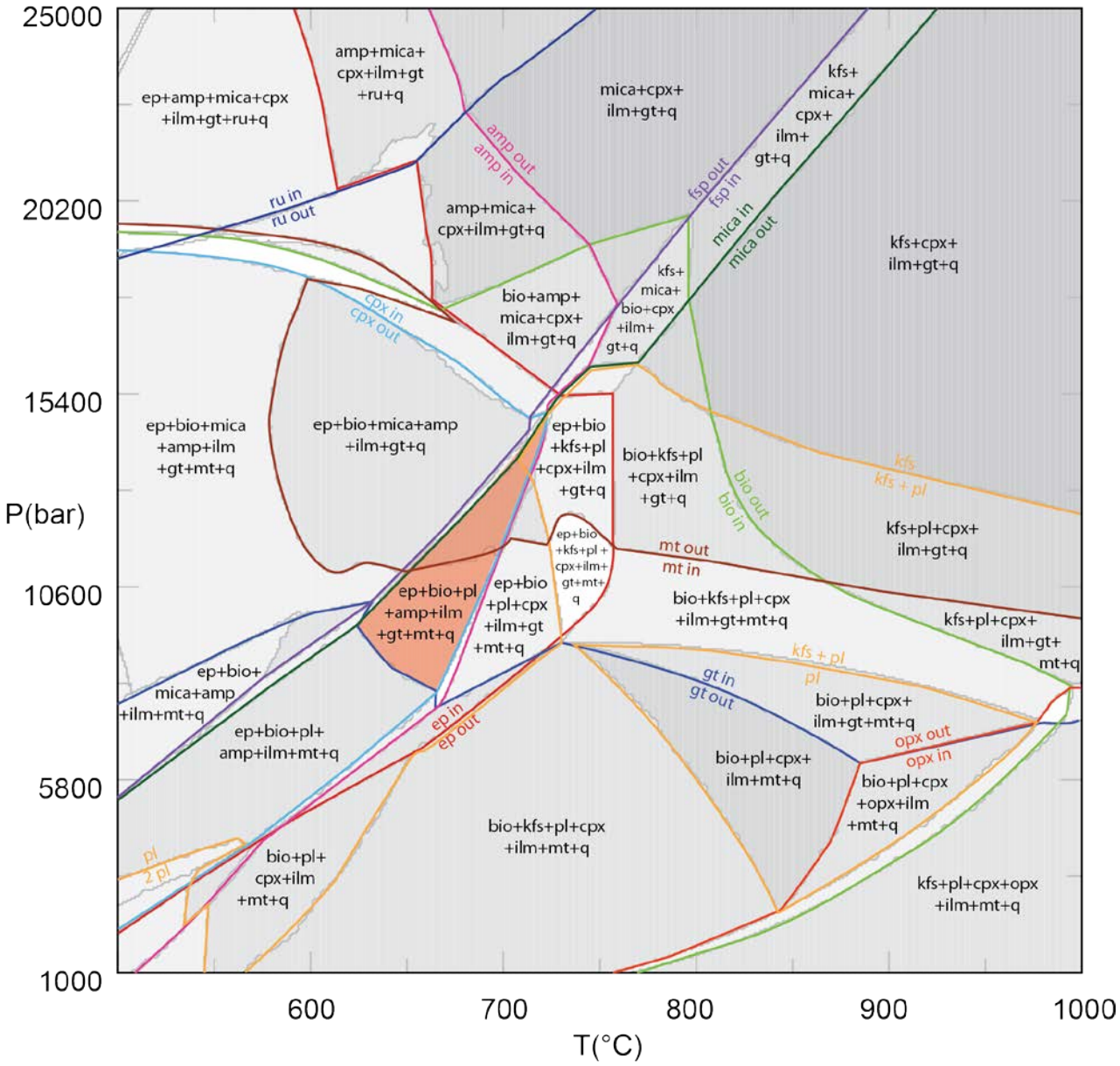

Figure 64. Pseudosection of JI 4-6. Stable mineral assemblage of ep + bio + amp + pl + gt + ilm + q ± mt is indicated with the red field. Phase boundaries are indicated with coloured lines and stable mineral assemblages of most fields are indicated.

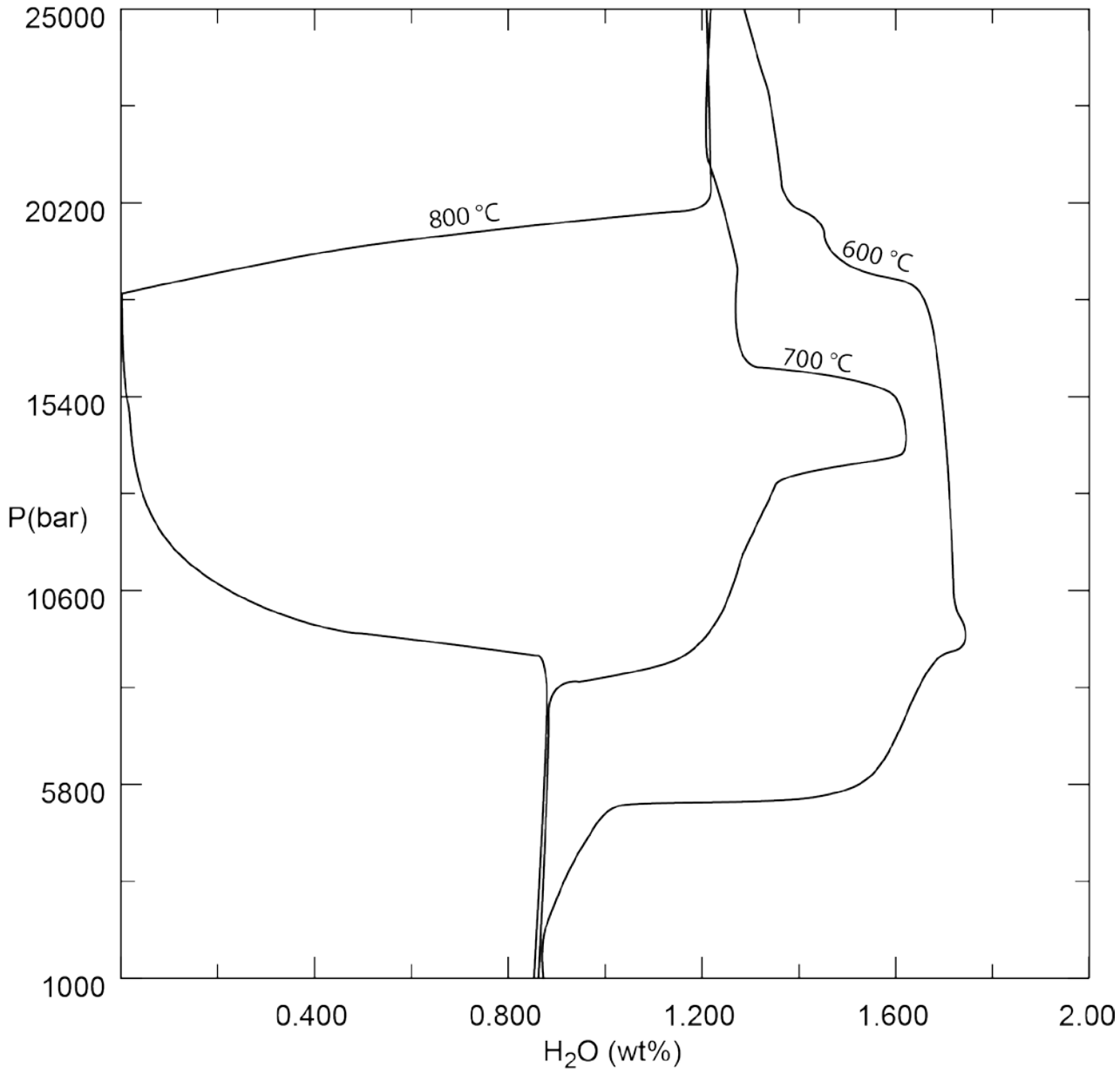

Figure 65. Water content used in the pseudosection of Figure 64 at given pressure and temperature conditions. The stability field indicated in red in the former figure corresponds to a water content of roughly 1.3 – 1.7 wt%.

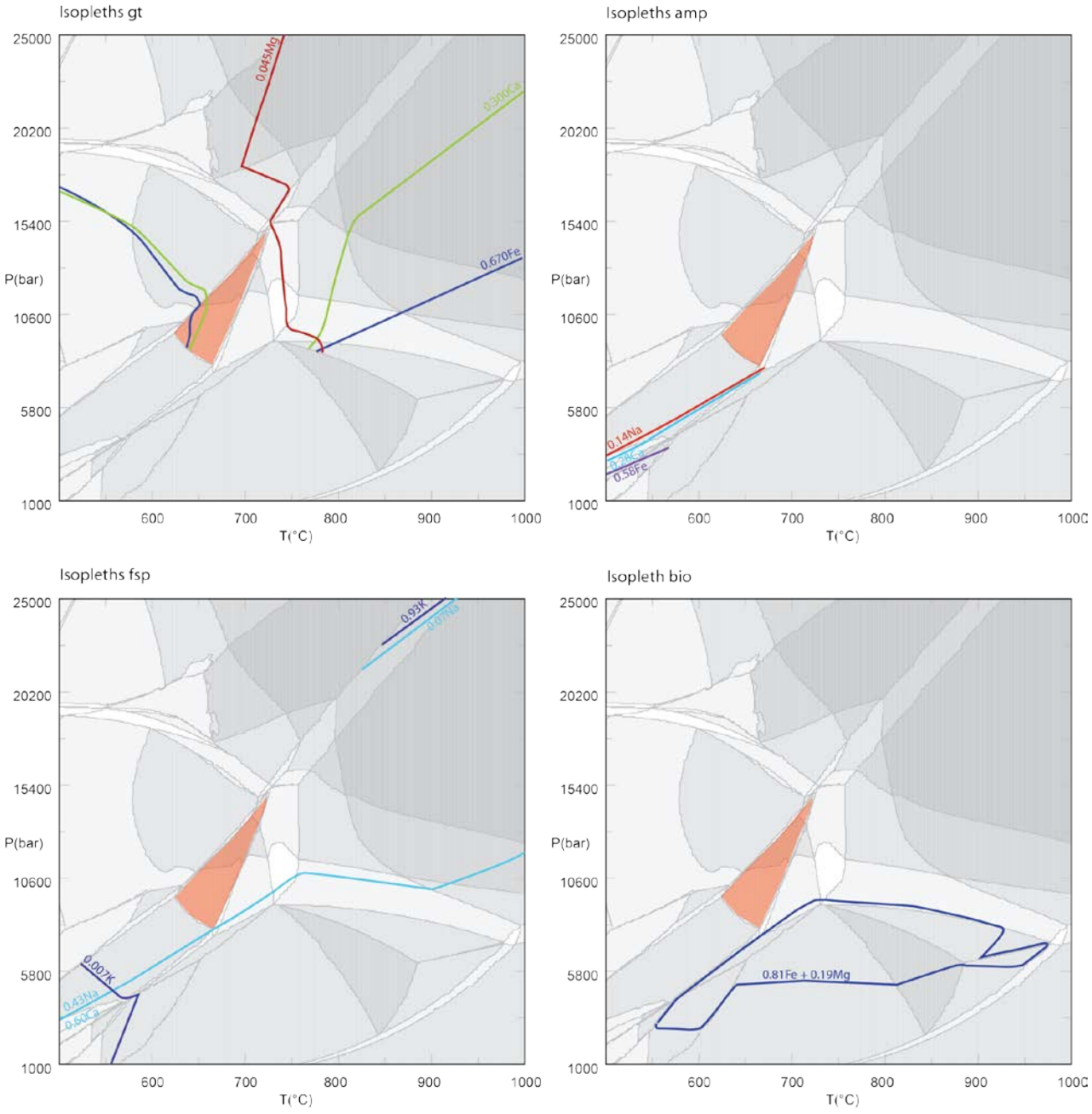

Figure 66. Isopleths of gt, amp, fsp and bio of sample JI 4-6.

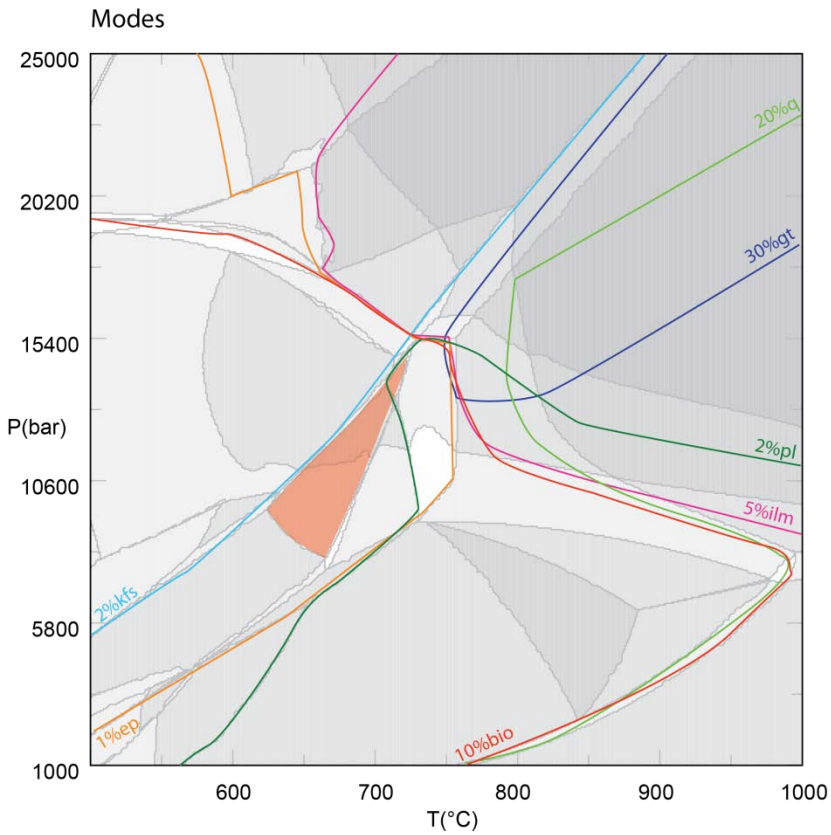

Figure 67. Mineral modes of ep, bio, gt, kfs, pl, q and ilm as observed in the thin section. Amphibole is not shown as modes do not exceed 10% whereas 25% is observed in thin section.

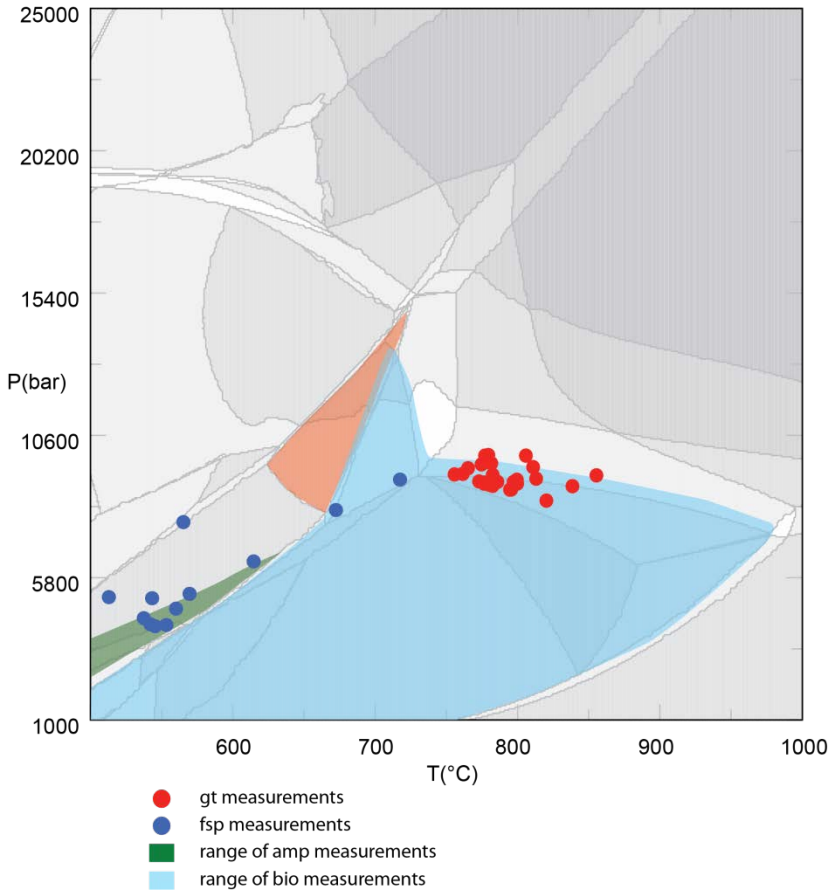

Figure 68. Single EMP measurements of feldspar, garnet, amphibole and biotite. For amphibole and biotite isopleths are generally parallel, so fields of possible stability are indicated. The red field indicates the stable mineral assemblage of ep + bio + amp + pl + gt + ilm + mt + q.

6.5.1. JI 4-6 model discussion

Sample JI 4-6 has a stable mineral assemblage of gt + amp + pl + kfs + bio + ep + q + ilm + ap and contains only a small amount (1%) of epidote. In order to model this epidote, a certain amount of O_2 was added in the model in order to transform Fe^{2+} to Fe^{3+}. As the amount of O_2 is determined based on visual best fit of modal abundances of pertinent minerals in the sample and chemical compositional isopleths of garnet, discrepancies in the model may arrive. However, the choice of not modelling epidote because of the low modal abundance and thus not including O_2 proved to influence the model extensively. This leads to lower pressure estimates for both garnet stability and the stability field of the pertinent mineral assemblage. The higher pressure estimates when including epidote agree very well with the estimates of other samples from the same location (e.g. JI 4-3 (Huijgen, 2015.) and the entire Jinshuikou group (this study, Figure 75). Therefore it was chosen to use the model including epidote.

As Bio(TCC), Amph(DPW) and Ep(HP) all three use Fe^{3+} in the model, but it is not taken into account in Gt(HP), it can be expected that this leads to underestimation of the stability of Fe-rich garnet in the sample. A correction for this would result in higher pressure stability of garnet and therefore a shift in the P-T path which would agree with other P-T paths within the Jinshuikou group.

The inability to correctly model isopleths for magnesium in amphibole, plus the too high estimates of Na and Fe isopleths and too low estimate of Ca isopleths may be related to each other as they all exchange for each other in the mineral B-site. When modelling without addition of O_2, these discrepancies were lower but still present. Therefore part of it can be ascribed to the introduction of Fe^{3+}, but not all. The reason for the remaining discrepancy and for the underestimation of stability with 15% is unknown.

Peak estimates are based on garnet stability with an average at 800°C and 10 kbar (Figure 69). As explained above, with better constraints of Fe^{3+} in garnet, this estimate may shift towards higher pressures. Feldspar and amphibole are considered to be retrograde minerals and are therefore used to determine the retrograde part of the P-T path.

Although part of the data seems to fit very precise, intersection of modal abundances and the position of the stability field do not agree with each other and with the rest of the data. A solution for this problem was not found so far.

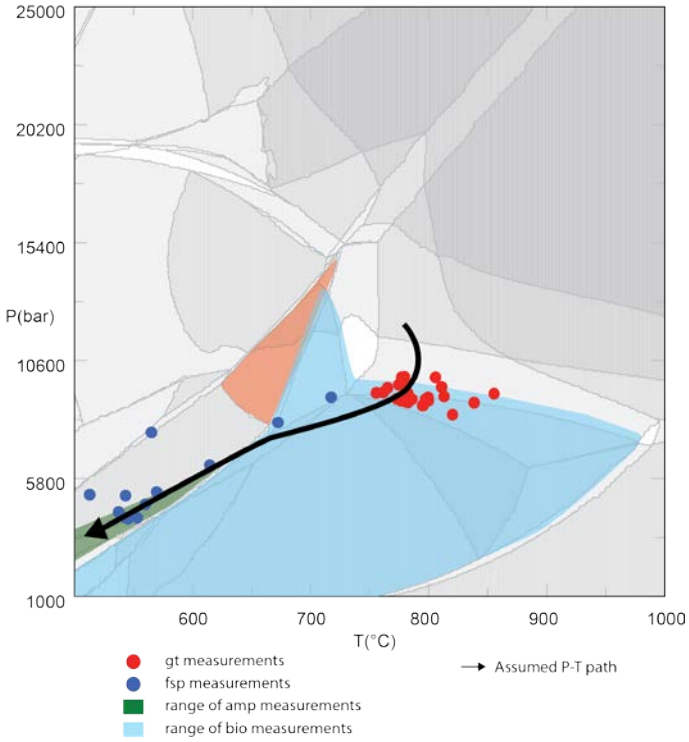

Figure 69. P-T path of sample JI 4-6. Garnet stability is thought to represent peak conditions. The shape of the path is based on garnet, amphibole and feldspar single measurements.

6.6. Hornblende hornfels JI 5-3

Sample JI 5-3 shows a mineral assemblage of amp + pl + bio + ru + chl + q. This mineral assemblage is modelled using the following solution models: GlTrTsPg, Bio(TCC), Pl(h), IlHm(A), Chl(LWV), Opx(HP), Mica(CHA) and Cpx(I). Model runs are calculated for a FeO + TiO_2 + CaO + K_2O + MgO + Na_2O + SiO_2 + Al_2O_3 + H_2O system with SiO_2 used as a saturated component and H_2O as a saturated fluid. MnO was left out of the model as none of the solution models used incorporates MnO.

Figure 70 shows the pseudosection as modelled for JI 5-3 in the P-T range of 0.001-15 kbar and 250-750°C. The stability field which corresponds best with the observed mineral assemblage in thin section is indicated with a red field and contains amp + bio + pl + ru + chl + q. It ranges between 490 – 625°C and 2.3 – 7.2 kbar. The modelled mineral assemblage is exactly the same as the one observed in the thin section.

In order to assess the effect of the amount of water in the system, and to determine the amount of water used to form the above mentioned stability fields, P-H_2O pseudosections were produced for three different temperatures, 500, 600 and 700°C. Figure 71 shows a P-H_2O diagram with H_2O ranging from 0 – 3 wt%. Lines in the diagram indicate the amount of H_2O used in Figure 70 to form the stable mineral assemblage at the given P and T conditions. Larger amounts of water results in excess water. The amount of water used by the model varies strongly throughout the pseudosection. The red stability field as indicated in Figure 70 corresponds to a H_2O concentration of roughly 1.2 wt%. The availability of water strongly affects the stability of opx and aluminosilicates. With decreasing water content, opx and aluminosilicates become stable. Above 1.2 wt% H_2O these phases are not stable at all.

Compositional isopleths of amphibole, plagioclase rims and biotite and mineral modes of all stable minerals in the sample are shown in Figure 72. Isopleths of Mg and Fe of amphibole do not intersect or come close to the isopleths of Ca and Na. However the latter two do intersect at 525°C and 6 kbar. Isopleths of plagioclase follow the same path as sodium and calcium exchange for eachother. Isopleths of biotite fall between 580 – 680°C and 6.75 – 8 kbar. Intersection of modal abundances of the stable mineral assemblage amp + pl + bio + chl + ru + q occurs roughly at 525°C and 7.5 kbar. Intersections of isopleths and mineral modes all occur at slightly higher (±0.75 kbar) than the stability field of JI 5-3 as indicated in Figure 70.

Single EMP measurements of hornblende, biotite and plagioclase rim and core are plotted on the pseudosection as isopleth intersections in Figure 73 in case of an error smaller than 20°C and 0.5 kbar and are tabulated in Appendix IV. For hornblende, only the measurements of the core of the phenocrysts are displayed as other measurements do not show stability in this model. As isopleths for feldspar are parallel over a large range, stability fields for this mineral are displayed, subdivided into rim and core measurements.

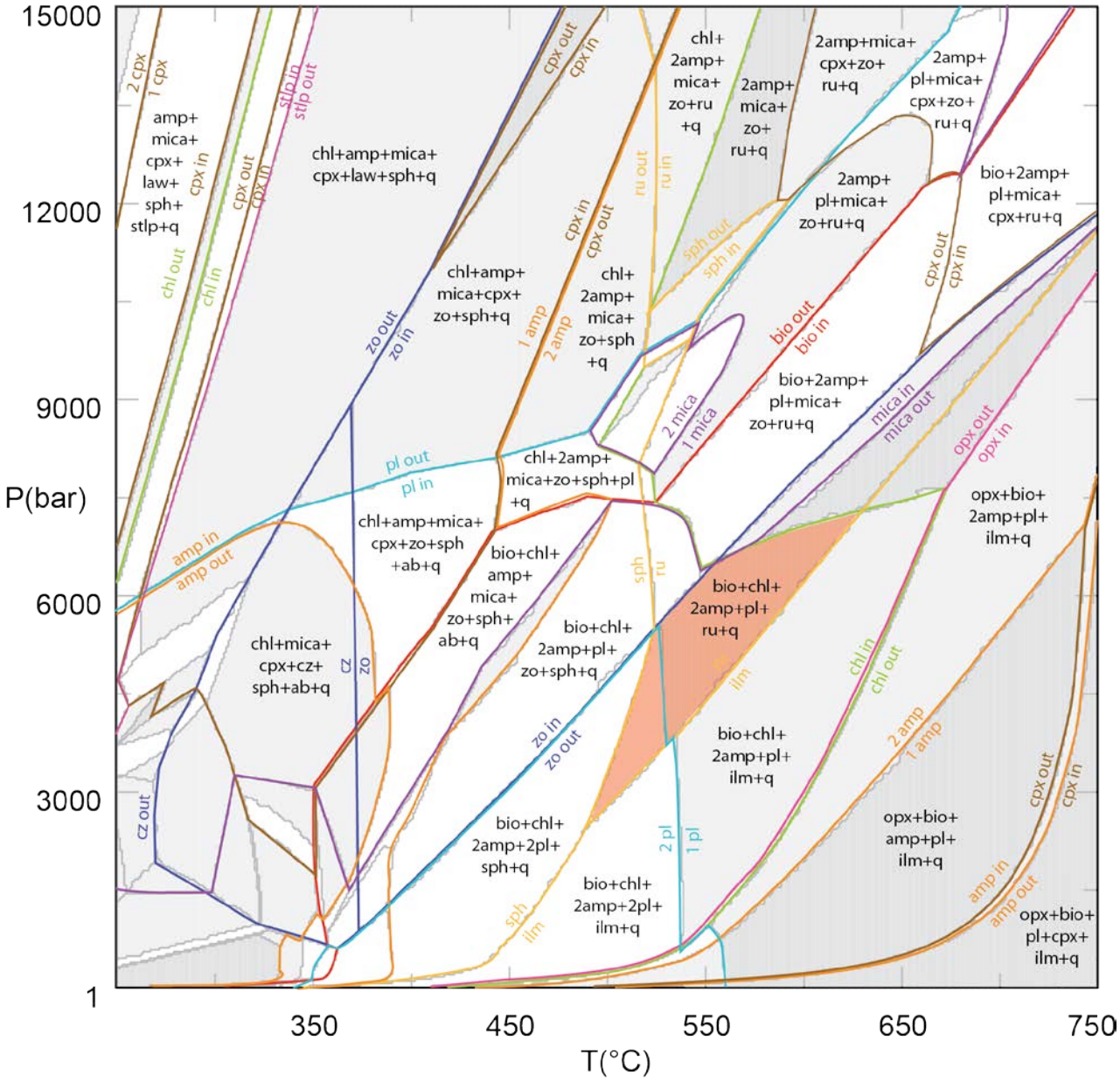

Figure 70. Pseudosection of JI 5-3. Stable mineral assemblage of amp + pl + bio + chl + ru + q is indicated with the red field. Important phase boundaries are indicated with coloured lines and stable mineral assemblages of most fields are indicated.

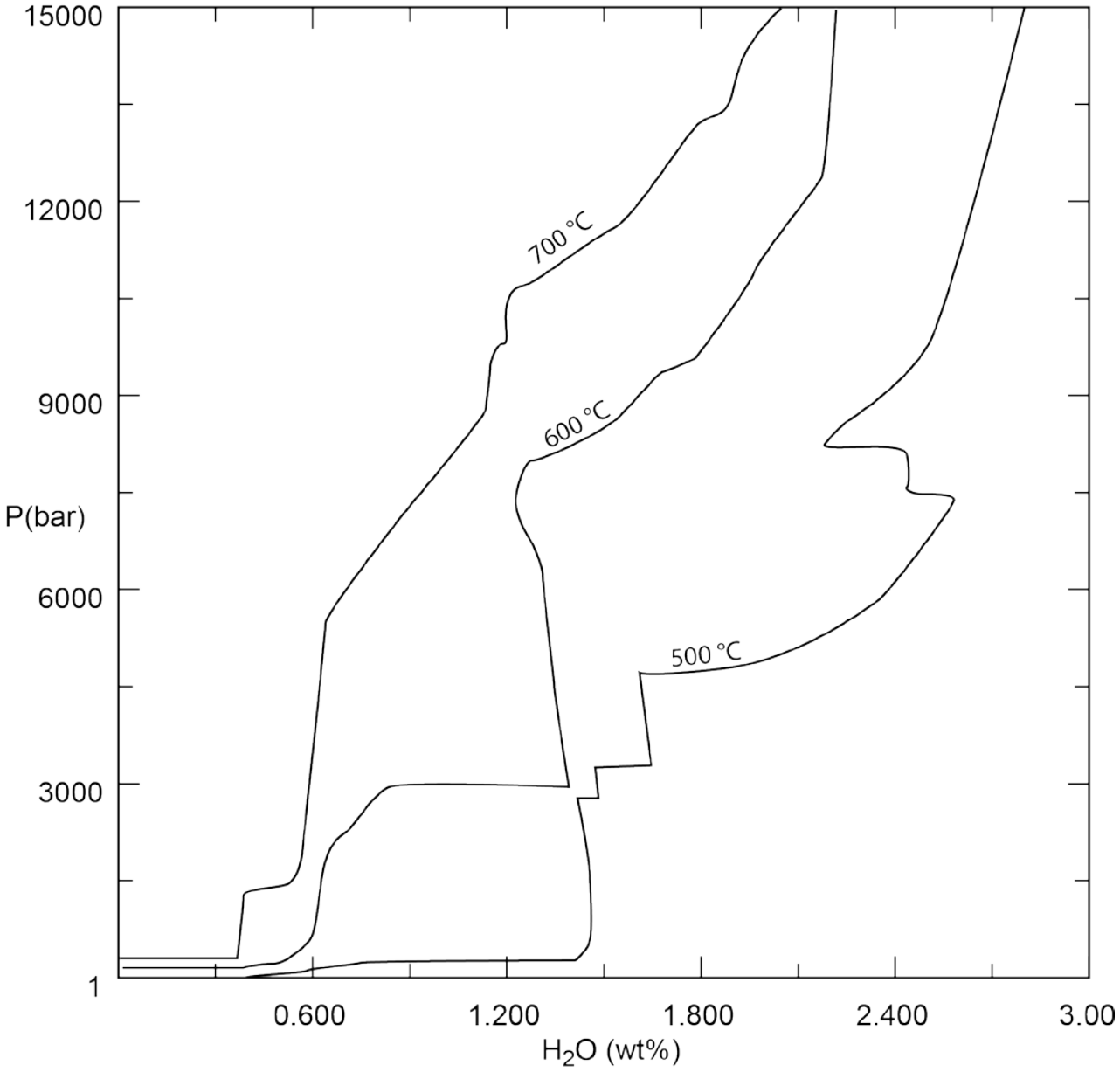

Figure 71. Water content used in the pseudosection of Figure 70 at given pressure and temperature conditions. The stability field indicated in red in the former figure corresponds to a water content of roughly 1.2 wt%.

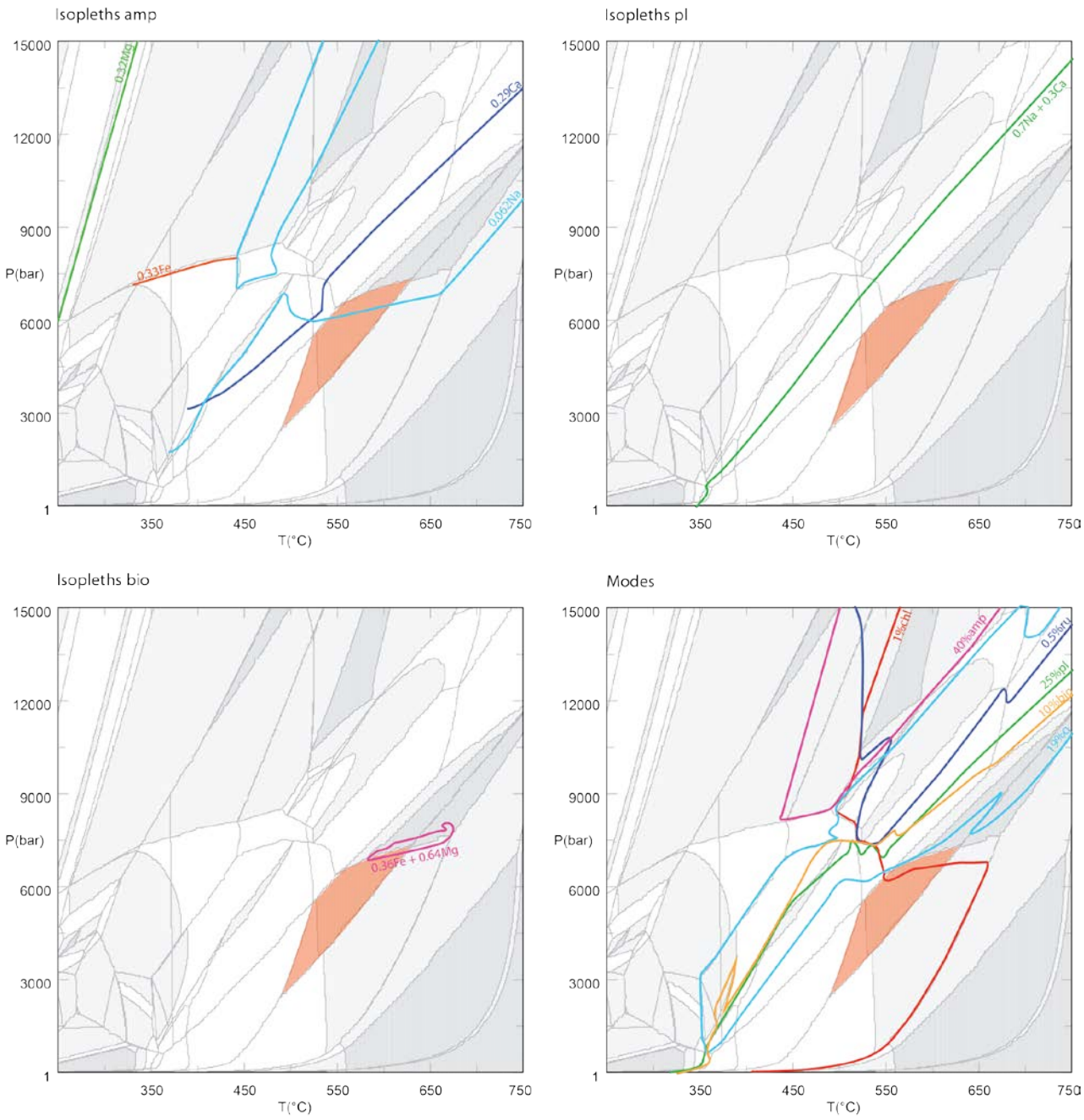

Figure 72. Isopleths of amphibole, plagioclase and biotite and modal abundances of all stable minerals within the sample. Isopleths of plagioclase are based on EMP measurements of plagioclase rims.

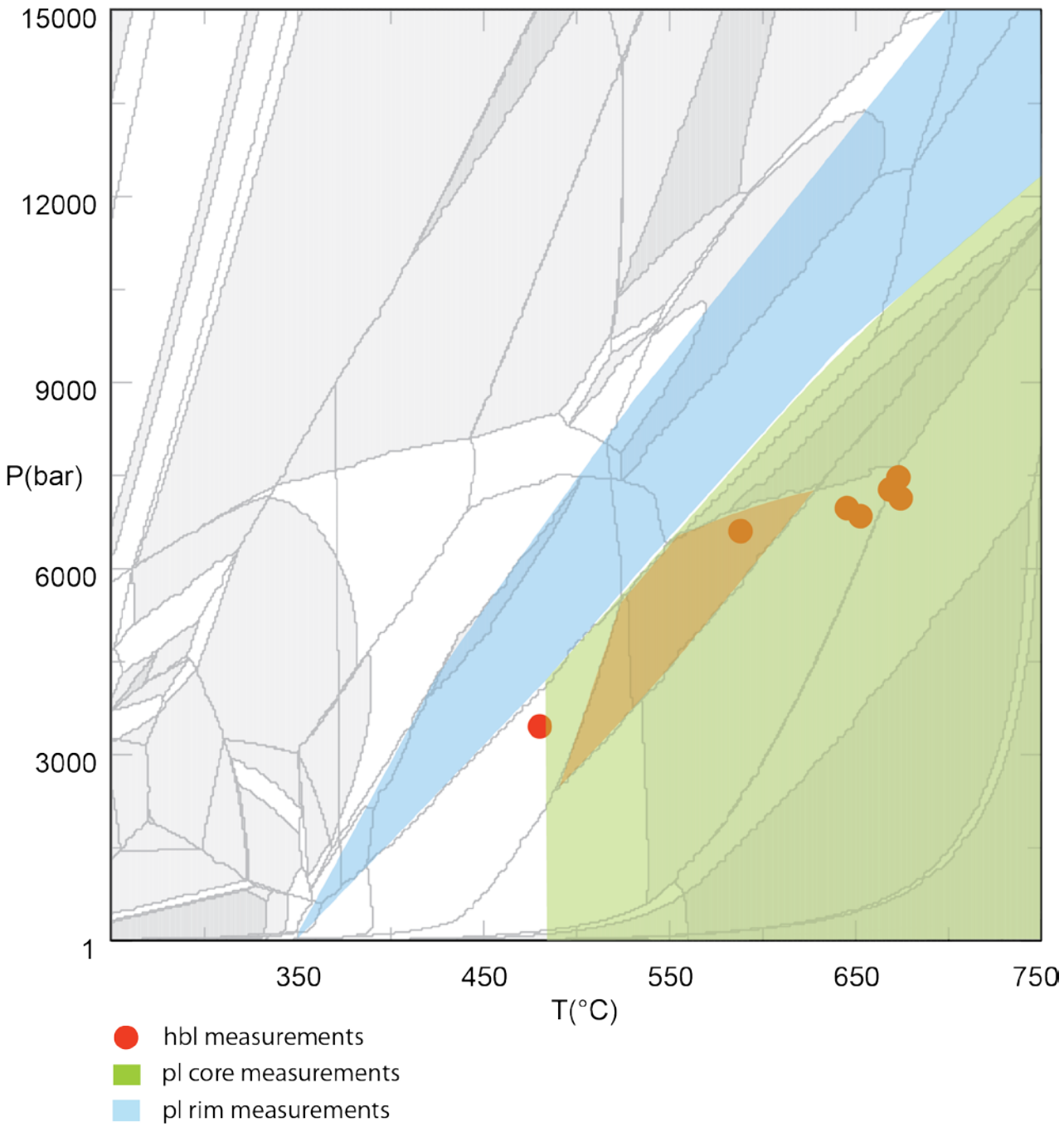

Figure 73. EMP measurements of hornblende, biotite and plagioclase rim and core plotted on the pseudosection based on isopleth intersections. Plagioclase measurements occur throughout the displayed fields.

6.6.1. JI 5-3 model discussion

Sample JI 5-3 is a hornblende hornfels and should therefore be stable in the range of 450 – 650°C and <3 kbar. The stability field of the mineral assemblage of this rock of amp + pl + bio + chl + ru + q falls partly within this ranges with the lowest pressure limits. However, stable hornblende measurements of the phenocryst cores (Figure 73) and isopleths of biotite and modal abundances (Figure 72) all intersect at higher pressure and temperature conditions. Measurements of rims of hornblende phenocrysts and hornblende in the matrix are not stable at all in the modelled pseudosection. However, a better fit could not be obtained. Therefore a P-T path is made based on hornblende core measurements which probably display the chemistry of the protolith, the stability field of the rock within the hornblende hornfels range of conditions and the chemistry of plagioclase core and rim measurements. However, as the real conditions of the rock could not be modelled, this path is less reliable and should be used with caution.

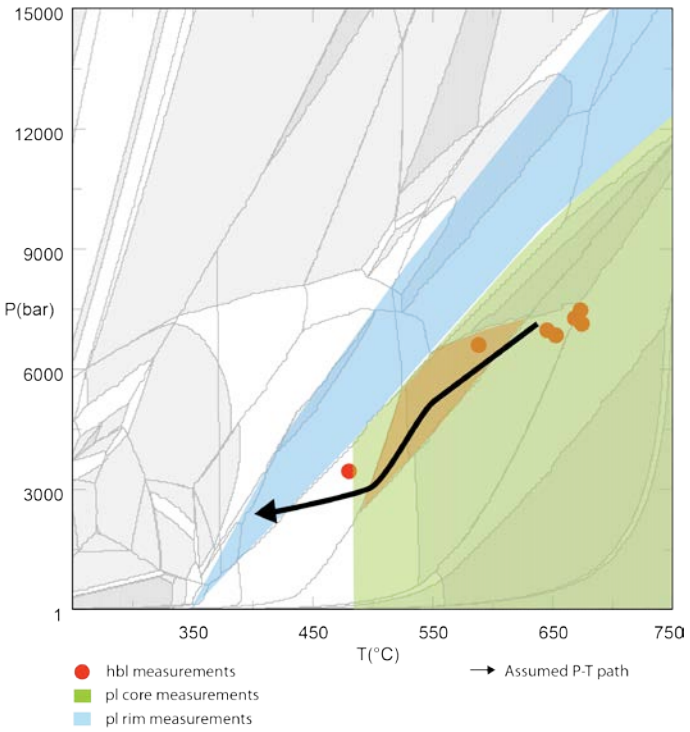

Figure 74. P-T path of sample JI 5-3 from a protolith amphibolite to a hornblende hornfels.

7. Discussion

In this chapter a discussion of the methodology used and the results obtained will be given. Furthermore, a geological interpretation and suggestions for future research will follow.

7.1. Discussion of methodology

Significance and interpretation of the data presented in this study strongly depends on the used methodology. Some of the choices made were based on well thought-through reasoning, whereas others were not intended but inevitable, a discussion will follow on the implications of these choices.

7.1.1. Fieldwork and sample selection

Due to the limited time available in the field, only four locations over a large spatial distance of ± 400 km within the Jinshuikou group were sampled. At three locations metamorphosed rocks were sampled. Unfortunately no metamorphosed rocks apart from one hornfels were sampled from the easternmost location. At these four locations a variety of amphibolites and biotite gneisses were sampled that could be used to carry out $^{40}Ar/^{39}Ar$ dating and thermodynamic modelling.

In particular the amphibolites were quite weathered and the surface parts of the rocks had to be removed before XRF measurements could be done in order to minimize the effects of the altered chemistry of the weathered parts. However, removing more material, revealing the deeper inside of the rock would have resulted in samples that were too small for obtaining a realistic whole rock chemical composition. As the grain size was relatively large (~1mm average) this will result in inhomogeneity problems. Therefore the XRF measurements which are the basis of the thermodynamic modelling may still contain a slight weathering signature which could have an influence on the outcome of the models. For instance more water-bearing clay minerals could be present on the outside of the rock when compared with the water-poor inside.

A complication of sampling biotite/chlorite gneisses with a general mineral assemblage of bio + pl + kfs + q for thermodynamic modelling was the limited amount of minerals in the sample to model. This makes it very hard to define good constraints on the P-T estimates. More mafic samples would have simplified the job of modelling P-T estimates of the Jinshuikou group. However, time constraints in the field made it impossible to search for more mafic samples both at the same sample locations and at a larger number of locations in the Jinshuikou group.

For argon dating, preferably a rock with three different potassium bearing minerals should be selected in order to constrain an uplift history for the rock. However, such kinds of rocks were not found and only one or two different potassium bearing minerals could be separated per sample.

7.1.2. Dating limitations

The argon dating system is suitable for the 'mid-range' temperature spectrum of the thermal history of a rock as maximum closure temperatures are at 525 °C for hornblende and lower for the other K-bearing minerals. It therefore gives only a small part of the thermal history of the samples based on the P-T-t paths derived in Chapters 5 and 6. As shown in Chapter 4 and 6, the chemistry of amphiboles and micas which are used for dating are determined to have conditions that relate to higher temperatures than their closure temperature. It is therefore certain that cooling rather than forming ages were determined.

As is shown by stepwise heating patterns and inverse isochrons in Chapter 5, all but the biotite samples give strong evidence for the presence of excess argon. Ages are calculated based on the inverse isochron and are therefore more accurate but less precise than when plateau ages can be used. Fine-

tuning the ages could be done when the exact influx of excess ^{40}Ar is known (Smye et al., 2013). A possibility for doing this is by measuring the amount of ^{40}Ar in a K-lacking mineral such as plagioclase (personal communication with Andriessen (2015)). Defining the amount of excess argon in the surroundings of the samples by this method will enable us to make a better estimate of the ages as the source of the isotopes is better constrained. It is therefore advisable to implement this method on the available samples in further research.

In this case excess argon was encountered in all rock samples of the entire research area. Therefore, one would expect excess argon to be present in all minerals and not just in some. However, evidence for excess argon in biotite is not visible. Reason for this is probably due to the high amounts of potassium in a biotite grain. When the closure age is high (> 100 Ma), the amount of potassium being decayed is large, obscuring the excess argon. For K-feldspar you would expect the same effect. However, K-feldspars have different degassing domains which in some cases keeps excess argon still visible in the high temperature domain (Lovera et al., 1989).

One could argue that stepwise heating patterns give evidence for partial resetting and thus provide more detail on the thermal history of the sample. However, as many of the dates found are obscured by excess ^{40}Ar, it is hard to tell the exact effect of partial resetting and interpretation should be treated with caution.

7.1.3. Model limitations

As described above, the sample selection already had an influence on the outcome and reliability of the thermodynamic models. In addition, a couple of the model based limitations and choices further influenced the outcome.

7.1.3.1. Omission of MnO

Only a limited amount of solution models includes manganese endmembers. Therefore including MnO in the model results in overestimation of stability of these few endmembers and underestimating stability of others. For this reason it is common practice to omit MnO in the model to overcome obvious discrepancies (Powell and Holland, 2008). However as shown by Tinkham et al. (2001) and references therein, leaving MnO out results in large discrepancies in garnet stability (± 150 °C and 4 kbar for the combined effect of MnO and CaO). This implies that cautiousness is needed when interpreting garnet stability in a MnO-absent system. For all samples in this study MnO was left out of the model and therefore real stability of all samples could be lowered with a maximum of (± 150 °C and 4 kbar).

Another effect which has to be addressed when omitting MnO is that this oxide has to be replaced by the remaining oxides. In this case it was chosen to not recalculate the amount of oxides as MnO only counted for a maximum of 0.238 wt%, which is relatively small compared to the deviation of the sum of all oxides from 100%. However, even though small, the missing amount of Mn in the model has to be replaced by cations occupying the same site in a mineral and will thus have more effect on certain oxides (e.g. CaO, FeO and MgO in the case of garnet) than it will on for instance SiO_2 and Al_2O_3.

7.1.3.2. Ferrous versus ferric iron

Iron measured during XRF measurements is reported as Fe_2O_3, but actually includes also FeO. For modelling pseudosections, the assumption was made that all iron was present in the ferrous state. Therefore XRF measurements of Fe_2O_3 were recalculated to FeO. Only if ferric iron bearing phases such as epidote were present in a sample, a certain amount of O_2 was added to the model in order to transform (part of) the iron from Fe^{2+} to Fe^{3+} (See Paragraph 6.2 for details on how the amount of O_2 is determined). However, also biotite, amphibole, pyroxene and garnet can contain Fe^{3+}, so the stability of these phases are also affected by changes in the amount of O_2 in the model. The solution models used

for biotite, amphibole and pyroxene all include Fe^{3+}, although the model for garnet does not. Therefore the stability of garnet will be affected when adding O_2 to the system as predictions will be further deviating from reality than they are for the other Fe^{3+}-bearing minerals. As apparently both the absence of MnO and the presence of Fe^{3+} influence the stability of garnet, stability fields calculated for this mineral should be treated with caution. Unfortunately garnet is the only mineral which is appropriate for estimating peak metamorphic conditions in most rocks used in this study and therefore peak temperature and pressure estimates are likely to be less reliable than assumed at first.

Garnet is not the only mineral influenced by changes in the amount of Fe^{3+} in the model. Within biotite, Fe^{2+} and Mg substitute for each other and Fe^{3+} and Ti do so too. When assuming all iron to be ferrous, the bulk Fe/Mg ratio is generally assumed to be equal to this ratio in the mineral site occupation within the biotite (Powell and Holland, 2008). However, this will directly influence the amount of Ti needed to fill the second mineral site and thus the amount of Ti available for other minerals such as rutile. In the models produced in this study, rutile is generally underestimated in modal abundance, which is assumed to be a direct result of the overestimation of the Ti-occupation of the biotite mineral sites.

Also amphibole and pyroxene are influenced by the absence of Fe^{3+} as mineral stabilities will be different and thus phase boundaries are situated differently. It is therefore better to include O_2 in every model in order to have Fe^{3+} present. However, estimating the right amount of ferric iron is a very difficult and imprecise task which becomes even harder when no epidote is present in the sample as estimates are based on the modal abundance of epidote. A discussion on the O_2 estimation in order to produce enough Fe^{3+} is given in the next section.

7.1.3.3. O_2 estimation

The amount of O_2 added in the model in order to produce Fe^{3+} is fully based on the stability of epidote in this model. Getting to the right amount of O_2 is relatively imprecise as a trial and error method at different O_2 concentrations has been applied. First a certain amount of O_2 was discarded based on the absence of a stability field containing the stable mineral assemblage of the sample. However, as it can be very hard to actually define the equilibration volume (paragraph 7.1.3.6), an estimate which is only slightly off, can already cause discarding the right amount of O_2. A further narrowing of the range of possible O_2 concentrations was done by intersecting modal abundance isopleths of the stable mineral assemblage and, depending on the type of minerals present in the sample, also intersection of chemical compositional isopleths. As this is a very time consuming process, the interval of O_2 concentrations at which these tests were performed could not be too small and was generally set at 0.2 wt% for a first try and subsequently 0.1 or 0.05 wt% for further narrowing down. In practice, a true intersection of modal abundance and chemical compositional isopleths rarely occurs as the solution models that are used are a simplification of reality. The lack of this true intersection was the case for every model within this study. Therefore determining a best fit is hard, especially when two tests give an equally good result on visual basis. A statistically best fit was not determined and thus the choice only relies on visual and personal interpretation of a best fit. Furthermore, the actual best amount of O_2 can be 0.05 - 0.1 wt% off as tests were not further narrowed down.

As already explained in paragraph 6.2.1, having both O_2 and a CO_2 fluid in the model makes it even harder to predict how much O_2 should be present, as the mineral stability will be affected by both components. Modelling is only possible in 2D with contours of a third variable. Therefore, either O_2 or CO_2 had to be fixed in order to determine the effect of varying concentrations of the component on the stability field. In theory it would be possible to produce an extensive dataset for the whole range of O_2 and CO_2 concentrations. However this would take several weeks of processing data and is therefore not performed in this study.

7.1.3.4. H_2O saturation

For all models, H_2O is assumed to be a saturated component. However, this is not a realistic assumption as most samples have experienced temperatures over 700 °C so it can be expected that most water has been removed during dehydration reactions in the prograde part of the path. Water was therefore probably not available anymore for retrograde reactions. Sample JI 4-6 gives clear evidence for water undersaturation during the retrograde path as garnet still seems (meta-) stable instead of being replaced by hydrous phases such as biotite or chlorite. However, for the prograde part of the path a H_2O saturation is realistic as protoliths consist of sedimentary rocks and basic volcanics which generally contain high amounts of H_2O. For sample JI 2-1 the same counts but in a less extreme manner as garnet is partly replaced.

Sample JI 2-2 is an example of most probably H_2O saturation during the entire metamorphic history as only tiny hints of remaining garnets and relatively large amounts of hydrous phases (14%) such as chlorite, muscovite and biotite are present.

Water was chosen to be saturated for modelling purposes as all samples contain reasonable amounts of water bearing minerals such as amphibole, biotite, chlorite and muscovite. As is shown for samples JI 2-2, JI 4-6 and JI 5-3 in Chapter 6, the effect of including less water than the saturation volume leads to large changes in mineral stability. Especially for the retrograde part of the paths this is an important aspect to take into account. However due to time constraints the exact amount of water for each sample is not defined. Therefore, the retrograde part of the P-T paths can be subject to changes when including the right amount of water.

7.1.3.5. CO_2 estimation

To estimate the amount of CO_2 fluid in the model, the same procedure as for O_2 is used, using the stability of calcite instead of epidote. This is again a relatively imprecise trial and error method with a test interval of 10% CO_2 fluid (e.g. 0.1 CO_2 + 0.9 H_2O etc.), assuming a saturated CO_2 + H_2O fluid. For detailed thoughts on the inaccuracy, see paragraph 7.1.3.3.

7.1.3.6. Estimating the equilibration volume

In order to correctly model the pertinent stable mineral assemblage in a rock, the equilibration volume needs to be correctly estimated. However, this was complicated for some samples as they contain a suite of assemblages being stable throughout their history. Zoning and (partly) unstable minerals make it hard to correctly estimate the right distribution of minerals at stable conditions (Powell and Holland, 2008). This is especially the case for sample JI 2-1, which contains parts of remaining garnet and ingrowth of amphiboles, feldspars and calcite. Based on exchange of elements between these minerals an estimate could be made of which mineral assemblages were stable at the same time. However estimating modal abundances of this stable mineral assemblage is harder as part of the minerals may be completely vanished, which may lead to flaws in the model. Also for sample JI 5-3 it is hard to make a proper estimate as both amphibole and plagioclase are highly zoned. This results in certain elements being locked in a minerals' core and thus will affect the mineral assemblage that can be stable.

7.1. Discussion of argon ages

As shown in Chapter 5, the $^{40}Ar/^{39}Ar$ ages are not all very straightforward crystallization ages, but rather cooling ages, obscured by excess argon and partial resetting. This makes it difficult to form a comprehensive geological story out of them, but not impossible. Ages from literature named in this paragraph are listed in Table 11.

A reason for this 'imperfect' behaviour of the minerals can be found in the complex geological history the rocks and minerals have experienced. Plate subduction and the associated presence of a fluid which can mobilize argon, enabled the build-in of excess argon into the minerals. This excess argon was

locked into the grains as diffusion within minerals became inefficient after cooling below the closure temperature (Smye et al., 2013). Furthermore, minerals were partly reset during granite intrusion phases in the Ordovician – Devonian and Permian – Triassic. Another complicating factor is the overprinting of high temperature mineral assemblages by low temperature minerals such as chlorite, which does not contain any potassium, whereas its preliminary mineral (often biotite or amphibole) often do.

Based on closure temperature, ages within one sample, and preferably also within the entire Jinshuikou group, follow a trend of oldest towards youngest age from hornblende, muscovite, biotite, K-feldspar. Closure temperatures of these minerals are: 450 – 525°C, 325 – 375°C, 260 – 350°C and 125 – 350°C (Harrison, 1982; Spear, 1993). However, these numbers can vary up to 75°C according to literature. (Partial) resetting gives evidence for re-heating above the minerals closure temperature.

Based on the argon ages found in this study, four different age groups were determined. The first group exists of metamorphic hornblende and muscovite cooling ages of granulite facies rocks between 450.27 ± 22.60 Ma and 403.25 ± 17.89 Ma. This group corresponds to the accretion of the South Tarim- and Qaidam block to the North Tarim and North China block during Silurian – Mid Devonian (Figure 1) and associated closure of the Paleo-Tethys. This is further strengthened by a 427 ± 4 Ma hornblende- and 408 Ma muscovite plateau age found by Chen et al. (2002) and a granulite facies hornblende age of 395.8 ± 7.2 Ma (Liu et al., 2005). This age group also coincides with zircon SHRIMP ages of granulite-facies metamorphism of 460 ± 8 Ma and granitic anatexis of 402 ± 6 Ma as found by Zhang et al. (2003). Also U-Pb zircon ages coming from granitic intrusions within the Jinshuikou group between 484.6 ± 7.3 Ma and 396 ± 18 Ma are in agreement with the ages related to the first age group as found in this study (Dai et al., 2013; Li et al., 2013; Long et al., 2006; Long et al., 2005).

The second age group ranges from 353.40 ± 14.62 Ma to 263.43 ± 9.97 Ma and consists of metamorphic biotite and K-feldspar ages and one hornblende age. This age group corresponds to the accretion of the former blocks to Siberia and the indention of South China from the south during Carboniferous – Permian. One matching granitic K-feldspar age of 338.4 ± 0.4 Ma was found in literature (Mock et al., 1999). In the literature, matching ages of intrusive rocks based on U-Pb zircon ages were only found approximately 200 km to the west of the westernmost sample location. As this is thought to be spatially too far apart from each other, these ages were not used for comparison.

The third age group ranges from 252.58 ± 8.87 Ma to 199.86 ± 43.37 Ma for metamorphic K-feldspar ages and magmatic hornblende, biotite and K-feldspar ages. The hornblende age of 273.92 ± 4.26 Ma from age group 2 could also be counted to this age group due to its higher closure temperature. This age group corresponds to the still ongoing indention of the South China block and the accretion of the Qiangtang terrain during Late Permian – Late Triassic. Liu et al. (2005) found a similar age group of 242 – 212 Ma which relates to magmatic intrusions. These ages are well in agreement with ages found by Mock et al. (1999) for the Golmud Hydro Batholith 30 km south of Golmud (Geermu) of 252 ± 5 Ma for biotite and 224 ± 4 Ma for K-feldspar. Also the a U-Pb zircon age of 253.1 ± 4.7 Ma found by Dai et al. (2013) is in agreement.

The last age group ranges from 215.11 ± 5.48 Ma to 184.26 ± 7.52 Ma for metamorphic K-feldspar and magmatic hornblende, biotite and K-feldspar. This group corresponds to accretion of the Lhasa terrain and still ongoing closure of the Tethys sea during Late Triassic – Cretaceous. U-Pb zircon crystallization ages between 228.4 ± 2.4 Ma and 194.9 ± 1.0 Ma and ZHe ages between 215 ± 31 Ma and 185.8 ± 9.1 Ma found by Dai et al. (2013) are in agreement with the age group found in this study.

From the second age group of 353.40 ± 14.62 Ma to 263.43 ± 9.97 Ma, partial resetting both in biotite and K-feldspar towards the third age group took place. This implies that temperatures in the Jinshuikou group exceeded the minimum closure temperature of K-feldspar and biotite of 260 °C during this event. As muscovite does not show evidence of partial resetting, the temperatures probably did not exceed 325 °C which is the minimum closure temperature for muscovite.

For the magmatic ages, we see partial resetting within the third age group for biotite ages. This is probably caused by a series of magmatic pulses during the accretion of the South China block and accretion and subduction of the Qiangtang terrain. New magmatic pulses increased the local temperature, causing partial resetting of the argon system. Partial resetting from the third to the fourth age group is only observed for the K-feldspar ages and one single biotite age. Accretion and subduction of the Lhasa terrain and the associated granitic intrusions are assumed to have caused heating up of the surroundings, but due to the larger distance of the Jinshuikou group to the suture zone, temperatures reached only slightly over 125 °C. This is high enough to partially reset the K-feldspar ages, but not sufficient to reset the biotite system. The single biotite age that has been reset, is probably caused by a local heat source that added to the heat caused by the accretion phase.

For biotite single grain ages, we can observe a similar pattern of resetting, resulting in age clusters corresponding to the second to fourth age group. For sample location 4, Figure 46 shows an overlap of youngest metamorphic ages and oldest magmatic ages. This implies that the onset of magmatism resulted in resetting of part of the metamorphic biotite grains, which resulted in younger ages than the bulk. Also within the magmatic sample of location 4 we observe a main age group corresponding to the indention of the South China block during Carboniferous – Permian, but also ages corresponding to the third and fourth age group of accretion of the Qiangtang and Lhasa terrains.

Lithology	Method	Age (Ma)	Source
Granitic gneiss	$^{40}Ar/^{39}Ar$ biotite	233.4 ± 4.3	(Liu et al., 2005)
Granitic gneiss	$^{40}Ar/^{39}Ar$ biotite	218.6 ± 4.1	
Granitic gneiss	$^{40}Ar/^{39}Ar$ biotite	212.2 ± 4.1	
Granulite	$^{40}Ar/^{39}Ar$ biotite	222.1 ± 4.4	
Granulite	$^{40}Ar/^{39}Ar$ hornblende	395.8 ± 7.2	
Granitic gneiss	$^{40}Ar/^{39}Ar$ muscovite	242.0 ± 4.3	
Epidote-amphibolite	$^{40}Ar/^{39}Ar$ hornblende	427 ± 4	(Chen et al., 2002)
Gneiss	$^{40}Ar/^{39}Ar$ muscovite	408	
Granitoid	ZHe	215 ± 31	(Dai et al., 2013)
Granitoid	AHe	93.0 ± 17.0	
Granitoid	SHRIMP Zircon U-Pb	253.1 ± 4.7	
Granitoid	SHRIMP Zircon U-Pb	228.4 ± 2.4	
Granitoid	SHRIMP Zircon U-Pb	194.9 ± 1.0	
Granite	LA-ICP-MS Zircon U-Pb	484.6 ± 7.3	(Li et al., 2013)
Granite	LA-ICP-MS Zircon U-Pb	439.0 ± 5.9	
Granite	LA-ICP-MS Zircon U-Pb	424.0 ± 3.5	
Granite	LA-ICP-MS Zircon U-Pb	261.5 ± 3.7	
Granodiorite	SHRIMP Zircon U-Pb	407 ± 3	(Liu et al., 2012)
Granite	$^{40}Ar/^{39}Ar$ K-feldspar	338.4 ± 0.4	(Mock et al., 1999)
Granite	$^{40}Ar/^{39}Ar$ biotite	252 ± 5	
Granite	$^{40}Ar/^{39}Ar$ K-feldspar	224 ± 4	
Granite	AHe	24 ± 4.2	(Clark et al., 2010)
Metasediment	AHe	24 ± 4.2	
Granodiorite	LA-ICP-MS Zircon U-Pb	396 ± 18	(Long et al., 2006)
Granulite	SHRIMP Zircon U-Pb	460 ± 8	(Zhang et al., 2003)
Granite	SHRIMP Zircon U-Pb	402 ± 6	

Table 11. Ages from literature.

7.2. Discussion of thermodynamic modelling

Pressure-Temperature paths for samples modelled in this study and the study of Huijgen (2015) are combined in Figure 75. Although numeral assumptions were made and models showed discrepancies from the observed pertinent mineral assemblages in the samples as described in Chapter 6, all P-T paths follow a quite similar metamorphic history as is shown in Figure 75. In this section, all samples including the ones modelled in this study and in Huijgen (2015) are discussed and compared with each other. Modelling details of samples JI 1-3, JI 1-4 and JI 4-3 can be found in Huijgen (2015).

Part of the samples (e.g. JI 1-1, JI 1-3, JI 1-4, JI 4-3 and JI 5-3) only contain retrograde minerals. Therefore the prograde path could not be determined and peak metamorphic conditions could only be displayed as minimum peak conditions as explained in Chapter 6. For samples that do display part of the prograde path, peak metamorphic conditions plot in the low eclogite/upper granulite facies of 13.5 kbar and 780-830°C for sample location 2 (JI 2-1 and JI 2-2) and in the granulite facies of 10 kbar and 800°C for sample location 4 (JI 4-6). Sample JI 4-3 follows a similar path as JI 4-6 and reaches almost the same conditions as peak conditions of JI 4-6. Samples JI 1-1 and JI 1-4 follow the same retrograde path although JI 1-1 lies at 50°C higher temperature conditions for similar pressure. JI 1-3 shows similar conditions for the upper part of the P-T path as JI 1-4, although discrepancies between the two arise at pressures below 7 kbar. However, as these samples are modelled by Huijgen (2015), and details on this process are missing at this moment, a decent explanation for this discrepancy cannot be given here. A possibility is that EMP measurements which plot at 5 kbar and 470°C belong to prograde minerals rather than retrograde as was the case for sample JI 2-2. In that case the P-T path could more or less follow the path of sample JI 2-2. However, due to lack of information within this study this could not be verified.

The P-T path of sample JI 1-1 reveals a higher temperature compared to that of sample JI 1-4. The discrepancy between the two could have resulted from differences in the solution models used. The main difference is the choice for GlTrTsPg as the amphibole model in JI 1-1 and Amph(DPW) in JI 1-4. As shown in paragraph 6.5, choosing GlTrTsPg instead of Amph(DPW) resulted in an unrealistic amphibole stability up to much higher temperatures (>200°C) for pressures below 12kbar. Therefore the path of JI 1-4 could be argued more realistic than the path of JI 1-1 for sample location 1. The same issue could be the case for sample JI 2-1 which means that the path of JI 2-2 (which does not contain amphibole and is therefore not prone to this problem), is the most realistic for sample location 2.

When adapting the temperature profile of samples JI 1-1 and JI 2-1 to a profile based on the Amph(DPW) model, we could state that sample location 2 has experienced the highest pressure-temperature conditions of 13.5 kbar and 780°C. Location 4 has experienced similar to slightly higher temperatures of 800°C and lower pressure conditions of 10 kbar. For location 1, no peak conditions could be determined, although based on the shape of the other P-T paths and the retrograde part of the paths at location 1, it can be argued that peak conditions are probably similar to those of location 2. This results in an asymmetric metamorphic stage with higher pressures in the western part of the Kunlun Mountains, and lower pressures with similar to slightly higher temperatures in the eastern part of the Kunlun Mountains.

Only little research on metamorphic conditions in the Kunlun Mountains and especially in the Jinshuikou group has been carried out so far. Chen et al. (2002) and Liu et al. (2005) both report of metamorphosed sequences of epidote-amphibolite with relics of granulite facies, which corresponds to results found in this study. Liu et al. (2005) also performed thermodynamic modelling on three granitic gneisses of amphibolite facies and two granulites from the Jinshuikou group. This data is displayed in Figure 75 with black stars and corresponding error bars. Part of the data of Liu et al. (2005) agrees with data found in this study and is in equilibrium at amphibolite facies, or, just within P-T error, of upper granulite facies. However, sample conditions corresponding to middle granulite facies with pressures between 7.1 and 4.5 kbar and temperatures of 826 - 885°C as obtained by Liu et al. (2005) were not

found in this study. This discrepancy could be due to sample limitations, as according to Liu et al. (2005) granulite facies can only be found as relics north of the Central Kunlun Fault. It is therefore likely that these granulite facies samples were just missed in the field and not sampled.

This study seems to be the first to report of rocks having experienced eclogite facies metamorphism, overprinted by amphibolite and/or greenschist facies. No other report on eclogite facies rocks in the Jinshuikou group have been found.

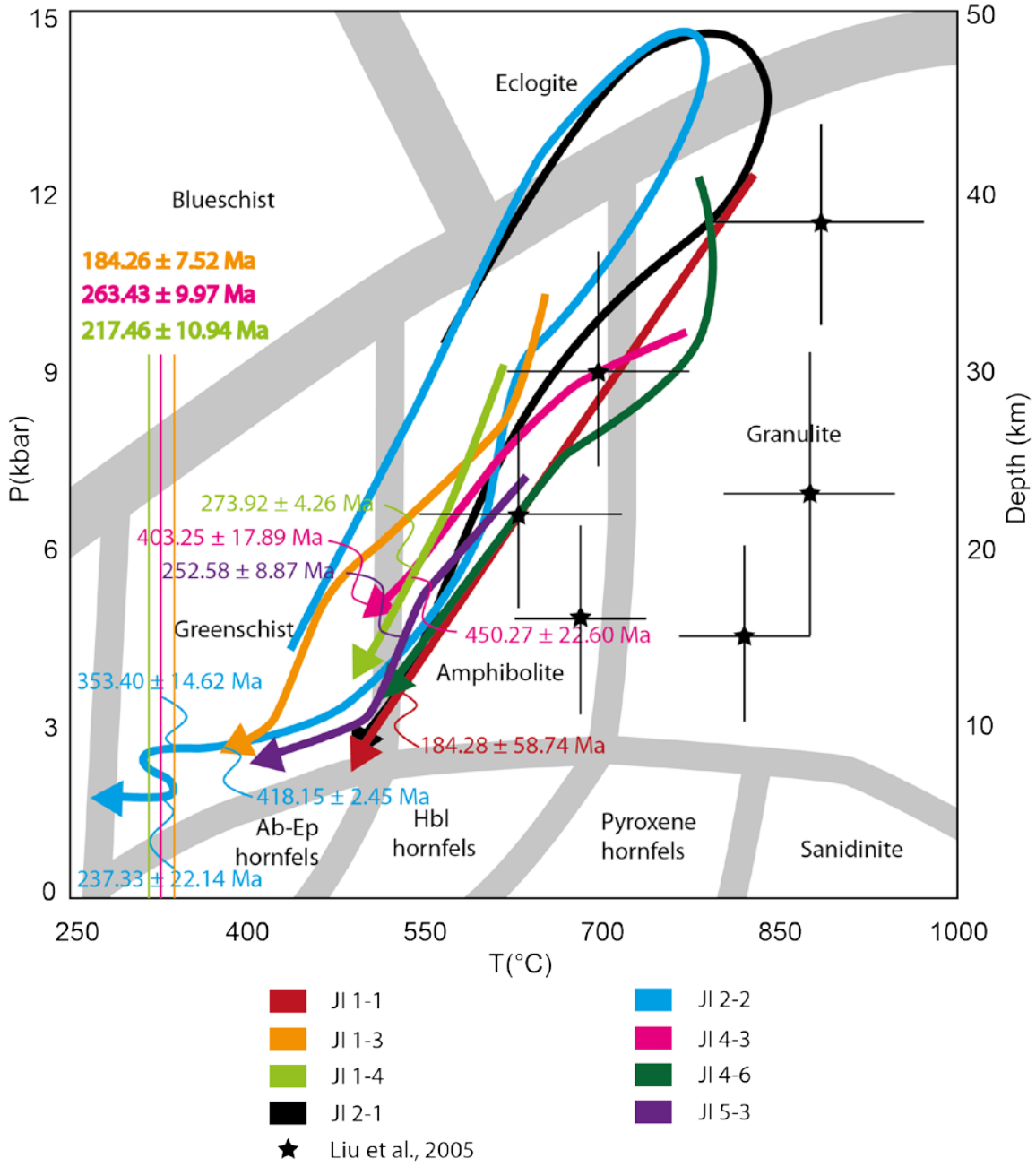

Figure 75. P-T-t paths of this study and the study of Huijgen (2015) All follow a similar path with peak conditions of lower eclogite/granulite facies and retrogression through amphibolite and greenschist facies. Note that the wiggle in the lowest part of the path of sample JI 2-2 is an exaggeration based on partial resetting. P-T conditions of Liu et al. (2005) are displayed with stars and correspond partly to the data found in this study. Ages are displayed onto the path at the right closure temperatures if possible and otherwise displayed with a line where the path could cross the closure temperature.

7.3. Geological implications

In Figure 76 age data obtained in this study and from literature is displayed and correlated based on spatial distribution. Literature based ages are displayed in Table 11 and references are listed in the legend of Figure 76. Cooling histories for each sample location are displayed with a thick line, which approximately represents the vertical error. Zircon U-Pb data is correlated with ages found in this study within the vicinity (<50km) of the sample location. As not much published data exists from the western part of the Eastern Kunlun Mountains, it was not possible to correlate sample location 2 with zircon U-Pb data. Furthermore, the thermal history of location 2 is based on only two data points, which both suffered from complications concerning excess argon. It is therefore possible that the resulting cooling history for this location is less meaningful.

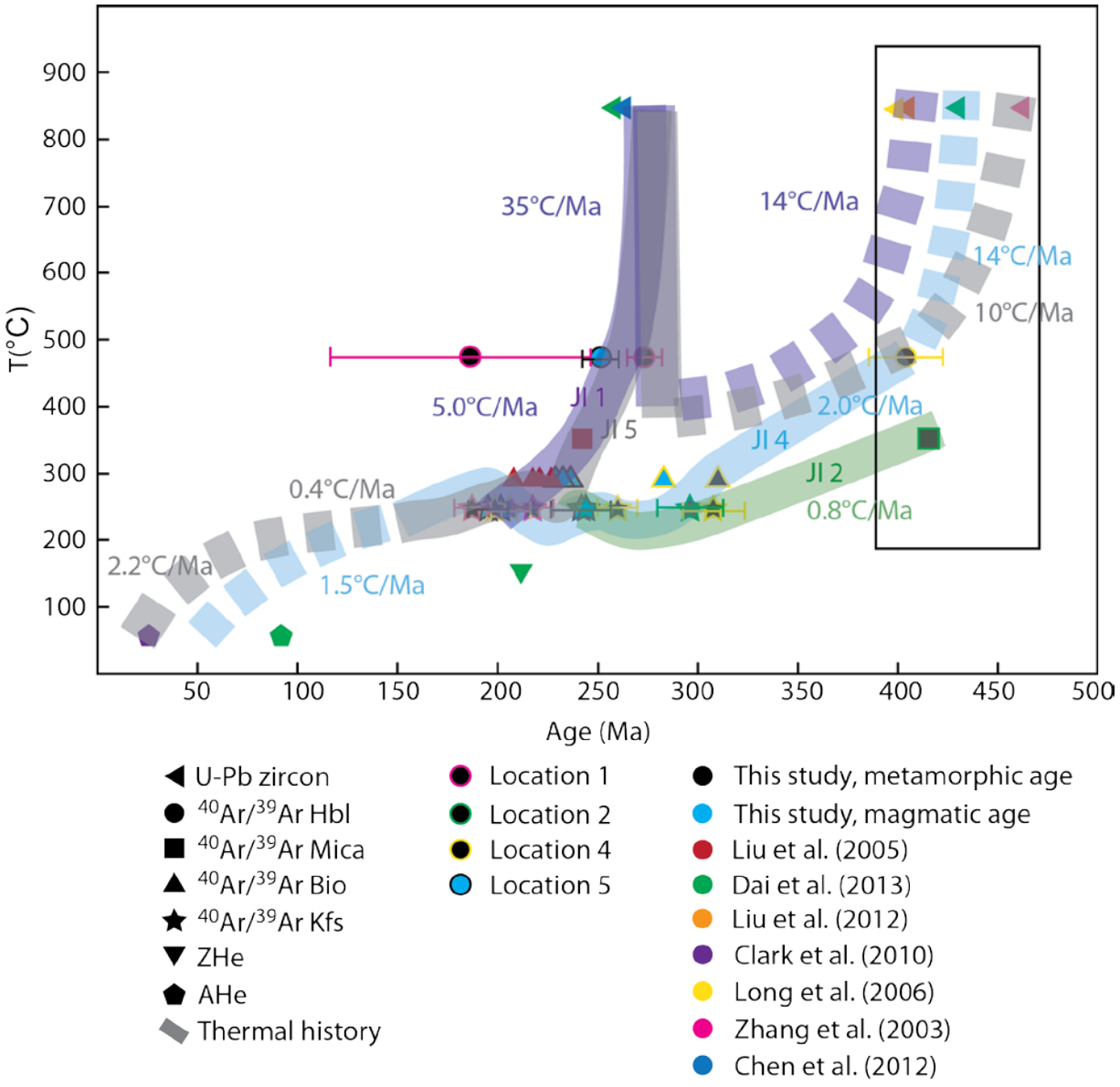

Figure 76. Thermal history of the Jinshuikou group. Different symbols indicate various dating methods whereas colours stand for the source. The cooling speed for different segments is indicated. As the cooling path of JI 2 is based on only two measurements with major issues concerning excess argon, this may not be very conclusive for the thermal history of location 2. Age errors (2σ) are displayed in case they are smaller than the symbol indicating the age.

Figure 76 shows Silurian – Devonian ages for U-Pb zircon and $^{40}Ar/^{39}Ar$ hornblende and muscovite, which are outlined by the black box. Based on peak temperature conditions in Figure 75 and temperature-time constraints in Figure 76, metamorphism of the Jinshuikou group is thought to have taken place during the this period. The metamorphic event is thought to have occurred simultaneously with granitic intrusions. From the high (850°C) temperatures of sample locations 1, 4 and 5 exponential cooling took place with an initial estimated rate of 10 – 14°C/Ma. The cooling rate is dependent on the depth placement of the intrusion within the crust. The intrusion at location 5 was situated lower in the crust than at locations 1 and 4, which caused a lower relative temperature difference and thus slower cooling. The hornblende age of 403 Ma at location 4 was probably also present at locations 1 and 5, but due to later resetting not preserved. Location 1 and 5 experienced strong heating due to intrusion of new granitic plutons with a Permian – Triassic age which is demonstrated by U-Pb zircon ages and visible in Figure 77 by Chen et al. (2012). This extensive emplacement of granitic intrusions is also known as the Kunlun Batholith, which formed during active subduction of the Paleo Tethys (Harris et al., 1988). This completely reset the argon dating system and only ages from this event on are preserved. The hornblende hornfels from location 5 contains dated phenocrysts of Permian – Triassic age but a modelled chemistry of amphibolite facies (Paragraph 6.6). This seemingly contradiction can probably be explained as the amphibolite facies chemistry resulted from the Silurian – Devonian metamorphic event, whereas the hornfels texture was formed during granitic intrusions in the Permian – Triassic.

From the onset of magmatism around 270 Ma until ~225 Ma, exponential cooling took place with an initial rate of 35°C/Ma and gradually decreasing to 5.0°C/Ma. For sample location 1, no age data younger than 200 Ma is available and so no further cooling history is determined. For sample location 5, age data both from this study and the study of Liu et al. (2005) show evidence of cooling biotite and K-feldspar ages between 250 and 200 Ma, and subsequent partial resetting of these ages. This might be related to the accretion of the Qiangtang and Lhasa terrain to the already existing complex.

At sample location 2, only small (<10 km) Permian-Triassic plutons are present. Therefore, rocks were not heated extensively and could retain their former age information of Silurian-Devonian age. Only partial resetting in K-feldspar took place during the magmatic event.

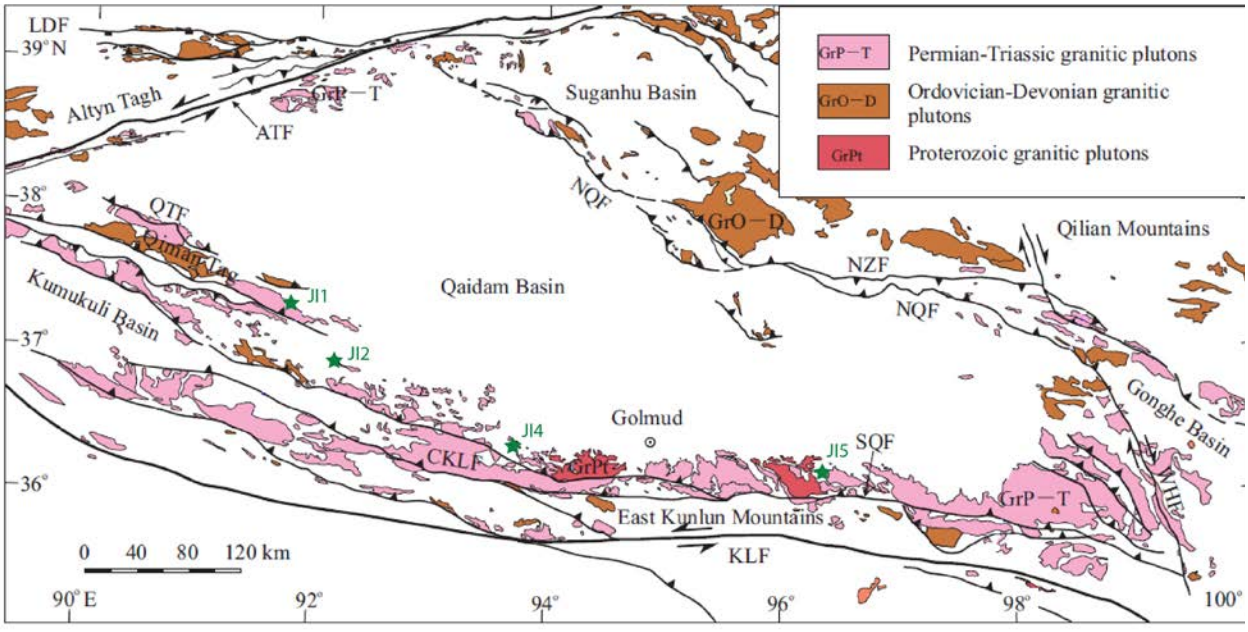

Figure 77. Simplified tectonic map showing the distribution of magmatism in the Eastern Kunlun mountains. Modified after Chen et al. (2012). Sample locations in this study are indicated with green stars.

Various small (<20 km) Permian-Triassic plutons are present at location 4 which probably caused partial resetting of all but the hornblende systems. The temperatures reached during this stage were either not high enough, or not prolonged enough to (partially) retain the hornblende age of 403 Ma. Cooling between ~400 and ~300 Ma occurred at a rate of 2.0°C/Ma. Subsequently, two phases of partial resetting can be found in biotite and K-feldspar ages. These are related to the tectonic activity during the indention of the South China block and accretion of the Qiangtang and Lhasa terrains. The temperature did not exceed 450°C as the hornblende age was not reset.

It is found probable that AHe ages found by Clark et al. (2010) and Dai et al. (2013) are the result of accretion of India to Eurasia. Therefore an initially tectonic inactive period was interpreted from ~175 Ma with a cooling rate of 0.4°C/Ma. Active cooling started again around 70 Ma with a cooling rate of 1.5 – 2.2°C/Ma, which is supported by Arnaud et al. (2003).

According to literature, cooling rates vary highly north and south of the Central Kunlun fault due to northward tectonic thrusting both during the Devonian and Palaeogene (Chen et al., 2002; Mock et al., 1999). Around 25-30 Ma, related to this tectonic thrusting, an important cooling event took place. The rate of cooling varies among authors between 9-15°C/Ma based on K-feldspar diffusion modelling of Mock et al., (1999) and 40°C/Ma based on argon release spectra and apatite dating by Arnaud et al. (2003). The increased amount of cooling is further supported by (U-Th)/He dating by Clark et al. (2010) who comes to cooling of 30°C/Ma. This late stage of fast cooling can only be explained by exhumation.

Based on the combined study of pressure-temperature constraints of the metamorphic rocks in the Jinshuikou group, and temperature-time constraints on the entire Kunlun Mountains north of the Central Kunlun fault, we could construct a local thermal gradient of ~50°C/km between peak metamorphism and present. This corresponds to an average denudation rate of 0.1 km/Ma and a total unroofing of 40 km in this period. Based on research by AHe dating, this geothermal gradient decreased to 15-30°C/km from 30 Ma due to the collision of India and Eurasia South of the Central Kunlun fault (Clark et al., 2010).

7.4. Suggestions for future research

As very little is known so far about the metamorphic history of the Jinshuikou group and the Eastern Kunlun Mountains as a whole, it is advisable to further investigate the metamorphic sequences in this area to expand the available dataset and provide more material for comparison. At this moment only this study, the study of Huijgen (2015) and Liu et al. (2005) provide information on the P-T-t history of the Jinshuikou group. At some points, major differences exist between these studies, especially on the estimates of the peak metamorphic conditions. Therefore it is recommended to carry out a more extensive sampling study throughout the entire Jinshuikou group to obtain more and better distributed samples for modelling purposes. Subsequently it would be good to perform more dating work on metamorphosed samples, both in the low (<250°C) and in the high (>500°C) temperature domain in order to better constrain the thermal history of the samples.

In this study, modelling was carried out with the assumption that water was saturated at all times. As explained in Chapter 6 this is not entirely realistic and therefore, a better reconsideration of the full effect that water can have is needed. Also an iterating modelling of CO_2 and O_2 concentrations is needed to better constrain these amounts in the sample during mineral stability. Furthermore, replacing the amphibole model GlTrTsPg by the more extensive Amph(DPW) model would improve constraints on the amphibole stability.

In order to define the amount of excess argon present in the samples, testing with a K-poor mineral is advised. By degassing for instance plagioclase in the same way as is done for K-feldspar, the amount of excess ^{40}Ar can be measured and a quantified correction could be applied to the age measurements within this study. This will lead to more realistic ages and therefore to better constraints on the geological impact and consequences of certain events.

8. Conclusions

Based on the P-T modelling and $^{40}Ar/^{39}Ar$ dating results the following conclusions were drawn:

I. Metamorphic samples from the Jinshuikou group experienced amphibolite to granulite facies metamorphism. Only part of the rocks show real evidence for granulite facies, but based on the P-T paths of the other samples, extension into the granulite field is assumed for the whole unit.

II. Peak metamorphic conditions of 750°C and 13 kbar for samples JI 1-1, JI 2-1 and JI 2-2 and conditions of 800°C and 10 kbar for samples JI 4-3 and JI 4-6 are at higher pressure and lower temperature than those found by Liu et al. (2005).

III. Peak metamorphic conditions might shift to lower pressure if adjustments are made for MnO and water undersaturation.

IV. Four age groups are determined as cooling ages based on $^{40}Ar/^{39}Ar$ dating: 1) 450.27 ± 22.60 Ma till 403.25 ± 17.89 Ma. This group corresponds to the accretion of the South Tarim- and Qaidam block to the North Tarim and North China block during Silurian – Mid Devonian and associated closure of the Paleo-Tethys. 2) 353.40 ± 14.62 Ma till 263.43 ± 9.97 Ma. This age group corresponds to the accretion of the aforementioned blocks to Siberia and the indention of South China from the south during Carboniferous – Permian. 3) 252.58 ± 8.87 Ma to 199.86 ± 43.37 Ma. This age group corresponds to the still ongoing indention of the South China block and the accretion of the Qiangtang terrain during Late Permian – Late Triassic. 4) 215.11 ± 5.48 Ma to 184.26 ± 7.52 Ma. This group corresponds to accretion of the Lhasa terrain and ongoing closure of the Tethys sea during Late Triassic – Cretaceous.

V. The distribution of argon ages can be explained with the presence of granitic plutons throughout the Jinshuikou group and the associated (partial) resetting. Presence of Permian – Triassic plutons in the vicinity of sample locations 1 and 5 caused complete resetting of the argon system.

VI. Peak metamorphism is assumed to have occurred during a Silurian – Devonian metamorphic event.

VII. Cooling rates after metamorphism changed exponentially from 10 – 14°C/Ma between 430 and 400 Ma to 2.0°C/Ma between 400 and 300 Ma. Reheating of sample locations 1 and 5 caused another phase of exponential cooling, whereas sample locations 2 and 4 fluctuated around 250°C due to several phases of granitic intrusions. The approach/collision of India with Eurasia caused another tectonically active period which caused increased cooling from ~175 Ma onward of 2.2°C/Ma.

VIII. A paleo geothermal gradient between peak metamorphism and present of 50°C/km is found. This corresponds to a denudation rate of 0.1 km/Ma and total unroofing of 40 km over this period.

Acknowledgements

First I would like to thank Jan Wijbrans and Fraukje Brouwer for giving me the opportunity to participate in this project and giving guidance and help wherever needed during the project. The fruitful discussions helped me to get to this final work. Furthermore I would like to thank Jan Wijbrans, Maarten Huijgen and Hanwen Zhou for their company in the field and the nice atmosphere during our stay in China.

Analyses would not have been possible without the help of Bouk Lacet and Wynanda Koot for thin section and mineral mount preparations, and Roel van Elzas for help with mineral separation. Sergei Matveev has been a great help with preparation for XRF measurements and performing EMP measurements. Furthermore, this project was financially supported by the Molengraaff fonds, which is highly appreciated.

References

Aitchison, J. C., Ali, J. R., and Davis, A. M., 2007, When and where did India and Asia collide?: Journal of Geophysical Research: Solid Earth, v. 112, no. B5, p. B05423.

Andersen, D. J., and Lindsley, D. H., 1988, Internally consistent solution models for Fe-Mg-Mn-Ti oxides; Fe-Ti oxides: American Mineralogist, v. 73, no. 7-8, p. 714-726.

Andriessen, P. A. M., 2015.

Arnaud, N., Tapponnier, P., Roger, F., Brunel, M., Scharer, U., Wen, C., and Zhiqin, X., 2003, Evidence for Mesozoic shear along the western Kunlun and Altyn-Tagh fault, northern Tibet (China): Journal of Geophysical Research: Solid Earth, v. 108, no. B1, p. 2053.

Auzanneau, E., Schmidt, M. W., Vielzeuf, D., and Connolly, J. A. D., 2010, Titanium in phengite: a geobarometer for high temperature eclogites: Contributions to Mineralogy and Petrology, v. 159, p. 1-24.

Ba, J., Chen, N., Wang, Q., wang, X., Zhang, L., and Wang, S., 2012, Nd-Sr-Pb Isotopic compositions of cordierite granite on southern margin of the Qaidam block, NW China, and constraints on tis petrogenesis, tectonic affinity of source region and tectonic implications.: Earth Science - Journal of China University of Geosciences, v. 37, p. 80-92.

Chen, N., Sun, M., He, L., Zhang, K., and Wang, G., 2002, Precise timing of the Early Paleozoic metamorphism and thrust deformation in the Eastern Kunlun Orogen: Chinese Science Bulletin, v. 47, no. 13, p. 1130-1133.

Chen, X. H., Gehrels, G., Yin, A., Li, L., and Jiang, R. B., 2012, Paleozoic and Mesozoic Basement Magmatisms of Eastern Qaidam Basin, Northern Qinghai-Tibet Plateau: LA-ICP-MS Zircon U-Pb Geochronology and its Geological Significance: Acta Geologica Sinica - English Edition, v. 86, no. 2, p. 350-369.

Ching-Hua, L., and Onstott, T. C., 1989, 39Ar recoil artifacts in chloritized biotite: Geochimica et Cosmochimica Acta, v. 53, no. 10, p. 2697-2711.

Clark, M. K., Farley, K. A., Zheng, D., Wang, Z., and Duvall, A. R., 2010, Early Cenozoic faulting of the northern Tibetan Plateau margin from apatite (U–Th)/He ages: Earth and Planetary Science Letters, v. 296, no. 1–2, p. 78-88.

Coggon, R., and Holland, T. J. B., 2002, Mixing properties of phengitic micas and revised garnet-phengite thermobarometers: Journal of Metamorphic Geology, v. 20, no. 7, p. 683-696.

Connolly, J. A. D., 1990, Multivariable phase diagrams: an algorithm based on generalized thermodynamics: American Journal of Science, v. 290, p. 666-718.

Connolly, J.A.D., 2005, Computation of phase equilibria by linear programming: A tool for geodynamic modeling and its application to subduction zone decarbonation: Earth and Planetary Science Letters, v. 236, no. 1–2, p. 524-541.

Connolly, J.A.D., 2012, Perple_X 6.6.8.: ETH Zürich.

Dai, J., Wang, C., Hourigan, J., and Santosh, M., 2013, Multi-stage tectono-magmatic events of the Eastern Kunlun Range, northern Tibet: Insights from U–Pb geochronology and (U–Th)/He thermochronology: Tectonophysics, v. 599, no. 0, p. 97-106.

Dale, J., Powell, R., White, R. W., Elmer, F. L., and Holland, T. J. B., 2005, A thermodynamic model for Ca–Na clinoamphiboles in Na2O–CaO–FeO–MgO–Al2O3–SiO2–H2O–O for petrological calculations: Journal of Metamorphic Geology, v. 23, no. 8, p. 771-791.

Dewey, J. F., Shackleton, R. M., Chengfa, C., and Yiyin, S., 1988, The Tectonic Evolution of the Tibetan Plateau: Philosophical Transactions of the Royal Society of London. Series A, Mathematical and Physical Sciences, v. 327, no. 1594, p. 379-413.

Fuhrman, M. L., and Lindsley, D. H., 1988, Ternary-feldspar modeling and thermometry: American Mineralogist, v. 73, no. 3-4, p. 201-215.

Gasparik, T., 1984, Experimental study of subsolidus phase relations and mixing properties of pyroxene in the system CaO-Al2O3-SiO2: Geochimica et Cosmochimica Acta, v. 48, no. 12, p. 2537-2545.

Gasparik, T., 1985, Experimental study of subsolidus phase relations and mixing properties of pyroxene and plagioclase in the system Na_2O-CaO-Al_2O_3-SiO_2: Contributions to Mineralogy and Petrology, v. 89, p. 346-357.

Harris, N. B. W., Ronghua, X., Lewis, C. L., Hawkesworth, C. J., and Yuquan, Z., 1988, Isotope Geochemistry of the 1985 Tibet Geotraverse, Lhasa to Golmud: Philosophical Transactions of the Royal Society of London. Series A, Mathematical and Physical Sciences, v. 327, no. 1594, p. 263-285.

Harrison, M. T., 1982, Diffusion of 40Ar in hornblende: Contributions to Mineralogy and Petrology, v. 78, no. 3, p. 324-331.

Harrison, T. M., and McDougall, I., 1980, Investigations of an intrusive contact, northwest Nelson, New Zealand—II. Diffusion of radiogenic and excess 40Ar in hornblende revealed by 40Ar39Ar age spectrum analysis: Geochimica et Cosmochimica Acta, v. 44, no. 12, p. 2005-2020.

Hess, J. C., and Lippolt, H. J., 1986, Kinetics of Ar isotopes during neutron irradiation: 39Ar loss from minerals as a source of error in 40Ar/39Ar dating: Chemical Geology: Isotope Geoscience section, v. 59, no. 0, p. 223-236.

Hess, J. C., Lippolt, H. J., and Wirth, R., 1987, Interpretation of 40Ar39Ar biotites: Evidence from hydrothermal degassing experiments and TEM studies: Chemical Geology: Isotope Geoscience section, v. 66, no. 1–2, p. 137-149.

Holland, T. J. B., and Powell, R., 1996, Thermodynamics of order-disorder in minerals: II. Symmetric formalism applied to solid solutions: American Mineralogist, v. 81, p. 1425-1437.

Holland, T. J. B., and Powell, R., 1998a, An internally consistent thermodynamic data set for phases of petrological interest: Journal of metamorphic Geology, v. 16, p. 309-343.

Huijgen, M., 2015, Metamorphic conditions of the Jinshuikou Group in the Eastern Kunlun Mountains, China: Master thesis, VU Amsterdam.

Koppers, A. A. P., 2002, ArArCALC—software for 40Ar/39Ar age calculations: Computers & Geosciences, v. 28, no. 5, p. 605-619.

Leake, B. E., Woolley, A. R., Arps, C. E. S., Birch, W. D., Gilbert, M. C., Grice, J. D., Hawthorne, F. C., Kato, A., Kisch, H. J., Krivovichev, V. G., Linthout, K., Laird, J., Mandarino, J. A., Maresch, W. V., Nickel, E. H., Rock, N. M. S., Schumacher, J. C., Smith, D. C., Stephenson, N. C. N., Ungaretti, L., Whittaker, E. J. W., and Youzhi, G., 1997, Nomenclature of amphiboles; Report of the Subcommittee on Amphiboles of the International Mineralogical Association, Commission on New Minerals and Mineral Names: American Mineralogist, v. 82, no. 9-10, p. 1019-1037.

Lee, J. Y., Marti, K., Severinghaus, J. P., Kawamura, K., Yoo, H. S., Lee, J. B., and Kim, J. S., 2006, A redetermination of the isotopic abundances of atmospheric Ar: Geochimica et Cosmochimica Acta, v. 70, p. 4507-4512.

Lexa, O., 2011, PyWerami.

Li, W., Neubauer, F., Liu, Y., Genser, J., Ren, S., Han, G., and Liang, C., 2013, Paleozoic evolution of the Qimantagh magmatic arcs, Eastern Kunlun Mountains: Constraints from zircon dating of granitoids and modern river sands: Journal of Asian Earth Sciences, v. 77, no. 0, p. 183-202.

Liu, B., Ma, C.-Q., Zhang, J. Y., Xiong, F.-H., Huang, J., and Jiang, H.-A., 2012, Petrogenesis of early Devonian intrusive tocks in the east part of Eastern Kunlun Orogen and implication for Early Palaeozoic orogenic processes: Acta Petrologica Sinica, v. 28, no. 6, p. 1785-1807.

Liu, Y., Genser, J., Neubauer, F., Jin, W., Ge, X., Handler, R., and Takasu, A., 2005, 40Ar/39Ar mineral ages from basement rocks in the Eastern Kunlun Mountains, NW China, and their tectonic implications: Tectonophysics, v. 398, no. 3–4, p. 199-224.

Long, X., Jin, W., Ge, W., and Yu, N., 2006, Zircon U-Pb geochronology and geological implications of the granitoids in Jinshuikou, East Kunlun, NW China: Geochimica, v. 35, no. 4, p. 333-345.

Long, X., Jin, W., and Yu, N., 2005, Raman spectroscopic study of zircons in the Jinshuikou gneissic Al-rich granite in east Golmud, East Kunlun: Geological Bulletin of China, v. 24, no. 1, p. 36-40.

Lovera, O. M., Richter, F. M., and Harrison, T. M., 1989, The 40Ar/39Ar thermochronometry for slowly cooled samples having a distribution of diffusion domain sizes: Journal of Geophysical Research: Solid Earth, v. 94, no. B12, p. 17917-17935.

Mattauer, M., Matte, P., Malavieille, J., Tapponnier, P., Maluski, H., Zhiqin, X., Yilun, L., and Yaoqin, T., 1985, Tectonics of the Qinling Belt: build-up and evolution of eastern Asia: Nature, v. 317, p. 496-500.

McDougall, I., and Harrison, T. M., 1999, Geochronology and thermochronology by the $^{40}Ar/^{39}Ar$ method, New York, Oxford, Oxford University Press.

Mo, X., Niu, Y., Dong, G., Zhao, Z., Hou, Z., Zhou, S., and Ke, S., 2008, Contribution of syncollisional felsic magmatism to continental crust growth: A case study of the Paleogene Linzizong volcanic Succession in southern Tibet: Chemical Geology, v. 250, no. 1–4, p. 49-67.

Mock, C., Arnaud, N. O., and Cantagrel, J.-M., 1999, An early unroofing in northeastern Tibet? Constraints from 40Ar/39Ar thermochronology on granitoids from the eastern Kunlun range (Qianghai, NW China): Earth and Planetary Science Letters, v. 171, no. 1, p. 107-122.

Newton, R. C., Charlu, T. V., and Kleppa, O. J., 1980, Thermochemistry of the high structural state plagioclases: Geochimica et Cosmochimica Acta, v. 44, no. 7, p. 933-941.

Pietersen, J. L., 2013, Reconstruction of PT-conditions and (dis-)equilibria in a blueschist and eclogite facies metabasite domain at western Syros (Cyclades, Creece) [MSc MSc-thesis]: VU University.

Powell, R., and Holland, T. J. B., 2008, On thermobarometry: Journal of Metamorphic Geology, v. 26, no. 2, p. 155-179.

Reed, S. J. B., 2005, Electron Microprobe Analysis and Scanning Electron Microscopy in Geology, Cambridge University Press.

Rieder, M., Cavazzini, G., D'yakonov, Y. S., Frank-Kamenetskii, V. A., Gottardi, G., Guggenheim, S., Koval', P. V., Mueller, G., Neiva, A. M. R., Radoslovich, E. W., Robert, J.-L., Sassi, F. P., Takeda, H., Weiss, Z., and Wones, D. R., 1998, Nomenclature of the micas: The Canadian Mineralogist, v. 36, no. 3, p. 905-912.

Roger, F., Arnaud, N., Gilder, S., Tapponnier, P., Jolivet, M., Brunel, M., Malavieille, J., Xu, Z., and Yang, J., 2003, Geochronological and geochemical constraints on Mesozoic suturing in east central Tibet: Tectonics, v. 22, no. 4, p. 1037.

Royden, L. H., Burchfiel, B. C., and van der Hilst, R. D., 2008, The Geological Evolution of the Tibetan Plateau: Science, v. 321, no. 5892, p. 1054-1058.

Smye, A. J., Warren, C. J., and Bickle, M. J., 2013, The signature of devolatisation: Extraneous 40Ar systematics in high-pressure metamorphic rocks: Geochimica et Cosmochimica Acta, v. 113, no. 0, p. 94-112.

Spear, F. S., 1993, Metamorphic phase equilibria and Pressure-Temperature-Time paths, Washington, Mineralogical society of America.

Tajčmanová, L., Connolly, J. A. D., and Cesare, B., 2009, A thermodynamic model for titanium and ferric iron solution in biotite: Journal of Metamorphic Geology, v. 27, no. 2, p. 153-165.

Tinkham, D. K., Zuluaga, C. A., and Stowell, H. H., 2001, Metapelite phase equilibria modeling in MnNCKFMASH: The effect of variable Al_2O_3 and MgO/(MgO+FeO) on mineral stability: Geological Materials Research, v. 3, no. 1, p. 1-42.

Tracy, J. R., 1975, High grade metamorphic reactions and partial melting in pelitic schist, Quabbin reservoir area, Massachusetts [Ph.D: University of Massachusetts, 127 p.

Van der Woerd, J., Ryerson, F. J., Tapponnier, P., Meriaux, A. S., Gaudemer, Y., Meyer, B., Finkel, R. C., Caffee, M. W., Guoguang, Z., and Zhiqin, X., 2000, Uniform slip-rate along the Kunlun Fault: Implications for seismic behaviour and large-scale tectonics: Geophysical Research Letters, v. 27, no. 16, p. 2353-2356.

Wei, C., and Powell, R., 2003, Phase relations in high-pressure metapelites in the system KFMASH (K2O–FeO–MgO–Al2O3–SiO2–H2O) with application to natural rocks: Contributions to Mineralogy and Petrology, v. 145, no. 3, p. 301-315.

Wijbrans, J. R., Pringle, M. S., Koppers, A. A. P., and Scheveers, R., 1995, Argon geochronology of small samples using the Vulkaan argon laserprobe: Proc. Kon. Ned. Akad. v. Wetensch., v. 98 no. 2, p. 185-218.

Xiao, W., Han, F., Windley, B. F., Yuan, C., Zhou, H., and Li, J., 2003, Multiple Accretionary Orogenesis and Episodic Growth of Continents: Insights from the Western Kunlun Range, Central Asia: International Geology Review, v. 45, no. 4, p. 303-328.

Yin, A., and Harrison, T. M., 2000, Geologic Evolution of the Himalayan-Tibetan Orogen: Annual Review of Earth and Planetary Sciences, v. 28, no. 1, p. 211-280.

Yin, A., and Nie, S., 1996, A Phanerozoic palinspastic reconstruction of China and its neighboring regions, The tectonic evolution of Asia: Cambridge, Cambridge University Press, p. 666.

Yu, N., Jin, W., Ge, W., and Long, X., 2005, Geochemical study on peraluminous granite from Jinshuikou in East Kunlun: Global Geology, v. 24, no. 2, p. 123-128.

Zhang, J.-Y., Ma, C.-Q., Xiong, F.-H., and Liu, B., 2012, Petrogenesis and tectonic significance of the Late Permian–Middle Triassic calc-alkaline granites in the Balong region, eastern Kunlun Orogen, China: Geological Magazine, v. 149, no. 05, p. 892-908.

Zhang, J., Meng, F., Wan, Y., Yang, J., and Tung, K. A., 2003, Early Paleozoic tectono-thermal event of the Jinshuikou Group on the southern margin of Qaidam: Zircon U-Pb SHRIMP age evidence: Geological Bulletin of China, v. 22, no. 6, p. 397-404.

Zhang, Y., and Zheng, J., 1994, Geologic Overview in Kokshili, Qinghai and Adjacent Areas, Beijing, Seismological Publishing House, 177 p.:

Zhiqin, X., Mei, J., and Jingsui, Y., 1997, Deep Tectonophysical Process of the Uplift of the Northern Qinghai—Tibet Plateau: Acta Geologica Sinica - English Edition, v. 71, no. 1, p. 1-14.

Zhu, B., Kidd, W. S. F., Rowley, D. B., Currie, B. S., and Shafique, N., 2005, Age of Initiation of the India-Asia Collision in the East-Central Himalaya: The Journal of Geology, v. 113, no. 3, p. 265-285.

Appendix I: Thin section descriptions

JI 1-1

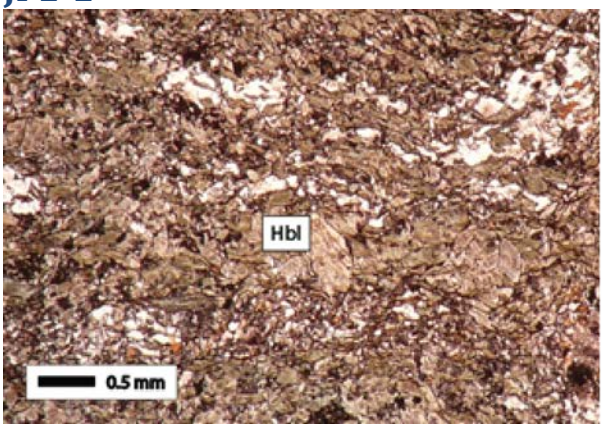

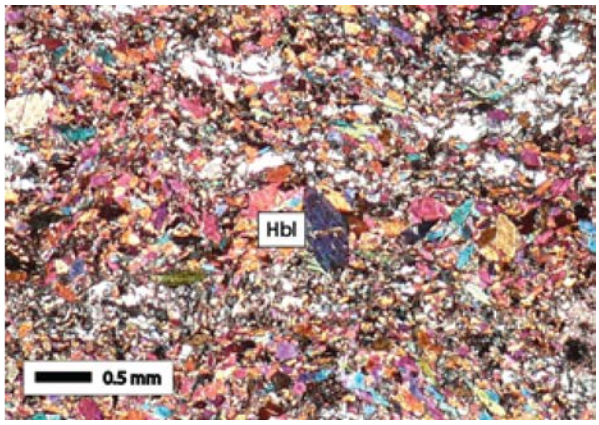

Mineral	Abundance (%)	Size (mm)	Average size (mm)	Habit
q	5	0.02-0.1	0.05	Anhedral
amp	60	0.1-0.5	0.15	Subhedral, fine grained, positioned in bands. Some grains lay perpendicular to the direction of the bands.
ce	2	0.05-0.1	0.1	Brown pleochroic, looks like biotite. Subhedral, in clusters with q and pl
ep	5	0.01-0.1	0.07	Anhedral, zoning, in clusters with cc + pl + cz (+q), replaces calcium-rich lumps.
cz	3	0.05-0.1	0.07	Anhedral, bluish in XPL, clusters with cc + ep + pl + (q)
pl	15	0.1-0.3	0.2	Anhedral, sometimes albite twinning.
cc-rich lumps	<1	1-1.5 original now replaced		Completely altered, replaced by clayminerals + amp + ep + cz + cc. Sigma-clast shape.
cc	5	0.05-0.15	0.1	Subhedral, in clusters with q and pl or in cracks.
sph	5	0.01-0.1	0.05	Very high relief, in sph clusters.
chl	1	0.05-0.3	0.2	Subhedral, green pleochroic.

Texture

The thin section shows clear banding of pl + cc + ep (+q) and amp + ce. In some places, there are very distinct bends/kinks in the banding. The elongated amphiboles lie in the direction of the banding and follow the kinks. The bigger (0.3-0.5 mm) amphibole grains are mostly positioned perpendicular to the banding. Completely altered lumps of calcite rich material are present as sigma clasts. These are replaced by clayminerals, epidote, clinozoisite, calcite and amphibole. Calcite also occurs as filling of cracks and in clusters with quartz and plagioclase.

Interpretation

This rock is an gneissic amphibolite with a calc-silicate as protolith. The rock is not in equilibrium as calcite rich lumps are being transformed. Sigma clast structures and bends/kinks point to a shear stress. The perpendicular amphibole would suggest the grow of amphibole before and after compression. However, only few (20%) of the crystals are post compression.

JI 1-3

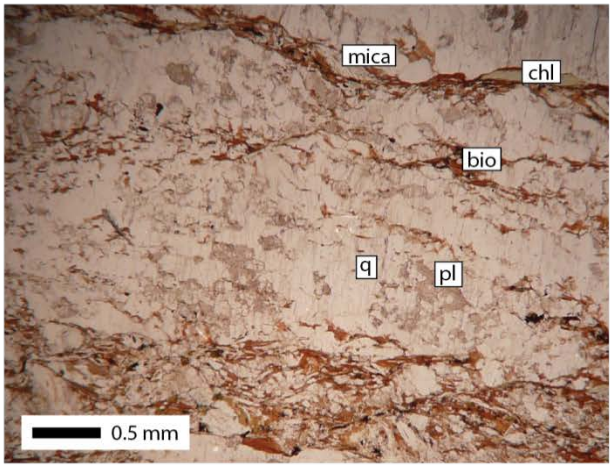

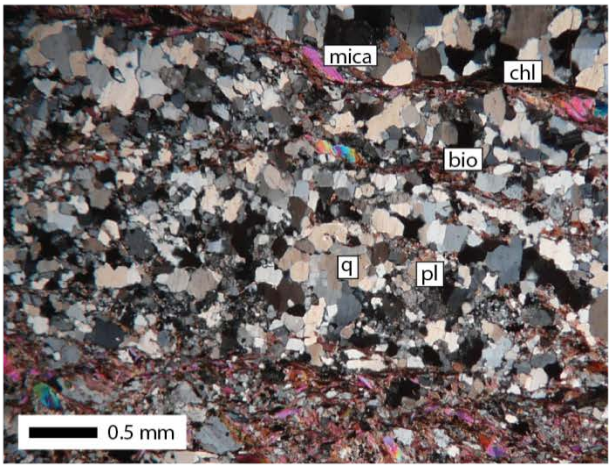

Mineral	Abundance (%)	Size (mm)	Average size (mm)	Habit
q	45	0.05-0.3	0.2	Undulose extinction, blue extinction on the edges. Recrystallized grains.
pl	7	0.1-0.6	0.3	Sometimes albite twinning visible.
kfs	5	0.2-0.8	0.5	Dusty appearance, mainly replaced by clay minerals.
mica	15	0.1-1	0.6	Intergrowing with biotite.
bio	20	0.1-1.5	0.5	Large grains > 0.5 mm generally have an elongated habit and preferred orientation. Smaller grains are more random in shape and occur around the larger grains.
chl	2	0.3-1	0.5	Intergrowing with biotite. Light green pleochroic.
zo	5	0.05-0.3	0.2	Blue extinction. Occurs together with quartz.

Texture

All micas focus in bands, which are generally cracked. In between the bands q + pl + kfs occurs. The quartz grains show undulose extinction and have relocated grain boundaries, giving it a mosaic-like structure. The K-feldspar grains are highly unstable and only visible as dusty looking mineral shapes, mainly replaced by clay-minerals.

Interpretation

This rock is a biotite gneiss with little remains of chlorite. The rock has experienced large deformational pressures, forming banding and recrystallization of quartz. The environment changed from a more potassium rich, to a more sodium + calcium rich one.

JI 1-4

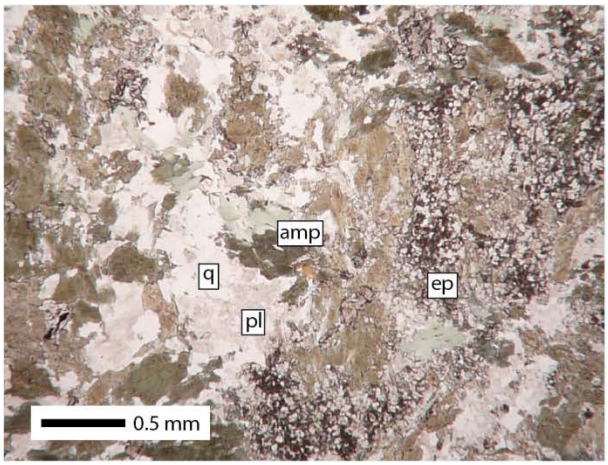

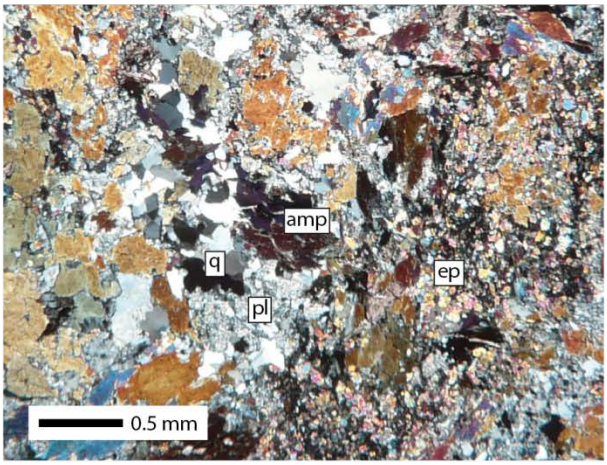

Mineral	Abundance (%)	Size (mm)	Average size (mm)	Habit
amp	40	0.8-1.5	1	Green pleochroic, very altered, sometimes distinct cleavage.
q	25	0.05-0.3	0.2	Rounded, anhedral grains occurring in clusters.
cc	5	0.1-1	0.3	Rounded grains, generally growing along altered amphiboles.
ep	5	0.03-0.1	0.05	Rounded minerals growing as a replacement of other, undefined, minerals.
pl	10	0.05-0.1	0.1	Anhedral, sometimes albite twinning.
kfs	2	0.05-0.1	0.08	Checkerboard twinning, quite altered.
chl	3	0.2-0.3	0.25	Light green pleochroic, very fresh grains.
bio	5	0.05-0.15	0.1	Brown pleochroic, elongated.
zo	2	0.1-0.3	0.2	Blue extinction. Occurs together with quartz.
ru	2	0.05-0.1	0.08	Occurs around chl.
sph	1	0.08-0.12	0.1	Eye-shaped, sometimes very clear cleavage.

Texture

This rock contains not very well defined bands of amp + ep, separated from q + fsp + zo + cc. Amphibole grains are very altered and no distinct grain boundaries are present anymore. Grains are partly replaced by epidote and calcite grains grow along the outside of the grains. Quartz grains are partly recrystallized. Part of them shows undulose extinction whereas other grains do not. Zoisite looks very similar to the quartz grains, except for the blue extinction.

Interpretation

This is an amphibolite which is no longer in equilibrium. Amphiboles are being replaced by epidote, chlorite, calcite and rutile. A non-uniform pressure enabled slight bands to form. A CO_2 fluid was at some point after peak metamorphism introduced, enabling calcite to form as a stable mineral in the current assemblage.

JI 2-1

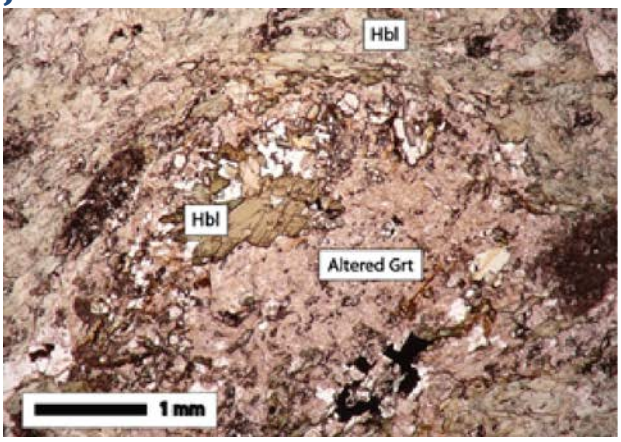

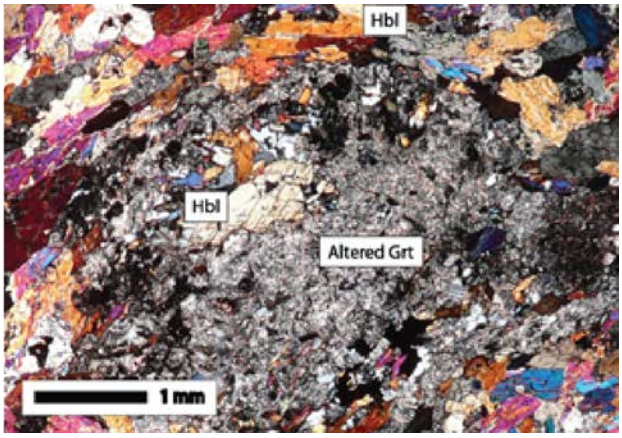

Mineral	Abundance (%) Present (early)	Size (mm)	Average size (mm)	Habit
amp	70 (66)	0.5-2	1.5	Subhedral, sometimes pretty cracked. Clear cleavage, light green pleochroic. Some grains grow over altered gt, most are folded around former garnets.
gt	3 (10)	0.2-0.5	0.4	Completely altered, tiny patches of gt left (max. 20% of grain).
sph	5	0.1-0.2	0.15	Sub/Euhedral. As inclusions in amp.
metal oxides	5	0.1-0.5	0.25	Anhedral, replacing the gt.
pl	10 (8)	0.05-0.5	0.3	Anhedral, replacing the gt. Unstable; exsolution between albite and anorthite
cz	3	0.1-0.5	0.2	Anhedral, heavily zoned. In bands together with ru.
cc	1 (0)	0.2-0.5	0.4	Subhedral, grows in pressure shadow of gt.
ru	1	0.1-0.5	0.2	Deep orange, in bands with cz and replacing gt.

Texture

This thin section shows vague bands of amphibole and altered plagioclase which are wrapped around altered garnets. The amphiboles have a weakly expressed preference orientation. In the pressure shadow of the garnet, calcite may occur. The altered garnets are replaced by pl + metal oxides + amp + sph + cz + ru. Mostly a rim-like structure of the garnet is still present, whereas the interior is completely altered away.

Interpretation

This is an amphibolites, formed from a mafic material. The garnets were formed before stress and shearing started. The rock is not in equilibrium anymore as minerals are being replaced but no stable structure is present yet. Calcite can only have formed in the presence of a CO_2 fluid, providing the necessary carbon.

JI 2-2

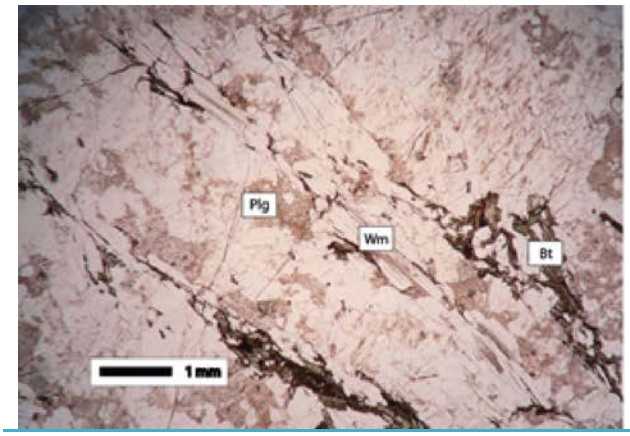

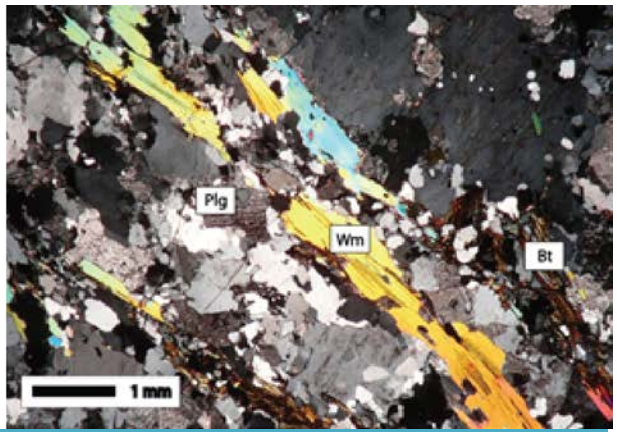

Mineral	Abundance (%)	Size (mm)	Average size (mm)	Habit
bio	<1	0.1-0.5	0.2	Almost completely replaced by chl.
chl	5	0.5-2	1.5	Replaced most of the biotite. Decay halos present as remains of biotite.
q	35	0.5-2	1	Anhedral, undulose extinction
pl	25	0.3-1	0.7	Anhedral, sometimes albite twinning. Unstable: satirization by clay minerals
kfs	25	0.3-1	0.5	Anhedral, sometimes checkerboard twinning.
wm	8	0.3-1	0.7	Anhedral, inclusions of zr and chl. Decay halos present.
zr	accessory	<0.1	<0.1	Euhedral, as inclusions in wm. Zoned.
ap	accessory	0.1-0.2	0.15	Euhedral, as inclusions in wm
metal oxides	1	0.2-0.5	0.3	Opaque areas, generally along or between biotite/chlorite grains
ru	<1	0.02	0.02	Deep orange in PPL and XPL
cz	<1	<0.1	<0.1	Anhedral, highly zoned, distinct blue color, inside pl grains.
gt	<1	<0.2	<0.2	Relics, being eaten away by chlorite. High relief, isotropic.

Texture

This thin section shows clear banding of bio + wm and q + pl + kfs. The plagioclase is not in equilibrium and satirization by clay minerals and minor amounts of clinozoisite occurs. However kfs does seem stable. Some micas show folding structures. Almost all biotite is being replaced by chlorite. Relics of garnet can be found.

Interpretation

This is a biotite gneiss. Fluid flow at relatively low temperatures caused alteration of the rock, including replacement of biotite by chlorite and plagioclase by clay minerals and clinozoisite. Remaining potassium from the biotite is used in kfs. Relics of garnet give evidence for an earlier eclogite or granulite facies. A pressure regime caused both folding of mica grains and undulose extinction in quartz grains.

JI 4-2

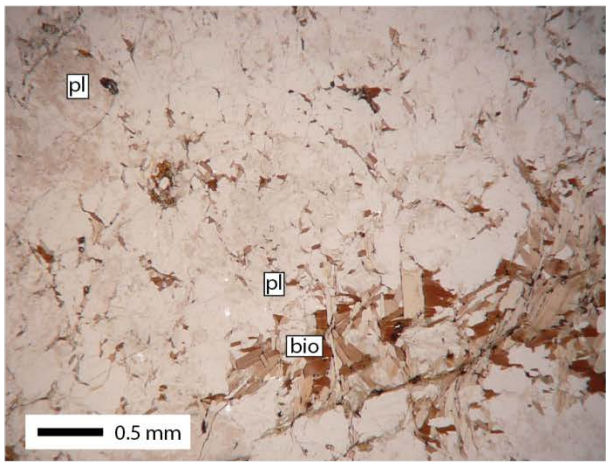

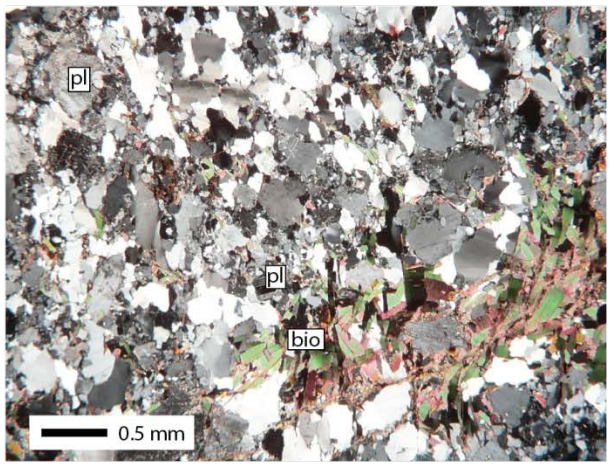

Mineral	Abundance (%)	Size (mm)	Average size (mm)	Habit
Q	65	0.1-1	0.4	Undulose extinction in most grains.
Bio	20	0.05-2	0.1	Elongated
Kfs	7	0.1-0.3	0.2	Checkerboard twinning
pl	10	0.1-0.5	0.3	Albite twinning
zr	Accessory	0.05-0.1	0.8	euhedral

Texture

This rock shows a wealth of felsic minerals occurring in bands, interspersed with bands containing also biotite up to 30% within the band. The biotite grains are generally finegrained (<0.1 mm) but also sometimes occur in clusters with much larger grains up to 2 mm.

Interpretation

This is a biotite gneiss, although the banding is not that well developed. Most quartz grains show undulose extinction pointing toward a fierce stress regime being plied on the rock.

JI 4-3

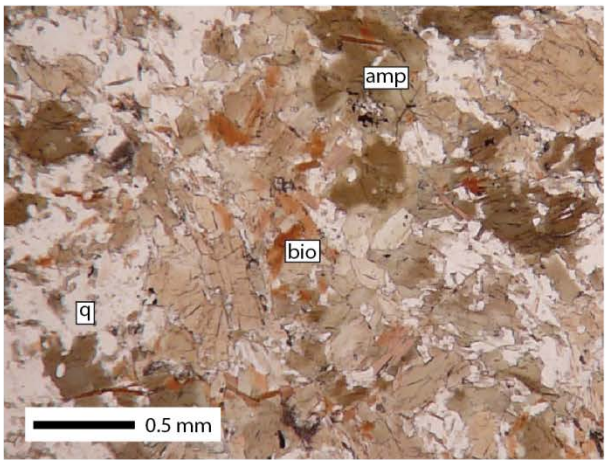

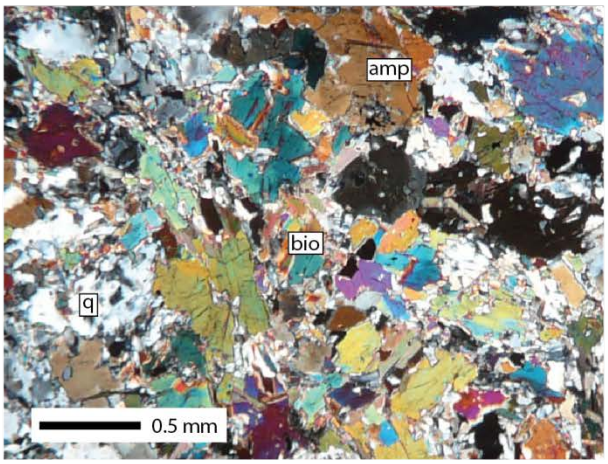

Mineral	Abundance (%)	Size (mm)	Average size (mm)	Habit
amp	50	0.1-1	0.5	Green pleochroic, anhedral, clear cleavage.
pl	10	0.1-0.3	0.2	Very clear albite twinning. Anhedral, dusty looking in PPL.
kfs	7	0.1-0.3	0.2	Checkerboard twinning, dusty looking in PPL.
q	20	0.05-0.8	0.2	Undulose extinction, sometimes yellowish on the rims.
sph	3	0.05-0.2	0.1	Very high relief, eye-shaped.
bio	5	0.05-0.5	0.3	Intergrown with amphibole grains. Blocky to elongated shape.
metal oxides	3	0.01-0.2	0.05	Generally as replacement of amphibole rims.
ap	2	0.05-0.1	0.1	Rounded, within amphibole grains

Texture

This rock shows a randomly orientated mineral assemblage. Amphiboles are not completely stable and partly replaced by metal oxides. Titanite grains are growing randomly over other minerals. Quartz shows undulose extinction with often pale yellow parts on the side of the grains. Both plagioclase and k-feldspar show very distinct twinning.

Interpretation

This is a amphibolite on the retrograde part of the metamorphic path. A slight pressure domain was applied on the rock creating undulose extinction in the quartz grains, but it was not enough for distinct banding to form.

JI 4-5

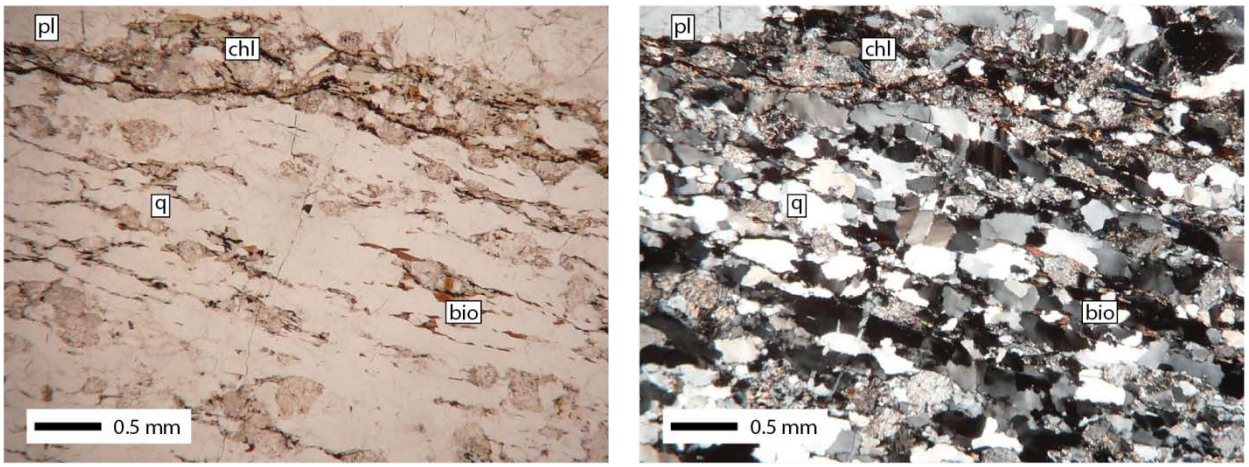

Mineral	Abundance (%)	Size (mm)	Average size (mm)	Habit
q	65	0.1-3	1	Elongated shape, undulose extinction
pl	10	0.2-0.8	0.5	Very dusty appearance in PPL, unstable. Some grains still show albite twinning.
kfs	5	0.7-1.5	1	Clear checkerboard twinning. Less dusty than pl.
zr	accessory	0.03-0.05	0.04	Rounded, very high interference colours.
chl	10	0.2-1	0.8	Light green pleochroic. Dark blue extinction in XPL. Elongated, clustered with biotite remains.
cc	3	0.01-0.1	0.05	Grows in between grains, along the grain boundaries.
bio	3	0.05-0.1	0.06	Grows together with chl, mostly replaced by chl.
Metal oxides	5	0.01-0.05	0.02	Opaque, anhedral grains on the edges of chlorite grains.

Texture

This rock shows a very clear preferred orientation of the grains, even resulting in occurrence of elongated quartz grains. Chlorite is gathered in bands together with a single biotite crystal every now and then. Plagioclase grains are not stable anymore, which gives them a very dusty appearance in PPL. K-felspars are stable and show checkerboard twinning.

Interpretation

This rock is a mylonite. Due to the very high pressures it must have experienced even quartz was able to deform to an elongated shape. The for the naked eye 'dark' bands consist out of unstable plagioclase together with chlorite and biotite, whereas the lighter bands consist mainly of quartz and k-feldspar.

JI 4-6

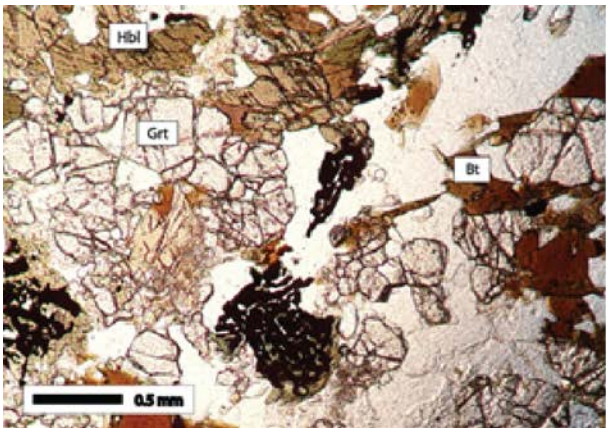

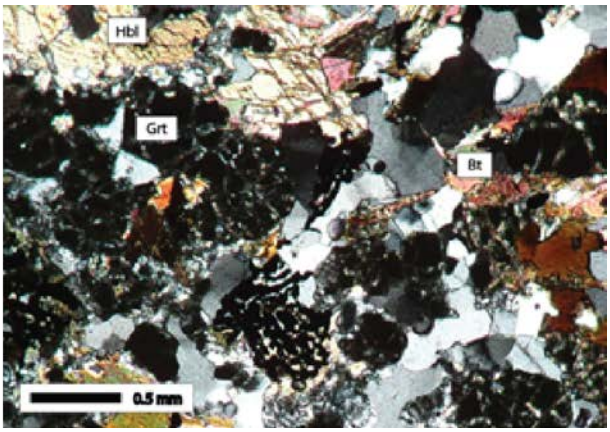

Mineral	Abundance (%)	Size (mm)	Average size (mm)	Habit
bio	10	0.5-1	0.8	Subhedral, sometimes ingrowth of ap and replaced by ilm.
gt	30	0.1-0.8	0.5	Sub/euhedral, many cracks running through. Occurs in clusters.
amp	25	0.5-0.8	0.7	Dark green/blue pleochroic. Sometimes almost completely replaced by ilm.
q	20	0.1-1.5	0.5	Anhedral. Most grains show undulose extinction.
ilm	5	0.1-1	0.7	Opaque patches of multiple grains, mostly overgrowing one or more amp grains.
pl	2	0.1-0.4	0.2	Unstable, wispy appearance with alternation of more Na- and Ca-rich parts.
kfs	2	0.1-0.4	0.2	Anhedral, patchy in PPL
ru	accessory	0.05-0.1	0.1	Deep orange in PPL and XPL
al (allanite)	accessory	0.05-0.1	0.08	Yellow in PPL. Occurs between ilm clusters replacing amp grains.
ep	1	0.1-1	0.5mm	Euhedral, zoning with diffuse borders.
ap	2	0.05-0.1	0.08mm	Euhedral. Occurs inside q, bio and amp.

Texture

This rock shows clusters of gt + bio + amp, separated by quartz and feldspars. Plagioclase grains seem to be unstable and show segregation of more sodic and more calcic parts. The gt + bio + amp clusters appear to be stable, although at some places complete amphibole + biotite grains are being replaced by ilmenite (+ allanite). Most amphiboles show a dark green pleochroism specific for hornblende, although some grains go towards a bluish color specific for barroisite.

Euhedral epidote occurs in the sample, but is not evenly distributed and grains cluster together at some places. Euhedral apatite is evenly distributed throughout the sample. Almost all quartz grains show undulose extinction.

Interpretation

This rock is a garnet amphibolite with a very stable mineral assemblage of gt + bio + amp. However at confined locations amp + bio is being replaced by ilm (+ al) indicating the assemblage as less stable. Undulose extinction in the quartz grains indicate a stress regime which was put on the rock.

JI 4-7

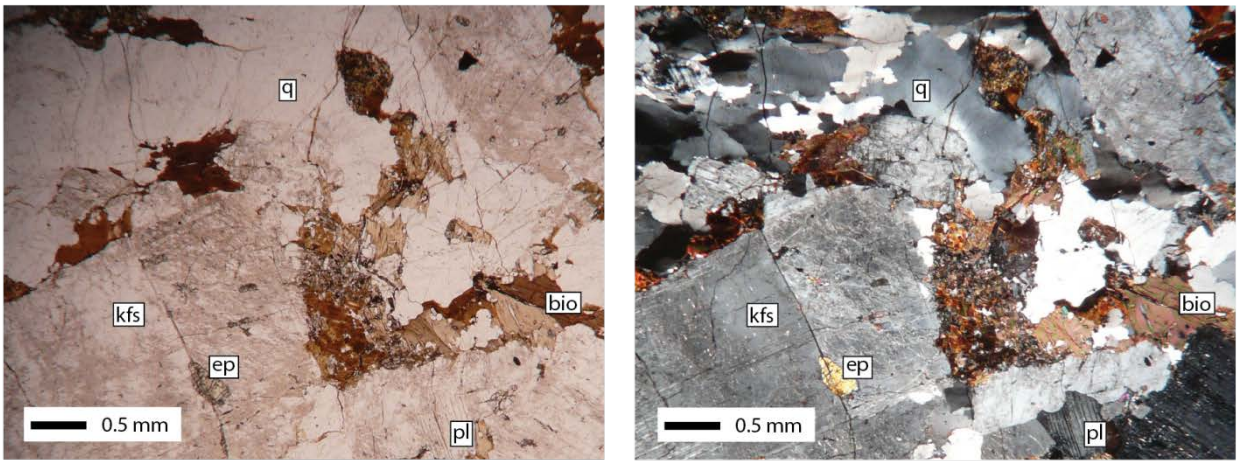

Mineral	Abundance (%)	Size (mm)	Average size (mm)	Habit
q	35	0.2-4	1	Undulose extinction. Partly recrystallized.
pl	25	0.2-6	3	Generally elongated with sometimes twinning, Subhedral. Dusty appearance. Sometimes albite twinning.
kfs	20	0.2-20	5	Elongated, subhedral, sometimes with checkerboard twinning.
bio	15	0.1-2	1	Brown pleochroic, some grains contain small grains of apatite inside.
ep	5	0.1-0.5	0.1	Small grains in cluster, probably remains of one larger grain. Blue extinction, high relief.
zo	1	0.1-0.8	0.5	High relief, blue extinction. Within pl.
metal oxides	3	0.1-0.5	0.2	Between biotite clusters.
zr	1	0.05-0.2	0.1	As inclusions in plagioclase.

Texture

This rock is equigranular with large (up to 20mm) grains of k-feldspar. Biotite clusters with metal oxides. Plagioclase is unstable and is sometimes partly replaced by epidote grains.

Interpretation

This is a granite which had quite some time to cool down, resulting in large feldspar grains. The chemical surrounding got more potassium rich resulting in breakdown of plagioclase and remaining stability of k-feldspar.

JI 5-1

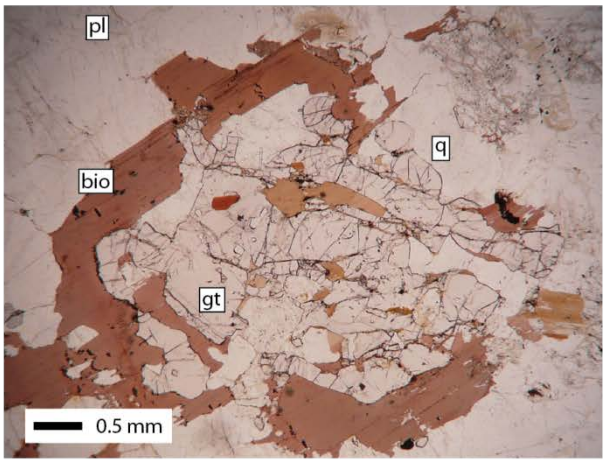

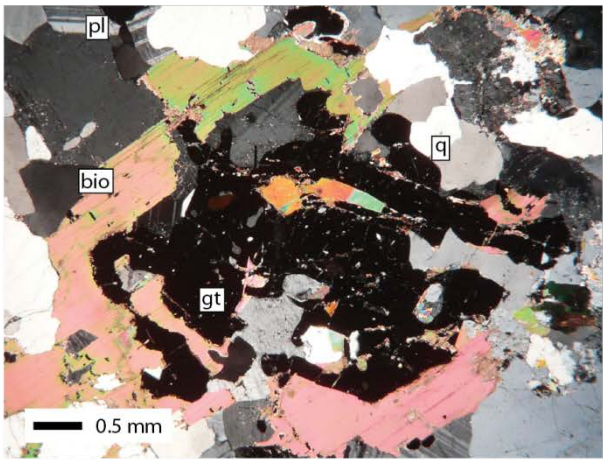

Mineral	Abundance (%)	Size (mm)	Average size (mm)	Habit
q	50	0.5-4	2	Subhedral, symplectitic structures running from the old garnets.
pl	10	0.5-3	2	Sub-/Euhedral grain, very clear albite twinning. Inclusions of zircon.
kfs	10	1-5	3	Dusty appearance in PPL, seemingly unstable.
bio	10	0.5-1	0.7	Brown pleochroic, black decay halos. Mostly overgrown by quartz. Sometimes symplectite formation in quartz and feldspar radiating from the biotite grains.
gt	5	1-5	2	High relief, pinkish in PPL. Subhedral, run through by cracks. Overgrowing biotite.
old gt	20	0.3-2	1	Subhedral, 6-sized grains, colourless in PPL. Low grey interference colours, neither isotropic nor showing normal interference habits. Grains ran through by green filled cracks like often in garnet.
zr	Accessory	0.01	0.01	As inclusions in quartz.

Texture

This rock contains an equigranular mineral assemblage. Part of the minerals used to be garnet according to their relief, shape and filled cracks resembling a garnet. They are completely replaced by quarts. Some garnets with a pinkish colour are still present and overgrow the biotite in the sample. K-feldspar seems relatively unstable compared to plagioclase as of its dusty appearance and less obvious mineral edges. Also symplectitic structures can be observed (Figure 78).

Interpretation

This rock is a granite, containing garnet. Potassium was reacted out of the rock, making K-feldspar and biotite less stable. Further back in its history, the surroundings were changed as well, making garnet unstable.

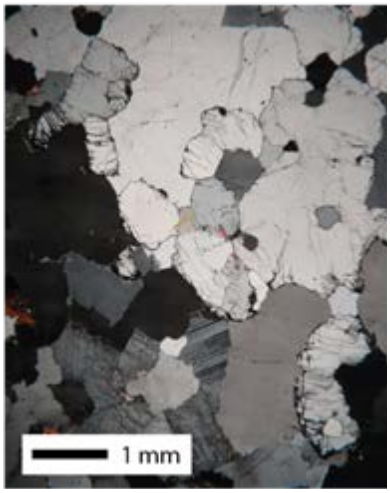

Figure 78. Symplectitic structures in sample JI 5-1.

JI5-2

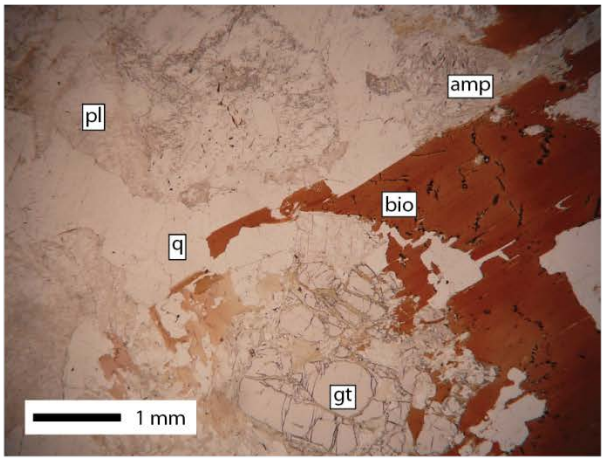

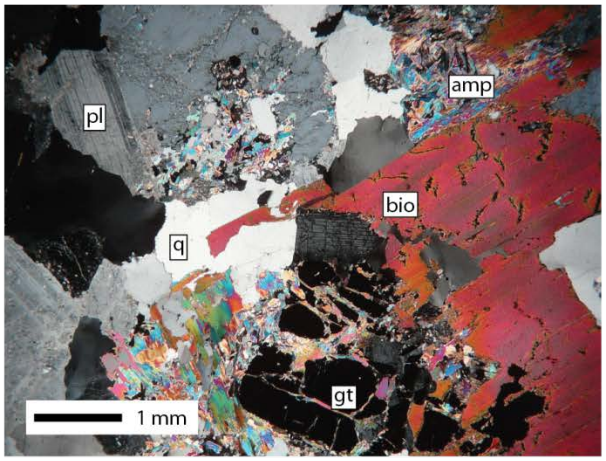

Mineral	Abundance (%)	Size (mm)	Average size (mm)	Habit
q	40	0.1-4	2	Anhedral, some recrystallization along the edges. Some grains show undulose extinction.
pl	20	0.5-3	1	Albite twinning, some grains are unstable, partly replaced by amphibole.
kfs	15	1-4	2	Dusty appearance, anhedral.
bio	10	1-8	5	Brown pleochroic, cleavage parallel to elongated shape of the grains.
gt	5	2-5	3	Unstable, partly replaced by amp + pl
amp	10	0.1-0.5	0.3	Finegrained needles, occurs as a replacement for altered minerals.

Texture

This rock contains large (1-5mm) crystals, of which some are completely replaced by a fine grained mineral cluster of amp + pl (+ bio) (<0.5mm) in a random order. Garnet and biotite crystals are unstable and are partly replaced by small grained amp + pl.

Interpretation

This rock is an unstable granite. Garnet and biotite are (partly) replaced by amphibole and plagioclase needles in a random order.

JI 5-3

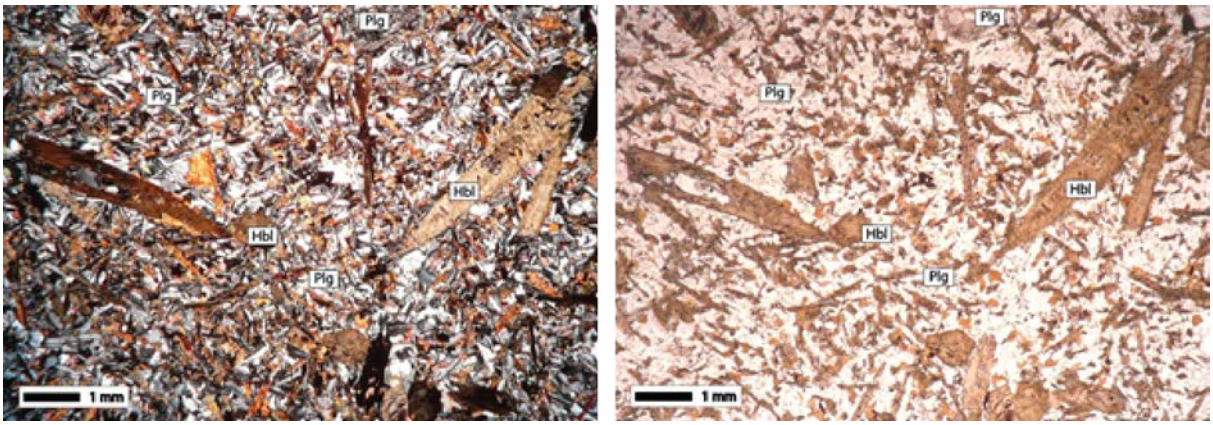

Mineral	Abundance (%)	Size (mm)	Average size (mm)	Habit
hbl (phenocrysts)	10	2-4	3	Euhedral, zoned, sometimes clear cleavage. Dark green pleochroic. Sometimes partly replaced by bio + metal oxides.
pl (phenocrysts)	2	1-2	1	Euhedral blocky shape, zoned, albite twinning. Unstable core filled with hbl, followed by anorthite zone and albite rim.
hbl (matrix)	30	0.5-2	1	Anhedral, partly being replaced by metal oxides. Dark green pleochroic.
pl (matrix)	25	<0.2	0.05	Euhedral elongated shape, sometimes albite twinning. An-rich core, Ab-rich rim.
q (matrix)	20	<0.2	0.05	Anhedral
bio (matrix)	10	0.01-0.1	0.02	Anhedral, light brown pleochroic. Stable appearance.
ru	1	0.05-0.1	0.08	Deep orange, Anhedral.
metal oxides	2	0.01-0.1	0.02	Anhedral to blocky shape. Often overgrows hbl or pl.

Texture

Fine grained matrix with coarse grained hbl and pl minerals. No preferred direction of growth visible. Phenocrysts seem unstable, especially in the core of the grains. Plagioclases show a clear zoning with an anorthite rich core and an albite rich rim.

Interpretation

This is a hornblende hornfels, formed as contact metamorphose with granite intrusions. Present conditions are different from original conditions, causing zoning and replacement of mineral cores.

JI 5-4

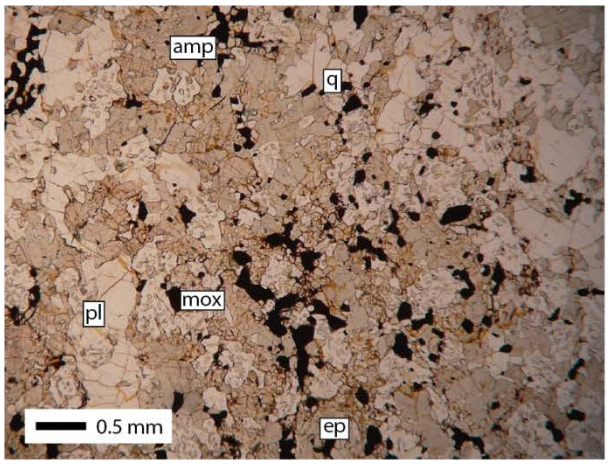

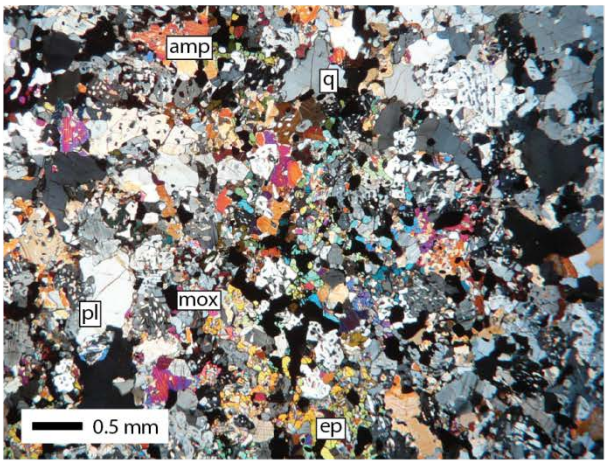

Mineral	Abundance (%)	Size (mm)	Average size (mm)	Habit
q	40	0.5-1	0.8	Anhedral, sometimes containing holes with ap inside.
pl	15	0.2-1	0.5	Albite twinning. Grains covered with holes, filled with amp.
amp	15	0.3-1.5	0.8	Green in PPL, not pleochroic. Clear 60/120 degree cleavage.
metal oxides	10	0.05-0.2	0.1	Anhedral, overgrowing ol, pl and q.
ol	10	0.05-0.2	0.1	Slightly higher relief than amphibole, green in PPL. Sometimes clear cleavage in one direction.
zo	5	0.05-0.1	0.08	Distinct blue extinction. Occurs along grain boundaries and as fill up of holes in pl.
chl	3	0.01-0.1	0.05	Along quartz and epidote grain boundaries. Green pleochroic.
ru	2	0.01-0.2	0.05	Along epidote grain boundaries.
bio	Accessory	0.1		Along metal oxide boundary.
ap	Accessory	0.03-0.08	0.05	Inside quartz grains.

Texture

This rock shows an unstable, equigranular mineral assemblage in which plagioclase is eaten away, resulting in holes inside the grains filled with amphibole. Metal oxides grow throughout the sample replacing olivine, plagioclase and quartz. The sample consists mainly of a mineral assemblage as described in the table. However there are some more felsic spots with mainly quartz, plagioclase and some amphibole. Here plagioclase grains show symplectitic structures.

Interpretation

This is a mafic intrusive rock, most likely a gabbro, which cooled pretty fast according to the mineral size. The chemistry of the surroundings changed drastically, resulting in plagioclase being replaced by amphibole and symplectitic structures to form. The more felsic part are probably lumps of minerals added to the melt at a later stage.

JI 5-5

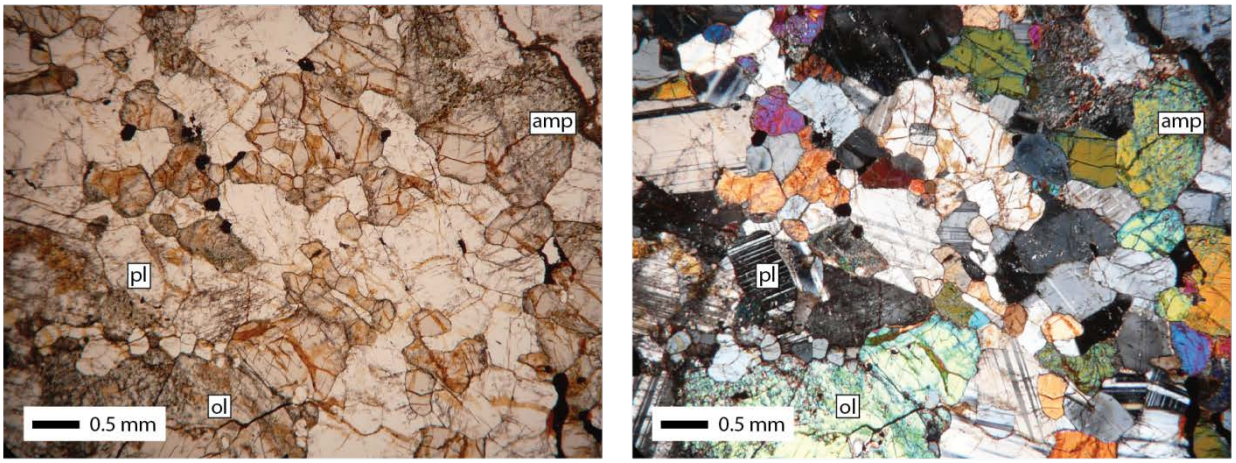

Mineral	Abundance (%)	Size (mm)	Average size (mm)	Habit
q	2	0.1-0.5	0.2	Anhedral, together with plagioclase.
pl	20	0.1-13	1	Anhedral, very distinct albite twinning.
ol	40	0.3-3	0.8	Rounded shape, slight higher relief than amphibole. Sometimes distinct cleavage in one direction.
amp	25	0.5-2	1	Distinct cleavage on 60/120 degree angle. Often dusty appearance.
metal oxides	5	0.1-2	0.5	Anhedral, often overgrowing plagioclase.
ru	2	0.05-0.1	0.08	Together with metal oxides and inside cracks.
cpx	5	0.2-0.5	0.3	Distinct 90 degree cleavage, inclined extinction.
bio	2	0.1-1	0.5	Randomly orientated, together with clayminerals in a crack running through the sample.

Texture

This rock shows a fairly coarse grained, equigranular mineral structure. Amphibole seems unstable regarding the dusty appearance. A crack running through the sample contains mainly plagioclase and random oriented clay minerals. The rock is divided in a mafic and more felsic part. The latter contains plagioclase grains up to 13 mm whereas within the mafic part these grain do not exceed 2 mm. However on the border between the two areas, minerals in the mafic section are slightly larger (<2 mm) than in the rest of the rock (<1 mm).

Interpretation

This is a mafic intrusive rock; most probably a gabbro. Introduction of a more felsic melt caused slower cooling in this area resulting in slightly larger crystals. Chemistry changes caused amphiboles to be unstable, although no evidence for such is found in zoning of olivines.

JI 5-7

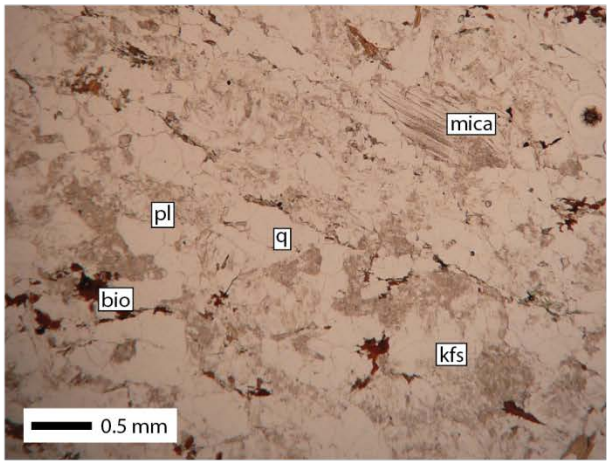

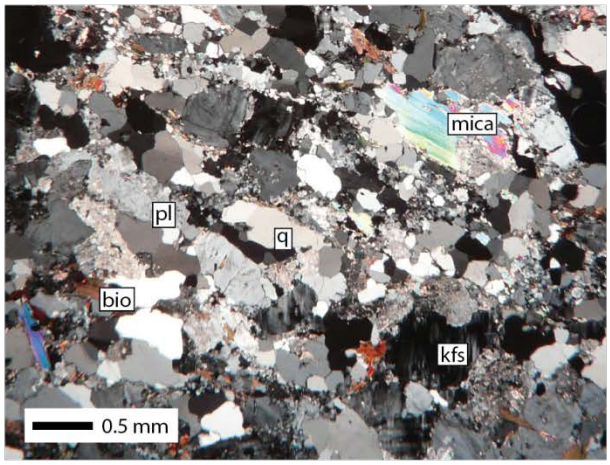

Mineral	Abundance (%)	Size (mm)	Average size (mm)	Habit
q	50	0.1-1	0.5	Subhedral, some grains show undulose extinction.
pl	15	0.3-1	0.7	Anhedral, dusty appearance.
kfs	10	0.5-1.5	1	Anhedral, checkerboard twinning.
bio	15	0.01-1	0.3	Elongated, slight preferred orientation. Mainly in between quartz grains.
mica	5	0.1-1	0.7	Elongated, slight preferred orientation. Mainly overgrowing quartz grains.
chl	5	0.01-0.3	0.1	Anhedral, small patches.

Texture

This rock shows a slight preferred orientation of the micas, although no banding of these grains is observed. The rock is much smaller grained (0.01-1.5mm) than the other granite samples in this study (0.1-8mm). Chlorite grains are small and thinly spread indicating they probably only had short time to grow.

Interpretation

This is a granite with slight schistose habits. It is probably part of a different generation of granites than the others described in this study because of its fine grained habit and lack of garnets.

Appendix II: XRF data

Sample name	LOI (%)	Fe_2O_3	MnO	TiO2	CaO	K2O	P_2O_5	SiO_2	Al_2O_3	MgO	Na_2O	BaO	Sum
JI-1-1	2.471	11.190	0.225	1.243	13.131	0.875	0.096	48.367	15.273	6.623	1.927	0.010	98.959
JI-1-3	1.294	5.358	0.118	0.615	1.737	3.156	0.133	68.480	14.242	2.605	2.228	0.046	98.716
JI-1-4	2.207	10.635	0.216	1.087	7.533	2.458	0.105	55.529	16.693	3.636	2.068	0.045	100.003
JI-2-1	1.396	12.058	0.197	1.210	11.471	0.609	0.087	49.222	13.906	7.964	2.332	0.008	99.064
JI-2-2	1.168	2.285	0.027	0.257	0.972	5.743	0.154	73.218	13.993	0.275	2.577	0.085	99.585
JI-4-2	0.613	3.356	0.040	0.449	2.151	4.383	0.106	67.623	14.053	1.241	2.783	0.093	96.278
JI-4-3	0.912	12.204	0.202	0.936	11.125	0.975	0.068	49.136	14.382	7.530	1.448	0.007	98.013
JI 4-6		18.684	0.238	2.000	6.394	3.084	0.788	49.587	13.549	1.635	0.685	0.176	96.820
JI-4-7	1.150	5.347	0.072	0.817	2.861	4.566	0.207	65.908	15.249	1.109	3.096	0.111	99.344
JI-5-3	0.914	9.126	0.173	0.908	8.049	1.150	0.209	54.976	18.653	3.822	2.419	0.045	99.530
JI-5-7	0.626	1.786	0.019	0.171	0.932	5.352	0.036	74.275	13.423	0.224	2.909	0.067	99.193

Table 12. Whole rock geochemistry from XRF analysis in wt%. Fe_2O_3 includes both Fe_2O_3 and FeO.

Appendix III: EMP data single grain

JI 1-1 K-feldspar

Na2O	SiO2	MnO	K2O	MgO	Al2O3	FeO	CaO	Total	Comment
0,197	65,208	0,000	16,527	0,000	18,673	0,000	0,000	100,637	core
0,353	65,298	0,000	15,962	0,120	18,791	0,126	0,036	100,725	core
0,145	64,246	0,022	16,507	0,003	18,618	0,000	0,000	99,598	core
0,673	64,219	0,040	15,988	0,000	18,756	0,000	0,000	99,676	core
0,180	64,939	0,000	16,304	0,011	18,415	0,012	0,000	99,861	core
0,219	65,560	0,009	16,300	0,004	18,612	0,007	0,012	100,723	core
0,124	66,121	0,009	16,156	0,011	18,522	0,019	0,000	100,963	core
7,020	59,002	0,000	0,245	0,013	26,568	0,081	7,661	100,590	core
0,141	65,875	0,011	16,365	0,000	18,617	0,032	0,000	101,057	core
0,213	65,579	0,000	16,277	0,008	18,701	0,000	0,002	100,802	core
0,134	65,460	0,022	16,598	0,001	19,003	0,026	0,000	101,244	core
0,149	65,011	0,013	16,615	0,000	18,552	0,035	0,000	100,375	middle
0,212	65,202	0,000	16,088	0,008	18,524	0,000	0,648	100,736	middle
0,210	64,007	0,004	16,392	0,000	18,593	0,000	0,010	99,216	middle
0,709	62,897	0,000	15,678	0,263	18,517	0,044	0,000	98,108	middle
0,209	65,876	0,011	16,278	0,000	18,672	0,040	0,000	101,086	middle
0,149	65,288	0,031	16,557	0,000	18,615	0,056	0,000	100,699	middle
0,146	66,065	0,013	16,251	0,000	18,673	0,000	0,000	101,160	middle
0,211	65,855	0,046	16,365	0,009	18,788	0,000	0,000	101,287	middle
0,207	64,858	0,000	16,463	0,000	18,622	0,000	0,000	100,201	middle
0,129	64,919	0,011	16,702	0,000	18,888	0,014	0,000	100,670	middle
0,231	65,472	0,029	16,327	0,005	18,386	0,033	0,000	100,483	rim
0,250	65,426	0,013	16,419	0,007	18,978	0,011	0,000	101,157	rim
0,207	65,084	0,000	16,514	0,000	18,814	0,000	0,000	100,667	rim
0,499	64,792	0,020	16,093	0,000	18,652	0,011	0,000	100,108	rim
0,201	65,765	0,011	16,378	0,000	19,041	0,032	0,000	101,430	rim
0,158	65,303	0,018	16,300	0,000	18,700	0,076	0,000	100,568	rim
0,130	66,040	0,015	16,290	0,000	18,809	0,000	0,015	101,358	rim
6,754	59,056	0,004	0,179	0,002	27,497	0,000	8,173	101,675	rim
0,163	65,200	0,000	16,640	0,014	18,731	0,000	0,000	100,748	rim
0,173	65,474	0,000	16,488	0,000	18,908	0,007	0,000	101,062	rim
0,110	65,597	0,022	16,599	0,000	19,103	0,000	0,000	101,451	rim

Table 13. Core, middle and rim measurements of K-felspar in JI 1-1.

JI 1-3 K-feldspar

Na2O	SiO2	MnO	K2O	MgO	Al2O3	FeO	CaO	Total	Comment
0,137	64,446	0,000	16,417	0,000	18,605	0,019	0,007	99,652	core
0,167	65,502	0,000	16,288	0,000	19,069	0,028	0,007	101,087	core
0,252	64,848	0,026	16,265	0,000	18,857	0,114	0,000	100,362	core
0,261	64,224	0,002	16,055	0,027	19,782	0,074	0,036	100,462	core
0,145	65,441	0,007	16,236	0,003	18,824	0,000	0,000	100,675	core
0,399	64,715	0,000	16,107	0,005	18,756	0,000	0,021	100,003	core
0,179	65,479	0,000	16,182	0,000	18,832	0,032	0,000	100,704	core
0,154	65,254	0,000	16,308	0,000	18,703	0,023	0,015	100,471	core
0,140	65,012	0,000	16,385	0,000	18,894	0,000	0,016	100,447	core
0,130	64,944	0,004	16,345	0,004	18,768	0,007	0,003	100,211	core
0,143	65,034	0,000	16,523	0,001	18,879	0,000	0,000	100,595	core
0,132	65,011	0,002	16,384	0,006	18,552	0,083	0,000	100,186	middle
0,169	65,607	0,011	16,308	0,004	18,897	0,035	0,012	101,056	middle
0,173	65,266	0,000	16,161	0,000	18,525	0,048	0,000	100,213	middle
0,183	64,336	0,000	16,045	0,012	19,830	0,009	0,025	100,445	middle
0,167	65,655	0,011	16,397	0,000	18,815	0,048	0,000	101,095	middle
0,136	64,615	0,000	16,570	0,000	18,644	0,000	0,000	99,974	middle
0,180	65,500	0,000	16,131	0,004	18,715	0,035	0,000	100,565	middle
0,180	65,356	0,000	16,323	0,000	18,688	0,018	0,000	100,568	middle
0,153	65,393	0,000	16,322	0,001	18,978	0,000	0,000	100,849	middle
0,166	65,217	0,000	16,296	0,003	18,701	0,055	0,000	100,496	middle
0,174	65,284	0,011	16,317	0,000	18,951	0,046	0,000	100,837	rim
0,167	64,620	0,000	16,176	0,049	18,434	0,058	0,003	99,507	rim
0,994	63,935	0,024	14,491	0,078	20,282	0,241	0,224	100,269	rim
0,132	65,399	0,007	16,357	0,000	18,843	0,012	0,000	100,750	rim
0,181	64,718	0,033	16,372	0,000	18,476	0,011	0,000	99,791	rim
0,230	65,677	0,013	16,059	0,000	18,721	0,016	0,000	100,755	rim
0,105	65,048	0,000	16,604	0,000	18,717	0,000	0,001	100,475	rim
0,364	65,456	0,000	16,213	0,000	18,858	0,000	0,000	100,905	rim
0,164	63,797	0,000	16,635	0,000	18,644	0,000	0,000	99,251	rim
0,116	65,288	0,000	16,570	0,002	18,890	0,083	0,000	100,953	rim

Table 14. Core, middle and rim measurements of K-felspar in JI 1-3.

JI 1-4 K-feldspar

Na2O	SiO2	MnO	K2O	MgO	Al2O3	FeO	CaO	Total	Comment
0,188	64,473	0,000	16,636	0,000	19,065	0,002	0,080	100,444	core
0,098	64,931	0,017	16,858	0,006	19,198	0,034	0,027	101,169	core
0,160	65,298	0,000	16,593	0,003	19,229	0,000	0,000	101,283	core
0,161	65,061	0,002	16,751	0,006	19,250	0,000	0,000	101,231	core
0,188	65,110	0,000	16,568	0,000	18,962	0,002	0,000	100,830	core
0,156	64,977	0,033	16,813	0,000	18,855	0,000	0,008	100,842	core
0,129	65,736	0,019	16,905	0,010	19,236	0,000	0,000	102,035	core
0,144	64,013	0,007	16,669	0,001	19,166	0,011	0,000	100,011	core
0,214	62,979	0,000	16,627	0,011	19,142	0,000	0,014	98,987	core
0,238	64,423	0,000	16,674	0,000	18,946	0,019	0,000	100,300	core
0,177	64,909	0,031	16,694	0,000	19,224	0,000	0,000	101,035	middle
0,166	63,395	0,019	16,636	0,017	18,952	0,000	0,000	99,185	middle
0,111	65,088	0,021	16,687	0,013	19,259	0,004	0,000	101,183	middle
0,183	65,431	0,000	16,632	0,000	18,801	0,044	0,264	101,355	middle
0,183	63,804	0,005	16,552	0,000	18,706	0,000	0,000	99,250	middle
0,194	65,085	0,000	16,779	0,000	19,102	0,000	0,000	101,160	middle
0,185	64,836	0,000	16,724	0,005	19,060	0,000	0,016	100,826	middle
0,167	63,037	0,000	16,584	0,000	18,857	0,000	0,000	98,645	middle
0,142	62,462	0,000	16,452	0,000	18,900	0,000	0,014	97,970	middle
0,146	65,000	0,000	16,677	0,004	18,836	0,013	0,011	100,687	middle
0,182	63,943	0,000	16,799	0,000	19,132	0,000	0,000	100,056	rim
0,187	65,105	0,000	16,480	0,018	19,052	0,021	0,011	100,874	rim
0,116	64,379	0,035	16,624	0,000	19,161	0,000	0,000	100,315	rim
0,154	65,607	0,000	16,713	0,000	19,149	0,000	0,000	101,623	rim
0,196	65,906	0,000	16,653	0,000	18,881	0,000	0,000	101,636	rim
0,149	63,998	0,064	16,596	0,002	18,846	0,000	0,007	99,662	rim
0,217	65,193	0,000	16,845	0,001	19,263	0,000	0,007	101,526	rim
0,175	63,826	0,012	16,642	0,012	18,913	0,000	0,017	99,597	rim
0,187	63,424	0,024	16,591	0,000	18,933	0,038	0,005	99,202	rim
0,236	64,538	0,000	16,717	0,000	18,894	0,002	0,000	100,387	rim

Table 15. Core, middle and rim measurements of K-felspar in JI 1-4.

JI 2-2 K-feldspar

Na2O	SiO2	MnO	K2O	MgO	Al2O3	FeO	CaO	Total	Comment
1,067	65,088	0,000	15,558	0,000	19,503	0,028	0,083	101,327	core
0,778	64,519	0,000	16,172	0,000	19,221	0,045	0,018	100,753	core
1,203	65,462	0,024	15,311	0,009	19,239	0,032	0,002	101,282	core
2,047	65,440	0,000	14,154	0,000	19,606	0,000	0,041	101,288	core
3,567	66,158	0,000	12,731	0,000	19,727	0,000	0,033	102,216	core
0,632	65,044	0,000	16,012	0,002	19,206	0,040	0,079	101,015	core
0,478	65,293	0,000	16,392	0,000	19,232	0,030	0,029	101,454	core
0,871	65,379	0,009	15,901	0,000	19,439	0,000	0,015	101,614	core
0,872	64,329	0,007	15,672	0,000	19,058	0,002	0,040	99,980	core
0,759	65,134	0,000	16,005	0,000	19,402	0,038	0,077	101,415	middle
1,222	64,916	0,000	15,290	0,000	19,331	0,000	0,040	100,799	middle
1,353	64,847	0,002	15,275	0,000	19,343	0,030	0,025	100,875	middle
0,932	65,617	0,000	15,827	0,000	19,309	0,028	0,015	101,728	middle
0,833	65,209	0,042	15,756	0,000	19,361	0,000	0,028	101,229	middle
0,804	64,977	0,007	15,963	0,000	19,370	0,006	0,005	101,132	middle
0,663	65,509	0,000	16,156	0,000	19,390	0,023	0,052	101,793	middle
0,891	65,871	0,016	15,841	0,000	19,465	0,017	0,038	102,139	middle
1,165	65,642	0,005	15,377	0,000	19,366	0,000	0,035	101,590	middle
0,980	65,742	0,000	15,728	0,000	19,557	0,013	0,038	102,058	middle
0,749	65,172	0,009	16,072	0,000	19,291	0,004	0,048	101,345	rim
0,967	64,466	0,005	15,868	0,000	19,088	0,004	0,037	100,435	rim
0,770	65,522	0,000	15,938	0,017	19,464	0,047	0,009	101,767	rim
1,412	65,424	0,000	14,990	0,000	19,414	0,049	0,024	101,313	rim
0,449	64,856	0,000	16,418	0,000	19,288	0,000	0,055	101,066	rim
0,895	65,505	0,000	15,771	0,010	19,529	0,011	0,009	101,730	rim
0,677	65,783	0,000	15,939	0,003	19,469	0,032	0,025	101,928	rim
0,966	65,737	0,012	15,597	0,000	19,471	0,008	0,043	101,834	rim
1,121	65,773	0,000	15,675	0,005	19,457	0,028	0,040	102,099	rim
1,042	65,037	0,000	15,728	0,000	19,371	0,009	0,070	101,257	rim

Table 16. Core, middle and rim measurements of K-felspar in JI 2-2.

JI 4-2 K-feldspar

Na2O	SiO2	MnO	K2O	MgO	Al2O3	FeO	CaO	Total	Comment
1,429	65,245	0,000	14,895	0,003	19,390	0,000	0,040	101,002	core
1,911	65,137	0,002	14,034	0,000	19,822	0,000	0,241	101,147	core
0,674	64,834	0,000	16,258	0,000	19,437	0,000	0,000	101,203	core
0,599	65,174	0,005	16,314	0,000	19,420	0,013	0,000	101,525	core
0,559	64,586	0,000	16,272	0,000	19,511	0,015	0,009	100,952	core
0,608	63,817	0,000	16,211	0,000	19,411	0,013	0,000	100,060	core
0,429	65,318	0,007	16,451	0,003	19,422	0,000	0,035	101,665	core
0,320	65,162	0,000	16,492	0,005	19,309	0,011	0,000	101,299	core
0,922	63,592	0,000	15,528	0,000	19,512	0,061	0,018	99,633	middle
2,336	66,112	0,017	13,564	0,006	19,845	0,030	0,198	102,108	middle
0,702	63,838	0,000	16,099	0,000	19,358	0,063	0,000	100,060	middle
0,570	64,944	0,014	16,333	0,018	19,308	0,009	0,000	101,196	middle
0,458	64,563	0,000	16,330	0,000	19,405	0,000	0,000	100,756	middle
0,640	64,722	0,000	16,268	0,000	19,516	0,000	0,000	101,146	middle
0,580	64,674	0,026	16,158	0,000	19,397	0,013	0,000	100,848	middle
0,751	65,033	0,000	16,118	0,000	19,523	0,000	0,004	101,429	middle
0,749	65,795	0,000	15,928	0,020	19,363	0,000	0,032	101,887	rim
0,976	65,324	0,000	15,714	0,008	19,507	0,015	0,031	101,575	rim
0,671	65,119	0,012	16,157	0,010	19,458	0,000	0,000	101,427	rim
0,645	65,891	0,000	16,296	0,000	19,487	0,000	0,000	102,319	rim
0,582	63,825	0,000	16,153	0,000	19,356	0,000	0,178	100,094	rim
0,562	65,332	0,033	16,285	0,006	19,513	0,023	0,244	101,998	rim
0,525	65,102	0,000	16,391	0,000	19,447	0,000	0,000	101,465	rim
0,810	63,826	0,000	15,958	0,004	19,261	0,000	0,007	99,866	rim
0,895	65,505	0,000	15,771	0,010	19,529	0,011	0,009	101,730	rim
0,677	65,783	0,000	15,939	0,003	19,469	0,032	0,025	101,928	rim
0,966	65,737	0,012	15,597	0,000	19,471	0,008	0,043	101,834	rim
1,121	65,773	0,000	15,675	0,005	19,457	0,028	0,040	102,099	rim
1,042	65,037	0,000	15,728	0,000	19,371	0,009	0,070	101,257	rim

Table 17. Core, middle and rim measurements of K-felspar in JI 4-2.

JI 4-3 K-feldspar

Na2O	SiO2	MnO	K2O	MgO	Al2O3	FeO	CaO	Total	Comment
0,524	63,871	0,000	15,746	0,302	18,962	0,477	0,033	99,917	core
0,323	65,340	0,020	16,615	0,003	19,093	0,014	0,000	101,433	core
0,461	65,321	0,000	16,348	0,000	19,161	0,000	0,000	101,305	core
0,377	64,724	0,009	16,346	0,000	18,981	0,000	0,010	100,447	core
0,349	65,304	0,035	16,406	0,000	18,949	0,000	0,024	101,067	core
0,507	65,776	0,018	16,006	0,000	19,033	0,016	0,000	101,373	core
0,116	65,294	0,033	16,631	0,001	18,849	0,000	0,000	100,924	core
0,485	65,320	0,000	16,311	0,005	19,014	0,007	0,015	101,157	core
0,488	65,782	0,000	16,041	0,000	19,053	0,011	0,000	101,419	core
0,244	65,509	0,000	16,532	0,011	18,999	0,007	0,000	101,302	core
0,559	65,380	0,000	15,878	0,040	19,198	0,072	0,019	101,157	core
0,266	64,419	0,000	16,044	0,013	18,954	0,000	0,017	99,753	middle
0,262	65,365	0,000	16,507	0,009	19,225	0,000	0,000	101,413	middle
0,482	65,264	0,000	16,174	0,000	18,974	0,004	0,004	100,902	middle
0,343	65,411	0,000	16,395	0,000	19,078	0,000	0,000	101,272	middle
0,266	65,028	0,024	16,416	0,000	19,062	0,000	0,000	100,796	middle
0,482	65,482	0,042	16,087	0,003	19,074	0,000	0,006	101,176	middle
0,492	65,446	0,009	16,099	0,000	19,067	0,000	0,000	101,113	middle
0,068	65,340	0,000	16,770	0,017	18,814	0,007	0,000	101,031	middle
0,437	65,523	0,002	16,218	0,021	19,158	0,000	0,000	101,381	middle
0,517	65,788	0,000	16,242	0,000	18,942	0,000	0,000	101,489	middle
0,082	65,894	0,009	16,805	0,001	18,981	0,000	0,000	101,796	middle
0,690	65,200	0,020	15,703	0,016	19,161	0,037	0,004	100,847	middle
0,379	64,257	0,000	16,188	0,000	19,046	0,000	0,016	99,886	rim
0,386	65,358	0,018	16,373	0,000	18,990	0,000	0,000	101,160	rim
0,596	64,505	0,029	15,895	0,000	19,170	0,000	0,000	100,218	rim
0,384	65,497	0,013	16,356	0,000	19,108	0,000	0,000	101,359	rim
0,317	65,265	0,018	16,381	0,004	19,247	0,000	0,000	101,239	rim
0,331	51,086	0,308	0,278	12,984	4,399	14,394	12,219	96,293	rim
0,353	65,251	0,000	16,220	0,007	18,841	0,025	0,000	100,697	rim
0,470	65,709	0,004	16,155	0,013	19,009	0,002	0,000	101,436	rim
0,063	65,533	0,000	16,782	0,000	18,944	0,021	0,000	101,366	rim
0,416	65,519	0,002	16,252	0,004	19,189	0,026	0,016	101,424	rim
0,451	65,764	0,000	16,170	0,000	19,024	0,000	0,000	101,421	rim
0,096	65,381	0,011	16,685	0,000	19,181	0,044	0,000	101,422	rim
0,478	64,519	0,027	15,702	0,003	18,777	0,023	0,000	99,529	rim

Table 18. Core, middle and rim measurements of K-felspar in JI 4-3.

JI 4-5 K-feldspar

Na2O	SiO2	MnO	K2O	MgO	Al2O3	FeO	CaO	Total	Comment
0,227	64,946	0,012	16,732	0,000	19,016	0,030	0,000	100,963	core
0,263	64,765	0,016	16,742	0,008	18,901	0,032	0,000	100,727	core
1,479	63,813	0,012	14,264	0,019	18,730	0,030	1,479	99,826	core
0,695	64,944	0,012	16,048	0,011	19,299	0,000	0,025	101,034	core
0,715	65,844	0,031	15,963	0,001	19,597	0,017	0,041	102,209	core
0,557	64,426	0,000	16,364	0,000	19,251	0,000	0,000	100,598	core
0,249	64,418	0,000	16,788	0,000	19,060	0,000	0,000	100,515	core
0,569	63,964	0,000	16,154	0,005	19,114	0,023	0,035	99,864	core
0,661	64,277	0,019	16,068	0,000	19,092	0,000	0,028	100,145	core
0,689	64,574	0,000	16,007	0,000	19,293	0,000	0,022	100,585	core
0,212	65,027	0,000	16,806	0,000	18,990	0,000	0,012	101,047	middle
0,250	64,991	0,000	16,787	0,000	18,924	0,000	0,000	100,952	middle
2,096	65,655	0,000	13,820	0,002	19,616	0,011	0,051	101,251	middle
0,498	65,336	0,000	16,308	0,000	19,449	0,004	0,024	101,619	middle
0,655	65,012	0,000	16,097	0,008	19,351	0,000	0,035	101,158	middle
0,648	65,315	0,033	16,122	0,000	19,274	0,045	0,012	101,449	middle
0,216	64,639	0,012	16,549	0,000	19,255	0,000	0,000	100,671	middle
0,504	64,488	0,012	16,412	0,000	19,254	0,019	0,022	100,711	middle
0,382	63,361	0,052	16,394	0,000	18,998	0,000	0,033	99,220	middle
0,666	64,153	0,028	16,128	0,002	19,315	0,013	0,027	100,332	middle
0,264	64,810	0,000	16,628	0,005	19,133	0,000	0,000	100,840	rim
0,278	65,035	0,005	16,627	0,000	18,963	0,038	0,002	100,948	rim
0,913	65,834	0,000	15,507	0,000	19,331	0,000	0,014	101,599	rim
0,955	65,602	0,000	15,706	0,002	19,456	0,015	0,000	101,736	rim
1,187	65,714	0,000	15,248	0,000	19,625	0,017	0,036	101,827	rim
0,876	65,644	0,000	15,678	0,000	19,450	0,000	0,000	101,648	rim
0,254	63,952	0,000	16,545	0,002	18,669	0,004	0,000	99,426	rim
0,275	64,690	0,045	16,595	0,002	19,373	0,011	0,000	100,991	rim
0,848	64,270	0,035	15,832	0,000	18,979	0,000	0,014	99,978	rim
0,748	65,001	0,033	15,968	0,000	19,513	0,000	0,004	101,267	rim

Table 19. Core, middle and rim measurements of K-felspar in JI 4-5.

JI 4-7 K-feldspar

Na2O	SiO2	MnO	K2O	MgO	Al2O3	FeO	CaO	Total	Comment
0,584	63,853	0,022	15,98	0	18,796	0,035	0,058	99,382	core
0,715	65,028	0,002	15,863	0,004	18,93	0,005	0	100,579	core
0,656	64,582	0	15,872	0	18,768	0	0	99,888	core
0,572	63,701	0	15,946	0	18,843	0,019	0,004	99,121	core
0,661	64,619	0,015	15,748	0	19,107	0	0,001	100,153	core
0,838	64,428	0	15,481	0	18,974	0,046	0	99,806	core
0,694	64,846	0	15,88	0	18,909	0	0	100,352	core
0,898	64,523	0	15,207	0	19,164	0,004	0,019	99,815	core
0,737	65,116	0	15,721	0	19,147	0,067	0,005	100,793	core
2,419	65,74	0	13,208	0	19,133	0,002	0,028	100,541	core
0,685	65,06	0,024	15,885	0	19,13	0,005	0	100,823	middle
0,727	64,293	0,024	15,845	0	18,649	0,002	0	99,615	middle
0,594	63,826	0	15,989	0,004	18,723	0,019	0,009	99,186	middle
0,602	64,849	0	15,916	0	19,032	0	0,005	100,411	middle
0,588	64,449	0,002	15,737	0	19,032	0,023	0,008	99,875	middle
0,842	63,933	0	15,431	0	18,967	0,033	0	99,27	middle
0,552	64,892	0,031	15,935	0	18,932	0,028	0	100,374	middle
0,449	64,66	0	16,105	0	19,002	0	0	100,216	middle
0,708	64,999	0	15,688	0,005	19,064	0,058	0,005	100,527	middle
0,664	65,18	0,004	15,871	0,001	19,067	0	0	100,829	middle
0,777	65,041	0,011	15,672	0	18,967	0,07	0,012	100,568	middle
0,717	64,972	0,026	15,721	0,015	19,039	0,023	0,012	100,537	rim
0,788	63,606	0	15,378	0	18,618	0	0	98,408	rim
0,478	64,193	0,042	16,157	0,002	18,739	0	0	99,687	rim
0,671	65,022	0	15,674	0	19,001	0,007	0	100,397	rim
0,678	64,259	0,002	15,603	0,004	18,868	0,037	0	99,462	rim
2,831	64,063	0	12,564	0	19,027	0	0,046	98,551	rim
0,587	65,288	0,046	16,015	0	19,046	0,058	0	101,048	rim
0,721	65,44	0,011	15,727	0,015	19,136	0,011	0	101,076	rim
0,76	65,098	0,013	15,717	0	19,026	0,011	0,003	100,628	rim
0,723	64,946	0	15,709	0	19,025	0	0	100,431	rim
0,668	65,188	0,007	15,769	0	19,055	0,018	0	100,714	rim

Table 20. Core, middle and rim measurements of K-felspar in JI 4-7.

JI 5-1 K-feldspar

Na2O	SiO2	MnO	K2O	MgO	Al2O3	FeO	CaO	Total	Comment
1,084	64,518	0,000	15,269	0,000	19,447	0,002	0,038	100,396	core
1,240	63,957	0,000	14,886	0,000	19,165	0,000	0,052	99,336	core
1,942	64,897	0,000	14,063	0,000	19,277	0,000	0,055	100,263	core
1,160	64,860	0,000	15,206	0,000	19,354	0,048	0,013	100,667	core
0,922	64,898	0,004	15,362	0,031	19,457	0,000	0,035	100,739	core
0,973	64,567	0,000	15,323	0,000	19,060	0,004	0,033	99,986	core
1,387	64,508	0,000	14,703	0,000	19,059	0,025	0,064	99,772	core
0,944	63,465	0,000	15,389	0,000	19,187	0,005	0,038	99,033	core
1,294	64,393	0,018	14,813	0,000	19,377	0,014	0,075	99,987	core
1,586	65,033	0,044	14,471	0,006	19,410	0,021	0,067	100,662	core
0,997	64,982	0,000	15,195	0,000	19,221	0,026	0,037	100,493	core
1,785	65,192	0,000	14,368	0,023	19,742	0,000	0,150	101,260	middle
1,409	64,451	0,007	14,674	0,000	19,363	0,030	0,060	100,021	middle
1,804	64,925	0,013	14,224	0,010	19,412	0,051	0,022	100,473	middle
1,174	64,571	0,000	15,174	0,002	19,272	0,011	0,020	100,224	middle
1,038	64,308	0,000	15,338	0,002	19,264	0,000	0,023	100,031	middle
1,214	65,167	0,002	14,918	0,008	19,420	0,000	0,044	100,784	middle
2,310	65,074	0,000	13,365	0,000	19,389	0,028	0,096	100,265	middle
2,126	63,819	0,022	13,273	0,000	18,972	0,026	0,105	98,343	middle
1,456	64,882	0,011	14,594	0,006	19,266	0,000	0,068	100,309	middle
1,426	65,023	0,000	14,601	0,000	19,471	0,000	0,054	100,575	middle
1,345	64,992	0,020	14,814	0,000	19,316	0,028	0,069	100,613	middle
1,221	64,821	0,000	14,969	0,001	19,429	0,039	0,040	100,539	rim
1,437	64,851	0,024	14,789	0,000	19,316	0,030	0,052	100,553	rim
1,920	65,046	0,000	13,954	0,016	19,390	0,033	0,048	100,438	rim
1,353	64,723	0,000	14,857	0,004	19,158	0,007	0,068	100,193	rim
0,810	64,358	0,000	15,572	0,007	19,295	0,000	0,035	100,085	rim
1,845	64,756	0,000	14,084	0,016	19,252	0,000	0,040	100,015	rim
0,655	64,707	0,000	15,713	0,012	19,302	0,011	0,000	100,419	rim
2,069	65,052	0,011	13,354	0,011	19,541	0,033	0,069	100,172	rim
1,047	65,299	0,018	15,125	0,000	19,450	0,000	0,052	101,041	rim
1,334	65,402	0,000	14,883	0,000	19,459	0,016	0,058	101,227	rim

Table 21. Core, middle and rim measurements of K-felspar in JI 5-1.

JI 5-2 K-feldspar

Na2O	SiO2	MnO	K2O	MgO	Al2O3	FeO	CaO	Total	Comment
0,960	64,384	0,000	15,729	0,005	19,238	0,000	0,000	100,316	core
0,977	64,340	0,000	15,406	0,000	19,078	0,030	0,052	99,883	core
0,839	64,001	0,000	15,663	0,004	18,862	0,024	0,019	99,412	core
0,950	64,018	0,000	15,300	0,000	18,780	0,000	0,041	99,089	core
1,376	64,244	0,039	14,993	0,012	19,100	0,031	0,098	99,893	core
1,495	64,319	0,046	14,788	0,000	19,256	0,000	0,049	99,953	core
1,145	64,341	0,023	15,324	0,005	18,769	0,000	0,000	99,607	core
1,024	64,071	0,000	15,466	0,001	18,894	0,000	0,023	99,479	core
0,458	63,113	0,023	15,984	0,003	18,669	0,000	0,013	98,263	core
1,355	63,008	0,005	14,936	0,000	18,463	0,026	0,202	97,995	core
1,094	64,268	0,000	15,418	0,000	19,016	0,022	0,049	99,867	core
0,964	63,937	0,000	15,474	0,000	18,870	0,000	0,000	99,245	middle
1,342	64,329	0,000	14,818	0,015	18,885	0,000	0,046	99,435	middle
0,762	64,010	0,000	15,801	0,014	19,078	0,000	0,019	99,684	middle
1,800	64,707	0,014	14,511	0,000	18,683	0,000	0,032	99,747	middle
0,721	63,776	0,000	15,759	0,006	19,193	0,000	0,013	99,468	middle
1,383	64,752	0,000	14,795	0,019	18,883	0,000	0,019	99,851	middle
1,241	64,301	0,000	15,091	0,000	18,908	0,013	0,006	99,560	middle
0,251	75,674	0,000	10,092	0,000	11,466	0,004	0,012	97,499	middle
0,852	64,178	0,007	15,500	0,004	18,601	0,000	0,111	99,253	middle
1,243	64,126	0,005	15,110	0,013	18,759	0,000	0,023	99,279	middle
1,459	64,292	0,000	14,724	0,000	18,647	0,024	0,083	99,229	middle
1,074	63,872	0,016	15,280	0,000	19,027	0,061	0,005	99,335	rim
1,439	64,606	0,000	14,812	0,000	18,999	0,000	0,052	99,908	rim
0,867	63,558	0,028	15,541	0,000	18,916	0,007	0,023	98,940	rim
0,904	64,536	0,014	15,523	0,005	18,743	0,000	0,000	99,725	rim
0,691	63,782	0,000	15,658	0,011	18,690	0,007	0,123	98,962	rim
2,726	64,268	0,005	12,974	0,002	18,710	0,007	0,074	98,766	rim
1,345	64,399	0,005	14,796	0,000	19,043	0,000	0,016	99,604	rim
0,418	65,459	0,028	15,615	0,000	17,983	0,000	0,000	99,503	rim
0,794	63,835	0,000	15,649	0,000	18,386	0,018	0,020	98,702	rim
1,269	64,029	0,000	15,050	0,000	18,632	0,000	0,016	98,996	rim
0,918	63,602	0,000	15,492	0,002	19,169	0,000	0,054	99,237	rim

Table 22. Core, middle and rim measurements of K-felspar in JI 5-2.

JI 5-5 K-feldspar

Na2O	SiO2	MnO	K2O	MgO	Al2O3	FeO	CaO	Total	Comment
1,008	64,485	0,000	15,401	0,000	18,956	0,007	0,003	99,871	core
0,711	65,017	0,000	15,821	0,000	19,193	0,000	0,000	100,775	core
0,880	65,365	0,000	15,447	0,000	19,121	0,000	0,048	100,901	core
0,998	64,945	0,007	15,111	0,000	19,221	0,042	0,026	100,409	core
0,976	64,230	0,000	15,259	0,000	19,282	0,023	0,078	99,880	core
0,782	65,463	0,026	15,855	0,000	18,996	0,000	0,000	101,122	core
1,298	64,711	0,022	14,948	0,000	19,187	0,000	0,001	100,194	core
0,765	65,155	0,015	15,574	0,000	19,351	0,000	0,009	100,887	core
1,066	65,425	0,000	15,314	0,002	19,344	0,000	0,038	101,189	core
0,100	64,616	0,000	16,527	0,066	18,828	0,116	0,001	100,289	core
0,732	65,388	0,000	15,748	0,000	19,163	0,056	0,003	101,129	core
0,783	65,058	0,000	15,555	0,000	19,144	0,000	0,018	100,611	middle
0,727	64,856	0,000	15,972	0,000	19,164	0,018	0,000	100,768	middle
0,883	65,743	0,000	15,426	0,005	19,172	0,044	0,028	101,337	middle
0,998	64,954	0,000	15,220	0,005	19,350	0,019	0,014	100,560	middle
0,917	64,687	0,009	15,357	0,000	19,233	0,000	0,063	100,266	middle
0,727	64,770	0,029	15,871	0,000	19,109	0,004	0,002	100,541	middle
0,750	65,221	0,000	15,519	0,000	19,198	0,000	0,001	100,709	middle
0,766	65,058	0,009	15,553	0,000	19,325	0,002	0,022	100,779	middle
1,147	64,999	0,000	15,120	0,000	19,090	0,000	0,000	100,366	middle
0,107	65,155	0,000	16,625	0,054	19,134	0,070	0,000	101,156	middle
0,731	65,122	0,040	15,706	0,009	19,131	0,004	0,001	100,744	middle
0,832	65,049	0,000	15,525	0,000	19,095	0,014	0,014	100,555	rim
0,875	65,379	0,000	15,611	0,000	19,208	0,012	0,028	101,113	rim
0,920	64,823	0,000	15,469	0,001	19,171	0,000	0,005	100,394	rim
0,898	64,922	0,000	15,326	0,009	19,311	0,000	0,083	100,584	rim
0,799	65,597	0,011	15,831	0,005	19,156	0,005	0,011	101,428	rim
0,790	65,151	0,000	15,496	0,000	19,092	0,037	0,008	100,651	rim
0,563	64,788	0,033	16,002	0,000	19,321	0,026	0,000	100,742	rim
1,023	64,786	0,000	15,324	0,000	19,071	0,028	0,018	100,276	rim
0,102	65,089	0,000	16,715	0,001	18,977	0,014	0,006	100,916	rim
0,703	64,914	0,000	15,601	0,006	19,089	0,021	0,000	100,351	rim

Table 23. Core, middle and rim measurements of K-felspar in JI 5-5.

JI 5-7 K-feldspar

Na2O	SiO2	MnO	K2O	MgO	Al2O3	FeO	CaO	Total	Comment
0,832	65,140	0,000	15,888	0,015	19,492	0,021	0,000	101,388	core
0,604	64,763	0,014	16,413	0,000	19,350	0,013	0,000	101,157	core
0,375	64,649	0,031	16,530	0,004	19,221	0,000	0,000	100,810	core
0,499	64,471	0,000	16,191	0,000	18,963	0,000	0,683	100,807	core
1,069	64,116	0,007	15,519	0,013	19,488	0,000	0,014	100,226	core
1,410	64,665	0,026	15,063	0,000	19,537	0,008	0,013	100,722	core
1,256	65,578	0,000	15,418	0,005	19,574	0,000	0,031	101,862	core
0,844	65,348	0,009	15,940	0,008	19,511	0,017	0,006	101,683	core
1,099	65,445	0,000	15,569	0,024	19,411	0,024	0,025	101,597	core
0,846	64,755	0,005	16,098	0,000	19,448	0,004	0,000	101,156	middle
0,990	65,230	0,002	15,720	0,014	19,507	0,015	0,026	101,504	middle
0,979	64,969	0,007	15,714	0,002	19,358	0,000	0,000	101,029	middle
0,387	64,531	0,023	16,554	0,001	19,387	0,028	0,016	100,927	middle
1,000	63,537	0,000	15,645	0,000	19,454	0,000	0,000	99,636	middle
1,187	65,158	0,016	15,428	0,000	19,541	0,000	0,028	101,358	middle
1,084	64,962	0,009	15,549	0,000	19,363	0,000	0,025	100,992	middle
0,966	65,097	0,000	15,749	0,000	19,408	0,013	0,000	101,233	middle
0,979	65,998	0,002	15,792	0,003	19,541	0,002	0,000	102,317	middle
1,078	65,180	0,000	15,596	0,016	19,323	0,011	0,000	101,204	middle
0,762	64,605	0,000	16,064	0,000	19,418	0,000	0,000	100,849	rim
0,537	63,076	0,000	16,392	0,000	19,130	0,026	0,002	99,163	rim
0,909	65,781	0,012	15,775	0,000	19,429	0,006	0,001	101,913	rim
1,059	65,775	0,000	15,637	0,000	19,573	0,000	0,027	102,071	rim
1,010	64,221	0,000	15,708	0,000	19,415	0,000	0,000	100,354	rim
1,238	65,392	0,009	15,330	0,000	19,585	0,000	0,014	101,568	rim
0,560	64,237	0,012	16,445	0,006	19,345	0,030	0,000	100,635	rim
0,764	65,348	0,012	16,072	0,000	19,567	0,047	0,000	101,810	rim
0,727	65,378	0,000	16,090	0,000	19,324	0,028	0,000	101,547	rim
0,613	64,694	0,000	16,247	0,000	19,280	0,047	0,000	100,881	rim

Table 24. Core, middle and rim measurements of K-felspar in JI 5-7.

Na2O	SiO2	MnO	K2O	MgO	Al2O3	FeO	CaO	F	TiO2	Cl	Total	Comment
0,405	49,524	0,016	10,648	1,392	30,840	3,361	0,014	0,726	0,482	0,000	97,102	core
0,441	47,279	0,044	10,909	0,732	33,517	2,810	0,000	0,559	0,838	0,004	96,897	core
0,415	47,921	0,039	10,702	1,172	31,267	3,810	0,001	0,667	0,753	0,000	96,466	core
0,488	47,445	0,032	10,812	0,982	32,539	3,626	0,000	0,570	0,738	0,006	96,997	core
0,430	48,324	0,046	10,824	1,168	31,844	3,356	0,000	0,801	0,622	0,000	97,081	core
0,519	47,346	0,055	10,939	0,760	33,819	2,967	0,000	0,364	0,695	0,000	97,311	core
0,344	48,406	0,000	10,893	1,186	31,590	3,517	0,000	0,657	0,622	0,007	96,943	core
0,637	45,594	0,032	10,620	0,511	34,869	2,819	0,063	0,391	0,579	0,050	95,989	core
0,473	48,026	0,042	10,644	1,174	31,344	3,964	0,010	0,828	0,732	0,004	96,891	core
0,467	48,508	0,081	10,796	1,155	32,018	3,558	0,000	0,901	0,856	0,000	97,979	core
0,428	49,838	0,030	10,599	1,368	30,729	3,353	0,000	0,894	0,561	0,000	97,450	middle
0,509	47,191	0,030	10,827	0,764	33,743	2,806	0,004	0,566	0,942	0,011	97,153	middle
0,458	47,910	0,005	10,817	1,175	31,511	3,822	0,000	0,627	0,783	0,000	96,867	middle
0,498	47,477	0,062	10,793	0,971	32,712	3,580	0,004	0,577	0,758	0,009	97,198	middle
0,500	48,608	0,000	10,715	1,096	32,252	3,313	0,000	0,578	0,674	0,000	97,498	middle
0,490	46,958	0,035	10,796	0,802	33,631	3,053	0,000	0,350	0,675	0,008	96,661	middle
0,443	48,536	0,053	10,741	1,156	31,890	3,369	0,000	0,557	0,599	0,000	97,109	middle
0,598	46,440	0,009	10,927	0,540	35,403	2,923	0,000	0,489	0,618	0,000	97,741	middle
0,499	47,776	0,042	10,510	1,162	31,489	3,857	0,000	1,001	0,803	0,002	96,725	middle
0,483	48,406	0,044	10,810	1,014	32,181	3,202	0,000	0,631	0,817	0,001	97,331	middle
0,383	49,376	0,016	10,753	1,246	31,371	3,217	0,000	0,571	0,674	0,007	97,372	rim
0,469	48,155	0,009	10,836	1,129	31,761	3,593	0,005	0,613	0,784	0,001	97,119	rim
0,508	47,004	0,000	10,765	0,790	33,467	3,308	0,000	0,554	0,765	0,004	96,931	rim
0,552	47,460	0,035	10,972	0,646	35,159	2,830	0,000	0,286	0,620	0,000	98,465	rim
0,403	48,561	0,044	10,756	1,191	31,886	3,394	0,000	0,641	0,641	0,002	97,249	rim
0,450	47,068	0,000	10,974	0,739	34,168	3,031	0,003	0,451	0,858	0,011	97,573	rim

Table 25. Core, middle and rim measurements of muscovite in JI 2-2.

Na2O	SiO2	MnO	K2O	MgO	Al2O3	FeO	CaO	F	TiO2	Cl	Total	Comment
0,062	36,111	0,277	9,643	8,515	15,844	22,053	0,000	0,027	3,091	0,115	95,701	core
0,075	35,723	0,300	9,600	8,330	15,992	20,881	0,055	0,007	3,152	0,125	94,211	core
0,083	36,133	0,285	9,609	8,707	15,889	20,804	0,000	0,140	3,239	0,130	94,931	core
0,107	36,176	0,291	9,756	8,944	16,012	21,309	0,074	0,080	2,871	0,118	95,677	core
0,077	35,855	0,299	9,529	8,255	15,967	21,026	0,021	0,031	2,772	0,158	93,971	core
0,109	36,082	0,265	9,493	8,748	15,791	21,720	0,054	0,000	2,809	0,135	95,179	core
0,074	36,223	0,298	9,508	8,737	15,877	21,240	0,000	0,000	2,907	0,131	94,978	core
0,081	35,927	0,293	9,633	8,458	15,207	21,655	0,031	0,098	3,462	0,119	94,919	core
0,072	36,100	0,345	9,634	8,964	15,737	21,159	0,026	0,060	3,162	0,153	95,365	core
1,014	46,306	0,429	0,809	10,213	8,990	17,185	11,701	0,000	0,744	0,044	97,560	core
0,075	35,837	0,326	9,650	8,489	15,924	21,634	0,035	0,099	3,052	0,105	95,160	middle
0,097	35,690	0,307	9,656	8,416	16,012	21,359	0,012	0,259	3,118	0,140	94,925	middle
0,060	35,959	0,263	9,693	8,867	15,554	20,501	0,011	0,000	3,365	0,124	94,405	middle
0,060	36,308	0,283	9,447	8,850	15,780	21,876	0,076	0,006	2,774	0,121	95,579	middle
0,093	35,827	0,303	9,413	8,380	15,848	20,642	0,039	0,068	2,789	0,150	93,497	middle
0,086	35,964	0,273	9,512	8,618	16,149	21,114	0,035	0,070	2,861	0,136	94,758	middle
0,110	36,004	0,253	9,506	8,804	15,654	20,775	0,064	0,017	2,771	0,131	94,070	middle
0,099	35,743	0,327	9,535	8,305	15,263	21,260	0,085	0,025	3,513	0,134	94,259	middle
0,101	36,111	0,300	9,652	9,095	15,985	20,971	0,021	0,047	3,252	0,118	95,606	middle
0,993	46,643	0,514	0,817	10,421	8,374	17,040	11,506	0,032	0,666	0,046	97,108	middle
0,073	35,840	0,266	9,612	8,771	16,649	20,482	0,014	0,095	2,312	0,120	94,167	rim
0,117	35,487	0,363	9,633	8,283	16,152	21,514	0,008	0,000	3,033	0,116	94,680	rim
0,064	20,291	0,211	5,346	5,723	9,181	13,535	0,009	0,066	1,945	0,446	56,705	rim
0,099	36,381	0,294	9,508	8,583	16,022	21,470	0,073	0,065	2,774	0,120	95,367	rim
0,050	29,274	0,225	7,421	7,257	13,307	18,424	0,020	0,061	2,166	0,308	78,447	rim
0,063	35,813	0,245	9,419	8,495	16,091	20,270	0,055	0,150	2,769	0,109	93,409	rim
0,061	30,499	0,180	7,884	7,731	13,585	18,573	0,075	0,009	2,194	0,174	80,939	rim
0,061	35,938	0,313	9,483	8,138	16,007	21,057	0,033	0,005	3,357	0,137	94,521	rim
0,081	35,860	0,276	9,797	8,841	16,764	20,154	0,046	0,050	3,008	0,117	94,947	rim
1,125	45,471	0,393	0,914	10,070	9,391	16,557	11,515	0,000	0,680	0,056	96,284	rim

Table 26. Core, middle and rim measurements of biotite in JI 4-2.

Na2O	SiO2	MnO	K2O	MgO	Al2O3	FeO	CaO	F	TiO2	Cl	Total	Comment
0,050	35,245	0,424	9,524	6,228	15,221	25,966	0,000	0,387	3,163	0,087	96,119	core
0,073	35,208	0,439	9,465	6,157	15,763	26,612	0,000	0,210	2,802	0,088	96,709	core
0,069	34,516	0,416	8,076	6,866	16,627	26,080	0,000	0,381	2,329	0,065	95,250	core
0,090	35,311	0,429	9,153	6,524	15,418	25,658	0,000	0,283	2,640	0,097	95,473	core
0,034	35,717	0,372	9,729	6,314	15,793	26,069	0,000	0,339	2,982	0,066	97,257	core
0,088	35,032	0,407	9,348	6,554	14,874	25,264	0,027	0,616	2,854	0,091	94,876	core
0,080	35,526	0,347	9,481	6,520	15,480	25,478	0,000	0,571	2,509	0,083	95,855	core
0,049	35,108	0,411	9,248	6,229	15,493	26,038	0,002	0,362	2,597	0,082	95,453	core
0,062	35,219	0,349	9,530	6,232	15,856	25,460	0,000	0,461	3,020	0,089	96,072	core
0,061	35,130	0,429	9,437	6,226	15,473	25,379	0,000	0,334	2,880	0,094	95,281	middle
0,078	35,186	0,362	9,451	6,223	15,672	26,747	0,000	0,392	2,685	0,072	96,687	middle
0,087	35,466	0,417	9,473	6,665	15,900	24,663	0,000	0,207	2,557	0,081	95,411	middle
0,043	29,887	0,598	2,916	7,838	17,461	30,770	0,159	0,169	1,599	0,061	91,438	middle
0,088	35,649	0,457	9,541	6,338	15,458	26,755	0,000	0,315	2,393	0,100	96,938	middle
0,104	34,581	0,377	8,208	6,783	15,588	25,974	0,026	0,395	2,456	0,084	94,391	middle
0,067	35,312	0,417	9,567	6,367	15,671	26,107	0,000	0,405	2,843	0,089	96,678	middle
0,097	35,172	0,399	9,285	6,606	14,686	25,680	0,000	0,280	2,692	0,095	94,860	middle
0,059	35,388	0,411	9,324	6,798	15,413	25,011	0,000	0,576	2,318	0,085	95,121	middle
0,089	35,423	0,392	9,376	6,351	15,390	25,962	0,000	0,230	2,772	0,075	95,946	middle
0,048	35,289	0,424	9,389	6,201	15,701	25,282	0,000	0,203	2,855	0,088	95,375	middle
0,068	33,891	0,436	8,010	6,549	15,818	27,067	0,001	0,243	2,500	0,074	94,538	rim
0,034	33,641	0,379	7,684	5,997	16,963	25,468	0,031	0,188	3,161	0,075	93,525	rim
0,063	35,306	0,445	9,291	6,243	15,766	26,905	0,000	0,271	2,039	0,096	96,289	rim
0,056	35,053	0,452	9,305	6,252	16,014	26,740	0,000	0,235	2,349	0,104	96,438	rim
0,045	35,366	0,425	9,592	6,153	16,012	25,946	0,000	0,267	2,852	0,076	96,605	rim
0,090	34,411	0,405	9,271	6,676	15,033	25,957	0,007	0,507	2,629	0,131	94,874	rim
0,043	34,219	0,345	9,357	6,761	15,837	23,632	0,000	0,426	2,208	0,096	92,734	rim
0,067	35,279	0,480	9,430	6,318	15,408	26,919	0,018	0,308	2,729	0,079	96,887	rim
0,050	34,917	0,417	9,340	6,296	15,383	25,481	0,000	0,281	2,874	0,087	94,988	rim

Table 27. Core, middle and rim measurements of biotite in JI 5-2.

Na2O	SiO2	MnO	K2O	MgO	Al2O3	FeO	CaO	F	TiO2	Cl	Total	Comment
0,256	35,007	0,092	9,361	7,981	18,482	19,785	0,001	0,072	3,642	0,094	94,757	core
0,253	34,589	0,054	9,281	7,929	18,438	19,918	0,035	0,322	3,727	0,105	94,537	core
0,190	35,277	0,059	9,691	8,125	18,773	20,983	0,000	0,244	3,049	0,114	96,434	core
0,216	34,769	0,052	9,341	7,860	18,228	19,928	0,040	0,109	3,576	0,114	94,240	core
0,195	33,916	0,168	9,228	7,440	18,177	21,668	0,151	0,278	2,677	0,085	93,918	core
0,293	35,032	0,024	9,201	8,305	18,230	20,640	0,056	0,158	3,215	0,107	95,269	core
0,204	34,713	0,049	9,390	8,039	18,294	20,130	0,143	0,119	3,470	0,115	94,635	core
0,207	34,907	0,032	9,461	7,806	18,803	20,102	0,007	0,309	3,699	0,135	95,465	core
0,209	34,783	0,039	9,428	8,130	18,059	20,378	0,000	0,223	3,599	0,111	94,933	core
0,262	35,206	0,039	9,340	8,315	18,959	19,481	0,000	0,275	3,252	0,097	95,156	core
0,276	34,836	0,076	9,252	7,754	18,087	19,791	0,031	0,211	3,916	0,107	94,264	middle
0,234	34,418	0,077	9,327	7,933	18,793	19,877	0,042	0,330	3,773	0,098	94,801	middle
0,198	34,556	0,079	9,473	8,093	18,712	20,937	0,123	0,167	2,875	0,121	95,311	middle
0,227	34,606	0,076	9,299	7,929	18,521	20,344	0,034	0,171	3,540	0,112	94,856	middle
0,174	34,165	0,186	9,370	7,326	17,812	21,903	0,012	0,249	2,706	0,099	93,935	middle
0,235	35,024	0,047	9,361	8,508	18,154	20,529	0,025	0,291	3,048	0,100	95,247	middle
0,181	35,092	0,067	9,345	8,118	18,267	19,767	0,060	0,246	3,225	0,090	94,402	middle
0,199	34,947	0,067	9,382	7,911	18,683	19,972	0,000	0,218	3,587	0,118	95,068	middle
0,233	34,658	0,020	9,291	8,048	18,118	20,234	0,029	0,200	3,548	0,101	94,467	middle
0,262	34,685	0,018	9,303	8,552	18,878	19,102	0,000	0,218	2,955	0,119	94,045	middle
0,299	33,695	0,072	9,186	7,984	17,129	19,876	0,000	0,167	3,847	0,133	92,325	rim
0,280	34,767	0,060	9,297	8,041	18,439	20,003	0,046	0,298	3,780	0,092	95,007	rim
0,130	34,438	0,099	9,532	7,990	18,196	21,168	0,020	0,317	3,147	0,118	95,070	rim
0,218	33,646	0,096	9,327	8,109	18,299	20,041	0,007	0,105	3,523	0,113	93,510	rim
0,203	34,778	0,052	9,103	8,613	18,781	20,383	0,015	0,249	2,616	0,113	94,843	rim
0,191	34,579	0,064	9,470	8,388	18,773	19,786	0,071	0,184	2,779	0,094	94,347	rim
0,251	35,050	0,075	9,294	7,864	18,620	19,917	0,112	0,144	3,533	0,134	94,997	rim
0,211	34,715	0,096	9,323	8,050	18,778	19,804	0,038	0,204	3,146	0,127	94,452	rim
0,231	33,374	0,054	9,119	8,726	18,292	18,814	0,000	0,217	3,186	0,095	92,069	rim

Table 28. Core, middle and rim measurements of biotite in JI 5-1.

Na2O	SiO2	MnO	K2O	MgO	Al2O3	FeO	CaO	F	TiO2	Cl	Total	Comment
0,150	35,275	0,130	9,678	8,775	19,134	18,333	0,037	0,076	3,108	0,053	94,835	core
0,137	35,296	0,174	9,699	8,645	19,198	18,645	0,000	0,057	3,239	0,048	95,229	core
0,095	35,220	0,177	9,725	9,748	18,737	17,257	0,000	0,000	2,758	0,049	93,916	core
0,096	34,790	0,174	9,598	9,042	18,793	17,550	0,090	0,014	2,807	0,071	93,155	core
0,120	35,252	0,149	9,612	8,691	18,443	18,053	0,009	0,012	3,422	0,116	93,982	core
0,126	35,029	0,147	9,596	9,058	18,628	17,886	0,020	0,000	3,222	0,122	93,941	core
0,125	35,054	0,206	9,495	8,911	18,192	18,299	0,000	0,033	3,228	0,050	93,711	core
0,128	34,869	0,192	9,692	8,447	19,055	18,114	0,015	0,096	3,036	0,155	93,870	core
0,086	34,907	0,130	9,675	8,643	18,794	18,236	0,000	0,096	2,800	0,134	93,569	core
0,138	35,191	0,194	9,557	8,871	18,998	18,289	0,005	0,032	3,114	0,054	94,552	middle
0,160	35,416	0,189	9,538	8,613	18,802	18,445	0,008	0,092	3,290	0,103	94,743	middle
0,089	35,160	0,196	9,645	9,675	18,988	17,504	0,000	0,174	2,604	0,030	94,140	middle
0,127	33,794	0,145	9,214	8,609	17,959	18,039	0,000	0,118	3,135	0,028	91,243	rim
0,076	35,262	0,152	9,796	9,767	19,062	17,548	0,000	0,000	2,590	0,044	94,428	rim
0,139	34,979	0,149	9,760	8,942	18,226	17,958	0,016	0,024	3,377	0,110	93,779	rim
0,169	31,728	0,120	8,576	7,842	16,631	16,038	0,083	0,071	2,952	0,117	84,411	rim
0,135	35,124	0,197	9,611	8,725	18,418	18,291	0,000	0,175	3,176	0,027	93,933	rim
0,115	34,731	0,163	9,630	8,643	18,775	18,237	0,037	0,000	2,791	0,159	93,377	rim

Table 29. Core, middle and rim measurements of biotite in JI 5-2.

Na2O	SiO2	MnO	K2O	MgO	Al2O3	FeO	CaO	F	TiO2	Cl	Total	Comment
0,062	33,650	0,377	9,645	3,146	18,949	27,370	0,000	0,260	2,914	0,189	96,416	core
0,039	33,431	0,377	9,562	3,197	19,049	27,100	0,000	0,322	2,756	0,250	95,891	core
0,052	33,366	0,334	9,628	3,083	18,341	27,494	0,015	0,288	2,893	0,220	95,543	core
0,029	33,759	0,334	9,526	3,161	18,563	27,160	0,000	0,341	2,903	0,235	95,814	core
0,056	33,534	0,375	9,713	3,065	18,632	27,456	0,000	0,069	2,817	0,219	95,871	core
0,041	33,715	0,300	9,403	3,182	18,122	27,461	0,000	0,230	2,942	0,253	95,511	core
0,082	33,613	0,326	9,469	3,072	18,789	26,914	0,000	0,256	2,871	0,218	95,461	core
0,051	33,678	0,301	9,571	3,074	18,442	26,529	0,000	0,233	2,865	0,208	94,809	core
0,055	33,821	0,297	9,572	3,106	18,427	27,114	0,000	0,220	2,990	0,183	95,651	core
0,053	33,693	0,365	9,564	3,158	18,692	27,004	0,010	0,196	2,981	0,226	95,814	core
0,089	33,662	0,347	9,612	3,157	18,393	26,875	0,000	0,295	2,898	0,195	95,355	core
0,084	33,581	0,334	9,671	3,185	19,081	27,763	0,002	0,423	2,896	0,166	96,971	middle
0,023	33,300	0,350	9,353	3,062	18,540	26,607	0,018	0,342	2,698	0,228	94,326	middle
0,055	33,843	0,351	9,519	3,123	18,412	27,097	0,004	0,311	2,934	0,224	95,691	middle
0,059	33,544	0,349	9,672	3,152	18,668	27,245	0,000	0,275	2,898	0,205	95,905	middle
0,066	33,545	0,399	9,533	3,155	18,751	27,309	0,000	0,353	2,629	0,206	95,751	middle
0,071	33,112	0,320	9,294	3,217	18,095	27,335	0,003	0,266	2,991	0,221	94,763	middle
0,060	33,259	0,334	9,483	3,065	18,487	26,756	0,000	0,346	2,783	0,213	94,592	middle
0,056	32,912	0,330	9,189	3,243	18,038	27,315	0,017	0,414	2,892	0,201	94,388	middle
0,058	33,324	0,398	9,594	3,074	18,193	27,105	0,000	0,325	3,057	0,195	95,142	middle
0,076	33,702	0,328	9,436	3,071	18,627	27,263	0,050	0,301	2,932	0,226	95,836	middle
0,046	33,482	0,373	9,524	3,153	18,323	27,546	0,000	0,364	2,911	0,208	95,730	middle
0,079	33,486	0,362	9,562	3,042	18,316	26,636	0,000	0,269	2,960	0,193	94,748	middle
0,063	33,413	0,314	9,598	3,207	18,535	27,627	0,017	0,137	2,993	0,164	95,973	rim
0,077	32,554	0,356	8,789	3,197	18,351	26,603	0,068	0,262	2,648	0,237	92,979	rim
0,089	31,708	0,291	8,937	2,989	17,537	25,777	0,016	0,161	2,706	0,211	90,306	rim
0,056	31,563	0,339	8,639	2,973	17,466	26,126	0,000	0,394	2,657	0,203	90,212	rim
0,087	33,362	0,391	9,599	3,178	18,689	27,042	0,016	0,224	2,638	0,233	95,312	rim
0,062	31,681	0,345	7,654	3,507	18,173	28,355	0,017	0,000	2,901	0,207	92,860	rim
0,041	33,062	0,355	9,388	3,075	18,330	25,885	0,005	0,175	2,786	0,223	93,201	rim
0,073	33,847	0,327	9,396	3,185	18,750	27,306	0,049	0,347	2,901	0,197	96,201	rim
0,059	33,048	0,345	9,535	3,145	18,236	26,973	0,026	0,186	2,952	0,204	94,585	rim

Table 30. Core, middle and rim measurements of biotite in JI 5-7.

Na2O	SiO2	MnO	K2O	MgO	Al2O3	FeO	CaO	F	NiO	TiO2	Total	Comment
1,113	43,500	0,469	0,881	8,260	14,040	17,350	11,840	0,061	0,035	0,748	98,366	core
0,959	45,580	0,387	0,682	9,610	12,060	16,750	12,040	0,000	0,017	0,482	98,597	core
0,965	45,340	0,360	0,641	9,550	12,600	16,520	12,120	0,098	0,013	0,384	98,641	core
0,924	46,290	0,347	0,570	10,470	11,230	15,410	12,200	0,000	0,022	0,605	98,092	core
1,011	44,630	0,337	0,686	9,130	13,110	16,170	11,870	0,096	0,028	0,509	97,676	core
0,929	45,610	0,432	0,655	10,030	11,880	15,780	12,080	0,000	0,026	0,454	98,082	core
1,019	44,400	0,395	0,675	9,380	12,450	16,430	11,830	0,256	0,000	0,808	97,689	core
1,012	44,740	0,301	0,707	9,360	12,390	16,150	11,970	0,000	0,058	0,814	97,563	core
0,616	48,280	0,363	0,381	11,540	8,840	14,850	11,840	0,000	0,044	0,212	97,014	core
0,841	46,350	0,340	0,690	10,010	11,090	15,680	11,940	0,141	0,042	0,647	97,795	core
0,825	46,460	0,311	0,615	10,550	10,510	15,590	11,950	0,000	0,038	0,692	97,579	core
0,910	45,380	0,371	0,630	9,630	11,110	15,450	11,750	0,000	0,000	0,426	95,745	core
0,962	45,520	0,380	0,665	9,600	11,730	16,840	11,930	0,044	0,000	0,569	98,286	middle
0,963	45,960	0,306	0,588	9,860	11,580	16,010	11,950	0,194	0,091	0,748	98,291	middle
0,864	46,370	0,416	0,500	10,750	10,670	15,740	12,000	0,133	0,029	0,461	98,010	middle
0,940	45,730	0,364	0,733	9,540	11,980	16,300	12,010	0,057	0,032	0,657	98,424	middle
0,979	44,840	0,367	0,657	9,300	12,670	15,580	11,840	0,000	0,020	0,763	97,060	middle
0,993	45,770	0,389	0,579	9,870	11,830	16,470	12,030	0,055	0,000	0,509	98,562	middle
0,759	47,940	0,371	0,595	11,020	9,610	15,520	12,040	0,000	0,042	0,560	98,482	middle
0,881	46,340	0,304	0,574	10,040	11,360	15,560	12,100	0,000	0,036	0,580	97,774	middle
0,733	47,950	0,352	0,467	11,130	9,310	15,380	11,960	0,000	0,000	0,332	97,614	middle
0,831	46,500	0,317	0,561	10,020	10,910	16,170	11,890	0,000	0,019	0,359	97,623	rim
0,983	45,560	0,393	0,743	9,660	11,430	16,800	11,850	0,019	0,054	0,594	98,143	rim
0,683	42,820	0,331	1,128	9,630	12,940	16,200	11,140	0,103	0,012	0,501	95,531	rim
0,788	46,660	0,385	0,501	10,310	10,270	15,110	11,960	0,106	0,000	0,549	96,703	rim
0,954	45,200	0,317	0,649	9,770	12,060	15,680	12,110	0,133	0,050	0,872	97,831	rim
1,128	44,190	0,319	0,641	9,620	12,710	15,950	11,920	0,085	0,000	0,608	97,262	rim
0,952	45,160	0,299	0,673	9,620	12,200	15,620	11,830	0,000	0,000	0,831	97,264	rim
0,850	46,070	0,380	0,696	10,200	10,540	16,290	11,970	0,000	0,000	0,732	97,735	rim
0,938	46,490	0,360	0,535	10,170	10,940	16,080	12,010	0,007	0,020	0,603	98,217	rim
0,737	47,470	0,383	0,501	10,580	9,690	15,530	12,030	0,125	0,000	0,818	97,922	rim
0,812	47,180	0,322	0,569	10,530	10,760	15,480	12,090	0,048	0,000	0,389	98,190	rim

Table 31. Core, middle and rim measurements of hornblende in JI 1-4.

Na2O	SiO2	MnO	K2O	MgO	Al2O3	FeO	CaO	F	NiO	TiO2	Total	Comment
1,182	41,130	0,494	1,120	6,630	15,880	19,290	11,610	0,040	0,000	0,472	97,911	core
1,196	39,510	0,604	0,630	6,740	13,180	18,220	14,180	0,068	0,000	0,578	94,998	core
1,270	40,580	0,510	1,045	6,430	16,550	18,820	11,560	0,000	0,013	0,803	97,632	core
1,165	41,440	0,483	0,561	6,120	16,890	19,350	11,540	0,000	0,030	0,296	97,920	core
1,070	43,500	0,551	0,933	7,560	13,260	19,250	11,550	0,036	0,008	0,687	98,479	core
1,012	43,040	0,427	1,230	7,800	12,690	19,550	11,740	0,000	0,029	0,589	98,295	core
1,233	41,640	0,515	0,826	6,740	15,270	18,900	11,760	0,000	0,009	0,526	97,479	core
1,179	40,740	0,481	1,440	6,610	17,020	18,900	10,060	0,000	0,010	0,383	96,950	core
1,324	40,750	0,562	0,845	6,120	17,290	19,060	11,420	0,024	0,028	0,449	97,921	core
1,153	41,210	0,487	1,137	6,330	16,400	19,500	11,510	0,000	0,053	0,395	98,230	core
1,184	41,570	0,510	1,186	7,460	15,170	19,030	11,700	0,000	0,039	0,596	98,484	core
1,216	41,360	0,538	0,903	6,850	15,300	19,440	11,650	0,074	0,009	0,599	97,985	middle
1,215	41,400	0,518	1,059	6,320	16,030	19,710	11,590	0,000	0,018	0,623	98,617	middle
1,158	43,100	0,470	0,614	7,460	13,570	17,760	11,380	0,044	0,000	0,380	95,961	middle
1,034	40,730	0,456	1,560	6,400	15,140	20,240	11,730	0,000	0,000	0,759	98,108	middle
0,978	42,500	0,554	1,360	7,480	13,160	20,200	11,790	0,029	0,000	0,894	98,996	middle
1,115	43,540	0,533	0,714	7,370	14,090	18,330	11,760	0,026	0,080	0,429	98,173	middle
1,283	42,170	0,477	0,746	6,810	15,640	19,230	11,510	0,073	0,000	0,567	98,573	middle
1,242	41,650	0,444	0,613	5,920	17,060	18,740	11,540	0,000	0,021	0,271	97,624	middle
1,329	41,820	0,459	0,698	6,750	16,480	18,950	11,570	0,000	0,043	0,394	98,506	middle
1,190	40,940	0,498	1,121	6,150	16,430	19,570	11,790	0,051	0,035	0,556	98,429	middle
1,156	41,640	0,472	1,240	7,510	15,120	19,020	11,760	0,055	0,020	0,625	98,645	middle
1,169	42,870	0,428	1,063	7,650	13,670	18,870	11,660	0,168	0,015	0,703	98,316	middle
1,279	40,100	0,454	0,646	6,410	16,930	19,210	11,020	0,000	0,000	0,308	96,357	rim
1,327	41,670	0,473	0,844	6,930	16,330	18,260	11,630	0,000	0,039	0,483	98,020	rim
1,273	40,880	0,421	0,961	6,660	16,720	18,810	11,800	0,000	0,000	0,558	98,113	rim
1,206	41,020	0,572	0,678	5,390	17,780	19,520	11,510	0,000	0,019	0,340	98,134	rim
0,994	43,710	0,482	1,010	7,830	12,730	18,940	11,520	0,000	0,011	0,714	97,959	rim
1,049	43,020	0,482	0,929	7,950	12,900	18,740	11,640	0,015	0,008	0,518	97,475	rim
1,240	41,630	0,434	1,055	6,740	15,860	19,560	11,620	0,000	0,018	0,606	98,823	rim
1,249	41,330	0,468	0,919	6,260	16,900	19,450	11,520	0,237	0,000	0,444	98,794	rim
1,236	41,920	0,447	0,885	6,790	15,060	19,190	11,870	0,000	0,000	0,606	98,150	rim
1,149	42,610	0,527	0,962	7,470	13,720	18,530	11,690	0,000	0,000	0,757	97,559	rim

Table 32. Core, middle and rim measurements of hornblende in JI 1-4.

Na2O	SiO2	MnO	K2O	MgO	Al2O3	FeO	CaO	F	NiO	TiO2	Total	Comment
1,167	42,780	0,289	1,390	9,680	13,420	16,050	11,750	0,088	0,070	0,933	97,640	core
1,071	42,250	0,262	1,300	9,070	13,110	17,000	11,800	0,037	0,000	0,944	97,104	core
1,172	43,350	0,249	1,270	10,320	13,140	14,860	11,850	0,035	0,022	0,883	97,183	core
1,155	43,270	0,278	1,430	9,530	13,660	16,120	11,600	0,083	0,048	0,995	98,201	core
0,968	43,310	0,336	1,270	9,040	12,560	16,960	11,870	0,210	0,000	0,947	97,519	core
1,095	42,160	0,238	1,310	8,660	14,350	16,860	11,930	0,000	0,000	1,099	97,819	core
1,142	43,330	0,336	1,270	9,590	13,360	15,810	11,800	0,000	0,018	0,896	97,563	core
1,086	43,460	0,345	1,220	9,400	12,380	16,870	11,870	0,147	0,000	1,013	97,812	core
1,063	43,490	0,269	1,290	10,130	13,290	15,310	11,960	0,189	0,000	0,858	97,921	core
1,084	43,930	0,218	1,168	10,040	12,540	15,360	11,860	0,026	0,000	0,868	97,106	core
1,140	42,450	0,287	1,430	9,590	14,220	15,460	11,800	0,246	0,000	1,079	97,739	core
1,169	43,120	0,303	1,370	9,960	13,680	15,570	11,750	0,209	0,028	1,069	98,310	core
1,110	43,080	0,294	1,320	9,280	13,590	16,000	12,020	0,093	0,016	0,943	97,825	core
1,039	43,390	0,290	1,260	9,590	13,450	16,030	11,900	0,000	0,026	1,006	98,032	core
1,149	43,750	0,330	1,210	9,980	13,090	15,620	11,840	0,178	0,010	0,922	98,129	core
1,070	42,530	0,298	1,380	8,760	14,090	16,620	11,810	0,195	0,000	1,098	97,937	middle
1,141	43,030	0,339	1,290	9,660	13,890	15,650	11,770	0,122	0,032	0,914	97,903	middle
1,099	43,670	0,294	1,061	9,930	13,010	16,120	11,810	0,000	0,032	0,820	97,883	middle
1,092	42,790	0,347	1,230	9,180	12,920	16,980	11,880	0,009	0,000	1,012	97,476	middle
1,049	42,770	0,330	1,310	9,530	12,990	15,790	11,910	0,011	0,010	1,067	96,808	middle
1,073	43,310	0,283	1,280	9,530	12,820	16,000	11,750	0,076	0,000	0,946	97,118	middle
1,198	41,980	0,271	1,540	9,200	14,420	16,010	11,900	0,291	0,015	1,113	97,979	middle
1,093	43,370	0,314	1,280	9,720	12,860	16,240	11,970	0,037	0,019	1,070	98,055	middle
1,140	43,780	0,265	1,185	9,480	13,010	17,090	11,890	0,152	0,000	0,890	98,934	middle

Table 33. Core and middle measurements of hornblende in JI 4-3.

Na2O	SiO2	MnO	K2O	MgO	Al2O3	FeO	CaO	F	NiO	TiO2	Total	Comment
1,119	42,200	0,316	1,270	9,330	12,650	16,250	11,970	0,161	0,000	1,045	96,349	rim
1,117	41,800	0,300	1,330	9,180	13,360	16,270	11,890	0,081	0,000	0,994	96,335	rim
1,051	42,610	0,262	1,310	9,000	13,180	16,610	11,970	0,168	0,015	0,916	97,274	rim
1,106	42,740	0,289	1,280	9,220	12,960	16,970	11,900	0,108	0,046	0,981	97,692	rim
1,079	44,030	0,348	1,137	10,050	12,450	15,760	11,810	0,105	0,000	0,919	97,716	rim
0,980	43,650	0,247	1,190	9,280	12,600	16,860	12,050	0,162	0,000	1,304	98,399	rim
1,082	43,150	0,319	1,175	9,790	12,980	16,160	11,940	0,087	0,012	0,880	97,621	rim
1,063	43,100	0,323	1,230	9,700	12,700	16,070	12,030	0,079	0,023	0,903	97,297	rim
1,118	43,190	0,321	1,280	9,580	12,990	15,980	12,000	0,000	0,000	0,948	97,437	rim
1,118	42,960	0,328	1,510	10,140	14,020	14,250	11,940	0,261	0,012	1,064	97,604	rim
1,072	44,170	0,247	1,141	9,920	12,370	16,290	11,780	0,094	0,000	0,922	98,050	rim
1,142	43,240	0,310	1,370	9,730	13,860	15,730	11,790	0,177	0,010	1,003	98,384	rim
1,022	43,460	0,283	1,300	9,050	12,940	17,430	12,050	0,105	0,018	1,114	98,772	rim

Table 34. Rim measurements of hornblende in JI 4-3.

Na2O	SiO2	MnO	K2O	MgO	Al2O3	FeO	CaO	F	TiO2	Cl	Total	Comment
1,830	40,835	0,180	0,541	12,933	14,161	11,464	11,767	0,109	2,187	0,020	95,996	core
1,256	42,331	0,324	0,908	11,751	13,260	13,531	10,871	0,012	2,125	0,104	96,491	core
1,570	41,530	0,278	0,935	12,128	14,371	11,987	11,500	0,061	2,186	0,067	96,599	core
2,107	42,172	0,244	0,523	13,826	13,419	10,747	11,534	0,000	2,097	0,008	96,694	core
1,716	42,487	0,285	0,562	13,081	13,149	11,722	11,605	0,108	2,070	0,016	96,771	core
1,398	42,574	0,380	0,535	11,279	13,307	13,813	11,615	0,128	1,969	0,077	97,004	core
1,764	41,247	0,238	0,548	13,414	13,206	11,337	11,756	0,146	2,245	0,012	95,855	core
1,390	42,130	0,319	0,664	11,470	13,459	13,336	11,500	0,040	2,164	0,129	96,613	core
1,985	42,099	0,199	0,558	13,907	13,659	10,458	11,648	0,231	2,134	0,006	96,806	core
1,126	42,469	0,371	1,095	9,265	13,641	16,016	10,710	0,000	1,563	0,259	96,488	core
2,058	41,575	0,221	0,561	13,612	13,949	10,617	11,833	0,111	2,224	0,020	96,775	middle
1,278	41,396	0,273	0,901	11,096	13,909	13,579	11,313	0,027	2,211	0,125	96,149	middle
1,667	41,842	0,259	0,571	13,001	14,196	10,783	11,866	0,094	2,236	0,031	96,552	middle
1,964	41,929	0,191	0,509	13,705	12,734	11,049	11,452	0,198	2,058	0,013	95,755	middle
1,199	41,590	0,366	0,923	10,257	13,767	14,722	11,037	0,158	1,878	0,180	95,971	middle
1,382	41,688	0,304	0,625	9,721	14,268	14,847	11,483	0,000	2,136	0,148	96,569	middle
1,994	41,726	0,165	0,616	13,984	14,097	10,511	11,630	0,137	2,215	0,016	97,067	middle
1,199	40,900	0,354	0,707	9,998	13,750	15,962	10,665	0,079	1,765	0,192	95,503	middle
1,612	41,791	0,345	0,595	11,668	14,242	12,806	11,709	0,210	2,230	0,072	97,187	middle
1,679	41,814	0,252	0,546	12,916	13,656	10,964	11,759	0,102	2,355	0,024	96,027	middle
1,127	42,431	0,480	1,071	9,374	13,194	16,284	10,535	0,105	2,174	0,177	96,868	middle
1,351	41,233	0,402	0,612	8,877	14,256	16,013	11,454	0,000	1,987	0,294	96,413	rim
1,192	40,741	0,386	0,727	9,079	13,483	15,791	11,207	0,141	1,853	0,273	94,787	rim
1,454	41,817	0,257	0,596	12,256	13,266	12,002	11,645	0,000	2,134	0,089	95,542	rim
1,697	43,089	0,237	0,512	13,920	12,402	10,463	11,941	0,148	1,890	0,045	96,296	rim
1,239	41,741	0,437	0,597	8,889	13,359	15,771	11,526	0,000	1,617	0,219	95,346	rim
1,239	40,825	0,339	0,721	9,440	13,303	15,663	11,698	0,021	1,821	0,245	95,267	rim
1,531	42,155	0,348	0,531	10,428	14,028	14,347	11,815	0,133	1,943	0,046	97,243	rim
1,187	41,551	0,379	0,540	9,139	12,727	16,512	10,799	0,000	1,662	0,209	94,658	rim
1,298	42,029	0,318	0,573	9,171	13,891	16,057	11,042	0,000	1,789	0,160	96,292	rim
1,334	42,158	0,373	0,556	9,418	14,196	15,537	11,392	0,000	2,116	0,085	97,190	rim

Table 35. Core, middle and rim measurements of hornblende in JI 5-3.

Appendix IV: EMP data thin sections

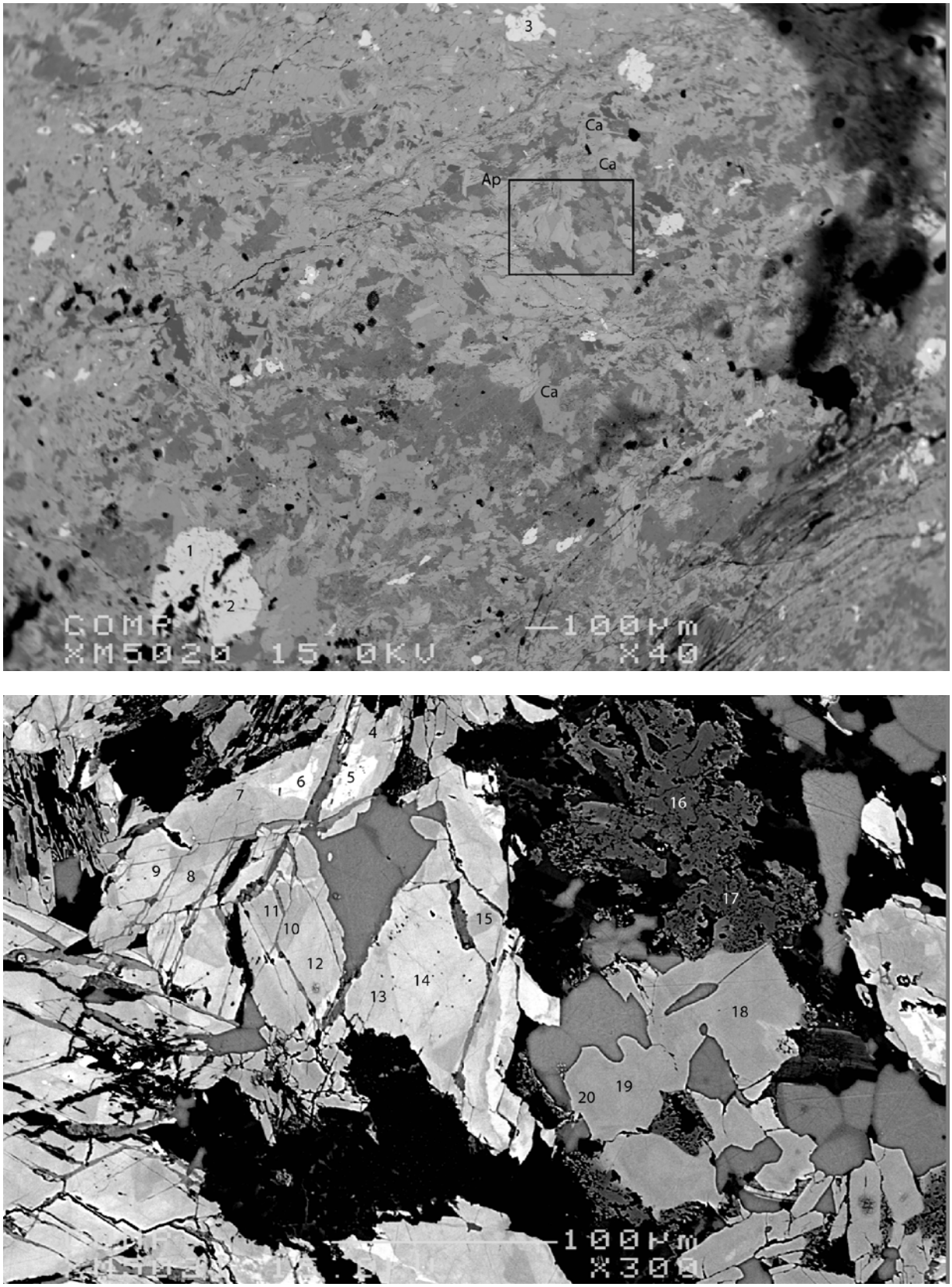

Figure 79. BSE of thin section JI 1-1, measuring location 1 (top) and zoom-in of the square (bottom).

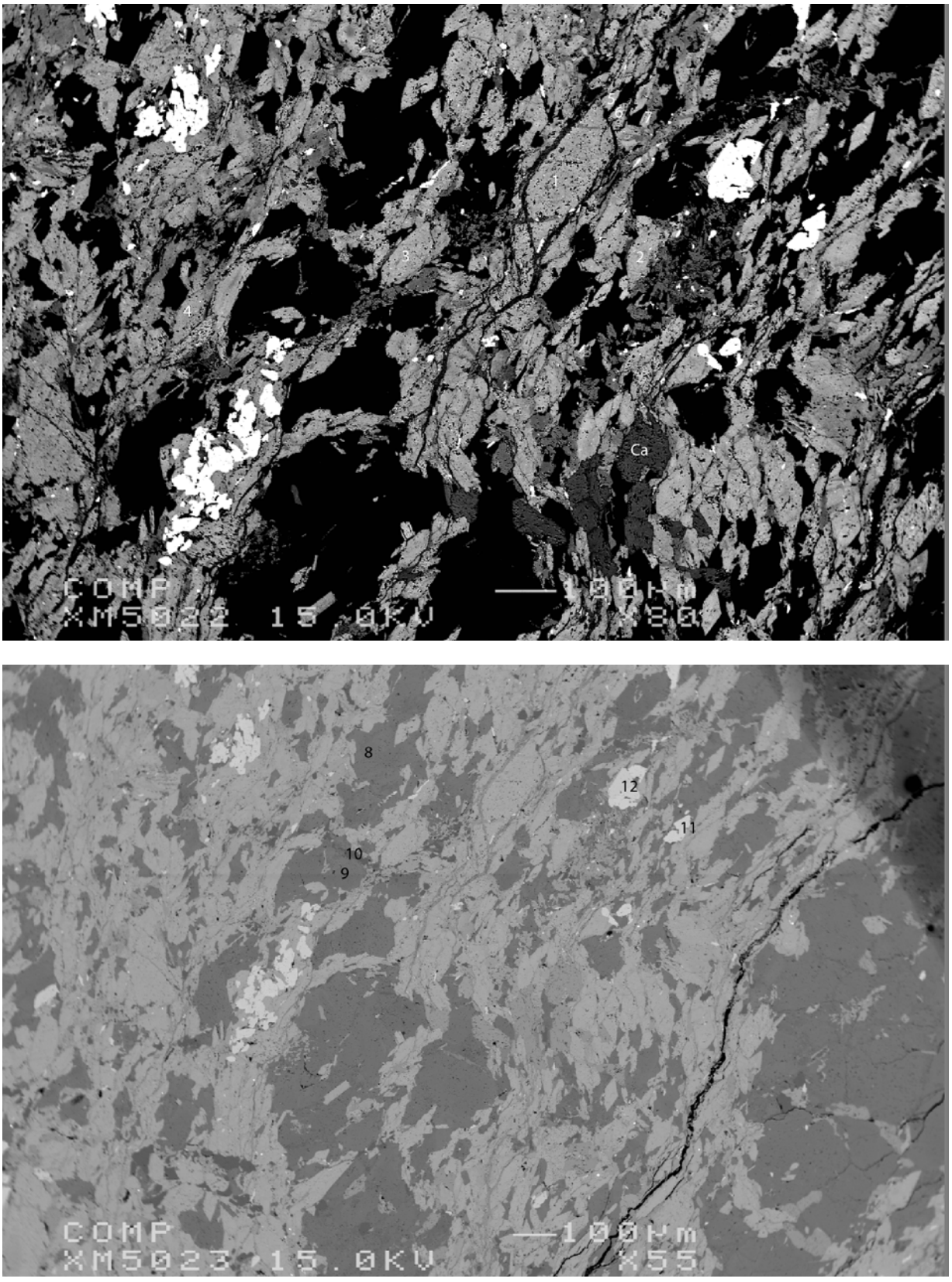

Figure 80. BSE of thin section JI 1-1, measuring location 3.

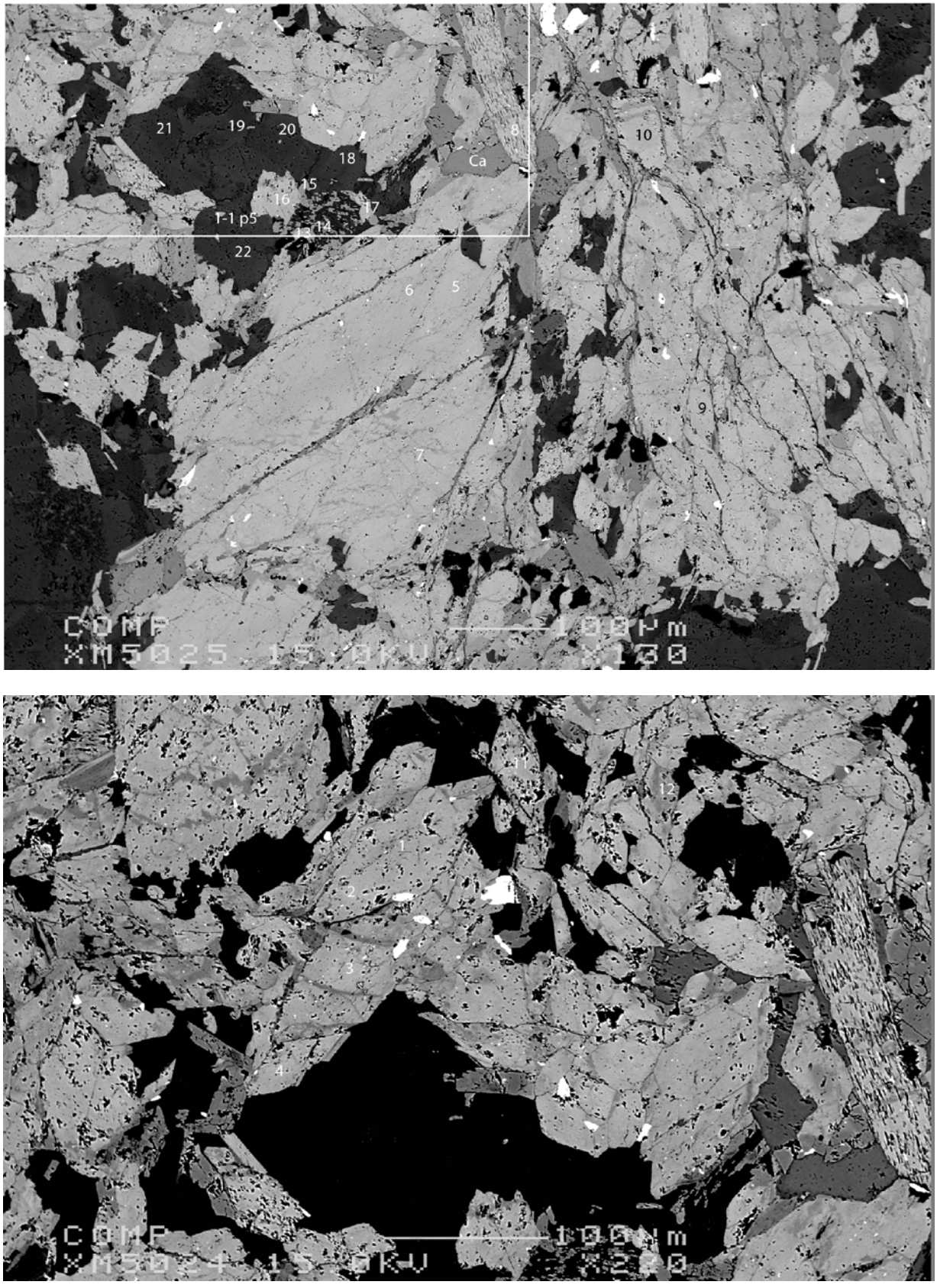

Figure 81. BSE of thin section JI 1-1, measuring location 4 (top) and zoom-in of the square (bottom).

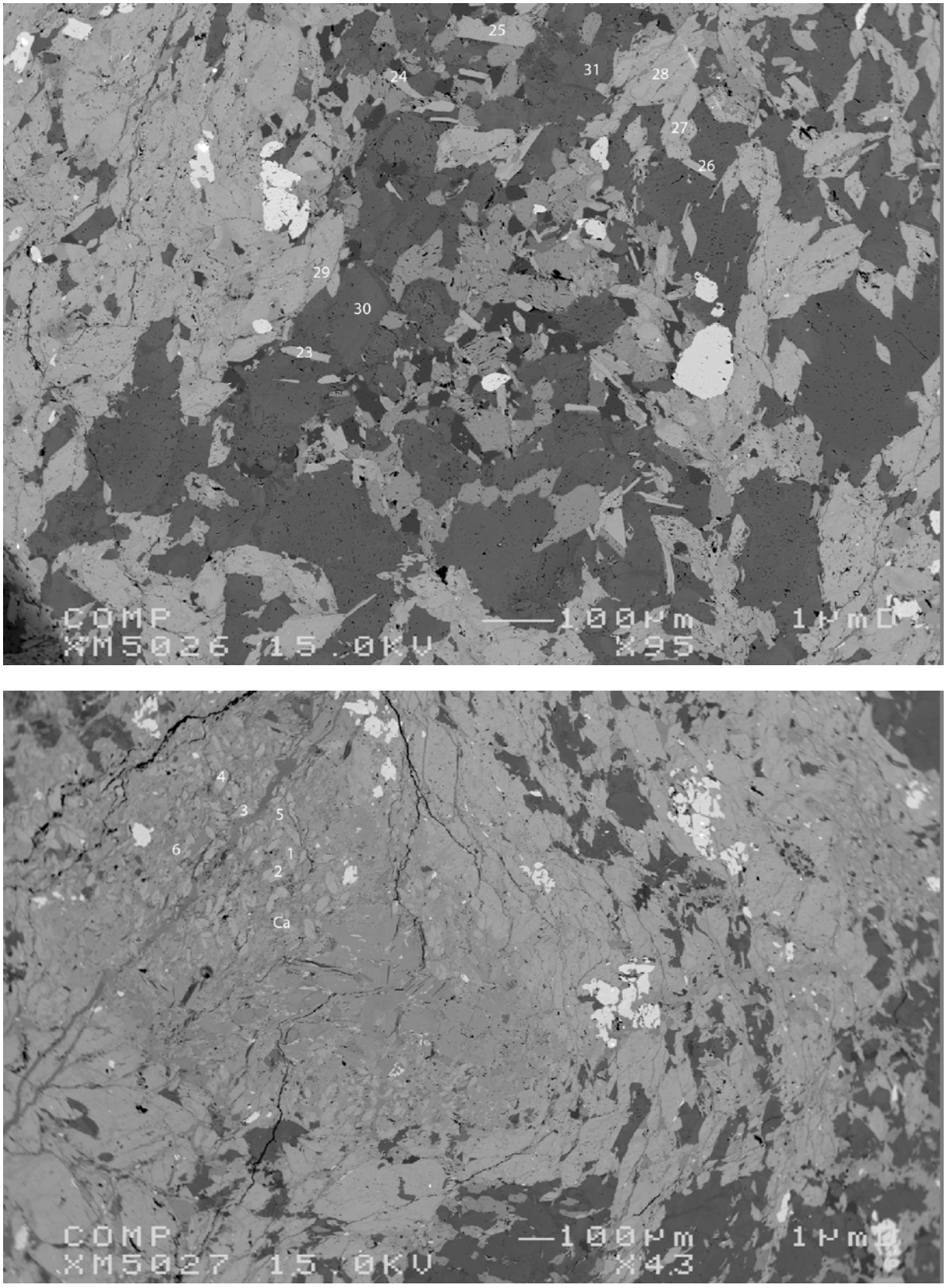

Figure 82. BSE of thin section JI 1-1, measuring locations 4 (top) and 5 (bottom).

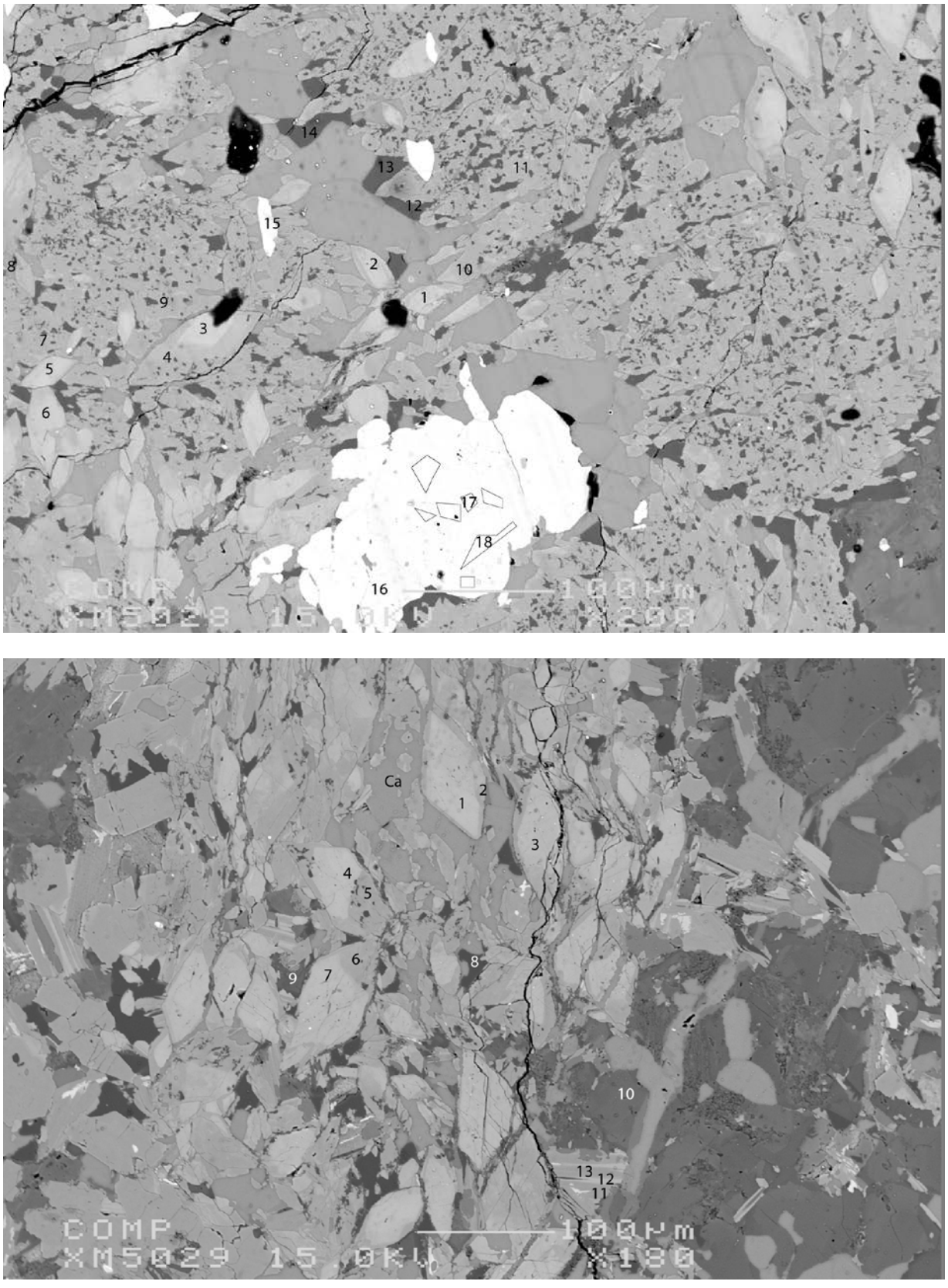

Figure 83. BSE of thin section JI 1-1, measuring locations 8 (top) and 9 (bottom).

point	1-4	1-5	1-6	1-7	1-8	1-9	1-10	1-11	1-12	1-13	1-14	1-15	3-1
Na2O	0,546	1,017	1,232	0,342	0,643	0,698	0,310	0,378	0,625	0,584	0,663	0,243	1,020
SiO2	50,944	44,917	42,347	52,593	49,166	48,567	53,229	52,936	49,056	50,124	48,442	54,045	44,905
MnO	0,357	0,304	0,370	0,406	0,400	0,331	0,479	0,403	0,371	0,396	0,377	0,332	0,361
K2O	0,275	0,860	1,003	0,167	0,415	0,545	0,151	0,149	0,350	0,299	0,508	0,165	0,541
MgO	12,906	8,671	7,682	13,767	12,033	11,292	14,231	13,785	12,238	12,684	11,197	14,485	9,247
Al2O3	6,014	13,401	15,760	3,932	7,557	8,895	3,371	4,066	7,556	6,801	8,644	2,827	12,469
FeO	13,790	16,185	17,139	13,314	14,796	15,604	13,511	13,634	14,637	14,218	15,657	13,245	16,159
CaO	12,362	12,230	12,196	12,486	12,519	12,382	12,460	12,537	12,481	12,342	12,393	12,498	12,170
TiO2	0,161	0,436	0,513	0,103	0,163	0,205	0,148	0,086	0,220	0,138	0,185	0,056	0,463
Cr2O3	0,120	0,178	0,056	0,002	0,020	0,041	0,046	0,010	0,013	0,064	0,068	0,027	0,058
Cl	0,011	0,000	0,011	0,005	0,000	0,000	0,000	0,000	0,000	0,009	0,000	0,000	0,002
F	0,021	0,000	0,000	0,000	0,234	0,010	0,000	0,058	0,000	0,043	0,088	0,000	0,044
Total	97,496	98,199	98,307	97,116	97,847	98,566	97,936	98,018	97,547	97,682	98,185	97,923	97,420
Na(I)	0,154	0,291	0,356	0,096	0,183	0,197	0,087	0,106	0,178	0,165	0,189	0,068	0,294
Si(IV)	7,421	6,633	6,308	7,650	7,221	7,085	7,682	7,642	7,195	7,314	7,108	7,774	6,683
Mn(II)	0,044	0,038	0,047	0,050	0,050	0,041	0,059	0,049	0,046	0,049	0,047	0,040	0,046
K(I)	0,051	0,162	0,191	0,031	0,078	0,101	0,028	0,027	0,065	0,056	0,095	0,030	0,103
Mg(II)	2,802	1,909	1,706	2,985	2,635	2,456	3,062	2,967	2,676	2,759	2,449	3,106	2,052
Al(III)	1,032	2,332	2,767	0,674	1,308	1,529	0,573	0,692	1,306	1,170	1,495	0,479	2,187
Fe(II)	1,680	1,999	2,135	1,620	1,817	1,904	1,631	1,646	1,795	1,735	1,921	1,593	2,011
Ca(II)	1,929	1,935	1,947	1,946	1,970	1,935	1,927	1,939	1,961	1,930	1,948	1,926	1,941
Ti(IV)	0,018	0,048	0,057	0,011	0,018	0,022	0,016	0,009	0,024	0,015	0,020	0,006	0,052
Cr(III)	0,014	0,021	0,007	0,000	0,002	0,005	0,005	0,001	0,002	0,007	0,008	0,003	0,007
F	0,010	0,000	0,000	0,000	0,109	0,005	0,000	0,026	0,000	0,020	0,041	0,000	0,021
Σ cations	15,145	15,369	15,521	15,065	15,282	15,277	15,070	15,080	15,249	15,201	15,280	15,027	15,375
charge	46,008	46,000	46,000	46,000	46,092	46,004	46,000	46,022	46,000	46,017	46,034	46,000	46,017

point	3-2	3-3	3-4	3-5	3-6	3-7	4-1	4-2	4-3	4-4	4-5	4-6	4-7
Na2O	1,024	1,038	0,935	0,909	0,932	1,005	0,998	0,952	1,126	0,719	0,896	0,966	0,912
SiO2	44,445	45,035	45,681	46,451	46,036	45,025	45,939	45,021	43,705	48,016	46,785	45,824	46,586
MnO	0,356	0,414	0,295	0,341	0,423	0,323	0,392	0,319	0,414	0,355	0,335	0,372	0,434
K2O	0,696	0,683	0,611	0,600	0,576	0,636	0,548	0,694	0,770	0,475	0,487	0,605	0,510
MgO	8,889	9,378	9,546	10,196	9,581	9,445	9,779	9,295	8,430	11,100	10,305	9,996	9,894
Al2O3	13,174	12,477	11,659	10,607	12,056	12,038	11,519	12,038	13,928	9,052	10,616	11,502	10,903
FeO	16,433	16,456	15,517	15,794	16,116	15,985	16,302	16,397	16,863	15,078	15,798	15,654	15,589
CaO	12,276	12,256	12,144	12,212	12,247	11,983	11,989	12,243	12,181	12,344	12,342	12,012	12,053
TiO2	0,631	0,589	0,651	0,600	0,316	0,835	0,514	0,656	0,712	0,396	0,264	0,499	0,278
Cr2O3	0,087	0,094	0,035	0,040	0,028	0,035	0,039	0,040	0,084	0,054	0,038	0,024	0,099
Cl	0,007	0,005	0,000	0,000	0,000	0,005	0,003	0,006	0,000	0,006	0,000	0,002	0,003
F	0,000	0,000	0,064	0,062	0,097	0,050	0,079	0,165	0,068	0,026	0,000	0,077	0,117
Total	98,016	98,424	97,111	97,786	98,367	97,343	98,067	97,756	98,252	97,609	97,866	97,501	97,328
Na(I)	0,294	0,297	0,270	0,261	0,266	0,290	0,286	0,275	0,324	0,205	0,256	0,278	0,262
Si(IV)	6,590	6,649	6,793	6,868	6,775	6,703	6,788	6,704	6,495	7,064	6,896	6,793	6,908
Mn(II)	0,045	0,052	0,037	0,043	0,053	0,041	0,049	0,040	0,052	0,044	0,042	0,047	0,055
K(I)	0,132	0,129	0,116	0,113	0,108	0,121	0,103	0,132	0,146	0,089	0,092	0,114	0,096
Mg(II)	1,965	2,064	2,116	2,247	2,102	2,096	2,154	2,063	1,868	2,434	2,264	2,209	2,187
Al(III)	2,302	2,171	2,043	1,848	2,091	2,112	2,006	2,113	2,439	1,569	1,844	2,009	1,905
Fe(II)	2,038	2,032	1,930	1,953	1,984	1,990	2,014	2,042	2,096	1,855	1,947	1,941	1,933
Ca(II)	1,950	1,939	1,935	1,935	1,931	1,911	1,898	1,953	1,940	1,946	1,949	1,908	1,915
Ti(IV)	0,070	0,065	0,073	0,067	0,035	0,094	0,057	0,073	0,080	0,044	0,029	0,056	0,031
Cr(III)	0,010	0,011	0,004	0,005	0,003	0,004	0,005	0,005	0,010	0,006	0,004	0,003	0,012
F	0,000	0,000	0,030	0,029	0,045	0,024	0,037	0,078	0,032	0,012	0,000	0,036	0,055
Σ cations	15,396	15,408	15,316	15,338	15,349	15,361	15,360	15,400	15,449	15,257	15,324	15,357	15,305
charge	46,000	46,000	46,025	46,024	46,038	46,020	46,031	46,065	46,027	46,010	46,000	46,030	46,046

Table 36. EMP measurements of representative amphibole of JI 1-1 based on 23 oxygens.

point	4-8	4-9	4-10	4-11	4-12	4-16	4-17	4-27	4-28	4-29	5-1	5-2	5-3
Na2O	0,935	0,953	0,821	1,031	0,485	0,898	0,769	0,962	1,034	0,898	1,070	1,095	0,936
SiO2	45,929	45,925	46,595	45,473	51,486	46,751	47,668	45,253	44,731	46,619	44,024	43,593	44,651
MnO	0,374	0,355	0,392	0,306	0,338	0,392	0,410	0,336	0,405	0,328	0,321	0,334	0,336
K2O	0,630	0,538	0,538	0,637	0,191	0,528	0,505	0,730	0,736	0,513	0,746	0,886	0,859
MgO	10,052	9,821	10,232	9,532	13,363	9,982	10,927	9,297	9,278	10,075	8,743	8,615	9,357
Al2O3	11,164	11,325	10,568	11,655	4,918	11,092	9,311	12,354	12,411	10,775	13,246	12,706	11,617
FeO	16,092	15,881	15,946	15,940	14,037	15,426	15,264	16,559	16,195	15,491	16,906	17,448	16,788
CaO	12,316	12,513	12,151	12,207	12,598	12,208	12,363	12,132	12,283	12,351	12,157	12,113	12,261
TiO2	0,399	0,877	0,446	0,536	0,159	0,315	0,580	0,717	0,775	0,410	0,743	0,917	0,831
Cr2O3	0,040	0,031	0,067	0,071	0,007	0,005	0,022	0,066	0,011	0,046	0,046	0,000	0,036
Cl	0,001	0,005	0,005	0,000	0,000	0,000	0,000	0,017	0,000	0,103	0,001	0,011	0,012
F	0,000	0,014	0,000	0,003	0,038	0,008	0,000	0,000	0,001	0,000	0,040	0,004	0,000
Total	97,932	98,231	97,760	97,390	97,604	97,602	97,819	98,419	97,860	97,586	98,026	97,718	97,681
Na(I)	0,268	0,272	0,235	0,297	0,137	0,257	0,219	0,275	0,298	0,257	0,309	0,318	0,271
Si(IV)	6,793	6,766	6,883	6,760	7,500	6,894	7,009	6,676	6,640	6,889	6,551	6,538	6,669
Mn(II)	0,047	0,044	0,049	0,039	0,042	0,049	0,051	0,042	0,051	0,041	0,040	0,042	0,043
K(I)	0,119	0,101	0,101	0,121	0,035	0,099	0,095	0,137	0,139	0,097	0,142	0,170	0,164
Mg(II)	2,216	2,157	2,253	2,112	2,902	2,194	2,395	2,045	2,053	2,219	1,939	1,926	2,083
Al(III)	1,946	1,967	1,840	2,042	0,844	1,928	1,614	2,148	2,171	1,877	2,323	2,246	2,045
Fe(II)	1,990	1,957	1,970	1,982	1,710	1,902	1,877	2,043	2,011	1,914	2,104	2,189	2,097
Ca(II)	1,952	1,975	1,923	1,944	1,966	1,929	1,948	1,918	1,954	1,956	1,938	1,947	1,962
Ti(IV)	0,044	0,097	0,050	0,060	0,017	0,035	0,064	0,080	0,087	0,046	0,083	0,103	0,093
Cr(III)	0,005	0,004	0,008	0,008	0,001	0,001	0,003	0,008	0,001	0,005	0,005	0,000	0,004
F	0,000	0,007	0,000	0,001	0,018	0,004	0,000	0,000	0,000	0,000	0,019	0,002	0,000
Σ cations	15,381	15,341	15,312	15,365	15,154	15,287	15,275	15,372	15,405	15,301	15,435	15,480	15,431
charge	46,000	46,005	46,000	46,001	46,015	46,003	46,000	46,000	46,000	46,000	46,016	46,002	46,000

point	5-4	5-6	8-1	8-2	8-3	8-4	8-5	8-6	8-7	8-8	8-9	8-10	8-11
Na2O	1,215	0,162	1,011	1,042	0,825	0,120	1,123	0,976	0,204	0,129	0,293	0,470	0,202
SiO2	44,297	54,257	44,549	44,506	46,062	54,577	43,178	45,095	56,480	55,099	53,981	51,539	53,909
MnO	0,385	0,392	0,405	0,429	0,482	0,398	0,351	0,323	0,285	0,372	0,412	0,393	0,325
K2O	0,601	0,031	0,811	0,918	0,647	0,027	0,969	0,793	0,049	0,030	0,087	0,233	0,044
MgO	8,967	14,788	9,081	8,830	9,241	14,720	7,937	9,099	14,472	15,141	14,496	13,275	14,288
Al2O3	12,450	1,914	12,590	12,034	9,480	1,453	12,643	11,677	1,043	1,338	2,874	5,205	2,406
FeO	17,185	13,116	16,611	16,807	17,762	13,117	18,154	16,844	12,466	13,154	13,174	13,889	13,296
CaO	12,103	12,967	12,261	12,191	12,174	12,503	11,784	12,120	12,120	12,496	12,476	12,618	12,947
TiO2	0,740	0,102	0,747	0,867	0,578	0,000	0,990	0,622	0,005	0,028	0,089	0,133	0,088
Cr2O3	0,066	0,055	0,196	0,157	0,128	0,015	0,125	0,119	0,000	0,058	0,073	0,000	0,085
Cl	0,002	0,004	0,003	0,007	0,010	0,000	0,003	0,000	0,042	0,001	0,006	0,000	0,000
F	0,000	0,028	0,000	0,000	0,000	0,009	0,025	0,041	0,000	0,046	0,092	0,000	0,067
Total	98,011	97,803	98,264	97,786	97,387	96,935	97,270	97,692	97,157	97,873	98,013	97,755	97,629
Na(I)	0,351	0,045	0,291	0,302	0,240	0,034	0,330	0,282	0,057	0,036	0,082	0,132	0,057
Si(IV)	6,599	7,824	6,605	6,646	6,915	7,919	6,535	6,725	8,105	7,919	7,768	7,486	7,798
Mn(II)	0,049	0,048	0,051	0,054	0,061	0,049	0,045	0,041	0,035	0,045	0,050	0,048	0,040
K(I)	0,114	0,006	0,153	0,175	0,124	0,005	0,187	0,151	0,009	0,006	0,016	0,043	0,008
Mg(II)	1,991	3,179	2,007	1,966	2,068	3,184	1,791	2,023	3,096	3,244	3,110	2,875	3,081
Al(III)	2,186	0,325	2,200	2,118	1,677	0,248	2,255	2,052	0,176	0,227	0,487	0,891	0,410
Fe(II)	2,141	1,582	2,060	2,099	2,230	1,592	2,298	2,101	1,496	1,581	1,586	1,687	1,608
Ca(II)	1,932	2,004	1,948	1,951	1,958	1,944	1,911	1,937	1,864	1,924	1,924	1,964	2,007
Ti(IV)	0,083	0,011	0,083	0,097	0,065	0,000	0,113	0,070	0,001	0,003	0,010	0,015	0,010
Cr(III)	0,008	0,006	0,023	0,019	0,015	0,002	0,015	0,014	0,000	0,007	0,008	0,000	0,010
F	0,000	0,013	0,000	0,000	0,000	0,004	0,012	0,019	0,000	0,021	0,042	0,000	0,031
Σ cations	15,454	15,030	15,422	15,426	15,355	14,977	15,480	15,396	14,839	14,991	15,041	15,141	15,028
charge	46,000	46,011	46,000	46,000	46,000	46,003	46,010	46,016	46,000	46,018	46,035	46,000	46,026

Table 37. EMP measurements of representative amphibole of JI 1-1 based on 23 oxygens (continued).

point	9-1	9-2	9-3	9-4	9-5	9-6	9-7
Na2O	1,671	0,392	1,056	1,248	0,364	0,410	1,196
SiO2	42,864	51,531	44,194	42,599	53,270	52,547	42,701
MnO	0,408	0,345	0,365	0,389	0,398	0,295	0,349
K2O	0,906	0,192	0,850	1,003	0,140	0,216	1,002
MgO	7,944	13,730	8,923	7,832	14,637	13,585	8,181
Al2O3	13,107	4,018	13,100	14,174	2,969	3,550	14,104
FeO	18,002	13,013	16,597	17,813	13,258	14,519	17,014
CaO	11,756	12,744	12,275	12,141	12,203	12,634	11,879
TiO2	0,902	0,156	0,739	1,186	0,092	0,102	1,068
Cr2O3	0,088	0,055	0,112	0,086	0,085	0,079	0,099
Cl	0,180	0,011	0,005	0,012	0,020	0,028	0,014
F	0,000	0,000	0,000	0,000	0,039	0,066	0,000
Total	97,787	96,185	98,215	98,480	97,454	97,997	97,604
Na(I)	0,489	0,112	0,304	0,362	0,102	0,116	0,348
Si(IV)	6,469	7,585	6,558	6,366	7,718	7,637	6,406
Mn(II)	0,052	0,043	0,046	0,049	0,049	0,036	0,044
K(I)	0,174	0,036	0,161	0,191	0,026	0,040	0,192
Mg(II)	1,787	3,013	1,974	1,745	3,162	2,944	1,830
Al(III)	2,331	0,697	2,291	2,496	0,507	0,608	2,494
Fe(II)	2,272	1,602	2,060	2,226	1,607	1,765	2,135
Ca(II)	1,901	2,010	1,952	1,944	1,894	1,967	1,909
Ti(IV)	0,102	0,017	0,082	0,133	0,010	0,011	0,121
Cr(III)	0,011	0,006	0,013	0,010	0,010	0,009	0,012
F	0,000	0,000	0,000	0,000	0,018	0,030	0,000
Σ cations	15,589	15,120	15,440	15,524	15,085	15,133	15,490
charge	46,000	46,000	46,000	46,000	46,015	46,026	46,000

point	4-23	4-24	4-25	4-26
Na2O	0,110	0,105	0,080	0,030
SiO2	36,774	36,924	36,963	35,721
MnO	0,185	0,209	0,293	0,242
K2O	9,305	9,819	9,917	8,451
MgO	11,163	10,893	10,509	11,271
Al2O3	18,345	18,473	18,242	18,882
FeO	17,983	17,912	18,063	18,908
CaO	0,085	0,160	0,116	0,075
TiO2	0,908	1,060	1,294	1,015
Cr2O3	0,010	0,032	0,011	0,045
Cl	0,002	0,002	0,006	0,005
F	0,219	0,140	0,271	0,203
Total	94,997	95,670	95,650	94,762
Na(I)	0,016	0,015	0,012	0,004
Si(IV)	2,789	2,784	2,798	2,720
Mn(II)	0,012	0,013	0,019	0,016
K(I)	0,900	0,945	0,958	0,821
Mg(II)	1,262	1,224	1,186	1,279
Al(III)	1,640	1,642	1,627	1,695
Fe(II)	1,141	1,130	1,143	1,204
Ca(II)	0,007	0,013	0,009	0,006
Ti(IV)	0,052	0,060	0,074	0,058
Cr(III)	0,001	0,002	0,001	0,003
F	0,053	0,033	0,065	0,049
Σ cations	7,819	7,828	7,826	7,806
charge	22,044	22,028	22,055	22,041

Table 38. EMP measurements of representative amphibole of JI 1-1 based on 23 oxygens (continued) (top) and biotite based on 11 oxygen (bottom).

point	1-16	1-17	1-18	1-19	1-20	4-13	4-14	4-15
Na2O	0,031	0,910	0,000	0,007	0,037	0,934	0,029	0,021
SiO2	40,466	42,423	38,815	39,286	39,114	45,545	39,103	39,029
MnO	0,000	0,000	0,105	0,123	0,143	0,337	0,139	0,103
K2O	0,134	0,053	0,009	0,003	0,005	0,603	0,000	0,022
MgO	0,016	0,000	0,024	0,005	0,008	9,818	0,020	0,016
Al2O3	34,665	33,673	29,461	29,053	29,619	11,587	29,006	28,901
FeO	0,154	0,174	5,804	6,394	5,800	15,593	6,553	6,802
CaO	24,418	23,347	24,000	23,843	24,085	12,209	23,841	23,883
TiO2	0,000	0,021	0,110	0,000	0,035	0,277	0,116	0,063
Cr2O3	0,007	0,000	0,011	0,015	0,000	0,000	0,000	0,000
Cl	0,011	0,013	0,007	0,009	0,001	0,002	0,000	0,004
F	0,000	0,043	0,000	0,079	0,000	0,000	0,042	0,000
Total	99,900	100,636	98,344	98,782	98,847	96,905	98,831	98,843
Na(I)	0,004	0,129	0,000	0,001	0,006	0,147	0,004	0,003
Si(IV)	2,999	3,112	3,021	3,053	3,028	3,689	3,040	3,036
Mn(II)	0,000	0,000	0,007	0,008	0,009	0,023	0,009	0,007
K(I)	0,013	0,005	0,001	0,000	0,000	0,062	0,000	0,002
Mg(II)	0,002	0,000	0,003	0,001	0,001	1,186	0,002	0,002
Al(III)	3,028	2,911	2,703	2,661	2,702	1,106	2,657	2,650
Fe(II)	0,010	0,011	0,378	0,416	0,376	1,056	0,426	0,443
Ca(II)	1,939	1,835	2,002	1,985	1,998	1,060	1,986	1,991
Ti(IV)	0,000	0,001	0,006	0,000	0,002	0,017	0,007	0,004
Cr(III)	0,000	0,000	0,001	0,001	0,000	0,000	0,000	0,000
F	0,000	0,010	0,000	0,019	0,000	0,000	0,010	0,000
Σ cations	7,995	8,003	8,121	8,125	8,122	8,346	8,131	8,138
charge	25,000	25,008	25,000	25,016	25,000	25,000	25,009	25,000

point	3-8	3-9	4-18	4-19	4-20	4-21	4-22	4-30	4-31	9-9	9-10
Na2O	6,313	5,887	4,810	5,770	5,616	6,223	5,182	5,630	4,841	7,302	5,738
SiO2	56,474	55,571	53,907	56,010	55,220	55,931	54,542	55,638	53,913	58,717	56,363
MnO	0,013	0,000	0,036	0,000	0,000	0,000	0,002	0,011	0,027	0,022	0,000
K2O	0,047	0,091	0,047	0,045	0,065	0,051	0,068	0,063	0,030	0,151	0,130
MgO	0,002	0,002	0,001	0,000	0,118	0,000	0,000	0,012	0,000	0,023	0,003
Al2O3	28,362	28,455	30,306	28,904	28,565	28,142	29,677	28,969	30,291	26,530	28,809
FeO	0,123	0,110	0,127	0,080	0,230	0,157	0,147	0,034	0,025	0,342	0,094
CaO	9,218	10,082	12,087	10,256	10,443	9,819	11,157	10,494	12,073	7,794	10,108
TiO2	0,000	0,023	0,000	0,000	0,000	0,027	0,000	0,000	0,000	0,019	0,012
Cr2O3	0,008	0,000	0,000	0,014	0,010	0,000	0,000	0,000	0,046	0,000	0,000
Cl	0,005	0,021	0,012	0,012	0,010	0,002	0,003	0,000	0,000	0,031	0,012
F	0,000	0,056	0,038	0,090	0,000	0,102	0,001	0,051	0,114	0,023	0,000
Total	100,564	100,269	101,352	101,140	100,275	100,411	100,778	100,881	101,312	100,937	101,266
Na(I)	0,546	0,513	0,417	0,498	0,489	0,542	0,450	0,487	0,420	0,629	0,494
Si(IV)	2,521	2,497	2,408	2,494	2,482	2,510	2,442	2,484	2,410	2,607	2,502
Mn(II)	0,000	0,000	0,001	0,000	0,000	0,000	0,000	0,000	0,001	0,001	0,000
K(I)	0,003	0,005	0,003	0,003	0,004	0,003	0,004	0,004	0,002	0,009	0,007
Mg(II)	0,000	0,000	0,000	0,000	0,008	0,000	0,000	0,001	0,000	0,002	0,000
Al(III)	1,492	1,507	1,595	1,517	1,513	1,489	1,566	1,524	1,596	1,388	1,507
Fe(II)	0,005	0,004	0,005	0,003	0,009	0,006	0,006	0,001	0,001	0,013	0,003
Ca(II)	0,441	0,485	0,578	0,489	0,503	0,472	0,535	0,502	0,578	0,371	0,481
Ti(IV)	0,000	0,001	0,000	0,000	0,000	0,001	0,000	0,000	0,000	0,001	0,000
Cr(III)	0,000	0,000	0,000	0,000	0,000	0,000	0,000	0,000	0,002	0,000	0,000
F	0,000	0,008	0,005	0,013	0,000	0,014	0,000	0,007	0,016	0,003	0,000
Σ cations	5,008	5,012	5,007	5,004	5,008	5,023	5,002	5,003	5,009	5,018	4,995
charge	16,000	16,007	16,005	16,011	16,000	16,012	16,000	16,006	16,014	16,003	16,000

Table 39. EMP measurements of representative epidote of JI 1-1 based on 12.5 oxygens (top) and plagioclase based on 8 oxygen (bottom).

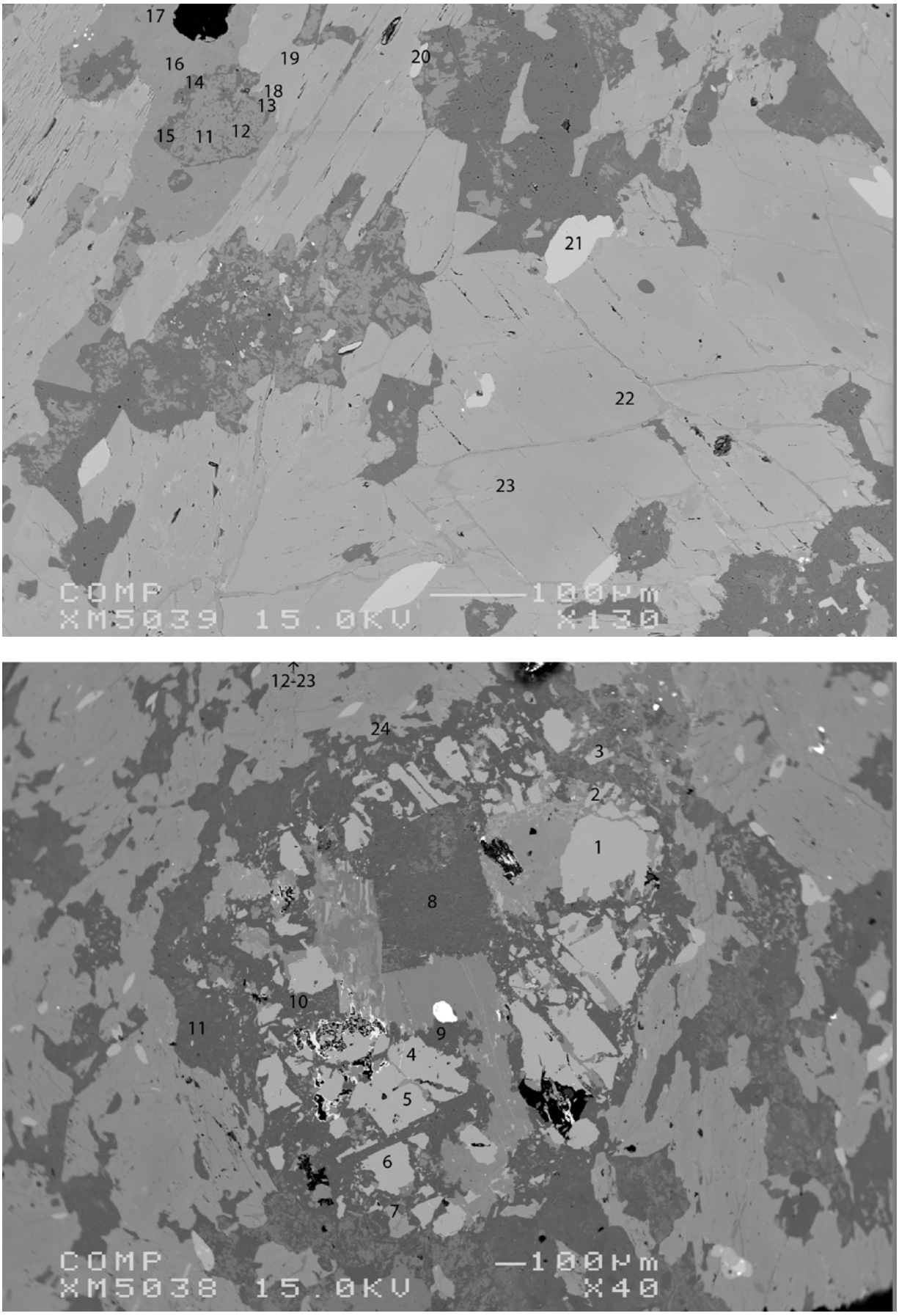

Figure 84. BSE of thin section JI 2-1, measuring location 1.

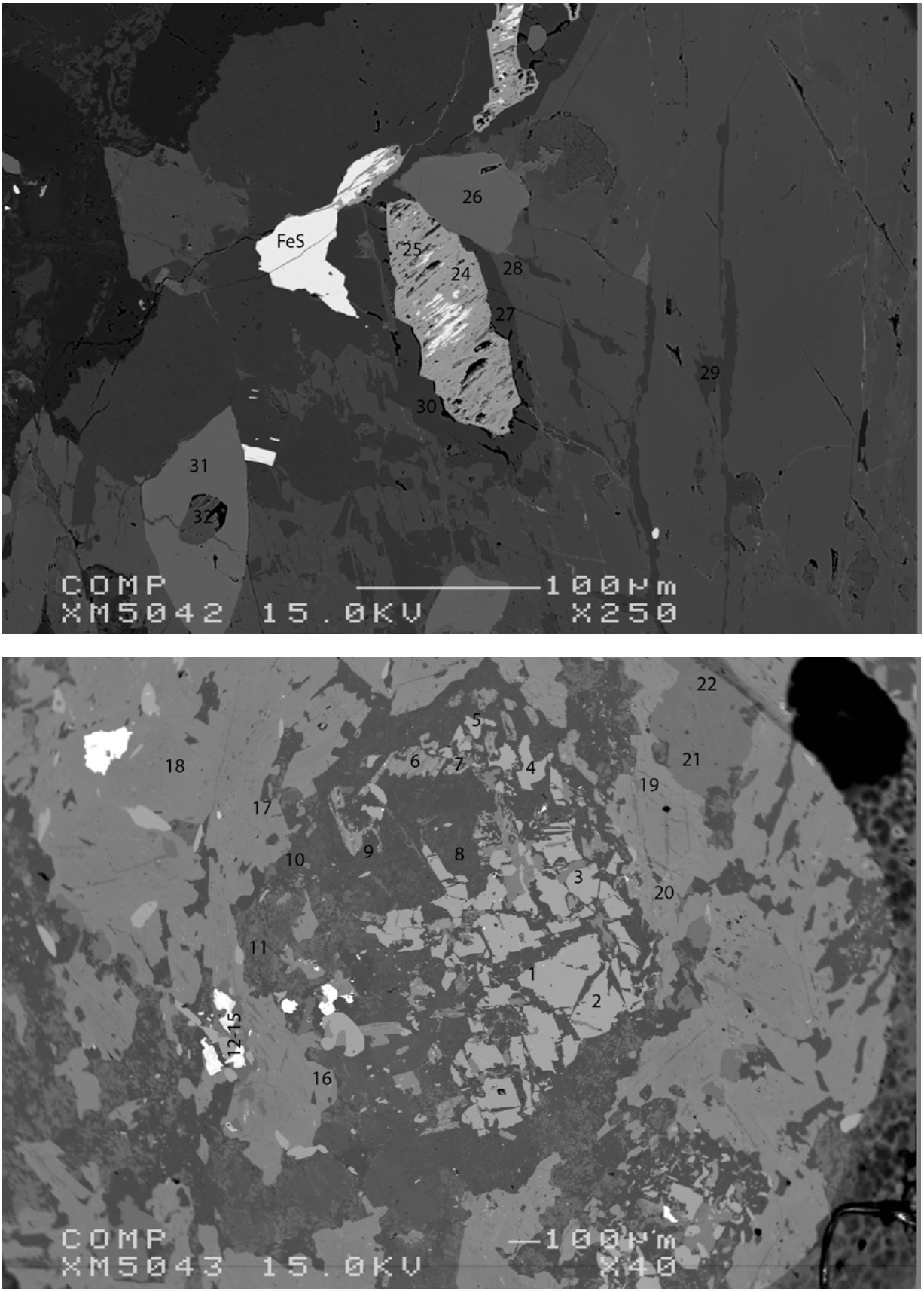

Figure 85. BSE of thin section JI 2-1, measuring location 1 (top) and 3 (bottom).

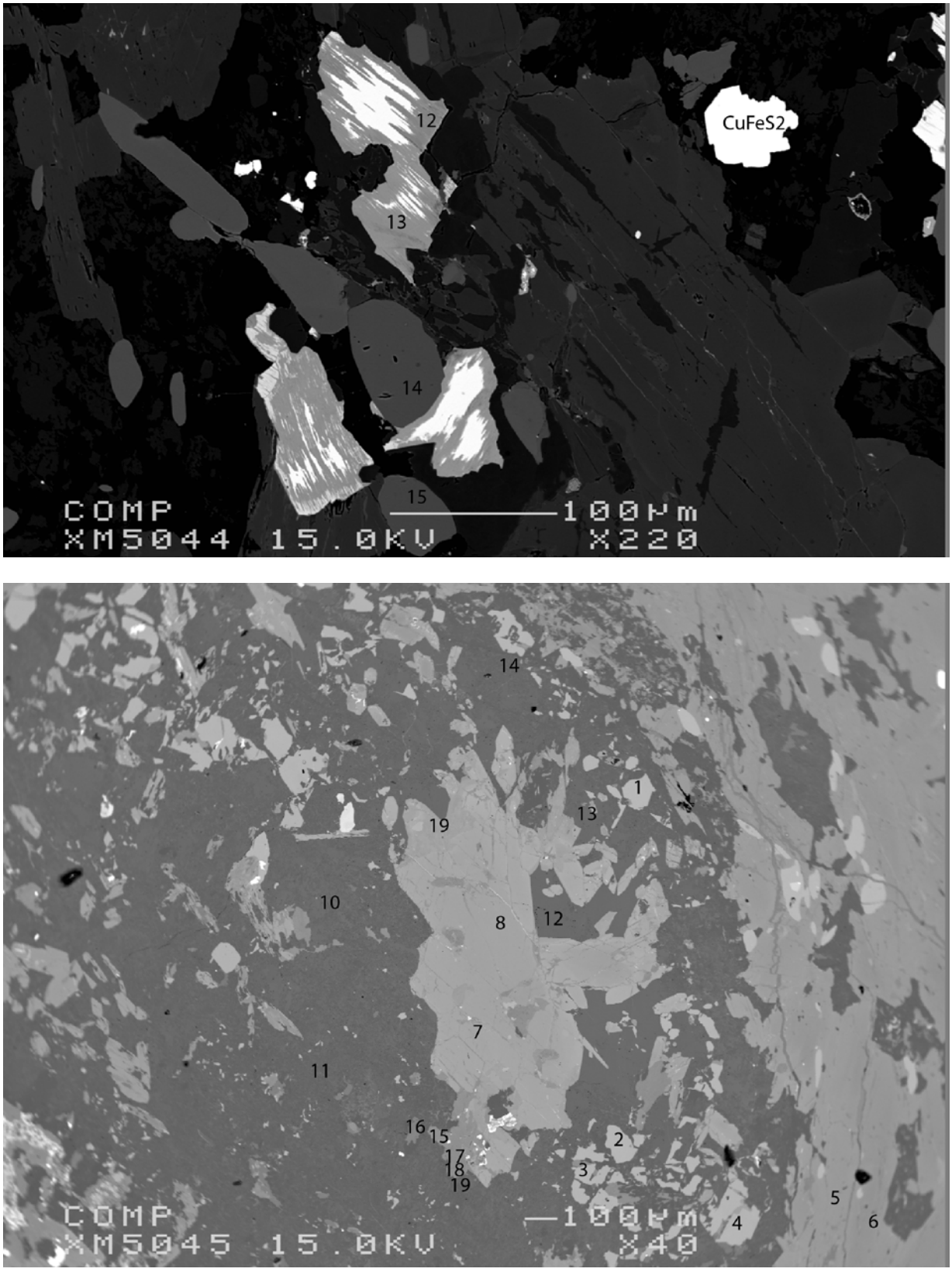

Figure 86. BSE of thin section JI 2-1, measuring location 3 (top) and 6 (bottom).

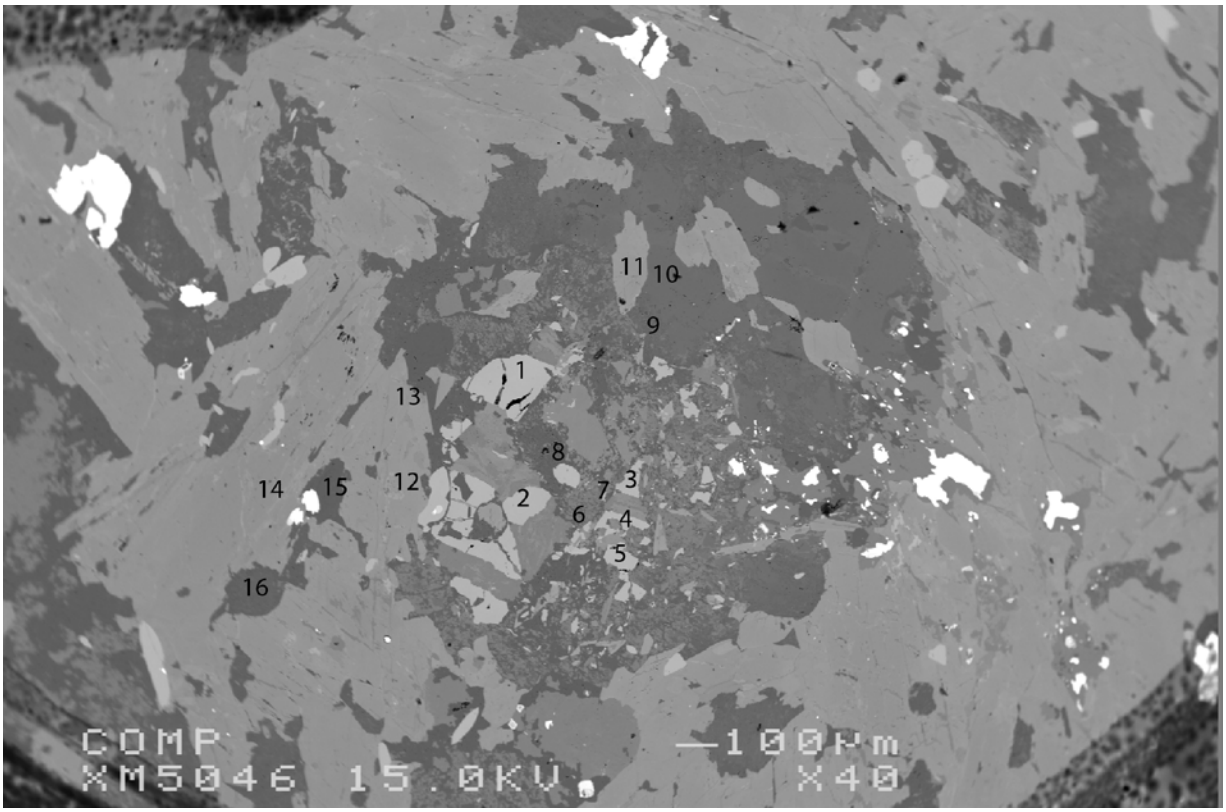

Figure 87. BSE of thin section JI 2-1, measuring location 1 (top) and 3 (bottom).

point	3-16	3-17	3-18	3-19	3-20	6-5	6-6	6-7	6-8	6-9	4-11	4-12	4-13	4-14
Na2O	1,100	1,287	1,610	1,067	0,384	1,290	1,400	1,174	1,190	0,635	1,530	1,460	1,181	1,340
SiO2	46,380	46,390	45,230	46,480	51,760	44,620	45,010	44,060	44,160	48,190	45,040	43,860	46,630	46,630
MnO	0,278	0,272	0,194	0,317	0,426	0,366	0,254	0,573	0,511	0,593	0,322	0,290	0,284	0,263
K2O	0,490	0,546	0,296	0,476	0,132	0,626	0,467	0,634	0,589	0,326	0,402	0,614	0,505	0,293
MgO	11,340	11,730	11,740	11,190	13,340	10,290	11,500	7,340	8,120	10,260	10,770	9,900	11,190	12,480
Al2O3	10,100	10,760	13,580	9,860	3,520	11,580	12,890	10,090	10,670	6,530	13,050	13,370	10,140	11,800
FeO	15,300	13,900	13,020	15,680	15,490	15,900	13,070	21,220	20,060	18,410	14,230	15,670	15,160	12,910
CaO	11,970	11,950	11,240	11,800	12,140	11,800	11,840	11,390	11,610	11,870	11,710	11,780	11,970	11,960
TiO2	0,541	0,522	0,531	0,480	0,184	0,619	0,428	0,894	0,795	0,233	0,527	0,583	0,507	0,420
Cr2O3	0,073	0,098	0,061	0,022	0,018	0,011	0,048	0,000	0,025	0,129	0,069	0,092	0,117	0,080
Cl	0,051	0,019	0,015	0,023	0,036	0,056	0,036	0,070	0,091	0,220	0,026	0,064	0,024	0,011
F	0,254	0,191	0,158	0,000	0,023	0,299	0,000	0,076	0,000	0,000	0,101	0,113	0,146	0,257
Total	97,877	97,664	97,676	97,395	97,452	97,457	96,944	97,521	97,821	97,395	97,777	97,797	97,854	98,445
Na(I)	0,316	0,367	0,456	0,307	0,109	0,375	0,400	0,349	0,350	0,185	0,436	0,421	0,338	0,377
Si(IV)	6,868	6,831	6,606	6,889	7,598	6,686	6,630	6,750	6,696	7,237	6,623	6,520	6,884	6,769
Mn(II)	0,035	0,034	0,024	0,040	0,053	0,046	0,032	0,074	0,066	0,075	0,040	0,037	0,036	0,032
K(I)	0,093	0,103	0,055	0,090	0,025	0,120	0,088	0,124	0,114	0,062	0,075	0,116	0,095	0,054
Mg(II)	2,503	2,575	2,556	2,472	2,919	2,299	2,525	1,676	1,835	2,297	2,361	2,194	2,463	2,701
Al(III)	1,763	1,867	2,338	1,722	0,609	2,045	2,238	1,822	1,907	1,156	2,262	2,342	1,764	2,019
Fe(II)	1,895	1,712	1,590	1,944	1,902	1,992	1,610	2,719	2,544	2,312	1,750	1,948	1,872	1,567
Ca(II)	1,899	1,885	1,759	1,874	1,909	1,894	1,869	1,870	1,886	1,910	1,845	1,876	1,894	1,860
Ti(IV)	0,060	0,058	0,058	0,054	0,020	0,070	0,047	0,103	0,091	0,026	0,058	0,065	0,056	0,046
Cr(III)	0,009	0,011	0,007	0,003	0,002	0,001	0,006	0,000	0,003	0,015	0,008	0,011	0,014	0,009
F	0,119	0,089	0,073	0,000	0,011	0,142	0,000	0,037	0,000	0,000	0,047	0,053	0,068	0,118
Σ cations	15,440	15,444	15,450	15,393	15,147	15,528	15,444	15,487	15,491	15,275	15,459	15,530	15,416	15,436
charge	46,100	46,075	46,061	46,000	46,009	46,119	46,000	46,031	46,000	46,000	46,040	46,045	46,057	46,099

Table 40. EMP measurements of representative amphibole of JI 2-1 based on 23 oxygen.

point	1-1	1-2	1-3	1-4	1-5	1-6	3-1	3-3	3-4	3-5
Na2O	0,040	0,025	0,000	0,013	0,016	0,047	0,024	0,038	0,055	0,036
SiO2	38,400	38,400	38,230	38,430	38,350	37,960	38,140	38,380	37,930	37,760
MnO	1,217	1,017	0,750	4,140	2,230	1,001	2,440	0,974	0,760	0,451
K2O	0,000	0,000	0,000	0,000	0,000	0,000	0,000	0,000	0,000	0,000
MgO	1,860	2,240	2,310	1,282	1,396	1,690	1,930	1,910	1,940	1,840
Al2O3	22,370	22,660	22,600	22,530	22,340	22,500	22,250	22,390	22,440	22,630
FeO	27,150	25,860	26,340	24,520	26,270	26,870	25,600	27,160	26,600	27,290
CaO	11,280	11,270	11,130	11,670	11,440	11,440	11,280	11,240	11,420	11,120
TiO2	0,115	0,089	0,102	0,104	0,110	0,110	0,123	0,142	0,076	0,038
Cr2O3	0,038	0,000	0,000	0,000	0,030	0,044	0,031	0,010	0,013	0,011
Cl	0,000	0,010	0,000	0,000	0,000	0,000	0,010	0,000	0,007	0,015
F	0,000	0,000	0,000	0,000	0,000	0,000	0,000	0,000	0,000	0,000
Total	102,469	101,571	101,462	102,689	102,182	101,663	101,828	102,244	101,240	101,191
Na(I)	0,006	0,004	0,000	0,002	0,002	0,007	0,004	0,006	0,008	0,005
Si(IV)	2,969	2,974	2,967	2,970	2,977	2,957	2,966	2,971	2,961	2,952
Mn(II)	0,080	0,067	0,049	0,271	0,147	0,066	0,161	0,064	0,050	0,030
K(I)	0,000	0,000	0,000	0,000	0,000	0,000	0,000	0,000	0,000	0,000
Mg(II)	0,214	0,259	0,267	0,148	0,162	0,196	0,224	0,220	0,226	0,214
Al(III)	2,039	2,069	2,067	2,052	2,044	2,066	2,039	2,043	2,064	2,085
Fe(II)	1,756	1,675	1,710	1,585	1,705	1,750	1,665	1,758	1,736	1,784
Ca(II)	0,934	0,935	0,926	0,966	0,951	0,955	0,940	0,932	0,955	0,931
Ti(IV)	0,007	0,005	0,006	0,006	0,006	0,006	0,007	0,008	0,004	0,002
Cr(III)	0,002	0,000	0,000	0,000	0,002	0,003	0,002	0,001	0,001	0,001
F	0,000	0,000	0,000	0,000	0,000	0,000	0,000	0,000	0,000	0,000
Σ cations	8,007	7,988	7,993	7,999	7,996	8,006	8,008	8,002	8,006	8,006
charge	24,000	24,000	24,000	24,000	24,000	24,000	24,000	24,000	24,000	24,000

point	6-1	6-2	6-3	6-4	4-1	4-2	4-3	4-4	4-5
Na2O	0,014	0,028	0,010	0,041	0,030	0,000	0,024	0,038	0,045
SiO2	38,360	38,200	38,290	38,140	37,990	37,990	38,100	37,760	37,980
MnO	0,469	1,900	2,130	1,020	0,633	0,425	0,885	0,680	0,575
K2O	0,000	0,000	0,000	0,000	0,013	0,000	0,000	0,000	0,000
MgO	1,910	1,690	1,530	2,110	1,594	2,000	1,900	1,645	1,603
Al2O3	22,540	22,360	22,260	22,450	22,470	22,490	22,500	22,330	22,540
FeO	27,850	26,160	25,810	26,330	27,300	26,700	26,700	27,530	27,530
CaO	11,190	11,410	11,480	11,180	11,390	11,720	11,240	11,220	11,280
TiO2	0,060	0,166	0,156	0,132	0,107	0,132	0,111	0,150	0,105
Cr2O3	0,010	0,048	0,000	0,016	0,011	0,075	0,068	0,031	0,010
Cl	0,000	0,000	0,000	0,000	0,025	0,009	0,010	0,000	0,000
F	0,000	0,000	0,000	0,000	0,000	0,000	0,000	0,000	0,000
Total	102,403	101,961	101,666	101,419	101,564	101,541	101,538	101,385	101,667
Na(I)	0,002	0,004	0,002	0,006	0,005	0,000	0,004	0,006	0,007
Si(IV)	2,966	2,967	2,981	2,967	2,963	2,955	2,965	2,954	2,959
Mn(II)	0,031	0,125	0,140	0,067	0,042	0,028	0,058	0,045	0,038
K(I)	0,000	0,000	0,000	0,000	0,001	0,000	0,000	0,000	0,000
Mg(II)	0,220	0,196	0,178	0,245	0,185	0,232	0,220	0,192	0,186
Al(III)	2,054	2,047	2,042	2,059	2,065	2,062	2,064	2,059	2,070
Fe(II)	1,801	1,699	1,680	1,713	1,781	1,737	1,738	1,801	1,794
Ca(II)	0,927	0,950	0,958	0,932	0,952	0,977	0,937	0,941	0,942
Ti(IV)	0,003	0,010	0,009	0,008	0,006	0,008	0,006	0,009	0,006
Cr(III)	0,001	0,003	0,000	0,001	0,001	0,005	0,004	0,002	0,001
F	0,000	0,000	0,000	0,000	0,000	0,000	0,000	0,000	0,000
Σ cations	8,004	8,000	7,990	7,998	8,001	8,004	7,996	8,009	8,003
charge	24,000	24,000	24,000	24,000	24,000	24,000	24,000	24,000	24,000

Table 41. EMP measurements of representative garnet of JI 2-1 based on 12 oxygen.

point	1-8	1-9	1-10	1-11	1-14	1-15	6-10	6-11	6-12	6-13
Na2O	7,810	10,430	10,190	8,360	11,390	11,860	9,930	5,450	7,460	7,430
SiO2	61,610	65,340	65,360	61,060	67,170	67,590	64,680	56,650	58,930	58,800
MnO	0,009	0,052	0,022	0,000	0,000	0,000	0,000	0,069	0,013	0,000
K2O	3,020	0,510	0,248	1,600	0,017	0,010	0,502	5,050	0,158	0,128
MgO	0,269	0,015	0,000	0,060	0,000	0,012	0,056	0,306	0,000	0,011
Al2O3	25,760	21,980	22,560	25,180	20,690	20,580	22,190	29,020	26,300	26,110
FeO	0,482	0,308	0,105	0,177	0,058	0,033	0,111	0,487	0,114	0,150
CaO	1,550	1,520	2,270	3,140	1,780	0,118	1,860	1,960	7,160	7,220
TiO2	0,040	0,028	0,013	0,010	0,010	0,010	0,000	0,000	0,025	0,009
Cr2O3	0,000	0,000	0,010	0,000	0,000	0,023	0,024	0,000	0,032	0,000
Cl	0,014	0,037	0,054	0,017	0,007	0,000	0,018	0,012	0,000	0,000
F	0,062	0,000	0,103	0,051	0,000	0,048	0,025	0,017	0,000	0,010
Total	100,625	100,220	100,936	99,656	101,122	100,283	99,396	99,021	100,192	99,869
Na(I)	0,670	0,889	0,863	0,723	0,960	1,004	0,852	0,480	0,644	0,644
Si(IV)	2,727	2,873	2,856	2,724	2,921	2,951	2,864	2,573	2,626	2,629
Mn(II)	0,000	0,002	0,001	0,000	0,000	0,000	0,000	0,003	0,000	0,000
K(I)	0,171	0,029	0,014	0,091	0,001	0,001	0,028	0,293	0,009	0,007
Mg(II)	0,018	0,001	0,000	0,004	0,000	0,001	0,004	0,021	0,000	0,001
Al(III)	1,344	1,139	1,162	1,324	1,061	1,059	1,158	1,554	1,381	1,376
Fe(II)	0,018	0,011	0,004	0,007	0,002	0,001	0,004	0,019	0,004	0,006
Ca(II)	0,074	0,072	0,106	0,150	0,083	0,006	0,088	0,095	0,342	0,346
Ti(IV)	0,001	0,001	0,000	0,000	0,000	0,000	0,000	0,000	0,001	0,000
Cr(III)	0,000	0,000	0,000	0,000	0,000	0,001	0,001	0,000	0,001	0,000
F	0,009	0,000	0,014	0,007	0,000	0,007	0,004	0,002	0,000	0,001
Σ cations	5,023	5,016	5,007	5,024	5,029	5,024	4,999	5,037	5,009	5,009
charge	16,007	16,000	16,012	16,006	16,000	16,006	16,003	16,002	16,000	16,001

point	6-14	6-15	6-16	6-18	4-6	4-7	4-10	4-15	4-16
Na2O	7,130	0,000	0,000	0,012	1,211	11,090	7,680	11,120	10,460
SiO2	59,240	38,660	36,910	38,570	46,350	67,560	59,360	67,340	65,570
MnO	0,034	0,082	0,029	0,078	0,000	0,018	0,000	0,000	0,000
K2O	2,820	0,012	0,010	0,000	0,010	0,309	0,322	0,135	0,030
MgO	0,041	0,030	0,587	0,032	0,009	0,052	0,010	0,000	0,000
Al2O3	26,960	28,700	27,410	29,190	24,450	21,090	25,670	20,570	21,780
FeO	0,255	7,430	5,880	6,940	0,269	0,131	0,080	0,208	0,116
CaO	2,940	23,800	22,510	23,560	23,160	0,270	6,590	0,570	1,900
TiO2	0,037	0,064	0,000	0,010	0,000	0,010	0,010	0,000	0,000
Cr2O3	0,000	0,000	0,015	0,048	0,000	0,009	0,000	0,000	0,000
Cl	0,000	0,000	0,000	0,000	0,016	0,014	0,014	0,307	0,010
F	0,000	0,000	0,000	0,100	0,149	0,000	0,032	0,009	0,063
Total	99,457	98,778	93,351	98,540	95,625	100,552	99,766	100,259	99,929
Na(I)	0,620	0,000	0,000	0,001	0,116	0,936	0,666	0,944	0,892
Si(IV)	2,657	1,933	1,940	1,930	2,289	2,939	2,655	2,949	2,885
Mn(II)	0,001	0,003	0,001	0,003	0,000	0,001	0,000	0,000	0,000
K(I)	0,161	0,001	0,001	0,000	0,001	0,017	0,018	0,008	0,002
Mg(II)	0,003	0,002	0,046	0,002	0,001	0,003	0,001	0,000	0,000
Al(III)	1,425	1,691	1,698	1,722	1,423	1,081	1,353	1,062	1,129
Fe(II)	0,010	0,311	0,258	0,290	0,011	0,005	0,003	0,008	0,004
Ca(II)	0,141	1,275	1,267	1,263	1,226	0,013	0,316	0,027	0,090
Ti(IV)	0,001	0,002	0,000	0,000	0,000	0,000	0,000	0,000	0,000
Cr(III)	0,000	0,000	0,001	0,002	0,000	0,000	0,000	0,000	0,000
F	0,000	0,000	0,000	0,016	0,023	0,000	0,005	0,001	0,009
Σ cations	5,020	5,219	5,212	5,215	5,067	4,996	5,012	4,997	5,001
charge	16,000	16,000	16,000	16,013	16,020	16,000	16,004	16,001	16,007

Table 42. EMP measurements of representative plagioclase of JI 2-1 based on 8 oxygen.

Comment	1-12	1-13	3-21	3-22
Na2O	0,256	0,011	0,018	0,029
SiO2	43,700	43,870	43,350	43,120
MnO	0,018	0,020	0,000	0,000
K2O	0,000	0,000	0,024	0,022
MgO	0,019	0,000	0,000	0,010
Al2O3	24,890	24,960	24,670	25,100
FeO	0,311	0,723	1,223	0,208
CaO	26,630	26,810	27,140	26,980
TiO2	0,090	0,026	0,000	0,010
Cr2O3	0,000	0,021	0,000	0,000
Cl	0,000	0,000	0,000	0,000
F	0,000	0,083	0,000	0,000
Total	95,914	96,524	96,425	95,479
Na(I)	0,039	0,002	0,003	0,004
Si(IV)	3,401	3,402	3,377	3,374
Mn(II)	0,001	0,001	0,000	0,000
K(I)	0,000	0,000	0,002	0,002
Mg(II)	0,002	0,000	0,000	0,001
Al(III)	2,283	2,281	2,265	2,314
Fe(II)	0,020	0,047	0,080	0,014
Ca(II)	2,220	2,228	2,265	2,262
Ti(IV)	0,005	0,002	0,000	0,001
Cr(III)	0,000	0,001	0,000	0,000
F	0,000	0,020	0,000	0,000
Σ cations	7,972	7,964	7,993	7,972
charge	25,000	25,017	25,000	25,000

Table 43. EMP measurements of representative clinozoisite of JI 2-1 based on 12.5 oxygen.

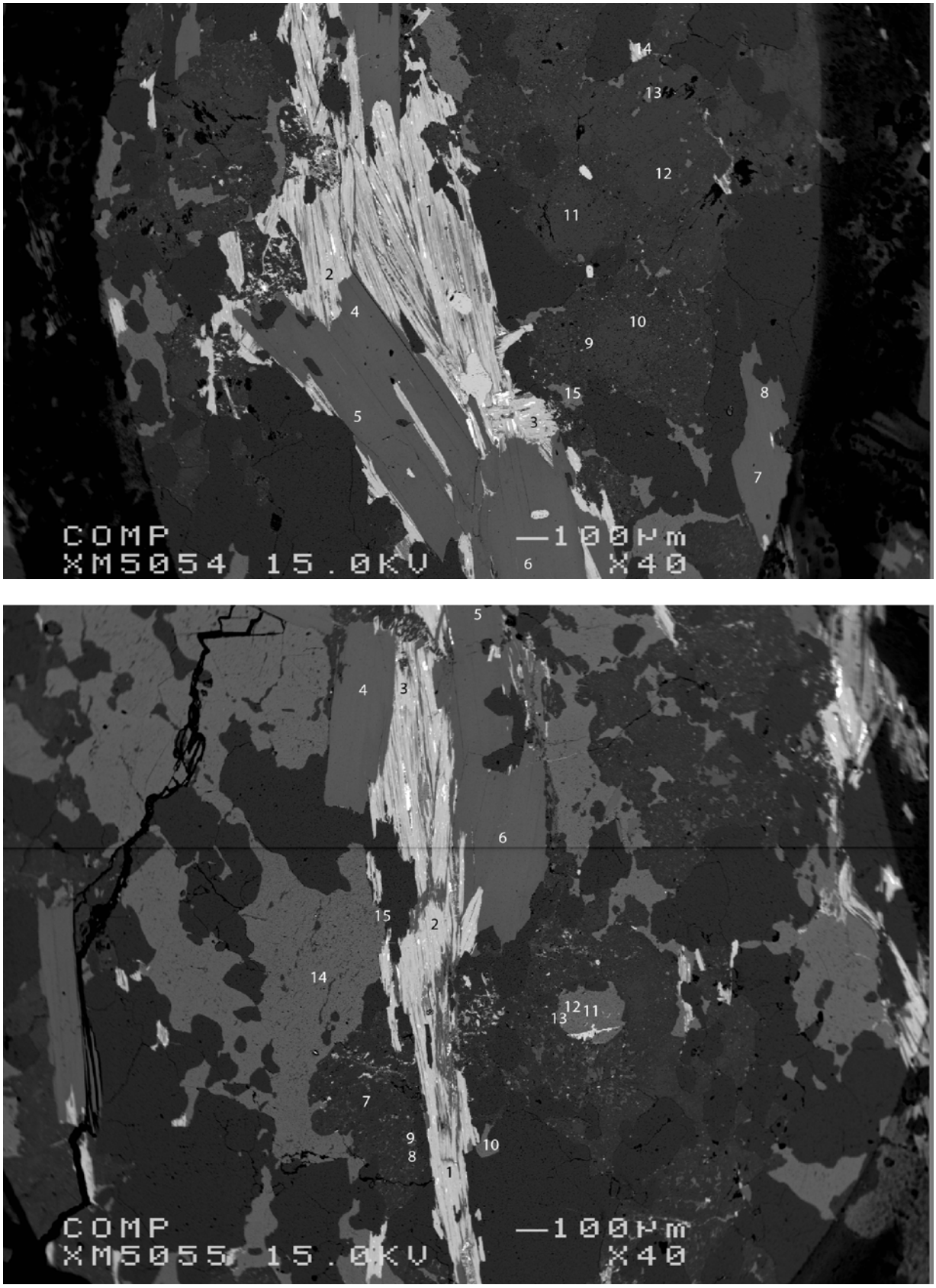

Figure 88. BSE of thin section JI 2-2, measuring locations 1 (top) and 2 (bottom).

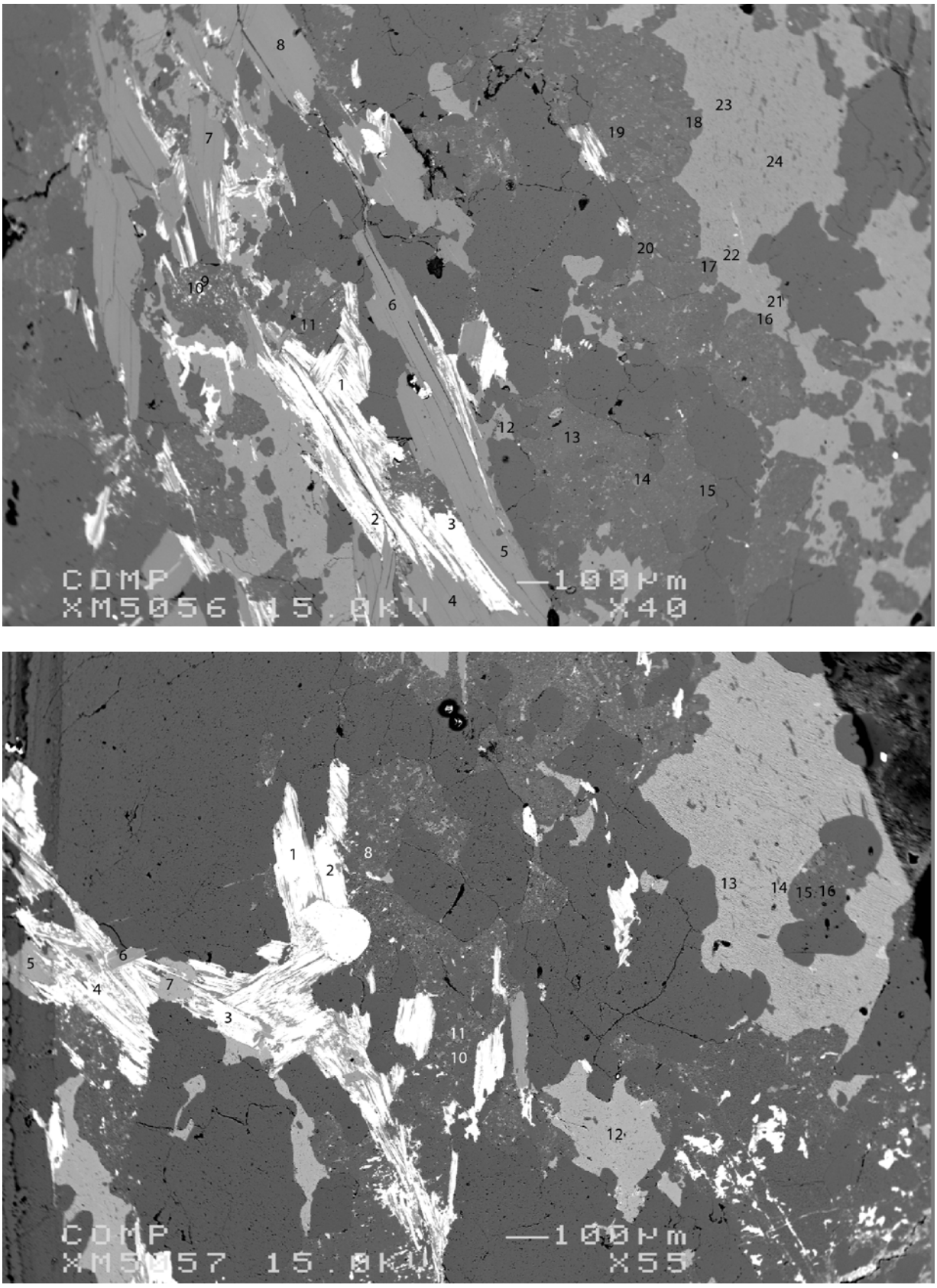

Figure 89. BSE of thin section JI 2-2, measuring locations 3 (top) and 4 (bottom).

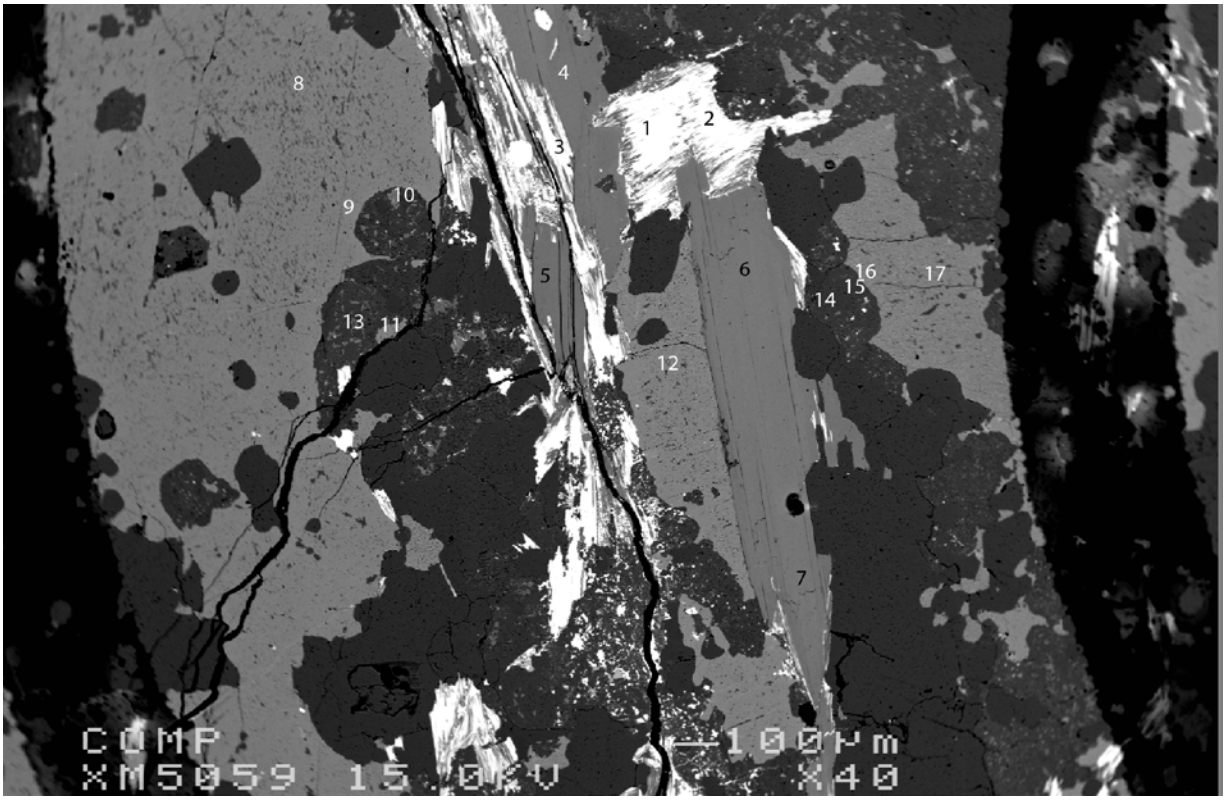

Figure 90. BSE of thin section JI 2-2, measuring location 5.

point	1-4	1-5	1-6	1-7	1-8	2-4	2-5	2-6	3-4
Na2O	0,466	0,500	0,459	0,458	0,478	0,488	0,553	0,482	0,409
SiO2	46,350	46,730	46,580	48,260	46,780	47,170	46,220	47,450	47,420
MnO	0,047	0,056	0,086	0,018	0,009	0,038	0,000	0,000	0,111
K2O	10,670	10,570	10,650	10,270	10,580	10,660	10,740	10,670	11,040
MgO	1,010	1,056	1,220	1,548	1,115	1,111	0,879	1,113	0,990
Al2O3	32,760	32,320	31,580	30,070	32,180	32,000	33,490	31,880	32,630
FeO	3,710	3,670	3,810	3,910	3,230	3,450	3,240	3,700	3,340
CaO	0,032	0,026	0,000	0,035	0,036	0,009	0,035	0,010	0,000
TiO2	0,950	0,793	0,805	0,539	0,772	0,754	0,633	0,747	1,016
Cr2O3	0,000	0,000	0,023	0,000	0,000	0,019	0,000	0,000	0,023
Cl	0,007	0,000	0,008	0,000	0,000	0,015	0,011	0,000	0,012
F	1,077	1,560	1,281	1,351	0,999	1,248	0,979	1,311	0,695
Total	97,079	97,280	96,501	96,459	96,180	96,961	96,778	97,363	97,686
Na(I)	0,061	0,066	0,061	0,061	0,063	0,064	0,072	0,063	0,053
Si(IV)	3,137	3,180	3,186	3,291	3,178	3,198	3,124	3,209	3,162
Mn(II)	0,003	0,003	0,005	0,001	0,001	0,002	0,000	0,000	0,006
K(I)	0,921	0,918	0,929	0,893	0,917	0,922	0,926	0,920	0,939
Mg(II)	0,102	0,107	0,124	0,157	0,113	0,112	0,089	0,112	0,098
Al(III)	2,613	2,592	2,545	2,417	2,577	2,557	2,668	2,541	2,564
Fe(II)	0,210	0,209	0,218	0,223	0,184	0,196	0,183	0,209	0,186
Ca(II)	0,002	0,002	0,000	0,003	0,003	0,001	0,003	0,001	0,000
Ti(IV)	0,048	0,041	0,041	0,028	0,039	0,038	0,032	0,038	0,051
Cr(III)	0,000	0,000	0,001	0,000	0,000	0,001	0,000	0,000	0,001
F	0,230	0,336	0,277	0,291	0,215	0,268	0,209	0,280	0,147
Σ cations	7,097	7,117	7,111	7,073	7,074	7,091	7,097	7,093	7,062
charge	22,194	22,283	22,233	22,245	22,181	22,225	22,176	22,236	22,123

Table 44. EMP measurements of representative muscovite of JI 2-2 based on 11 oxygen.

point	3-5	3-6	3-7	3-8	4-6	5-4	5-5	5-6	5-7
Na2O	0,451	0,471	0,512	0,487	0,511	0,541	0,517	0,476	0,324
SiO2	47,470	47,080	46,150	46,630	45,350	45,800	45,780	47,050	46,990
MnO	0,022	0,018	0,036	0,044	0,000	0,000	0,018	0,080	0,011
K2O	10,910	10,760	10,930	10,640	10,920	10,790	10,870	10,680	10,850
MgO	1,111	1,006	0,782	1,055	0,498	0,827	0,787	1,120	1,158
Al2O3	31,890	32,350	33,900	32,560	35,570	33,780	33,990	32,150	31,610
FeO	3,530	3,330	3,140	3,570	3,090	3,500	3,220	3,500	3,780
CaO	0,000	0,018	0,008	0,033	0,010	0,000	0,012	0,000	0,023
TiO2	0,884	0,977	0,726	0,938	0,688	0,707	0,698	0,774	0,545
Cr2O3	0,000	0,000	0,000	0,000	0,000	0,000	0,000	0,020	0,011
Cl	0,000	0,000	0,000	0,013	0,000	0,010	0,011	0,000	0,009
F	1,246	1,014	0,587	1,414	0,533	0,982	0,738	1,251	0,985
Total	97,514	97,023	96,771	97,384	97,170	96,936	96,641	97,100	96,298
Na(I)	0,059	0,062	0,067	0,064	0,066	0,071	0,068	0,063	0,043
Si(IV)	3,203	3,175	3,098	3,162	3,029	3,098	3,089	3,187	3,200
Mn(II)	0,001	0,001	0,002	0,003	0,000	0,000	0,001	0,005	0,001
K(I)	0,939	0,926	0,936	0,920	0,930	0,931	0,936	0,923	0,943
Mg(II)	0,112	0,101	0,078	0,107	0,050	0,083	0,079	0,113	0,118
Al(III)	2,536	2,571	2,682	2,602	2,800	2,693	2,703	2,567	2,537
Fe(II)	0,199	0,188	0,176	0,202	0,173	0,198	0,182	0,198	0,215
Ca(II)	0,000	0,001	0,001	0,002	0,001	0,000	0,001	0,000	0,002
Ti(IV)	0,045	0,050	0,037	0,048	0,035	0,036	0,035	0,039	0,028
Cr(III)	0,000	0,000	0,000	0,000	0,000	0,000	0,000	0,001	0,001
F	0,266	0,216	0,125	0,303	0,113	0,210	0,157	0,268	0,212
Σ cations	7,095	7,074	7,078	7,110	7,083	7,110	7,093	7,095	7,086
charge	22,224	22,182	22,105	22,255	22,095	22,177	22,133	22,226	22,179

point	1-1	1-2	1-3	2-1	2-2	2-3	3-1	3-2	3-3	4-1	4-2	4-3	4-4	5-1	5-2	5-3
Na2O	0,010	0,018	0,103	0,036	0,012	0,008	0,082	0,027	0,036	0,015	0,007	0,000	0,030	0,102	0,097	0,007
SiO2	26,110	23,810	24,510	25,200	25,380	27,330	23,800	24,830	23,590	23,400	23,550	23,500	24,130	23,350	23,350	23,600
MnO	0,318	0,442	0,313	0,352	0,288	0,305	0,386	0,332	0,410	0,376	0,552	0,459	0,375	0,459	0,454	0,459
K2O	1,230	0,013	0,070	0,460	1,023	1,790	0,019	0,035	0,035	0,007	0,000	0,142	0,421	0,022	0,014	0,062
MgO	4,260	4,110	4,470	4,820	4,130	4,660	4,160	4,500	3,910	4,250	4,410	4,380	4,860	4,540	4,570	4,310
Al2O3	21,480	21,600	21,280	21,090	20,420	19,760	21,410	20,410	22,030	21,850	21,960	22,260	21,030	21,720	21,810	21,350
FeO	32,580	39,200	39,370	37,440	33,080	34,990	39,970	39,490	39,480	39,790	38,950	38,580	38,270	39,180	38,960	38,760
CaO	0,031	0,000	0,063	0,009	0,129	0,031	0,022	0,095	0,013	0,025	0,020	0,000	0,009	0,079	0,067	0,014
TiO2	4,560	0,144	0,255	0,522	6,160	2,140	0,057	0,125	0,092	0,075	0,102	0,145	0,149	0,086	0,082	0,115
Cr2O3	0,000	0,000	0,032	0,000	0,000	0,026	0,000	0,028	0,000	0,010	0,000	0,000	0,000	0,000	0,013	0,008
Cl	0,000	0,010	0,000	0,017	0,000	0,000	0,010	0,018	0,000	0,008	0,000	0,000	0,013	0,010	0,000	0,000
F	0,043	0,000	0,000	0,000	0,000	0,000	0,000	0,000	0,000	0,000	0,000	0,000	0,000	0,000	0,000	0,000
Total	90,621	89,347	90,466	89,946	90,622	91,040	89,916	89,890	89,595	89,806	89,551	89,467	89,285	89,547	89,417	88,684
Na(I)	0,002	0,003	0,017	0,006	0,002	0,001	0,014	0,005	0,006	0,003	0,001	0,000	0,005	0,017	0,017	0,001
Si(IV)	2,181	2,090	2,121	2,172	2,131	2,304	2,084	2,165	2,067	2,051	2,061	2,054	2,114	2,049	2,049	2,087
Mn(II)	0,022	0,033	0,023	0,026	0,020	0,022	0,029	0,025	0,030	0,028	0,041	0,034	0,028	0,034	0,034	0,034
K(I)	0,131	0,001	0,008	0,051	0,110	0,192	0,002	0,004	0,004	0,001	0,000	0,016	0,047	0,002	0,002	0,007
Mg(II)	0,530	0,538	0,577	0,619	0,517	0,586	0,543	0,585	0,511	0,555	0,575	0,571	0,635	0,594	0,598	0,568
Al(III)	2,115	2,234	2,170	2,143	2,021	1,963	2,210	2,098	2,275	2,257	2,265	2,293	2,172	2,246	2,256	2,225
Fe(II)	2,276	2,877	2,849	2,699	2,323	2,467	2,927	2,880	2,893	2,916	2,850	2,820	2,804	2,875	2,859	2,866
Ca(II)	0,003	0,000	0,006	0,001	0,012	0,003	0,002	0,009	0,001	0,002	0,002	0,000	0,001	0,007	0,006	0,001
Ti(IV)	0,287	0,010	0,017	0,034	0,389	0,136	0,004	0,008	0,006	0,005	0,007	0,010	0,010	0,006	0,005	0,008
Cr(III)	0,000	0,000	0,002	0,000	0,000	0,002	0,000	0,002	0,000	0,001	0,000	0,000	0,000	0,000	0,001	0,001
F	0,011	0,000	0,000	0,000	0,000	0,000	0,000	0,000	0,000	0,000	0,000	0,000	0,000	0,000	0,000	0,000
Σ cations	7,546	7,786	7,789	7,751	7,525	7,675	7,815	7,781	7,794	7,818	7,801	7,798	7,816	7,832	7,826	7,797
charge	22,010	22,000	22,000	22,000	22,000	22,000	22,000	22,000	22,000	22,000	22,000	22,000	22,000	22,000	22,000	22,000

Table 45. EMP measurements of representative muscovite of JI 2-2 based on 11 oxygen (continued) (top) and biotite based on 11 oxygen (bottom).

point	1-9	1-10	1-11	1-12	1-13	1-14	1-15	2-7	2-8	2-10	2-11	2-12	2-13
Na2O	9,160	8,510	9,320	9,680	0,645	0,024	0,744	10,340	10,910	0,960	0,825	0,588	10,810
SiO2	63,820	60,640	63,130	63,690	64,900	25,380	64,220	65,530	67,270	64,770	65,550	64,470	66,260
MnO	0,000	0,000	0,000	0,040	0,011	0,335	0,000	0,022	0,000	0,022	0,000	0,000	0,036
K2O	0,649	2,080	0,282	0,169	16,470	0,379	15,980	1,152	0,181	15,770	16,060	16,490	0,790
MgO	0,009	0,080	0,013	0,000	0,010	4,720	0,013	0,095	0,041	0,000	0,000	0,019	0,073
Al2O3	23,630	24,610	23,250	23,310	19,250	21,580	19,270	21,590	20,710	19,000	19,220	19,310	21,310
FeO	0,009	0,132	0,010	0,009	0,025	37,490	0,097	0,323	0,058	0,099	0,056	0,061	0,209
CaO	3,030	1,440	3,630	3,500	0,034	0,016	0,045	0,409	0,795	0,012	0,033	0,033	0,672
TiO2	0,016	0,000	0,021	0,000	0,000	0,216	0,000	0,000	0,010	0,000	0,000	0,034	0,011
Cr2O3	0,000	0,007	0,000	0,000	0,007	0,010	0,000	0,000	0,000	0,000	0,010	0,000	0,000
Cl	0,000	0,014	0,013	0,000	0,025	0,011	0,000	0,024	0,000	0,000	0,000	0,000	0,000
F	0,018	0,000	0,000	0,040	0,105	0,000	0,162	0,079	0,000	0,052	0,000	0,060	0,118
Total	100,341	97,513	99,670	100,438	101,482	90,160	100,530	99,564	99,975	100,686	101,754	101,067	100,290
Na(I)	0,781	0,749	0,801	0,826	0,057	0,003	0,067	0,887	0,926	0,085	0,073	0,052	0,921
Si(IV)	2,806	2,754	2,798	2,802	2,968	1,584	2,964	2,900	2,944	2,975	2,976	2,960	2,911
Mn(II)	0,000	0,000	0,000	0,001	0,000	0,018	0,000	0,001	0,000	0,001	0,000	0,000	0,001
K(I)	0,036	0,121	0,016	0,009	0,961	0,030	0,941	0,065	0,010	0,924	0,930	0,966	0,044
Mg(II)	0,001	0,005	0,001	0,000	0,001	0,439	0,001	0,006	0,003	0,000	0,000	0,001	0,005
Al(III)	1,224	1,317	1,214	1,209	1,038	1,587	1,048	1,126	1,068	1,029	1,028	1,045	1,104
Fe(II)	0,000	0,005	0,000	0,000	0,001	1,956	0,004	0,012	0,002	0,004	0,002	0,002	0,008
Ca(II)	0,143	0,070	0,172	0,165	0,002	0,001	0,002	0,019	0,037	0,001	0,002	0,002	0,032
Ti(IV)	0,001	0,000	0,001	0,000	0,000	0,010	0,000	0,000	0,000	0,000	0,000	0,001	0,000
Cr(III)	0,000	0,000	0,000	0,000	0,000	0,000	0,000	0,000	0,000	0,000	0,000	0,000	0,000
F	0,003	0,000	0,000	0,006	0,015	0,000	0,024	0,011	0,000	0,008	0,000	0,009	0,016
Σ cations	4,991	5,022	5,003	5,013	5,028	5,629	5,026	5,017	4,990	5,019	5,011	5,029	5,026
charge	16,002	16,000	16,000	16,005	16,013	16,000	16,020	16,009	16,000	16,006	16,000	16,007	16,014

point	2-14	2-15	3-10	3-11	3-12	3-13	3-15	3-16	3-17	3-18	3-19	3-20	3-21
Na2O	0,936	1,003	10,270	0,753	0,780	9,600	11,000	9,610	10,160	9,540	10,410	10,400	0,372
SiO2	64,220	64,870	65,590	64,360	64,210	64,110	66,630	61,890	64,760	63,940	65,440	64,760	62,270
MnO	0,000	0,047	0,011	0,000	0,007	0,000	0,000	0,000	0,018	0,000	0,031	0,000	0,020
K2O	15,060	15,630	1,210	16,150	16,070	0,302	0,479	1,250	0,117	1,970	1,410	0,780	16,580
MgO	0,337	0,051	0,102	0,034	0,000	0,025	0,013	0,032	0,012	0,038	0,128	0,030	0,016
Al2O3	18,880	19,060	21,940	19,090	19,150	23,110	21,740	22,780	22,640	23,660	22,120	22,130	18,890
FeO	0,151	0,070	0,661	0,099	0,034	0,040	0,049	0,130	0,040	0,276	0,456	0,162	0,049
CaO	0,107	0,000	0,690	0,014	0,018	3,200	1,158	1,940	2,370	0,678	0,319	1,048	0,049
TiO2	0,010	0,023	0,020	0,000	0,010	0,029	0,000	0,000	0,000	0,000	0,030	0,010	0,000
Cr2O3	0,010	0,000	0,036	0,000	0,000	0,000	0,019	0,000	0,000	0,000	0,024	0,029	0,000
Cl	0,049	0,037	0,000	0,007	0,000	0,000	0,014	0,014	0,000	0,013	0,000	0,000	0,017
F	0,000	0,000	0,000	0,000	0,000	0,014	0,126	0,886	0,000	0,009	0,000	0,083	0,000
Total	99,761	100,791	100,531	100,507	100,278	100,430	101,228	98,532	100,116	100,124	100,369	99,432	98,263
Na(I)	0,084	0,089	0,874	0,067	0,070	0,818	0,928	0,851	0,866	0,817	0,887	0,894	0,034
Si(IV)	2,968	2,973	2,880	2,965	2,963	2,816	2,900	2,826	2,845	2,823	2,877	2,871	2,948
Mn(II)	0,000	0,002	0,000	0,000	0,000	0,000	0,000	0,000	0,001	0,000	0,001	0,000	0,001
K(I)	0,888	0,914	0,068	0,949	0,946	0,017	0,027	0,073	0,007	0,111	0,079	0,044	1,001
Mg(II)	0,023	0,003	0,007	0,002	0,000	0,002	0,001	0,002	0,001	0,003	0,008	0,002	0,001
Al(III)	1,028	1,029	1,135	1,037	1,042	1,197	1,115	1,226	1,172	1,231	1,146	1,156	1,054
Fe(II)	0,006	0,003	0,024	0,004	0,001	0,001	0,002	0,005	0,001	0,010	0,017	0,006	0,002
Ca(II)	0,005	0,000	0,032	0,001	0,001	0,151	0,054	0,095	0,112	0,032	0,015	0,050	0,002
Ti(IV)	0,000	0,001	0,001	0,000	0,000	0,001	0,000	0,000	0,000	0,000	0,001	0,000	0,000
Cr(III)	0,000	0,000	0,001	0,000	0,000	0,000	0,001	0,000	0,000	0,000	0,001	0,001	0,000
F	0,000	0,000	0,000	0,000	0,000	0,002	0,017	0,128	0,000	0,001	0,000	0,012	0,000
Σ cations	5,003	5,013	5,023	5,025	5,024	5,002	5,027	5,077	5,004	5,026	5,032	5,024	5,043
charge	16,000	16,000	16,000	16,000	16,000	16,002	16,015	16,108	16,000	16,001	16,000	16,010	16,000

Table 46. EMP measurements of representative plagioclase of JI 2-2 based on 8 oxygen.

point	3-22	3-23	3-24	4-8	4-9	4-10	4-12	4-13	4-14	4-15	4-16	5-8	5-9
Na2O	0,404	1,220	0,943	11,420	11,440	11,260	0,638	1,127	0,794	10,910	10,510	0,632	1,015
SiO2	61,770	63,850	62,560	66,650	66,730	67,140	62,780	61,720	63,680	65,580	65,760	60,770	64,620
MnO	0,020	0,000	0,036	0,000	0,027	0,000	0,016	0,013	0,000	0,000	0,011	0,058	0,000
K2O	16,410	15,210	15,780	0,193	0,095	0,148	16,360	15,510	16,200	0,430	0,736	15,860	15,800
MgO	0,056	0,000	0,078	0,000	0,010	0,013	0,000	0,039	0,010	0,028	0,019	0,265	0,008
Al2O3	19,040	19,370	19,080	20,610	20,460	20,600	19,230	18,950	19,130	21,020	21,680	18,490	19,210
FeO	0,014	0,000	0,032	0,067	0,029	0,089	0,000	0,000	0,023	0,038	0,087	0,115	0,025
CaO	0,056	0,021	0,054	0,305	0,420	0,303	0,013	0,034	0,044	0,467	0,580	0,079	0,011
TiO2	0,000	0,027	0,012	0,000	0,000	0,000	0,010	0,000	0,000	0,000	0,000	0,009	0,000
Cr2O3	0,000	0,000	0,000	0,000	0,000	0,027	0,000	0,000	0,000	0,012	0,000	0,000	0,000
Cl	0,015	0,000	0,038	0,010	0,000	0,000	0,000	0,014	0,000	0,044	0,023	0,030	0,010
F	0,162	0,000	0,072	0,020	0,000	0,000	0,000	0,000	0,084	0,016	0,240	0,000	0,000
Total	97,948	99,698	98,685	99,275	99,211	99,580	99,047	97,407	99,966	98,545	99,645	96,308	100,700
Na(I)	0,037	0,109	0,086	0,977	0,979	0,959	0,058	0,104	0,071	0,942	0,901	0,059	0,090
Si(IV)	2,941	2,954	2,944	2,941	2,945	2,949	2,943	2,938	2,958	2,919	2,908	2,936	2,966
Mn(II)	0,001	0,000	0,001	0,000	0,001	0,000	0,001	0,001	0,000	0,000	0,000	0,002	0,000
K(I)	0,997	0,898	0,947	0,011	0,005	0,008	0,978	0,942	0,960	0,024	0,042	0,977	0,925
Mg(II)	0,004	0,000	0,005	0,000	0,001	0,001	0,000	0,003	0,001	0,002	0,001	0,019	0,001
Al(III)	1,068	1,056	1,058	1,072	1,064	1,066	1,062	1,063	1,047	1,103	1,130	1,053	1,039
Fe(II)	0,001	0,000	0,001	0,002	0,001	0,003	0,000	0,000	0,001	0,001	0,003	0,005	0,001
Ca(II)	0,003	0,001	0,003	0,014	0,020	0,014	0,001	0,002	0,002	0,022	0,027	0,004	0,001
Ti(IV)	0,000	0,001	0,000	0,000	0,000	0,000	0,000	0,000	0,000	0,000	0,000	0,000	0,000
Cr(III)	0,000	0,000	0,000	0,000	0,000	0,001	0,000	0,000	0,000	0,000	0,000	0,000	0,000
F	0,024	0,000	0,011	0,003	0,000	0,000	0,000	0,000	0,012	0,002	0,034	0,000	0,000
Σ cations	5,052	5,020	5,047	5,018	5,015	5,001	5,044	5,053	5,040	5,013	5,013	5,056	5,022
charge	16,021	16,000	16,009	16,002	16,000	16,000	16,000	16,000	16,010	16,002	16,028	16,000	16,000

point	5-11	5-12	5-13	5-14	5-15	5-16	5-17
Na2O	0,737	0,746	10,960	11,400	11,390	0,799	0,719
SiO2	63,060	63,120	66,100	67,150	67,030	64,720	62,900
MnO	0,036	0,000	0,000	0,000	0,000	0,022	0,029
K2O	16,100	16,200	0,200	0,110	0,171	15,940	16,020
MgO	0,000	0,000	0,016	0,010	0,000	0,039	0,075
Al2O3	19,180	19,250	21,000	20,440	20,440	19,540	19,020
FeO	0,010	0,007	0,092	0,016	0,010	0,079	0,070
CaO	0,017	0,015	0,955	0,217	0,175	0,060	0,034
TiO2	0,012	0,000	0,000	0,000	0,000	0,047	0,014
Cr2O3	0,000	0,019	0,016	0,000	0,000	0,000	0,000
Cl	0,000	0,000	0,010	0,000	0,000	0,023	0,009
F	0,023	0,091	0,165	0,077	0,000	0,000	0,000
Total	99,174	99,449	99,513	99,420	99,217	101,268	98,890
Na(I)	0,067	0,068	0,939	0,973	0,973	0,071	0,065
Si(IV)	2,949	2,949	2,922	2,956	2,954	2,955	2,950
Mn(II)	0,001	0,000	0,000	0,000	0,000	0,001	0,001
K(I)	0,961	0,965	0,011	0,006	0,010	0,929	0,958
Mg(II)	0,000	0,000	0,001	0,001	0,000	0,003	0,005
Al(III)	1,057	1,060	1,094	1,061	1,062	1,052	1,051
Fe(II)	0,000	0,000	0,003	0,001	0,000	0,003	0,003
Ca(II)	0,001	0,001	0,045	0,010	0,008	0,003	0,002
Ti(IV)	0,000	0,000	0,000	0,000	0,000	0,002	0,000
Cr(III)	0,000	0,001	0,001	0,000	0,000	0,000	0,000
F	0,003	0,013	0,023	0,011	0,000	0,000	0,000
Σ cations	5,037	5,043	5,016	5,008	5,007	5,017	5,036
charge	16,003	16,011	16,019	16,009	16,000	16,000	16,000

Table 47. EMP measurements of representative plagioclase of JI 2-2 based on 8 oxygen (continued).

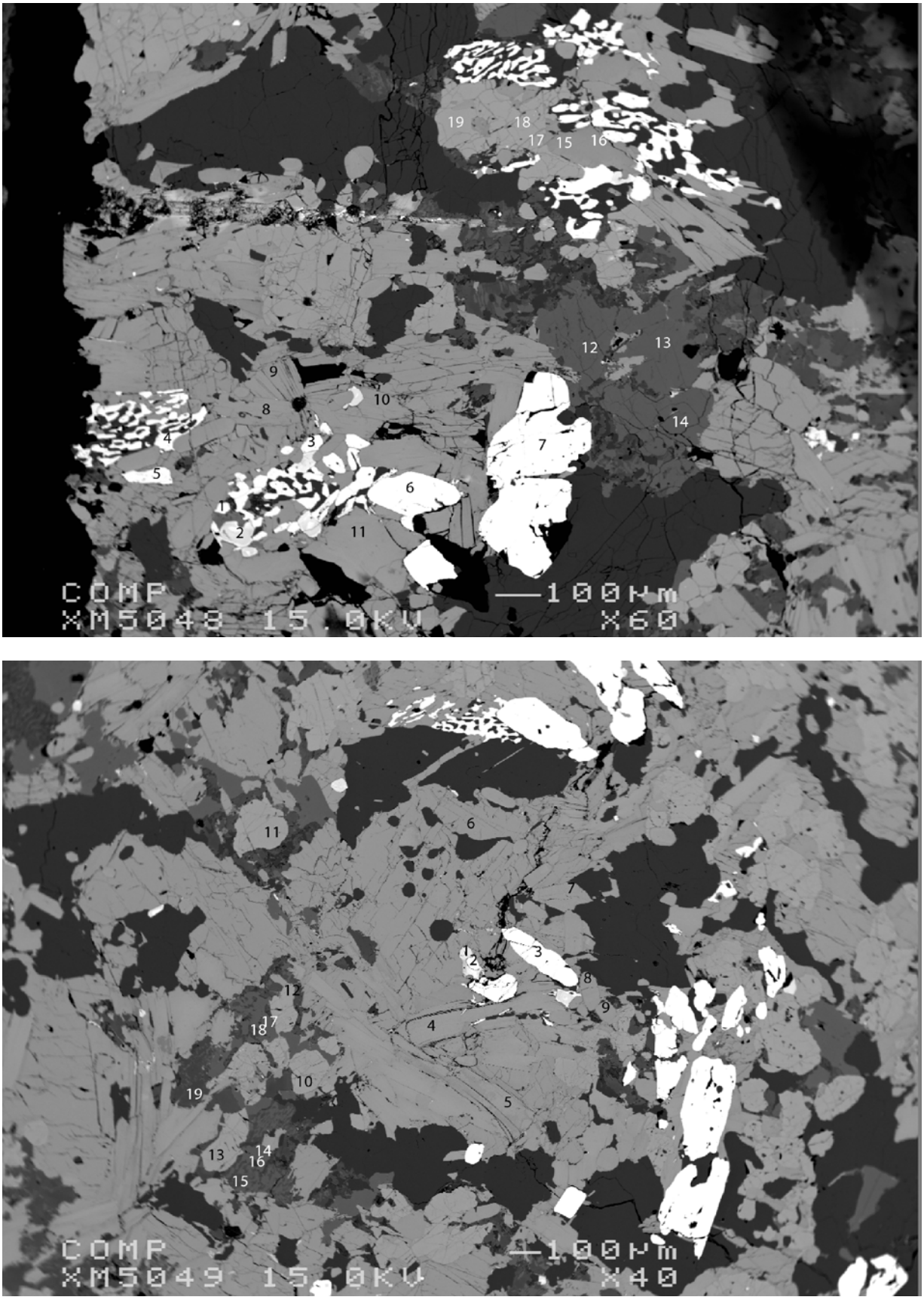

Figure 91. BSE of thin section JI 4-6, measuring locations 1 (top) and 2 (bottom).

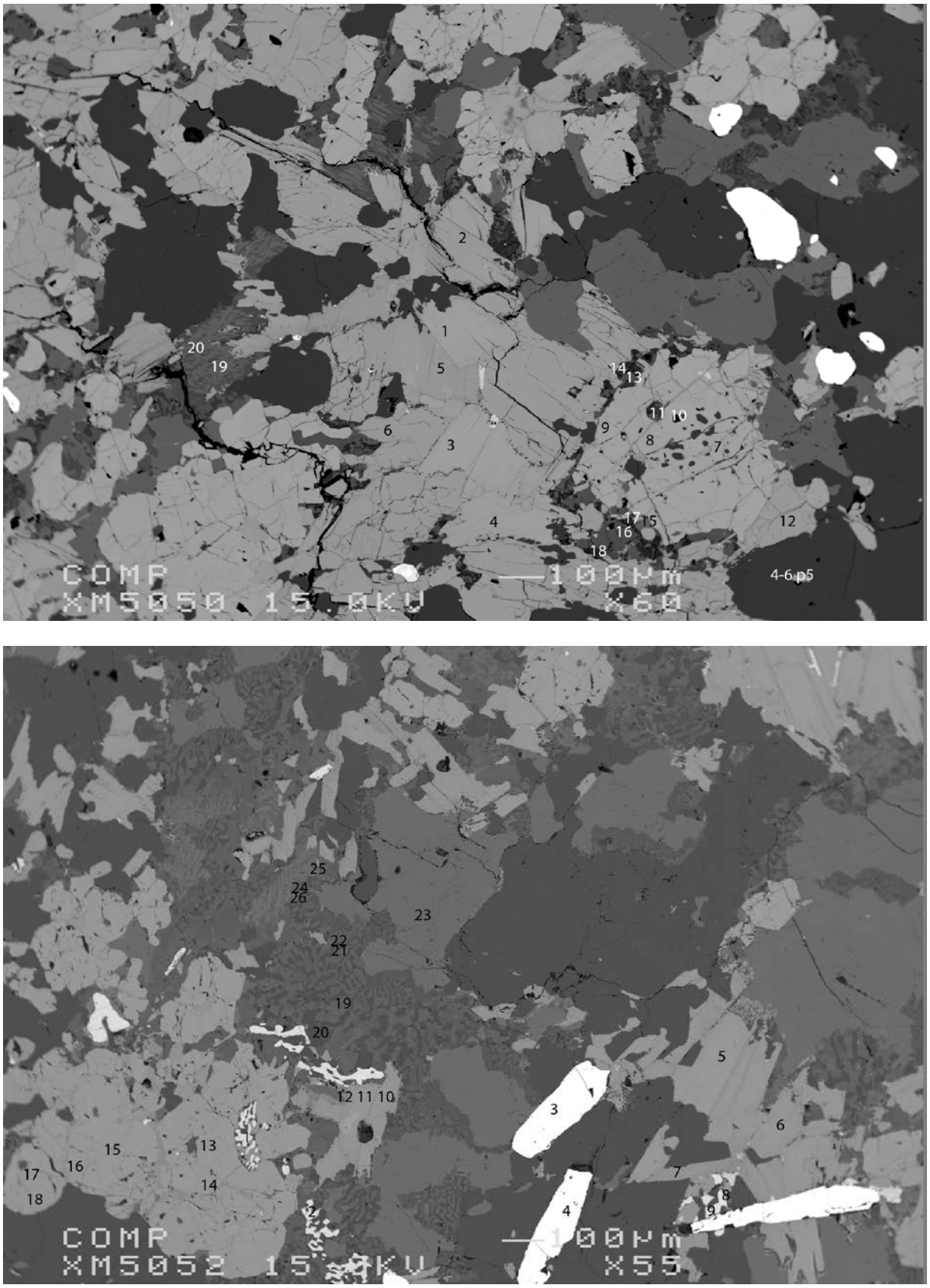

Figure 92. BSE of thin section JI 4-6, measuring location 3 (top) and 4 (bottom).

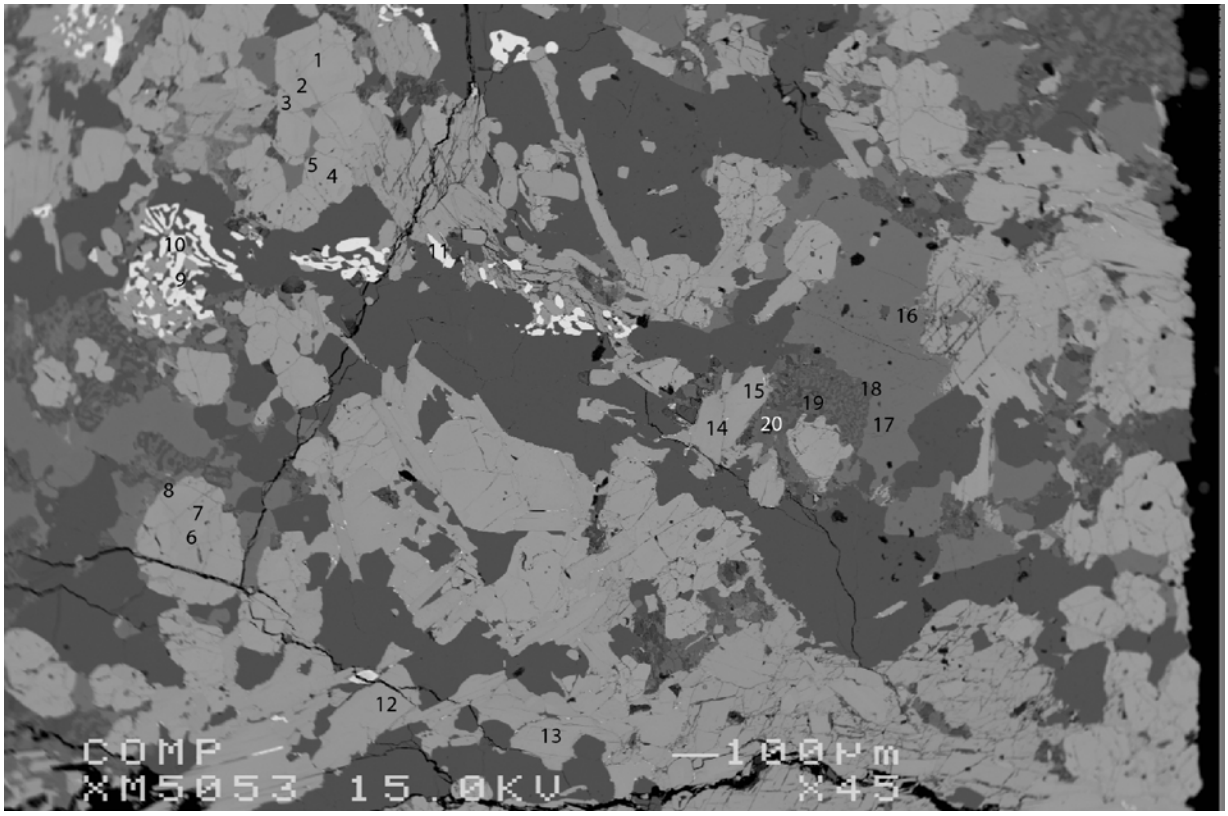

Figure 93. BSE of thin section JI 4-6, measuring location 7.

point	1-17	1-18	1-19	2-10	2-11	2-12	2-13	3-7	3-8	3-9	3-10	4-13	4-14
Na2O	0,000	0,000	0,027	0,040	0,036	0,014	0,065	0,111	0,071	0,085	0,023	0,027	0,098
SiO2	38,130	38,130	37,980	37,980	38,050	37,940	37,910	38,110	37,970	38,010	37,870	38,010	37,680
MnO	1,264	0,938	0,691	0,785	0,668	0,880	0,601	0,708	0,747	0,849	0,710	0,700	0,684
K2O	0,019	0,012	0,000	0,000	0,000	0,000	0,000	0,042	0,020	0,010	0,000	0,000	0,022
MgO	0,769	0,975	1,085	1,161	1,135	1,175	1,167	1,213	1,161	1,104	1,366	1,253	1,165
Al2O3	21,960	21,800	21,280	21,760	21,850	21,900	21,920	21,830	21,620	21,760	21,480	21,910	21,790
FeO	29,850	30,540	29,090	30,990	29,740	31,200	29,250	29,630	29,890	29,010	30,410	30,200	28,760
CaO	10,360	9,790	11,410	9,110	10,420	8,480	11,140	10,210	10,070	10,690	9,670	10,080	10,940
TiO2	0,101	0,014	0,101	0,070	0,069	0,039	0,214	0,077	0,010	0,124	0,056	0,055	0,052
Cr2O3	0,009	0,014	0,028	0,000	0,008	0,000	0,000	0,000	0,000	0,000	0,000	0,000	0,000
Cl	0,015	0,000	0,000	0,000	0,016	0,000	0,000	0,013	0,000	0,007	0,000	0,014	0,024
F	0,000	0,000	0,000	0,000	0,000	0,000	0,000	0,000	0,000	0,000	0,000	0,000	0,000
Total	102,476	102,213	101,691	101,896	101,992	101,627	102,267	101,944	101,558	101,650	101,584	102,248	101,215
Na(I)	0,000	0,000	0,004	0,006	0,005	0,002	0,010	0,017	0,011	0,013	0,004	0,004	0,015
Si(IV)	2,980	2,988	2,988	2,986	2,981	2,988	2,962	2,985	2,990	2,984	2,985	2,974	2,972
Mn(II)	0,084	0,062	0,046	0,052	0,044	0,059	0,040	0,047	0,050	0,056	0,047	0,046	0,046
K(I)	0,002	0,001	0,000	0,000	0,000	0,000	0,000	0,004	0,002	0,001	0,000	0,000	0,002
Mg(II)	0,090	0,114	0,127	0,136	0,133	0,138	0,136	0,142	0,136	0,129	0,161	0,146	0,137
Al(III)	2,023	2,014	1,973	2,016	2,018	2,033	2,018	2,015	2,006	2,013	1,995	2,020	2,025
Fe(II)	1,951	2,002	1,914	2,037	1,949	2,055	1,911	1,941	1,968	1,905	2,004	1,976	1,897
Ca(II)	0,868	0,822	0,962	0,767	0,875	0,716	0,932	0,857	0,850	0,899	0,817	0,845	0,924
Ti(IV)	0,006	0,001	0,006	0,004	0,004	0,002	0,013	0,005	0,001	0,007	0,003	0,003	0,003
Cr(III)	0,001	0,001	0,002	0,000	0,000	0,000	0,000	0,000	0,000	0,000	0,000	0,000	0,000
F	0,000	0,000	0,000	0,000	0,000	0,000	0,000	0,000	0,000	0,000	0,000	0,000	0,000
Σ cations	8,003	8,004	8,021	8,005	8,009	7,994	8,022	8,013	8,013	8,009	8,016	8,015	8,021
charge	24,000	24,000	24,000	24,000	24,000	24,000	24,000	24,000	24,000	24,000	24,000	24,000	24,000

Table 48. EMP measurements of representative garnet of JI 4-6 based on 12 oxygen.

point	4-15	4-16	4-17	4-18	5-1	5-2	5-3	5-4	5-5	5-6	5-7	5-8
Na2O	0,086	0,074	0,087	0,104	0,000	0,015	0,010	0,029	0,000	0,000	0,036	0,030
SiO2	37,840	37,790	37,900	37,700	37,850	38,260	37,740	37,220	37,770	38,130	38,330	37,930
MnO	0,685	0,714	0,708	0,750	0,745	0,423	0,790	1,125	0,857	0,401	0,505	0,611
K2O	0,028	0,025	0,015	0,006	0,000	0,000	0,000	0,031	0,000	0,021	0,000	0,000
MgO	1,089	1,200	1,105	1,067	1,416	0,595	1,003	1,024	0,928	0,491	0,582	1,067
Al2O3	21,590	21,710	22,020	21,950	22,140	22,650	21,560	21,940	21,410	22,550	22,510	22,200
FeO	29,080	30,730	30,180	28,640	31,480	26,300	29,120	30,850	28,750	25,760	26,030	28,590
CaO	11,050	9,310	10,100	10,950	8,400	13,500	11,390	9,450	11,390	14,430	14,140	11,220
TiO2	0,106	0,013	0,000	0,063	0,000	0,036	0,109	0,051	0,125	0,050	0,055	0,032
Cr2O3	0,000	0,000	0,010	0,021	0,000	0,000	0,000	0,000	0,000	0,000	0,000	0,010
Cl	0,028	0,007	0,014	0,000	0,000	0,016	0,000	0,000	0,000	0,000	0,010	0,000
F	0,000	0,000	0,000	0,000	0,000	0,000	0,000	0,000	0,000	0,000	0,000	0,000
Total	101,583	101,571	102,138	101,252	102,031	101,795	101,723	101,720	101,230	101,833	102,198	101,690
Na(I)	0,013	0,011	0,013	0,016	0,000	0,002	0,002	0,004	0,000	0,000	0,005	0,005
Si(IV)	2,978	2,981	2,970	2,970	2,970	2,975	2,970	2,943	2,983	2,966	2,972	2,970
Mn(II)	0,046	0,048	0,047	0,050	0,050	0,028	0,053	0,075	0,057	0,026	0,033	0,041
K(I)	0,003	0,003	0,001	0,001	0,000	0,000	0,000	0,003	0,000	0,002	0,000	0,000
Mg(II)	0,128	0,141	0,129	0,125	0,166	0,069	0,118	0,121	0,109	0,057	0,067	0,125
Al(III)	2,003	2,018	2,034	2,038	2,048	2,076	2,000	2,045	1,993	2,067	2,057	2,049
Fe(II)	1,914	2,027	1,978	1,887	2,066	1,710	1,916	2,040	1,899	1,676	1,688	1,872
Ca(II)	0,932	0,787	0,848	0,924	0,706	1,125	0,960	0,801	0,964	1,202	1,175	0,941
Ti(IV)	0,006	0,001	0,000	0,004	0,000	0,002	0,006	0,003	0,007	0,003	0,003	0,002
Cr(III)	0,000	0,000	0,001	0,001	0,000	0,000	0,000	0,000	0,000	0,000	0,000	0,001
F	0,000	0,000	0,000	0,000	0,000	0,000	0,000	0,000	0,000	0,000	0,000	0,000
Σ cations	8,022	8,016	8,020	8,015	8,006	7,986	8,025	8,035	8,013	7,999	8,000	8,005
charge	24,000	24,000	24,000	24,000	24,000	24,000	24,000	24,000	24,000	24,000	24,000	24,000

point	1-8	1-9	1-10	1-11	2-4	2-5	2-7	3-1	3-3	3-4
Na2O	0,077	0,101	0,052	0,130	0,114	0,146	0,126	0,152	0,118	0,121
SiO2	35,050	35,030	34,860	34,510	34,790	34,630	34,700	34,240	34,400	34,660
MnO	0,116	0,093	0,142	0,067	0,086	0,138	0,101	0,116	0,103	0,120
K2O	9,530	9,490	9,510	9,350	9,440	9,500	9,280	9,540	9,450	9,460
MgO	3,720	3,740	3,690	3,660	3,860	3,890	4,510	3,730	3,770	4,070
Al2O3	17,380	17,890	17,390	17,080	16,890	16,310	16,730	16,630	16,520	16,560
FeO	28,070	28,260	28,120	27,410	28,750	29,040	28,150	29,260	29,050	29,050
CaO	0,000	0,000	0,010	0,000	0,000	0,000	0,133	0,009	0,000	0,010
TiO2	3,040	2,460	3,010	3,480	3,470	3,630	2,570	3,460	3,240	2,780
Cr2O3	0,000	0,000	0,000	0,000	0,023	0,000	0,010	0,000	0,000	0,000
Cl	0,123	0,108	0,102	0,137	0,127	0,101	0,139	0,122	0,133	0,109
F	0,000	0,000	0,000	0,000	0,000	0,000	0,034	0,042	0,000	0,144
Total	97,106	97,172	96,887	95,824	97,550	97,385	96,484	97,302	96,785	97,084
Na(I)	0,012	0,015	0,008	0,020	0,017	0,022	0,019	0,023	0,018	0,019
Si(IV)	2,741	2,736	2,734	2,731	2,720	2,722	2,739	2,702	2,722	2,739
Mn(II)	0,008	0,006	0,009	0,004	0,006	0,009	0,007	0,008	0,007	0,008
K(I)	0,951	0,946	0,951	0,944	0,942	0,953	0,935	0,960	0,954	0,954
Mg(II)	0,434	0,435	0,431	0,432	0,450	0,456	0,531	0,439	0,445	0,479
Al(III)	1,602	1,647	1,607	1,593	1,556	1,511	1,557	1,547	1,541	1,542
Fe(II)	1,836	1,846	1,844	1,814	1,880	1,909	1,858	1,931	1,922	1,920
Ca(II)	0,000	0,000	0,001	0,000	0,000	0,000	0,011	0,001	0,000	0,001
Ti(IV)	0,179	0,145	0,178	0,207	0,204	0,215	0,153	0,205	0,193	0,165
Cr(III)	0,000	0,000	0,000	0,000	0,001	0,000	0,001	0,000	0,000	0,000
F	0,000	0,000	0,000	0,000	0,000	0,000	0,008	0,010	0,000	0,036
Σ cations	7,761	7,776	7,764	7,747	7,776	7,796	7,810	7,816	7,801	7,826
charge	22,000	22,000	22,000	22,000	22,000	22,000	22,007	22,009	22,000	22,030

Table 49. EMP measurements of representative garnet of JI 4-6 based on 12 oxygen (continued) (top) and biotite based on 11 oxygen (bottom).

point	3-5	4-5	4-6	4-7	4-10	4-11	5-12	5-13	5-14	5-15
Na2O	0,317	0,088	0,147	0,174	0,183	0,120	0,145	0,084	0,133	0,094
SiO2	33,840	37,400	34,640	34,260	33,480	33,690	33,880	34,270	33,600	33,770
MnO	0,142	0,178	0,112	0,114	0,078	0,088	0,142	0,144	0,131	0,118
K2O	9,240	10,160	9,410	9,230	9,290	9,240	9,370	9,470	9,310	9,110
MgO	3,850	3,920	3,760	3,720	3,730	3,600	3,770	3,630	3,650	3,650
Al2O3	16,400	17,600	16,760	16,560	16,490	16,580	16,520	16,670	16,710	15,810
FeO	29,050	31,020	28,720	28,570	26,880	28,260	28,020	28,810	28,780	28,900
CaO	0,051	0,010	0,000	0,019	0,056	0,036	0,000	0,000	0,000	0,013
TiO2	2,900	4,220	3,420	3,260	3,190	3,330	3,770	3,950	3,810	4,740
Cr2O3	0,000	0,000	0,010	0,000	0,000	0,009	0,000	0,020	0,000	0,000
Cl	0,133	0,126	0,129	0,125	0,118	0,113	0,096	0,120	0,118	0,136
F	0,000	0,000	0,000	0,000	0,000	0,000	0,000	0,000	0,032	0,000
Total	95,923	104,723	97,108	96,032	93,494	95,066	95,712	97,167	96,275	96,340
Na(I)	0,049	0,012	0,022	0,027	0,029	0,019	0,022	0,013	0,021	0,015
Si(IV)	2,708	2,729	2,723	2,725	2,724	2,708	2,702	2,698	2,676	2,687
Mn(II)	0,010	0,011	0,007	0,008	0,005	0,006	0,010	0,010	0,009	0,008
K(I)	0,943	0,946	0,944	0,936	0,964	0,948	0,953	0,951	0,946	0,925
Mg(II)	0,459	0,426	0,441	0,441	0,452	0,431	0,448	0,426	0,433	0,433
Al(III)	1,547	1,513	1,553	1,552	1,581	1,571	1,553	1,547	1,568	1,483
Fe(II)	1,944	1,893	1,888	1,900	1,829	1,900	1,869	1,897	1,917	1,923
Ca(II)	0,004	0,001	0,000	0,002	0,005	0,003	0,000	0,000	0,000	0,001
Ti(IV)	0,175	0,232	0,202	0,195	0,195	0,201	0,226	0,234	0,228	0,284
Cr(III)	0,000	0,000	0,001	0,000	0,000	0,001	0,000	0,001	0,000	0,000
F	0,000	0,000	0,000	0,000	0,000	0,000	0,000	0,000	0,008	0,000
Σ cations	7,840	7,762	7,781	7,786	7,786	7,788	7,783	7,776	7,798	7,758
charge	22,000	22,000	22,000	22,000	22,000	22,000	22,000	22,000	22,007	22,000

point	1-12	1-13	1-14	1-15	1-16	2-14	2-15	2-16	2-17	2-18	2-19	3-13	3-14	3-15	3-16
Na2O	0,791	0,683	0,688	0,163	0,194	0,737	5,370	10,770	0,782	5,860	5,560	3,830	0,418	0,657	4,400
SiO2	63,330	63,030	63,120	35,150	34,480	63,530	54,210	67,440	63,430	55,980	55,690	51,400	50,150	63,090	52,390
MnO	0,031	0,000	0,000	0,080	0,108	0,000	0,013	0,000	0,000	0,000	0,000	0,000	0,020	0,025	0,013
K2O	15,530	15,670	15,630	9,560	9,410	15,600	0,134	0,176	15,500	0,127	0,104	0,072	3,230	15,530	0,068
MgO	0,000	0,014	0,000	3,810	4,010	0,000	0,000	0,000	0,010	0,000	0,000	0,015	4,280	0,000	0,000
Al2O3	18,990	19,210	19,230	17,780	16,770	19,160	29,250	21,380	19,060	28,150	29,130	31,660	25,430	19,160	30,900
FeO	0,027	0,049	0,081	27,920	28,390	0,076	0,168	0,020	0,142	0,117	0,226	0,341	3,810	0,269	0,217
CaO	0,000	0,000	0,014	0,052	0,017	0,000	10,570	1,050	0,000	9,710	10,250	13,190	1,061	0,112	12,290
TiO2	0,053	0,015	0,020	3,120	3,350	0,027	0,012	0,000	0,016	0,043	0,013	0,013	0,015	0,044	0,000
Cr2O3	0,000	0,000	0,000	0,000	0,000	0,009	0,000	0,000	0,000	0,028	0,012	0,000	0,000	0,000	0,000
Cl	0,075	0,000	0,000	0,122	0,134	0,010	0,000	0,000	0,000	0,000	0,006	0,000	0,108	0,000	0,000
F	0,000	0,000	0,179	0,000	0,000	0,022	0,000	0,000	0,181	0,000	0,000	0,035	0,142	0,094	0,054
Total	98,827	98,670	98,964	97,758	96,864	99,170	99,728	100,836	99,122	100,016	100,990	100,555	88,665	98,980	100,331
Na(I)	0,072	0,062	0,062	0,018	0,022	0,067	0,471	0,906	0,071	0,510	0,480	0,336	0,041	0,060	0,386
Si(IV)	2,962	2,953	2,957	1,983	1,975	2,960	2,451	2,926	2,965	2,515	2,481	2,324	2,535	2,953	2,368
Mn(II)	0,001	0,000	0,000	0,004	0,005	0,000	0,000	0,000	0,000	0,000	0,000	0,000	0,001	0,001	0,000
K(I)	0,927	0,937	0,934	0,688	0,688	0,927	0,008	0,010	0,924	0,007	0,006	0,004	0,208	0,927	0,004
Mg(II)	0,000	0,001	0,000	0,320	0,342	0,000	0,000	0,000	0,001	0,000	0,000	0,001	0,322	0,000	0,000
Al(III)	1,047	1,061	1,062	1,182	1,132	1,052	1,559	1,093	1,050	1,490	1,530	1,687	1,515	1,057	1,646
Fe(II)	0,001	0,002	0,003	1,317	1,360	0,003	0,006	0,001	0,006	0,004	0,008	0,013	0,161	0,011	0,008
Ca(II)	0,000	0,000	0,001	0,003	0,001	0,000	0,512	0,049	0,000	0,467	0,489	0,639	0,057	0,006	0,595
Ti(IV)	0,002	0,001	0,001	0,132	0,144	0,001	0,000	0,000	0,001	0,001	0,000	0,000	0,001	0,002	0,000
Cr(III)	0,000	0,000	0,000	0,000	0,000	0,000	0,000	0,000	0,000	0,001	0,000	0,000	0,000	0,000	0,000
F	0,000	0,000	0,027	0,000	0,000	0,003	0,000	0,000	0,027	0,000	0,000	0,005	0,023	0,014	0,008
Σ cations	5,012	5,016	5,021	5,647	5,669	5,011	5,008	4,985	5,018	4,997	4,996	5,004	4,841	5,016	5,007
charge	16,000	16,000	16,022	16,000	16,000	16,003	16,000	16,000	16,023	16,000	16,000	16,004	16,019	16,012	16,007

Table 50. EMP measurements of representative biotite of JI 4-6 based on 11 oxygen (continued) (top) and feldspar based on 8 oxygen (bottom).

point	3-17	3-18	3-19	3-20	4-19	4-22	4-23	4-24	4-25	4-26	5-16	5-17	5-18	5-19
Na2O	0,206	0,381	0,887	5,110	2,730	4,770	1,048	0,863	0,700	2,630	0,752	0,653	7,720	4,750
SiO2	48,110	50,020	62,980	53,950	49,210	53,040	63,200	62,570	62,640	48,460	63,100	63,590	59,420	53,300
MnO	0,016	0,029	0,000	0,000	0,007	0,022	0,031	0,000	0,036	0,000	0,013	0,000	0,000	0,000
K2O	1,660	2,300	15,160	0,188	0,255	0,091	15,270	15,020	15,630	0,654	15,530	15,560	0,100	0,122
MgO	3,390	3,380	0,017	0,000	0,533	0,010	0,010	0,010	0,010	0,295	0,000	0,000	0,000	0,154
Al2O3	26,850	26,290	19,160	29,460	32,330	30,200	19,200	19,230	19,050	32,550	19,050	18,960	25,840	30,110
FeO	4,520	4,160	0,063	0,125	0,884	0,027	0,045	0,029	0,121	0,336	0,023	0,034	0,023	0,312
CaO	1,620	0,841	0,156	10,980	11,700	11,550	0,024	0,022	0,043	12,570	0,000	0,000	6,780	11,130
TiO2	0,037	0,041	0,059	0,028	0,049	0,000	0,022	0,027	0,056	0,000	0,036	0,060	0,010	0,011
Cr2O3	0,010	0,000	0,000	0,000	0,013	0,021	0,023	0,000	0,010	0,000	0,000	0,000	0,013	0,000
Cl	0,073	0,204	0,019	0,000	0,018	0,000	0,014	0,000	0,009	0,082	0,016	0,025	0,000	0,007
F	0,161	0,121	0,000	0,000	0,191	0,061	0,021	0,099	0,000	0,000	0,204	0,035	0,000	0,030
Total	86,652	87,767	98,501	99,840	97,921	99,793	98,909	97,871	98,304	97,576	98,725	98,918	99,907	99,926
Na(I)	0,021	0,037	0,081	0,448	0,246	0,419	0,095	0,079	0,064	0,238	0,068	0,059	0,668	0,416
Si(IV)	2,477	2,538	2,952	2,439	2,285	2,404	2,953	2,953	2,950	2,259	2,964	2,969	2,650	2,410
Mn(II)	0,001	0,001	0,000	0,000	0,000	0,001	0,001	0,000	0,001	0,000	0,001	0,000	0,000	0,000
K(I)	0,109	0,149	0,906	0,011	0,015	0,005	0,910	0,904	0,939	0,039	0,931	0,927	0,006	0,007
Mg(II)	0,260	0,256	0,001	0,000	0,037	0,001	0,001	0,001	0,001	0,021	0,000	0,000	0,000	0,010
Al(III)	1,629	1,572	1,058	1,570	1,769	1,613	1,057	1,070	1,057	1,788	1,055	1,043	1,358	1,605
Fe(II)	0,195	0,176	0,002	0,005	0,034	0,001	0,002	0,001	0,005	0,013	0,001	0,001	0,001	0,012
Ca(II)	0,089	0,046	0,008	0,532	0,582	0,561	0,001	0,001	0,002	0,628	0,000	0,000	0,324	0,539
Ti(IV)	0,001	0,002	0,002	0,001	0,002	0,000	0,001	0,001	0,002	0,000	0,001	0,002	0,000	0,000
Cr(III)	0,000	0,000	0,000	0,000	0,000	0,001	0,001	0,000	0,000	0,000	0,000	0,000	0,000	0,000
F	0,026	0,019	0,000	0,000	0,028	0,009	0,003	0,015	0,000	0,000	0,030	0,005	0,000	0,004
Σ cations	4,783	4,776	5,011	5,005	4,971	5,005	5,021	5,009	5,021	4,985	5,020	5,002	5,007	5,000
charge	16,022	16,016	16,000	16,000	16,024	16,007	16,003	16,012	16,000	16,000	16,026	16,004	16,000	16,004

point	2-6	3-2	3-6
Na2O	1,280	1,201	1,149
SiO2	39,860	40,400	40,480
MnO	0,056	0,156	0,093
K2O	1,850	1,710	1,730
MgO	3,490	3,510	3,550
Al2O3	12,920	12,350	12,870
FeO	25,920	26,390	25,700
CaO	11,070	11,150	11,300
TiO2	1,850	1,509	1,489
Cr2O3	0,031	0,000	0,000
Cl	0,146	0,154	0,123
F	0,000	0,000	0,000
Total	98,472	98,530	98,484
Na(I)	0,389	0,365	0,348
Si(IV)	6,254	6,341	6,328
Mn(II)	0,007	0,021	0,012
K(I)	0,370	0,342	0,345
Mg(II)	0,816	0,821	0,827
Al(III)	2,389	2,285	2,371
Fe(II)	3,401	3,464	3,360
Ca(II)	1,861	1,875	1,893
Ti(IV)	0,218	0,178	0,175
Cr(III)	0,004	0,000	0,000
F	0,000	0,000	0,000
Σ cations	15,711	15,693	15,659
charge	46,000	46,000	46,000

Table 51. EMP measurements of representative feldspar of JI 4-6 based on 8 oxygen (continued) (top) and amphibole based on 23 oxygen (bottom).

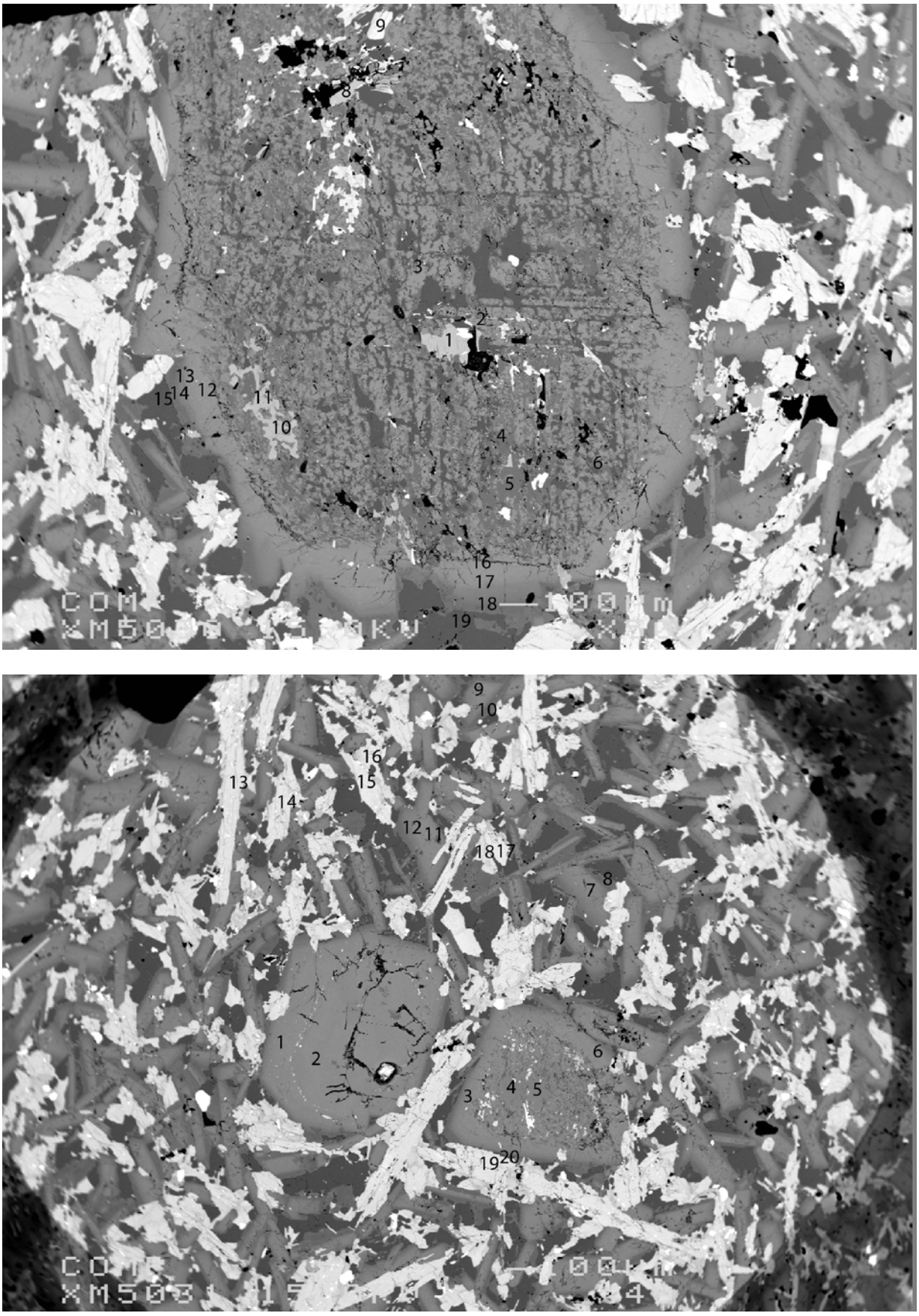

Figure 94. BSE of thin section JI 5-3, measuring locations 1 (top) and 2 (bottom).

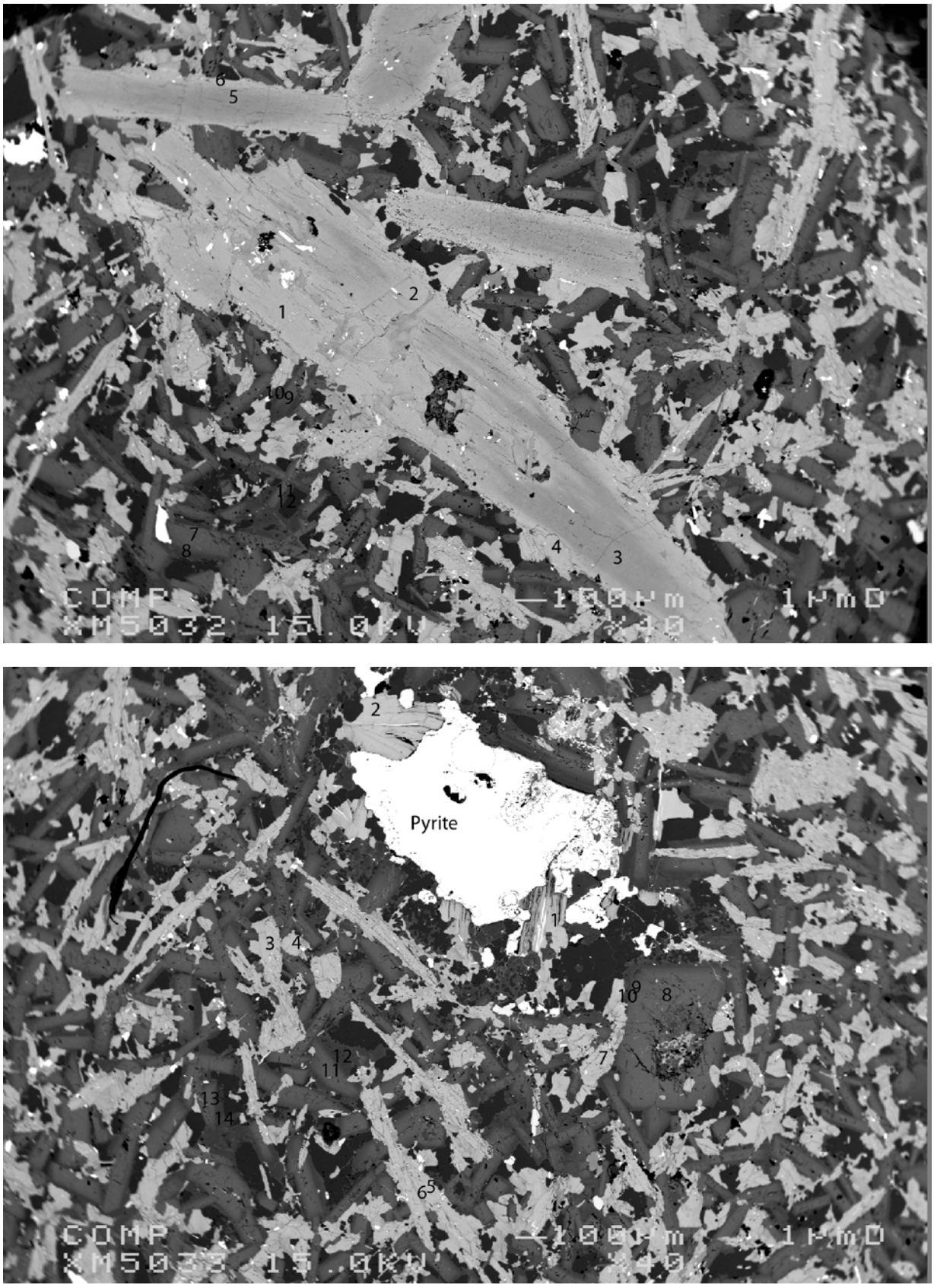

Figure 95. BSE of thin section JI 5-3, measuring locations 3 (top) and 5 (bottom).

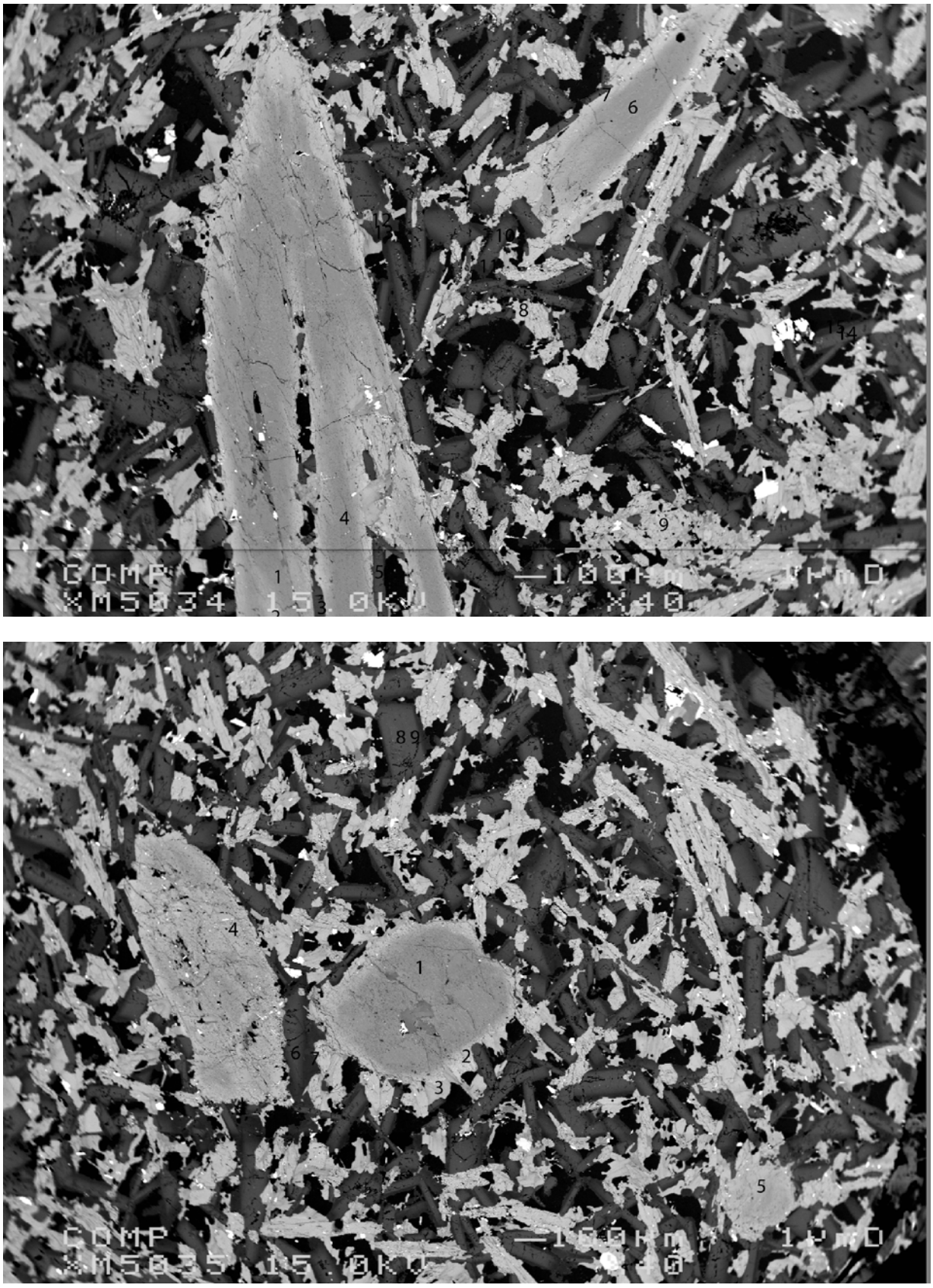

Figure 96. BSE of thin section JI 5-3, measuring locations 6 (top) and 7 (bottom).

point	2-13	2-14	2-15	2-17	2-19	3-1	3-2	3-3	3-4	3-5	3-6	5-3
Na2O	1,315	1,166	1,131	1,351	1,234	0,915	1,364	1,730	1,238	1,680	1,278	1,344
SiO2	41,401	42,271	42,718	41,132	43,478	42,498	41,748	42,043	41,877	42,358	41,087	41,435
MnO	0,395	0,410	0,413	0,434	0,375	0,415	0,391	0,231	0,371	0,328	0,382	0,427
K2O	0,501	0,563	0,543	0,507	0,502	1,047	0,564	0,569	0,750	0,531	0,568	0,619
MgO	7,895	8,039	8,378	7,897	8,777	9,282	9,410	13,104	8,626	12,719	9,204	7,525
Al2O3	14,957	14,217	13,505	14,810	13,219	13,582	14,754	14,487	13,895	14,055	14,077	14,735
FeO	17,414	17,778	17,426	17,449	17,082	16,268	15,477	10,794	16,806	11,444	16,206	18,025
CaO	11,392	11,505	11,419	11,338	11,414	10,860	11,641	11,818	11,273	11,735	11,149	11,425
TiO2	2,091	1,737	1,747	2,085	1,710	2,181	2,259	2,163	1,902	2,075	2,069	2,067
Cr2O3	0,029	0,025	0,000	0,006	0,004	0,020	0,000	0,000	0,031	0,007	0,000	0,000
Cl	0,186	0,284	0,187	0,213	0,194	0,238	0,097	0,010	0,259	0,014	0,278	0,369
F	0,000	0,044	0,000	0,072	0,000	0,000	0,141	0,043	0,000	0,025	0,000	0,000
Total	97,534	97,956	97,425	97,216	97,945	97,252	97,765	96,972	96,970	96,957	96,235	97,888
Na(I)	0,384	0,339	0,330	0,396	0,357	0,266	0,394	0,493	0,363	0,480	0,377	0,393
Si(IV)	6,228	6,343	6,420	6,224	6,479	6,376	6,225	6,185	6,328	6,245	6,245	6,244
Mn(II)	0,050	0,052	0,053	0,056	0,047	0,053	0,049	0,029	0,047	0,041	0,049	0,055
K(I)	0,096	0,108	0,104	0,098	0,095	0,200	0,107	0,107	0,145	0,100	0,110	0,119
Mg(II)	1,771	1,798	1,877	1,781	1,950	2,076	2,092	2,874	1,943	2,795	2,086	1,691
Al(III)	2,652	2,514	2,392	2,641	2,322	2,402	2,593	2,512	2,475	2,442	2,522	2,617
Fe(II)	2,191	2,231	2,190	2,208	2,129	2,041	1,930	1,328	2,124	1,411	2,060	2,272
Ca(II)	1,836	1,850	1,839	1,838	1,823	1,746	1,860	1,863	1,825	1,854	1,816	1,845
Ti(IV)	0,237	0,196	0,198	0,237	0,192	0,246	0,253	0,239	0,216	0,230	0,237	0,234
Cr(III)	0,003	0,003	0,000	0,001	0,000	0,002	0,000	0,000	0,004	0,001	0,000	0,000
F	0,000	0,021	0,000	0,034	0,000	0,000	0,066	0,020	0,000	0,012	0,000	0,000
Σ cations	15,448	15,435	15,403	15,480	15,394	15,409	15,504	15,629	15,470	15,599	15,501	15,469
charge	46,000	46,018	46,000	46,029	46,000	46,000	46,056	46,017	46,000	46,010	46,000	46,000

point	5-4	5-5	5-7	6-1	6-2	6-4	6-6	6-7	6-9	7-1	7-2	7-4
Na2O	1,228	1,313	1,309	1,270	1,486	1,685	1,541	1,213	0,317	1,629	1,502	1,220
SiO2	41,334	40,793	41,378	42,954	41,790	41,646	41,872	41,826	52,379	41,786	40,999	42,246
MnO	0,357	0,471	0,382	0,271	0,418	0,222	0,253	0,331	0,639	0,297	0,455	0,406
K2O	0,613	0,584	0,960	0,701	0,556	0,567	0,503	0,608	0,092	0,537	0,815	0,661
MgO	7,742	7,631	8,282	12,295	9,480	13,506	13,314	8,382	13,870	12,529	7,392	9,244
Al2O3	14,222	14,325	14,590	14,327	14,931	13,532	12,526	14,701	4,314	14,529	14,018	13,841
FeO	17,671	17,976	16,981	11,746	14,952	10,641	12,160	16,554	16,223	12,250	19,716	16,301
CaO	11,286	11,324	11,000	11,903	11,696	12,072	11,579	11,437	9,579	11,793	11,404	11,357
TiO2	1,940	2,236	2,041	2,297	2,231	1,960	2,670	2,055	0,173	2,325	0,658	0,410
Cr2O3	0,000	0,004	0,000	0,025	0,076	0,057	0,000	0,019	0,061	0,000	0,027	0,000
Cl	0,336	0,369	0,230	0,064	0,037	0,024	0,029	0,267	0,073	0,037	0,955	0,398
F	0,000	0,172	0,000	0,016	0,040	0,138	0,173	0,000	0,000	0,000	0,000	0,000
Total	96,653	97,043	97,101	97,848	97,668	95,987	96,540	97,333	97,704	97,704	97,725	95,994
Na(I)	0,363	0,389	0,384	0,360	0,428	0,487	0,446	0,353	0,089	0,464	0,447	0,360
Si(IV)	6,295	6,228	6,255	6,272	6,214	6,212	6,248	6,280	7,618	6,142	6,291	6,430
Mn(II)	0,046	0,061	0,049	0,034	0,053	0,028	0,032	0,042	0,079	0,037	0,059	0,052
K(I)	0,119	0,114	0,185	0,131	0,105	0,108	0,096	0,116	0,017	0,101	0,160	0,128
Mg(II)	1,758	1,737	1,866	2,676	2,101	3,003	2,962	1,876	3,007	2,745	1,691	2,098
Al(III)	2,553	2,578	2,599	2,466	2,616	2,379	2,203	2,601	0,740	2,517	2,535	2,483
Fe(II)	2,251	2,295	2,147	1,434	1,859	1,327	1,518	2,079	1,973	1,506	2,530	2,075
Ca(II)	1,842	1,853	1,782	1,862	1,863	1,929	1,851	1,840	1,493	1,857	1,875	1,852
Ti(IV)	0,222	0,257	0,232	0,252	0,250	0,220	0,300	0,232	0,019	0,257	0,076	0,047
Cr(III)	0,000	0,000	0,000	0,003	0,009	0,007	0,000	0,002	0,007	0,000	0,003	0,000
F	0,000	0,083	0,000	0,007	0,019	0,065	0,082	0,000	0,000	0,000	0,000	0,000
Σ cations	15,447	15,512	15,498	15,490	15,499	15,700	15,656	15,421	15,043	15,625	15,667	15,526
charge	46,000	46,070	46,000	46,006	46,016	46,055	46,069	46,000	46,000	46,000	46,000	46,000

Table 52. EMP measurements of representative amphibole of JI 5-3 based on 23 oxygen.

point	2-1	2-2	2-3	2-4	2-5	2-6	2-7	2-8	2-9	2-10	2-11	2-12	3-7
Na2O	2,058	1,508	2,470	3,503	3,705	2,098	3,807	7,648	3,221	7,709	2,691	7,401	3,115
SiO2	47,575	46,346	48,444	51,114	51,630	48,060	51,548	60,059	50,335	60,085	49,128	59,900	50,239
MnO	0,022	0,000	0,000	0,011	0,000	0,000	0,045	0,004	0,000	0,000	0,000	0,000	0,018
K2O	0,065	0,043	0,007	0,012	0,026	0,140	0,030	0,033	0,040	0,053	0,015	0,066	0,017
MgO	0,063	0,009	0,000	0,001	0,006	0,120	0,022	0,008	0,000	0,000	0,002	0,000	0,018
Al2O3	34,153	35,013	33,865	32,269	32,077	34,100	31,900	25,818	32,579	26,208	33,754	26,261	32,081
FeO	0,233	0,181	0,094	0,096	0,058	0,293	0,063	0,087	0,199	0,173	0,067	0,063	0,269
CaO	16,404	17,753	15,722	14,133	13,801	16,370	13,410	6,791	14,470	7,053	15,554	7,195	14,771
TiO2	0,019	0,006	0,014	0,000	0,025	0,000	0,020	0,031	0,019	0,008	0,000	0,000	0,015
Cr2O3	0,002	0,000	0,000	0,000	0,009	0,026	0,029	0,000	0,000	0,000	0,009	0,000	0,001
Cl	0,063	0,006	0,000	0,000	0,018	0,022	0,013	0,000	0,011	0,000	0,000	0,007	0,000
F	0,114	0,013	0,001	0,000	0,045	0,155	0,061	0,075	0,000	0,000	0,000	0,041	0,062
Total	100,709	100,872	100,617	101,139	101,377	101,314	100,919	100,522	100,872	101,289	101,220	100,915	100,580
Na(I)	0,182	0,133	0,218	0,305	0,322	0,185	0,332	0,657	0,282	0,658	0,235	0,634	0,274
Si(IV)	2,171	2,116	2,201	2,298	2,315	2,181	2,321	2,662	2,274	2,645	2,217	2,645	2,280
Mn(II)	0,001	0,000	0,000	0,000	0,000	0,000	0,002	0,000	0,000	0,000	0,000	0,000	0,001
K(I)	0,004	0,003	0,000	0,001	0,001	0,008	0,002	0,002	0,002	0,003	0,001	0,004	0,001
Mg(II)	0,004	0,001	0,000	0,000	0,000	0,008	0,001	0,001	0,000	0,000	0,000	0,000	0,001
Al(III)	1,837	1,884	1,813	1,710	1,695	1,824	1,693	1,349	1,734	1,360	1,795	1,367	1,716
Fe(II)	0,009	0,007	0,004	0,004	0,002	0,011	0,002	0,003	0,008	0,006	0,003	0,002	0,010
Ca(II)	0,802	0,868	0,765	0,681	0,663	0,796	0,647	0,322	0,700	0,333	0,752	0,340	0,718
Ti(IV)	0,001	0,000	0,000	0,000	0,001	0,000	0,001	0,001	0,001	0,000	0,000	0,000	0,001
Cr(III)	0,000	0,000	0,000	0,000	0,000	0,001	0,001	0,000	0,000	0,000	0,000	0,000	0,000
F	0,016	0,002	0,000	0,000	0,006	0,022	0,009	0,011	0,000	0,000	0,000	0,006	0,009
Σ cations	5,010	5,011	5,001	5,000	5,001	5,013	5,002	4,997	5,001	5,005	5,003	4,992	5,002
charge	16,014	16,002	16,000	16,000	16,005	16,019	16,007	16,009	16,000	16,000	16,000	16,005	16,007

point	3-8	3-9	3-10	3-11	3-12	5-8	5-9	5-10	5-11	5-12	5-13	5-14	6-10
Na2O	8,389	4,509	9,376	3,693	8,386	1,981	5,825	7,114	3,245	8,449	3,435	8,039	2,712
SiO2	61,509	53,289	63,437	51,460	61,127	47,593	56,327	58,932	50,644	61,463	50,294	60,972	49,194
MnO	0,007	0,000	0,045	0,000	0,002	0,000	0,011	0,000	0,000	0,000	0,029	0,004	0,000
K2O	0,055	0,037	0,070	0,025	0,052	0,038	0,055	0,599	0,020	0,071	0,010	0,077	0,105
MgO	0,002	0,000	0,001	0,000	0,000	0,012	0,000	0,077	0,000	0,000	0,003	0,001	0,099
Al2O3	24,628	30,664	23,633	31,610	24,667	34,070	28,589	26,395	32,475	24,700	31,728	25,322	32,330
FeO	0,020	0,094	0,079	0,005	0,000	0,056	0,083	0,317	0,045	0,056	0,061	0,038	0,276
CaO	5,792	12,100	4,181	13,529	5,608	16,626	10,129	6,676	14,916	5,548	14,204	6,168	15,176
TiO2	0,010	0,000	0,000	0,000	0,012	0,000	0,007	0,000	0,007	0,000	0,005	0,000	0,010
Cr2O3	0,000	0,000	0,008	0,000	0,000	0,000	0,010	0,000	0,000	0,002	0,000	0,000	0,000
Cl	0,000	0,000	0,004	0,000	0,000	0,017	0,015	0,000	0,000	0,011	0,000	0,007	0,006
F	0,138	0,031	0,015	0,058	0,084	0,030	0,007	0,031	0,000	0,000	0,000	0,000	0,000
Total	100,492	100,711	100,842	100,356	99,903	100,406	101,052	100,128	101,352	100,298	99,769	100,626	99,907
Na(I)	0,720	0,393	0,797	0,324	0,723	0,175	0,502	0,615	0,283	0,725	0,304	0,688	0,241
Si(IV)	2,722	2,393	2,783	2,328	2,718	2,173	2,506	2,629	2,278	2,719	2,295	2,692	2,250
Mn(II)	0,000	0,000	0,002	0,000	0,000	0,000	0,000	0,000	0,000	0,000	0,001	0,000	0,000
K(I)	0,003	0,002	0,004	0,001	0,003	0,002	0,003	0,034	0,001	0,004	0,001	0,004	0,006
Mg(II)	0,000	0,000	0,000	0,000	0,000	0,001	0,000	0,005	0,000	0,000	0,000	0,000	0,007
Al(III)	1,284	1,623	1,222	1,686	1,293	1,834	1,499	1,388	1,721	1,288	1,706	1,318	1,743
Fe(II)	0,001	0,004	0,003	0,000	0,000	0,002	0,003	0,012	0,002	0,002	0,002	0,001	0,011
Ca(II)	0,275	0,582	0,197	0,656	0,267	0,813	0,483	0,319	0,719	0,263	0,694	0,292	0,744
Ti(IV)	0,000	0,000	0,000	0,000	0,000	0,000	0,000	0,000	0,000	0,000	0,000	0,000	0,000
Cr(III)	0,000	0,000	0,000	0,000	0,000	0,000	0,000	0,000	0,000	0,000	0,000	0,000	0,000
F	0,019	0,004	0,002	0,008	0,012	0,004	0,001	0,004	0,000	0,000	0,000	0,000	0,000
Σ cations	5,005	4,995	5,008	4,995	5,004	5,001	4,997	5,003	5,004	5,001	5,004	4,995	5,001
charge	16,016	16,004	16,002	16,007	16,010	16,004	16,001	16,004	16,000	16,000	16,000	16,000	16,000

Table 53. EMP measurements of representative plagioclase of JI 5-3 based on 8 oxygen.

point	6-11	6-12	6-13	6-14	6-15	7-6	7-7	7-8	7-9
Na2O	8,584	5,365	9,351	2,743	7,992	4,309	7,134	2,633	7,318
SiO2	61,257	53,960	61,535	48,895	60,918	52,012	59,698	48,458	59,166
MnO	0,029	0,000	0,000	0,000	0,007	0,002	0,025	0,000	0,052
K2O	0,056	0,041	0,045	0,036	0,073	0,120	0,077	0,011	0,050
MgO	0,006	0,003	0,011	0,041	0,000	0,010	0,002	0,016	0,000
Al2O3	24,467	28,937	23,657	32,767	25,221	30,429	26,040	33,046	26,284
FeO	0,054	0,155	0,200	0,143	0,029	0,065	0,117	0,078	0,180
CaO	5,674	10,884	4,670	15,187	6,255	12,644	7,405	15,769	7,514
TiO2	0,022	0,000	0,008	0,015	0,000	0,000	0,000	0,011	0,012
Cr2O3	0,000	0,000	0,000	0,000	0,017	0,008	0,000	0,008	0,000
Cl	0,003	0,005	0,004	0,001	0,004	0,000	0,000	0,000	0,000
F	0,019	0,000	0,056	0,000	0,063	0,000	0,081	0,000	0,041
Total	100,162	99,349	99,512	99,828	100,551	99,599	100,545	100,030	100,600
Na(I)	0,739	0,473	0,810	0,243	0,685	0,380	0,614	0,233	0,630
Si(IV)	2,718	2,451	2,748	2,237	2,694	2,368	2,648	2,216	2,628
Mn(II)	0,001	0,000	0,000	0,000	0,000	0,000	0,001	0,000	0,002
K(I)	0,003	0,002	0,003	0,002	0,004	0,007	0,004	0,001	0,003
Mg(II)	0,000	0,000	0,001	0,003	0,000	0,001	0,000	0,001	0,000
Al(III)	1,280	1,549	1,245	1,767	1,315	1,633	1,361	1,781	1,376
Fe(II)	0,002	0,006	0,007	0,005	0,001	0,002	0,004	0,003	0,007
Ca(II)	0,270	0,530	0,223	0,744	0,296	0,617	0,352	0,773	0,358
Ti(IV)	0,001	0,000	0,000	0,001	0,000	0,000	0,000	0,000	0,000
Cr(III)	0,000	0,000	0,000	0,000	0,001	0,000	0,000	0,000	0,000
F	0,003	0,000	0,008	0,000	0,009	0,000	0,011	0,000	0,006
Σ cations	5,013	5,011	5,038	5,002	4,997	5,009	4,985	5,009	5,003
charge	16,002	16,000	16,007	16,000	16,007	16,000	16,010	16,000	16,005

point	1-9	2-16	2-18	5-1	5-2	5-6	6-8	7-3
Na2O	0,137	0,151	0,203	0,165	0,225	0,190	0,155	0,232
SiO2	36,311	35,247	33,436	35,385	36,190	34,755	36,418	35,257
MnO	0,153	0,154	0,142	0,107	0,173	0,189	0,105	0,134
K2O	8,911	8,335	5,669	8,470	8,481	6,533	8,356	8,069
MgO	10,770	11,200	12,433	10,542	10,556	11,978	11,205	11,416
Al2O3	16,635	17,140	16,546	16,504	16,549	16,848	16,332	16,429
FeO	20,401	19,428	20,913	20,159	19,935	18,749	18,676	19,650
CaO	0,007	0,038	0,105	0,064	0,095	0,161	0,071	0,075
TiO2	1,840	2,360	1,502	2,431	2,341	1,731	2,653	2,301
Cr2O3	0,000	0,016	0,000	0,000	0,000	0,000	0,000	0,000
Cl	0,409	0,427	0,415	0,504	0,389	0,389	0,378	0,401
F	0,000	0,000	0,095	0,000	0,001	0,000	0,019	0,000
Total	95,482	94,400	91,325	94,217	94,847	91,435	94,275	93,874
Na(I)	0,020	0,023	0,031	0,025	0,033	0,029	0,023	0,035
Si(IV)	2,776	2,712	2,659	2,743	2,775	2,728	2,789	2,730
Mn(II)	0,010	0,010	0,010	0,007	0,011	0,013	0,007	0,009
K(I)	0,869	0,818	0,575	0,838	0,830	0,654	0,816	0,797
Mg(II)	1,228	1,285	1,474	1,218	1,207	1,402	1,279	1,318
Al(III)	1,499	1,555	1,551	1,508	1,496	1,559	1,474	1,500
Fe(II)	1,304	1,250	1,391	1,307	1,279	1,231	1,196	1,273
Ca(II)	0,001	0,003	0,009	0,005	0,008	0,014	0,006	0,006
Ti(IV)	0,106	0,137	0,090	0,142	0,135	0,102	0,153	0,134
Cr(III)	0,000	0,001	0,000	0,000	0,000	0,000	0,000	0,000
F	0,000	0,000	0,024	0,000	0,000	0,000	0,005	0,000
Σ cations	7,813	7,794	7,789	7,793	7,774	7,732	7,743	7,802
charge	22,000	22,000	22,020	22,000	22,000	22,000	22,004	22,000

Table 54. EMP measurements of representative plagioclase of JI 5-3 based on 8 oxygen (continued) (top) and biotite based on 11 oxygen (bottom).

Appendix V: Argon dating

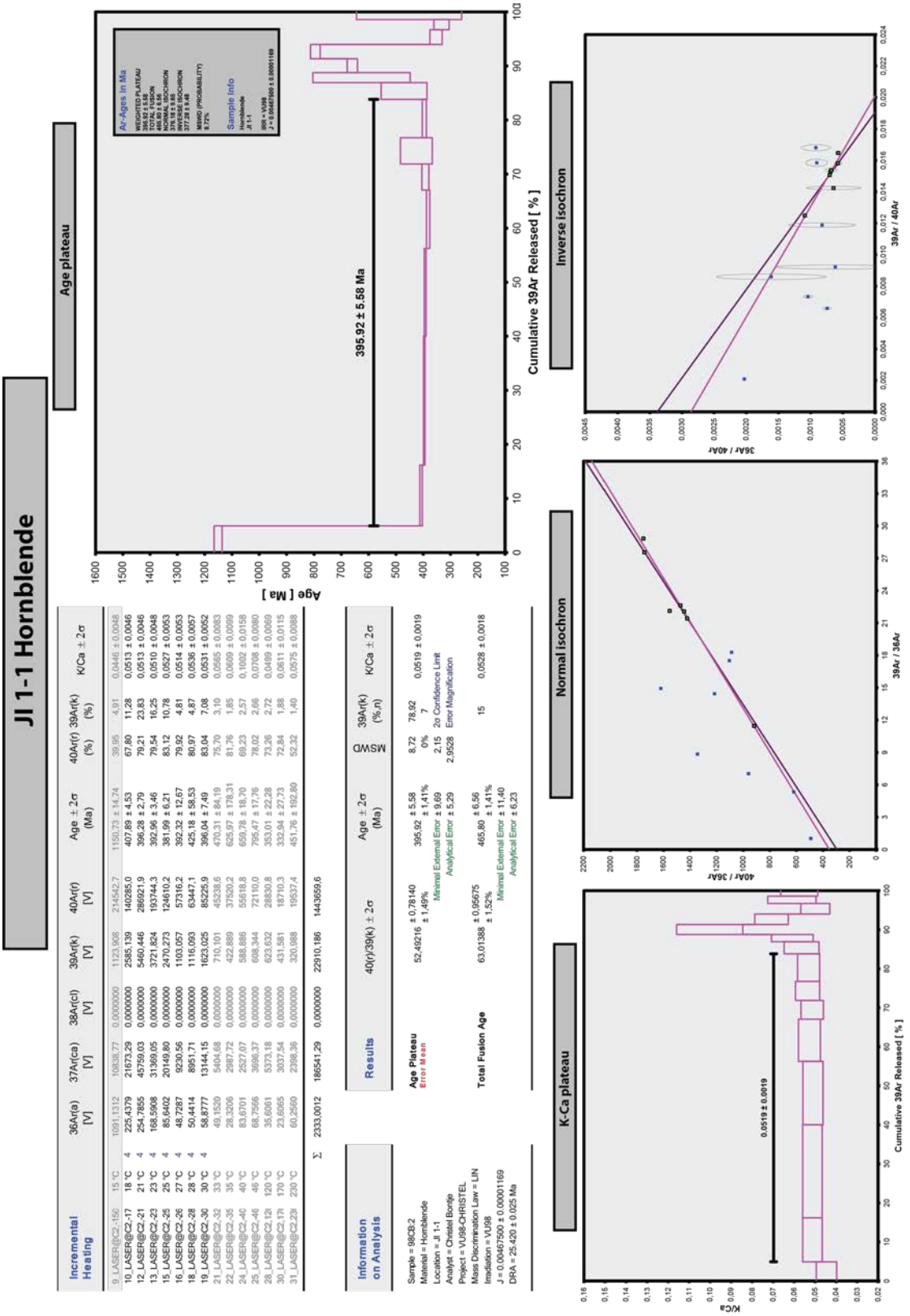

Incremental Heating			36Ar(a) [V]	37Ar(ca) [V]	38Ar(cl) [V]	39Ar(k) [V]	40Ar(r) [V]	Age ± 2σ (Ma)	40Ar(r) (%)	39Ar(k) (%)	K/Ca ± 2σ
9_LASER@C2-150	15 °C		1091,1312	10838,77	0,0000000	1123,908	214542,7	1150,73 ± 14,74	39,95	4,91	0,0446 ± 0,0048
10_LASER@C2-17	18 °C	4	225,4379	21673,29	0,0000000	2585,139	140285,0	407,89 ± 4,53	67,80	11,28	0,0513 ± 0,0046
12_LASER@C2-21	21 °C	4	254,7855	45759,03	0,0000000	5460,446	286921,9	396,28 ± 2,79	79,21	23,83	0,0513 ± 0,0046
13_LASER@C2-23	23 °C	4	168,5908	31366,05	0,0000000	3721,824	193744,3	392,96 ± 3,46	79,54	16,25	0,0510 ± 0,0048
15_LASER@C2-25	25 °C	4	86,6402	20149,80	0,0000000	2470,273	124610,2	381,99 ± 6,21	83,12	10,78	0,0527 ± 0,0053
16_LASER@C2-26	27 °C	4	48,7287	9230,56	0,0000000	1103,057	57316,2	392,32 ± 12,67	79,92	4,81	0,0514 ± 0,0053
18_LASER@C2-28	28 °C	4	50,4414	8951,71	0,0000000	1116,093	63447,1	425,18 ± 58,53	80,97	4,87	0,0536 ± 0,0057
19_LASER@C2-30	30 °C	4	58,8777	13144,15	0,0000000	1623,025	85225,9	396,04 ± 7,49	83,04	7,08	0,0531 ± 0,0062
21_LASER@C2-32	33 °C		49,1520	5404,68	0,0000000	710,101	45238,6	470,31 ± 84,19	75,70	3,10	0,0565 ± 0,0083
22_LASER@C2-35	35 °C		28,3206	2987,72	0,0000000	422,889	37520,2	625,97 ± 178,31	81,76	1,85	0,0609 ± 0,0099
24_LASER@C2-40	40 °C		83,6701	2527,07	0,0000000	588,886	55618,8	659,78 ± 18,70	69,23	2,57	0,1002 ± 0,0158
25_LASER@C2-46	46 °C		68,7566	3898,37	0,0000000	668,344	72110,0	795,47 ± 17,76	78,02	2,66	0,0708 ± 0,0080
28_LASER@C2-120	120 °C		35,6061	5373,18	0,0000000	623,632	28830,8	353,01 ± 22,28	73,26	2,72	0,0489 ± 0,0089
30_LASER@C2-170	170 °C		23,6065	3037,54	0,0000000	431,581	18710,3	332,94 ± 27,73	72,84	1,88	0,0611 ± 0,0115
31_LASER@C2-230	230 °C		60,2560	2398,36	0,0000000	320,988	19537,4	451,76 ± 192,80	52,32	1,40	0,0575 ± 0,0088
		Σ	2333,0012	186541,29	0,0000000	22910,186	1443659,6				

Information on Analysis	Results	40(r)/39(k) ± 2σ	Age ± 2σ (Ma)	MSWD	39Ar(k) (%,n)	K/Ca ± 2σ
Sample = 98CB-2						
Material = Hornblende	**Age Plateau**	52,49216 ± 0,78140	395,92 ± 5,58	8,72	78,92	0,0519 ± 0,0019
Location = JI 1-1	Error Mean	± 1,49%	± 1,41%	0%	7	
Analyst = Christel Bordje		Minimal External Error ± 9,69		2,15	2σ Confidence Limit	
Project = VU98-CHRISTEL		Analytical Error ± 5,29		2,9528	Error Magnification	
Mass Discrimination Law = LIN	**Total Fusion Age**	63,01388 ± 0,95675	465,80 ± 6,56		15	0,0528 ± 0,0018
Irradiation = VU98		± 1,52%	± 1,41%			
J = 0,00467500 ± 0,00001169		Minimal External Error ± 11,40				
DRA = 25,420 ± 0,025 Ma		Analytical Error ± 6,23				

Figure 97. Stepwise heating results of hornblende in JI 1-1.

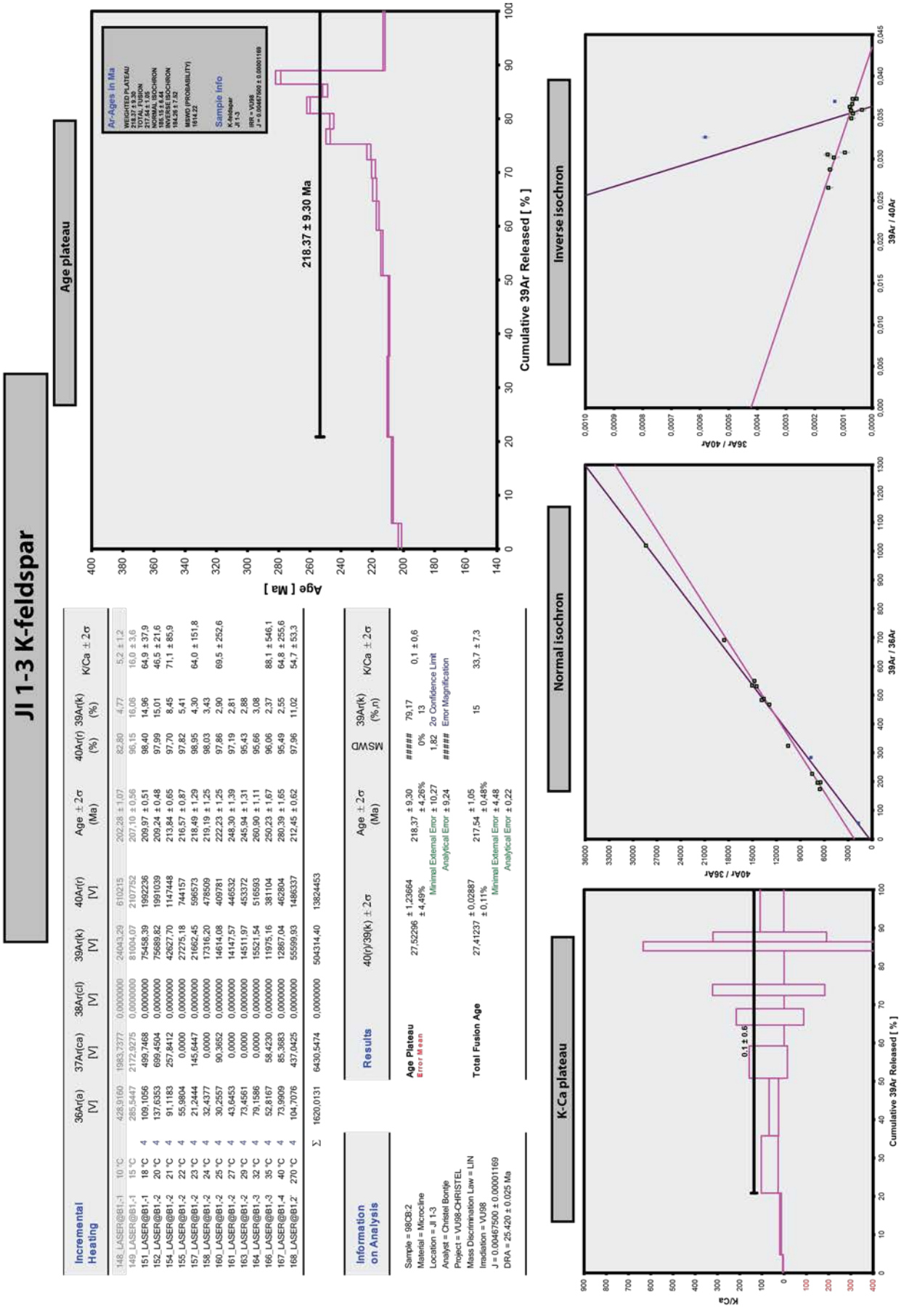

Incremental Heating		36Ar(a) [V]	37Ar(ca) [V]	38Ar(cl) [V]	39Ar(k) [V]	40Ar(r) [V]	Age ± 2σ (Ma)	40Ar(r) (%)	39Ar(k) (%)	K/Ca ± 2σ
148_LASER@B1-1	10 °C	428,9160	1983,7377	0,0000000	24043,29	610215	202,28 ± 1,07	82,80	4,77	5,2 ± 1,2
149_LASER@B1-1	15 °C	285,5447	2172,9275	0,0000000	81004,07	2107752	207,10 ± 0,56	96,15	16,06	16,0 ± 3,6
151_LASER@B1-1	18 °C 4	109,1056	499,7468	0,0000000	75458,39	1992236	209,97 ± 0,51	98,40	14,96	64,9 ± 37,9
152_LASER@B1-2	20 °C 4	137,6353	699,4504	0,0000000	75689,82	1991039	209,24 ± 0,48	97,99	15,01	46,5 ± 21,6
154_LASER@B1-2	21 °C 4	91,1183	257,8412	0,0000000	42627,70	1147448	213,84 ± 0,65	97,70	8,45	71,1 ± 85,9
155_LASER@B1-2	22 °C 4	55,9804	0,0000	0,0000000	27275,18	744157	216,57 ± 0,87	97,82	5,41	
157_LASER@B1-2	23 °C 4	21,2444	145,6447	0,0000000	21662,45	596573	218,49 ± 1,29	98,95	4,30	64,0 ± 151,8
158_LASER@B1-2	24 °C 4	32,4377	0,0000	0,0000000	17316,20	478509	219,19 ± 1,25	98,03	3,43	
160_LASER@B1-2	25 °C 4	30,2557	90,3652	0,0000000	14614,08	409781	222,23 ± 1,25	97,86	2,90	69,5 ± 252,6
161_LASER@B1-2	27 °C 4	43,6453	0,0000	0,0000000	14147,57	446532	248,30 ± 1,39	97,19	2,81	
163_LASER@B1-2	29 °C 4	73,4561	0,0000	0,0000000	14511,97	453372	245,94 ± 1,31	95,43	2,88	
164_LASER@B1-3	32 °C 4	79,1586	0,0000	0,0000000	15521,54	516593	260,90 ± 1,11	95,66	3,08	
166_LASER@B1-3	35 °C 4	52,8167	58,4230	0,0000000	11975,16	381104	250,23 ± 1,67	96,06	2,37	88,1 ± 546,1
167_LASER@B1-4	40 °C 4	73,9909	85,3683	0,0000000	12867,04	462804	280,39 ± 1,65	95,49	2,55	64,8 ± 255,6
168_LASER@B1-2	270 °C 4	104,7076	437,0425	0,0000000	55599,93	1486337	212,45 ± 0,62	97,96	11,02	54,7 ± 53,3
	Σ	1620,0131	6430,5474	0,0000000	504314,40	13824453				

Information on Analysis	Results	40(r)/39(k) ± 2σ	Age ± 2σ (Ma)	MSWD	39Ar(k) (%,n)	K/Ca ± 2σ
Sample = 98CB-2						
Material = Microcline	**Age Plateau**	27,52296 ± 1,23664	218,37 ± 9,30	#####	79,17	0,1 ± 0,6
Location = JI 1-3	Error Mean	± 4,49%	± 4,26%	0%	13	
Analyst = Christel Bonjé		Minimal External Error ± 10,27		1,82	2σ Confidence Limit	
Project = VU98-CHRISTEL		Analytical Error ± 9,24		#####	Error Magnification	
Mass Discrimination Law = LIN	**Total Fusion Age**	27,41237 ± 0,02887	217,54 ± 1,05		15	33,7 ± 7,3
Irradiation = VU98		± 0,11%	± 0,48%			
J = 0.00467500 ± 0.00001169		Minimal External Error ± 4,48				
DRA = 25.420 ± 0.025 Ma		Analytical Error ± 0,22				

Figure 98. Stepwise heating results of K-feldspar in JI 1-3.

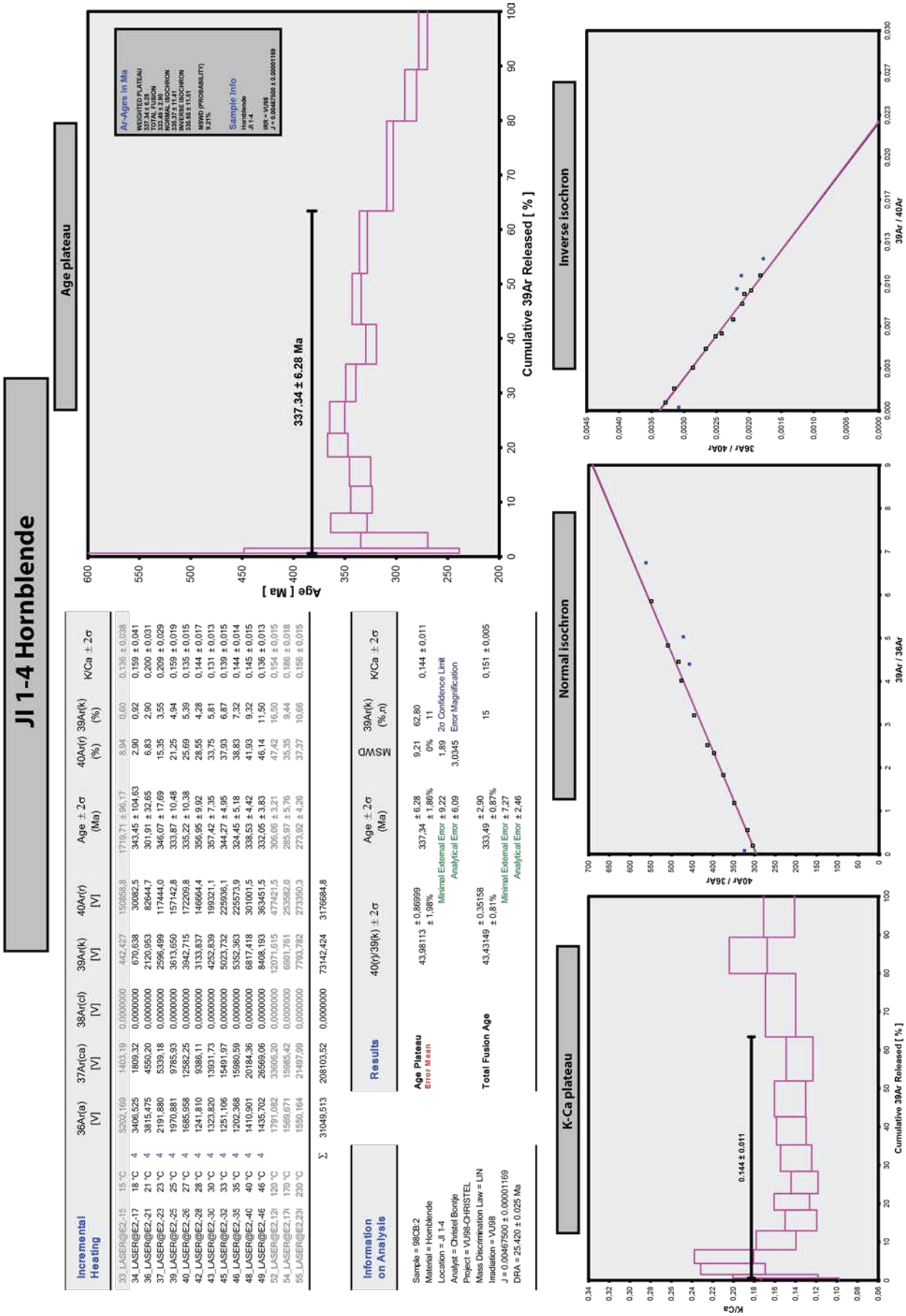

Incremental Heating	36Ar(a) [V]	37Ar(ca) [V]	38Ar(cl) [V]	39Ar(k) [V]	40Ar(r) [V]	Age ± 2σ (Ma)	40Ar(r) (%)	39Ar(k) (%)	K/Ca ± 2σ
33_LASER@E2-15 15 °C	5202,169	1403,19	0,0000000	442,427	150858,8	1719,71 ± 96,17	8,94	0,60	0,136 ± 0,038
34_LASER@E2-17 18 °C 4	3406,525	1809,32	0,0000000	670,638	30082,5	343,45 ± 104,63	2,90	0,92	0,159 ± 0,041
36_LASER@E2-21 21 °C 4	3815,475	4550,20	0,0000000	2120,953	82644,7	301,91 ± 32,65	6,83	2,90	0,200 ± 0,031
37_LASER@E2-23 23 °C 4	2191,880	5339,18	0,0000000	2596,499	117444,0	346,07 ± 17,69	15,35	3,55	0,209 ± 0,029
39_LASER@E2-25 25 °C 4	1970,881	9785,93	0,0000000	3613,650	157142,8	333,87 ± 10,48	21,25	4,94	0,159 ± 0,019
40_LASER@E2-26 27 °C 4	1685,958	12582,25	0,0000000	3942,715	172209,8	335,22 ± 10,38	25,69	5,39	0,135 ± 0,015
42_LASER@E2-28 28 °C 4	1241,810	9386,11	0,0000000	3133,837	146664,4	356,95 ± 9,92	28,55	4,28	0,144 ± 0,017
43_LASER@E2-30 30 °C 4	1323,820	13931,73	0,0000000	4252,839	199321,1	357,42 ± 7,35	33,75	5,81	0,131 ± 0,013
45_LASER@E2-32 33 °C 4	1251,106	15491,97	0,0000000	5023,732	225936,1	344,27 ± 4,95	37,93	6,87	0,139 ± 0,015
46_LASER@E2-35 35 °C 4	1202,368	15980,59	0,0000000	5352,363	225573,9	324,45 ± 5,18	38,83	7,32	0,144 ± 0,014
48_LASER@E2-40 40 °C 4	1410,901	20184,36	0,0000000	6817,418	301001,5	338,53 ± 4,42	41,93	9,32	0,145 ± 0,015
49_LASER@E2-46 46 °C 4	1435,702	26569,06	0,0000000	8408,193	363451,5	332,05 ± 3,83	46,14	11,50	0,136 ± 0,013
52_LASER@E2-12I 120 °C	1791,082	33606,20	0,0000000	12071,615	477421,5	306,06 ± 3,21	47,42	16,50	0,154 ± 0,015
54_LASER@E2-17I 170 °C	1569,671	15985,42	0,0000000	6901,761	253582,0	285,97 ± 5,76	35,35	9,44	0,186 ± 0,018
55_LASER@E2-23I 230 °C	1550,164	21497,99	0,0000000	7793,782	273350,3	273,92 ± 4,26	37,37	10,66	0,156 ± 0,015
Σ	31049,513	208103,52	0,0000000	73142,424	3176684,8				

Information on Analysis	Results	40(r)/39(k) ± 2σ	Age ± 2σ (Ma)	MSWD	39Ar(k) (%,n)	K/Ca ± 2σ
Sample = 98CB:2	**Age Plateau**	43,98113 ± 0,86999	337,34 ± 6,28	9,21	62,80	0,144 ± 0,011
Material = Hornblende	Error Mean	± 1,98%	± 1,86%	0%	11	
Location = JI 1-4		Minimal External Error ± 9,22		1,89	2σ Confidence Limit	
Analyst = Christel Bonije		Analytical Error ± 6,09		3,0345	Error Magnification	
Project = VU98-CHRISTEL						
Mass Discrimination Law = LIN						
Irradiation = VU98	**Total Fusion Age**	43,43149 ± 0,35158	333,49 ± 2,90		15	0,151 ± 0,005
J = 0,00467500 ± 0,00001169		± 0,81%	± 0,87%			
DRA = 25,420 ± 0,025 Ma		Minimal External Error ± 7,27				
		Analytical Error ± 2,46				

Figure 99. Stepwise heating results of hornblende in JI 1-4.

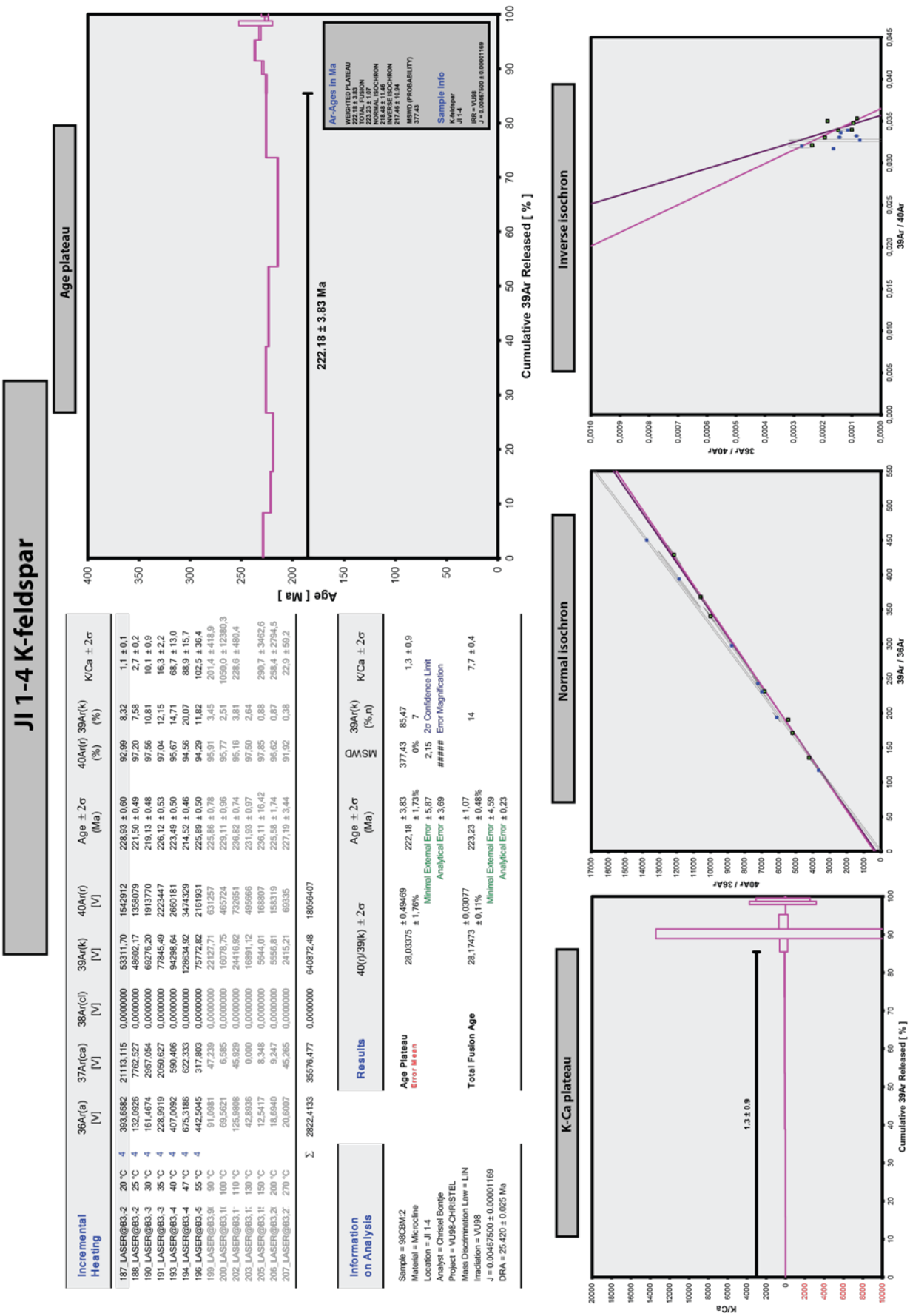

Incremental Heating		36Ar(a) [V]	37Ar(ca) [V]	38Ar(cl) [V]	39Ar(k) [V]	40Ar(r) [V]	Age ± 2σ (Ma)	40Ar(r) (%)	39Ar(k) (%)	K/Ca ± 2σ
187_LASER@83.2	20 °C	393,6582	21113,115	0,0000000	53311,70	1542912	228,93 ± 0,60	92,99	8,32	1,1 ± 0,1
188_LASER@83.2	25 °C	132,0926	7762,527	0,0000000	48602,17	1358079	221,50 ± 0,49	97,20	7,58	2,7 ± 0,2
190_LASER@83.3	30 °C	161,4674	2957,054	0,0000000	69276,20	1913770	219,13 ± 0,48	97,56	10,81	10,1 ± 0,9
191_LASER@83.3	35 °C	228,9919	2050,627	0,0000000	77845,49	2223447	226,12 ± 0,53	97,04	12,15	16,3 ± 2,2
193_LASER@83.4	40 °C	407,0092	590,406	0,0000000	94298,64	2660181	223,49 ± 0,50	95,67	14,71	68,7 ± 13,0
194_LASER@83.4	47 °C	675,3186	622,333	0,0000000	128634,92	3474329	214,52 ± 0,46	94,56	20,07	88,9 ± 15,7
196_LASER@83.5	55 °C	442,5045	317,803	0,0000000	75772,82	2161931	225,89 ± 0,50	94,29	11,82	102,5 ± 36,4
199_LASER@83.9	90 °C	91,0081	47,239	0,0000000	22127,71	631257	225,86 ± 0,78	95,91	3,45	201,4 ± 418,9
200_LASER@83.1	100 °C	69,5621	6,585	0,0000000	16078,75	465724	229,11 ± 0,96	95,77	2,51	1050,0 ± 12380,3
202_LASER@83.1	110 °C	125,9808	45,929	0,0000000	24416,92	732651	236,82 ± 0,74	95,16	3,81	228,6 ± 480,4
203_LASER@83.1	130 °C	42,8936	0,000	0,0000000	16891,12	495666	231,93 ± 0,97	97,50	2,64	
205_LASER@83.1	150 °C	12,5417	8,348	0,0000000	5644,01	168807	236,11 ± 16,42	97,85	0,88	290,7 ± 3462,6
206_LASER@83.2	200 °C	18,6940	9,247	0,0000000	5556,81	158319	225,58 ± 1,74	96,62	0,87	258,4 ± 2794,5
207_LASER@83.2	270 °C	20,6007	45,265	0,0000000	2415,21	69335	227,19 ± 3,44	91,92	0,38	22,9 ± 59,2
	Σ	2822,4133	35576,477	0,0000000	640872,48	18056407				

Information on Analysis	Results	40(r)/39(k) ± 2σ	Age ± 2σ (Ma)	MSWD	39Ar(k) (%,n)	K/Ca ± 2σ
Sample = 98CBM.2	**Age Plateau**	28,03375 ± 0,49469	222,18 ± 3,83	377,43	85,47	1,3 ± 0,9
Material = Microcline	Error Mean	± 1,76%	± 1,73%	0%	7	
Location = JI 1-4		Minimal External Error ± 5,87		2,15	2σ Confidence Limit	
Analyst = Christel Bonjé		Analytical Error ± 3,69		#####	Error Magnification	
Project = VU98-CHRISTEL						
Mass Discrimination Law = LIN						
Irradiation = VU98	**Total Fusion Age**	28,17473 ± 0,03077	223,23 ± 1,07		14	7,7 ± 0,4
J = 0.00467500 ± 0.00001169		± 0,11%	± 0,48%			
DRA = 25.420 ± 0.025 Ma		Minimal External Error ± 4,59				
		Analytical Error ± 0,23				

Figure 100. Stepwise heating results of K-feldspar in JI 1-4.

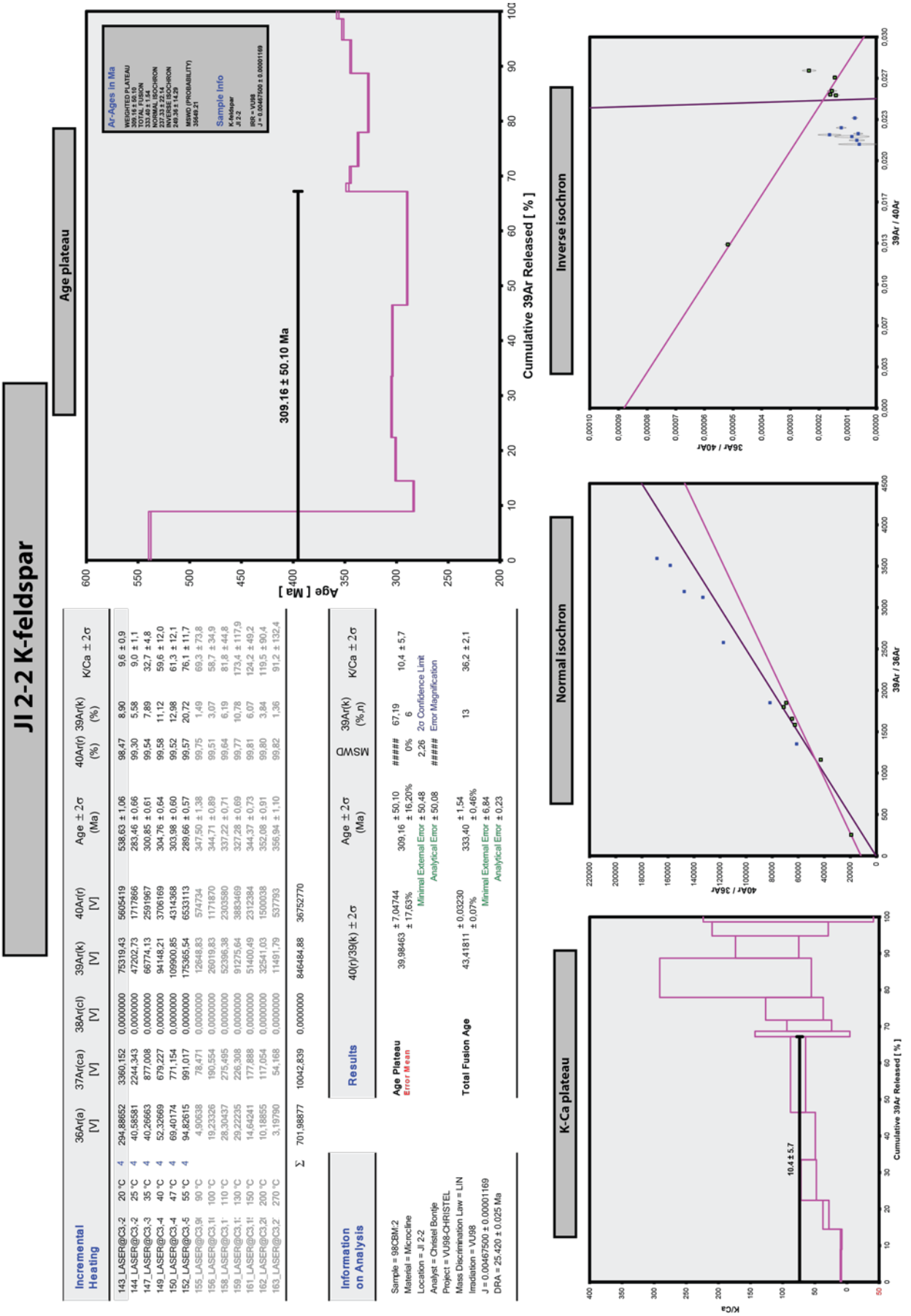

Incremental Heating			36Ar(a) [V]	37Ar(ca) [V]	38Ar(cl) [V]	39Ar(k) [V]	40Ar(r) [V]	Age ± 2σ (Ma)	40Ar(r) (%)	39Ar(k) (%)	K/Ca ± 2σ
143_LASER@C3:-2	20 °C	4	294,88652	3360,152	0,0000000	75319,43	5605419	538,63 ± 1,06	98,47	8,90	9,6 ± 0,9
144_LASER@C3:-2	25 °C	4	40,58581	2244,343	0,0000000	47202,73	1717866	283,46 ± 0,66	99,30	5,58	9,0 ± 1,1
147_LASER@C3:-3	35 °C	4	40,26663	877,008	0,0000000	66774,13	2591967	300,85 ± 0,61	99,54	7,89	32,7 ± 4,8
149_LASER@C3:-4	40 °C	4	52,32669	679,227	0,0000000	94148,21	3706169	304,76 ± 0,64	99,58	11,12	59,6 ± 12,0
150_LASER@C3:-4	47 °C	4	69,40174	771,154	0,0000000	109900,85	4314368	303,98 ± 0,60	99,52	12,98	61,3 ± 12,1
152_LASER@C3:-5	55 °C	4	94,82615	991,017	0,0000000	175365,54	6533113	289,66 ± 0,57	99,57	20,72	76,1 ± 11,7
155_LASER@C3:9(	90 °C		4,90638	78,471	0,0000000	12648,83	574734	347,50 ± 1,38	99,75	1,49	69,3 ± 73,8
156_LASER@C3:1(	100 °C		19,23326	190,554	0,0000000	26019,83	1171870	344,71 ± 0,89	99,51	3,07	58,7 ± 34,9
158_LASER@C3:1:	110 °C		28,30437	275,495	0,0000000	52396,38	2303580	337,22 ± 0,71	99,64	6,19	81,8 ± 44,8
159_LASER@C3:1:	130 °C		29,22235	226,308	0,0000000	91275,64	3883469	327,28 ± 0,69	99,77	10,78	173,4 ± 117,9
161_LASER@C3:1!	150 °C		14,64241	177,888	0,0000000	51400,49	2312384	344,37 ± 0,73	99,81	6,07	124,2 ± 49,2
162_LASER@C3:2(	200 °C		10,18855	117,054	0,0000000	32541,03	1500038	352,08 ± 0,91	99,80	3,84	119,5 ± 90,4
163_LASER@C3:2'	270 °C		3,19790	54,168	0,0000000	11491,79	537793	356,94 ± 1,10	99,82	1,36	91,2 ± 132,4
		Σ	701,98877	10042,839	0,0000000	846484,88	36752770				

Information on Analysis	Results	40(r)/39(k) ± 2σ	Age ± 2σ (Ma)	MSWD	39Ar(k) (%,n)	K/Ca ± 2σ
Sample = 98CBM:2	**Age Plateau**	39,98463 ± 7,04744	309,16 ± 50,10	#####	67,19	10,4 ±5,7
Material = Microcline	Error Mean	± 17,63%	± 16,20%	0%	6	
Location = JI 2-2		Minimal External Error ± 50,48		2,26	2σ Confidence Limit	
Analyst = Christel Bonjé		Analytical Error ± 50,08		#####	Error Magnification	
Project = VU98-CHRISTEL						
Mass Discrimination Law = LIN						
Irradiation = VU98	**Total Fusion Age**	43,41811 ± 0,03230	333,40 ± 1,54		13	36,2 ± 2,1
J = 0,00467500 ± 0,00001169		± 0,07%	± 0,46%			
DRA = 25,420 ± 0,025 Ma		Minimal External Error ± 6,84				
		Analytical Error ± 0,23				

Figure 101. Stepwise heating results of K-feldspar in JI 2-2.

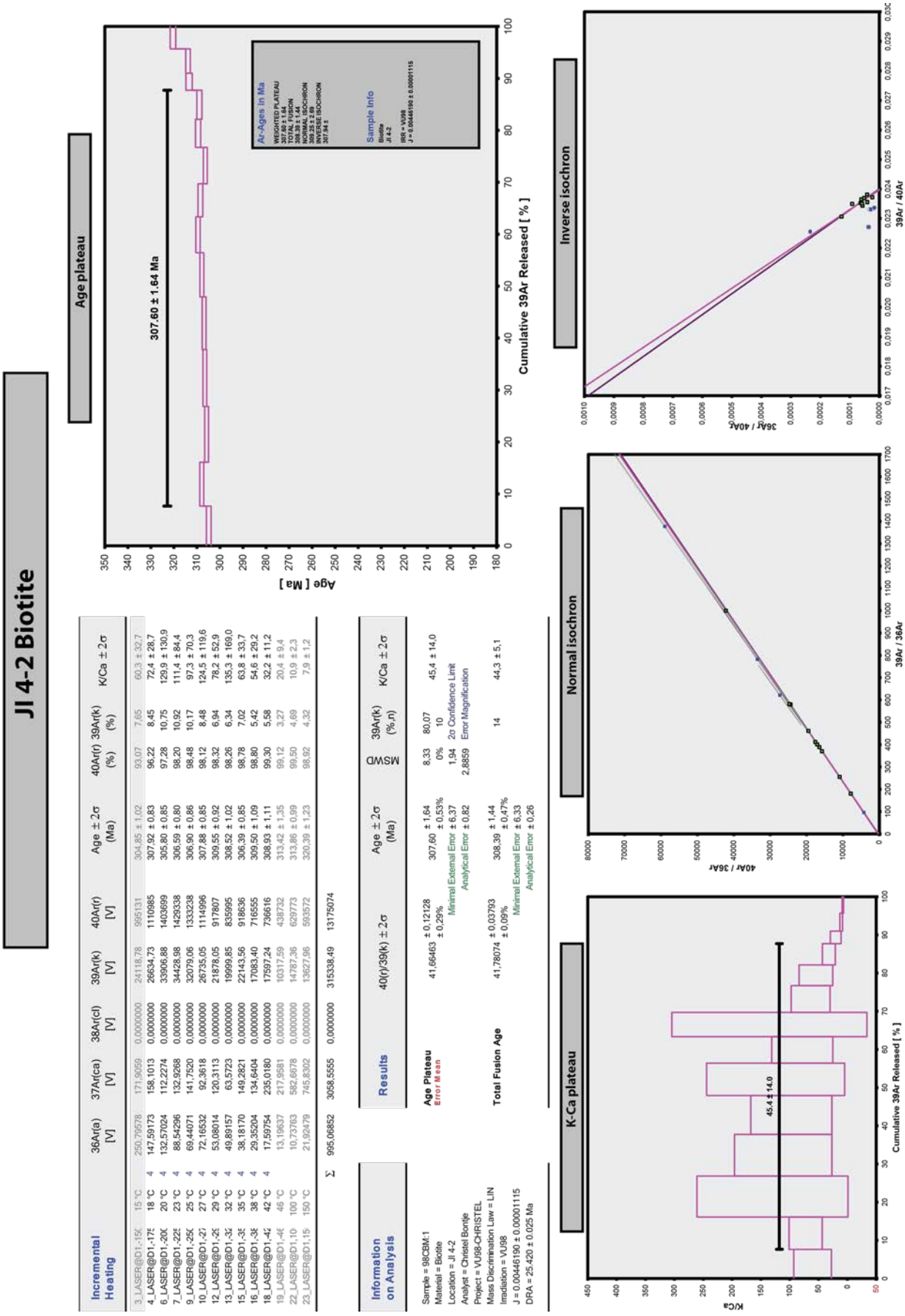

Incremental Heating		36Ar(a) [V]	37Ar(ca) [V]	38Ar(cl) [V]	39Ar(k) [V]	40Ar(r) [V]	Age ± 2σ (Ma)	40Ar(r) (%)	39Ar(k) (%)	K/Ca ± 2σ
3_LASER@D1,15C	15 °C	250.79578	171.9059	0.0000000	24118.78	995131	304.85 ± 1.02	93.07	7.65	60.3 ± 32.7
4_LASER@D1,17:	18 °C	147.59173	158.1013	0.0000000	26634.73	1110985	307.92 ± 0.83	96.22	8.45	72.4 ± 28.7
6_LASER@D1,20(	20 °C	132.57024	112.2274	0.0000000	33906.88	1403699	305.80 ± 0.85	97.28	10.75	129.9 ± 130.9
7_LASER@D1,22:	23 °C	88.54296	132.9268	0.0000000	34428.98	1429338	306.59 ± 0.80	98.20	10.92	111.4 ± 84.4
9_LASER@D1,25(	25 °C	69.44071	141.7520	0.0000000	32079.06	1333238	306.90 ± 0.86	98.48	10.17	97.3 ± 70.3
10_LASER@D1,27	27 °C	72.16532	92.3618	0.0000000	26735.05	1114996	307.88 ± 0.85	98.12	8.48	124.5 ± 119.6
12_LASER@D1,2:	29 °C	53.08014	120.3113	0.0000000	21878.05	917807	309.55 ± 0.92	98.32	6.94	78.2 ± 52.9
13_LASER@D1,3(	32 °C	49.89157	63.5723	0.0000000	19999.85	835995	308.52 ± 1.02	98.26	6.34	135.3 ± 169.0
15_LASER@D1,3:	35 °C	38.18170	149.2821	0.0000000	22143.56	918636	306.39 ± 0.85	98.78	7.02	63.8 ± 33.7
16_LASER@D1,3(	38 °C	29.35204	134.6404	0.0000000	17083.40	716555	309.50 ± 1.09	98.80	5.42	54.6 ± 29.2
18_LASER@D1,4:	42 °C	17.59754	235.0180	0.0000000	17597.24	736616	308.93 ± 1.11	99.30	5.58	32.2 ± 11.2
19_LASER@D1,4(	46 °C	13.19637	217.9581	0.0000000	10317.59	438732	313.42 ± 1.35	99.12	3.27	20.4 ± 9.4
22_LASER@D1,10	100 °C	10.73763	582.6678	0.0000000	14787.36	629773	313.86 ± 0.99	99.50	4.69	10.9 ± 2.3
23_LASER@D1,15	150 °C	21.92479	745.8302	0.0000000	13627.96	593572	320.39 ± 1.23	98.92	4.32	7.9 ± 1.2
	Σ	995.06852	3058.5555	0.0000000	315338.49	13175074				

Information on Analysis	Results	40(r)/39(k) ± 2σ	Age ± 2σ (Ma)	MSWD	39Ar(k) (%,n)	K/Ca ± 2σ
Sample = 98CBM:1	**Age Plateau**	41,66463 ± 0,12128	307,60 ± 1,64	8,33	80,07	45,4 ± 14,0
Material = Biotite	Error: Mean	± 0,29%	± 0,53%	0%	10	
Location = JI 4-2		Minimal External Error ± 6,37		1,94	2σ Confidence Limit	
Analyst = Christel Bonjé		Analytical Error ± 0,82		2,8859	Error Magnification	
Project = VU98-CHRISTEL						
Mass Discrimination Law = LIN	**Total Fusion Age**	41,78074 ± 0,03793	308,39 ± 1,44		14	44,3 ± 5,1
Irradiation = VU98		± 0,09%	± 0,47%			
J = 0.00446190 ± 0.00001115		Minimal External Error ± 6,33				
DRA = 25.420 ± 0.025 Ma		Analytical Error ± 0,26				

Figure 102. Stepwise heating results of biotite in JI 4-2.

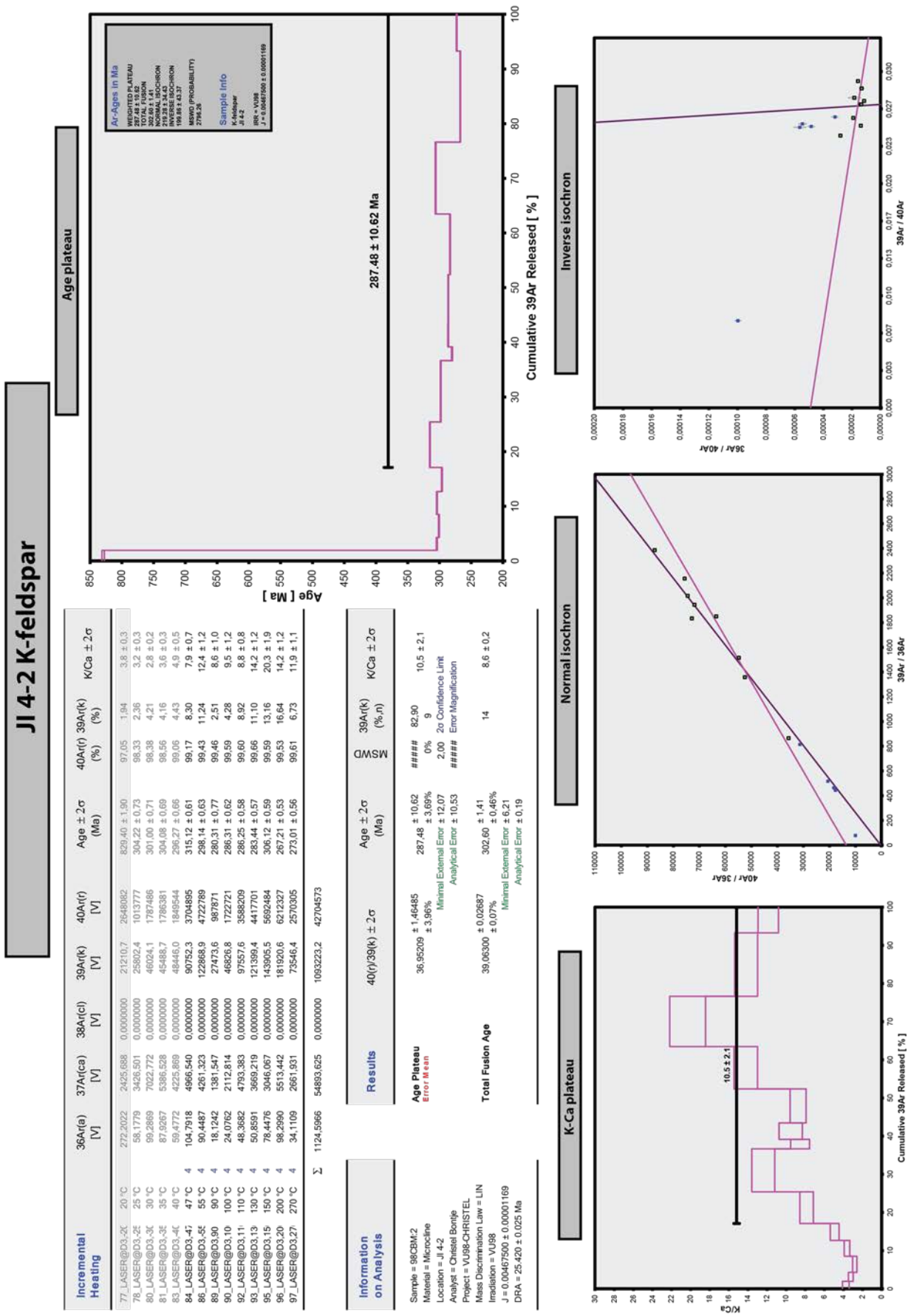

Incremental Heating		36Ar(a) [V]	37Ar(ca) [V]	38Ar(cl) [V]	39Ar(k) [V]	40Ar(r) [V]	Age ± 2σ (Ma)	40Ar(r) (%)	39Ar(k) (%)	K/Ca ± 2σ
77_LASER@D3_2(	20 °C	272,2022	2425,688	0,0000000	21210,7	2648082	829,40 ± 1,90	97,05	1,94	3,8 ± 0,3
78_LASER@D3_2(	25 °C	58,1779	3426,501	0,0000000	25802,4	1013777	304,22 ± 0,73	98,33	2,36	3,2 ± 0,3
80_LASER@D3_3(	30 °C	99,2869	7022,772	0,0000000	46024,1	1787486	301,00 ± 0,71	98,38	4,21	2,8 ± 0,2
81_LASER@D3_3(	35 °C	87,9267	5386,528	0,0000000	45488,7	1786381	304,08 ± 0,69	98,56	4,16	3,6 ± 0,3
83_LASER@D3_4(	40 °C	59,4772	4225,869	0,0000000	48446,0	1849544	296,27 ± 0,66	99,06	4,43	4,9 ± 0,5
84_LASER@D3_47	47 °C 4	104,7918	4966,540	0,0000000	90752,3	3704895	315,12 ± 0,61	99,17	8,30	7,9 ± 0,7
86_LASER@D3_5(	55 °C 4	90,4487	4261,323	0,0000000	122868,9	4722789	298,14 ± 0,63	99,43	11,24	12,4 ± 1,2
89_LASER@D3_90	90 °C 4	18,1242	1381,547	0,0000000	27473,6	987871	280,31 ± 0,77	99,46	2,51	8,6 ± 1,0
90_LASER@D3_10	100 °C 4	24,0762	2112,814	0,0000000	46826,8	1722721	286,31 ± 0,62	99,59	4,28	9,5 ± 1,2
92_LASER@D3_11	110 °C 4	48,3682	4793,383	0,0000000	97557,6	3588209	286,25 ± 0,58	99,60	8,92	8,8 ± 0,8
93_LASER@D3_13	130 °C 4	50,8591	3669,219	0,0000000	121399,4	4417701	283,44 ± 0,57	99,66	11,10	14,2 ± 1,2
95_LASER@D3_15	150 °C 4	78,4476	3046,067	0,0000000	143905,5	5692484	306,12 ± 0,59	99,59	13,16	20,3 ± 1,9
96_LASER@D3_20	200 °C 4	98,2990	5513,442	0,0000000	181920,6	6212327	267,21 ± 0,53	99,53	16,64	14,2 ± 1,2
97_LASER@D3_27	270 °C 4	34,1109	2661,931	0,0000000	73546,4	2570305	273,01 ± 0,56	99,61	6,73	11,9 ± 1,1
	Σ	1124,5966	54893,625	0,0000000	1093223,2	42704573				

Information on Analysis	Results	40(r)/39(k) ± 2σ	Age ± 2σ (Ma)	MSWD	39Ar(k) (%,n)	K/Ca ± 2σ
Sample = 98CBM-2	**Age Plateau**	36,95209 ± 1,46485	287,48 ± 10,62	#####	82,90	10,5 ± 2,1
Material = Microcline	Error Mean	± 3,96%	± 3,69%	0%	9	
Location = JI 4-2		Minimal External Error ± 12,07		2,00	2σ Confidence Limit	
Analyst = Christel Bonjé		Analytical Error ± 10,53		#####	Error Magnification	
Project = VU98-CHRISTEL						
Mass Discrimination Law = LIN	**Total Fusion Age**	39,06300 ± 0,02687	302,60 ± 1,41		14	8,6 ± 0,2
Irradiation = VU98		± 0,07%	± 0,46%			
J = 0,00467500 ± 0,00001169		Minimal External Error ± 6,21				
DRA = 25.420 ± 0.025 Ma		Analytical Error ± 0,19				

Figure 103. Stepwise heating results of K-feldspar in JI 4-2.

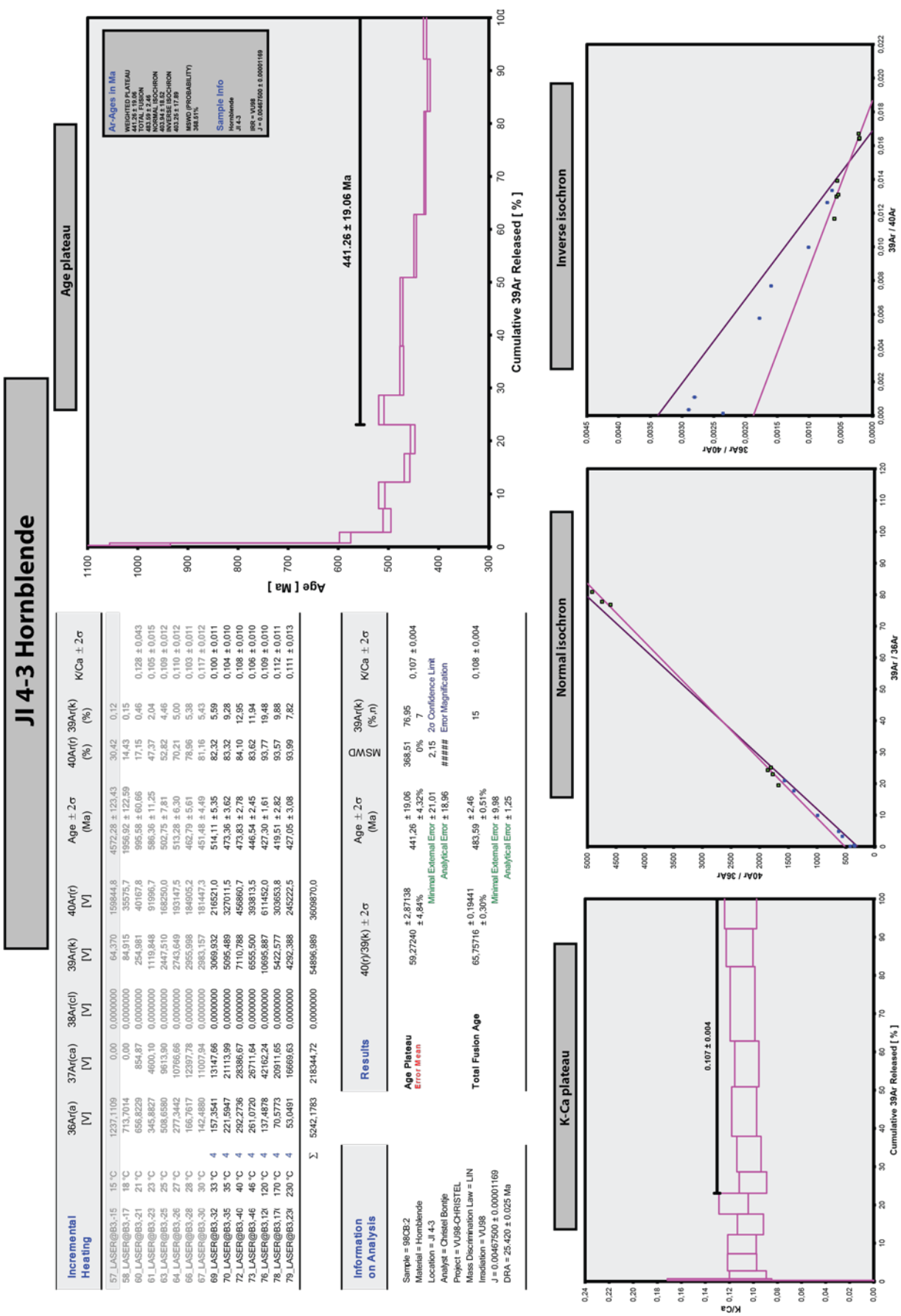

Incremental Heating		36Ar(a) [V]	37Ar(ca) [V]	38Ar(cl) [V]	39Ar(k) [V]	40Ar(r) [V]	Age ± 2σ (Ma)	40Ar(r) (%)	39Ar(k) (%)	K/Ca ± 2σ
57_LASER@B3,-15	15 °C	1237,1109	0,00	0,0000000	64,370	159844,8	4572,28 ± 123,43	30,42	0,12	
58_LASER@B3,-17	18 °C	713,7014	0,00	0,0000000	84,915	35575,7	1956,92 ± 122,59	14,43	0,15	
60_LASER@B3,-21	21 °C	656,8229	854,87	0,0000000	254,981	40167,8	995,58 ± 60,66	17,15	0,46	0,128 ± 0,043
61_LASER@B3,-23	23 °C	345,8827	4600,10	0,0000000	1119,848	91996,7	586,36 ± 11,25	47,37	2,04	0,105 ± 0,015
63_LASER@B3,-25	25 °C	508,6580	9613,90	0,0000000	2447,510	168250,0	502,75 ± 7,81	52,82	4,46	0,109 ± 0,012
64_LASER@B3,-26	27 °C	277,3442	10766,66	0,0000000	2743,649	193147,5	513,28 ± 6,30	70,21	5,00	0,110 ± 0,012
66_LASER@B3,-28	28 °C	166,7617	12397,78	0,0000000	2955,998	184905,2	462,79 ± 5,61	78,96	5,38	0,103 ± 0,011
67_LASER@B3,-30	30 °C	142,4880	11007,94	0,0000000	2983,157	181447,3	451,48 ± 4,49	81,16	5,43	0,117 ± 0,012
69_LASER@B3,-32	33 °C 4	157,3541	13147,66	0,0000000	3069,932	216521,0	514,11 ± 5,35	82,32	5,59	0,100 ± 0,011
70_LASER@B3,-35	35 °C 4	221,5947	21113,99	0,0000000	5095,489	327011,5	473,36 ± 3,62	83,32	9,28	0,104 ± 0,010
72_LASER@B3,-40	40 °C 4	292,2736	28386,67	0,0000000	7110,788	456860,7	473,83 ± 2,78	84,10	12,95	0,108 ± 0,010
73_LASER@B3,-46	46 °C 4	261,0720	26711,64	0,0000000	6555,500	393813,5	446,54 ± 2,45	83,62	11,94	0,106 ± 0,010
76_LASER@B3,12(	120 °C 4	137,4878	42162,24	0,0000000	10695,887	611452,0	427,30 ± 1,61	93,77	19,48	0,109 ± 0,010
78_LASER@B3,17(	170 °C 4	70,5773	20911,65	0,0000000	5422,577	303653,8	419,51 ± 2,82	93,57	9,88	0,112 ± 0,011
79_LASER@B3,23(	230 °C 4	53,0491	16669,63	0,0000000	4292,388	245222,5	427,05 ± 3,08	93,99	7,82	0,111 ± 0,013
	Σ	5242,1783	218344,72	0,0000000	54896,989	3609870,0				

Information on Analysis	Results	40(r)/39(k) ± 2σ	Age ± 2σ (Ma)	MSWD	39Ar(k) (%,n)	K/Ca ± 2σ
Sample = 98CB-2	**Age Plateau**	± 2,87138	441,26 ± 19,06	368,51	76,95	0,107 ± 0,004
Material = Hornblende	Error Mean	± 4,84%	± 4,32%	0%	7	
Location = JI 4-3		Minimal External Error ± 21,01		2,15	2σ Confidence Limit	
Analyst = Christel Bonjé		Analytical Error ± 18,96		#####	Error Magnification	
Project = VU98-CHRISTEL						
Mass Discrimination Law = LIN	**Total Fusion Age**	± 0,19441	483,59 ± 2,46		15	0,108 ± 0,004
Irradiation = VU98		± 0,30%	± 0,51%			
J = 0.00467500 ± 0.00001169		Minimal External Error ± 9,98				
DRA = 25.420 ± 0.025 Ma		Analytical Error ± 1,25				

Figure 104. Stepwise heating results of hornblende in JI 4-3.

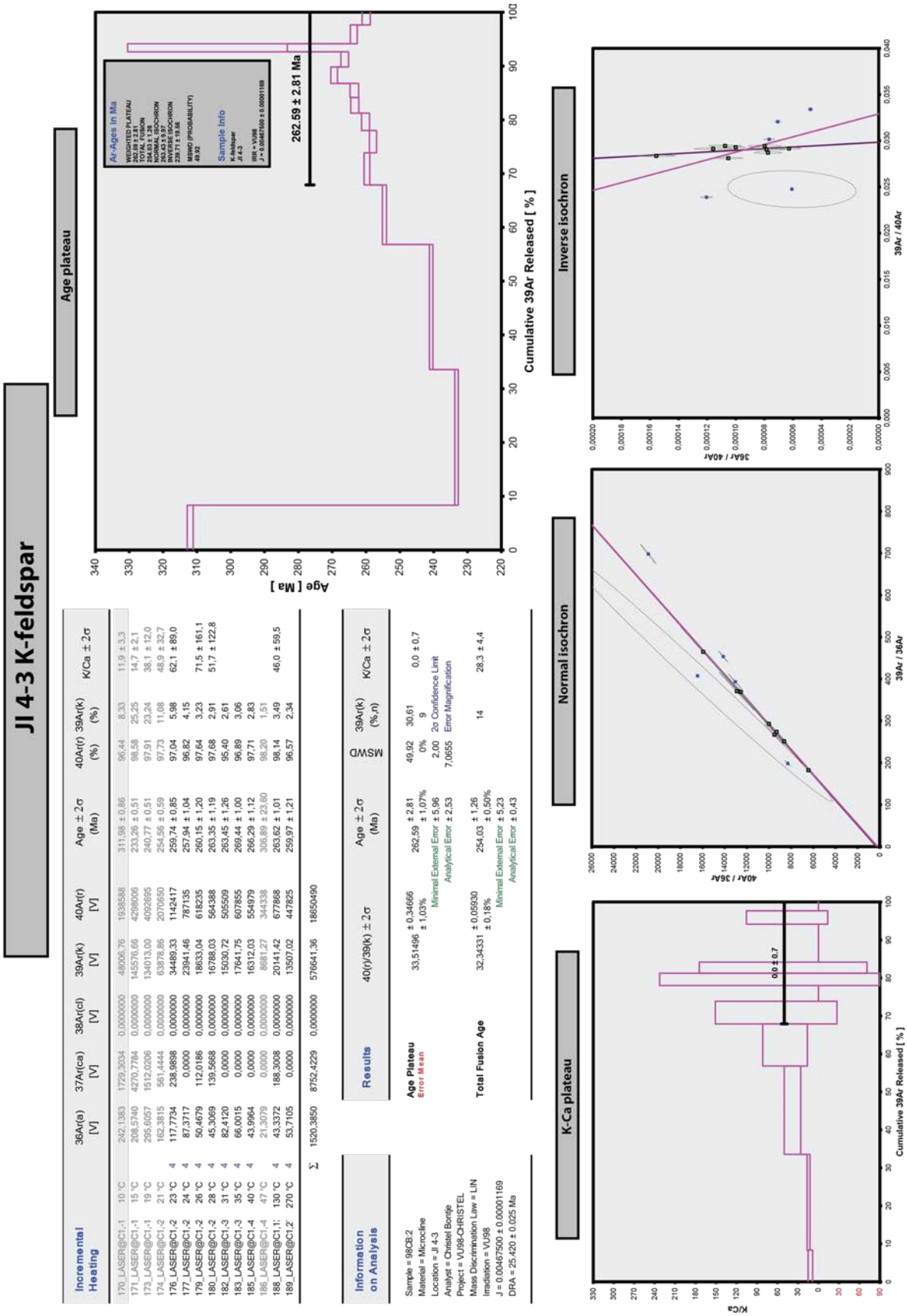

Incremental Heating		36Ar(a) [V]	37Ar(ca) [V]	38Ar(cl) [V]	39Ar(k) [V]	40Ar(r) [V]	Age ± 2σ (Ma)	40Ar(r) (%)	39Ar(k) (%)	K/Ca ± 2σ
170_LASER@C1,-1	10 °C	242,1383	1729,3034	0,0000000	48006,76	1938588	311,88 ± 0,86	96,44	8,33	11,9 ± 3,3
171_LASER@C1,-1	15 °C	208,5740	4270,7784	0,0000000	145576,66	4298006	233,26 ± 0,51	98,58	25,25	14,7 ± 2,1
173_LASER@C1,-1	19 °C	295,6057	1512,0206	0,0000000	134013,00	4092695	240,77 ± 0,51	97,91	23,24	38,1 ± 12,0
174_LASER@C1,-2	21 °C	162,3815	561,4444	0,0000000	63878,86	2070650	254,96 ± 0,59	97,73	11,08	48,9 ± 32,7
176_LASER@C1,-2	23 °C 4	117,7734	238,9898	0,0000000	34489,33	1142417	259,74 ± 0,85	97,04	5,98	62,1 ± 89,0
177_LASER@C1,-2	24 °C 4	87,3717	0,0000	0,0000000	23941,46	787135	257,94 ± 1,04	96,82	4,15	
179_LASER@C1,-2	26 °C 4	50,4679	112,0186	0,0000000	18633,04	618235	260,15 ± 1,20	97,64	3,23	71,5 ± 161,1
180_LASER@C1,-2	28 °C 4	45,3069	139,5668	0,0000000	16788,03	564388	263,35 ± 1,19	97,68	2,91	51,7 ± 122,8
182_LASER@C1,-3	31 °C 4	82,4120	0,0000	0,0000000	15030,72	505509	263,45 ± 1,26	95,40	2,61	
183_LASER@C1,-3	35 °C 4	66,0015	0,0000	0,0000000	17641,75	607855	269,44 ± 1,00	96,89	3,06	
185_LASER@C1,-4	40 °C 4	43,9964	0,0000	0,0000000	16312,03	554979	266,29 ± 1,12	97,71	2,83	
186_LASER@C1,-4	47 °C	21,3079	0,0000	0,0000000	8681,27	344338	306,89 ± 23,60	98,20	1,51	
188_LASER@C1,1:	130 °C 4	43,3372	188,3008	0,0000000	20141,42	677868	263,62 ± 1,01	98,14	3,49	46,0 ± 59,5
189_LASER@C1,2	270 °C 4	53,7105	0,0000	0,0000000	13507,02	447825	259,97 ± 1,21	96,57	2,34	
	Σ	1520,3850	8752,4229	0,0000000	576641,36	18650490				

Information on Analysis	Results	40(r)/39(k) ± 2σ	Age ± 2σ (Ma)	MSWD	39Ar(k) (%,n)	K/Ca ± 2σ
Sample = 98CB:2	**Age Plateau**	33,51496 ± 0,34666	262,59 ± 2,81	49,92	30,61	0,0 ± 0,7
Material = Microcline	Error Mean	± 1,03%	± 1,07%	0%	9	
Location = JI 4-3		Minimal External Error ± 5,96		2,00	2σ Confidence Limit	
Analyst = Christel Bontje		Analytical Error ± 2,53		7,0655	Error Magnification	
Project = VU98-CHRISTEL						
Mass Discrimination Law = LIN						
Irradiation = VU98	**Total Fusion Age**	32,34331 ± 0,05930	254,03 ± 1,26		14	28,3 ± 4,4
J = 0.00467500 ± 0.00001169		± 0,18%	± 0,50%			
DRA = 25.420 ± 0.025 Ma		Minimal External Error ± 5,23				
		Analytical Error ± 0,43				

Figure 105. Stepwise heating results of K-feldspar in JI 4-3.

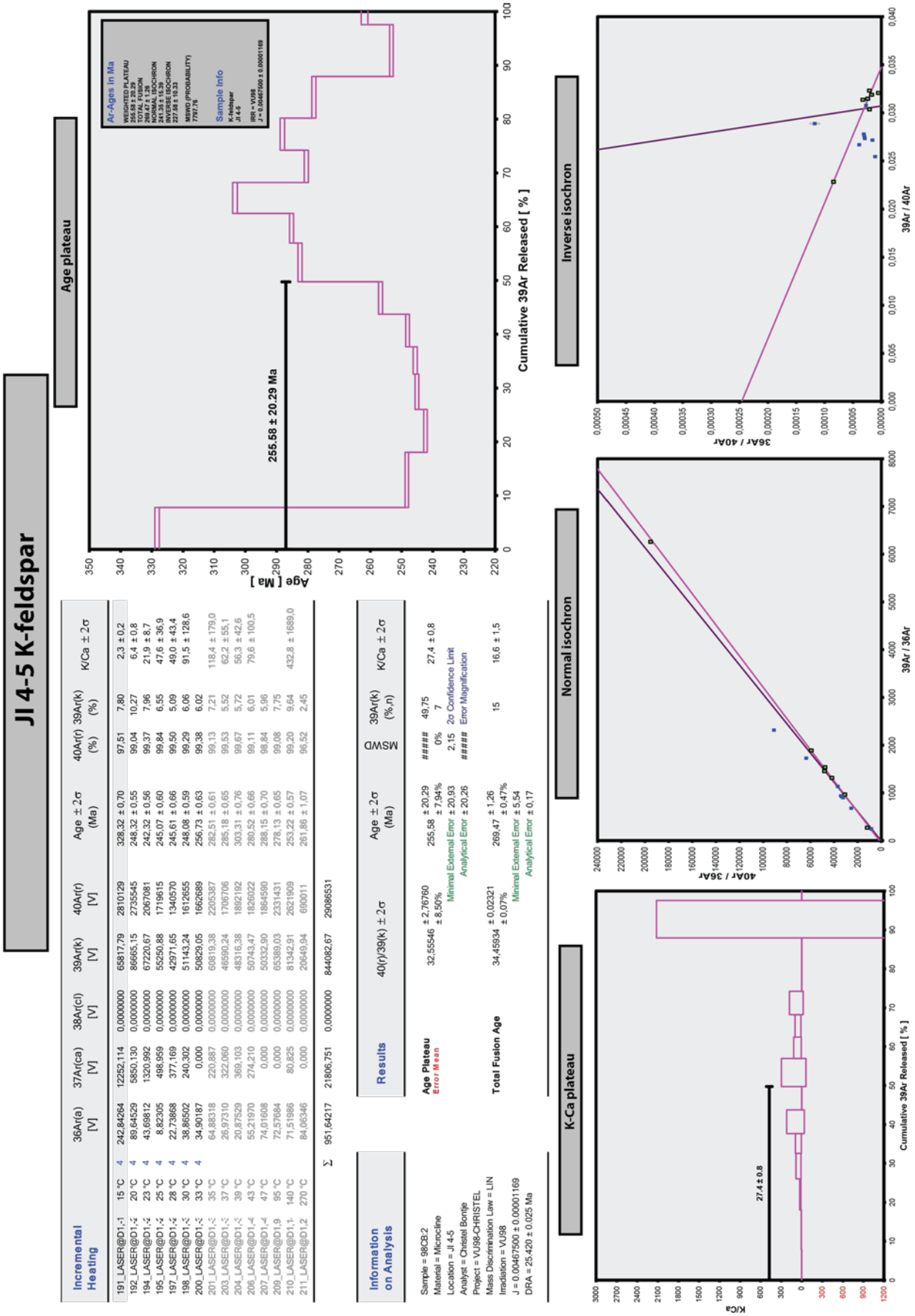

Figure 106. Stepwise heating results of K-feldspar in JI 4-5.

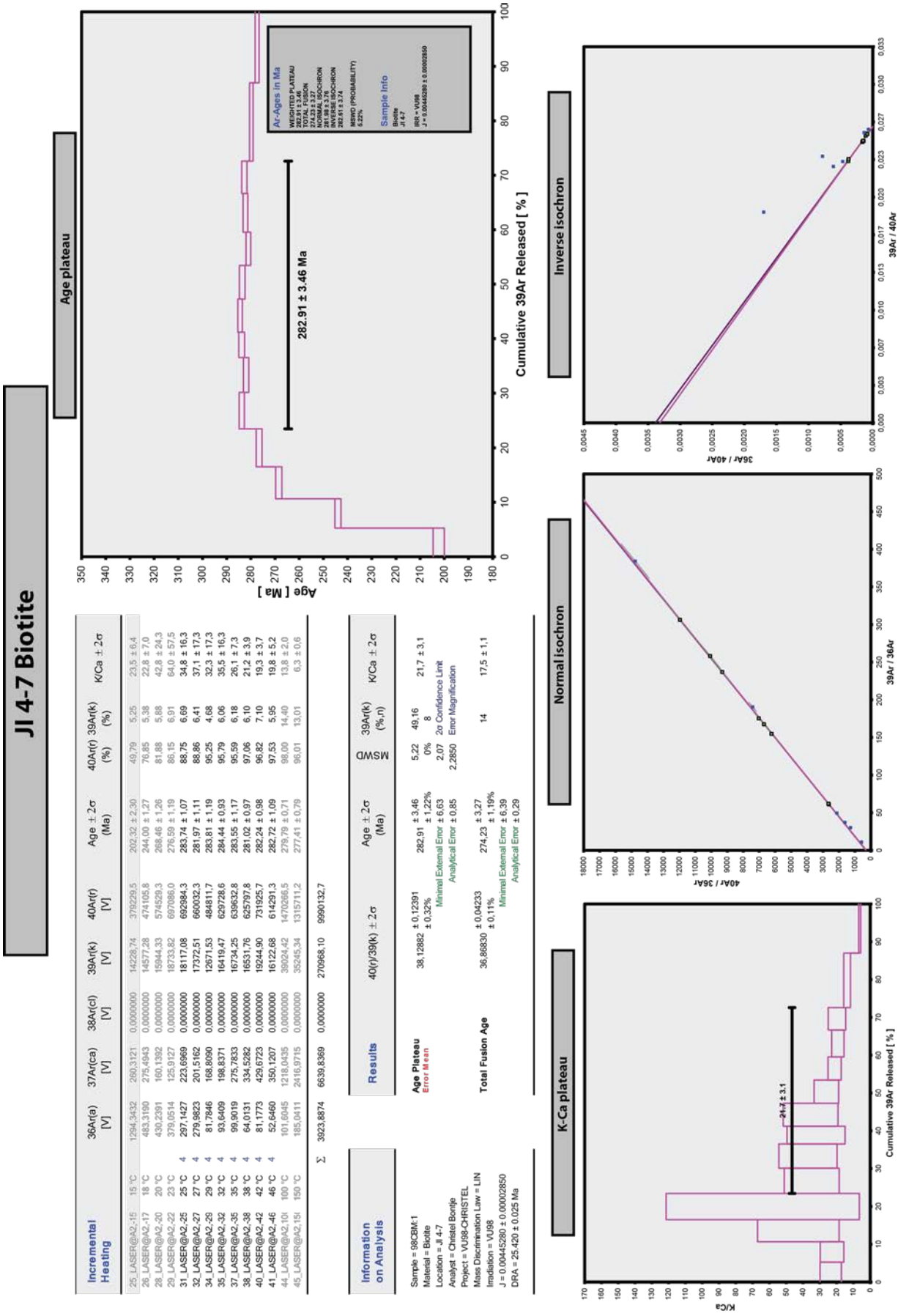

Incremental Heating		36Ar(a) [V]	37Ar(ca) [V]	38Ar(cl) [V]	39Ar(k) [V]	40Ar(r) [V]	Age ± 2σ (Ma)	40Ar(r) (%)	39Ar(k) (%)	K/Ca ± 2σ
25_LASER@A2-15	15 °C	1294,3432	260,3121	0,0000000	14228,74	379229,5	202,32 ± 2,30	49,79	5,25	23,5 ± 6,4
26_LASER@A2-17	18 °C	483,3190	275,4943	0,0000000	14577,28	474105,8	244,00 ± 1,27	76,85	5,38	22,8 ± 7,0
28_LASER@A2-20	20 °C	430,2391	160,1392	0,0000000	15944,33	574529,3	268,46 ± 1,26	81,88	5,88	42,8 ± 24,3
29_LASER@A2-22	23 °C	379,0514	125,9127	0,0000000	18733,82	697086,0	276,59 ± 1,19	86,15	6,91	64,0 ± 57,5
31_LASER@A2-25	25 °C 4	297,1427	223,6969	0,0000000	18117,08	692984,3	283,74 ± 1,07	88,75	6,69	34,8 ± 16,3
32_LASER@A2-27	27 °C 4	279,9823	201,5162	0,0000000	17372,51	660032,3	281,97 ± 1,11	88,86	6,41	37,1 ± 17,3
34_LASER@A2-29	29 °C 4	81,7846	168,8090	0,0000000	12671,53	484811,7	283,81 ± 1,19	95,25	4,68	32,3 ± 17,3
35_LASER@A2-32	32 °C 4	93,6409	198,8371	0,0000000	16419,47	629728,6	284,44 ± 0,93	95,79	6,06	35,5 ± 16,3
37_LASER@A2-35	35 °C 4	99,9019	275,7833	0,0000000	16734,25	639632,8	283,55 ± 1,17	95,59	6,18	26,1 ± 7,3
38_LASER@A2-38	38 °C 4	64,0131	334,5282	0,0000000	16531,76	625797,8	281,02 ± 0,97	97,06	6,10	21,2 ± 3,9
40_LASER@A2-42	42 °C 4	81,1773	429,6723	0,0000000	19244,90	731925,7	282,24 ± 0,98	96,82	7,10	19,3 ± 3,7
41_LASER@A2-46	46 °C 4	52,6460	350,1207	0,0000000	16122,68	614291,3	282,72 ± 1,09	97,53	5,95	19,8 ± 5,2
44_LASER@A2-100	100 °C	101,6045	1218,0435	0,0000000	39024,42	1470266,5	279,79 ± 0,71	98,00	14,40	13,8 ± 2,0
45_LASER@A2-150	150 °C	185,0411	2416,9715	0,0000000	35245,34	1315711,2	277,41 ± 0,79	96,01	13,01	6,3 ± 0,6
	Σ	3923,8874	6639,8369	0,0000000	270968,10	9990132,7				

Information on Analysis	Results	40(r)/39(k) ± 2σ	Age ± 2σ (Ma)	MSWD	39Ar(k) (%,n)	K/Ca ± 2σ
Sample = 98CBM:1 Material = Biotite Location = JI 4-7 Analyst = Christel Bontje Project = VU98-CHRISTEL Mass Discrimination Law = LIN Irradiation = VU98 J = 0.00445280 ± 0.00002850 DRA = 25.420 ± 0.025 Ma	**Age Plateau** Error Mean	38,12882 ± 0.12391 ± 0.32%	282,91 ± 3.46 ± 1.22% Minimal External Error ± 6.63 Analytical Error ± 0.85	5.22 0% 2,07 2,2850	49,16 8 2σ Confidence Limit Error Magnification	21,7 ± 3,1
	Total Fusion Age	36,86830 ± 0.04233 ± 0.11%	274,23 ± 3.27 ± 1.19% Minimal External Error ± 6.39 Analytical Error ± 0.29		14	17,5 ± 1,1

Figure 107. Stepwise heating results of Biotite in JI 4-7.

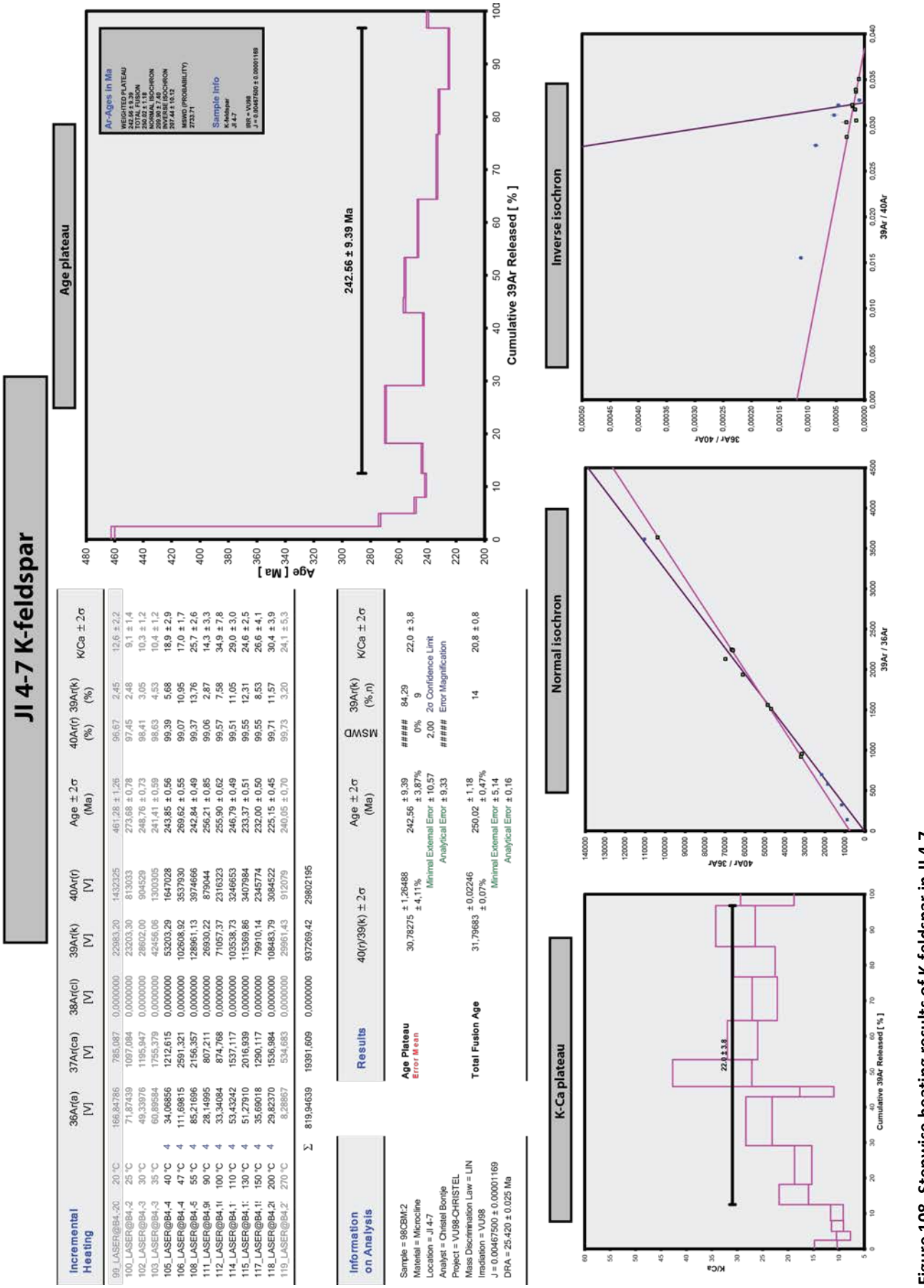

Incremental Heating		36Ar(a) [V]	37Ar(ca) [V]	38Ar(cl) [V]	39Ar(k) [V]	40Ar(r) [V]	Age ± 2σ (Ma)	40Ar(r) (%)	39Ar(k) (%)	K/Ca ± 2σ
99_LASER@B4.20	20 °C	166,84786	785,087	0,0000000	22983,20	1432325	461,28 ± 1,26	96,67	2,45	12,6 ± 2,2
100_LASER@B4.2	25 °C	71,87439	1097,084	0,0000000	23203,30	813033	273,68 ± 0,78	97,45	2,48	9,1 ± 1,4
102_LASER@B4.3	30 °C	49,33976	1195,947	0,0000000	28602,00	904529	248,76 ± 0,73	98,41	3,05	10,3 ± 1,2
103_LASER@B4.3	35 °C	60,89584	1755,379	0,0000000	42456,06	1300305	241,41 ± 0,59	98,63	4,53	10,4 ± 1,2
105_LASER@B4.4	40 °C 4	34,06856	1212,615	0,0000000	53203,29	1647028	243,85 ± 0,56	99,39	5,68	18,9 ± 2,9
106_LASER@B4.4	47 °C 4	111,69815	2591,321	0,0000000	102608,92	3537930	269,62 ± 0,55	99,07	10,95	17,0 ± 1,7
108_LASER@B4.5	55 °C 4	85,21696	2156,357	0,0000000	128961,13	3974666	242,84 ± 0,49	99,37	13,76	25,7 ± 2,6
111_LASER@B4.9	90 °C 4	28,14995	807,211	0,0000000	26930,22	879044	256,21 ± 0,85	99,06	2,87	14,3 ± 3,3
112_LASER@B4.1	100 °C 4	33,34084	874,768	0,0000000	71057,37	2316323	255,90 ± 0,62	99,57	7,58	34,9 ± 7,8
114_LASER@B4.1	110 °C 4	53,43242	1537,117	0,0000000	103538,73	3246653	246,79 ± 0,49	99,51	11,05	29,0 ± 3,0
115_LASER@B4.1	130 °C 4	51,27910	2016,939	0,0000000	115369,86	3407984	233,37 ± 0,51	99,55	12,31	24,6 ± 2,5
117_LASER@B4.1	150 °C 4	35,69018	1290,117	0,0000000	79910,14	2345774	232,00 ± 0,50	99,55	8,53	26,6 ± 4,1
118_LASER@B4.2	200 °C 4	29,82370	1536,984	0,0000000	108483,79	3084522	225,15 ± 0,45	99,71	11,57	30,4 ± 3,9
119_LASER@B4.2	270 °C	8,28867	534,683	0,0000000	29961,43	912079	240,05 ± 0,70	99,73	3,20	24,1 ± 5,3
	Σ	819,94639	19391,609	0,0000000	937269,42	29802195				

Information on Analysis	Results	40(r)/39(k) ± 2σ	Age ± 2σ (Ma)	MSWD	39Ar(k) (%,n)	K/Ca ± 2σ
Sample = 98CBM.2	**Age Plateau**	30,78275 ± 1,26488	242,56 ± 9,39	#####	84,29	22,0 ± 3,8
Material = Microcline	Error Mean	± 4,11%	± 3,87%	0%	9	
Location = JI 4-7		Minimal External Error ± 10,57		2,00	2σ Confidence Limit	
Analyst = Christel Bonije		Analytical Error ± 9,33		#####	Error Magnification	
Project = VU98-CHRISTEL						
Mass Discrimination Law = LIN	**Total Fusion Age**	± 0,02246	± 1,18		14	20,8 ± 0,8
Irradiation = VU98		31,79683 ± 0,07%	250,02 ± 0,47%			
J = 0,00467500 ± 0,00001169		Minimal External Error ± 5,14				
DRA = 25.420 ± 0.025 Ma		Analytical Error ± 0,16				

Figure 108. Stepwise heating results of K-feldspar in JI 4-7.

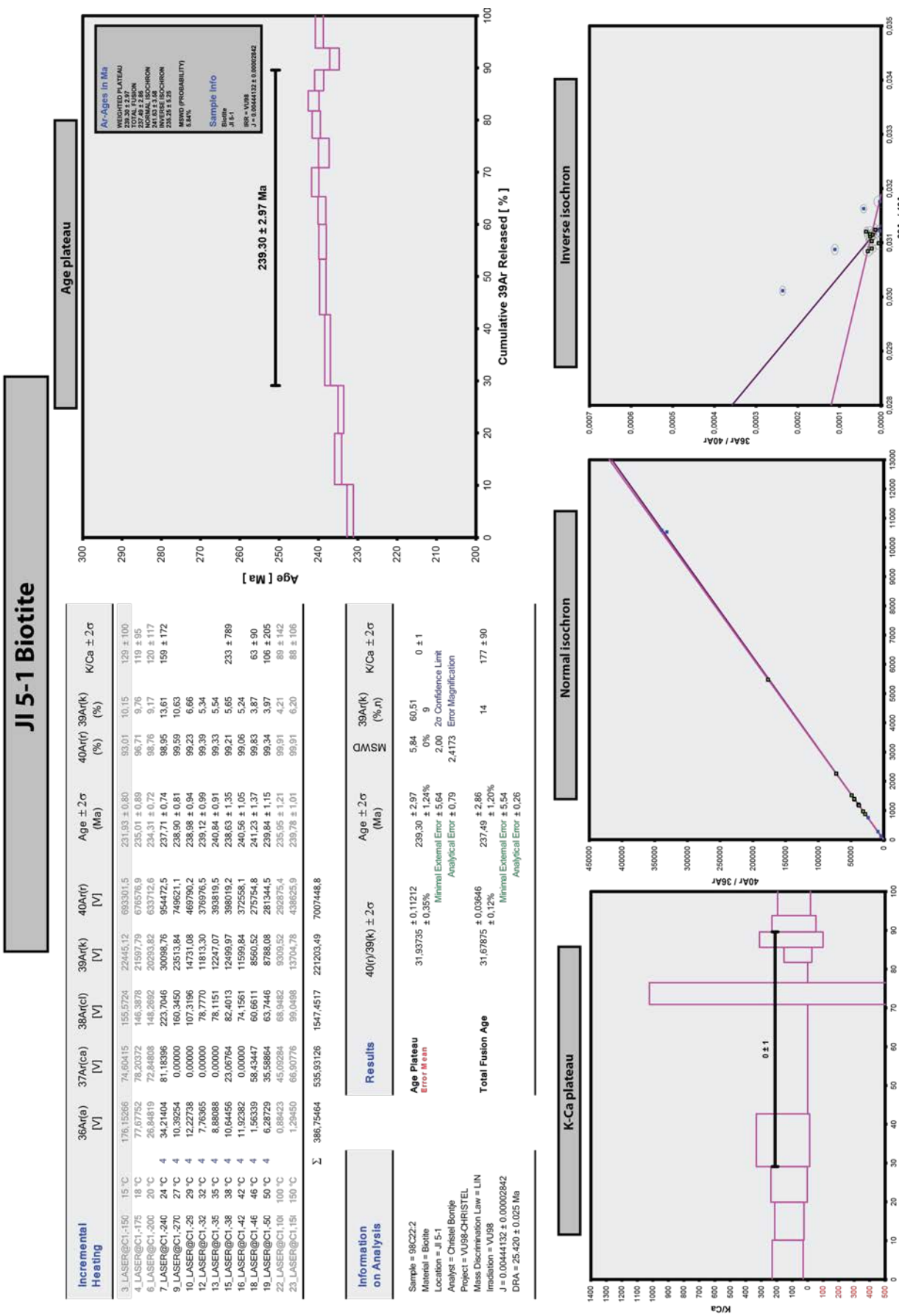

Figure 109. Stepwise heating results of Biotite in JI 5-1.

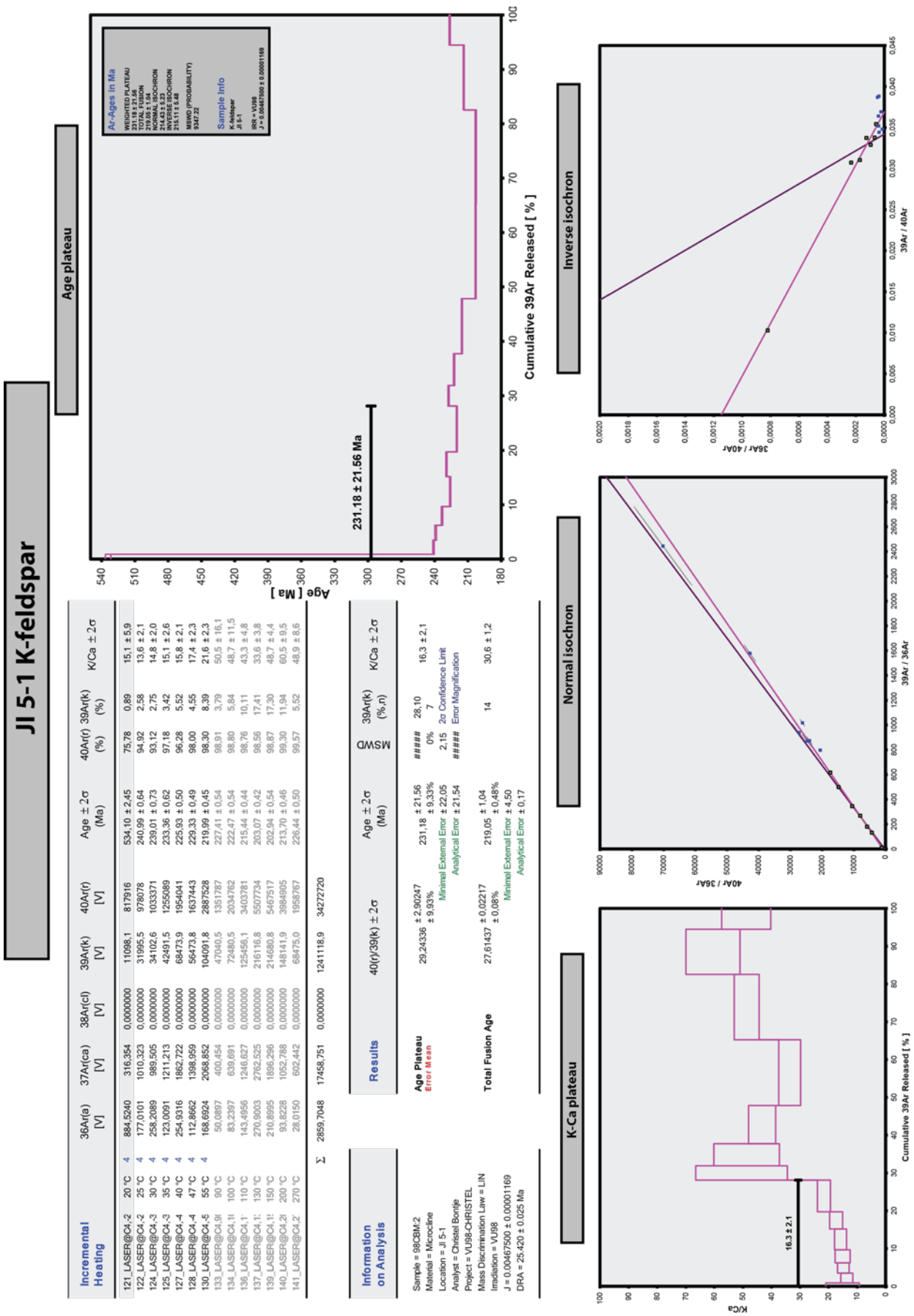

Figure 110. Stepwise heating results of K-feldspar in JI 5-1.

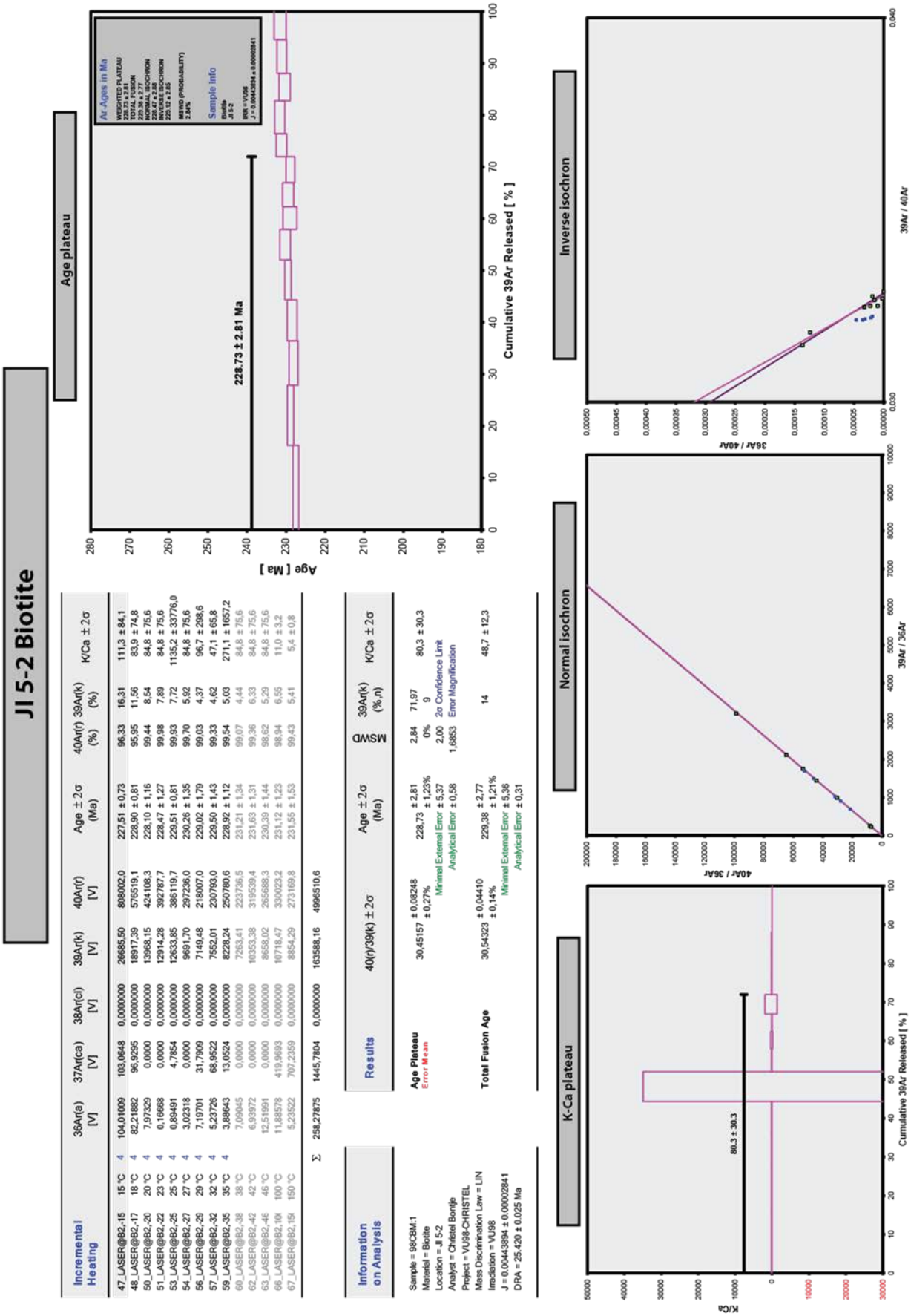

Incremental Heating			36Ar(a) [V]	37Ar(ca) [V]	38Ar(cl) [V]	39Ar(k) [V]	40Ar(r) [V]	Age ± 2σ (Ma)	40Ar(r) (%)	39Ar(k) (%)	K/Ca ± 2σ
47_LASER@B2,-15	15 °C	4	104,01009	103,0648	0,0000000	26685,50	808002,0	227,51 ± 0,73	96,33	16,31	111,3 ± 84,1
48_LASER@B2,-17	18 °C	4	82,21882	96,9295	0,0000000	18917,39	576519,1	228,90 ± 0,81	95,95	11,56	83,9 ± 74,8
50_LASER@B2,-20	20 °C	4	7,97329	0,0000	0,0000000	13968,15	424108,3	228,10 ± 1,16	99,44	8,54	84,8 ± 75,6
51_LASER@B2,-22	23 °C	4	0,16668	0,0000	0,0000000	12914,28	392787,7	228,47 ± 1,27	99,98	7,89	84,8 ± 75,6
53_LASER@B2,-25	25 °C	4	0,89491	4,7854	0,0000000	12633,85	386119,7	229,51 ± 0,81	99,93	7,72	1135,2 ± 33776,0
54_LASER@B2,-27	27 °C	4	3,02318	0,0000	0,0000000	9691,70	297236,0	230,26 ± 1,35	99,70	5,92	84,8 ± 75,6
56_LASER@B2,-29	29 °C	4	7,19701	31,7909	0,0000000	7149,48	218007,0	229,02 ± 1,79	99,03	4,37	96,7 ± 298,6
57_LASER@B2,-32	32 °C	4	5,23726	68,9522	0,0000000	7552,01	230793,0	229,50 ± 1,43	99,33	4,62	47,1 ± 65,8
59_LASER@B2,-35	35 °C	4	3,88643	13,0524	0,0000000	8228,24	250780,6	228,92 ± 1,12	99,54	5,03	271,1 ± 1657,2
60_LASER@B2,-38	38 °C		7,09045	0,0000	0,0000000	7263,41	223736,5	231,21 ± 1,34	99,07	4,44	84,8 ± 75,6
62_LASER@B2,-42	42 °C		6,93972	0,0000	0,0000000	10353,38	319539,4	231,63 ± 1,31	99,36	6,33	84,8 ± 75,6
63_LASER@B2,-46	46 °C		12,51991	0,0000	0,0000000	8638,02	265688,3	230,39 ± 1,44	98,62	5,29	84,8 ± 75,6
66_LASER@B2,-100	100 °C		11,88578	419,9693	0,0000000	10718,47	330023,2	231,12 ± 1,23	98,94	6,55	11,0 ± 3,2
67_LASER@B2,-150	150 °C		5,23522	707,2359	0,0000000	8854,29	273169,8	231,55 ± 1,53	99,43	5,41	5,4 ± 0,8
		Σ	258,27875	1445,7804	0,0000000	163588,16	4996510,6				

Information on Analysis	Results	40(r)/39(k) ± 2σ	Age ± 2σ (Ma)	MSWD	39Ar(k) (%,n)	K/Ca ± 2σ
Sample = 98CBM-1	**Age Plateau**	30,45157 ± 0,08248	228,73 ± 2,81	2,84	71,97	80,3 ± 30,3
Material = Biotite	Error Mean	± 0,27%	± 1,23%	0%	9	
Location = JI 5-2		Minimal External Error ± 5,37		2,00	2σ Confidence Limit	
Analyst = Christel Bonjé		Analytical Error ± 0,58		1,6853	Error Magnification	
Project = VU98-CHRISTEL						
Mass Discrimination Law = LIN	**Total Fusion Age**	30,54323 ± 0,04410	229,38 ± 2,77		14	48,7 ± 12,3
Irradiation = VU98		± 0,14%	± 1,21%			
J = 0,00443894 ± 0,00002841		Minimal External Error ± 5,36				
DRA = 25,420 ± 0,025 Ma		Analytical Error ± 0,31				

Figure 111. Stepwise heating results of biotite in JI 5-2.

JI 5-2 K-feldspar

Incremental Heating			36Ar(a) [V]	37Ar(ca) [V]	38Ar(cl) [V]	39Ar(k) [V]	40Ar(r) [V]	Age ± 2σ (Ma)	40Ar(r) (%)	39Ar(k) (%)	K/Ca ± 2σ
55_LASER@D4,-2(	20 °C	4	2452,1631	1280,998	0,0000000	18744,5	1727744	646,42 ± 2,86	70,45	1,19	6,3 ± 0,9
56_LASER@D4,-2[	25 °C	4	279,1271	1830,199	0,0000000	40357,0	1246792	243,38 ± 0,78	93,79	2,57	9,5 ± 1,0
58_LASER@D4,-3(	30 °C	4	183,3239	3701,186	0,0000000	55680,2	1654065	234,61 ± 0,58	96,82	3,55	6,5 ± 0,7
59_LASER@D4,-3[	35 °C	4	210,1160	4340,750	0,0000000	79752,9	2306163	228,75 ± 0,59	97,37	5,08	7,9 ± 0,7
61_LASER@D4,-4(	40 °C	4	172,5027	3534,535	0,0000000	89160,9	2538418	225,43 ± 0,55	98,03	5,68	10,8 ± 1,0
62_LASER@D4,-47	47 °C	4	266,5930	2164,515	0,0000000	136646,3	3756967	218,15 ± 0,47	97,94	8,71	27,1 ± 3,1
64_LASER@D4,-5[	55 °C	4	227,4865	1708,637	0,0000000	161602,7	4336169	213,20 ± 0,42	98,47	10,30	40,7 ± 5,7
67_LASER@D4,90	90 °C	4	152,5151	803,485	0,0000000	129879,5	3518848	215,15 ± 0,51	98,73	8,28	69,5 ± 12,2
68_LASER@D4,10	100 °C	4	177,8207	809,791	0,0000000	145284,7	3908458	213,72 ± 0,43	98,67	9,26	77,1 ± 13,4
70_LASER@D4,11	110 °C		243,5002	901,213	0,0000000	193215,8	5008435	206,36 ± 0,42	98,58	12,32	92,2 ± 14,7
71_LASER@D4,13	130 °C		305,1495	1706,648	0,0000000	300794,6	7166356	190,52 ± 0,38	98,75	19,18	75,8 ± 9,1
73_LASER@D4,15	150 °C		57,8052	524,813	0,0000000	83311,7	2375462	225,75 ± 0,49	99,28	5,31	68,3 ± 16,4
74_LASER@D4,20	200 °C		65,2783	450,426	0,0000000	99181,9	2778060	222,00 ± 0,49	99,31	6,32	94,7 ± 27,4
75_LASER@D4,27	270 °C		23,0084	184,922	0,0000000	35023,8	1036276	233,73 ± 0,62	99,34	2,23	81,4 ± 43,7
		Σ	4816,3896	23942,120	0,0000000	1568636,6	43358211				

Information on Analysis

Sample = 98CBM:2
Material = Microcline
Location = JI 5-2
Analyst = Christel Bontje
Project = VU98-CHRISTEL
Mass Discrimination Law = LIN
Irradiation = VU98
J = 0.00467500 ± 0.00001169
DRA = 25.420 ± 0.025 Ma

Results	40(r)/39(k) ± 2σ	Age ± 2σ (Ma)	MSWD	39Ar(k) (%,n)	K/Ca ± 2σ
Age Plateau	28,01188 ± 2,43205	222,01 ± 18,17	#####	54,64	8,3 ± 3,0
Error Mean	± 8,68%	± 8,18%	0%	9	
	Minimal External Error	± 18,70	2,00	2σ Confidence Limit	
	Analytical Error	± 18,14	#####	Error Magnification	
Total Fusion Age	27,64070 ± 0,02009	219,24 ± 1,04		14	28,2 ± 1,0
	± 0,07%	± 0,48%			
	Minimal External Error	± 4,51			
	Analytical Error	± 0,15			

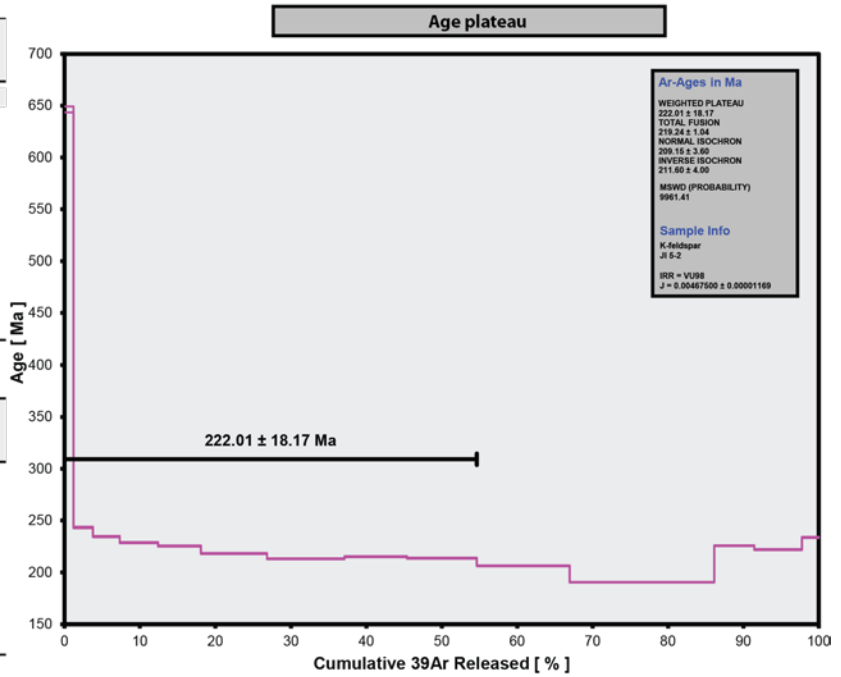

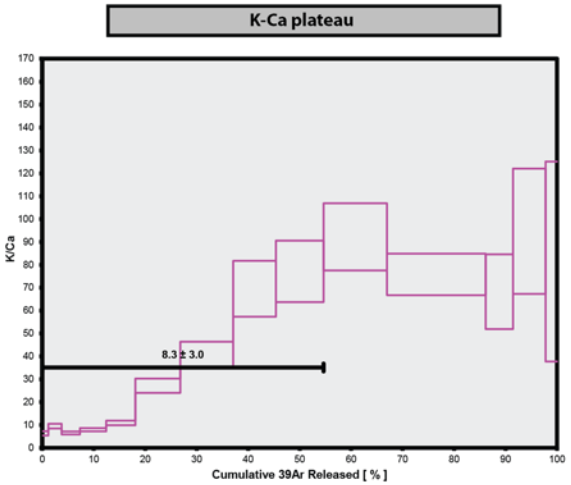

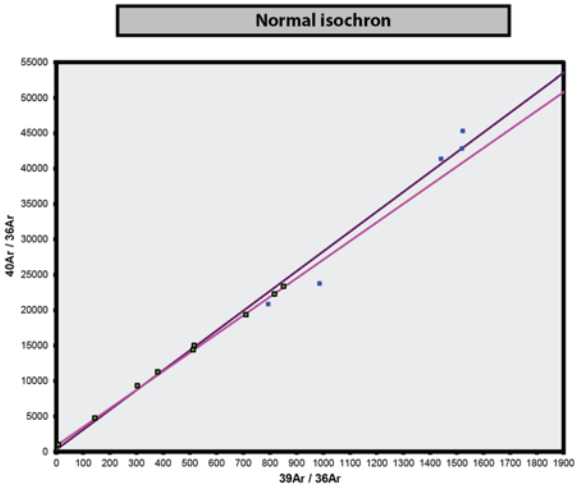

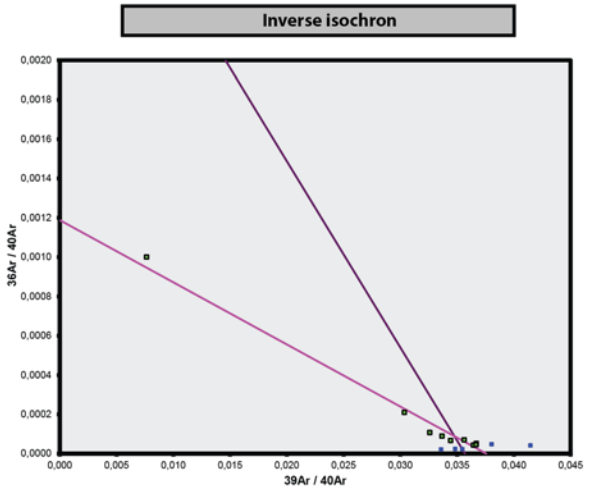

Figure 112. Stepwise heating results of K-feldspar in JI 5-2.

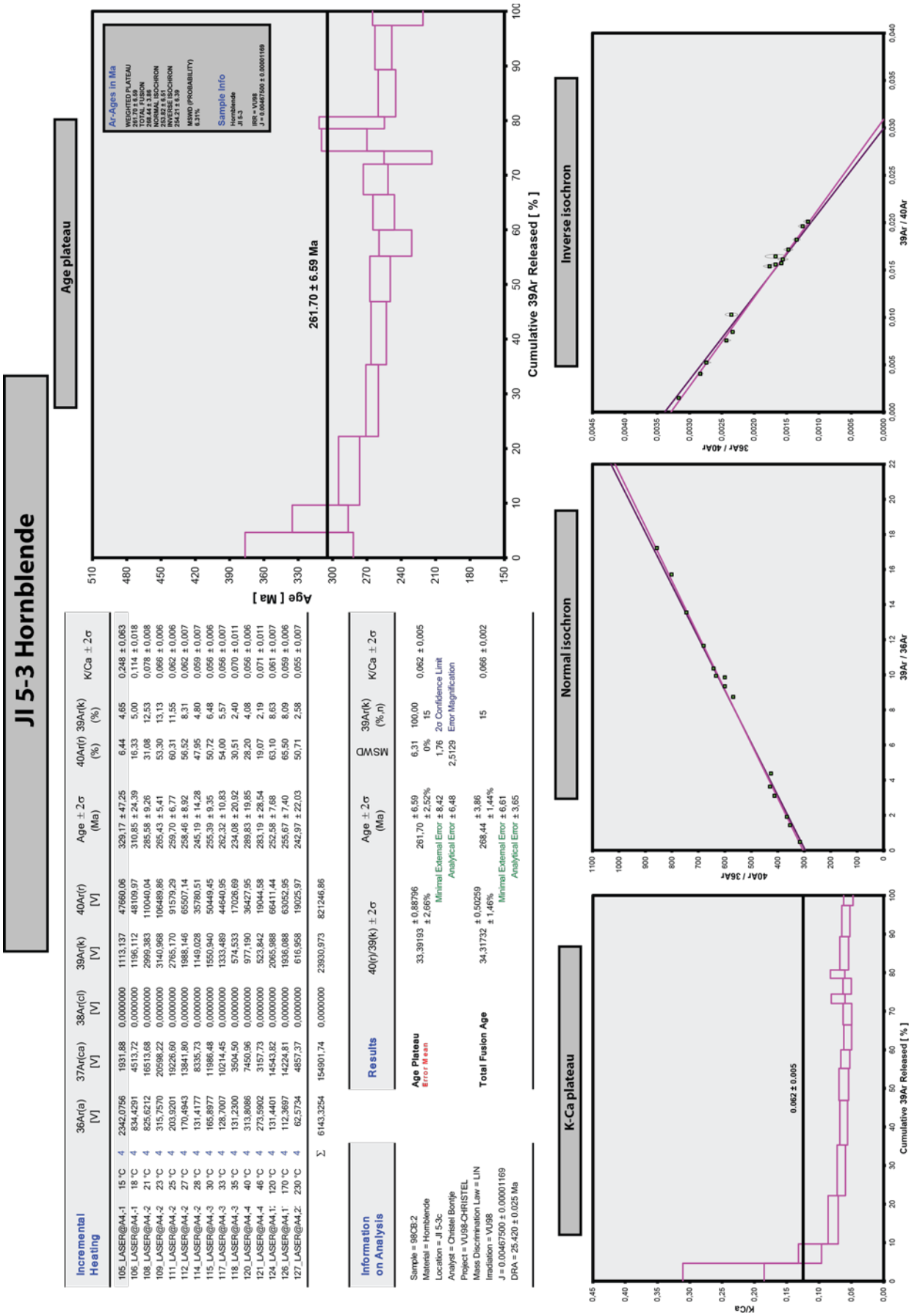

Incremental Heating			36Ar(a) [V]	37Ar(ca) [V]	38Ar(cl) [V]	39Ar(k) [V]	40Ar(r) [V]	Age ± 2σ (Ma)	40Ar(r) (%)	39Ar(k) (%)	K/Ca ± 2σ
105_LASER@A4.-1	15 °C	4	2342,0756	1931,88	0,0000000	1113,137	47660,06	329,17 ± 47,25	6,44	4,65	0,248 ± 0,063
106_LASER@A4.-1	18 °C	4	834,4291	4513,72	0,0000000	1196,112	48109,97	310,85 ± 24,39	16,33	5,00	0,114 ± 0,018
108_LASER@A4.-2	21 °C	4	825,6212	16513,68	0,0000000	2999,383	110040,04	285,58 ± 9,26	31,08	12,53	0,078 ± 0,008
109_LASER@A4.-2	23 °C	4	315,7570	20598,22	0,0000000	3140,968	106489,86	265,43 ± 5,41	53,30	13,13	0,066 ± 0,006
111_LASER@A4.-2	25 °C	4	203,9201	19226,60	0,0000000	2765,170	91579,29	259,70 ± 6,77	60,31	11,55	0,062 ± 0,006
112_LASER@A4.-2	27 °C	4	170,4943	13841,80	0,0000000	1988,146	65507,14	258,46 ± 8,92	56,52	8,31	0,062 ± 0,007
114_LASER@A4.-2	28 °C	4	131,4177	8335,73	0,0000000	1149,028	35780,51	245,19 ± 14,28	47,95	4,80	0,059 ± 0,007
115_LASER@A4.-3	30 °C	4	165,8977	11986,48	0,0000000	1550,940	50449,45	255,39 ± 9,35	50,72	6,48	0,056 ± 0,006
117_LASER@A4.-3	33 °C	4	128,7007	10214,45	0,0000000	1333,489	44640,95	262,32 ± 10,83	54,00	5,57	0,056 ± 0,007
118_LASER@A4.-3	35 °C	4	131,2300	3504,50	0,0000000	574,533	17026,69	234,08 ± 20,92	30,51	2,40	0,070 ± 0,011
120_LASER@A4.-4	40 °C	4	313,8086	7450,96	0,0000000	977,190	36427,95	289,83 ± 19,85	28,20	4,08	0,056 ± 0,006
121_LASER@A4.-4	46 °C	4	273,5902	3157,73	0,0000000	523,842	19044,58	283,19 ± 28,54	19,07	2,19	0,071 ± 0,011
124_LASER@A4.1:	120 °C	4	131,4401	14543,82	0,0000000	2065,988	66411,44	252,58 ± 7,68	63,10	8,63	0,061 ± 0,007
126_LASER@A4.1'	170 °C	4	112,3697	14224,81	0,0000000	1936,088	63052,95	255,67 ± 7,40	65,50	8,09	0,059 ± 0,006
127_LASER@A4.2:	230 °C	4	62,5734	4857,37	0,0000000	616,958	19025,97	242,97 ± 22,03	50,71	2,58	0,055 ± 0,007
		Σ	6143,3254	154901,74	0,0000000	23930,973	821246,86				

Information on Analysis	Results	40(r)/39(k) ± 2σ	Age ± 2σ (Ma)	MSWD	39Ar(k) (%,n)	K/Ca ± 2σ
Sample = 98CB-2						
Material = Hornblende	**Age Plateau**	33,39193 ± 0,88796	261,70 ± 6,59	6,31	100,00	
Location = JI 5-3c	Error M ean	± 2,66%	± 2,52%	0%	15	0,062 ± 0,005
Analyst = Christel Bontje		Minimal External Error ± 8,42		1,76	2σ Confidence Limit	
Project = VU98-CHRISTEL		Analytical Error ± 6,48		2,5129	Error Magnification	
Mass Discrimination Law = LIN						
Irradiation = VU98	**Total Fusion Age**	34,31732 ± 0,50259	268,44 ± 3,86		15	0,066 ± 0,002
J = 0.00467500 ± 0.00001169		± 1,46%	± 1,44%			
DRA = 25.420 ± 0.025 Ma		Minimal External Error ± 6,61				
		Analytical Error ± 3,65				

Figure 113. Stepwise heating results of hornblende in JI 5-3.

JI 5-5 K-feldspar

Incremental Heating			36Ar(a) [V]	37Ar(ca) [V]	38Ar(cl) [V]	39Ar(k) [V]	40Ar(r) [V]	Age ± 2σ (Ma)	40Ar(r) (%)	39Ar(k) (%)	K/Ca ± 2σ
275_LASER@E4,-2	20 °C	4	357,69764	14926,227	0,0000000	128980,27	4079147	248,77 ± 0,54	97,47	28,03	3,72 ± 0,28
276_LASER@E4,-2	25 °C	4	94,36081	6438,482	0,0000000	90388,03	2678792	234,09 ± 0,50	98,97	19,65	6,04 ± 0,48
278_LASER@E4,-3	30 °C	4	72,88119	5810,175	0,0000000	65441,97	1991643	239,99 ± 0,52	98,93	14,22	4,84 ± 0,38
279_LASER@E4,-3	35 °C	4	34,26463	2799,007	0,0000000	39584,42	1223991	243,58 ± 0,63	99,18	8,60	6,08 ± 0,59
281_LASER@E4,-4	40 °C	4	15,44475	1891,532	0,0000000	25205,50	780259	243,84 ± 0,75	99,41	5,48	5,73 ± 0,73
284_LASER@E4,-5	55 °C	4	20,72700	2269,928	0,0000000	24190,15	727717	237,40 ± 0,84	99,16	5,26	4,58 ± 0,48
287_LASER@E4,9(	90 °C	4	0,50847	428,577	0,0000000	9776,11	302823	243,98 ± 1,50	99,95	2,12	9,81 ± 4,02
288_LASER@E4,1(	100 °C	4	4,62701	1279,594	0,0000000	10240,27	319224	245,44 ± 1,57	99,57	2,23	3,44 ± 0,45
290_LASER@E4,1'	110 °C	4	22,76080	935,443	0,0000000	10718,42	320595	236,12 ± 1,18	97,94	2,33	4,93 ± 0,97
291_LASER@E4,1:	130 °C	4	23,82549	1974,891	0,0000000	19022,74	566568	235,18 ± 0,81	98,77	4,13	4,14 ± 0,39
293_LASER@E4,1!	150 °C	4	7,08581	1459,561	0,0000000	13953,02	415750	235,27 ± 1,09	99,49	3,03	4,11 ± 0,47
294_LASER@E4,2(	200 °C	4	11,14261	1155,420	0,0000000	13883,36	410835	233,76 ± 1,19	99,20	3,02	5,17 ± 0,92
295_LASER@E4,2!	250 °C	4	1,89949	1053,775	0,0000000	8694,51	270577	245,05 ± 1,58	99,79	1,89	3,55 ± 0,63
		Σ	667,22570	42422,612	0,0000000	460078,77	14087922				

Information on Analysis

Sample = 98CBM:2
Material = Microcline
Location = JI 5-5
Analyst = Christel Bontje
Project = VU98-CHRISTEL
Mass Discrimination Law = LIN
Irradiation = VU98
J = 0.00467500 ± 0.00001169
DRA = 25.420 ± 0.025 Ma

Results	40(r)/39(k) ± 2σ	Age ± 2σ (Ma)	MSWD	39Ar(k) (%,n)	K/Ca ± 2σ
Age Plateau	30,46934 ± 0,40739	240,25 ± 3,21	198,05	100,00	4,42 ± 0,50
Error Mean	± 1,34%	± 1,34%	0%	13	
	Minimal External Error ± 5,78		1,82	2σ Confidence Limit	
	Analytical Error ± 3,01		#####	Error Magnification	
Total Fusion Age	30,62067 ± 0,03069	241,37 ± 1,15		13	4,66 ± 0,16
	± 0,10%	± 0,48%			
	Minimal External Error ± 4,96				
	Analytical Error ± 0,23				

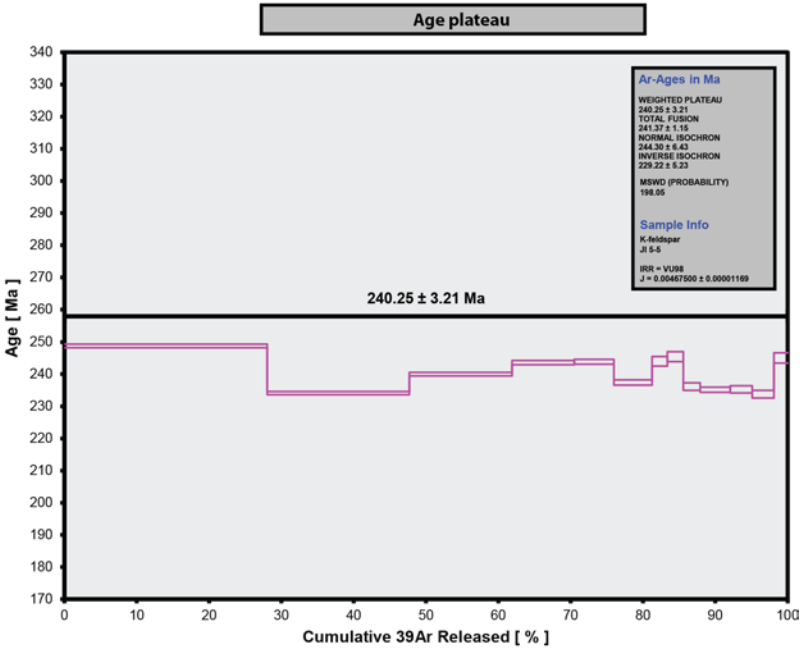

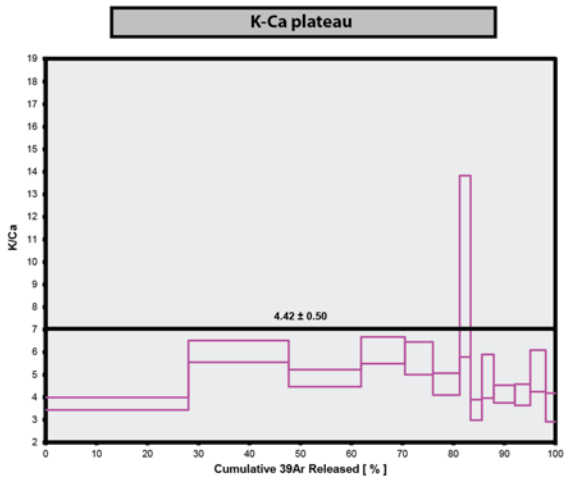

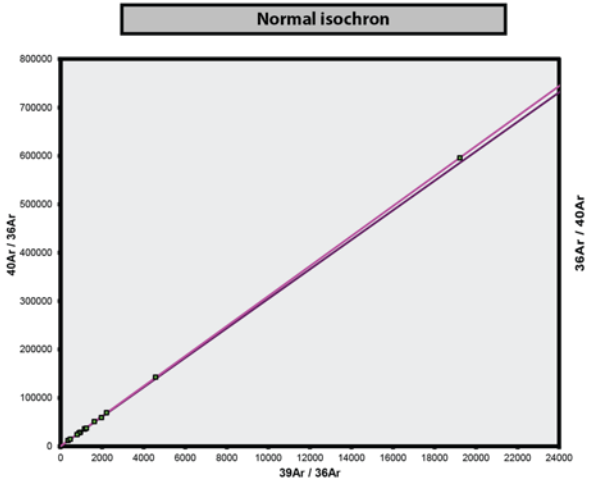

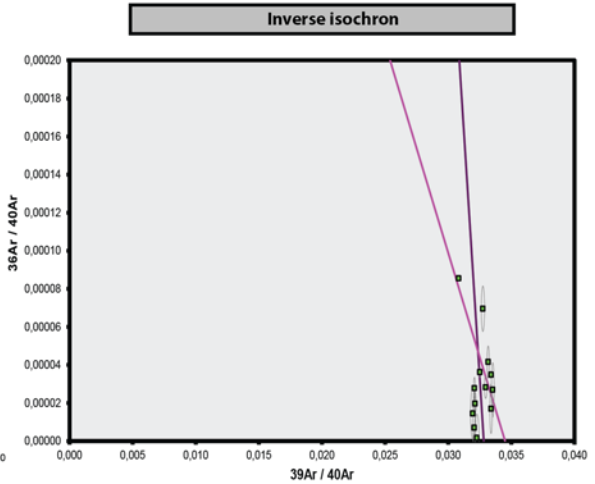

Figure 114. Stepwise heating results of K-feldspar in JI 5-5.

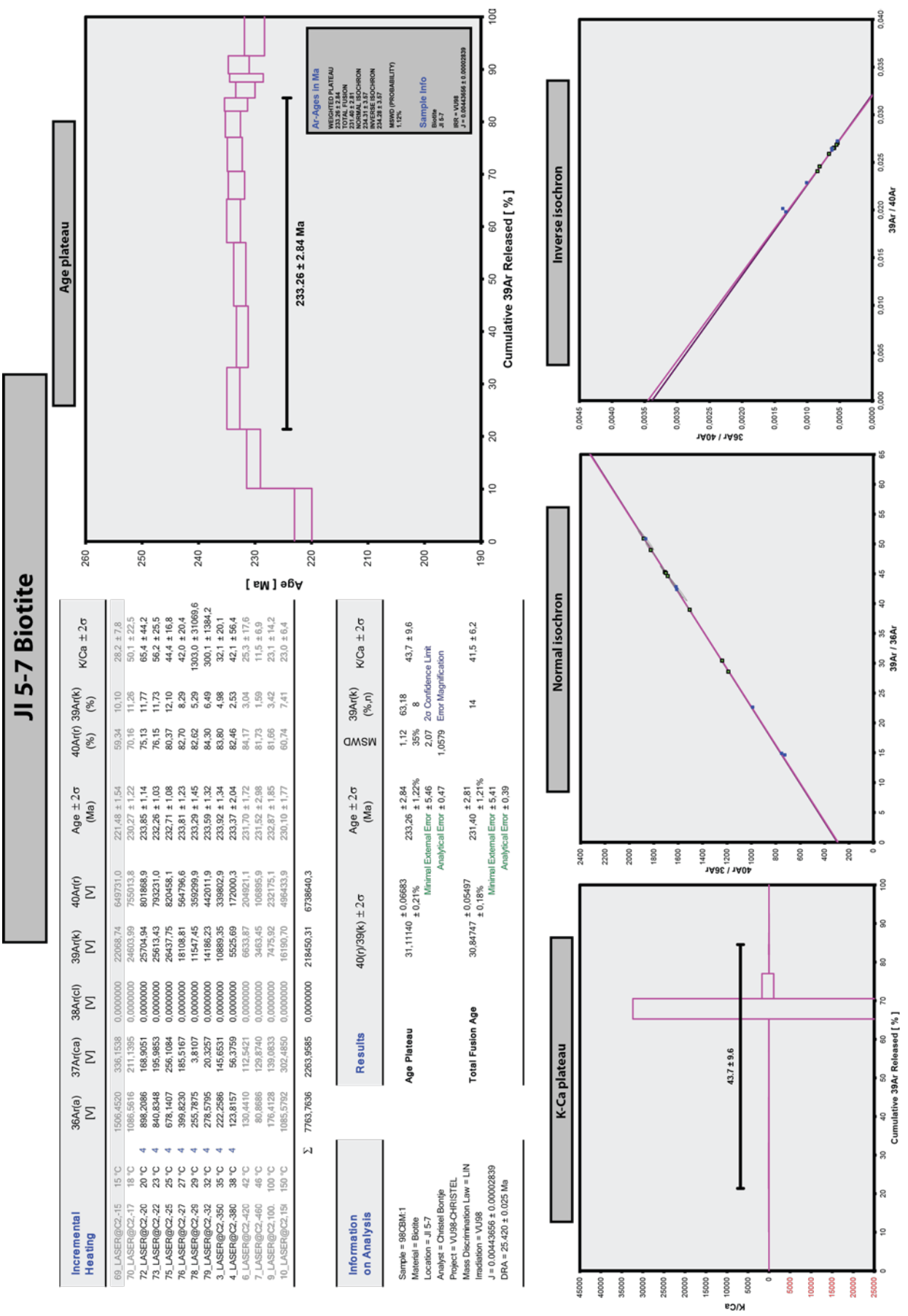

Incremental Heating			36Ar(a) [V]	37Ar(ca) [V]	38Ar(cl) [V]	39Ar(k) [V]	40Ar(r) [V]	Age ± 2σ (Ma)	40Ar(r) (%)	39Ar(k) (%)	K/Ca ± 2σ
69_LASER@C2,-15	15 °C		1506,4520	336,1538	0,0000000	22068,74	649731,0	221,48 ± 1,54	59,34	10,10	28,2 ± 7,8
70_LASER@C2,-17	18 °C		1086,5616	211,1395	0,0000000	24603,99	755013,8	230,27 ± 1,22	70,16	11,26	50,1 ± 22,5
72_LASER@C2,-20	20 °C	4	898,2086	168,9051	0,0000000	25704,94	801868,9	233,85 ± 1,14	75,13	11,77	65,4 ± 44,2
73_LASER@C2,-22	23 °C	4	840,8348	195,9853	0,0000000	25613,43	793231,0	232,26 ± 1,03	76,15	11,73	56,2 ± 25,5
75_LASER@C2,-25	25 °C	4	678,1407	256,1084	0,0000000	26437,75	820458,1	232,71 ± 1,08	80,37	12,10	44,4 ± 16,8
76_LASER@C2,-27	27 °C	4	399,8230	185,5167	0,0000000	18108,81	564796,6	233,81 ± 1,23	82,70	8,29	42,0 ± 20,4
78_LASER@C2,-29	29 °C	4	255,7875	3,8107	0,0000000	11547,45	359299,9	233,29 ± 1,45	82,62	5,29	1303,0 ± 31069,6
79_LASER@C2,-32	32 °C	4	278,5795	20,3257	0,0000000	14186,23	442011,9	233,59 ± 1,32	84,30	6,49	300,1 ± 1384,2
3_LASER@C2,-350	35 °C	4	222,2586	145,6531	0,0000000	10889,35	339802,9	233,92 ± 1,34	83,80	4,98	32,1 ± 20,1
4_LASER@C2,-380	38 °C	4	123,8157	56,3759	0,0000000	5525,69	172000,3	233,37 ± 2,04	82,46	2,53	42,1 ± 56,4
6_LASER@C2,-420	42 °C		130,4410	112,5421	0,0000000	6633,87	204921,1	231,70 ± 1,72	84,17	3,04	25,3 ± 17,6
7_LASER@C2,-460	46 °C		80,8686	129,8740	0,0000000	3463,45	106895,9	231,52 ± 2,98	81,73	1,59	11,5 ± 6,9
9_LASER@C2,-100	100 °C		176,4128	139,0833	0,0000000	7475,92	232175,1	232,87 ± 1,85	81,66	3,42	23,1 ± 14,2
10_LASER@C2,15(	150 °C		1085,5792	302,4850	0,0000000	16190,70	496433,9	230,10 ± 1,77	60,74	7,41	23,0 ± 6,4
		Σ	7763,7636	2263,9585	0,0000000	218450,31	6738640,3				

Information on Analysis	Results	40(r)/39(k) ± 2σ	Age ± 2σ (Ma)	MSWD	39Ar(k) (%,n)	K/Ca ± 2σ
Sample = 98CBM-1	**Age Plateau**	31,11140 ± 0,06683	233,26 ± 2,84	1,12	63,18	43,7 ± 9,6
Material = Biotite		± 0,21%	± 1,22%	35%	8	
Location = JI 5-7		Minimal External Error ± 5,46		2,07	2σ Confidence Limit	
Analyst = Christel Bontje		Analytical Error ± 0,47		1,0579	Error Magnification	
Project = VU98-CHRISTEL						
Mass Discrimination Law = LIN	**Total Fusion Age**	30,84747 ± 0,05497	231,40 ± 2,81		14	41,5 ± 6,2
Irradiation = VU98		± 0,18%	± 1,21%			
J = 0,00443656 ± 0,00002839		Minimal External Error ± 5,41				
DRA = 25.420 ± 0.025 Ma		Analytical Error ± 0,39				

Figure 115. Stepwise heating results of biotite in JI 5-7.

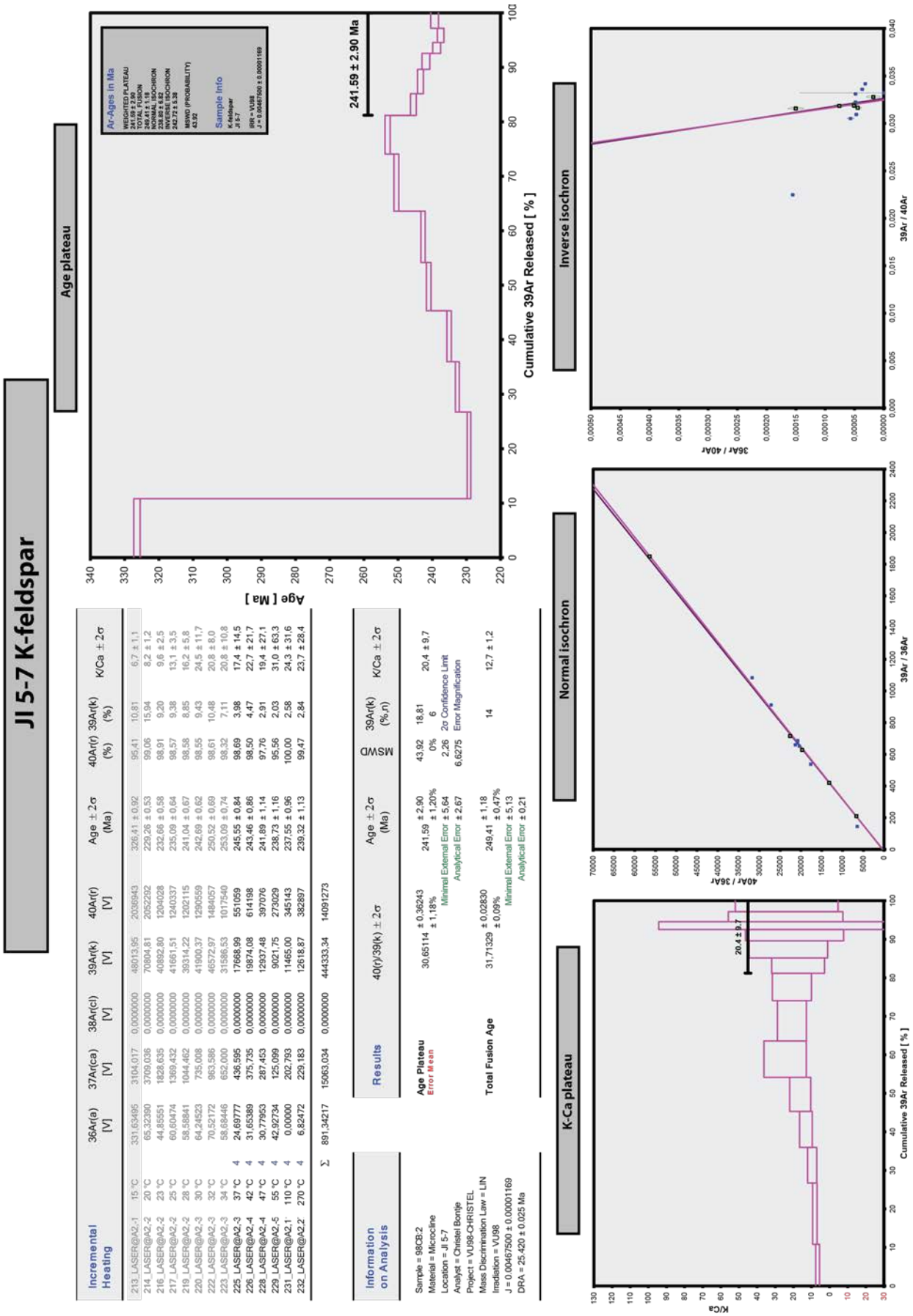

Incremental Heating		36Ar(a) [V]	37Ar(ca) [V]	38Ar(cl) [V]	39Ar(k) [V]	40Ar(r) [V]	Age ± 2σ (Ma)	40Ar(r) (%)	39Ar(k) (%)	K/Ca ± 2σ
213_LASER@A2-1	15 °C	331,63495	3104,017	0,0000000	48013,95	2036943	326,41 ± 0,92	95,41	10,81	6,7 ± 1,1
214_LASER@A2-2	20 °C	65,32390	3709,036	0,0000000	70804,81	2052292	229,26 ± 0,53	99,06	15,94	8,2 ± 1,2
216_LASER@A2-2	23 °C	44,85551	1828,635	0,0000000	40892,80	1204028	232,66 ± 0,58	98,91	9,20	9,6 ± 2,5
217_LASER@A2-2	25 °C	60,60474	1369,432	0,0000000	41661,51	1240337	235,09 ± 0,64	98,57	9,38	13,1 ± 3,5
219_LASER@A2-2	28 °C	58,58841	1044,462	0,0000000	39314,22	1202115	241,04 ± 0,67	98,58	8,85	16,2 ± 5,8
220_LASER@A2-3	30 °C	64,24523	735,008	0,0000000	41900,37	1290559	242,69 ± 0,62	98,55	9,43	24,5 ± 11,7
222_LASER@A2-3	32 °C	70,52172	963,586	0,0000000	46572,97	1484057	250,52 ± 0,69	98,61	10,48	20,8 ± 8,0
223_LASER@A2-3	34 °C	58,68446	652,000	0,0000000	31586,53	1017540	253,09 ± 0,74	98,32	7,11	20,8 ± 10,8
225_LASER@A2-3	37 °C 4	24,69777	436,595	0,0000000	17668,99	551059	245,55 ± 0,84	98,69	3,98	17,4 ± 14,5
226_LASER@A2-4	42 °C 4	31,65389	375,735	0,0000000	19874,08	614198	243,46 ± 0,86	98,50	4,47	22,7 ± 21,7
228_LASER@A2-4	47 °C 4	30,77953	287,453	0,0000000	12937,48	397076	241,89 ± 1,14	97,76	2,91	19,4 ± 27,1
229_LASER@A2-5	55 °C 4	42,92734	125,099	0,0000000	9021,75	273029	238,73 ± 1,16	95,56	2,03	31,0 ± 63,3
231_LASER@A2-1	110 °C 4	0,00000	202,793	0,0000000	11465,00	345143	237,55 ± 0,96	100,00	2,58	24,3 ± 31,6
232_LASER@A2-2	270 °C 4	6,82472	229,183	0,0000000	12618,87	382897	239,32 ± 1,13	99,47	2,84	23,7 ± 28,4
	Σ	891,34217	15063,034	0,0000000	444333,34	14091273				

Information on Analysis	Results	40(r)/39(k) ± 2σ	Age ± 2σ (Ma)	MSWD	39Ar(k) (%,n)	K/Ca ± 2σ
Sample = 98CB.2 Material = Microcline Location = JI 5-7 Analyst = Christel Bontje Project = VU98-CHRISTEL Mass Discrimination Law = LIN Irradiation = VU98 J = 0.00467500 ± 0.00001169 DRA = 25.420 ± 0.025 Ma	**Age Plateau** Error Mean	30,65114 ± 0,36243 ± 1,18%	241,59 ± 2,90 ± 1,20% Minimal External Error ± 5,64 Analytical Error ± 2,67	43,92 0% 2,26 6,6275	18,81 6 2σ Confidence Limit Error Magnification	20,4 ± 9,7
	Total Fusion Age	31,71329 ± 0,02830 ± 0,09%	249,41 ± 1,18 ± 0,47% Minimal External Error ± 5,13 Analytical Error ± 0,21		14	12,7 ± 1,2

Figure 116. Stepwise heating results of K-feldspar in JI 5-7.

JI 4-2 Biotite Single Grain

Single Grain			36Ar(a) [V]	37Ar(ca) [V]	38Ar(cl) [V]	39Ar(k) [V]	40Ar(r) [V]	Age ± 2σ (Ma)	40Ar(r) (%)	39Ar(k) (%)	K/Ca ± 2σ
46_LASER@J12,8(	80 °C	4	23,2500	72,2206	0,0000000	7413,67	284914	285,52 ± 1,59	97,64	1,64	44,1 ± 50,1
59_LASER@I7,80.)	80 °C	4	100,5018	164,8868	0,0000000	6381,72	246022	286,34 ± 1,91	89,23	1,41	16,6 ± 8,6
43_LASER@J9,80..	80 °C	4	28,9051	106,9156	0,0000000	9289,22	367508	293,28 ± 1,51	97,73	2,06	37,4 ± 29,5
44_LASER@J10,8(	80 °C	4	310,7652	356,6042	0,0000000	32843,85	1307084	294,88 ± 0,84	93,43	7,28	39,6 ± 10,3
53_LASER@I2,80.)	80 °C	4	25,0082	81,1893	0,0000000	14790,44	592025	296,46 ± 1,18	98,76	3,28	78,3 ± 69,4
66_LASER@I13,80	80 °C	4	194,3075	217,2543	0,0000000	44596,86	1800162	298,76 ± 0,70	96,91	9,88	88,3 ± 41,4
48_LASER@J13,8(	80 °C	4	70,6248	144,1266	0,0000000	21943,39	885828	298,79 ± 0,80	97,70	4,86	65,5 ± 41,6
50_LASER@J15,8(	80 °C	4	31,7904	288,4424	0,0000000	17704,90	717621	299,90 ± 0,94	98,70	3,92	26,4 ± 8,5
56_LASER@I5,80.)	80 °C	4	80,3886	101,6835	0,0000000	9082,85	369266	300,74 ± 1,59	93,95	2,01	38,4 ± 33,6
64_LASER@I11,80	80 °C	4	112,7297	216,1357	0,0000000	22489,19	915435	301,08 ± 0,82	96,49	4,98	44,7 ± 22,4
58_LASER@I6,80.)	80 °C	4	41,6396	221,4317	0,0000000	6877,45	280958	302,08 ± 1,81	95,80	1,52	13,4 ± 5,4
60_LASER@I8,80.)	80 °C	4	95,9927	172,1373	0,0000000	15373,80	628578	302,31 ± 1,20	95,68	3,41	38,4 ± 18,8
71_LASER@H2,80	80 °C	4	52,2374	85,5804	0,0000000	31482,21	1295673	304,15 ± 0,73	98,82	6,98	158,2 ± 177,8
68_LASER@I14,80	80 °C	4	236,7400	262,7058	0,0000000	19816,94	816647	304,51 ± 0,89	92,11	4,39	32,4 ± 8,9
61_LASER@I9,80.)	80 °C	4	129,9810	160,4156	0,0000000	11368,08	469242	304,97 ± 1,13	92,43	2,52	30,5 ± 12,9
75_LASER@H5,80	80 °C	4	50,2072	423,6989	0,0000000	13376,03	552180	305,00 ± 1,06	97,38	2,96	13,6 ± 3,7
51_LASER@I1,80.)	80 °C		21,2614	123,8522	0,0000000	22770,93	944822	306,44 ± 0,93	99,34	5,05	79,1 ± 46,9
45_LASER@J11,8(	80 °C	4	777,4103	876,1035	0,0000000	22830,34	947937	306,63 ± 1,17	80,49	5,06	11,2 ± 1,3
65_LASER@I12,80	80 °C	4	165,3892	105,2938	0,0000000	17468,45	725496	306,70 ± 1,02	93,69	3,87	71,3 ± 67,8
49_LASER@J14,8(	80 °C		10,5890	543,5311	0,0000000	8042,54	334456	307,07 ± 1,60	99,07	1,78	6,4 ± 1,2
41_LASER@J8,80..	80 °C	4	25,4587	0,0000	0,0000000	7392,25	308948	308,48 ± 1,78	97,62	1,64	
70_LASER@H1,80	80 °C		7,2687	45,8486	0,0000000	12299,42	517329	310,29 ± 1,16	99,58	2,73	115,4 ± 164,2
74_LASER@H4,80	80 °C	4	90,9635	373,5431	0,0000000	18783,63	790393	310,41 ± 0,94	96,71	4,16	21,6 ± 4,7
73_LASER@H3,80	80 °C		66,2189	113,9782	0,0000000	19209,95	815330	312,88 ± 1,04	97,65	4,26	72,5 ± 50,2
55_LASER@I4,80.)	80 °C	4	0,0000	0,0000	0,0000000	3376,83	143989	314,21 ± 1,62	100,00	0,75	
69_LASER@I15,80	80 °C		6,5343	155,5598	0,0000000	9994,09	426473	314,43 ± 1,28	99,55	2,21	27,6 ± 15,8
63_LASER@I10,80	80 °C		33,1129	182,0834	0,0000000	11774,63	504712	315,73 ± 1,41	98,10	2,61	27,8 ± 16,4
40_LASER@J7,80..	80 °C		40,8900	17,3773	0,0000000	7161,71	314601	322,90 ± 1,87	96,30	1,59	177,2 ± 836,3
54_LASER@I3,80.)	80 °C		351,3227	0,0000	0,0000000	5372,67	242655	331,21 ± 2,82	70,03	1,19	
		Σ	3181,4888	5612,5998	0,0000000	451308,04	18546283				

Information on Analysis
Sample = JI 4-2
Material = Biotite
Location = Jinshuikou
Analyst = Christel Bontje
Project = 98CB
Mass Discrimination Law = LIN
Irradiation = VU98
J = 0.00446190 ± 0.00001115
DRA = 25.420 ± 0.025 Ma

Results	40(r)/39(k) ± 2σ		Age ± 2σ (Ma)		MSWD	39Ar(k) (%,n)	K/Ca ± 2σ
Age Plateau	40,77528	± 0,35540	301,56	± 2,79	112,46	78,59	2,1 ± 0,4
Error Mean		± 0,87%		± 0,93%	0%	21	
		Minimal External Error		± 6,65	1,63	2σ Confidence Limit	
		Analytical Error		± 2,42	#####	Error Magnification	
Total Fusion Age	41,09451	± 0,03088	303,73	± 1,41		29	34,6 ± 2,9
		± 0,08%		± 0,47%			
		Minimal External Error		± 6,24			
		Analytical Error		± 0,21			

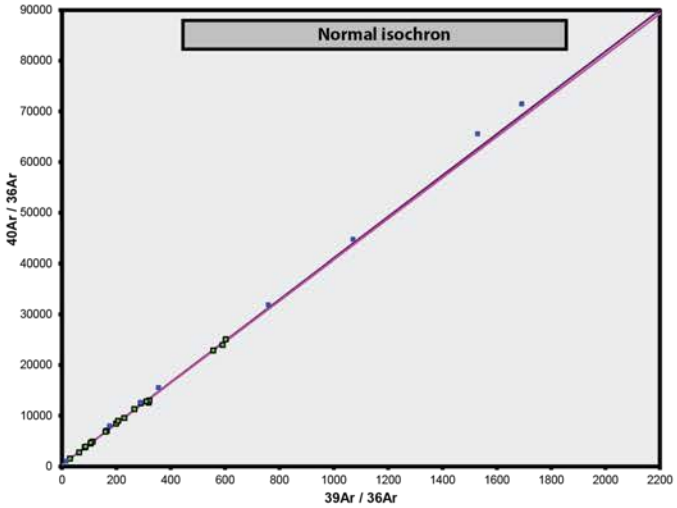

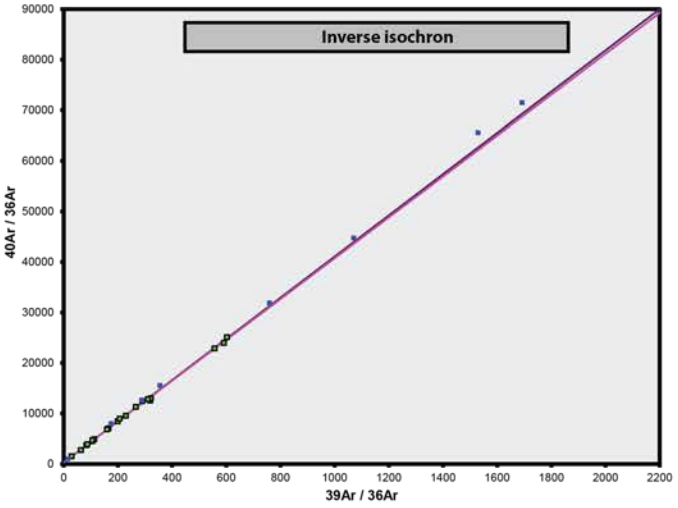

Figure 117. Single grain results of biotite in JI 4-2.

JI 4-7 Biotite Single Grain

Single Grain			36Ar(a) [V]	37Ar(ca) [V]	38Ar(cl) [V]	39Ar(k) [V]	40Ar(r) [V]	Age ± 2σ (Ma)	40Ar(r) (%)	39Ar(k) (%)	K/Ca ± 2σ
10B_LASER@O11,	80 °C	4	1335,336	1408,643	0,0000000	4321,38	109673	193,16 ± 6,58	21,75	0,76	1,3 ± 0,2
9C_LASER@O10,8	80 °C	4	1527,100	1011,456	0,0000000	2627,50	82402	235,82 ± 12,97	15,44	0,46	1,1 ± 0,2
16_LASER@M11,8	80 °C	4	4893,212	2552,443	0,0000000	53493,65	1763631	247,12 ± 1,75	54,95	9,36	9,0 ± 0,8
16B_LASER@N8,8	80 °C	4	3385,387	1259,979	0,0000000	15256,86	505177	248,12 ± 4,51	33,55	2,67	5,2 ± 0,6
15B_LASER@N7,8	80 °C	4	4134,177	1041,336	0,0000000	9660,76	323368	250,64 ± 9,16	20,93	1,69	4,0 ± 0,6
15_LASER@M10,8	80 °C	4	5329,200	594,291	0,0000000	58708,77	1972369	251,51 ± 1,64	55,60	10,27	42,5 ± 8,0
11_LASER@N4,80	80 °C	4	5508,678	1327,164	0,0000000	41551,31	1402753	252,65 ± 2,23	46,29	7,27	13,5 ± 1,8
14_LASER@M9,80	80 °C	4	3574,077	2193,387	0,0000000	68364,18	2336069	255,52 ± 1,09	68,86	11,96	13,4 ± 1,2
13B_LASER@N5,8	80 °C	4	3662,441	1914,486	0,0000000	12511,82	427871	255,71 ± 5,64	28,33	2,19	2,8 ± 0,3
19_LASER@N10,8	80 °C	4	5078,858	171,796	0,0000000	42003,41	1439258	256,18 ± 2,16	48,95	7,35	105,1 ± 77,0
5_LASER@N12,80	80 °C	4	6025,490	1065,890	0,0000000	21985,53	754973	256,70 ± 4,72	29,78	3,85	8,9 ± 0,8
12_LASER@M8,80	80 °C	4	3283,655	402,215	0,0000000	13116,76	457032	260,20 ± 4,32	32,02	2,30	14,0 ± 3,8
21B_LASER@L3,8	80 °C	4	2198,466	501,608	0,0000000	5153,65	183070	264,92 ± 7,58	21,98	0,90	4,4 ± 0,9
6_LASER@M3,80.)	80 °C		684,410	353,634	0,0000000	12051,97	428748	265,28 ± 1,58	67,95	2,11	14,7 ± 2,9
17_LASER@M12,8	80 °C	4	4054,521	468,004	0,0000000	29559,47	1052431	265,48 ± 2,56	46,76	5,17	27,2 ± 5,2
3_LASER@O5,80.)	80 °C	4	5120,570	542,790	0,0000000	17123,05	610585	265,86 ± 4,98	28,75	3,00	13,6 ± 2,8
14B_LASER@N6,8	80 °C	4	2561,761	725,895	0,0000000	10757,52	385882	267,34 ± 4,90	33,76	1,88	6,4 ± 1,4
19B_LASER@M13,	80 °C	4	1938,380	1636,887	0,0000000	7580,94	272234	267,61 ± 4,92	32,22	1,33	2,0 ± 0,2
18_LASER@N9,80	80 °C	4	5661,235	376,538	0,0000000	33087,98	1189682	267,92 ± 2,88	41,56	5,79	37,8 ± 14,2
10_LASER@M6,80	80 °C	4	3017,693	327,944	0,0000000	6160,39	232557	280,31 ± 8,61	20,68	1,08	8,1 ± 2,8
8B_LASER@O9,80	80 °C		2958,061	843,104	0,0000000	12413,10	470827	281,54 ± 4,35	35,01	2,17	6,3 ± 0,7
7B_LASER@M4,80	80 °C		1414,962	661,494	0,0000000	3852,44	148902	286,49 ± 8,24	26,26	0,67	2,5 ± 0,4
5B_LASER@O7,80	80 °C		3179,760	1004,103	0,0000000	17664,50	687424	288,30 ± 3,18	42,25	3,09	7,6 ± 1,4
20_LASER@L2,80.	80 °C		2809,448	235,931	0,0000000	10740,70	418068	288,36 ± 4,98	33,49	1,88	19,6 ± 8,5
6B_LASER@O8,80	80 °C		2344,043	878,725	0,0000000	6948,42	270539	288,44 ± 6,31	28,09	1,22	3,4 ± 0,5
9B_LASER@M5,80	80 °C		2875,020	1032,716	0,0000000	22181,14	870646	290,60 ± 2,48	50,61	3,88	9,2 ± 1,2
11_LASER@M7,80	80 °C		2614,601	379,445	0,0000000	21409,61	851980	294,31 ± 2,21	52,44	3,75	24,3 ± 7,4
4B_LASER@O6,80	80 °C	4	1377,418	438,841	0,0000000	2810,44	113905	299,32 ± 11,66	21,87	0,49	2,8 ± 0,6
4B_LASER@N11,8	80 °C		1469,797	390,804	0,0000000	8437,78	354901	309,71 ± 3,66	44,97	1,48	9,3 ± 2,2
		Σ	94017,757	25741,547	0,0000000	571535,03	20116958				

Information on Analysis
Sample = JI 4-7
Material = Biotite
Location = Jinshuikou
Analyst = Christel Bontje
Project = 98CB
Mass Discrimination Law = LIN
Irradiation = VU98
J = 0.00445280 ± 0.00001113
DRA = 25.420 ± 0.025 Ma

Results	40(r)/39(k) ± 2σ		Age ± 2σ (Ma)		MSWD	39Ar(k) (%,n)		K/Ca ± 2σ
Age Plateau	34,10220	± 0,57964	255,04	± 4,21	42,70	79,76		2,3 ± 1,0
Error Mean		± 1,70%		± 1,65%	0%	20		
			Minimal External Error	± 6,62	1,65	2σ Confidence Limit		
			Analytical Error	± 4,04	6,5346	Error Magnification		
Total Fusion Age	35,19812	± 0,08874	262,67	± 1,37		29		9,5 ± 0,3
		± 0,25%		± 0,52%				
			Minimal External Error	± 5,43				
			Analytical Error	± 0,62				

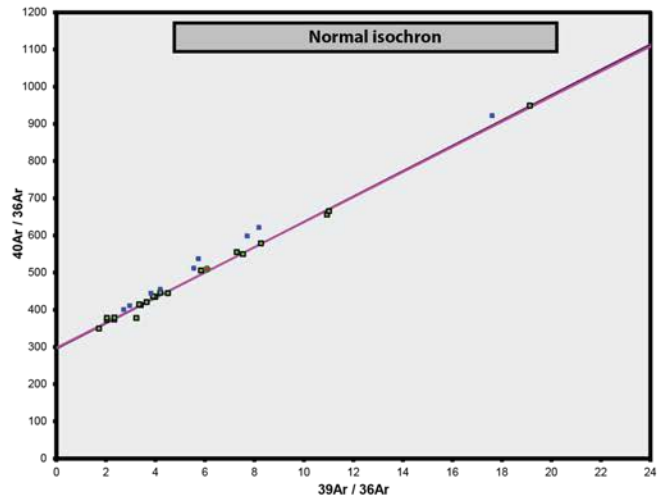

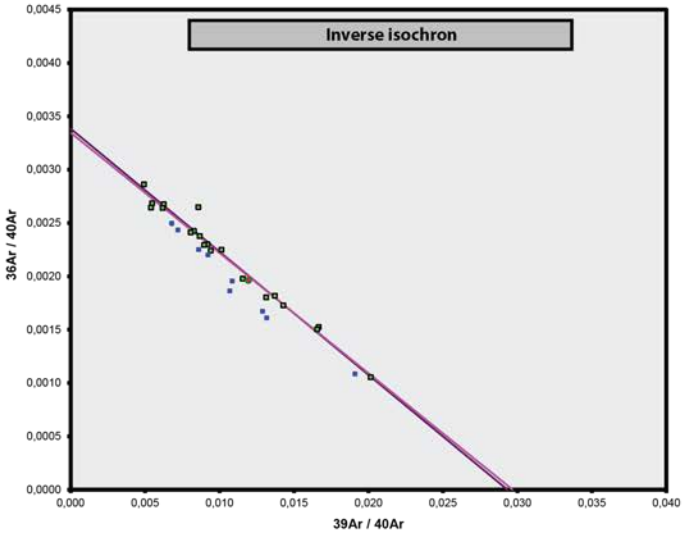

Figure 118. Single grain results of biotite in JI 4-7.

JI 5-1 Biotite Single Grain

Single Grain			36Ar(a) [V]	37Ar(ca) [V]	38Ar(cl) [V]	39Ar(k) [V]	40Ar(r) [V]	Age ± 2σ (Ma)	40Ar(r) (%)	39Ar(k) (%)	K/Ca ± 2σ
25_LASER@K10,8	80 °C	4	64,0227	58,3782	0,0000000	90260,19	2738388	228,05 ± 0,48	99,31	9,95	665 ± 573
15_LASER@K2,80.	80 °C	4	114,9487	42,0657	0,0000000	59549,16	1822627	229,94 ± 0,54	98,17	6,57	609 ± 758
21_LASER@K7,80.	80 °C	4	309,2882	47,7070	0,0000000	69601,90	2147709	231,70 ± 0,50	95,91	7,67	627 ± 577
26_LASER@K11,8	80 °C	4	111,2215	5,1975	0,0000000	38459,05	1190866	232,46 ± 0,61	97,31	4,24	3182 ± 27152
36_LASER@J4,80.	80 °C	4	248,5879	518,1657	0,0000000	31396,00	981338	234,52 ± 0,70	93,03	3,46	26 ± 4
9_LASER@L11,80.	80 °C	4	343,4759	196,4061	0,0000000	107475,21	3362258	234,71 ± 0,49	97,07	11,85	235 ± 48
14_LASER@K1,80.	80 °C	4	10,3633	21,0023	0,0000000	26103,71	817642	234,98 ± 0,78	99,62	2,88	534 ± 967
11_LASER@L13,8	80 °C	4	21,6394	5,3492	0,0000000	4136,82	129628	235,07 ± 2,06	95,30	0,46	333 ± 2448
33_LASER@J1,80.	80 °C	4	0,8683	34,0585	0,0000000	24114,60	755790	235,12 ± 0,65	99,96	2,66	304 ± 626
19_LASER@K5,80.	80 °C	4	135,9029	66,7471	0,0000000	28917,39	909708	235,94 ± 0,63	95,77	3,19	186 ± 145
10_LASER@L12,8	80 °C	4	42,0786	0,0000	0,0000000	12348,92	388629	236,02 ± 1,01	96,90	1,36	
34_LASER@J2,80.	80 °C	4	0,8727	17,3224	0,0000000	11162,62	352210	236,60 ± 1,16	99,92	1,23	277 ± 895
28_LASER@K12,8	80 °C	4	35,9304	12,7772	0,0000000	18763,96	592272	236,68 ± 0,81	98,23	2,07	631 ± 2445
31_LASER@K15,8	80 °C	4	0,8773	0,0000	0,0000000	15550,84	491514	236,98 ± 0,95	99,94	1,71	
35_LASER@J3,80.	80 °C		11,9758	25,0416	0,0000000	9953,40	316100	238,04 ± 1,15	98,89	1,10	171 ± 422
6_LASER@L9,80.X	80 °C		184,6412	0,0000	0,0000000	6075,51	193470	238,65 ± 1,87	78,00	0,67	
18_LASER@K4,80.	80 °C		80,1732	31,0583	0,0000000	8368,89	267913	239,83 ± 1,53	91,87	0,92	116 ± 150
8_LASER@L10,80.	80 °C		1223,9257	204,3214	0,0000000	34960,28	1123348	240,67 ± 0,97	75,64	3,85	74 ± 17
38_LASER@J5,80.	80 °C	4	590,6610	508,6611	0,0000000	131178,95	4218096	240,83 ± 0,49	96,02	14,46	111 ± 25
5_LASER@L8,80.X	80 °C		321,9191	0,0000	0,0000000	16265,89	524068	241,27 ± 1,07	84,63	1,79	111 ± 25
16_LASER@K3,80.	80 °C		134,2756	83,6507	0,0000000	11572,32	374858	242,49 ± 1,09	90,42	1,28	59 ± 36
30_LASER@K14,8	80 °C		19,4539	0,0000	0,0000000	15320,02	496262	242,50 ± 0,98	98,85	1,69	
4_LASER@L7,80.X	80 °C		292,8999	0,0000	0,0000000	11769,26	381277	242,52 ± 1,54	81,50	1,30	111 ± 25
3_LASER@L6,80.X	80 °C		10,1125	0,0000	0,0000000	8142,98	264152	242,82 ± 1,16	98,88	0,90	339 ± 316
20_LASER@K6,80.	80 °C		458,5138	30,6371	0,0000000	27044,45	878085	243,02 ± 0,92	86,63	2,98	380 ± 613
24_LASER@K9,80.	80 °C		280,5744	16,0061	0,0000000	15628,19	513135	245,58 ± 1,11	86,09	1,72	420 ± 1403
29_LASER@K13,8	80 °C		145,9060	36,9619	0,0000000	29108,36	960717	246,78 ± 0,79	95,70	3,21	339 ± 316
23_LASER@K8,80.	80 °C		1885,7600	0,0000	0,0000000	31453,59	1045007	248,31 ± 1,31	65,22	3,47	
13_LASER@L14,8	80 °C		20,9667	0,0000	0,0000000	12219,84	413760	252,74 ± 1,01	98,52	1,35	
		Σ	7101,8368	1961,5154	0,0000000	906902,33	28650826				

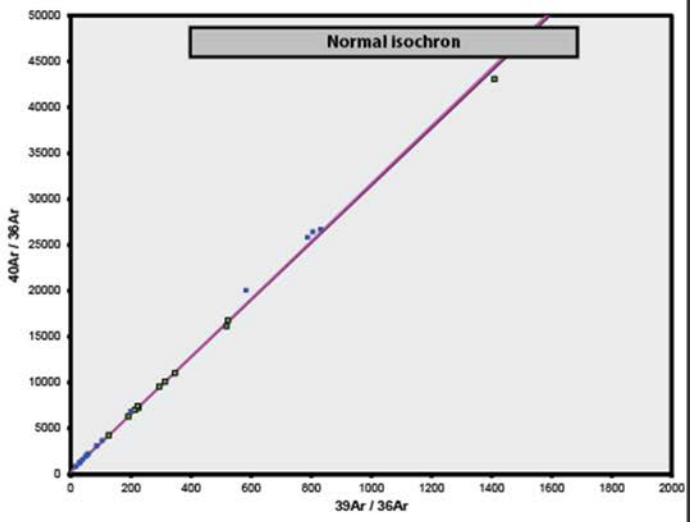

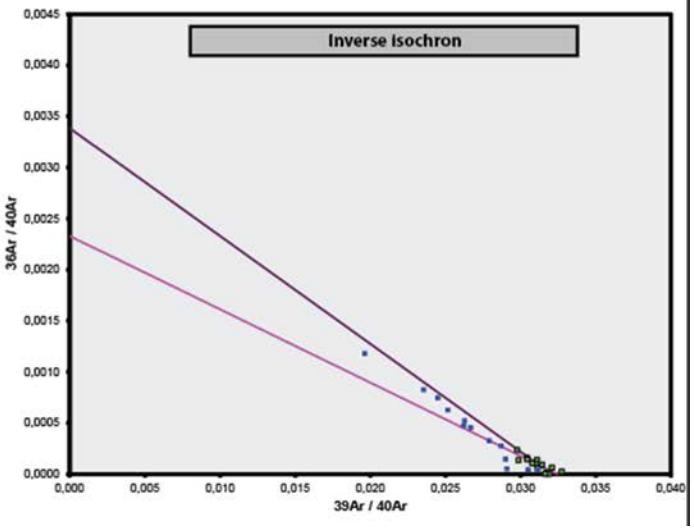

Information on Analysis
Sample = JI 5-1
Material = Biotite
Location = Jinshuikou
Analyst = Christel Bontje
Project = 98CB
Mass Discrimination Law = LIN
Irradiation = VU98
J = 0.00444132 ± 0.00001110
DRA = 25.420 ± 0.025 Ma

Results	40(r)/39(k) ± 2σ		Age ± 2σ (Ma)		MSWD	39Ar(k) (%,n)	K/Ca ± 2σ
Age Plateau	31,18119	± 0,27831	233,99	± 2,25	138,07	73,77	1 ± 1
Error Mean		± 0,89%		± 0,96%	0%	15	
		Minimal External Error		± 5,19	1,76	2σ Confidence Limit	
		Analytical Error		± 1,96	#####	Error Magnification	
Total Fusion Age	31,59196	± 0,02216	236,88	± 1,12		29	199 ± 28
		± 0,07%		± 0,47%			
		Minimal External Error		± 4,87			
		Analytical Error		± 0,16			

Figure 119. Single grain results of biotite in JI 5-1.

Appendix VI: Pseudosections

Modal abundances JI 1-1

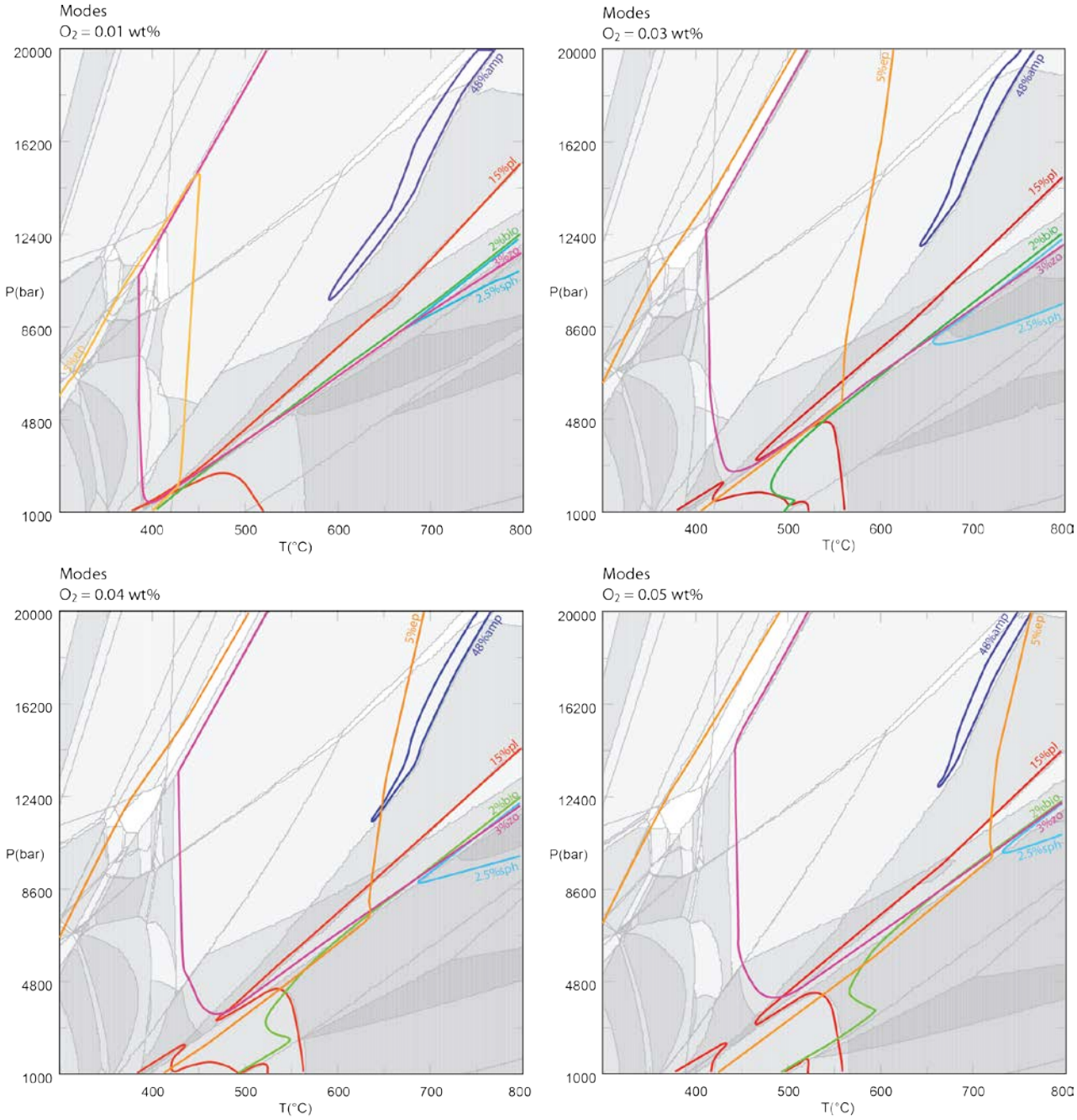

Figure 120. Modal abundance isopleths plotted onto a pseudosection for varying O_2 concentrations. The best fit of the cluster of isopleths is used for further modelling. See next page for continuation. O_2 = 0.04 wt% was found the best fit.

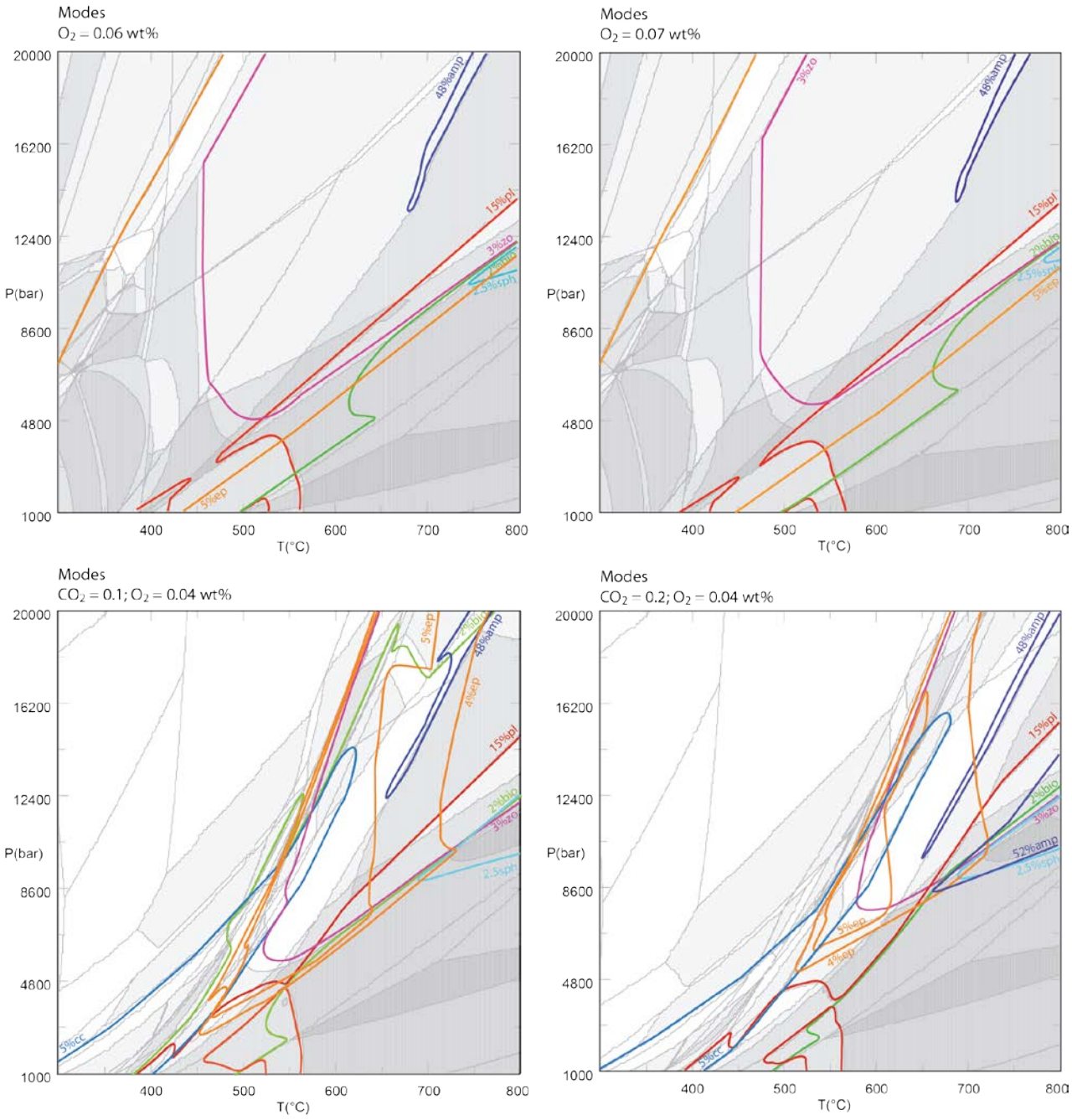

Figure 121. Modal abundance isopleths plotted onto a pseudosection for varying O_2 concentrations (top) and varying CO_2 concentration with O_2 fixed at 0.04 wt% (bottom). The best fit of the cluster of isopleths is used for further modelling. See next page for continuation.

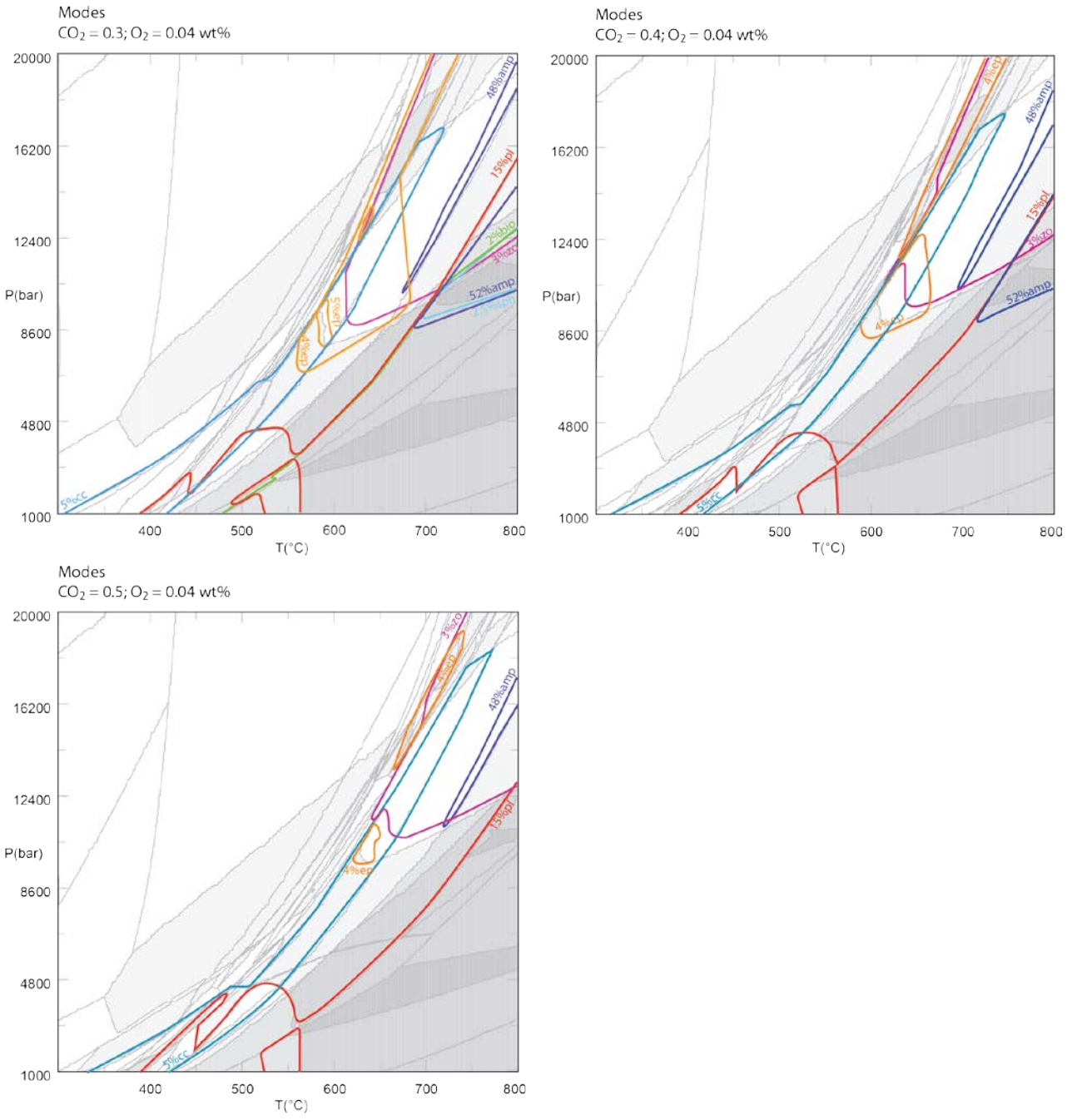

Figure 122. Modal abundance isopleths plotted onto a pseudosection for varying CO_2 concentration with O_2 fixed at 0.04 wt%. The best fit of the cluster of isopleths is used for further modelling. A CO_2 fraction of 0.3 (0.3 CO_2 + 0.7 H_2O) was found as best fit.

Isopleths JI 1-1

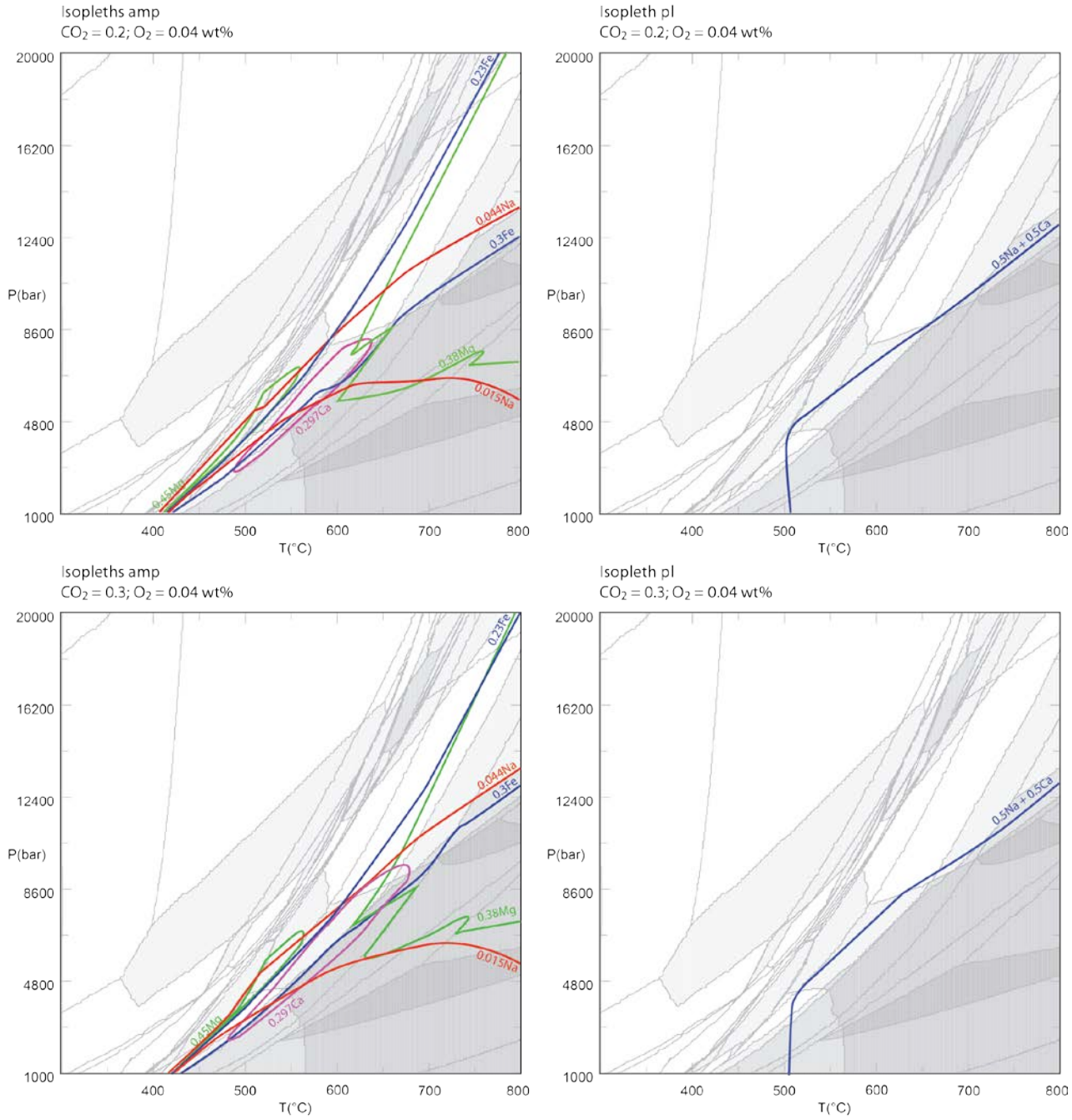

Figure 123. Chemical compositional isopleths of amphibole and plagioclase at a CO_2 fraction of 0.2 and 0.3. A best clustered fit of chemistry and modal abundances is found for CO_2 = 0.3.

Modal abundances JI 2-1

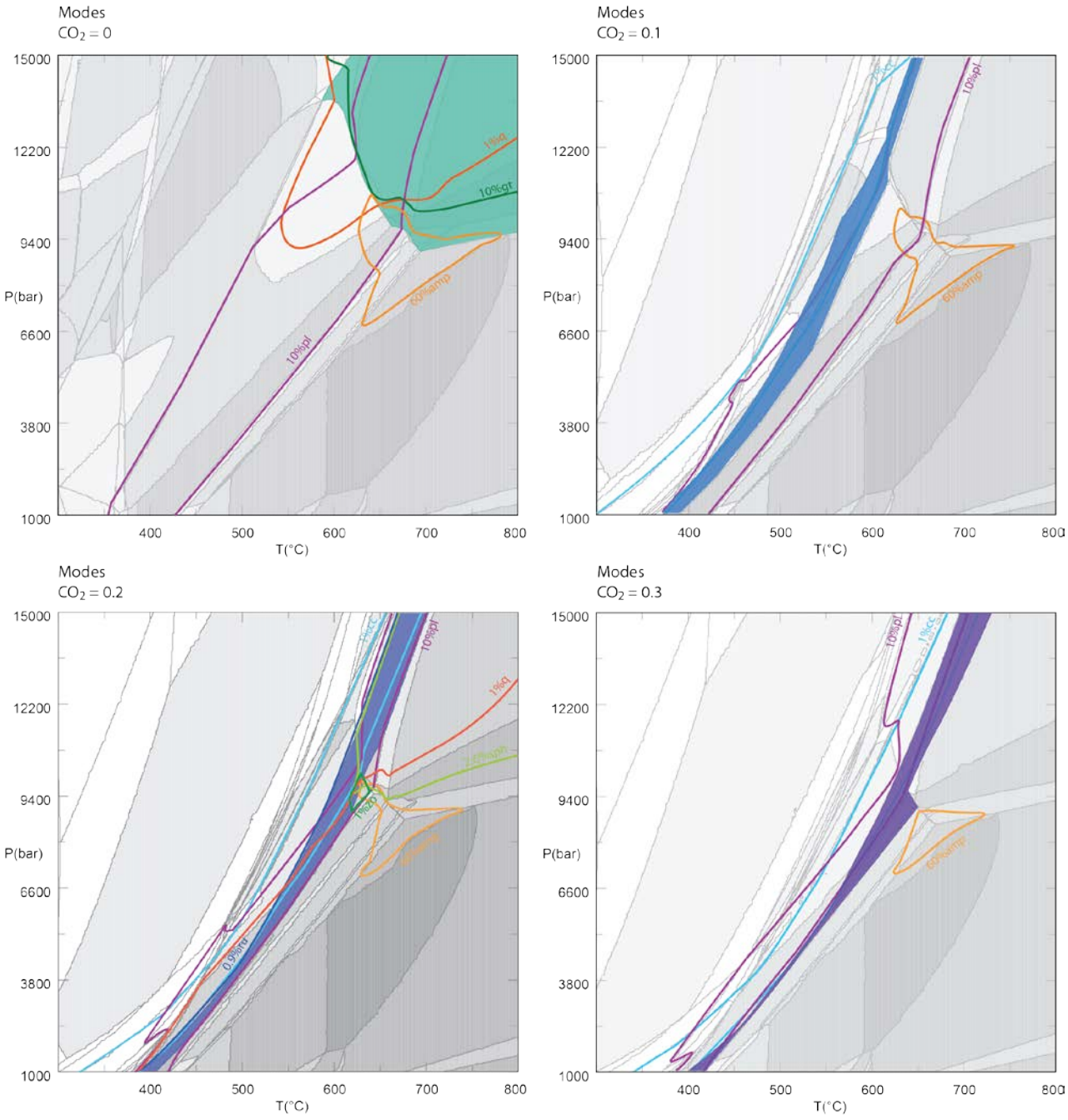

Figure 124. Modal abundance isopleths plotted onto a pseudosection for varying CO_2 concentrations. The best fit of the cluster of isopleths with the stable mineral assemblage of the pertinent minerals in thin section is used for further modelling. See next page for continuation. CO_2 = 0.2 was found the best fit.

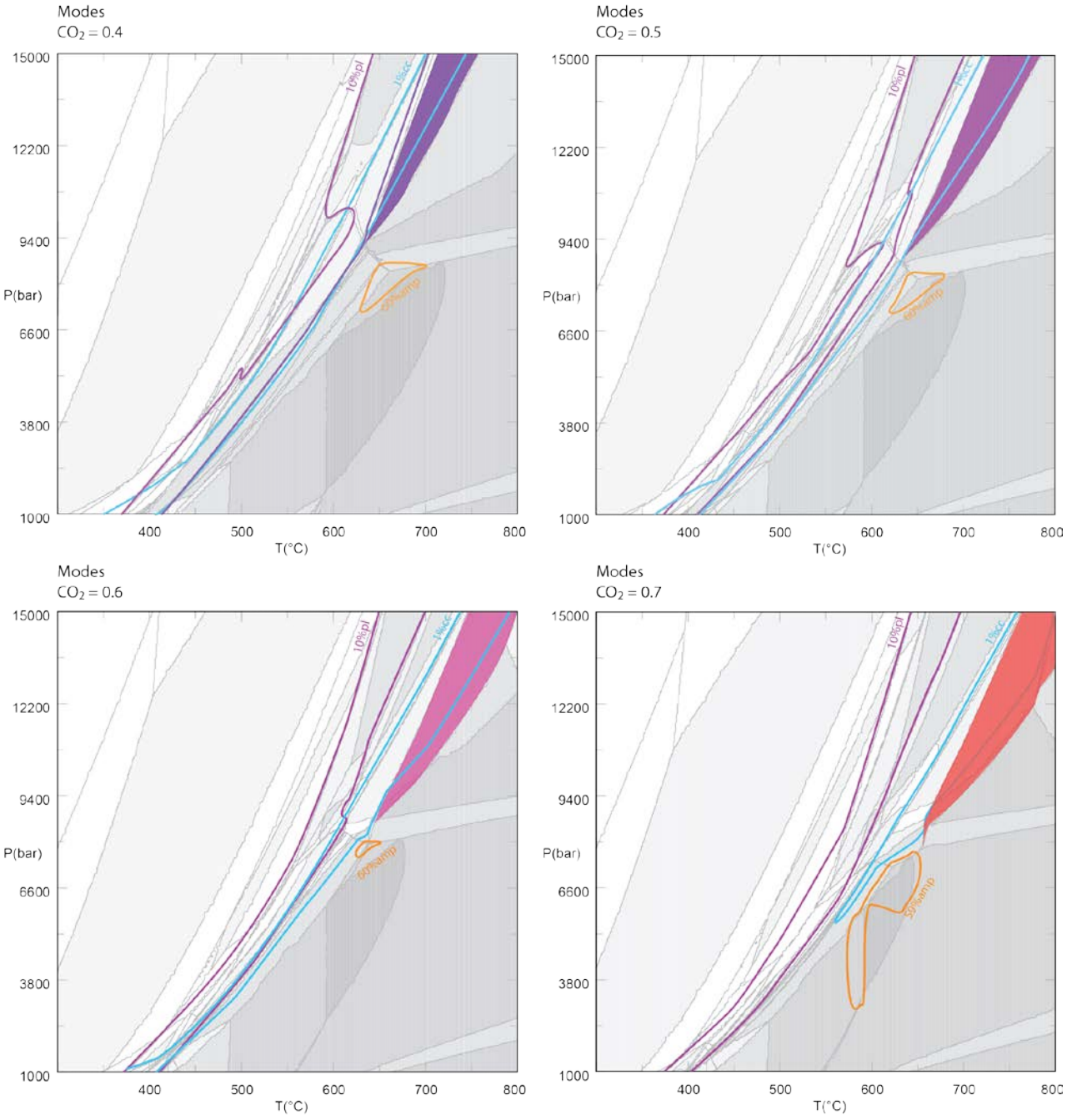

Figure 125. Continuation of Figure 124. Modal abundance isopleths plotted onto a pseudosection for varying CO_2 concentrations. The best fit of the cluster of isopleths with the stable mineral assemblage of the pertinent minerals in thin section is used for further modelling. See next page for continuation. CO_2 = 0.2 was found the best fit.

Isopleths JI 2-1

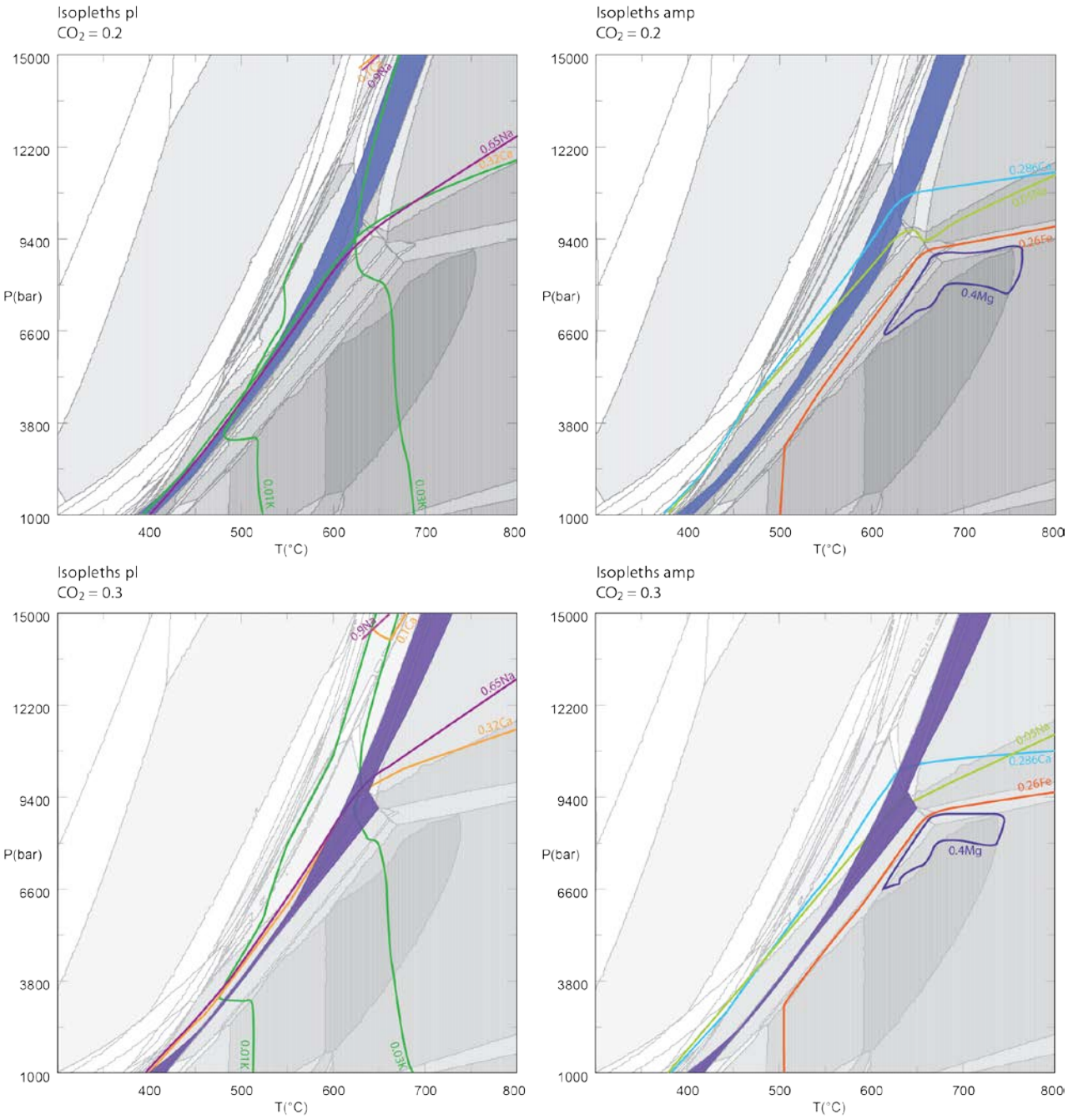

Figure 126. Chemical compositional isopleths of plagioclase and amphibole at varying CO_2 fractions (to be continued in Figure 127 and Figure 128). A best clustered fit of chemistry and the pertinent mineral assemblage in thin section is found for CO_2 = 0.2.

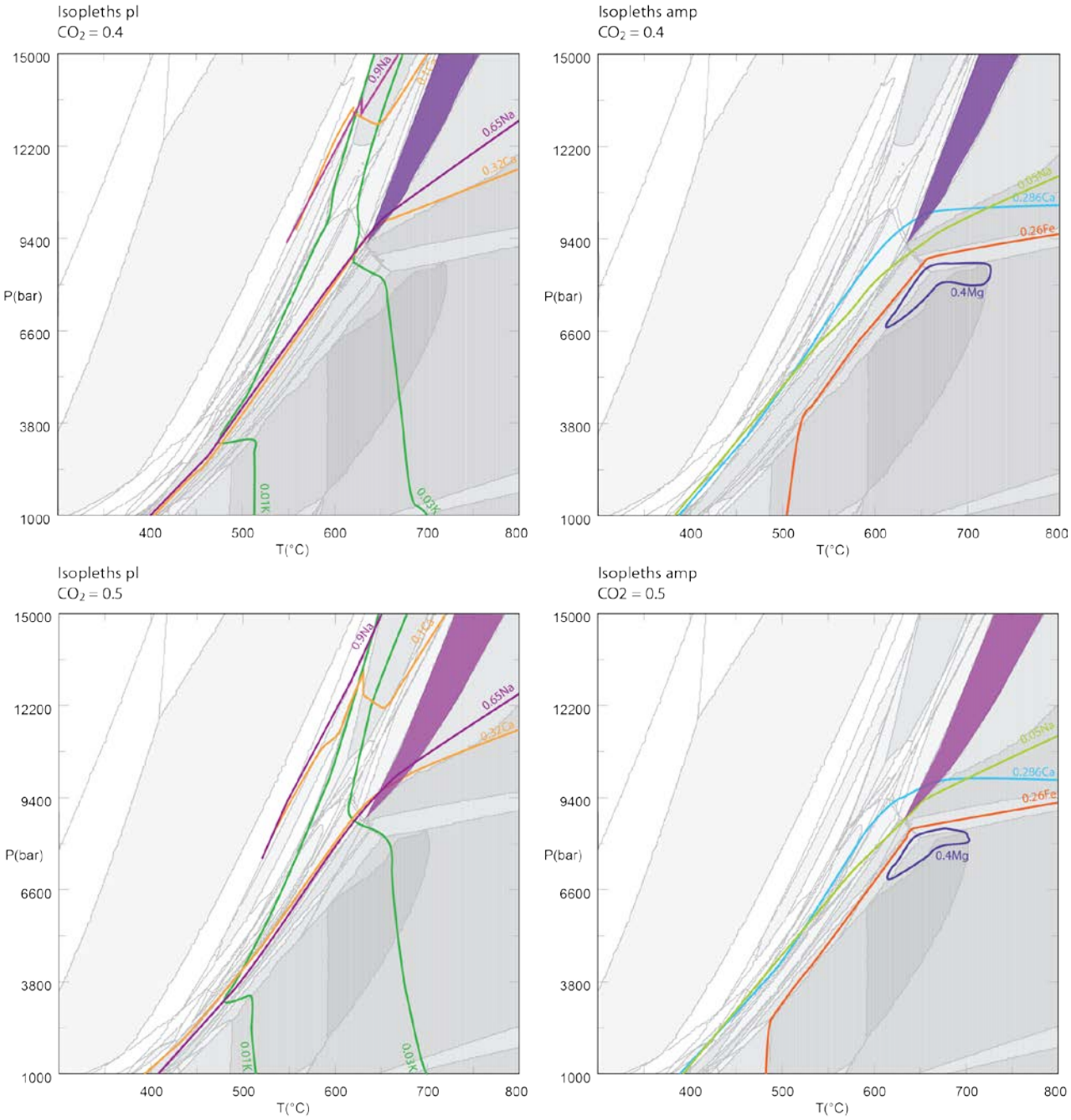

Figure 127. Continuation of chemical compositional isopleths of plagioclase and amphibole at varying CO_2 fractions. A best clustered fit of chemistry and the pertinent mineral assemblage in thin section is found for CO_2 = 0.2.

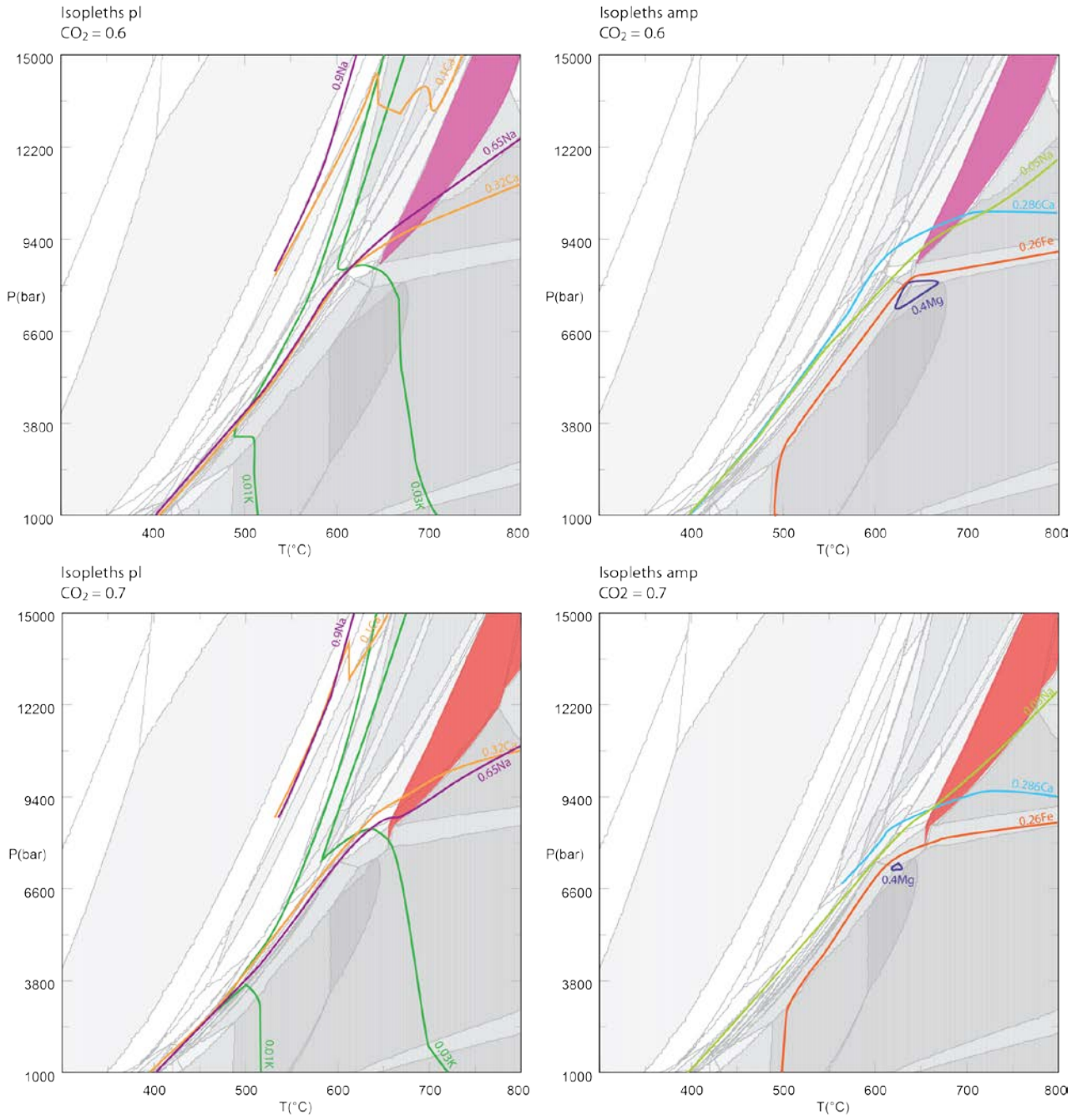

Figure 128. Continuation of chemical compositional isopleths of plagioclase and amphibole at varying CO_2 fractions. A best clustered fit of chemistry and the pertinent mineral assemblage in thin section is found for CO_2 = 0.2.

Modal abundances JI 4-6

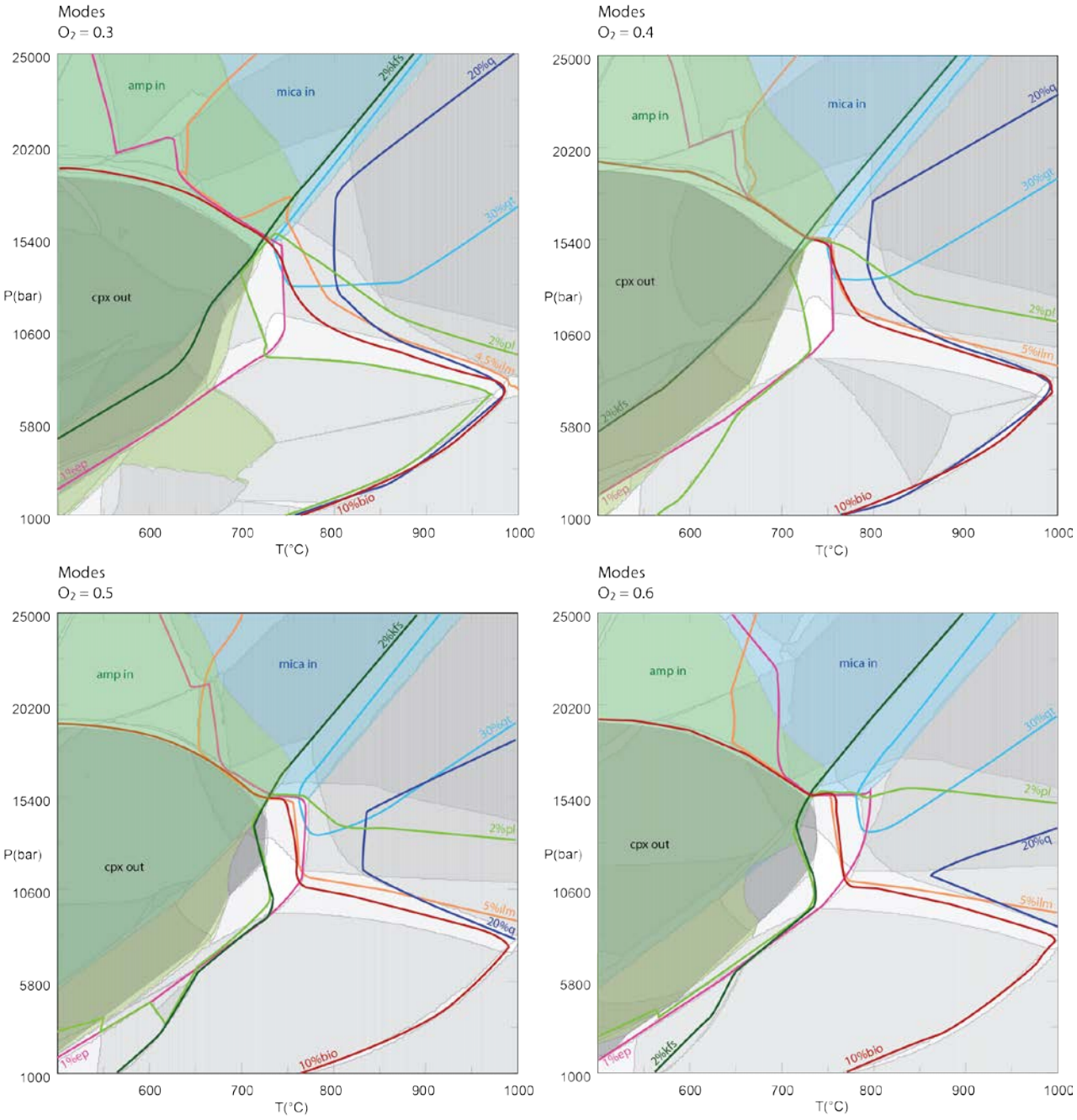

Figure 129. Modal abundance isopleths plotted onto a pseudosection for varying O_2 concentrations. The best fit of the cluster of isopleths with the stable mineral assemblage of the pertinent minerals in thin section is used for further modelling. See next page for continuation. O_2 = 0.4 was found the best fit.

Modal abundance and isopleths JI 4-6

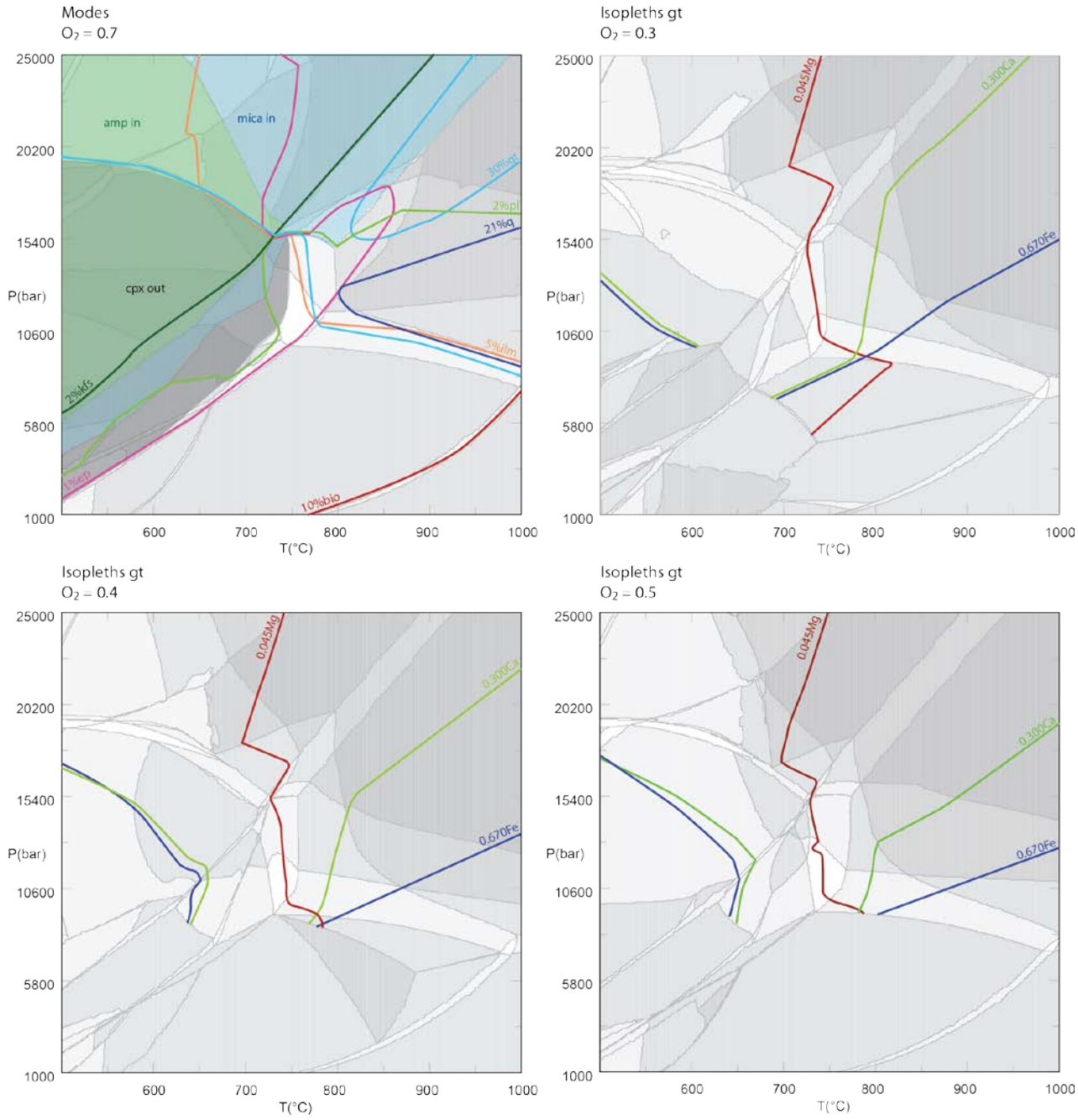

Figure 130. Continuation of modal abundance isopleths plotted onto a pseudosection for varying O_2 concentrations (top left) and chemical compositional isopleths of garnet for varying O_2 concentrations. The best combined fit of the cluster of isopleths with the stable mineral assemblage of the pertinent minerals in thin section and compositional isopleths for garnet is used for further modelling. O_2 = 0.4 was found the best fit.